Advances in
QUANTUM CHEMISTRY

VOLUME **62**

Editors

JOHN R. SABIN
Quantum Theory Project
University of Florida
Gainesville, Florida

ERKKI BRÄNDAS
Department of Quantum Chemistry
Uppsala University
Uppsala, Sweden

ELSEVIER

Amsterdam • Boston • Heidelberg • London • NewYork • Oxford
Paris • SanDiego • SanFrancisco • Singapore • Sydney • Tokyo

Academic Press is an imprint of Elsevier

Academic Press is an imprint of Elsevier
525 B Street, Suite 1900, San Diego, CA 92101-4495, USA
225 Wyman Street, Waltham, MA 02451, USA
32 Jamestown Road, London NW1 7BY, UK

First edition 2011

ISBN: 978-0-12-386477-2
ISSN: 0065-3276

Printed and bounded in USA
11 12 13 10 9 8 7 6 5 4 3 2 1

PREFACE

This volume contains six chapters on various aspects of quantum chemistry, ranging from the mathematical to the biological. We hope that there is something here for many theorists with a wide range of interests.

Recent advances in laser technology have resulted in new phenomena involving radiation-induced interparticle forces being observed such as the cooling, trapping, and manipulating atoms and molecules, and their optical binding is the subject of Chapter 1. The study of the last mentioned of these processes from a theoretical standpoint is the subject of this chapter. This is carried out within the framework of nonrelativistic quantum electrodynamics. Since light modifies the intermolecular potential, a brief summary of the calculation of the retarded van der Waals dispersion energy between a pair of molecules is given. This is followed by the evaluation of the radiation-induced energy shift using two different physical viewpoints and calculational techniques. One involves fourth-order diagrammatic time-dependent perturbation theory, whereas the other entails the coupling of electric dipole moments at each center induced by the externally applied radiation field. Identical results are obtained for interaction energies for two identified mechanisms—dynamic and static. The contribution to the optical binding force arising from coupling of chiral molecules is also derived in order to ascertain whether discriminatory effects occur. This is done via the fluctuating moment method. Applications of the theory are then made to spherical and cylindrical nanoparticles by investigating the topology of the potential energy surface. Regions where forces and torques are maximized, minimized, and vanished are identified, as well as conditions under which particle array formation is favored. The effect of broadband, coherent, or Laguerre–Gaussian radiation, in addition to a second counter-propagating beam, on the energy shift is also examined.

In Chapter 2, the author describes state- and property-specific quantum chemistry including comments on certain aspects of the separation of electron correlation into its dynamical and nondynamical parts. The account contains also a historic appraisal of multiconfigurational schemes comparing Brueckner–Goldstone many-body perturbation theory, MBPT,

to modern-day multireference configuration interaction, MRCI, techniques to computationally powerful methods on the level of complete active space SCF, CASSCF. In particular, very accurate results for atomic, molecular, and metallic Beryllium are presented including both the discrete and the continuous spectrum.

Among the most successful theories of quantum physics are those that have been formulated in terms of propagators. Sequences of propagators, also known as Green's functions, have been used to reformulate many-body problems. Instead of solving the many-body Schrödinger equation, one may introduce a coupling of propagators corresponding to numbers of particles from one to the full, N-particle limit. The electron propagator, also known as the one-electron Green's function, of an N-electron system is a function with poles that correspond to all possible electron binding energies. In molecular calculations subject to the Born–Oppenheimer approximation, these poles are equal to negative vertical detachment energies (VDEs) or negative vertical attachment energies (VAEs). Propagator concepts in molecular electronic structure theory and their applications to large molecules and anions is the subject of Chapter 3.

Chapter 4 presents a review of the exact formulations and evaluations for the rotations of free asymmetric molecules and for treatment of the systems when confined by boundary conditions including elliptical cones. In addition, some tools and advances in development in the theory of angular momentum in bases of spheroconal harmonics are discussed.

The last two chapters in this volume deal with more biologically oriented subjects.

Chapter 5 deals with the effects of energy transfer from swift ion radiation to biomolecules. Such effects are best described by the stopping cross section of the target for the projectile ion. In turn, the mean excitation energy of the target is the determining factor in the stopping cross section. Using polarization propagator methodology, the mean excitation energies of components of several biomolecular systems, ranging from amino acids to nucleotides, are reviewed and reported. The calculated mean excitation energies can then be used to determine the stopping cross sections of various biomolecular systems.

In Chapter 6, the theoretical analysis of the Fast-Padé Transform, FPT, of Chapter 4 (AQC Vol. 61) is applied to a wide class of biomedical time signals. The quantification problem, via FPT, is illustrated on magnetic resonance spectroscopy, MRS, for diagnostic purposes in clinical oncology. A rich background material of benign and malignant cancer samples is discussed and examined, and it is found that FPT resolves and quantifies many overlapping resonances in exceedingly difficult spectra. Validation studies in vitro and in vivo should open up new avenues for early cancer detection without exposing the patient to ionizing radiation.

We offer this volume of *Advances in Quantum Chemistry* to the readers with the belief that it will be both interesting and informative.

John R. Sabin and Erkki Brändas
Editors

CONTRIBUTORS

A. Salam, Department of Chemistry, Wake Forest University, Winston-Salem, NC, USA.

Alexander V. Zakjevskii, Department of Chemistry and Biochemistry, Auburn University, Auburn AL, USA.

Cleanthes A. Nicolaides, Theoretical and Physical Chemistry Institute, Hellenic Research Foundation, Athens, Greece.

Dževad Belkić, Nobel Medical University, Karolinska Institute, Department of Oncology and Pathology, Stockholm, Sweden.

Eugenio Ley-Koo, Instituto de Física, Universidad Nacional Autónoma de México. Apartado Postal, México, D. F., México.

J. V. Ortiz, Department of Chemistry and Biochemistry, Auburn University, Auburn AL, USA.

Jens Oddershede, Department of Physics and Chemistry, University of Southern Denmark, Odense Denmark; Quantum Theory Project, Department of Physics, University of Florida, Gainesville, Florida, USA.

John R. Sabin, Department of Physics and Chemistry, University of Southern Denmark, Odense Denmark; Quantum Theory Project, Department of Physics, University of Florida, Gainesville, Florida, USA.

Karen Belkić, Nobel Medical University, Karolinska Institute, Department of Oncology and Pathology, Stockholm, Sweden; Claremont Graduate University, School of Community and Global Health, Claremont, California, US; University of Southern California, School of Medicine, Institute for Health Promotion and Disease Prevention Research, Los Angeles, California, US.

Olga Dolgounitcheva, Department of Chemistry and Biochemistry, Auburn University, Auburn AL, USA.

Ricardo Méndez-Fragoso, Instituto de Física, Universidad Nacional Autónoma de México. Apartado Postal, México, D. F., México.

Stephan P. A. Sauer, Department of Chemistry, University of Copenhagen, Copenhagen, Denmark.

Viatcheslav G. Zakrzewski, Department of Chemistry and Biochemistry, Auburn University, Auburn AL, USA.

CHAPTER 1

Molecular Quantum Electrodynamics of Radiation-Induced Intermolecular Forces

A. Salam[a]

Contents

Abstract Recent advances in laser technology have resulted in new phenomena involving radiation-induced interparticle forces being observed such as the cooling, trapping and manipulation of atoms and molecules, and their optical binding. The study of the last mentioned of these processes from a theoretical standpoint is the subject of the present article. This is carried out within

[a] Department of Chemistry, Wake Forest University, Winston-Salem, NC, USA
E-mail address: salama@wfu.edu

Advances in Quantum Chemistry, Volume 62
ISSN 0065-3276, DOI: 10.1016/B978-0-12-386477-2.00001-2

the framework of nonrelativistic quantum electrodynamics, whose background is first explicated. Because light modifies the intermolecular potential, a brief summary of the calculation of the retarded van der Waals dispersion energy between a pair of molecules is given. This is followed by the evaluation of the radiation-induced energy shift using two different physical viewpoints and calculational techniques. One involves fourth-order, diagrammatic, time-dependent perturbation theory, whereas the other entails the coupling of electric dipole moments at each center induced by the externally applied radiation field. Identical results are obtained for interaction energies for two identified mechanisms—dynamic and static. The contribution to the optical binding force arising from coupling of chiral molecules is also derived in order to ascertain whether discriminatory effects occur. This is done through the fluctuating moment method. Applications of the theory are then made to spherical and cylindrical nanoparticles by investigating the topology of the potential energy surface. Regions where forces and torques are maximized, minimized, and vanish are identified, as well as conditions under which particle array formation is favored. The effect of broadband, or coherent, or Laguerre–Gaussian radiation, in addition to a second counter-propagating beam, on the energy shift is also examined.

1. INTRODUCTION

A notable success of the theory of quantum electrodynamics (QED) [1] was the calculation of the retarded van der Waals dispersion force between a pair of neutral nonpolar bodies in their ground electronic states [2]. Instead of the usual inverse sixth power law behavior of the energy shift on interparticle separation distance, R, the potential was found to be weaker at long-range by a factor of R^{-1}, displaying an R^{-7} dependence. This modification was rationalized on the basis of the proper allowance being made in the QED formalism of the propagation of electromagnetic signals between two centers at the correct speed of light. This feature arises naturally in the QED theory because the radiation field forms an intrinsic part of the total system dynamics, the entirety of which is subject to quantum mechanical rules, unlike various semiclassical approaches where light is treated classically in contrast to the material system which is described quantum mechanically. Over the years, the formula for the retarded dispersion interaction energy has been rederived using a number of different physical viewpoints and computational methods within the framework of quantum field theory, establishing the veracity of the Casimir–Polder result as well as insight into its origin [3–12].

Other landmark achievements of QED attributable to radiative effects include the explanation and calculation of the anomalous magnetic moment of the electron, and the Lamb shift in atomic hydrogen [1]. In order to treat processes involving the interaction of electromagnetic fields with atoms and molecules, the latter containing bound electrons moving at a small fraction

of the speed of light, a nonrelativistic version of QED in the Coulomb gauge that is termed molecular QED [13–18] has been developed. It has been applied judiciously to a number of problems in theoretical chemistry and chemical physics that require a quantized radiation field approach for a thorough understanding of the process. Some of these include laser-molecule interactions as manifest in single- and multiphoton absorption, emission and scattering of light, optical activity and chiroptical spectroscopies, and nonlinear and quantum optical phenomena, as well as intermolecular interactions such as two-, three- and many-body dispersion forces, the resonant exchange of electronic excitation energy, and chiral discriminatory energy shifts.

A prediction using molecular QED that combined both radiation–molecule and molecule–molecule coupling that showed an especially high degree of foresight was made by Thirunamachandran in 1980 and concerned the change in dispersion interaction energy resulting from the presence of an intense radiation field [19]. Although the effect is small in magnitude—typically being of the order of a few percent of the short-range dispersion force, recent advances in the production of coherent sources of light have led to the phenomenon being studied spectroscopically [20]. Influential in this regard has been the pioneering experimental work of Ashkin [21], involving the trapping and manipulation of particles, to the actual experimental demonstration of optical binding by Burns, Fournier, and Golovchenko [22]. These and subsequent experiments [23–30] have stimulated further theoretical work involving the development of alternate calculational methods and physical viewpoints for the evaluation of the optical binding energy following its initial computation using the fourth-order, time-dependent, diagrammatic perturbation theory technique. Notable among these options has been the induced multipole moment approach in which the applied electromagnetic field induces an electric dipole moment to a first approximation at each molecular center which couple through the resonant dipole–dipole interaction tensor, leading to a straightforward computation of the field-modified interaction energy. Other advances include accounting for additional contributions to the potential when either one or both species are polar, relaxing the electric dipole approximation to account for higher multipole terms—some combinations of which result in the field-modified intermolecular energy depending on the handedness of the interacting species, application to quantum dots, spherical and cylindrical nanoparticles, examining the effect of Laguerre–Gaussian beams and optical vortices, and other forms of structured light, exploring the topology of the generated potential energy landscapes, and investigating the consequences of coherent state and broadband throughput radiation versus the conventional treatment of the process in terms of number states of the field. These aspects will be discussed in this retrospective article, beginning in the following section by a presentation of the characteristic features and key equations of the theory of molecular QED. The treatment given is of sufficient generality to enable its application to any

particular problem in atomic, molecular, and optical physics involving the perturbative coupling of electromagnetic radiation with matter. Before going on in Section 4 to evaluate the optical binding energy, Section 3 contains a brief summary according to molecular QED of the origin and manifestation of the retarded van der Waals dispersion force along with formulae for the Casimir–Polder potential and its near- and far-zone asymptotic limits. This is useful because it is this energy shift that is modified by the presence of an intense beam of electromagnetic radiation, which will be examined in the subsequent section. Hence, in Section 4, the diagrammatic perturbation theory computation of the radiation-induced intermolecular interaction energy between a pair of neutral, ground state polarizable molecules is detailed within the electric dipole approximation, including the contribution arising when either one or both species are polar. Results are obtained for the case in which the propagation direction of the external electric field is held at a fixed orientation relative to the internuclear join, as well as for the freely tumbling situation, for which the so-called static mechanism vanishes. In Section 5, an alternative physical viewpoint and calculational method is outlined in which application of an external field to a polarizable molecule induces multipole moments. These moments associated with different centers couple to each other through resonance. Field-induced energy shifts are then obtained on evaluating expectation values over the ground electronic state of both species with the field described by a high occupation number state. It is shown how identical results are derived for interaction energies to those obtained by using time-dependent, perturbation theory techniques. In Section 6, the electric dipole approximation is relaxed, and the discriminatory radiation-modified energy shifts are computed by including magnetic dipole interaction terms and extracting contributions proportional to the handedness of each optical isomer. The general form of the results obtained is then applied to different types of optically bound particles in Section 7, along with consideration of different forms of applied electromagnetic radiation, and their subsequent influence in further affecting the induced energy shift is studied. A short summary is then given in Section 8.

2. THEORY OF MOLECULAR QED

The key feature of the theory of QED—whether it is cast in nonrelativistic or fully covariant forms is that the electromagnetic field obeys quantum mechanical laws. A frequent first step in the construction of either version of the theory is the writing of the classical Lagrangian function for the interaction of a charged particle with a radiation field. For a particle of mass m, electronic charge $-e$, located at position vector $\vec{q}$, and moving with velocity $|\mathrm{d}\vec{q}/\mathrm{d}t| \ll c$ in a position-dependent potential $V(\vec{q})$ subject to electromagnetic radiation described by scalar and vector potentials $\varphi(\vec{r})$ and $\vec{a}(\vec{r})$, at field point

$\vec{r}$ in the Coulomb gauge (div $\vec{a}(\vec{r}) = 0$), a suitable Lagrangian is given by

$$L = \frac{1}{2}m\dot{\vec{q}}^2 - V(\vec{q}) + \frac{1}{2}\varepsilon_0 \int \left\{\dot{\vec{a}}^2(\vec{r}) - c^2(\mathrm{curl}\,\vec{a}(\vec{r}))^2\right\}\mathrm{d}^3\vec{r} + \int \vec{j}^{\perp}(\vec{r}) \cdot \vec{a}(\vec{r})\mathrm{d}^3\vec{r}, \quad (1)$$

where $\vec{j}^{\perp}(\vec{r})$ is the transverse component of the current density $\vec{j}(\vec{r}) = -e\dot{\vec{q}}\delta(\vec{r} - \vec{q})$ on extracting the perpendicular component with use of the transverse delta function dyadic $\delta^{\perp}_{ij}(\vec{r})$. Latin subscripts designate Cartesian tensor components with an implied summation convention being adopted for indices that repeat. Easily identifiable from expression (1) is the decomposition of the Lagrangian into a sum of particle, field, and interaction terms. It is evident that the radiation field is included at the outset. Beginning with (1), it is straightforward to obtain a quantum mechanical Hamiltonian operator describing the total radiation-field matter system on carrying out the well-known canonical quantization procedure [31]. First, a classical Hamiltonian function is derived from (1) through

$$H = \vec{p} \cdot \dot{\vec{q}} + \int \vec{\Pi}(\vec{r}) \cdot \dot{\vec{a}}(\vec{r})\mathrm{d}^3\vec{r} - L, \quad (2)$$

by eliminating the particle and field velocities in favor of the corresponding momenta. In formula (2), $\vec{p} = \partial L/\partial\dot{\vec{q}}$ is the canonically conjugate particle momentum, $\vec{\Pi}(\vec{r}) = \partial\mathcal{L}/\partial\dot{\vec{a}}$ is the analogous quantity for the electromagnetic field, with $\mathcal{L}$ being the Lagrangian density for the radiation, defined as $\mathcal{L} = \frac{1}{2}\varepsilon_0\{\dot{\vec{a}}^2(\vec{r}) - c^2(\mathrm{curl}\,\vec{a}(\vec{r}))^2\}$, and $L_{\mathrm{rad}} = \int\mathcal{L}\mathrm{d}^3\vec{r}$. Elevating the canonically conjugate dynamical variables to quantum mechanical operators produces a quantum mechanical Hamiltonian function for the coupling of the charged particle to the electromagnetic field. Extension to include many particles, which may be grouped into aggregates, results in a quantum many-body Hamiltonian. The operators satisfy the equal-time commutation relations

$$[q_{i(\alpha)}(\zeta), p_{j(\beta)}(\xi)] = i\hbar\,\delta_{ij}\delta_{\alpha\beta}\delta_{\zeta\xi}, \quad (3)$$

for two charged particles α and β associated with entities ζ and ξ, and

$$[a_i(\vec{r}), \Pi_j(\vec{r}')] = i\hbar\,\delta^{\perp}_{ij}(\vec{r} - \vec{r}'), \quad (4)$$

for the field variables. It should be remarked that the choice of Lagrangian should lead to the correct equations of motion. In the case of Eq. (1), insertion into the Euler–Lagrange equations yield Newton's equations of motion with an added Lorentz force law term for the coupling of charged particles to the radiation field, and Maxwell–Lorentz equations. The resulting Hamiltonian is often called the *minimal-coupling* Hamiltonian as Hamilton's equations of

motion are obtained by variationally minimizing the Lagrangian (1). Details may be found in a number of texts dealing with the foundations of molecular QED [13–18]. The terms that represent coupling of radiation and matter in this formulation are

$$H_{\text{int}}^{\text{min}}(\zeta,\xi) = \frac{e}{m}\sum_{\alpha}\vec{p}_{\alpha}(\xi)\cdot\vec{a}(\vec{q}_{\alpha}(\xi)) + \frac{e^2}{2m}\sum_{\alpha}\vec{a}^2(\vec{q}_{\alpha}(\xi)) + V_{\text{inter}}(\zeta,\xi), \quad (5)$$

where $V_{\text{inter}}(\zeta,\xi)$ is a two-center intermolecular potential energy contribution. Although quantum mechanical probability amplitudes for any molecule–field or molecule–molecule process can be computed using the minimal-coupling interaction Hamiltonian (5), the ensuing calculation is frequently lengthy and complicated. This is because of the appearance of momentum and vector potential operators instead of other more chemically insightful atomic and molecular properties, and lack of explicit presence of electromagnetic field operators, as well as the need to account for interparticle coupling terms when examining processes involving two or more bodies.

An alternative coupling scheme, that proves to be advantageous in many regards, and is now the preferred theoretical method, is the multipolar framework [32, 33] of molecular QED. In this formulation, molecules couple directly to the radiation fields through their molecular multipole moments. Because the Maxwell fields obey Einstein causality, interactions between species is properly retarded, which is mediated by the emission and absorption of transverse photons. It is convenient to partition the total many-body QED matter-field multipolar Hamiltonian into a sum of particle, radiation field, and interaction terms as follows:

$$H^{\text{mult}} = \sum_{\xi} H_{\text{part}}(\xi) + H_{\text{rad}} + \sum_{\xi} H_{\text{int}}^{\text{mult}}(\xi). \quad (6)$$

The first term is the standard molecular Hamiltonian within the Born–Oppenheimer approximation

$$H_{\text{part}}(\xi) = \sum_{\alpha}\frac{\vec{p}_{\alpha}^2(\xi)}{2m} + V(\xi), \quad (7)$$

with $V(\xi)$ being the intramolecular potential energy operator. In the absence of matter, the electromagnetic field propagates in free space. Application of the variational calculus to the Lagrangian density $\mathcal{L}$ given earlier in this section leads to the source-free Maxwell equations as the correct equations of motion with the vector potential $\vec{a}(\vec{r})$, serving as the generalized coordinate. Evaluating the canonical momentum in the usual way, the Hamiltonian density for the free radiation field is readily arrived at, and is seen to be

identical to the electromagnetic energy density. Because in a fixed volume V, the equations for the modes of the radiation field are formally isomorphic with those of a set of independent harmonic oscillators, quantization of the electromagnetic field in vacuo is immediate. This is most easily achieved in the second quantized representation by introducing two mutually adjoint mode annihilation and creation operators $a^{(\lambda)}(\vec{k})$ and $a^{\dagger(\lambda)}(\vec{k})$, which respectively reduce and increase the number of quantized particles associated with the electromagnetic field—the photons with index of polarization λ, propagation direction $\vec{k}$, and circular frequency $\omega = ck$. Hence, the quantum mechanical Hamiltonian operator for the radiation field is written as

$$H_{\text{rad}} = \sum_{\vec{k},\lambda} \left[a^{\dagger(\lambda)}(\vec{k}) a^{(\lambda)}(\vec{k}) + \frac{1}{2} \right] \hbar\omega, \tag{8}$$

having familiar eigenvalue spectrum $\left(n + \frac{1}{2}\right)\hbar\omega$, where n are nonnegative integers,

$$a^{\dagger(\lambda)}(\vec{k}) a^{(\lambda)}(\vec{k}) |n(\vec{k},\lambda)\rangle = n|n(\vec{k},\lambda)\rangle, \quad n = 0, 1, 2, \ldots \tag{9}$$

The raising and lowering operators act on the normalized number state of the radiation field $|n(\vec{k},\lambda)\rangle$ according to

$$a^{\dagger(\lambda)}(\vec{k})|n(\vec{k},\lambda)\rangle = (n+1)^{\frac{1}{2}}|(n+1)(\vec{k},\lambda)\rangle, \quad n = 0, 1, 2, \ldots, \tag{10}$$

and

$$a^{(\lambda)}(\vec{k})|n(\vec{k},\lambda)\rangle = \begin{cases} 0, & n = 0 \\ n^{\frac{1}{2}}|(n-1)(\vec{k},\lambda)\rangle, & n = 1, 2, \ldots, \end{cases} \tag{11}$$

and obey the commutator

$$[a^{(\lambda)}(\vec{k}), a^{\dagger(\lambda')}(\vec{k}')] = \delta_{\lambda\lambda'}\delta_{\vec{k}\vec{k}'}, \tag{12}$$

all other combinations vanishing.

Alternatively, the Hamiltonian for the radiation field in multipolar formalism may be written explicitly in terms of the Maxwell field operators. From the second term of Eq. (2), the Hamiltonian density for the electromagnetic field is

$$\mathcal{H} = \frac{1}{2}\left\{ \vec{\Pi}^2(\vec{r})/\varepsilon_0 + \varepsilon_0^2 c^2 (\text{curl}\, \vec{a}(\vec{r}))^2 \right\} = \frac{1}{2\varepsilon_0}\left\{ \vec{d}^{\perp 2}(\vec{r}) + \varepsilon_0^2 c^2 \vec{b}^2(\vec{r}) \right\}, \tag{13}$$

on using the relation $\vec{b}(\vec{r}) = \text{curl}\,\vec{a}(\vec{r})$, and the field canonical momentum in multipolar coupling

$$\vec{\Pi}(\vec{r}) = \frac{\partial \mathcal{L}}{\partial \dot{\vec{a}}(\vec{r})} = -\vec{d}^{\perp}(\vec{r}), \tag{14}$$

where $\vec{d}^{\perp}(\vec{r}) = \varepsilon_0 \vec{e}^{\perp}(\vec{r}) + \vec{p}^{\perp}(\vec{r})$ is the transverse electric displacement field operator and $\vec{p}\perp(\vec{r})$ is the transverse electric polarization field. It is noteworthy that in the multipolar framework, the canonically conjugate field momentum is equal to the negative electric displacement field, while in the minimal-coupling, $\vec{\Pi}(\vec{r}) = -\varepsilon_0 \vec{e}^{\perp}(\vec{r})$. Hence, $\vec{d}^{\perp}(\vec{r})$ appears explicitly in the multipolar version of the theory. It includes the effects of bound charges and currents comprising the material system. Atoms and molecules, therefore, couple directly to the displacement and magnetic fields through their multipole moment distributions.

Fourier series mode expansions for the multipolar electric displacement and magnetic field operators may be written in terms of the creation and destruction operators as

$$\vec{d}^{\perp}(\vec{r}) = i \sum_{\vec{k},\lambda} \left(\frac{\hbar c k \varepsilon_0}{2V} \right)^{1/2} \left[\vec{e}^{(\lambda)}(\vec{k}) a^{(\lambda)}(\vec{k}) e^{i\vec{k}\cdot\vec{r}} - \bar{\vec{e}}^{(\lambda)}(\vec{k}) a^{\dagger(\lambda)}(\vec{k}) e^{-i\vec{k}\cdot\vec{r}} \right], \tag{15}$$

and

$$\vec{b}(\vec{r}) = i \sum_{\vec{k},\lambda} \left(\frac{\hbar k}{2\varepsilon_0 c V} \right)^{1/2} \left[\vec{b}^{(\lambda)}(\vec{k}) a^{(\lambda)}(\vec{k}) e^{i\vec{k}\cdot\vec{r}} - \bar{\vec{b}}^{(\lambda)}(\vec{k}) a^{\dagger(\lambda)}(\vec{k}) e^{-i\vec{k}\cdot\vec{r}} \right], \tag{16}$$

respectively, where $\vec{e}^{(\lambda)}(\vec{k})$ is a complex unit electric polarization vector, $\vec{b}^{(\lambda)}(\vec{k}) = \hat{k} \times \vec{e}^{(\lambda)}(\vec{k})$ is its magnetic analog, and V is the volume of the quantization box.

The third and final term of the total multipolar Hamiltonian (6) is the interaction Hamiltonian. Excluding the transverse polarization term [17], which is important only when considering self-energy corrections, the coupling Hamiltonian is

$$\begin{aligned} H_{\text{int}}^{\text{mult}}(\xi) = &-\varepsilon_0^{-1} \vec{\mu}(\xi) \cdot \vec{d}^{\perp}(\vec{R}_\xi) - \varepsilon_0^{-1} Q_{ij}(\xi) \nabla_j d_i^{\perp}(\vec{R}_\xi) + \cdots - \vec{m}(\xi) \cdot \vec{b}(\vec{R}_\xi) \\ &+ \cdots + \frac{e^2}{8m} \{ \vec{q}(\xi) \times \vec{b}(\vec{R}_\xi) \}^2 + \cdots \end{aligned} \tag{17}$$

and is seen to be a sum of electric, magnetic, and diamagnetic interaction terms, each of which is expanded as an infinite series of multipole moment

distributions, with for example, $\vec{\mu}(\xi)$ is the electric dipole moment operator, $Q_{ij}(\xi)$ is the electric quadrupole moment tensor, $\vec{m}(\xi)$ is the magnetic dipole moment operator, and the last term written explicitly in the expression above is the leading order diamagnetic interaction term, of species ξ located at position vector $\vec{R}_\xi$. Absent from Eq. (17) relative to the minimal-coupling interaction Hamiltonian (5) is the intermolecular coupling V_{inter} because in the multipolar scheme, molecules directly interact with electromagnetic fields through their multipole moments. For the majority of applications, retaining the first perturbation term, namely the electric dipole contribution, is often sufficient as it is the largest in magnitude. The next two multipole moments written in Eq. (17) are both a factor of the fine structure constant smaller than $\vec{\mu}(\xi)$ and are commonly disregarded. They must be included when the molecular species belongs to a point group containing low elements of symmetry. Spectroscopic selection rules are then less restrictive and contributions to optical transitions from higher multipole terms come into play. This is the case with chiral molecules, which undergo a wide range of chiroptical processes such as optical rotation and circular dichroism, which manifest in terms of interference of electric dipole with magnetic dipole and electric quadrupole contributions. Discriminatory effects in radiation-induced interparticle forces will be explored in Section 6.

Earlier in this section it was commented on how the minimal-coupling QED Hamiltonian is obtained from the classical Lagrangian function. A few words are in order regarding the derivation of the multipolar Hamiltonian (6). One method involves the application of a canonical transformation to the minimal-coupling Hamiltonian [32]. In classical mechanics, such a transformation renders the Poisson bracket and Hamilton's canonical equations of motion invariant. In quantum mechanics, a canonical transformation preserves both the commutator and Heisenberg's operator equation of motion. The appropriate generating function that converts $H_{\text{min}} \rightarrow H_{\text{mult}}$ is proportional to $\int \vec{p}^{\perp}(\vec{r}) \cdot \vec{a}(\vec{r}) \mathrm{d}^3\vec{r}$ [32, 34]. Because the quantities appearing in the generator are functions only of the generalized coordinates, these remain unchanged, with only the canonically conjugate momenta being transformed. A second method involves the addition of the time derivative of a function of $\vec{q}$ and $\vec{a}(\vec{r})$ only to the classical (or quantum) minimal-coupling Lagrangian (1) [35]. Such an addition produces an equivalent Lagrangian that satisfies identical Euler–Lagrange equations of motion. If the added function is proportional to the generator mentioned above, the multipolar Lagrangian results. From this new Lagrangian, the multipolar QED Hamiltonian follows on promotion of dynamical variables to quantum operators. A third method involves effecting a gauge transformation on the minimal-coupling Lagrangian. If the gauge function is a prescribed function of the generalized coordinates of the system, equivalent Lagrangians ensue. If the gauge function is taken to be a line integral of the Coulomb gauge

vector potential, and the Coulomb energy is added and subtracted to $L_{\min}$, L_{mult} results after a gauge transformation. Further details may be found in Chapter 7 Section 3 of Ref. [14] and in Ref. [36].

The form of H_{mult} having been obtained, it now remains to discuss how to solve the subsequent eigenvalue equation. For radiation-matter coupling that is small relative to intramolecular Coulomb potential energies, the interaction Hamiltonian may be considered as a perturbation on the particle-field system. A perturbation theory solution is then the most obvious choice. The first two terms of Eq. (6) are taken to constitute the unperturbed Hamiltonian H_0, so that

$$H_{\text{mult}} = H_0 + H_{\text{int}}, \tag{18}$$

with

$$H_0 = H_{\text{part}} + H_{\text{rad}}. \tag{19}$$

When particles and radiation do not interact, H_0 is separable, yielding product eigenfunctions of particle and electromagnetic field and total energy that is a sum of the eigenenergies of the two subsystems. The wavefunctions and energies associated with matter are taken to be known, the former represented by appropriate quantum numbers that serve to label the state vector, with a species in quantized level m having state designation $|m\rangle$, with energy eigenvalue E_m, namely $H_{\text{part}}|m\rangle = E_m|m\rangle$. States of the radiation field are given by the occupation number representation outlined earlier, with typically only nonzero states of the electromagnetic field being specified. Hence for the number state $|n(\vec{k},\lambda)\rangle$, $H_{\text{rad}}|n(\vec{k},\lambda)\rangle = n|n(\vec{k},\lambda)\rangle$. Thus, the base states used in the perturbation theory solution are the product states

$$|\text{part; rad}\rangle = |\text{part}\rangle|\text{rad}\rangle = |E_m\rangle|n(\vec{k},\lambda)\rangle = |E_m; n(\vec{k},\lambda)\rangle. \tag{20}$$

Standard application of time-dependent perturbation theory yields a series expansion in powers of the perturbation H_{int} of the probability amplitude for a transition from the initial state of the system to the final state under the influence of H_{int},

$$M_{fi} = \langle f|H_{\text{int}}|i\rangle + \sum_I \frac{\langle f|H_{\text{int}}|I\rangle\langle I|H_{\text{int}}|i\rangle}{E_{Ii}} + \cdots, \tag{21}$$

where the sum is executed over a complete set of intermediate states $|I\rangle$ that connect $|i\rangle$ to $|f\rangle$, with $E_{Ii} = E_I - E_i$ the difference in energy between system states $|I\rangle$ and $|i\rangle$. Energy shifts are readily computed using formula

(21) as now $|f\rangle = |i\rangle$. In addition, expression (21) may be used to evaluate spectroscopic transition rates through the Fermi golden rule

$$\Gamma = \frac{2\pi\rho}{\hbar}|M_{fi}|^2, \tag{22}$$

where ρ is the density of final states.

In this section, the basic working equations of molecular QED have been given which enable the perturbative solution to be obtained for the quantum mechanical observable quantity for any spectroscopic or intermolecular process. Before going on to apply the formalism presented to the computation of the optical binding energy in Section 4, the QED calculation of the retarded dispersion potential is briefly discussed in the following section.

3. van der WAALS DISPERSION FORCE

A fundamental interaction between neutral nonpolar atoms and molecules, and one that is also everpresent, is the van der Waals dispersion force [37]. This is a purely quantum mechanical phenomenon commonly understood as arising from the coupling of fluctuations in the electronic charge distribution associated with the centers of material particles. In early quantum chemical calculations of the potential between two species in their electronic ground states, the electric dipole approximation was invoked on expanding the charge density in an electric multipole series, along with the assumption that the interaction between any two sites is instantaneous in its manifestation. This led to the well-known London dispersion energy, whose formula is given by [38]

$$\Delta E = -\frac{1}{24\pi^2\varepsilon_0^2 R^6}\sum_{r,s}\frac{|\vec{\mu}^{r0}(\mathrm{A})|^2|\vec{\mu}^{0s}(\mathrm{B})|^2}{E_{r0}^{\mathrm{A}}+E_{s0}^{\mathrm{B}}}, \tag{23}$$

exhibiting familiar inverse sixth power dependence on relative separation distance between the two centers A and B, $\vec{R} = \vec{R}_{\mathrm{B}} - \vec{R}_{\mathrm{A}}$. In the result (23), $\vec{\mu}^{0t}(\xi) = \langle 0^{\xi}|\vec{\mu}(\xi)|t^{\xi}\rangle$ is the transition electric dipole moment of species $\xi = \mathrm{A}$, B between ground and excited electronic states $|0^{\xi}\rangle$ and $|t^{\xi}\rangle$, respectively, with energy difference $E_{t0}^{\xi} = E_t^{\xi} - E_0^{\xi} = \hbar\omega_{t0}$ expressed in terms of the energy eigenvalues of the relevant state vectors, and ω_{t0}^{ξ} is the circular transition frequency. The summation is executed over a complete set of eigenstates of A and B, $|r^{\mathrm{A}}\rangle$ and $|s^{\mathrm{B}}\rangle$, respectively, excluding the electronic ground state. The result (23) applies to randomly oriented bodies for all separation distances beyond the wavefunction overlap.

It was soon realized that the energy shift (23) is unphysical, and that the correct expression for the dispersion force must properly account for the effects due to the finite speed of propagation of light signals, by which the interaction is mediated. That this must be so is clearly understood on the grounds that the distortion resulting from the quantum mechanical behavior of electrons comprising the charge and current densities give rise to microscopic Maxwell fields that are strictly causal, irrespective of their multipole order. With considerable advances having been made in the theory of QED in both its nonrelativistic version immediately after the development of quantum mechanics in the 1920s [31, 39], and the fully covariant formulation in the early 1950s, thereby enabling the quantum theory of electron–photon coupling to rest on solid theoretical foundations, ensured that field theoretic calculations of interparticle interactions could then be carried out with greater confidence and accuracy. Casimir and Polder first tackled the application of this method to the problem of the van der Waals dispersion potential in a pioneering computation in 1948 [2]. Their calculation involved the use of the minimal-coupling Hamiltonian and accounted for all contributions arising in second-, third-, and fourth-order perturbation theory [13].

Including retardation effects resulted in the dispersion potential at large internuclear separations possessing the functional form

$$\Delta E = -\frac{23\hbar c\alpha(\mathrm{A};0)\alpha(\mathrm{B};0)}{64\pi^3\varepsilon_0^2 R^7}, \tag{24}$$

displaying an inverse seventh power distance dependence, with $\alpha(\xi;0)$ the static isotropic electric dipole polarizability of entity $\xi = \mathrm{A}, \mathrm{B}$ given by

$$\alpha(\xi;0) = \frac{2}{3}\sum_t \frac{|\vec{\mu}^{0t}(\xi)|^2}{E_{t0}^{\xi}}. \tag{25}$$

The delay in the traversal of electromagnetic influences between interacting species and the ensuing loss of orientational correlation in the respective dipolar charge distributions results in a weakening of the energy shift (24) relative to its static counterpart (23). In fact, Casimir and Polder were able to derive an expression for the dispersion potential valid for all distances outside the region of overlapping charge clouds. Their eponymous formula is

$$\Delta E = -\frac{\hbar c}{16\pi^3\varepsilon_0^2 R^2}\int_0^\infty du u^4 e^{-2uR}\alpha(\mathrm{A};iu)\alpha(\mathrm{B};iu) \times\left[1+\frac{2}{uR}+\frac{5}{u^2R^2}+\frac{6}{u^3R^3}+\frac{3}{u^4R^4}\right], \tag{26}$$

where $\alpha(\xi; iu)$ is the isotropic polarizability evaluated at the imaginary wavevector $k = iu$,

$$\alpha(\xi; iu) = \frac{2}{3} \sum_t \frac{|\vec{\mu}^{0t}(\xi)|^2 E_{t0}^{\xi}}{(E_{t0}^{\xi})^2 + (\hbar cu)^2}. \tag{27}$$

Although it is perfectly legitimate to use the minimal-coupling form of interaction Hamiltonian in application of QED formalism calculations, the ensuing complexity and lengthy nature of the computations commonly prohibits its use in a wide range of problems, especially those concerning intermolecular processes. Alternative coupling schemes have therefore been sought, in particular, to avoid the occurrence of static multipole interaction terms that are present in the minimal-coupling framework. By far the most successful of these competing approaches is the multipolar formalism of QED [32, 33]. Atoms and molecules couple directly to second-quantized electric displacement and magnetic field operators through their electric, magnetic, and diamagnetic multipole moments. The Casimir–Polder potential (26) is now well understood as arising from two-virtual photon exchange between a pair of ground state polarizable atoms or molecules and derived using fourth-order diagrammatic time-dependent perturbation theory [13, 17, 18, 40]. Because the dispersion energy shift is evaluated by taking the expectation value of the matter-field coupling over both species in the electronic ground state, and the electromagnetic field containing no photons, the potential provides a classic example of an observable phenomenon attributable to the effect of fluctuations of the vacuum radiation field [15]. Others include spontaneous emission rates when excited species undergo decay, and the Lamb shift [13, 17].

4. OPTICAL BINDING ENERGY: PERTURBATION THEORY CALCULATION

In the previous section, an expression for the energy shift between a pair of neutral, polarizable molecules was obtained. Both species were in their electronic ground states, and the electromagnetic field contained no photons—being in the vacuum state. The resulting potential is the van der Waals dispersion energy. In this section, the effect of an incident beam of laser light in modifying the pair interaction energy is presented.

Cooling and trapping of a single particle by optical means is now commonplace [20–22]. Microscopic entities undergo radiative attraction to the focal area of the high-intensity radiation field, with control and manipulation now also being possible. Introducing two or more bodies complicates the picture as now interparticle couplings have to be accounted for, as well

as those forces induced by the external electromagnetic source. The theory of molecular QED outlined in Section 2 is readily applicable to the study of optomechanical forces and torques.

Consider two interacting molecules A and B that are both in the electronic ground state, located at $\vec{R}_{\rm A}$ and $\vec{R}_{\rm B}$, respectively, and separated by a distance $\vec{R} = \vec{R}_{\rm B} - \vec{R}_{\rm A}$.They are subject to an intense beam of electromagnetic radiation. Each species will individually undergo a dynamic Stark shift, but as this is independent of R, it is ignored. To begin the calculation of the radiation-induced energy shift, the total Hamiltonian for the system comprising of A and B, the radiation field and their mutual interaction is written as

$$H = H_{\rm part}({\rm A}) + H_{\rm part}({\rm B}) + H_{\rm rad} - \varepsilon_0^{-1}\vec{\mu}({\rm A})\cdot\vec{d}^{\perp}(\vec{R}_{\rm A}) - \varepsilon_0^{-1}\vec{\mu}({\rm B})\cdot\vec{d}^{\perp}(\vec{R}_{\rm B}), \quad (28)$$

on using Eq. (6), with the electric dipole approximation being made to leading order for the coupling Hamiltonian (17). The modification of the dispersion force by external radiation may be interpreted as because of scattering of a real photon from the laser by the two particles, which are themselves coupled through the transfer of a single virtual photon. Distinguishing between the two types of photons is largely semantic in that real photons are detected, while virtual ones are not, being emitted and absorbed on so short a timescale that detection is not possible, although ultimately all photons are emitted and eventually absorbed. From the statement of the problem, it is a simple matter to write down the initial and final states of the system. If the electromagnetic field contains N photons of mode $(\vec{k},\lambda)$, with virtual photons designated by the mode label $(\vec{p},\varepsilon)$, and A and B in the ground state $|0^{\xi}\rangle$, then both states are seen to be equivalent and are given by

$$|i\rangle = |f\rangle = |0^{\rm A}, 0^{\rm B}; N(\vec{k},\lambda), 0(\vec{p},\varepsilon)\rangle. \quad (29)$$

At this level of theory, the change in interaction energy is calculated using the fourth-order, time-dependent perturbation theory because overall the process is a four-photon one, in which two photons are absorbed and two are emitted. It is given by the following formula:

$$\Delta E = -\sum_{I,II,III} \frac{\langle f|H_{\rm int}|III\rangle\langle III|H_{\rm int}|II\rangle\langle II|H_{\rm int}|I\rangle\langle I|H_{\rm int}|i\rangle}{E_{IIIi}E_{IIi}E_{Ii}}. \quad (30)$$

At this stage, it is convenient to distinguish between the photon creation and destruction events occurring at each center. The first case to be considered is when absorption and emission of the real photon occurs at different sites. In the second situation, scattering of a real photon takes place at the same

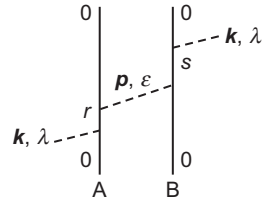

Figure 1.1 One of 48 time-orderings contributing to radiation-induced energy shift with scattering taking place at different centers.

species, either A or B. In both cases, the virtual photon propagates in either direction between the pair.

A visual aid that helps in the evaluation of the energy shift is time-ordered diagrams, a variant of the space-time diagrams introduced by Feynman [41, 42]. For the first case described above, 48 distinct time-orderings of the individual photon annihilation and creation events can be drawn that connect initial and final system states (29). One such sequence is illustrated in Figure 1.1. Labels r and s denote excited intermediate states of A and B, respectively. This contribution to ΔE has been identified as the dynamic mechanism [43] because a real and finite amount of excitation energy migrates between the pair. Evaluation of the energy shift requires summing over all 48 graphs. In doing so, and carrying out the summation over virtual photon polarization and wavevector, the following equation results [17–19, 43, 44]:

$$\Delta E = \frac{I}{\varepsilon_0 c}\alpha_{ik}(\mathrm{A};k)\alpha_{jl}(\mathrm{B};k)e_i^{(\lambda)}(\vec{k})\bar{e}_j^{(\lambda)}(\vec{k})\mathrm{Re}\, V_{kl}(k,\vec{R})\cos\vec{k}\cdot\vec{R}. \tag{31}$$

In the result (31), $I = N\hbar c^2 k/V$ is the incident beam irradiance, and

$$\alpha_{ij}(\xi;k) = \sum_p \left\{ \frac{\mu_i^{0p}(\xi)\mu_j^{p0}(\xi)}{(E_{p0} - \hbar ck)} + \frac{\mu_j^{0p}(\xi)\mu_i^{p0}(\xi)}{(E_{p0} + \hbar ck)} \right\}, \tag{32}$$

is the ground state electric dipole polarizability tensor of species ξ. It is interesting to see that appearing in Eq. (31) is the retarded electric dipole–dipole coupling tensor $V_{ij}(k,\vec{R})$, which has the functional form

$$V_{ij}(k,\vec{R}) = \frac{1}{4\pi\varepsilon_0 R^3}[(\delta_{ij} - 3\hat{R}_i\hat{R}_j)(1 - ikR) - (\delta_{ij} - \hat{R}_i\hat{R}_j)k^2R^2]e^{ikR}, \tag{33}$$

a direct consequence of the single virtual photon coupling A and B. It is the same interaction tensor occurring in the expression for the matrix element

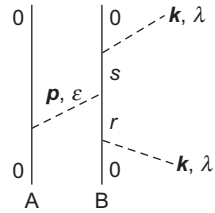

Figure 1.2 One of 48 time-orderings contributing to radiation-induced energy shift with scattering taking place at the same center.

for resonant transfer of energy between an excited and an unexcited pair, but instead evaluated at the value of the resonant wavevector of the downward transition between excited and ground states [45–50]. Hence, the energy shift (31) is directly proportional to the incident beam intensity, the dynamic polarizability of each molecule, the polarization of the laser, and the strength of the intermolecular coupling.

Now considering the second contribution, that arising from absorption and emission of a real photon at either one of the scattering centers, 48 possible time-ordered sequences may be drawn. The diagram displayed in Figure 1.2 represents one term. Evaluating the contribution from each of the graphs in the usual way, and adding them yields the energy shift expression [18, 43]

$$\Delta E = \frac{1}{2\varepsilon_0 c}\left[\beta_{ijk}(\mathrm{A};k)\mu_l^{00}(\mathrm{B}) + \mu_l^{00}(\mathrm{A})\beta_{ijk}(\mathrm{B};k)\right]e_i^{(\lambda)}(\vec{k})\bar{e}_j^{(\lambda)}(\vec{k})V_{kl}(0,\vec{R}). \tag{34}$$

In formula (34), $\mu_i^{00}(\xi) = \langle 0^\xi|\mu_i(\xi)|0^\xi\rangle$ is the ground state, permanent, electric dipole moment of species ξ, while $\beta_{ijk}(\xi;k)$ is the molecular first hyperpolarizability tensor defined by

$$\beta_{ijk}(\xi;k) = \sum_{r,s}\left\{\begin{array}{l}\dfrac{\mu_i^{0s}(\xi)\mu_j^{sr}(\xi)\mu_k^{r0}(\xi)}{(E_{s0}+\hbar ck)E_{r0}} + \dfrac{\mu_i^{0s}(\xi)\mu_k^{sr}(\xi)\mu_j^{r0}(\xi)}{(E_{r0}+\hbar ck)(E_{s0}+\hbar ck)} + \dfrac{\mu_j^{0s}(\xi)\mu_i^{sr}(\xi)\mu_k^{r0}(\xi)}{(E_{s0}-\hbar ck)E_{r0}} \\ + \dfrac{\mu_j^{0s}(\xi)\mu_k^{sr}(\xi)\mu_i^{r0}(\xi)}{(E_{r0}-\hbar ck)(E_{s0}-\hbar ck)} + \dfrac{\mu_k^{0s}(\xi)\mu_i^{sr}(\xi)\mu_j^{r0}(\xi)}{(E_{r0}+\hbar ck)E_{s0}} + \dfrac{\mu_k^{0s}(\xi)\mu_j^{sr}(\xi)\mu_i^{r0}(\xi)}{(E_{r0}-\hbar ck)E_{s0}}\end{array}\right\}. \tag{35}$$

In contrast to the result (31), where the retarded coupling tensor $V_{ij}(k,\vec{R})$ appears, in Eq. (34), the zero frequency form is present, namely

$$V_{ij}(0,\vec{R}) = \frac{1}{4\pi\varepsilon_0 R^3}(\delta_{ij} - 3\hat{R}_i\hat{R}_j). \tag{36}$$

For this reason, the energy shift (34) is often termed the static mechanism because no net energy is transferred between the pair and for its dependence on static moments and static electric dipole–dipole coupling. It arises when either or both species are polar, in contrast to the dynamic term which occurs for nonpolar A and B. Note that the static term vanishes if either A or B is centrosymmetric as both the permanent moment and hyperpolarizability are zero for such species.

The total laser-induced intermolecular energy shift is given by the sum of the two contributions (31) and (34) and applies for radiation propagating in a fixed direction relative to the two oriented molecules. A molecular average can be carried out for all possible orientations of A and B relative to each other. In this case, the static contribution (34) vanishes while the dynamic term becomes

$$\Delta E = \frac{I}{\varepsilon_0 c}\alpha(\mathrm{A};k)\alpha(\mathrm{B};k)e_i^{(\lambda)}(\vec{k})\bar{e}_j^{(\lambda)}(\vec{k})\mathrm{Re}\,V_{ij}(k,\vec{R})\cos\vec{k}\cdot\vec{R}. \tag{37}$$

For Eq. (37) to be applicable to systems in the fluid phase, a pair orientational average has to be performed. This accounts for all possible directions of the wavevector $\vec{k}$ of the impinging beam with respect to the pair separation distance vector $\vec{R}$. After tumble averaging,

$$\langle\Delta E\rangle = -\frac{I}{8\pi\varepsilon_0^2 cR^3}\alpha(\mathrm{A};k)\alpha(\mathrm{B};k) \times\left[kR\sin 2kR + 2\cos 2kR - 5\frac{\sin 2kR}{kR} - 6\frac{\cos 2kR}{k^2R^2} + 3\frac{\sin 2kR}{k^3R^3}\right], \tag{38}$$

and which is the isotropic optical binding energy. It is directly proportional to the beam irradiance, independent of the polarization characteristics of the latter, and linearly proportional to the polarizability of each entity. Near- and far-zone limits are readily obtainable from the result valid for all R. At the former asymptote $kR \ll 1$, and Eq. (38) reduces to

$$\langle\Delta E_{\mathrm{NZ}}\rangle = -\frac{11Ik^2}{60\pi\varepsilon_0^2 cR}\alpha(\mathrm{A};k)\alpha(\mathrm{B};k), \tag{39}$$

exhibiting inverse dependence on R. This contribution can be significant relative to the London dispersion energy (23) for an assembly in which molecules are close together. In addition, the contribution (39) can be further increased if the incident laser is tuned to near-resonance to a molecular transition, thereby significantly enhancing the polarizability. In the far-zone, $kR \gg 1$ and

the limiting form is

$$\langle \Delta E_{\mathrm{FZ}} \rangle = -\frac{Ik}{8\pi\varepsilon_0^2 cR^2}\alpha(\mathrm{A};k)\alpha(\mathrm{B};k)\sin 2kR, \tag{40}$$

which has a modulated inverse square behavior.

From expression (37), it is possible to study the effect of beam polarization on the interaction energy. This may be carried out for linearly and circularly polarized radiation propagating in directions parallel and perpendicular to the intermolecular join, $\vec{R}$. Details and results may be found in Refs. [18, 19].

5. INDUCED MULTIPOLE MOMENT METHOD

An alternative approach to the evaluation of the results obtained in the previous section, and one that provides additional physical insight into the manifestation of the process, is through the coupling of induced multipole moments [51–53]. This method also enables results for energy shifts to be obtained with considerably reduced computational effort, as will be shown in what follows.

Consider a collection of charged particles forming an atom or molecule. A key attribute of such a body is that it is polarizable. Application of an electromagnetic field induces multipole moments in the system. The first few terms of the electric response, resulting in an electric dipole moment being induced, is given by the expansion

$$\mu_i^{\mathrm{ind}}(\xi) = \mu_i^{\mathrm{s}}(\xi) + \varepsilon_0^{-1}\alpha_{ij}(\xi;\omega)d_j^{\perp}(\omega;\vec{R}_\xi) + \varepsilon_0^{-2}\beta_{ijk}(\xi;\omega)d_j^{\perp}(\omega;\vec{R}_\xi)d_k^{\perp}(\omega;\vec{R}_\xi) + \cdots, \tag{41}$$

where $\mu_i^{\mathrm{s}}(\xi)$ is the static dipole moment of species ξ induced along the ith Cartesian axis, $\alpha_{ij}(\xi;\omega)$ is the frequency-dependent electric dipole polarizability tensor (32), $\beta_{ijk}(\xi,\omega)$ is the first-order hyperpolarizability tensor, given explicitly by Eq. (35), and $d_j^{\perp}(\omega,\vec{r})$ is the transverse electric displacement field, whose mode expansion is written in Eq. (15). The first term contributing to the energy shift because of the interaction of multipole moments fluctuating at each center arises from the coupling of induced electric dipole moments (41). For coupling through the retarded interaction tensor $V_{ij}(k,\vec{R})$ given by Eq. (33), the energy shift associated with electric dipoles induced at A and B is

$$\Delta E = \mu_i^{\mathrm{ind}}(\mathrm{A})\mu_j^{\mathrm{ind}}(\mathrm{B})\mathrm{Re}\,V_{ij}(\omega,\vec{R}), \quad \text{where} \quad \vec{R} = \vec{R}_{\mathrm{B}} - \vec{R}_{\mathrm{A}}. \tag{42}$$

An expression for the interaction energy written explicitly in terms of the response tensors is easily derived on substituting Eq. (41) into Eq. (42). This

yields the following equation:

$$\begin{aligned}\Delta E = \big[&\mu_i^{\mathrm{s}}(A) + \varepsilon_0^{-1}\alpha_{im}(\mathrm{A};\omega)d_m^{\perp}(\omega;\vec{R}_{\mathrm{A}}) \\ &+ \varepsilon_0^{-2}\beta_{imn}(\mathrm{A};\omega)d_m^{\perp}(\omega;\vec{R}_{\mathrm{A}})d_n^{\perp}(\omega;\vec{R}_{\mathrm{A}}) + \cdots\big]\big[\mu_j^{\mathrm{s}}(\mathrm{B}) + \varepsilon_0^{-1}\alpha_{jp}(\mathrm{B};\omega)d_p^{\perp}(\omega;\vec{R}_{\mathrm{B}}) \\ &+ \varepsilon_0^{-2}\beta_{jpq}(\mathrm{B};\omega)d_p^{\perp}(\omega;\vec{R}_{\mathrm{B}})d_q^{\perp}(\omega;\vec{R}_{\mathrm{B}}) + \cdots\big]\mathrm{Re}\, V_{ij}(\omega,\vec{R}). \end{aligned} \tag{43}$$

For both molecules in the electronic ground state, and the radiation field of the intense laser containing N photons of mode $(\vec{k},\lambda)$, the expectation value of Eq. (43) is taken over the matter-field state $|0^{\mathrm{A}},0^{\mathrm{B}};N(\vec{k},\lambda)\rangle$. The result for the molecular factors is straightforward, producing ground state permanent moments, polarizabilities, and hyperpolarizabilities. Individual terms contributing to the interaction energy are easily extracted on multiplying the two factors in square brackets of Eq. (43). The first term, for example, proportional to $\mu_i^{00}(\mathrm{A})\mu_j^{00}(\mathrm{B})$, is simply the static dipolar Coulomb energy. Similarly, the so-called dynamic mechanism term is readily seen to be given by

$$\Delta E = \varepsilon_0^{-2}\alpha_{im}(\mathrm{A};\omega)\alpha_{jp}(\mathrm{B};\omega)d_m^{\perp}(\omega;\vec{R}_{\mathrm{A}})d_p^{\perp}(\omega;\vec{R}_{\mathrm{B}})\mathrm{Re}\, V_{ij}(\omega,\vec{R}). \tag{44}$$

It is seen from Eq. (44) that for the radiation field, the expectation value is taken over the spatial correlation function, which is easily found to be

$$\begin{aligned}&\langle N(\vec{k},\lambda)|d_i^{\perp}(\vec{R}_{\mathrm{A}})d_j^{\perp}(\vec{R}_{\mathrm{B}})|N(\vec{k},\lambda)\rangle \\ &\quad = \left(\frac{\hbar ck\varepsilon_0}{2V}\right)\big[(N+1)e_i^{(\lambda)}(\vec{k})\bar{e}_j^{(\lambda)}(\vec{k})e^{-i\vec{k}\cdot\vec{R}} + N\bar{e}_i^{(\lambda)}(\vec{k})e_j^{(\lambda)}(\vec{k})e^{i\vec{k}\cdot\vec{R}}\big]. \end{aligned} \tag{45}$$

Inserting the right-hand side of Eq. (45) into Eq. (44) gives

$$\Delta E = \left(\frac{N\hbar ck}{2\varepsilon_0 V}\right)\alpha_{im}(\mathrm{A};\omega)\alpha_{jp}(\mathrm{B};\omega)e_m^{(\lambda)}(\vec{k})\bar{e}_p^{(\lambda)}(\vec{k})(e^{i\vec{k}\cdot\vec{R}} + e^{-i\vec{k}\cdot\vec{R}})\mathrm{Re}\, V_{ij}(\omega,\vec{R}), \tag{46}$$

which is equivalent to result (31), after making the approximation $N+1 \sim N$ for an intense beam of laser light. The static term can be evaluated similarly from Eq. (43) on isolating the contribution proportional to the product of permanent moment and hyperpolarizability. It is given by

$$\begin{aligned}\Delta E = \langle N(\vec{k},\lambda);0^{\mathrm{B}},\ 0^{\mathrm{A}}\Big|&\frac{1}{2}\varepsilon_0^{-2}\mu_i^{\mathrm{s}}(\mathrm{A})\beta_{jpq}(\mathrm{B};\omega)d_p^{\perp}(\omega;\vec{R}_{\mathrm{B}})d_q^{\perp}(\omega;\vec{R}_{\mathrm{B}})V_{ij}(0,\vec{R})\Big|0^{\mathrm{A}},0^{\mathrm{B}}; \\ &N(\vec{k},\lambda)\rangle + \mathrm{A}\leftrightarrow\mathrm{B}. \end{aligned} \tag{47}$$

As a result of index symmetry, a factor of one-half arises from the cross-term, with the identities of the two species being clearly distinguished. Note

the appearance of the static coupling tensor (36). Evident from Eq. (47) is that the expectation value of the product of electric displacement fields at the *same* point in space is required. This follows from Eq. (45) on letting $\vec{R} = 0$. For a high occupation number state of the field,

$$\langle N(\vec{k},\lambda)|d_i^{\perp}(\vec{r})d_j^{\perp}(\vec{r})|N(\vec{k},\lambda)\rangle = \left(\frac{N\hbar ck\varepsilon_0}{V}\right) e_i^{(\lambda)}(\vec{k})\bar{e}_j^{(\lambda)}, \tag{48}$$

yielding for the static term, the energy shift

$$\Delta E = \left(\frac{N\hbar ck}{2\varepsilon_0 V}\right) \mu_i^{00}(\mathrm{A})\beta_{jpq}(\mathrm{B};\omega)e_p^{(\lambda)}(\vec{k})\bar{e}_q^{(\lambda)}(\vec{k})V_{ij}(0,\vec{R}) + \mathrm{A} \leftrightarrow \mathrm{B}, \tag{49}$$

which is identical to result (34).

Another major advantage associated with the induced moment method is that it is easy to generalize the results for the radiation-induced energy shift to more than two interacting particles. From the form of the expression for the two-body potential (46), the extension to n bodies is compactly written as follows [54]:

$$\begin{aligned}\Delta E^{\{\xi_1,\ldots,\xi_n\}} = &\left(\frac{N\hbar ck}{2\varepsilon_0 V}\right) e_{i_0}^{(\lambda)}(\vec{k})\bar{e}_{i_n}^{(\lambda)}(\vec{k})\alpha_{i_0 i_1}^{(\xi_1)}(-k;k) \\ &\times \prod_{p=1}^{n-1}\left[V_{i_p i_{p+1}}\left(k,\vec{R}_{\xi_p\xi_{p+1}}\right)\alpha_{i_{p+1}i_{p+2}}^{(\xi_{p+1})}(-k;k)\right] e^{-i\vec{k}\cdot\vec{R}_{\xi_n\xi_1}},\end{aligned} \tag{50}$$

where $\{\xi_1,\ldots,\xi_n\}$ means a permutation over all ξ_i, $i = 1\ldots n$ must be carried out. Formulae for three-, four-, ..., body optical binding energy shifts follow from Eq. (50). Particles varying in size from micro to nanometer diameter frequently exhibit optical binding, formed by molecules whose number is p. As this number grows, an effective polarizability associated with aggregate ζ is introduced,

$$\chi_{ij}^{\zeta} = \sum_{\xi}^{p} \alpha_{\lambda\mu}^{\xi} l_{i\lambda}^{\xi} l_{j\mu}^{\xi} e^{i\vec{k}\cdot\Delta\vec{R}_{\xi}}, \tag{51}$$

where $l_{i\lambda}^{\xi}$ is the direction cosine of the angle relating space (i) to molecule (λ) fixed Cartesian axes, and the relative position of each species ξ within collection ζ is denoted by $\Delta\vec{R}_{\xi}$.

Finally, it is worth remarking that retarded van der Waals dispersion potentials between molecules in ground and excited electronic states may also be calculated [12, 51] using the fluctuating moment method. Because dispersion forces arise from the perturbation induced by the zero-point energy associated with the vacuum electromagnetic field, the expectation value of

the spatial field–field correlation function (45) is taken over the radiation field state $|0(\vec{k},\lambda)\rangle$, obtained on inserting $N = 0$. The Casimir–Polder potential then follows from

$$\Delta E = \sum_{\vec{k},\lambda} \langle 0(\vec{k},\lambda);$$

$$0^{\mathrm{B}}, 0^{\mathrm{A}} \left| \varepsilon_0^{-2} \alpha_{ik}(\mathrm{A};k)\alpha_{jl}(\mathrm{B};k) d_k^{\perp}(\vec{R}_{\mathrm{A}}) d_l^{\perp}(\vec{R}_{\mathrm{B}}) \mathrm{Re}\, V_{ij}(k,\vec{R}) \right| 0^{\mathrm{A}}, 0^{\mathrm{B}}; 0(\vec{k},\lambda)\rangle, \quad (52)$$

on evaluating the mode sum in the usual way.

6. DISCRIMINATORY EFFECTS

Application of the molecular QED formalism to the computation of the radiation-induced intermolecular energy shift has been restricted, thus far, to the electric dipole approximation, with contributions to ΔE dependent on the electric permanent moment, polarizability, and hyperpolarizability evaluated explicitly. It is well known that intermolecular processes can be discriminatory in nature [55]. The interaction energy depends on the handedness of the coupled species. Manifestations occur in resonant transfer of excitation energy [49, 51, 56, 57] and in van der Waals dispersion [4, 58–60]. In the former process, discriminatory effects cause a change in the sign of the transfer rate when one enantiomer is replaced by its mirror image form, whereas in the dispersion force, identical chemical species with opposite chirality exhibit an attractive interaction, with a repulsive energy shift found for isomers possessing the same handedness; for chemically distinct bodies, the dispersion energy changes sign when one species is substituted by its antipode. To leading order, these effects are understood as arising from the interference of electric and magnetic dipole coupling terms, thereby necessitating the relaxation of the electric dipole approximation. Hence higher multipole moment terms are required to fully describe the chiral entities, largely because of their symmetry properties, which permit electronic transitions to occur with less strict selection rules, with magnetic dipole and electric quadrupole contributions to absorption often commonplace.

In the previous section, it was shown how the induced multipole moment method offered a number of advantages relative to perturbation theory for the calculation of the optical binding energy. There was no need to sum over a large number of time-ordered diagrams, the method could straightforwardly be extended to evaluate field-modified interaction energies between two-, three-, and many-bodies, and the Casimir–Polder dispersion potential could also be computed. Therefore, it seems logical to apply the fluctuating moment approach to higher multipole moment–dependent contributions to

the radiation-induced interaction energy, extending the electric dipole case presented earlier.

Application of a time-varying electromagnetic field to a chiral molecule results in magnetic dipole, electric quadrupole, and higher order multipole moments being induced in addition to the electric dipole moment. Retaining only the induced electric and magnetic dipole terms, whose coupled product survives orientational averaging, and ignoring the induced electric quadrupole moment, whose interference term with the electric dipole moment vanishes for isotropic systems, the correction to $\mu_i^{\text{ind}}(\xi)$ given by Eq. (41) as a result of chiral response is

$$\mu_i^{\text{ind}}(\xi) = G_{ij}(\xi;\omega) b_j(\omega;\vec{R}_\xi), \tag{53}$$

where $G_{ij}(\xi;\omega)$ is the dynamic mixed electric-magnetic dipole polarizability tensor

$$G_{ij}(\xi;\omega) = \sum_t \left\{ \frac{\mu_i^{0t}(\xi) m_j^{t0}(\xi)}{E_{t0} - \hbar\omega} + \frac{m_j^{0t}(\xi)\mu_i^{t0}(\xi)}{E_{t0} + \hbar\omega} \right\}, \tag{54}$$

which depends on the optical activity of the chiral chromophore. In a similar fashion, the induced magnetic dipole moment is

$$m_j^{\text{ind}}(\xi) = \varepsilon_0^{-1} G_{ij}(\xi;\omega) d_i^{\perp}(\omega;\vec{R}_\xi) + \chi_{ij}(\xi;\omega) b_i(\omega;\vec{R}_\xi) + \cdots, \tag{55}$$

where $\chi_{ij}(\xi;\omega)$ is the magnetic dipole analog of the electric dipole polarizability tensor (32). It doesn't discriminate between enantiomers. To describe discriminatory effects, coupling between induced electric moments, induced magnetic moments, as well as between induced electric and magnetic moments, at different centers need to be accounted for. The term in the energy shift proportional to the chirality of each molecule is calculated from

$$\begin{aligned} \Delta E = &\left[\mu_i^{\text{ind}}(\text{A}) \mu_j^{\text{ind}}(\text{B}) + \frac{1}{c^2} m_i^{\text{ind}}(\text{A}) m_j^{\text{ind}}(\text{B}) \right] \text{Re}\, V_{ij}(\omega,\vec{R}) \\ &+ [\mu_i^{\text{ind}}(\text{A}) m_j^{\text{ind}}(\text{B}) + m_i^{\text{ind}}(\text{A}) \mu_j^{\text{ind}}(\text{B})] \text{Im}\, U_{ij}(\omega,\vec{R}), \end{aligned} \tag{56}$$

on substituting Eq. (53) and the first term of Eq. (55). In addition to the previously encountered interaction tensor $V_{ij}(\omega,\vec{R})$ appearing in Eq. (56), coupling between $\mu_i^{\text{ind}}(\text{A})$ and $m_j^{\text{ind}}(\text{B})$, and $\text{A} \leftrightarrow \text{B}$ occurs through the retarded tensor [49, 56, 57]

$$U_{ij}(\omega,\vec{R}) = \frac{1}{4\pi\varepsilon_0 c R^3} \varepsilon_{ijk} \hat{R}_k \left(\frac{i\omega R}{c} - \frac{\omega^2 R^2}{c^2} \right) e^{i\omega R/c}, \tag{57}$$

which mediates the resonant transfer of electronic excitation energy between chiral systems and where ε_{ijk} is the Levi–Civita tensor. Expectation values are again taken over state (29), yielding ground state molecular polarizability tensors (54), and additional field–field spatial correlation functions involving magnetic–magnetic and electric–magnetic combinations. These may be found elsewhere [60]. The pair-averaged energy shift is calculated to be

$$\Delta E = \left(\frac{N\hbar k}{\varepsilon_0 cV}\right) G(\mathrm{A};\omega)G(\mathrm{B};\omega)\{[b_i^{(\lambda)}(\vec{k})\bar{b}_j^{(\lambda)}(\vec{k}) + e_i^{(\lambda)}(\vec{k})\bar{e}_j^{(\lambda)}(\vec{k})]\mathrm{Re}\, V_{ij}(\omega,\vec{R}) + c[b_i^{(\lambda)}(\vec{k})\bar{e}_j^{(\lambda)}(\vec{k}) + e_i^{(\lambda)}(\vec{k})\bar{b}_j^{(\lambda)}(\vec{k})]\mathrm{Im}U_{ij}(\omega,\vec{R})\}\cos(\vec{k}\cdot\vec{R}). \tag{58}$$

This result is the next highest-order correction term to the isotropic electric dipole polarizability energy shift (37). It should be mentioned that while there is a contribution to the radiation-induced interparticle interaction energy between an oriented electric dipole polarizable molecule A and an oriented chiral molecule B, or vice versa, this term vanishes on pair averaging. Similarly, the energy shift between an electric dipole polarizable body and an electric dipole–quadrupole polarizable body in a radiation field equals zero on averaging [61]. Results of the analysis of the behavior of the energy shift (58) for linearly and circularly polarized incoming light propagating parallel and perpendicular to $\vec{R}$ may be found in Ref. [60]. Averaging overall relative orientations of $\vec{k}$ and $\vec{R}$ produces the optical binding energy between two chiral molecules

$$\Delta E = \frac{I}{8\pi\varepsilon_0^2 c^3 R^3} G(\mathrm{A};\omega)G(\mathrm{B};\omega)\left[4\frac{\sin 2kR}{kR} + 6\frac{\cos 2kR}{k^2R^2} - 3\frac{\sin 2kR}{k^3R^3}\right], \tag{59}$$

which exhibits linear dependence on the laser irradiance. Both of the results (58) and (59) are discriminatory, changing sign when one enantiomeric form is replaced by its optical isomer as witnessed by the product of $G_{ij}(\xi;\omega)$ tensors for each species appearing in the expressions for the energy shift. Note that Eq. (59) is independent of laser polarization. Asymptotic limits readily follow and are

$$\Delta E(\mathrm{NZ}) = -\frac{4Ik^2}{15\pi\varepsilon_0^2 c^3 R} G(\mathrm{A};\omega)G(\mathrm{B};\omega), \tag{60}$$

and

$$\Delta E(\mathrm{FZ}) = \frac{I}{2\pi\varepsilon_0^2 c^3 kR^4} G(\mathrm{A};\omega)G(\mathrm{B};\omega)\sin 2kR, \tag{61}$$

in the near- and far-zones, respectively.

A nondiscriminatory contribution to the optical binding energy arising from purely magnetic dipole coupling is easily obtainable from the second term of Eq. (55) through the expression

$$\Delta E = m_i^{\text{ind}}(\text{A}) m_j^{\text{ind}}(\text{B}) \text{Re}\, V_{ij}(\omega, \vec{R}). \tag{62}$$

The result analogous to the dynamic contribution (37) is written down immediately on substituting transition electric dipoles by $\frac{1}{c}\vec{m}^{0t}(\xi)$ and electric polarization vectors by their magnetic counterparts. Whence

$$\Delta E = \left(\frac{N\hbar k}{\varepsilon_0 c V}\right) \chi(\text{A};\omega)\chi(\text{B};\omega) b_i^{(\lambda)}(\vec{k}) \bar{b}_j^{(\lambda)}(\vec{k}) \text{Re}\, V_{ij}(\omega, \vec{R}) \cos(\vec{k}\cdot\vec{R}), \tag{63}$$

for isotropic paramagnetically susceptible A and B held in fixed orientation with respect to the incoming beam propagation direction. Identical results to the electric dipole example then follow for a variety of beam polarizations and configurations, and for a freely tumbling pair [62]. Because of the small size of $\vec{m}$ relative to $\vec{\mu}$, the purely magnetic dipole term (63) is commonly neglected in comparison with the dominant electric dipole contribution, in addition to the fact that the former is independent of molecular chirality.

7. APPLICATIONS

The results of Section 4 have been applied to a number of different types of particles subject to radiation with varying characteristics to further understand the nature of the optical binding force, and to compare with experimental investigations, where possible. Some of these cases are examined below, although more detailed studies may be found in the literature cited.

7.1. Spherical particles

A common application has been to spherical particles. For nonpolar species, only the dynamic term (31) contributes to the interaction potential. From the form of the energy shift, it is clear that the surface containing the laser propagation direction and polarization vectors form a plane, which when combined with its perpendicular produces a Cartesian axis frame which may be used to express the orientation of the coupled pair through the separation distance vector, $\vec{R}$. This gives rise to a minimum of three degrees of geometric freedom comprising this length and two angular variables, θ, the angle R makes to the electric polarization vector, and ϕ, which corresponds to the angle formed between the plane containing $\vec{e}$ and $\vec{R}$, and the radiation wavevector, $\vec{k}$. Spherical particles therefore exhibit this minimal

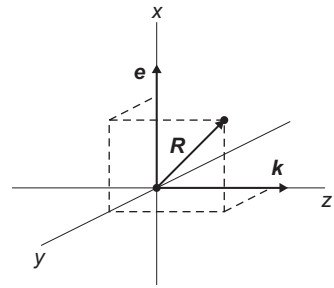

Figure 1.3 Two particles in a plane wave of polarization ***e***, and wavevector ***k***. The vector ***R*** denotes the displacement between the particles A and B, where A can be considered as located at the origin. The *x*- and *z*-axes are defined along ***e*** and ***k***, respectively. Copyright (2008) by the American Physical Society.

descriptive configuration, as illustrated in Figure 1.3. For linear polarization, the isotropic energy shift (37) becomes

$$\Delta E = \frac{I}{2\pi c\varepsilon_0^2 R^3}\alpha(\mathrm{A})\alpha(\mathrm{B})\cos[kR\sin\theta\cos\phi] \times \{(1-ikR)(1-3\cos^2\theta) - k^2R^2\sin^2\phi\}e^{ikR}, \tag{64}$$

in terms of the newly defined coordinates. Model calculations [63] showed that the field-induced interaction energy becomes larger in magnitude than the dispersion energy for separation distances of the order of 50 nm at fixed orientations when subject to radiation of wavelength 355 nm at the reasonable irradiance of 10^{12} Wm^{-2}. Shown in Fig. 1.2 of Ref. [64] is the variation of the energy shift (64) with separation distance R for different values of kR resolved along the three Cartesian axes for the configuration of Figure 1.3. A corresponding plot in the y, z-plane for $kR_x = 0$ is displayed in Figure 1.4. Clearly visible is the anisotropic nature of the radiation-induced interaction energy. Distinct regions representing attractive and repulsive pair interactions emerge, with differently colored islands depicting alternating local maxima and minima. As kR_x increases, the minima along the z-axis gradually disappear. Also apparent from these surfaces is the increasing long-range order as R increases. When investigating the angular dependence of the laser-induced energy shift, an interesting finding was that the regions of positive and negative force exist, the former therefore resulting in repulsive pair particle interactions. Plots of the potential energy landscape revealed that optical binding configurations are distinguished by local minima, displaying an even dependence on each angular coordinate. For an arbitrary configuration, both forces and torques will, in general, be manifested.

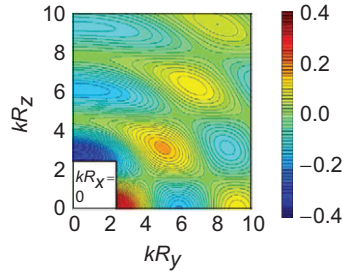

Figure 1.4 Optically induced interparticle energy surface on the (*y*, *z*) plane of Figure 1.3. The scale is in $2I\alpha^2k^3/4\pi\varepsilon_0^2c$ units. Field polarization directed along the *x*-axis, wavevector on the *z*-axis. Copyright (2008) by the American Physical Society.

7.2. Cylindrically symmetric particles

It is interesting to note that formula (64) is applicable to two cylindrically symmetric particles, such as between two nanotubes [43, 61], if the applied field is the only source of radiation. If this is the case, only the principal axis (diagonal elements) of the polarizability tensors contribute, corresponding to the component aligned in the same direction as the laser polarization.

An important consequence of the topological features of the potential energy surfaces mentioned above is the possibility to produce ordered arrays of particles. This is most starkly visible when comparing polarized with nonpolarized laser beams. The phenomenon has been observed for nanoparticles originating on a silicon surface [65, 66]. For radiation that is nonpolarized, only two variables are necessary to characterize the geometric behavior of ΔE, and they are the interparticle distance vector, and its direction relative to the throughput radiation vector. Points of stability, which favor particle localization, are clearly evident from the contour plots, and these regions are characterized by zero torques acting on the pair. For specific arrangements contributing to the sum of all pair energy shifts, it is possible to generate ordered linear chains and two-dimensional arrays of particles. Other configurations can also be formed, including ring structures, and four bodies occupying sites at the vertices of a square. Examples of the dependence of the energy shift for three and four identical particles as a function of the distance of one of them from the remainder are shown in Fig. 1.4 of Ref. [64] and Fig. 1.5 for the configuration of Fig. 1.3. Again islands of stability are clearly evident, along with attractive and repulsive regions. No torques are in effect because the energy is minimized at values of $\phi = 0$ or 90°, being independent of θ. Comparing Figure 1.5 with Fig. 1.4 of Ref. [64], it is seen that on going from three to four particles, the number of possible physically stable arrays increases significantly. In the plot for four particles, noticeably large extrema are found at kR_y values of around 3, 6, and 9. In both cases, the most

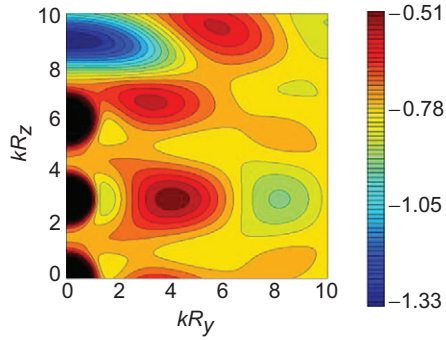

Figure 1.5 Optically induced potential energy landscapes for four identical interacting particles as a function of the vector positions of one of them, when the other three are at (0, 0, 0), (0, 0, 3), and (0, 0, 6). Scale in $2I\alpha^2k^3/4\pi\varepsilon_0^2c$ units. Polarization and wavevector as in Figure 1.3. Black circular shapes represent local divergences in energy shift in the proximity of the fixed particles. Copyright (2008) by the American Physical Society.

stable minima are found along the z-axis, indicating a preference for chain formation along this direction.

7.3. Effect of a second laser beam

Interesting effects arise on the introduction of an additional laser field [67]. If a beam propagating in a direction opposite to that inducing optical binding is applied, then cancellation of radiation pressure occurs, leaving the energy shift as the only effective potential operating. One possible arrangement is illustrated in Figure 1.6. Additional secondary laser action can further modify the total field influencing the interacting particles. Typically, this secondary field propagates perpendicularly to the counter-propagating beams, and with polarization that is orthogonal. Now the local minima on the potential energy surface, which determine stable particle arrangements, are dependent on the relative irradiances of the primary and secondary radiation. For the near-field separation distance regime, control of aggregate shapes is possible as they metamorphose between linear, spherical, and lamellar structures. At large separation distances, comparable with the laser wavelength, for specific-threshold intensity of the secondary laser relative to the primary field, potential energy minima disappear leading to collapse of the structure. This is predicted to take place for micrometer-sized particles. Fig. 1.2 of Ref. [67] shows the change in interparticle potential energy as a function of kR for $\zeta = 0$ and $\phi = 90^\circ$ as the secondary beam irradiance is increased from zero to four times the strength of the primary field. Instability increases as the minimum energy configuration giving rise to particle conglomeration slowly disappears. Instead, substructures comprised of smaller

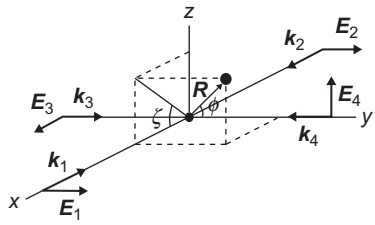

Figure 1.6 Pair of particles irradiated by two counter-propagating beams designated *primary* ($\boldsymbol{E}_1$, $\boldsymbol{k}_1$) and ($\boldsymbol{E}_2$, $\boldsymbol{k}_2$) (standard optical binding) and *secondary* beams ($\boldsymbol{E}_3$, $\boldsymbol{k}_3$) reflected with transverse polarization as ($\boldsymbol{E}_4$, $\boldsymbol{k}_4$). The angle subtended by the interparticle displacement vector **R** on the *y* axis is ϕ, and the angle between the ***R*** projection on the *zx* plane and the *x*-axis is ζ.

numbers of particles form, governed by optical binding or retarded van der Waals dispersion energy shifts.

7.4. Coupling of particles by broadband radiation

To minimize the effects of interference arising when monochromatic counter-propagating laser beams are used in forming particle arrays in optical traps, broadband or continuum radiation is often used in its place because of the resulting small coherence length [68]. For broadband radiation propagating in the z-direction and polarized along the x-axis, the time-averaged energy shift is [69]

$$\Delta\bar{E} = \sum_k \mathrm{Re}\,\{P_x^{\mathrm{ind}}(\mathrm{A})V_{xx}(k,\vec{R})P_x^{\mathrm{ind}}(\mathrm{B})\}_{\mathrm{av}}, \tag{65}$$

where $\vec{P}^{\mathrm{ind}}(\xi)$ is the induced electric polarization. Carrying out the mode sum on introducing continuum mode raising and lowering operators yields for isotropic A and B,

$$\langle\Delta\bar{E}\rangle = \mathrm{Re}\left[\frac{\varepsilon_0}{2c}\int S(\omega)V_{xx}(k,\vec{R})\big\{\sigma(\mathrm{A};\omega)\sigma(\mathrm{B};-\omega)e^{-i\omega R_z/c} + \sigma(\mathrm{A};-\omega)\sigma(\mathrm{B};\omega)e^{i\omega R_z/c}\big\}\mathrm{d}\omega\right], \tag{66}$$

where $\sigma(\xi)$ is the isotropic electric susceptibility, defined through the induced electric polarization as

$$P_i^{\mathrm{ind}}(\xi) = \sigma_{ij}(\xi)d_j^{\perp}(\vec{r}_\xi), \tag{67}$$

and the spectral beam irradiance is

$$S(\omega) = \langle\{x\}|a^{\dagger}(\omega)a(\omega)|\{x\}\rangle\hbar c\omega/V, \tag{68}$$

and is expressed in terms of the expectation value of the number operator over the continuum state $|\{x\}\rangle$. Choosing a particular form for the function $S(\omega)$, such as a Lorentzian, enables particle arrays to be manipulated and molded using broadband radiation, providing an alternative to the use of a secondary source. Chain length may then be controlled through suitable frequency filtering.

7.5. Coherent state description

The inclusion of coherent states of the radiation field in the formalism describing optically induced forces is most conveniently carried out within the induced multipole moment method delineated in Section 5. Instead of number states $|n(\vec{k},\lambda)\rangle = |a^{\dagger(\lambda)}(\vec{k})a^{(\lambda)}(\vec{k})\rangle$, coherent states $|\alpha^{\pm}\rangle$ are defined to describe the state of the field, with the upper/lower signs referring to propagation in the $\vec{k}$ and $-\vec{k}$ directions, respectively. Such states are of minimum uncertainty, satisfying the relation $\Delta n\Delta\cos\varphi \geq \frac{1}{2}|\langle\sin\varphi\rangle|$, where φ is the phase operator. Interference therefore ensues when several lasers superpose. The averaged interparticle interaction energy is given by [69]

$$\langle\Delta E\rangle = \frac{2I\varepsilon_0}{c}\sigma(\mathrm{A})\sigma(\mathrm{B})V_{xx}(k,\vec{R})f(kR), \tag{69}$$

where $f(kR) = \cos kR_z$. When the mismatch between wavevector moduli of the two counter-propagating beams, $\Delta k \neq 0$, this corresponds to no interference, and $f(kR) = \cos kR_z^{\mathrm{A}}\cos kR_z^{\mathrm{B}}$, while when $\Delta k = 0$, a standing wave forms. The irradiance, $I = \alpha^{+}\bar{\alpha}^{+}\hbar c^2k/V$, on letting $\alpha^{+} = \alpha^{-}$, since the fields of the two counter-propagating beams are near identical. From the surfaces generated, it is found that for particles trapped in the standing wave, both transverse and longitudinal optical binding can occur. When $\Delta k \neq 0$, and there is no interference, either parallel or perpendicular chains of particles form, as well as planar arrangements. The enhancement of the interaction energy as particle size increases is clearly seen in Fig. 1.6 of Ref. [64]. Figure 1.7 illustrates the behavior of the pair-interaction energy as a function of increasing particle size in the presence of two counter-propagating fields. Clearly visible is the disappearance of minima as the radius of the particle increases, which favors collapse of individual particles and the formation of conglomerates.

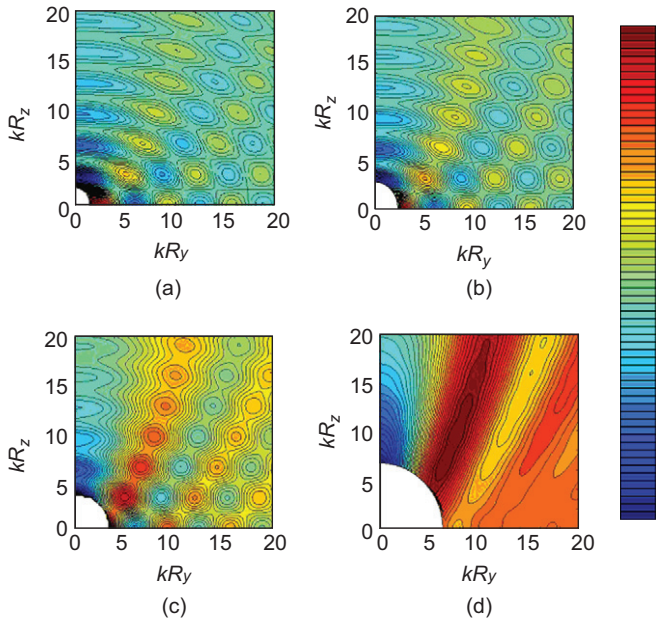

Figure 1.7 Contour maps of the optically induced interparticle potential energy for two particles in counter-propagating beams, with a slight shift in their wavelength, against kR_z and kR_y (R_z and R_y being the projection on the z- and y-axes, respectively, of the separation between particles A and B, $\mathbf{R}^{(AB)}$) for particle radius (a) $L = 0.5/k$, (b) $L = 1/k$, (c) $L = 2/k$, and (d) $L = 3/k$. In the greyscale, bottom and top values in each panel are (a) -0.0488 and 0.0604; (b) -2.40 and 2.38; (c) -50.2 and 23; (d) -340 and 108. Energy units are $I\alpha^2\rho^2/4\pi\varepsilon_0 ck^6$. One beam has its Poynting vector along the direction of the z-axis, and the other one in the opposite direction; both beams have their polarization along the x-axis.

7.6. Interparticle coupling in Laguerre–Gaussian beams

Recent novel developments in the field of optics have included the use of bifurcated gratings to produce structured beams of light, containing regions of high intensity that may be used to trap particles [20]. One such type of exotic radiation is the Laguerre–Gaussian beam [70]. It may also be defined through a coherent state and characterized in terms of a modulus $|\Lambda(r, z)|$ and a phase angle $\varphi(z, r, \theta)$, these last two factors depending on indices l, the Azimuthal mode, and p, which quantifies the number of radial nodes, which together serve to classify specific modal structures of the beam. A common beam structure involves high-intensity annular rings of different radius around the center of the propagation wavevector. For two particles A and B trapped in two different rings of radii r_A and r_B, making angles θ_A and θ_B,

respectively, the energy shift can be written as [69]

$$\langle \Delta E \rangle = \left(\frac{\hbar c k \varepsilon_0^2}{2V} \right) \frac{1}{4\pi c R^3} \sigma(\mathrm{A}) \sigma(\mathrm{B}) |\Lambda(0, r_\mathrm{A})| |\Lambda(0, r_\mathrm{B})| \mathrm{Re}\, e^{i[\varphi(0, r_\mathrm{B}, \theta_\mathrm{B}) - \varphi(0, r_\mathrm{A}, \theta_\mathrm{A})]}$$
$$\times \left\{ \sum_{i=x,y} \left[1 - 3 \left(\frac{R_i}{R} \right)^2 \right] (\cos kR + kR \sin kR) \right.$$
$$\left. - \left[1 - \left(\frac{R_i}{R} \right)^2 \right] k^2 R^2 \cos kR \right\}, \tag{70}$$

and the Cartesian components of the displacement vectors are $R_x = r_\mathrm{B} \sin\theta_\mathrm{B} - r_\mathrm{A} \sin\theta_\mathrm{A}$, $R_y = r_\mathrm{B} \cos\theta_\mathrm{B} - r_\mathrm{A} \cos\theta_\mathrm{A}$, and $R^2 = R_x^2 + R_y^2$. It is found that for $l = 0$, diametrically opposed particle configuration leads to the most favorable energy. And varying the parameter $k\omega_0$, where ω_0 is the width of the Gaussian beam at $z = 0$, allows particle arrangements on individual rings to be controlled.

8. SUMMARY

Two theoretical approaches within the framework of molecular quantum electrodynamics in the Coulomb gauge have been outlined for the evaluation of the energy shift between a pair of interacting particles in the presence of an intense beam of laser light. One method involved standard time-dependent perturbation theory together with Feynman diagrams to visualize the sequence of photon creation and annihilation events, which for the process of interest corresponds to the scattering of a real photon and exchange of a virtual photon between the two optically bound centers. Two distinct mechanisms were unveiled depending on the polarity of the individual species. A contribution proportional to the polarizability of each molecule is found for interaction between nonpolar substances, termed the dynamic one, while if either one or both species are polar, then a term depending on the product of the ground state permanent moment and the first hyperpolarizability and denoted the static mechanism occurs. Identical results for the interaction energy were obtained using a second physical picture, one that involved the coupling of multipole moments induced at each site by the applied electric field. Expectation values over the ground electronic state of both particles, and the field containing N photons yielded the energy shift directly. This method proved amenable to the study of higher multipole contributions to the field-modified intermolecular potential. By including magnetic dipole coupling, and extracting the term resulting from interference of electric and magnetic dipole moments, the energy shift was

shown to be discriminatory, depending on the chirality of each molecule. Application of the theory by others to different types of interacting particles and differing forms of radiation were then reviewed. These included spherically and cylindrically symmetric systems, as well as the effect of broadband, coherent, and secondary radiation on ΔE. Model calculations enabled the topology of the potential energy landscape to be explored, regions of stability to be located corresponding to points at which the force and/or torque vanish and the energy minimized, to particle array formation. These and other aspects will continue to be studied as long as progress in laser technology ensures that difficult experiments advance.

ACKNOWLEDGMENT

J. J. Rodriguez is gratefully acknowledged for producing all of the figures used in this article.

REFERENCES

[1] J. Schwinger (Ed.), Selected Papers on Quantum Electrodynamics, Dover, New York, 1958, pp. 1–424.
[2] H.B.G. Casimir, D. Polder, The Influence of Retardation on the London van der Waals Forces. Phys. Rev. 73 (1948) 360.
[3] I.E. Dzyaloshinskii, E.M. Lifshitz, L.P. Pitaevskii, General theory of van der Waals forces. Sov. Phys. Usp. 4 (1961) 153.
[4] C. Mavroyannis, M.J. Stephen, Dispersion forces. Mol. Phys. 5 (1962) 629.
[5] A.D. McLachlan, Retarded dispersion forces between molecules. Proc. Roy. Soc. Lond. A 271 (1963) 287.
[6] D.P. Craig, E.A. Power, The Asymptotic Casimir-Polder Potential From Second-Order Perturbation Theory and Its Generalization for Anisotropic Polarizabilities. Int. J. Quant. Chem. 3 (1969) 903.
[7] G. Feinberg, J. Sucher, General theory of the van der Waals interaction: A model independent approach. Phys. Rev. A 2 (1970) 2395.
[8] Y.S. Barash, V.L. Ginzburg, Electromagnetic fluctuations in matter and molecular (Van-der-Waals) forces between them. Sov. Phys. Usp. 18 (1975) 305.
[9] E.A. Power, T. Thirunamachandran, Quantum Electrodynamics With Nonrelativistic Sources. III. Intermolecular Interactions. Phys. Rev. A 28 (1983) 2671.
[10] P.W. Milonni, Casimir forces without the vacuum radiation field. Phys. Rev. A 25 (1982) 1315.
[11] G. Compagno, F. Persico, R. Passante, Interference in the virtual photon clouds of two hydrogen atoms. Phys. Lett. A 112 (1985) 215.
[12] E.A. Power, T. Thirunamachandran, Casimir-Polder Potential as an Interaction Between Induced Dipoles. Phys. Rev. A 48 (1993) 4761.
[13] E.A. Power, Introductory Quantum Electrodynamics, Longmans, London, 1964.
[14] W.P. Healy, Non-Relativistic Quantum Electrodynamics, Academic Press, London, 1982.
[15] P.W. Milonni, The Quantum Vacuum, Academic Press, San Diego, 1994.
[16] G. Compagno, R. Passante, F. Persico, Atom-Field Interactions and Dressed Atoms, Cambridge University Press, Cambridge, 1995.

[17] D.P. Craig, T. Thirunamachandran, Molecular Quantum Electrodynamics, Dover, New York, 1998.
[18] A. Salam, Molecular Quantum Electrodynamics, Wiley, New Jersey, 2010.
[19] T. Thirunamachandran, Intermolecular Interactions in the Presence of an Intense Radiation Field. Mol. Phys. 40 (1980) 393.
[20] D.L. Andrews, (Ed.), Structured Light and Its Applications, Elsevier, Burlington, MA, 2008, 1–341.
[21] A. Ashkin, Acceleration and trapping of particles by radiation pressure. Phys. Rev. Lett. 24 (1970) 156.
[22] M.M. Burns, J.-M. Fournier, J.A. Golovchenko, Optical binding. Phys. Rev. Lett. 63 (1989) 1233.
[23] M. M. Burns, J.-M. Fournier, J.A. Golovchenko, Optical matter-crystallization and binding in intense optical fields. Science 249 (1990) 749.
[24] T.M. Grzegorczyk, B.A. Kemp, J.A. Kong, Trapping and binding of an arbitrary number of cylindrical particles in an in-plane electromagnetic field. J. Opt. Soc. Am. A 23 (2006) 2324.
[25] N.K. Metzger, E.M. Wright, W. Sibbett, K. Dholakia, Visualization of optical binding of microparticles using a femtosecond fiber optical trap. Opt. Exp. 14 (2006) 3677.
[26] F. Chen, G.L. Klimchitskaya, V.M. Mostepanenko, U. Mohideen, Demonstration of optically modulated dispersion forces. Opt. Exp. 15 (2007) 823.
[27] K. Dholakia, P. Reece, M. Gu, Optical micromanipulation. Chem. Soc. Rev. 37 (2008) 42.
[28] A. Jonas, P. Zemanek, Light at work: the use of optical forces for particle manipulation, sorting, and analysis. Electrophoresis 29 (2008) 4813.
[29] J.R. Moffitt, Y.R. Chemla, S.B. Smith, C. Bustamante, Recent advances in optical tweezers. Annu. Rev. Biochem. 77 (2008) 205.
[30] V. Kerasek, O. Brzobohaty, P. Zemanek, Longitudinal optical binding of several spherical particles studied by the coupled dipole method. J. Opt. A: Pure Appl. Opt. 11 (2009) 034009.
[31] P.A.M. Dirac, The Principles of Quantum Mechanics, Oxford University Press, Oxford, 1958.
[32] E.A. Power, S. Zienau, Coulomb Gauge in Non-Relativistic Quantum Electrodynamics and the Shape of Spectral Lines. Phil. Trans. Roy. Soc. Lond. A 251 (1959) 427.
[33] R.G. Woolley, Molecular Quantum Electrodynamics. Proc. Roy. Soc. Lond. A 321 (1971) 557.
[34] E.A. Power, in: Multiphoton Processes, J.H. Eberly, P. Lambropoulos, (Eds.), Wiley, New York, 1978, pp. 11–34.
[35] E.A. Power, T. Thirunamachandran, On the Nature of the Hamiltonian for the Interaction of Radiation With Atoms and Molecules: (e/mc) $\mathbf{p}'\mathbf{A}$, $-\boldsymbol{\mu}'\mathbf{E}$, and All That. Am. J. Phys. 46 (1978) 370.
[36] R.G. Woolley, Gauge invariant wave mechanics and the Power-Zienau-Woolley transformation. J. Phys. A 13 (1980) 2795.
[37] H. Margenau, N.R. Kestner, Theory of Intermolecular Forces, Pergamon, Oxford, 1969.
[38] F. London, Zur Theorie und Systematik der Molekularkräfte. Zeits. fur Phys. 63 (1930) 245.
[39] P.A.M. Dirac, The Quantum Theory of the Emission and Absorption of Radiation. Proc. Roy. Soc. Lond. A 114 (1927) 243.
[40] B.W. Alligood, A. Salam, On the Application of State Sequence Diagrams to the Calculation of the Casimir-Polder Potential. Mol. Phys. 105 (2007) 395.
[41] R.P. Feynman, Space-time Approach to Non-Relativistic Quantum Mechanics. Rev. Mod. Phys. 20 (1948) 367.
[42] R.P. Feynman, The Theory of Positrons. Phys. Rev. 76 (1949) 769.
[43] D.S. Bradshaw, D.L. Andrews, Optically Induced Forces and Torques: Interactions Between Nanoparticles in a Laser Beam. Phys. Rev. A 76 (2005) 033816.
[44] P.W. Milonni, M.-L. Shih, Source theory of the Casimir force. Phys. Rev. A 45 (1992) 4241.
[45] R.R. McLone, E.A. Power, On the Interaction Between Two Identical Neutral Dipole Systems, One in an Excited State and the Other in the Ground State. Mathematika 11 (1964) 91.

[46] J.S. Avery, Resonance Energy Transfer and Spontaneous Photon Emission. Proc. Phys. Soc. Lond. 88 (1966) 1.
[47] D.L. Andrews, B.S. Sherborne, Resonant Excitation Transfer: A Quantum Electrodynamical Study. J. Chem. Phys. 86 (1987) 411.
[48] D.P. Craig, T. Thirunamachandran, Third-Body Mediation of Resonance Coupling Between Identical Molecules. Chem. Phys. 135 (1989) 37.
[49] G.J. Daniels, R.D. Jenkins, D.S. Bradshaw, D.L. Andrews, Resonance Energy Transfer: The Unified Theory Revisited. J. Chem. Phys. 119 (2003) 2264.
[50] A. Salam, A General Formula for the Rate of Resonant Transfer of Energy Between Two Electric Multipole Moments of Arbitrary Order Using Molecular Quantum Electrodynamics. J. Chem. Phys. 122 (2005) 044112.
[51] D.P. Craig, T. Thirunamachandran, New Approaches to Chiral Discrimination in Coupling Between Molecules. Theo. Chem. Acc. 102 (1999) 112.
[52] A. Salam, Intermolecular Interactions in a Radiation Field via the Method of Induced Moments. Phys. Rev. A 73 (2006) 013406.
[53] A. Salam, Two Alternative Derivations of the Static Contribution to the Radiation-Induced Intermolecular Energy Shift. Phys. Rev. A 76 (2007) 063402.
[54] L.C. Dávila Romero, D.L. Andrews, A retarded coupling approach to intermolecular interactions. J. Phys. B 42 (2009) 085403.
[55] S.F. Mason, Optical Activity and Chiral Discrimination, Reidel, Dordrecht, Holland, 1979.
[56] D.P. Craig, T. Thirunamachandran, Chiral Discrimination in Molecular Excitation Transfer. J. Chem. Phys. 109 (1998) 1259.
[57] A. Salam, Resonant Transfer of Excitation Between Two Molecules Using Maxwell Fields. J. Chem. Phys. 122 (2005) 044113.
[58] J.K. Jenkins, A. Salam, T. Thirunamachandran, Retarded Dispersion Interaction Energies Between Chiral Molecules. Phys. Rev. A 50 (1994) 4767.
[59] A. Salam, Intermolecular Energy Shifts Between Two Chiral Molecules in Excited Electronic States. Mol. Phys. 87 (1996) 919.
[60] A. Salam, On the Effect of a Radiation Field in Modifying the Intermolecular Interaction Between Two Chiral Molecules. J. Chem. Phys. 124 (2006) 014302.
[61] L.C. Dávila Romero, J. Rodríguez, D.L. Andrews, On the Electrodynamic mechanism and array stability in optical binding. Opt. Comm. 281 (2008) 865.
[62] A. Salam, Effect of Magnetic ipole Coupling on optical binding Energies between Molecules. J. Comp. Meth. Sci. Eng. 10, 559–567 (2010).
[63] T. Czimár, L.C. Dávila Romero, K. Dholakia, D.L. Andrews, Multiple optical trapping and binding: new routes to self-assembly. J. Phys. B 43 (2010) 102001.
[64] J. Rodriguez, L.C. Dávila Romero, D.L. Andrews, Optical binding in nanoparticle assembly: Potential energy landscapes. Phys. Rev. A 78 (2008) 043805.
[65] P.C. Chaumet, M. Nieto-Vesperinas, Optical binding of particles with or without the presence of a flat dielectric surface. Phys. Rev. B 64 (2001) 035422.
[66] A.J. Pedraza, J.D. Fowlkes, D.A. Blom, H.M. Meyer, Laser-induced nanoparticle ordering. J. Mater. Res. 17 (2002) 2815.
[67] D.L. Andrews, J. Rodríguez, Collapse of optical binding under secondary irradiation. Opt. Lett. 33 (2008) 1830.
[68] J. Rodríguez, D.L. Andrews, Inter-particle interaction induced by broadband radiation. Opt. Comm. 282 (2009) 2267.
[69] J. Rodríguez, D.L. Andrews, Influence of the state of light on the optically induced interparticle interaction. Phys. Rev. A 79 (2009) 022106.
[70] L. Allen, M.J. Padgett, M. Babiker, The orbital angular momentum of light. Prog. Opt. 39 (1999) 291.

CHAPTER 2

State- and Property-Specific Quantum Chemistry

Cleanthes A. Nicolaides[a]

Contents

[a] Theoretical and Physical Chemistry Institute, Hellenic Research Foundation, Athens, Greece
E-mail address: caan@eie.gr

Advances in Quantum Chemistry, Volume 62
ISSN 0065-3276, DOI: 10.1016/B978-0-12-386477-2.00008-5

Abstract The basic argument of the *state- and property-specific approach* (SPSA) to quantum chemistry is that many problems in atomic and molecular physics can be understood conceptually and quantitatively without necessarily trying to obtain as accurately as possible the *total energy* and the corresponding wavefunction of the state(s) involved. Instead, their solution can be achieved economically by using symmetry-adapted, *state-specific* wavefunctions whose computation, following analysis and computational experience, is geared so as to account for at least those parts that describe reliably the characteristics of closed-and open-(sub)shell electronic structures that contribute overwhelmingly to the property or phenomenon of interest. If additional terms in the wavefunction are required by the problem, this is feasible via methods of configuration-interaction or low-order perturbation theory.

This chapter discusses the SPSA assumptions and computational procedures and the related concept of the state-specific *multiconfigurational* (*Fermi-sea*) zero-order description of ground and excited states of the discrete and the continuous spectrum, Ψ_n^0. For each state, Ψ_n, the Ψ_n^0 is used as

reference for analysis and for further improvement of the overall calculation if necessary. Thus, the aim is to obtain Ψ_n in the form $a_0\Psi_n^0 + \Phi_n^{\text{corr}}$, where $a_0 \approx 1$, and the level of accuracy of Φ_n^{corr} depends on the property under investigation.

In this context, certain aspects of the issue of the separation of electron correlation into *nondynamical* (ND) and *dynamical* (D) parts are commented. Optimally, the function spaces of the ND and the D correlations are different, and both depend on how the Fermi-sea orbitals for each problem are chosen and computed.

The arguments are supported by a number of results on prototypical ground and excited states of atoms and molecules. Most of these are compared with results from conventional methods of quantum chemistry, where single basis sets, orbital- or Hylleraas-type, are used.

One set of examples illustrates the computational capacity of the SPSA and concepts such as Fermi-sea or ND correlations, by presenting, or referring to, new and old results for certain properties of the ground and the excited states of the Be atom and its derivative species, Be^-, $(Be)_n$ cluster and Be metal, and Be_2.

Special attention is given to the weak bond of the Be_2 $X^1\Sigma_g^+$ state, which has attracted the interest of quantum chemists for decades. By asserting that the formation of the bond at about 2.5 Å is influenced by the interactions involving excited states, I point to the corresponding significance in zero order (Fermi-sea) not only of *p*-waves but also of *d*-waves, whose origin is in the *valence-Rydberg state mixing* of the lowest ^1D and $^1P^o$ states of Be. Therefore, the Fermi-sea (*active space*) is represented by the Be set of {2*s*, 2*p*, 3*s*, 3*p*, 3*d*} orbitals. The initially heuristic predictions are supported by calculations (using the MOLPRO code) of the lowest 11 Be_2 $^1\Sigma_g^+$ states, whose Ψ_n^0 are obtained at the CASSCF level. These results are verified by the computation of $a_0\Psi_n^0 + \Phi_n^{\text{corr}}$ of the lowest 7 states at the MRCISD level, where indeed $a_0 \approx 1$ over the whole potential energy curve. This type of analysis and the corresponding results imply that by a properly justified choice of the zero-order orbital set, the Be_2 bond can be understood in terms of ND-type correlations, a conclusion which disagrees with that of Schmidt et al. J. Phys. Chem. A 114, 8687 (2010).

1. INTRODUCTION

This chapter reviews the main characteristics of a *state- and property-specific approach* (SPSA) to quantum chemistry as developed and implemented since the early 1970s by the author and collaborators. I discuss several examples and, in addition, I point to key elements of the background from the 1960s.

I also include new results and analysis on the unusual bond of Be_2 in its ground state, $X^1\Sigma_g^+$, and on the spectrum of the *potential energy curves* (PES) of the first 10 excited states of $^1\Sigma_g^+$ symmetry, which were obtained at the level of two models of the theory of electronic structure that have

become major tools in modern computational quantum chemistry (CQC) and whose basic features are both algorithmic and conceptual. These are, the *complete–active space self-consistent field* (CASSCF) as implemented and applied extensively by Björn Roos, Per Siegbahn, and their collaborators [1–3] and the corresponding *multireference configuration-interaction, singles and doubles* (MRCISD). This type of approach to the analysis and computation of electronic structure is keen to concepts and computational steps that constitute elements of the framework of the SPSA.

In appreciation of Roos' very significant contributions to quantum chemistry, I would like to dedicate this chapter to his memory. A shorter version has been published in the special volume of the International Journal of Quantum Chemistry, 2011, dedicated to Roos.

I first came in contact with a publication of Roos about 40 years ago, when my research interests necessitated the calculation of analytic Hartree–Fock (HF) functions in the Roothaan scheme [4–6], for the computation and analysis of electron correlation and its effect on atomic properties [7], with special emphasis on open-shell states whose energy is in the continuous spectrum [8]. Indeed, guided by Roothaan et al. [4, 5] and using the computer code written by Roos et al. [6], this became possible. Until that time, HF calculations on multiply excited configurations of negative ions (see below) had not been carried out, and it was not clear how the analytic HF method would behave. Such valid solutions were vital to the justification and implementation of a polyelectronic theory of resonance (autoionizing) states, which is based on the direct, *state-specific* computation of the localized part of resonance (autoionizing) states [8–10]. This proposal implied the appropriate separation of function spaces describing wavefunctions of states belonging to the continuous spectrum to allow a multistep computational approach that starts with the computation of a square-integrable HF (at that time) or a MCHF solution for such states and proceeds with the incorporation of electron correlation terms representing the remaining of the *localized* and the totality of the *asymptotic* components of the resonance eigenfunction [8–10]. Specifically, the program of Ref. [6] was employed (with small adjustments having to do with orthogonality requirements to one or two lower lying orbitals) in order to compute successfully, for the first time, analytic HF wavefunctions for multiply excited and diffuse open-shell structures corresponding to resonances in He + e inelastic scattering of $^2P^o$ and ^2D symmetry, which could be labeled as $He^-\ {}'2s^2 2p'\ {}^2P^o$ and $'2s2p^{2'}\ {}^2D$ [8–10].

It is worth pointing out that the idea of searching directly for a state-specific solution for the wavefunctions of *multiply excited states* (MES) implies projections on distinct function spaces with separate optimization of some type, thereby avoiding serious problems having to do with the undue mixing of states and channels of the same symmetry. This idea has since been a central element of our analyses and state-specific computations. In fact, in recent years, such concerns have led to appropriate modifications of conventional methods of quantum chemistry, such as perturbation or coupled-cluster,

albeit only for low-lying discrete states, for dealing with problems of lack of proper convergence or instabilities caused by *intruder states*. For a sample of publications on methods of computational chemistry in which a state-specific type of approach has been adopted and/or the problem of intruder states is tackled, see Refs. [11–15].

My next contact with Roos was in person, in September 1978, at a meeting near Lund. Björn had just moved to the University of Lund as a professor of theoretical chemistry. I remember how impressed I was with Björn's kind and lively personality. Part of the discussion at the meeting was on the *direct CI*, a genuine breakthrough for large-scale *configuration-interaction* (CI) methodology that Roos had proposed and applied in 1972 [16] to avoid storing the whole of the energy matrix. Roos' idea and practical demonstrations unleashed the potential for the drastic reduction of the computational requirements accompanying conventional CI methods that are used to solve the *time-independent Schrödinger equation* (TISE). A couple of years later, he, Per Siegbahn, and collaborators published their papers on the CASSCF model [1, 2]. For some applications and literature, see the recent review by Roos and Ryde [3].

The possibility of incorporating the recipe-like model of CASSCF into computer codes of CQC allowed the extensive and successful application over the years by a large number of research groups, including of course that of Roos, thereby creating a huge amount of useful and reliable information on molecular structures and properties. In order to briefly describe here the corresponding concept and practice, I quote from Ref. [3]:

> *The CASSCF model has been developed to make it possible to study situations with near-degeneracy between different electronic configurations and considerable configurational mixing*. . . . ([3], p. 528).
> *The CASSCF method is based on some knowledge of the electronic structure and its transformation during a molecular process (chemical reaction, electronic excitation, etc.). This knowledge can, if necessary, be achieved by making experiments on the computer*. . . . ([3], p. 526).

For statements of similar content concerning the state-specific *Fermi-sea*, see Section 8.

Also in Ref. [3] and in other publications in quantum chemistry, the concepts of *nondynamical* (ND) and *dynamical* (D) correlation are brought up. Since their nature and their practical implementations are, in principle, of critical importance to interpretation and computation and since the SPSA discussed herein contains aspects of such concepts, sections of this chapter have to do with their background, with their *a priori* identification as decoupled components of the total wavefunction, and with their possible use.

As it will be discussed in the following sections, the SPSA does not aim, except when necessary, at obtaining accurate *total energies*. Instead, depending on the problem under consideration, it aims to identify and compute economically, yet reliably, the important relevant parts of the wavefunction

for each state of interest. This has proven beneficial, especially for excited and highly excited states, and has led to the possibility of the practical and transparent solutions of the *complex-eigenvalue Schrödinger equation* for unstable states that are created when *ac* external fields are included [10] and of the *time-dependent Schrödinger equation* (TDSE) for various types of problems [17].

Returning to the content of the first paragraph, I end this introduction with the following:

The direct solution of the open-shell HF equations for configurations such as the He^- ones above was the prerequisite for creating the possibility of computing in a state-specific way correlated wavefunctions and energies of the corresponding resonance states [8–10]. It is recalled that such states normally have nearby states and an infinity of lower states of the same symmetry, and therefore, this approach bypassed the fundamental difficulty stemming from CI diagonalization methods that used (that use) fixed basis sets in conjunction with the search for signs of root stabilization, and which were (are) restricted, by computational necessity, to two- or three-electron systems, for example, Ref. [10]. Instead, it justified the implementation of general polyelectronic methods of computing electron correlation that use a *self-consistent-field* (SCF) solution as a zero-order reference wavefunction corresponding to a particular configuration or to a very limited superposition of important configurations, and which at that time, (1971–72), had been carried out only for ground or lowest-lying excited discrete states. In fact, the state-specific HF wavefunction for such excited open-shell configurations accounts very effectively for the strong orbital *relaxation effects*, which, in the alternative approach of diagonalization of the Hamiltonian matrix with a fixed basis set, normally requires the wavefunction expansion to be very large, and even then, if the basis is inadequate, inaccuracies may remain.

Given the scope of the present paper, I point out that the initial computations of the localized part of resonance states in Ref. [8] employed energy matrices of very small dimensions. Going beyond the HF calculation, the first stage of computation accounted for those configurations that appeared as contributing heavily to the character of the wavefunction and can be attributed to ND electron correlation. The second stage consisted of adding ("by hand" at that time) only a couple of doubly excited configurations and obtaining the total energy and wavefunction with a single diagonalization of the full small matrix using the correlation orbitals computed earlier for the ND part of the wavefunction. This calculation revealed that for certain open-(sub)shell states, many, rather than, say, one or two, configurations could acquire relatively large coefficients, thereby reducing the degree of validity of the single-configuration HF approximation and the models of electron correlation that depend on it.

For example, let me consider the localized component of the He^- $'2s2p^{2'}\ ^2D$ resonance state mentioned above. In 1971, before the publication of [8],

no HF, let alone MCHF, calculations on such states existed. In fact, at that time, the theory and experience from ground-state many-electron calculations was not enlightening as regards the extent to which, and the manner in which, various states, mainly excited, ought to be represented in zero order by superpositions of a number of configurations. Such a solution was obtained in later years numerically [9]. It turns out that it is characterized by the following six-term superposition of *symmetry-adapted configurations* (SACs), involving orbitals from two hydrogenic shells:

$$|\mathrm{He}^{-}\ {}^{\prime}2s2p^{2\prime}\ {}^{2}D\rangle\colon 0.880(2s2p^2) - 0.266[(2s2p)^1P^o3p] - 0.234(2s3p^2) - 0.195(2s^23d) - 0.127[3d(2p^2)^3P] + 0.111[3d(2p^2)^1D] \quad (1)$$

It is such types of heavy mixing that, together with additional evidence (see following sections), led to the proposal of optimizing the quantitative description of electronic structures by computing appropriately chosen multiconfigurational Fermi-sea zero-order wavefunctions (Sections 3 and 8).

With respect to the above, I note that following the publication by Froese Fischer [18] and by McCullough [19] of codes for the numerical solution of HF (or MCHF) equations for atomic and for diatomic states respectively, it has been demonstrated on prototypical unstable states (neutral, negative ion, molecular diabatic) that the state-specific computation of correlated wavefunctions representing the localized component of states embedded in the continuous spectrum can be done economically and accurately, for example, [9, 10, 17, 20–22] and references there in.

1.1. Two notions that are considered in the discussion of this article

Summarizing, the above brief discussion contains two notions that this chapter covers together with various descriptive and numerical examples.

The first notion constitutes the quintessence of the SPSA. It is the possibility of obtaining useful and reliable information using relatively small, and manageable for further application, wavefunctions constructed so as to (hopefully) contain those features that are pertinent to the property or process (i.e., off-diagonal matrix elements) under investigation, especially for problems involving excited states. Of course, there are always problems in which it is necessary to know the total energy of a state to high accuracy. By choice, such cases have been tackled within the SPSA only for prototypical excited states of few-electron systems, where reasonably fast convergence to energies of acceptable accuracy is possible without the need of large-size calculations.

In this context, it is important to remember that the solution of the *many electron problem* (MEP) in quantum chemistry is not exhausted with the

calculation of total energies and properties of the ground or the low-lying excited states of either small or large systems. For example, consider three classes of states, normally described as *highly excited states*, which are present in various modern fields of many-electron atomic and molecular physics and chemistry and with the absorption, internal transfer, and emission of energy in the form of radiation or of particles.

1. *Mixed valence-Rydberg-scattering states*. For example, the effects of this type of interaction are often observed via high-resolution laser spectroscopy of high-n Rydberg states perturbed by *doubly excited states* (DES). The proper treatment of such states and the demands imposed by the related measurements (e.g., high-resolution laser spectroscopy) requires the combination of some type of theory of the *quantum defect* capable of producing, from first principles and not semiempirically, usable polyelectronic wavefunctions [21–25].
2. States whose zero-order labels are configurations with one or two holes in the inner subshells (*inner-hole* states). Depending on the system and the stage of its ionization, these are produced by probes whose energy normally ranges from the UV to the soft and main X-ray regions. Theoretical considerations, which are supported by quantitative results, indicate that electron correlations are always important, not only because of the large number of correlating electrons (especially in heavy atoms) but also because of the possibility of both *valence* and *hole-filling* electron rearrangements [10, 22] and references there in. State-specific electron correlation treatments of such states were carried out in the 1970s and early 1980s for atomic and metallic systems [26a, 27a, 27b, 27c, 28], thereby recognizing the special significance of particular types of electron correlations for such states. Regarding metals, advantage was taken of the atom-like inner shells and the state-specific nature of wavefunctions of large atomic clusters with and without an inner hole.

   For example, the SPSA prediction of the binding energy (BE) of the 1s electron in the Be metal (115.4 eV) was in perfect agreement with experiment (115.2–115.6 eV) [28]. This was computed by assuming the relationship [28],

$$(\text{core level BE})_{\text{metal}} \approx (\Delta\text{SCF})_{\text{cluster}} + (\Delta E)_{\text{atomic correlation}} \tag{2}$$

   In the approximation (2), Δ indicates that the two quantities on the right-hand side are obtained by computing separately the initial and the final (hole) states. I note that in the 1970s and early 1980s, the problem of determining the BE of the 1s electron in the Be metal (in general, of inner electrons in metals), which is measured via photoelectron spectroscopy, was mostly tackled via models of the independent particle type, with

notions such as *chemical shift*, *hole-screening*, and *intra- and extra-atomic relaxation*." See Refs. [26a, 28].

The computation of $(\Delta E)_{\text{atomic correlation}}$ is a many-body problem by itself [26a–26c, 27a–27c]. The SPSA calculation for Be is presented in [27a].

Solving the problem from the point of view of the SPSA, Eq. (2), also renders interpretation and possibility of prediction easier. For example, one of the findings in Ref. [28], which has general validity as regards the understanding of possible valence electron rearrangement in such metallic clusters when near-degeneracies are present, is that, "Upon creation of the 1*s* hole, the p character of the valence band increases" (abstract of Ref. [28]). The consequence of this finding was understood as follows: "The calculated significant contribution of p character in the valence band for the excited state provides the first semiquantitative explanation for the fact that the observed fluorescence in the solid state is larger than that calculated in the free atom: A p-character electron is allowed a radiative transition to the 1*s*-hole, something which is forbidden for the 2*s* electron in the atomic case." ([28], p. 859).

Another prediction that has to do with *inner-hole* states is that the combination of valence and hole-filling electron rearrangements normally increases, compared with the standard case of ground states, the relative significance of *three-electron correlations* principally because of the relatively smaller energy denominators that are due to *hole-filling* rearrangements [22]. This is mentioned because, as is well known, in the normal case of electron correlation energy and wavefunction in the ground state, the significance of triple excitations is minimal.

3. States whose zero-order labels are configurations, which are *multiply excited* (e.g., doubly, triply, or even quadruply excited) with respect to the ground main configuration, for example, see Ref. [10]. They can be created by the absorption of one or more photons. It is important to stress that these states are determined as solutions of their state-specific Schrödinger equations and do not correspond, except perhaps by occasional accident, to the hierarchy of *virtual* excitations that appear in the many-electron treatments of electron correlation in ground states by the conventional methods of computational chemistry.

Of the three categories: (1), (2) and (3), only (3) is discussed briefly in this chapter. Guidance for the other two can be found in the references.

The second notion is concerned with aspects of the issue of the *a priori* identification of ND and D correlations and the choice of the state-specific set of zero-order orbitals and multiconfigurational wavefunctions in terms of which this identification is assumed and implemented. In this context, I use examples from published results and from new computations.

I close by pointing out that the herein discussed concepts regarding the general criteria for the choice of function spaces remain essentially the same

for relativistic Hamiltonians, although the overall theoretical construction and computational implementation become more complex.

2. COMMENTS ON FACTS FROM THE THEORY AND COMPUTATION OF GROUND STATES WITH SINGLE DETERMINANTAL ZERO-ORDER WAVEFUNCTIONS

"It is now perfectly clear that a single-configuration wavefunction must inevitably lead to a poor energy."

C. A. Coulson at the conference on Molecular Quantum Mechanics, Boulder, Colorado, June 21–27, 1959, published in Rev. Mod. Phys. ***32****, 170 (1960)*

In the many decades of quantum chemistry, the MEP was a problem of computing accurately the contribution of *electron correlations* to the *total energy* and of obtaining the corresponding N-electron wavefunction. In this context, even to this day, most of the relevant publications on formalism and on computational methodology have been applied only to *closed-shell ground states*, and their zero-order reference wavefunction being a single Slater determinant. This situation includes a few atomic states and, fortunately for molecular chemistry, many molecular ground states in the region of equilibrium geometry. A clear presentation of the essence of the computational methods that have dominated the literature of quantum chemistry for ground states can be found in the book of Szabo and Ostlund [29]. In this section, I simply recall certain facts of this area, which can be used as reference points.

After the computation of Φ_{HF} became routinely feasible in the 1960s [4], much of the work in quantum computational chemistry has been devoted to the computation from first principles of the total energy, E, via the calculation of the correlation energy, E_{corr}, moving from systems with a few electrons to larger ones, with lighter or heavier atoms. In the latter case, relativistic effects make an increasingly important contribution.

For the sake of this discussion, I assume the formal use of complete sets of one-electron and N-electron basis functions that are obtained from the solution of the HF equations as occupied and as unoccupied ('virtual') orbitals. The exact wavefunction, Ψ, can be written formally as a sum of two orthogonal parts:

$$\Psi = \Phi_{\mathrm{HF}} + \sum_i c_i \Delta_i \equiv \Phi_{\mathrm{HF}} + X_{\mathrm{corr}} \tag{3}$$

$$\text{with } \langle \Phi_{\mathrm{HF}} | X_{\mathrm{corr}} \rangle = 0, \text{ and normalization } \langle \Phi_{\mathrm{HF}} | \Psi \rangle = 1 \tag{3a}$$

Δ_i are N-electron Slater determinants, representing virtual electron excitations from the occupied Φ_{HF}, in terms of one, two, three, etc. *virtual* spin orbitals, appropriately replacing occupied ones. We may then write

symbolically

$$X_{\text{corr}} = \chi_s + \chi_d + \chi_t + \chi_q \ldots . \tag{4}$$

The total energy is obtained from the TISE, $E|\Psi\rangle = \mathbf{H}|\Psi\rangle$, as $E\langle\Phi_{\text{HF}}|\Psi\rangle = \langle\Phi_{\text{HF}}|\mathbf{H}|\Psi\rangle$ so that

$$E = E_{\text{HF}} + E_{\text{corr}} \tag{5a}$$

$$E_{\text{HF}} = \langle\Phi_{\text{HF}}|\mathbf{H}|\Phi_{\text{HF}}\rangle, \quad E_{\text{corr}} = \langle\Phi_{\text{HF}}|\mathbf{H}|X_{\text{corr}}\rangle \tag{5b}$$

$$\text{with } E = \langle\Psi|\mathbf{H}|\Psi\rangle/\langle\Psi|\Psi\rangle \tag{6}$$

Given that the Hamiltonian is a one- and two-electron operator, basis set orthogonality and the restriction of Brillouin's theorem, $\langle\Phi_{\text{HF}}|\mathbf{H}|\chi_s\rangle = 0$, introduce a formally and heuristically valuable selection rule for the MEP. It follows from Eqs. (4 and 5b) that

$$E_{\text{corr}} = \langle\Phi_{\text{HF}}|\mathbf{H}|\chi_d\rangle \tag{7}$$

Of course, in the actual computation, one first has to go to all orders to establish the exact X_{corr} of Eq. (4) from which Eq. (7) follows. Nevertheless, in practice, for atomic and molecular ground states where the shell model holds well and the zero-order reference is a closed-shell, single determinantal HF wavefunction, it remains true that the dominant contribution to the E_{corr} comes from the double excitations (electron pair correlations), although for a given state, the exact magnitude of each term of Eq. (4) depends on the computational method and on the function spaces that are used.

The next type of electron correlation contributing the most to the total energy is the one representing products of pair correlations that are present in χ_q. This fact was first stated explicitly by Sinanoğlu [30] following a penetrating many-electron formalism and guided by the detailed electron correlation results and conclusions of Watson [31] on Be and Ebbing on LiH [32]. A simple formal justification of this fact can be summarized as follows: In terms of Schrödinger perturbation theory (PT), the correlations in the wavefunction to first order, $\Psi^{(1)} = \Phi_{\text{HF}} + X^{(1)}_{\text{corr}}$, are determined by double excitations. Brillouin's theorem implies that the coefficients in χ_s result at a higher order and are very small. The corresponding total energy contains the contribution from the terms up to third order, that is, up to $\langle X^{(1)}_{\text{corr}}|V - E_1|X^{(1)}_{\text{corr}}\rangle$. Therefore, the total energy in a systematic calculation of ground states of relatively small systems is determined to a good level of accuracy by the sum of the following terms: $E_{\text{HF}}(\equiv E_0 + E_1), E_2 = \langle\Phi_{\text{HF}}|V|X^{(1)}_{\text{corr}}\rangle$ (pair energies and a very small contribution from single excitations coming from higher order), and $E_3 = \langle X^{(1)}_{\text{corr}}|V - E_1|X^{(1)}_{\text{corr}}\rangle$ (mainly pair–pair interactions). If higher accuracy is desired, one has to compute the terms that enter in higher

orders of perturbation theory. Obviously, the precise magnitude of such contributions depends on the degree of completeness and numerical accuracy of the basis functions. Even for second-order PT energies in various atoms and molecules, the question of their exact values with complete sets was studied exhaustively only recently [33].

The basic attribute of ground-state electronic structures that are labeled by a single determinantal $\Phi_{\rm HF}$, which renders Eq. (3) valid and makes things work, is that, in general, $E_{\rm HF}$ represents about 98–99% of E while the contribution of $X_{\rm corr}$ to Ψ is very small, that is, $\langle X_{\rm corr}|X_{\rm corr}\rangle \equiv \sum_i c_i^2$ is less than 0.2, say. In spite of this, physically (chemically) relevant properties that depend on very small differences (e.g., stability of negative ions, certain barriers in chemical reactions, or dipole moments along a coordinate) very often are determined by these small differences, either in the total energy (which is sometimes required to be of "chemical accuracy" (∼1kcal/mol)) or in the wavefunction, induced by small but numerous (in principle infinite) terms in $X_{\rm corr}$.

I now come to a well-known issue in quantum chemistry: On the one hand, the widely applied approaches to the solution of the TISE obtain solutions that are normally judged by the degree of convergence to the (generally unknown) exact total energy. For ground states, the minimum principle is a safe guide when full CI is applied. On the other hand, properties and observable quantities depend either on energy differences or on diagonal or off-diagonal matrix elements of operators whose characteristics are different than those of $\mathbf{H}$ and therefore must have a different dependence on characteristics of the N-electron wavefunctions, such as expansion coefficients and basis functions. Hence, even when terms in $X_{\rm corr}$ do not contribute much to the total energy, such as the singly excited determinants, χ_s, in Eq. (4), they may contribute in a significant way to that property. And vice versa: A few of the doubly excited determinants, contributing significantly to the correlation energy, may have a small contribution to the property.

For example, suppose that after a full CI calculation with a complete N-electron set, we have obtained the exact wavefunction, Ψ. The formal relations regarding energy are given by Eqs. (3–7). Now consider a one-electron Hermitian operator, representing a property, say $\boldsymbol{O}(i)$, where i are electron coordinates. From Eqs. (3 and 4), $\Psi = \Phi_{\rm HF} + \chi_s + \chi_d + \chi_t + \cdots$. Considering that the coefficient of $\Phi_{\rm HF}$ is by far the largest, normally larger than 0.92 when Ψ is normalized to one, and that the next important coefficient is χ_d, say about 0.25, the expectation value $\langle\Psi|\boldsymbol{O}(i)|\Psi\rangle$ ought to be determined mainly by $\langle\Phi_{\rm HF}|\boldsymbol{O}(i)|\Phi_{\rm HF}\rangle$. However, in certain situations, it is the corrections due to $X_{\rm corr}$ that matter, for example, Ref. [7]. The origin, the significance, and the degree of such corrections depend on the state and the operator. Specifically, consider the corrections due to χ_s and χ_t, whose contributions to the correlation energy are consistently very small and whose coefficients are also very small. Yet, because of the coupling that χ_s has with the dominant

components Φ_{HF} and χ_d, that is, because of the matrix elements $\langle \Phi_{\mathrm{HF}} | \boldsymbol{O}(i) | \chi_s \rangle$ and $\langle \chi_d | \boldsymbol{O}(i) | \chi_s \rangle$, its contribution to the final result may be critical. To a much lesser extent, this must hold for χ_t because of the matrix element $\langle \chi_d | \boldsymbol{O}(i) | \chi_t \rangle$.

One may argue that the concern about such details is eliminated when an accurate computation of a *total-energy wavefunction* is achieved. This is true. On the other hand, in any approach that is based on the separation (3) and aims at the calculation of total energies, it is inevitable that, regardless of the digit of numerical accuracy of the total energy, if the method produces wavefunctions as well (a couple of methods do not), these are huge (by the criterion of the number of Slater determinants in their expansion), especially if they are obtained by the conventional methods of using a large basis set that is common for the occupied and the unoccupied ("virtual") orbitals. One may then find himself "lost in the translation" of such calculations as regards transparency of crucial features that are often necessary for the understanding of, say, the main sources of electron correlation and notions of transferability of information on various properties from system to system.

Furthermore, as is well known, approaches whose basic aim has been to obtain accurate total energies of closed-shell states cannot be considered optimal or feasible, or even relevant, for a multitude of challenging problems of quantum chemistry, such as the following:

1. Structures and dynamics that have to do with the plethora of types of electronic excited states, in the discrete or the continuous spectrum.
2. Properties of atomic and molecular states, the latter along the potential energy surfaces (PES) that are known up to their fragmentation thresholds, rather than at just the region of equilibrium geometries. These include rates of transitions between states.
3. Time-dependent dynamics requiring the nonperturbative solution of the TDSE.

In cases (1) and (2), the HF *single-configuration approximation* (SCA) is, in general, inadequate as a zero-order model, either for purposes of efficient high-level computation or for purposes of semiquantitative understanding of the main features of a process or a property.

Furthermore, the quantum chemistry of the ground state is obviously limited as regards the variety of possible physical and chemical problems. For example, it has nothing to do with the possibility of treating the MEP that is present in all time-dependent phenomena of electronic excitation induced by the currently available great variety of photon sources (case 3, above). Instead, such time-dependent MEPs require the development and implementation of theory that can handle effectively the ab initio solution of the N-electron TDSE. Since I will not discuss this subject here, the reader is referred to a recently published review of the *state-specific expansion approach*

(SSEA) that was introduced in the early 1990s as a practical and transparent methodology for the solution of the *N*-electron TDSE [17]. The SSEA is possible because it is based on the use of small but efficient state-specific wavefunctions for the discrete and the continuous spectrums, whose choice is supposed to follow the requirements of each problem.

3. STATE- AND PROPERTY-SPECIFIC WAVEFUNCTIONS

The essence of the concepts and the results that are discussed in this chapter is that the MEP should not be considered only in the context of the requirement of solving "exactly" the TISE with the purpose of obtaining accurately the total energy and the corresponding wavefunction. This is because the MEP is omnipresent in many physical and chemical situations, in addition to those that require accurate numerical knowledge of the total energy of the ground state of a particular symmetry. The theoretical needs for these other situations, which are often more demanding and challenging, can be understood via the use of wavefunctions that do not necessarily produce an accurate total energy.

For example, the MEP is present in the plethora of problems involving excitation of one or more electrons to excited states that are located either in the discrete or the continuous spectrum (i.e., resonance or autoionizing states). Such excitation or de-excitation processes require the computation of their excitation energies (i.e., of energy differences) and transition probabilities. It is also present in problems where the desideratum is the calculation of observable properties other than total energies, ranging from fine and hyperfine structures to, say, hyperpolarizabilities. In such and other cases, the *total-energy wavefunctions* (the meaning of the term must be considered in the context of the discussion) need not necessarily be the most appropriate to use without further analysis.

Indeed, the success of computations of total energies that has been generally observed from the implementation of algorithms capable of producing and processing huge wavefunction expansions (up to a few billion (!) of determinants), may obscure the fact that, sometimes, in spite of its size, a conventional computation may not be as accurate as anticipated regarding a particular property because of corresponding intrinsic deficiencies in the basis set that is used, for example, [21].

In view of the above, the following assertion is made:

Indeed, for certain crucial cases of very small energy differences in the discrete or the continuous spectrum, it is often necessary to aim at computing highly accurate total energies. This is also necessary when the rovibrational spectrum for a particular Born–Oppenheimer (B-O) state must be known with great precision. In fact, in certain cases, going beyond the B-O approximation may be desirable.

However, for many other properties and phenomena, this is not necessary, provided a sufficient understanding of the dominant characteristics of the wavefunctions corresponding to the problem under study is possible. If such wavefunctions can be produced optimally and understood systematically, then selected parts of the remaining electron correlation can be computed economically while considering the particularities of the problem of interest. In this way, a variety of properties of stationary electronic states in the discrete and the continuous spectrums and their use for solving the TDSE can be computed reliably while avoiding additional efforts toward the gathering of information of diminishing returns. The domain of such problems is much larger than that of the quantum chemistry of the ground state.

The essence of the above argument permeates much of our work since the early 1970s, for example, [7–10, 17, 20–22, 26a–26c, 34], a basic element of which, namely the utility of the proper choice of the zero-order model, Fermi-sea zero-order function space, is reviewed here. Here, I use the generic name SPSA (also called *state-specific theory* (SST)) because of the special attention that is given to the nature of each state and property of interest and to the related theoretical and computational requirements of optimized function spaces.

3.1. The form of state-specific wavefunctions

Although the concepts behind the choice of the form given below are briefly presented in the next section, I write the equation here, eq. (8), in order to underline the fact that the aim of the SPSA is to treat problems of quantum chemistry by producing suitably correlated wavefunctions with short expansions, ostensibly containing, to a very good approximation, the information that is relevant to the problem of interest than to try to first compute accurate total energies.

The fundamental fixed-nuclei approximation, in which the nuclei are treated as distinguishable classical particles with positions in physical space, allows for the electronic structure of ground and excited states of both atoms and molecules to be ruled by the same principles, concepts, and approximations, such as the occupation of symmetry-adapted atomic or molecular orbitals by electrons, subject to the Pauli exclusion principle. The resulting basic interpretative and computational tool is the N-electron *symmetry-adapted configuration* (SAC), be it atomic or molecular. It is denoted here by Φ. When the SAC is adopted as a conceptual and computational tool, it is possible to use the same concepts and theoretical methods in order to treat the electronic eigenfunctions of states of both atoms and small molecules for each fixed geometry.

For example, the understanding that can be drawn from the study of atomic wavefunctions and spectra as a function of the nuclear charge,

Z (taken as a mathematical continuous parameter) as to the choice of zero-order wavefunctions when *valence-Rydberg state mixing* is present, is in principle applicable to situations of avoided crossings of potential energy curves of diatomics. Such mixings are often of crucial importance in defining the proper zero-order multiconfigurational wavefunction since both valence and Rydberg structures play a role in defining the 'Fermi-sea wavefunction' (Sections 4, 7, 8, 9, 10).

The wavefunction analogous to Eq. (3) for an arbitrary N-electron electronic state Ψ_n can be written, in terms of SACs, as follows:

$$\Psi_n = a_0\Psi_n^0 + \sum_{i=1}^{K} a_i\Phi_n^i, \quad |a_0|^2 + \sum_{i=1}^{K} |a_i|^2 = 1, \quad K \to \infty \tag{8}$$

$$\equiv a_0\Psi_n^0 + \Phi_n^{\text{corr}} \tag{8a}$$

The form (8) is now invoked in order to make the following statement:

3.2. Criterion of the SPSA

The most important characteristic of a good many-electron theory should be to decrease in an optimal way the labor of computation and the complexity of formalism without losing the physically significant accuracy while bringing out the basic features of the solution to the problem under study. With regards to Eq. (8), the effort must be on choosing and computing a compact zero order Ψ_n^0 so as to obtain a $|a_0|$ that is close to unity, in which case Ψ_n^0 is a reliable zero-order label of the state Ψ_n. This simple condition is the analog of that which characterizes the case of Eqs. (3–6). It is exemplified by the wavefunction of Eq. (1).

Then, for the understanding of various problems and properties other than the numerically exact value of the total energy, only a small part of Φ_n^{corr} needs to be considered beyond Ψ_n^0, if at all, depending on the nature of the relevant operator that acts on Ψ_n^0 (e.g., Coulomb Hamiltonian, dipole operator, or hyperfine structure operators).

In general, the steps of the SPSA toward the computation of the correlated wavefunction for each state and the property under consideration are as follows (adjustments in special cases are inevitable): Once Ψ_n^0 is established with self-consistent orbitals that are numerically accurate, one should seek the form of the part of the remaining wavefunction that results from the action on the Fermi-sea Ψ_n^0 of two operators: The Hamiltonian and the operator of the property that is being studied. This provides the information to first order beyond the MCHF (or nearly so) Ψ_n^0 on the symmetry and the spatial characteristics of the function space that is created by the action of the two operators. The final result for the total wavefunction is obtained *to all orders* via diagonalization of the total matrix after judicious choices and

optimization of the correlation and perturbed virtual orbitals. The procedure is exemplified in the next section in terms of the *first-order theory of oscillator strengths* (FOTOS).

In order for compactness and accuracy to be satisfied by Ψ_n^0, the orbitals of the constituent configurations must be obtained self-consistently and as accurately as possible. For atoms and diatomic molecules, this can be achieved by solving the relevant MCHF equations numerically. A rough but reliable criterion for the initial choice of the important configurations is based on the use of the fundamental result of perturbation theory, whereby the mixing coefficient is obtained, to first order, by {interaction matrix element/energy difference} with respect to the main reference configuration. The normally useful criterion of location of orbitals according to the shell structure is certainly relevant, but one need not use it as a strict constraint, especially for excited states (e.g., valence-Rydberg state mixing) and/or for large atoms where the density of subshells increases.

Our work has used the Coulomb (i.e., nonrelativistic) or the Breit–Pauli (i.e., quasi-relativistic) Hamiltonian. Relativistic structures and wavefunctions, without or with relativistic radials, follow the same concepts as in the nonrelativistic treatment, only that here, the differences between the level energies are generally smaller and, hence, the sensitivity of the mixing coefficients to the choice of orbitals and of the mixing configurations is expected to be much higher.

Finally, in certain problems involving mainly excited states, it is preferable to first partition the total function space into two or more (rarely) zero order separately optimized spaces, each representing one or more moieties of physical significance, which are then allowed to mix. This implies the application of *nonorthonormal configuration interaction* (NONCI).

I point out that Eq. (8) also holds for the SPSA of isolated highly excited states whose energy is in the continuous spectrum and are *unstable* [10]. In this approach, which solves a *complex eigenvalue Schrödinger equation*, real and complex functions are used together with the complex scaling of the appropriate coordinates. Hence, the mixing coefficients are complex, and this is why the absolute values appear in the normalization condition in Eq. (8). The work that is explained in [10] has shown how advanced methods of electronic structure can be amalgamated with appropriate theory of resonance (autoionizing) N-electron states.

An additional remark has to do with the quantum chemistry of doubly or multiply excited states embedded in *channels of series of Rydberg and scattering states*. In such cases, the SPSA has been implemented by first dividing the total function space into two parts: One containing the separately optimized valence states and the other containing the physically relevant channels. The theory for this approach and applications to prototypical cases can be found in Refs. [8, 10, 22–25]. A discussion on special topics concerning MES is given in Section 4.

The choice of Ψ_n^0 so as to satisfy $a_0 \approx 1$ is what the introduction of the concept of the Fermi-sea of orbitals is all about. (I note that the methodology toward the satisfaction of this criterion is understood much better today than in the late 1960s and early 1970s.) It may involve either *state-specific diabatic states*, for example [35a, 35b], MCHF-type calculations, or in special cases as in the example (4.1) on the ethylene molecule and in example (4.2) on the computation of electron correlation in Be, NONCI calculations. The background and the syllogism that led to the Fermi-sea is discussed in the following sections. The implementation of the criterion is demonstrated in Section 10 with new calculations at the CASSCF (Ψ_n^0) and MRCISD ($a_0\Psi_n^0 + \Phi_n^{\rm corr}$) level for the first 11 $^1\Sigma_g^+$ states of Be_2.

4. EXAMPLES OF THE APPLICATION OF THE SPSA FROM PUBLISHED WORK

4.1. Separate optimization of the relevant function spaces: zwitterionic excited states of polyenes and the sudden polarization effect

In the introduction of Ref. [36] on the topic of this example, the justification of using the SPSA and its methods is given in several paragraphs. I quote the following one:

> *"In the state-specific theory, the zeroth order and the virtual orbital space for each excited state of interest is optimized separately. In many interesting problems, the corresponding zeroth-order configurations yield near degeneracies and strong mixings – which, in general, are functions of geometry. In such cases, their rigorous calculation requires the explicit consideration of nonorthonormality (NON) corrections."* ([36], p. 3161).

In other words, in problems in which two or more electronic structure moieties are perceived as having distinct function spaces, instead of expanding the wavefunctions in a very large common basis set (see below), it should be physically more relevant and transparent to identify the main parts of the corresponding wavefunctions and to compute them separately in a state-specific way. When the total wavefunction is put together, it is then necessary to apply methods of NONCI, e.g., see [36, 37] for problems in polyenes. Actually, the possible alternative, namely that of an MCHF calculation in the full space of the important states, may not even converge properly when the mixing is strong and the energy differences are small. Such situations can be met not only in molecules but also in highly excited atomic states, for example, triply excited, where, due to the increased density of states, the degree of zero-order configurational mixing increases (see example (4.5) on multiply excited states). In atoms, what saves the day is the possibility of solving

the MCHF equations numerically, provided suitable considerations, such as appropriate orbital rotations, are applied when needed.

By the early 1980s, the quantitative understanding of the phenomenon *sudden polarization* in polyenes had attracted the interest of a few quantum chemists, for example, Ref. [38–40]. Later and more recent works on the excited states of such systems can be found in Refs. [41–43].

This is a typically difficult problem in which the crucial element is the possibility of understanding the electronic structures and properties of the relevant excited states than that of determining total energies. The closely lying states of ethylene (Z and V) and butadiene (Z_1 and Z_2) were chosen as the first application of the state-specific *NONCI-for-molecules* approach that was published and applied in Refs. [36, 37]. Each excited state of interest was optimized separately as a small expansion in terms of the Fermi-sea configurations, and then, the NONCI was carried out in order to allow their mixing. The important relaxation and correlation effects, which are state specific, are thus accounted for in a transparent way while avoiding the large expansions that are needed for such problems when the conventional CI is applied.

In 90° twisted ethylene, there are two zwitterionic singlet states, Z and V [36, 38–40], which in C_s symmetry are described in zero order by the superpositions.

$$\mathrm{Z}\colon \frac{1}{\sqrt{2}}\{7a'^2 + 2a''^2\}, \quad \mathrm{V}\colon \frac{1}{\sqrt{2}}\{7a'^2 - 2a''^2\}$$

In the 90° conformation (D_{2d}), these states possess no permanent dipole moment. However, pyramidalization of one of the C atoms (i.e., bending of one of the CH_2 groups) gives rise to a "sudden" polarization by breaking the symmetry. The sharp variation and magnitude of this polarization were investigated 30 years ago via large (for that time) CI (5000–6000 configurations) with a variety of basis sets [39, 40]. On the other hand, the SPSA NONCI theory of Ref. [36] was constructed as just a 6×6 problem. Comparison with the large, conventional CI results showed very good agreement [36]. The sudden rise takes place from 0° to about 20°. For angles around and larger than 20°, the mixing is reduced, the Z state is described well by MOs from the $7a'^2$ configuration, and the dipole moment becomes stabilized in all theoretical approaches. This result suggests similar descriptions for other symmetry-breaking or valence-Rydberg state mixing situations in molecules. I note that when a 6×6 CI using the same configurations but with an orthonormal basis set was carried out, the results were totally wrong for small angles, where it cannot restore the symmetry of the D_{2d} group.

In the case of butadiene, there is no sudden polarization since there is asymmetry already in the twisted conformation. Table 2.1 contains the results for butadiene from Ref. [37].

Table 2.1 Results for the zwitterionic states (Z_1 and Z_2) of terminally twisted butadiene[1]

		Dipole moment (in D)		
		MRD-CI	SPSA-NONCI	
Angle	Excited state	(~8500 configurations)	2 × 2	6 × 6
0°	Z_1	5.73	5.77	5.66
	Z_2	6.11	6.15	6.11
26°	Z_1	5.74	5.80	5.70
	Z_2	6.27	6.33	6.28
			Energy differences (Kcal/mol)	
0°		17.1	16.1	17.2
26°		26.8	25.7	26.3

[1] Dipole moments and energy differences as a function of the pyramidalization angle. Comparison between results from conventional CI with about 8500 configurations and from the SPSA-NONCI of dimensions 2 × 2 and 6 × 6 (From Ref. [37]).

Table 2.2 Convergence and efficiency of two different types of calculations for the Be^1 *S* ground state[1]

	Conventional full CI	SPSA
Number of basis functions	24	3 Fermi-sea (Ψ_n^0 of Eq. (8)) and 16 virtual orbitals
SCF energy (au)	−14.57207	−14.57302
Fermi-Sea energy (au)		−14.61685
CI (first column) and NONCI	−14.65689	−14.65826
Number of spin-adapted configurations	27,600	31 (177 determinants)
CPU time micro-VAXII	20 h	1.5 h

[1] Calculations from 1988. See text.

4.2. Rate of convergence: the ground state of Beryllium

This example is given as Table 2.2 and illustrates the efficiency of methods of the SPSA even for ground states when near-degeneracy is present (see Section 5). The example has to do with the rate of convergence to a total energy and wavefunction of practical accuracy, not to an exact energy [34].

The work was done in 1988 on a micro-VAXII and concerns hierarchical calculations on the Be^1 *S* state by two methods. The SPSA results, obtained

according to Eq. (7), are compared with those obtained using conventional methods of quantum chemistry that use large basis sets. The "full CI" calculations were done with an old version of the code "GAMESS" [44] and employed an uncontracted atomic basis set. The SPSA computations used the MCHF—Fermi-sea orbitals, 1*s*, 2*s*, and 2*p*, obtained numerically with the code of Froese Fischer [18] and analytic virtual Slater-type orbitals (STOs) representing the single, double, triple, and selected quadruple correlation functions. For the pair functions for the $1s^2$, $1s2s$, and $2s^2$ electrons, optimization was done separately and NONCI was applied.

In other words, for atoms and diatomics, in the SPSA computational methodology that was first implemented in the 1970s, a mixture of numerical and analytic orbitals is used to improve convergence and accuracy, for example, [20, 26a–26c]. Specifically, on the one hand, the accuracy of Ψ_n^0 is secured in terms of the radial details. On the other hand, the overall calculation, which involves $a_0\Psi_n^0$ and parts of Φ_n^{corr}, remains flexible by using analytic virtual orbitals that are optimized variationally.

In the case of the Be calculation above, the optimization of the virtual orbitals for each pair was done separately. Since such sets of virtual orbitals are not orthonormal among them, the final results were obtained from a total NONCI.

4.3. Transition properties: first-order theory of oscillator strengths (FOTOS)

It is not necessary to explain the significance of being able to compute reliable transition probabilities. These quantities are at the heart of spectroscopy.

The calculation of off-diagonal matrix elements means that two, rather than one, wavefunctions must be accurate for the transition of interest. In fact, when the total response of a state is studied with respect to its *energy shift and broadening* (decay into the continuous spectrum [10]), there are many different field-induced off-diagonal matrix elements.

In accordance with the meaning of the title of the paper, the claim is that given the characteristics of the perturbing operator, a convenient strategy for the understanding and computation of transition probabilities can avoid the burden of first computing accurate total energies for initial and final states in order to obtain wavefunctions that are suitable for reliable computations of transition probabilities. Instead, FOTOS explains how it is possible to deduce systematically the form of both wavefunctions and to compute consistently the important for each transition correlation effects beyond the zero-order Fermi-sea multiconfigurational wavefunction [26b, 45]. I underline that these effects are first identified formally and then computed via CI to all orders. This is achieved as follows [26b, 45]:

Let us consider an electric dipole transition (with operator $\vec{\boldsymbol{D}}$) from the initial state Ψ_i to the final discrete state Ψ_f. I write each of the wavefunctions

in the form (8), where, as already mentioned and as it will be discussed in the next section, Ψ_i^0 and Ψ_f^0 are, in general, the multiconfigurational Fermi-sea zero-order wavefunctions for initial and final states, satisfying the criterion for Eq. (8). Then, formally, the exact wavefunctions can be written as

$$\Psi_i = \Psi_i^0 + \Phi_i^{\rm corr}, \quad \Psi_f = \Psi_f^0 + \Phi_f^{\rm corr}, \tag{9}$$

and the transition matrix element is given by

$$\langle \Psi_i | \boldsymbol{D} | \Psi_f \rangle = \langle \Psi_i^0 | \boldsymbol{D} | \Psi_f^0 \rangle + \langle \Psi_i^0 | \boldsymbol{D} | \Phi_f^{\rm corr} \rangle + \langle \Phi_i^{\rm corr} | \boldsymbol{D} | \Psi_f^0 \rangle + \langle \Phi_i^{\rm corr} | \boldsymbol{D} | \Phi_f^{\rm corr} \rangle \tag{10}$$

The principal contribution to $|\langle \Psi_i | \boldsymbol{D} | \Psi_f \rangle|^2$ comes from the first term, $\langle \Psi_i^0 | \boldsymbol{D} | \Psi_f^0 \rangle$. Furthermore, since the coefficients of Ψ_i^0 and of Ψ_f^0 are, according to the criterion of Eq. (8), completely dominant, the next two terms of Eq. (10) dictate the part of the function spaces of $\Phi_i^{\rm corr}$ and of $\Phi_f^{\rm corr}$, which are connected directly with the zero-order Fermi-sea components and therefore contribute to $|\langle \Psi_i | \boldsymbol{D} | \Psi_f \rangle|^2$ the most. Note that the recognition of these function spaces from direct dipole connection involves the consideration of N-electron integrals and not just one-electron dipole (or quadrupole, etc) integrals. Therefore, *nonorthonormality* (NON) between the two sets of orbitals also becomes a criterion of selection of the correlation components.

In view of the above, the function spaces of $\Phi_i^{\rm corr}$ and $\Phi_f^{\rm corr}$ are written as

$$\Phi_i^{\rm corr} = \Phi_i^{\rm corr}({\rm int}) + \Phi_i^{\rm corr}(\textit{non}\,{\rm int}), \quad \Phi_f^{\rm corr} = \Phi_f^{\rm corr}({\rm int}) + \Phi_f^{\rm corr}(\textit{non}\,{\rm int}), \tag{11}$$

where $\Phi_i^{\rm corr}({\rm int})$ and $\Phi_f^{\rm corr}({\rm int})$ are those parts that interact directly, via $\boldsymbol{D}$, with the corresponding components of Ψ_f^0 and Ψ_i^0, and $\Phi_i^{\rm corr}(\textit{non}\,{\rm int})$ and $\Phi_f^{\rm corr}(\textit{non}\,{\rm int})$ are the remaining parts that do not interact directly. Therefore, the total transition amplitude of Eq. (10) is rewritten as

$$\begin{aligned}\langle \Psi_i | \boldsymbol{D} | \Psi_f \rangle = {} & \langle \Psi_i^0 | \boldsymbol{D} | \Psi_f^0 \rangle + \langle \Psi_i^0 | \boldsymbol{D} | \Phi_f^{\rm corr}({\rm int}) \rangle + \langle \Phi_i^{\rm corr}({\rm int}) | \boldsymbol{D} | \Psi_f^0 \rangle + \\ & \langle \Phi_i^{\rm corr}({\rm int}) | \boldsymbol{D} | \Phi_f^{\rm corr}({\rm int}) \rangle + \langle \Phi_i^{\rm corr}(\textit{non}\,{\rm int}) | \boldsymbol{D} | \Phi_f^{\rm corr}({\rm int}) \rangle + \\ & \langle \Phi_i^{\rm corr}({\rm int}) | \boldsymbol{D} | \Phi_f^{\rm corr}(\textit{non}\,{\rm int}) \rangle + \langle \Phi_i^{\rm corr}({\rm int}) | \boldsymbol{D} | \Phi_f^{\rm corr}(\textit{non}\,{\rm int}) \rangle \end{aligned} \tag{12}$$

In the early 1970s, when it had been recognized that experiments of beam-foil spectroscopy could produce lifetimes for many types of atomic transitions, we carried out a number of computations and analyses of transition probabilities in atoms, with and without heavy *valence-Rydberg state mixing*. As we wrote in Ref. [26b], that work revealed that "$\Phi^{\rm corr}(\textit{non}\,{\rm int})$ *corresponds to correlation vectors with small coefficients which are reasonably well decoupled from* Ψ^0 *and* $\Phi^{\rm corr}({\rm int})$. *This implies: A) Their direct contribution to* $|\langle \Psi_i | \boldsymbol{D} | \Psi_f \rangle|^2$ *is very small. I.e., the last three terms of eq. (12) are negligible because of the small*

coefficients and because not all correlation vectors in Φ_i^{corr} *and in* Φ_f^{corr} *are connected via* $\boldsymbol{D}$. *B) Their neglect does not affect the coefficients of* Ψ^0 *and* $\Phi^{\text{corr}}(\text{int})$ *significantly."* ([26b], p. 153).

It is important to repeat that in making the selection of the correlation configurations in initial and final states, NON considerations between the two sets of orbitals are applied. This implies that even though the dipole operator is a one-electron operator, certain configurations that differ by more than one orbital can indeed be selected and added to the total wavefunctions of initial and final states [26b, 45].

On the other hand, by emphasizing the state-specific calculation of the wavefunctions of initial and final states and by taking into account orbital NON, it is possible to understand semiquantitatively multiple electron excitations in atoms even at the SCF level. Such one-photon excitations may reach *doubly*, *triply*, or even *quadruply* excited unstable states. Given the existing high-energy photon sources, in atoms these are measurable. Two examples of transitions whose oscillator strengths are finite and reasonable even without the inclusion of electron correlation, are as follows: Li $1s^2 2s\ ^2S \overset{\text{one photon}}{\longrightarrow} 2p^3\ ^2P^o$ (triple excitation) and Be $1s^2 2s^2\ ^1S \overset{\text{one photon}}{\longrightarrow} 2p^3 3s^1 P^o$ (quadruple excitation) [46].

The above theoretical scheme has been implemented by first obtaining the forms of the wavefunction for initial and final states as predicted by FOTOS and then carrying out a CI so that the coefficients are obtained to all orders within the finite expansion. Obviously, in special cases, adjustments can be made, without, however, demanding much additional work, for example, Ref. [22]. The final calculation of the transition probability amplitude takes into account the overall NON between initial and final sets of orbitals.

A variety of transitions, including multiple-electron excitations, have been computed by the FOTOS method over the years. By 1980, its basic features had also been demonstrated in calculations of molecular transitions, with application to H_2O [47a, 47b].

Due to economy, I give only two numerical examples of such calculations (see Refs. [20, 22, 26b, 45] and references therein). The first concerns the oscillator strengths (f – values) of the $^1P^o \rightarrow {}^1D$ *valence-Rydberg state* spectrum of Be, where the 1978 results from FOTOS [26b], page 170 (obtained at that time in Athens in terms of very inadequate computational facilities), are compared with those from large MCHF calculations by Saha and Froese-Fischer [48a] and with experiment [48b, 48c]—see Table 2.3. This case is one of the few characteristic ones in the spectra of atoms and molecules in which almost all the oscillator strength to the lowest valence state of a given symmetry ($'1s^2 2p^{2'}\ ^1D$ in this case) is lost to the higher lying (mixed) Rydberg states. Because of this, the f-values are very sensitive to electron correlation in both initial and final states.

The second example is the FOTOS computation of the *electric quadrupole transition* Ca $4s^2\ ^1S \rightarrow 4s3d\ ^1D$ [49]. The 1983 prediction in Ref. [49] for

Table 2.3 Oscillator strengths (length f_L, velocity, f_V) for the $1s^2 2s2p\,^1P^o \rightarrow {}^1D$ valence-Rydberg state spectrum of Be. Comparison of the FOTOS results [26b] with those from large-scale MCHF calculations [48a] and with experiment [48b, 48c]

	FOTOS [26b]		Large MCHF [48a]		Experiment	
	f_L	f_V	f_L	f_V	[48b]	[48c]
$^1P^o \rightarrow {}'2p^{2\prime}$	0.0086	0.0016	0.0016	0.0010		⟨0.048
$'2s3d'$	0.64	0.41	0.404	0.425	0.43	0.50
$'2s4d'$	0.19	0.16	0.181	0.190	0.19	0.25
$'2s5d'$	0.08	0.07	0.079	0.082		0.16
$'2s6d'$	0.05	0.05	0.045	0.045		0.07

the transition probability in length and velocity forms was $A_L = 60.2(s^{-1})$, $A_V = 65.9(s^{-1})$. Later on, larger-size computations by different methods gave $A_L = 39.6(s^{-1})$ [50] and $A_L = 70.5(s^{-1})$ and $A_V = 78.5(s^{-1})$ [51]. A 2003 experimental publication reported $A_{exp} = 54.4 \pm 4.0$ [52], which is close to the FOTOS results.

Finally, it is relevant to cite the prediction of the SPSA of the *polarizabilities* and *hyperpolarizabilities* of the ground state and the low-lying excited states of Be, which was accompanied by a transparent analysis of the choice of the relevant function spaces. For example, for the ground state, ^1S, $\alpha = 37.62$ a.u. and $\gamma = 3.05 \times 10^4$ a.u., whereas for the lowest state of ^1D symmetry (normally labeled by $1s^2 2p^2$), these values are much larger: $\alpha = 492.73$ a.u. and $\gamma = 0.48 \times 10^7$ a.u. [53]. The reason for the latter is the fact that the wavefunction has a mixed valence-Rydberg character, which makes it easily polarizable. (The theme of the nature of the low-lying excited states of Be is discussed in Section 9). The SPSA results for the ^1S state could be compared with results of other types of calculation whose size is much larger, and there is general agreement, for example, references cited in Ref. [53]. Subsequent theory and computations by Bégué et al. [54a, 54b] on the ^1S and on the 2^3P^o and 2^1P^o excited states showed excellent agreement with the SPSA results.

4.4. Calculations of total energies and widths of doubly excited states using the Breit–Pauli Hamiltonian and comparison with results from the use of Hylleraas-type basis functions [55]

The traditional wisdom of quantum chemistry says that Hylleraas basis functions improve convergence due to the better handling of the cusp at short interelectronic distances. This conclusion is based on analysis and on many computations of ground states. For example, by 1960, it was known that small expansions could produce most of the correlation energy of the He and H_2 ground states [56a, 56b].

Of course, it is not only in the ground-state quantum chemistry, where high accuracy for the total energy has been of interest. A good example is the class of DES in He, where a different type of "high" accuracy is often needed, in relation to experimental requirements. To this purpose, in the late 1960s and early 1970s Bhatia and Temkin, for example, Ref. [57], introduced Hylleraas basis sets into the computational methodology of the Feshbach formalism for the calculation of resonance states in Helium-like atoms. According to the SPSA of resonance (autoionizing) states [8, 10], during the early 1970s, it was also demonstrated that HF and MCHF equations for such states can also be made to converge properly in spite of the fact that they are embedded in the continuous spectrum. Since the present section intends only to demonstrate the capabilities of the SPSA to deal with such states with high accuracy, I do not discuss the theory [10]. Instead, in Table 2.4, I present SPSA results from 1984 [55] on the total energies of a few DESs in He of ^3D and ^1D symmetry and compare them with those from large-scale calculations using Hylleraas basis functions [57]. In fact, the SPSA computations also included autoionization widths and relativistic effects at the Breit-Pauli level of the Hamiltonian, in order to compute for the first time *fine structures* in such states.

In the SPSA calculations of Table 2.4, the Fermi-sea wavefunctions (see Section 8) were obtained by solving the state-specific MCHF equations subject to suitable orthogonal conditions to lower orbitals [8, 10]. Obviously, as it is explained in the following sections, they are not restricted by the condition of the hydrogenic near-degeneracy. In fact, the mixing is so strong that no single configurational label is appropriate. There are a few additional configurations that one might consider as contributing to $a_0\Psi_n^0$ of Eq. (8). The ones reported are by far the dominant ones.

Table 2.4 Total energies (a.u.) of the first five $^{3,1}D$ doubly excited states of He

	SPSA [55]		
(Fermi-sea) MCHF[1]	Fermi-sea plus CI	CI with 112 Hylleraas terms [57]	
3^1D	−0.5493	−0.5561 (46 terms)	−0.5564
2^3D	−0.5540	−0.5599 (21 terms)	−0.5607
2^1D	−0.5632	−0.5684 (40 terms)	−0.5693
1^3D	−0.5827	−0.5837 (32 terms)	−0.5838
1^1D	−0.6970	−0.7019 (46 terms)	−0.7028

[1] The Fermi-sea wavefunctions (Section 8) were restricted to the largest components of Ψ_n^0 of Eq. (8). They were computed self-consistently. They are as follows:
$1^1D: 0.895(2p^2) - 0.338(2p3p) + 0.290(2s3d)$
$1^3D: 0.885(2p3p) - 0.466(2s3d)$
$2^1D: 0.881(2p3p) - 0.381(2s3d) + 0.279(2p^2)$
$2^3D: 0.869(2s3d) - 0.494(2p3p)$
$3^1D: 0.903(2s3d) - 0.420(2p3p) - 0.092(2p^2)$

As Table 2.4 shows, the SPSA results [55] were obtained by using 21–46 term expansions. They are essentially the same as those obtained from a 112-term Hylleraas expansion [57]. The corresponding autoionization widths are also similar. These findings on prototypical and heavily mixed DESs suggested that the quantum chemistry of multiply excited states, a field which is still largely untapped for large systems, can benefit from the implementation of SPS-type approaches. In addition to accuracy, such wavefunctions are compact, physically more transparent, and computationally more manageable and useful than those of the Hylleraas type that use large basis sets. One reason is that in describing such excited states, the systematically chosen SPSA one-electron function spaces are more effective than the r_{12}^n-type terms that were introduced into quantum chemistry in order to account for short-range correlations.

4.5. Multiply excited states

4.5.1. Multiple excitations and nonorthonormality in the context of the SPSA

High-energy MES in the continuous electronic spectrum, especially those corresponding to the excitation of more than two electrons from the ground state, represent a rather exotic class of states, for which the available quantitative information as to their existence, their properties, and their role in processes, *especially in molecules*, is very limited. There are a number of theoretical and experimental reasons for this fact. The conventional wisdom that permeates the literature is that in order to understand the excitation by one photon of MES, one has to introduce electron correlation to high order. Indeed, this is the case if the determinants comprising the initial and the final wavefunctions consist of a single orthonormal basis set, as is normal in conventional methods.

However, aspects of the problem of photon-induced excitation of MES can be understood from the point of view of the SPSA even at the SCF level, provided that the proper combination of state-specific orbital symmetries is present. This is because NON of the two sets of orbitals emerges naturally as a physically meaningful (it accounts for *relaxation* in a simple way) quantitative factor that contributes to the amplitude of the simultaneous excitation of many electrons. Of course, when good accuracy is desired, electron correlation in initial and final states must be added.

The application of the SPSA to atoms has demonstrated this fact. For example, see examples in Section 4.3 on FOTOS [46].

A corresponding example in a simple molecular system would be the multielectron excitation of Li_2 $1\sigma_g^2 1\sigma_u^2 2\sigma_g^{2\,1}\Sigma_g^+$, where three or four of the electrons in the $1\sigma_u^2 2\sigma_g^2$ subshells could be excited to relatively low-lying states labeled by their own SCF orbital configurations such as $2\sigma_u'^2 3\sigma_g' 1\pi_u'^{\,1}\Pi_u$ (quadruple

physical excitation). The SPSA treatment would require the computation of a state-specific SCF wavefunction for the configuration $1\sigma_g'^2 2\sigma_u'^2 3\sigma_g' 1\pi_u'\ ^1\Pi_u$, either in a single configuration treatment or in an MCHF treatment. Note that such a calculation would have to exclude lower states such as $1\sigma_g'^2 1\sigma_u'^2 2\sigma_g' n\pi_u'$, $n = 1, 2, 3\ldots\ ^1\Pi_u$.

The main N-electron matrix element of the one-electron dipole operator in the single configuration approximation would be $\langle 1\sigma_g{}^2|1\sigma_g'^2\rangle\langle 1\sigma_u{}^2|2\sigma_u'^2\rangle\langle 2\sigma_g|3\sigma_g'\rangle\langle 2\sigma_g|D|1\pi_u'\rangle$. This is not zero if the orbitals are obtained self-consistently for each configuration separately.

4.5.2. Regular ladders of doubly, triply, and quadruply excited states tending to fragmentation thresholds where the electronic geometry is symmetric

It is clear that, assuming the model of orbital configurations, one can construct, formally, an infinity of MES for each atom or molecule, at least as a superposition of such configurations for each symmetry. For example, the *two-electron ionization threshold* (TEIT) of He is at 79.0 eV. No bound or quasi-bound DES exist above this energy. However, below this TEIT, the spectrum contains one-electron continua for each hydrogenic threshold, $n = 1, 2, \ldots$, and a very large number of unstable quasi-bound DES (and a few stable ones due to nonrelativistic symmetry restrictions) of many symmetries for even and odd parity. Obviously, for the photoabsorption process in the non-relativistic context, only the DES of $^1P^o$ symmetry is excited. Assuming the basis of orbital configurations, these can be labeled, at least formally, by superposition of configurations such as $2s2p$, ($2s3p$, $2p3s$, $2p3d$), ($4s4p$, $4p4d$, $4d4f$), etc.

One important question is whether one can identify classes of such states exhibiting some type of *regularity* as a function of excitation energy, just like the Rydberg levels do as they reach the ionization threshold. Indeed, for MES without a complex electronic core, that is, for DES in H^-, He, Li^+, and Li^-, for triply excited states in $He^-$and Li, and for quadruply excited states in Be, such regularities have been identified in terms of a Rydberg-like energy formula and in terms of the symmetric geometries of the electrons as they reach the fragmentation thresholds—Ref. [58] and references below.

On the other hand, recent work on the double-electron excitation from the $2s^2$ subshell of Neon to newly established DES embedded in one- and two-electron continua, although they obey an effective Rydberg-like energy formula, show no tendency toward a symmetric geometry of fragmentation due to valence-core electron interactions [59].

These calculations and findings were made possible in the framework of the analyses that were published in the 1980s, for example, Refs. [60a, 60b, 61, 62]. Accordingly, the zero-order wavefunction was chosen as the direct, state-specific MCHF solution with only the *intrashell* configurations for each

hydrogenic shell, having the lowest energy. These multiconfigurational SCF wavefunctions account for most of angular correlation and part of radial correlation. This is sufficient for the quantitative understanding of the properties of interest, such as geometric arrangements of the correlated electrons or absorption oscillator strengths.

The first domain of investigations was that of classes of DES of H^-, He, Li^+, and Li^-. The crucial issue was how to choose and compute the zero-order multiconfigurational (Fermi-sea) wavefunctions, so as to be able to recognize without ambiguity possible regular series that tend to the Wannier state at $E = 0$, with $\langle r_1 \rangle = \langle r_2 \rangle$ and $\vartheta = 180^\circ$. Up to $n = 10$, intrashell states were computed and analyzed from first principles [60a, 60b]. When needed, additional radial and angular electron correlations were calculated variationally. In this way, accurate energies and oscillator strengths to the whole series of such DES were computed for the first time. The regular opening, as a function of excitation, of the angle between the two electrons with maximum density at $\langle r_1 \rangle = \langle r_2 \rangle$ was established from conditional probability densities. These quantities were computed quantum mechanically and demonstrated clearly that, for such cases, it is strong *angular correlations* that dominate the nature of the wavefunctions [58–64].

Later work produced the first ab initio results on the degree and mechanism of their stability by computing the partial and the total autoionization widths of Wannier *two-electron ionization ladders* (TEILs) for the $1sn\ell^2\ ^2S$ and ^4P states of He^- [63, 64] and the $1s^2n\ell^2$ TEIL states of Li^- [61]. The same general approach was implemented in order to establish and to analyze novel regular series of excited unstable states labeled by *triply* and *quadruply* excited configurations. Specifically, by combining notions of angular momentum and spin symmetry and of electronic structure, we determined from first principles that identifiable series of intrashell states lead to symmetric fragmentation thresholds [58, 62].

I give two examples from the aforementioned published results:

1. Let us consider the quadruply excited states in Be of $^5S^o$ symmetry having as zero-order wavefunction the MCHF intrashell superposition [58]. For the lowest principal quantum number, $n = 2$, the reference wavefunction is the single configuration $(2s2p^3)$. As n increases, angular correlation (hydrogenic near-degeneracy) dominates. Thus, for $n = 6$, the state-specific zero-order MCHF solution with the lowest energy is $0.77(6s6p^3) + 0.48(6s6p6d^2) + 0.23(6s6f6d^2) - 0.28(6d6f6p^2) + 0.13(6p6d6f^2) - 0.11(6f6d^3)$. As n increases and angular correlation contributes more, the average angle between the four electrons opens up, tending to that of a tetrahedron [58].
2. Table 2.5 presents two sets of results for the DES TEIL states in H^- $('n\ell^{2'}\ ^1S)$, He^- $('1sn\ell^{2'}\ ^2S)$, and Li^- $('1s^2n\ell^{2'}\ ^1S)$, $n = 3, 4, 5\ldots$, which were expected to have similar characteristics, produced by the strong electron

Table 2.5 Average radii, r_n, (in a.u.) and energies from threshold, ΔE, (in eV) for the TEIL states, H^- ($n\ell^2\,{}^1S$), He^- ($1sn\ell^2\,{}^2S$), and Li^- ($1s^2n\ell^2\,{}^1S$), $n = 3, 4, 5\ldots$[1]

	H^-		He^-		Li^-	
n	r_n	ΔE	r_n	ΔE	r_n	ΔE
3	16.3	1.885	14.2	2.156	13.3	2.285
4	28.7	1.088	26.5	1.180	25.8	1.213
5	44.9	0.706	42.6	0.745	41.8	0.755
6	66.5	0.493	62.9	0.511	62.0	0.517
7	90.9	0.366	87.0	0.375	86.9	0.376
8	120.1	0.282	114.7	0.287	114.7	0.287
9	152.0	0.224	144.1	0.227	144.0	0.227

[1] From Ref. [61]. Note that the results are very similar, reflecting the similar behavior of the excited pair of electrons in specific states.

pair correlations. One set contains the computed average values (in a.u.) of the radii of the two electrons, $\langle r_1\rangle_n \approx \langle r_2\rangle_n \equiv r_n$. The second set contains the energy distance from the fragmentation threshold (in eV). It turns out that these energies fit the Rydberg-like analytic formula $E_n = A\frac{n(n-1)}{{r_n}^2}$, where A is a slowly varying proportionality constant [61].

In order to acquire more definitive knowledge as to the properties of various types of DES in He, (effective Coulomb attractive potential) and in H^-, the SPSA computations have dealt with *intrashell* and *intershell* DES up to the hydrogenic threshold $N = 25$ and have been accompanied by analysis and a brief commentary concerning other approaches [65–67].

This became possible not only by the state-specific nature of the computations but also by the realization that the *natural orbitals* produced from hydrogenic basis sets were the same as the MCHF orbitals that are computable for the intrashell states up to about $N = 10 - 12$. Therefore, for DES with very high N, instead of obtaining the multiconfigurational zero-order wavefunction from the solution of the SPSA MCHF equations (which are very hard to converge numerically if at all), we replaced the MCHF orbitals by natural orbitals obtained from the diagonalization of the appropriate density matrices with hydrogenic orbitals.

In fact, by being able to obtain and use wavefunctions of different degrees of accuracy regarding the contribution of electron correlation, we explored the degree of validity of the Herrick–Sinanoğlu (K, T) quantum numbers [68] and of new ones, namely the Komninos et al. (F, T) classification scheme that was introduced in 1993 [65–67]. It was demonstrated that the accurate wavefunctions of the series of DES are best represented by the (F, T) scheme compared with the (K, T) one [65–67].

5. TWO TYPES OF NEAR-DEGENERACIES IN GROUND STATES, AND THEIR IMPACT ON THE THEORY AND COMPUTATION OF ELECTRON CORRELATION

Equations (3–7) and the related computational methods are formally applicable to closed-shell ground states of systems such as He, Ne, or H_2, CH_4, and H_2O (and many others) in the equilibrium geometry. The conventional objective is to add terms beyond Φ_{HF}, with functions of the same type, until a very good total energy is obtained. In principle, the computation of the numerically exact energy requires the inclusion of an infinite number of these terms.

In 1954, Moffit [69] called the requirement of computing even portions of the infinity of terms in X_{corr} of Eq. (1) the *nightmare of second-order CI*. On the other hand, given the nature of the problem that he was examining, he pointed out that, as an elementary approximation, one could focus on the contribution of two closely lying states in a simple model of conjugated molecules, thereby accounting to some extent for the dominant effects via *first-order CI*, that is, via the diagonalization of the corresponding 2×2 Hamiltonian matrix [69]. Of course at that time, the thoughts regarding practical computational models beyond the equivalent of Φ_{HF} were quite vague and without quantitative foundation.

Starting in the late 1950s, it was recognized, in the beginning descriptively and vaguely and in later years specifically and quantitatively, that, for many categories of states and problems, the formal and computational treatment of electron correlation must pay special attention to effects that result from the relatively strong mixing of only a few configurations. *In this context, the fundamental question is: Given a state, how are these identified and computed?*

In the 1960s, this identification was based on two features of electronic structure: The *hydrogenic near-degeneracy* (H-ND), with prototypical example, the Be $1s^2 2s^2 {}^1S$ state and the *dissociation near-degeneracy* (D-ND), with prototypical example, the H_2 $1\sigma_g^2 {}^1\Sigma_g^+$ state. Both cases require a simple, yet crucial, 2×2 CI. The former depends mildly (essentially linearly) on the nuclear charge Z, and the latter depends critically on the internuclear distance R.

As discussed below, in the 1960s, the consequences of these two near-degeneracies were incorporated in the 1960s in formalism and were accounted for in computations. However, they are not the only possible mixings that affect heavily the nature of the wavefunction as symbolized by Eq. (8). Indeed, in the 1970s, a broader framework of systematic treatment of electron correlation in ground and in excited states was understood, where, because of the criterion for Ψ_n^0 of Eq. (8), other types of possible mixings must also be examined. For example, when Hamiltonian parameter-dependent *valence-Rydberg state mixing* (VRSM) or *mixing of neutral states with charge-transfer states* (in molecules) are also considered, critical components of

possible zero-order superpositions, a more economic understanding of electronic structures, as well as more efficient methods of computation, can be achieved. (For example, see examples and discussion on the Fermi-sea and CASSCF ideas and methods in this paper—Sections 4, 7–10).

5.1. Concerning the dissociation near-degeneracy (D-ND)

In their 1961, critical review on simple molecules, Kotani, Ohno and Kayama [70] singled out two types of correlations, which are in conceptual analogy to the names of CI used by Moffit earlier: They pointed out the presence of special interactions in the dissociation region which give rise to *exchange correlation* ([70], p. 90). In the same context, they called parts of the remaining correlation *dynamical correlation* and suggested that this "is at work between electrons in atoms and in molecules with equilibrium internuclear separation." ([70], p. 90). They wrote "In the intermediate separation between nuclei both types of correlation may be considered to exist, but the separation into two parts is not without ambiguity." There are no quantitative results in Ref. [70] in support of this statement. However, according to computational experience from modern quantum chemistry, there is general validity in it, especially when it comes to *excited* PESs.

After many decades of ab initio calculations, the computational significance of D-ND is established firmly. In the prototypical case of the H_2 $1\sigma_g^2\,{}^1\Sigma_g^+$ state, this is represented by the mixing of configurations $1\sigma_g^2$ and $1\sigma_u^2$, where $1\sigma_g$ and $1\sigma_u$ are the bonding and antibonding orbitals that are degenerate in the dissociation region of H_2^+. In other words, as is well known, when only the $1\sigma_g^2$ molecular orbital configuration is used, the wavefunction does not dissociate correctly to the energy and the wavefunctions of two hydrogen atoms in the ground state 1*s*. Instead, physically irrelevant (for this dissociation channel) charge-transfer configurations ($H^+ + H^-(1s^2)$) are also present.

The D-ND for $R \to \infty$ can be recognized from theoretical considerations. However, because of the strong dependence of the CI mixing on R, it is not possible to predict quantitatively its importance at equilibrium or further in, where, normally, the united atom limit also plays an important role. For the sake of completeness, it is useful to quantify the above. I write the two-term superposition wavefunction as (I omit the dependence of the orbitals on the parameter),

$$\Psi^0(H_2; X^1\Sigma_g^+) = a(R)1\sigma_g^2 + b(R)1\sigma_u^2 \tag{13}$$

A systematic MCHF study of valence electron configurational mixing for H_2 $1\sigma_g^2\,{}^1\Sigma_g^+$ and for other small diatomics was published in a comprehensive paper by Wahl et al. [71] in 1967. In the example (13), two characteristic

coefficients from the calculations of Wahl et al. [71] (which actually included more configurations than just the two above) are

$$\text{At } R = 1.40\,\text{a.u}, \quad \text{(equilibrium) } a = 0.992 \text{ and } b = 0.092 \tag{14a}$$

$$\text{At } R = 8.0\,\text{a.u}, \quad \text{(dissociation) } a = 0.717 \text{ and } b = 0.697 \tag{14b}$$

Given that the potential energy curve indeed converges correctly to the $H(1s) + H(1s)$ dissociation limit, it follows that the breakdown of the SCA, which occurs as the atoms in the molecular ground state move away from the equilibrium geometry, is corrected in zero order by an economical two-term wavefunction, with one attractive SAC, $(1\sigma_g^2)$, and one repulsive $(1\sigma_u^2)$. Such a wavefunction, although it does not produce the exact energy curve, easily accounts for major observable effects in properties and phenomena such as polarizability, photoionization, photodissociation, etc. over the whole internuclear range.

The generalization to larger systems with more complicated situations is conceptually possible. However, in many such cases, the task of identifying the computationally and physically important configurations using as reference the D-ND and of computing their correct mixing as a function of geometry is very demanding and certainly more difficult computationally. The concepts of the Fermi-sea and active space, which are discussed later on, and the current possibility of computing systematically CASSCF wavefunctions for small to large molecules have provided the tools for making substantial progress with the understanding of such problems.

5.2. Concerning the hydrogenic near-degeneracy (H-ND)

Unlike the r_{12} singularity, the $2s - 2p$ "degeneracy" is handled well by the configuration interaction method and poorly by the Hylleraas method. Perhaps the two-configuration $1s^2 2s^2 - 1s^2 2p^2$ function would be a good starting point for a Hylleraas expansion.

R. E. Watson, 1961, [72], p. 252

The recognition of the hydrogenic near-degeneracy is straight forward since its origin is the hydrogenic spectrum and the shell model. It implies the superposition of *intrashell configurations*. The first steps toward the understanding of its significance in the theory and computation of *ground-state* electronic structures started in 1939 with the pioneering paper of Hartree, Hartree and Swirles [73], which presents the application of their MC-SCF approach to the $1s^2 2s^2 2p^3\ {}^2P^o \leftrightarrow 1s^2 2p^5\ {}^2P^o$ mixing in OII.

In order to set the stage, I give two examples that concern the electronic structure of Be $1s^2 2s^2\ {}^1S$. One refers to the 1960 calculation and analysis of Watson [31] in terms of systematic CI whose reference wavefunction is

the H-F solution. The second refers to Kelly's pioneering demonstration of the implementation of Brueckner–Goldstone *many-body perturbation theory* (MBPT) to electronic structure, in the early 1960s [74]. Among other things, Kelly's computations showed that the consequence of the strong mixing of the configurations $(1s^2 2s^2, 1s^2 2p^2)$, which is due to the large value of the interaction matrix element $\langle 2s^2|\mathbf{H}|2p^2\rangle$, is taken into account much more effectively if the basis orbitals are obtained in a $V_{\mathrm{HF}}^{(N-1)}$ potential (i.e., Be^+ $1s^2 2s\ ^2S$) rather than in a V_{HF}^{N} potential. For example, Kelly found that the MBPT pattern of convergence for the $2s^2$ correlation energy in Be changes significantly, with about 90% of the second-order result coming from the $2s^2 \rightarrow 2p^2$ HN-D correlation energy.

The 1960–1961 publications of Watson [31, 72] on results and the cataloguing of electron correlation based on systematic CI calculations of the wavefunction of the ^1S ground state of Be and its isoelectronic positive ions are linked directly to the discussion of this section. Among other things, he made the following important observations that are still relevant to the evolved methods of modern computational chemistry: Electron correlation in this state could be separated into the following two classes.

One was similar to the one that was known in the case of He $1s^2\ ^1S$ and was responsible for the slow convergence of orbital CI for this system (*correlation hole*). This is in the class of what Kotani et al. [70] and later Sinanoğlu and coworkers (see below) called *dynamical* (D) correlations. This name and its implication have become part of the nomenclature and discussions of modern quantum chemistry. From work prior to 1960, it was known that in the case of He $1s^2\ ^1S$, straightforward orbital CI is not performing efficiently with respect to convergence to the exact energy. This is due to the impossibility, in principle, for orbital CI to account exactly for the notorious *cusp conditions* that the eigenfunction must satisfy at the point $r_1 = r_2$. As Hylleraas had already shown in 1929–1930, for this case, convergence is greatly accelerated if terms containing r_{12} are incorporated into the trial wavefunction.

The other class that Watson identified was the $2s^2 \leftrightarrow 2p^2$ HN-D, which could be handled by a 2×2 CI or, better, by a 2×2 MCHF computation. Its dependence on the nuclear charge, Z, was essentially linear, rather than being nearly independent of Z, as in the case of the He $1s^2$-like correlation. In fact, Watson suggested that the two-term $1s^2 2s^2 - 1s^2 2p^2$ wavefunction could be used as a *reference wavefunction* for further computation. As is well known, such a procedure is now followed, on a computationally much more sophisticated level, by the *multireference CI* (MRCI) methods. The simpler alternative to CI, that is, that of *second-order perturbation theory*, was also considered by Watson. In the abstract of Ref. [31] he wrote: "The errors introduced by handling "high-lying" configurations by second-order perturbation theory rather by exact configuration interaction are also investigated." (This is the *nightmare of second-order CI* quoted above [69]).

Nowadays, the HN-D type of electron correlation, later classified by Sinanoğlu and coworkers as *internal* correlation, is placed in the category of *nondynamical* (ND) correlations. The remaining correlation, which is *dynamical* (D) *correlation*, was later also classified as *external* in the formalism presented in the 1960s by Sinanoğlu and coworkers, see below. D correlation is computable by methods that either use orbital functions or, in special cases, a Hylleraas-type expansion.

As in the case of the D-ND above, for the sake of completeness I close the present subsection by quantifying the H-ND in the Be ^1S isoelectronic sequence. The energy for Be will be used in Section 9 on the Fermi-sea wavefunctions and energies of the low-lying states of Be.

Omitting in the symbolism the dependence of the orbitals on the parameter Z, I write

$$\Psi^0(^1S) = c(Z)(1s^2 2s^2)\,^1S + d(Z)(1s^2 2p^2)\,^1S \tag{15}$$

A 2×2 numerical MCHF calculation of the Be sequence using the code of Froese-Fischer [18] yields

$$Z = 4, \quad \mathrm{Be}: c = 0.950, \quad d = 0.312 \quad E = -14.61685\,\text{a.u.} \tag{16a}$$

$$Z = 5, \quad \mathrm{B}^+: c = 0.957, \quad d = 0.290 \quad E = -24.29638\,\text{a.u.} \tag{16b}$$

$$Z = 6, \quad \mathrm{C}^{++}: c = 0.961, \quad d = 0.277 \quad E = -36.48096\,\text{a.u.} \tag{16c}$$

When the single-configuration HF energy is subtracted, the energy (16a) represents 46% of the total electron correlation nonrelativistic energy of Be ^1S, which is 1.19 eV. Nevertheless, it will be used in Section 9 for the calculation of excitation energies of low-lying excited states of Be, whose wavefunctions are also truncated appropriately.

It must be pointed out that the results (16a) are in perfect agreement with the pioneering computations of Watson [72] from 1961, who used the Roothaan analytic method.

It is clear that the label of the ground state of Be and Be-like ions should include the $1s^2 2p^2\ ^1S$ SAC, provided no other configuration also acquires a comparably large coefficient. (There is none.) Hence, regardless of the fact that the exact total energies are lower, it can be seen immediately that when this state is perturbed, either chemically (e.g., formation of BeH_2 or of Be_2) or by an external field (e.g., absorption oscillator strengths), the results of the response should depend directly and in a significant way on the presence of the $1s^2 2p^2\ ^1S$ SAC, even though its energy is about 9.5 eV above that of $1s^2 2s^2\ ^1S$. Similar considerations hold, of course, for longer zero-order superpositions that are necessary for the description of other states.

The two types of near-degeneracies that were discussed above, as well as the classification of electron correlation into two parts having the features

that were pointed out by Kotani et al. [70] and by Watson [31, 72], were integrated into a formal theory and analysis of the electronic structures of ground states by Sinanoğlu and coworkers in the 1960s [75–79], who, as the opposite to the name *dynamical* used the word *nondynamical* (ND) to describe them. For example, an explicit description given by Tuan and Sinanoğlu [75] reads as follows: "Pair correlations may have a dynamical part (slowly convergent CI, short-range part of the Coulomb repulsion) and a nondynamical part (near-degeneracy). The former is insensitive to immersion and exclusion effects, while the latter are very sensitive to both. Thus in building up atoms or ions step by step the dynamical part is transferable from system to system, but the nondynamical part, being strongly dependent on the two environmental effects, is untransferable." ([75], p. 2677).

6. OPEN-(SUB)SHELL STATES

The existence of the HN-D and DN-D effects that were discussed above implies that a single-determinantal description in zero order of a quasi-closed-shell ground state is inappropriate. Inevitably, the same is true for many N-electron ground or excited states (especially those having lower lying states of the same symmetry) for which the shell model implies that the occupied spin orbitals lead to an (assumed) open-(sub)shell configuration. For example, this is recognized when first-order perturbation theory is applied to states of atoms and small (relatively speaking) molecules, where the atomic or molecular orbital shell structure retains its validity.

In 1966, Silverstone and Sinanoğlu [77] and Kelly [80] published their extension of previous formal developments and applications of the cluster expansion of the wavefunction and MBPT for closed-(sub)shell ground states to analogous formalisms for open-(sub)shell states. In fact, Kelly demonstrated his methods with an impressive calculation of parts of electron correlation in the oxygen atom, with emphasis on the correlation of pairs of electrons [80]. Among other things, he pointed to the inevitable appearance of terms that correspond to spin-orbital pair excitations such as $\{2p(+1^+), 2p(0^+\} \rightarrow \{2p(-1^+), 4f(+2^+\}$, which are called *semi-internal* by Silverstone and Sinanoğlu [77], see below.

Silverstone and Sinanoğlu [77] wrote the cluster expansion of the nonrelativistic N-electron eigenfunction in terms of a zero-order reference wavefunction that is *multiconfigurational*, in accordance with the earlier suggestion of Watson [31] and the study of H-ND in Be [75, 76]. In their formalism, the one-, two-, three-, etc. correlation functions (i.e., the virtual electron-excitations in the language of CI) are linked to spin orbitals from an extended zero-order set of occupied and unoccupied spin orbitals. This set was named the *Hartree–Fock sea* (H-F sea). Optimally, the H-F sea spin orbitals are supposed to be computed self-consistently.

The essence of the suggestions and ground-state formalisms of [31, 72, 77] regarding the use of a multiconfigurational reference wavefunction is reflected in the large-scale computations of modern-day *multireference configuration interaction* (MRCI), whose introduction into CQC also goes back to the late 1960s, for example, Ref. [81].

Given the H-F sea of spin orbitals, Silverstone and Sinanoğlu [77] separated again electron correlation into *dynamical* (D) and *nondynamical* (ND). Accordingly, the ND part consists of the aforementioned HN-D and DN-D (called *internal* correlations) and of the possible virtual electron-pair (mainly) excitations from the occupied spin orbitals where one spin orbital belongs to the H-F sea (called *semi-internal* correlations). The remaining ones represent the D correlations and were called *external* correlations. In general, the external ones are supposed to be of the type represented, for closed-shell single-determinantal states, by X_{corr} of Eq. (3). All terms in Ref. [77] are defined in terms of spin orbitals and Slater determinants [82].

In the formalism of [77], the construction of the zero-order multiconfigurational wavefunction and the recognition of the ND and D parts of the remaining correlation are based in a fundamental way on the assumption and the actual choice of the H-F sea spin orbitals. In that work, and in subsequent developments and applications, the H-F sea was defined in terms of easily recognizable paradigms, such as the previously discussed H-ND [77–79], or in simple models of π-electron systems [83], all in the framework of one- and two-electron virtual excitations. For example, in the 1972 paper by Beck and Sinanoğlu [84], where the ND wavefunctions of the third-row-atoms were computed and applied to the calculation of oscillator strengths, it is written, as in earlier papers, that "To apply the theory to third-row KLM configurations, the restricted Hartree–Fock function Φ_{HF} is used as a starting point, the 'Hartree–Fock Sea' consisting of all 1*s*, 2*s*, 2*p*, 3*s*, 3*p*, and 3*d* spin orbitals. For the second row, only 1*s*, 2*s* and 2*p* were included in the 'sea"'. ([84], p. 945).

For *molecules, especially in excited states*, the choice of the proper, for each problem, extended set of zero-order orbitals and corresponding configurations that would allow, to a good approximation, the recognition, in quantitative terms, of the main features of the wavefunction and the bonds constitutes a challenging problem. For example, such a problem is discussed in Sections 9 and 10, where the exceptional bond of Be_2 $X^1\Sigma_g^+$ is examined in the framework of ND versus D correlation using as reference points the Fermi-seas of the low-lying states of Be.

For the normal ground states of molecules, the simplest route to choosing a suitable extended set of zero-order orbitals à la Hartree–Fock sea is to invoke the sequence of the shell model for the low-lying molecular orbitals in conjunction with the DN-D. Indeed, doing just that, together with the usual trial computations, in 1970 Das and Wahl [85] produced the first reliable results from MCHF calculations on the PES of the $^1\Sigma_g^+$

ground state of F_2, where the wavefunction is small and contains configurations that can be associated with *internal* and *semi-internal* correlations. Shortly afterwards, Schaefer [86, 87] reported results from CI calculations on the $^3\Sigma_g^-$ state of O_2 and on the $^1\Sigma^+$ ground state of BeO. For example, for BeO Schaefer's choice of the H-F sea was the extended zero-order set of valence orbitals $\{3\sigma, 4\sigma, 5\sigma, 6\sigma, 1\pi, 2\pi\}$, when the occupied zero-order configuration is $1\sigma^2 2\sigma^2 3\sigma^2 4\sigma^2 1\pi^2\, ^1\Sigma^+$ [87].

7. ON THE SEPARATION OF ELECTRON CORRELATION INTO DYNAMICAL (D) AND NONDYNAMICAL (ND)

The success of a practical theory that is applicable to various types of electronic structures as a function of the parameters of the Hamiltonian, that is, of Z and of geometry, at separating formally the exact wavefunction into orthogonal parts, which are supposed to be computed separately, depends critically on the degree of *actual decoupling* that is present computationally when truncated spaces are used. This decoupling is often difficult to foresee, especially in excited states where state energy-differences often vary rapidly as a function of geometry and/or of variational parameters, and small energy shifts of roots corresponding to correlation determinants may cause significant changes in certain mixing coefficients, for example, see examples (1) and (4) of Section 4.

Since the choice of the zero-order set of orbitals is crucial to an economical understanding of properties of electronic structures and of bonding, it is significant to elaborate mildly on the separations proposed in Ref. [77] in relation to the classification into ND and D correlations.

The *zero-order* and the *internal* multideterminantal wavefunctions, ϕ_0 and χ_{int}, respectively, are specified by those determinants that are created by the distribution of N electrons among M spin orbitals, and their number is fixed by the binomial term, $\frac{M!}{N!(M-N)!}$ (see Eqs. (3 and 9) of Ref. [77]).

The existence of an upper bound in the expansion of ϕ_0 plus χ_{int} suggests an automated procedure of creating determinants in zero order. In practice, although this number may be high, *symmetry* may reduce it drastically. This is especially true in small atoms. For example, for the first row of atoms, assuming that the $1s^2$ core is kept inert, the *HF-sea* for the valence electrons of each state consists of the eight spin orbitals of the $2s$ and $2p$ orbitals, according to the HN-D. Then, if the atomic state of interest has, say, two valence electrons (e.g., the extensively studied Be ground state, ^1S), the number of their possible unconstrained distributions over the eight spin orbitals is 28. Yet, the actual number after the restrictions of parity, the Pauli exclusion principle, and coupling to total angular momentum and spin of ^1S is reduced to only four determinants and two SACs, $1s^2 2s^2$ (one determinant) and $1s^2 2p^2$ [82]. Of course, for molecules, where symmetry is

lower than that of atoms, the reduction of the number of terms from Slater determinants to SACs is less drastic, ranging by factors, in general, of two to four.

The self-consistently computed sum of ϕ_0 and χ_{int} in the formalism of [77], whose simplest implementation is the case of the Be ground state discussed earlier, can be recognized as the formal description of the widely used, in later decades, computationally powerful model of the CASSCF wavefunction implemented in a very effective way by Roos and Siegbahn [1, 2]. The key question has to do with the choice of the *active space* of zero-order spin orbitals. In fact, these concepts follow from the general criterion of Eq. (8) that has led to the analysis of electronic structures in terms of state-specific Fermi-seas (see next section).

Indeed, as implied by the SPSA criterion (Eq. (8)) and suggested by the examples already discussed, the proper and optimal computation of the zero-order extended set of orbitals is directly linked to well-converged solutions that contain the essential information on electronic structures and properties. For example, the important to spectroscopy and chemical bonding over the whole PES *valence-Rydberg-scattering configuration mixing* was not considered or discussed in [31, 70, 72, 77] since such problems were not even part of the language of many-electron methods at that time.

The argument of the SPSA is that it is advantageous to computation for this choice to be as state specific as possible. In other words, the problem is defined not only with regards to the formal separation of the exact wavefunction into orthogonal parts. This is a matter of definition. The choice of the hydrogenic degeneracy, that is, of the H-F sea, provides one such formal separation. The problem is in deciding correctly on how to choose consistently the optimal zero-order set of orbitals to be computed self-consistently from a multiconfigurational calculation, for each state of interest and at each nuclear geometry. It is this choice that defines in practice the overall computational methodology while producing the preconditions of a systematic "model" of electron correlation that is based on the criterion of Eq. (8). This is the meaning of the introduction of the Fermi-sea in the early 1970s [7, 22, 26a–26c, 45], which is noted in Section 3 and is discussed below and in Section 8.

In modern times (compared to the 1960s), the use of the terms *nondynamical* (ND) and *dynamical* (D) electron correlation has increased in the literature of computational and of quantum chemistry, for example, Ref. [88–95]. However, it seems that there is some vagueness and confusion as to the practical definition of these terms, and especially, as to their a priori identification before large-scale computations have been carried out.

For example, in 1996, Mok, Neumann and Handy [90] suggested the "definition" for the ND correlation as $E_{\text{ND}} = E_{\text{CASSCF}} - E_{\text{HF}}$ (Eq. (2) of Ref. [90]). This is not what the initial definition of ND correlations was (see above and [77, 82]). Instead, given the normal choices of the "active space," what Mok et al. [90] have defined is essentially just the *internal* correlation in the formalism of [77]. On the other hand, Valderrama, Mercero and

Ugalde [92] have proposed a separation criterion according to which "*The wavefunction that maximizes the electron–electron counterbalance density contains all the nondynamical electron correlation*" (Abstract of Ref. [92]).

The critical examination of the degree of accuracy and consistency of the a priori separation between D and ND correlations was first done in the early 1970s in atomic systems, where, at the time, this could be done with reasonable economy. This is discussed below in terms of examples that involve the dependence of the spectra on Z (equivalent to R in the diatomics and to molecular geometry along a reaction coordinate in general). Specifically, in systems with high-effective Coulomb attraction, that is, in positive ions, the separation of electron correlation into ND and D can be recognized clearly. However, this is not the case when the nuclear attraction is reduced and the spectra become, in general, less distinct.

In the "Introduction," I referred to the approximate implementation of separate computations of ND and D correlations in resonance multiply excited states [8]. In 1974, Beck and the author [7] discussed the physical and computational significance of the choice of the zero-order wavefunction beyond the HF approximation, in conjunction with the calculation of internal and semi-internal correlations. At that time, both of us had the experience of computing [84, 96, 97] correlated wavefunctions of low-lying states of atoms and ions of the first and the second rows of the Periodic Table containing the spin-orbital excitations that Sinanoğlu and coworkers [77–79] labeled as ND electron correlation. For example, given the finiteness of the expansion of the corresponding singly and doubly excited ND wavefunctions that is imposed by symmetry, in the appendix of Ref. [96], we demonstrated the satisfaction of sum rules in this function space and their possible use in computation.

In one of those applications, which included the computation of various states of the highly ionized Silicon atom, two trends had been observed, and this, in conjunction with other trial computations, was the impetus for introducing the concept of the Fermi-sea to be discussed in the next section.

1. When the effective nuclear charge becomes larger than that of the neutrals or singly ionized species, the separation between ND and D correlations in low-lying states becomes rather clear, as can be concluded by inspection of the observed spectra and by applying notions of lowest order perturbation theory. In other words, doubly excited correlation determinants representing *external* correlation were too far from the "interaction zone" to be able to contribute significantly to the wavefunction. Therefore, instead of first obtaining total energies by first computing *external pair energies* via the semiempirical method of Ref. [79] to approximate the total energy as $E_T \approx E_{ND} + E_D$, we computed *energy differences* based on the hypothesis that given the types of initial and final states that are involved in the transition, the totality of dynamical and relativistic contributions would, to a good approximation, cancel out. A few indicative results from Ref. [96] are included in Table 2.6, together with the experimental values and

Table 2.6 Oscillator strengths and energy differences, (as wavelengths in Å, λ(Å)), for transitions of the type $1s^2 2s^a 2p^b \rightarrow 1s^2 2s^{a-1} 2p^{b+1}$ in ionized Silicon.[1]

		λ_{exp}(Å)	λ_{HF}(Å)	λ_{ND}(Å)	f_{HF}	f_{ND}
SiIX	$2s^2 2p^2\ ^3P \rightarrow 2s2p^3\ ^3D^o$	350	364	351	0.100	0.066
SiVIII	$2s^2 2p^3\ ^4S^o \rightarrow 2s2p^4\ ^4P$	319	324	317	0.217	0.170
SiVII	$2s^2 2p^4\ ^3P \rightarrow 2s2p^5\ ^3P^o$	275	248	275	0.203	0.135
SiVI	$2s^2 2p^5\ ^2P^o \rightarrow 2s2p^6\ ^2S$	246	239	246	0.113	0.076

[1] The wavefunctions contained configurations representing the ND correlations as defined in Refs. [77–79]. The λ(Å) were computed as differences of ND energies only, with E_{ND} defined with respect to the "Hartree–Fock sea" of zero-order spin orbitals (From Ref. [96]). The work was done in order to explore the hypothesis (confirmed by its results) that as the effective Coulomb attraction increases the decoupling of ND correlations from D ones becomes distinct and, consequently, the D contribution to two states with similar configurational structures cancels out on subtraction. Furthermore, the coefficients of the external-correlation configurations become too small to influence transition probabilities in a significant way.

the theoretical oscillator strengths, f, for the corresponding transitions, using the HF and the ND wavefunctions. I point out that those computations were not fully optimized in terms of flexible basis sets. Similarly good results were obtained for the $(S-D)/(D-P)$ term-splitting ratios.

2. On the other hand, in the neutrals, even from rough calculations, it emerges that the ND-D separation that is based on the *HF-sea* and the minimal spin-orbital expansion of the correlation functions in terms of a small set of atomic orbitals [78, 79, 84, 96] is much less distinct in many cases. In fact, in certain calculations of the ND correlation I had experienced abrupt energy near-degeneracies of roots during the optimization of correlation orbitals, represented, according to the then applied methodology, by single Slater-type orbitals (STOs). Unless corrected by an appropriate expansion of the relevant function spaces, such root peculiarities affect the composition of the wavefunction and consequently affect quantities such as transition probabilities. It was realized that these simulated the *mixing of valence-Rydberg configurations*, such as NI $1s^2 2s 2p^4\ ^4P$, $1s^2 2s^2 2p^2 3s\ ^4P$, even though these are the lowest lying states of their symmetry. In other words, such mixings, which do not enter the *HF-sea* from considerations of the standard HN-D (analogous situations may occur in molecules with respect to the DN-D), may affect significantly the wavefunction, so the basis sets must be flexible enough to accommodate their proper representation. These findings were reported in Ref. [97], where it was stated:

> *However, it was also found that for some of the neutrals agreement (between experimental and theoretical oscillator strengths) is not as good. This could be due to the relative diffusiveness of charge in the upper states and the proximity*

of these states to perturbing Rydberg levels, or to the neglect of D correlation components or both. ([97], p. 243).

It was thus evident that the choice of the *HF-sea*, which was defined in terms of the spin orbitals that complete the closed-shell structure, was convenient but in general insufficient and could not be applied consistently, without concern about "hidden," structure-dependent "near-degeneracies" (in a relative sense). In other words, the a priori decoupling of function spaces into D and ND correlations based on an apparently relevant *HF-sea* clearly entailed the danger of mishandling *parameter-dependent near-degeneracies*, most notably those due to the mixing of valence and Rydberg configurations.

The same conclusion would obviously be applicable to molecular states for which the adopted zero-order model is the one which results from the use of just a minimal basis set.

8. THE FERMI-SEA ("ACTIVE SPACE") OF ZERO-ORDER ORBITALS. THE SPSA CRITERION OF $a_0 \approx 1$ IN EQ. (8)

In view of the results that were discussed in the "Introduction" (see Eq. (1)) and in the previous section, in the early 1970s [7, 26b, 26c, 45] we proposed that the choice of the zero-order extended set of orbitals should not be confined to just the conditions of completing a closed shell, (H-ND) or satisfying the appropriate dissociation superpositions (D-ND).

Instead, it should be made using general criteria of dominant contributions to the eigenfunction of interest. This implies using as guiding principle the criterion that is associated with Ψ_n^0 of Eq. (8), namely $a_0 \approx 1$, for each value of the effective Z and molecular geometry. To achieve this, its ab initio choice should depend on the problem and should utilize any information from empirical data of spectra or from trial small computations (e.g., see Table 2.4 for doubly excited states). In this context, it was considered advantageous to construct and implement the formalism and the computations in terms of *symmetry-adapted* orbitals and configurations rather than of spin orbitals and Slater determinants. For example, in this way one has a direct link to spectroscopic states.

This type of zero-order orbital set was named the Fermi-sea, and depending on symmetry and the states under consideration, the corresponding configurations are to be computed self-consistently. Its heuristic description was given as follows in Refs. [7, 45]:

The 'Fermi – sea' is the set of orbitals formed from all orbitals appearing in the single configurational assignment to the state (the occupied orbitals), together with all other orbitals degenerate or nearly-degenerate (in a relative sense, not necessarily based on the hydrogenic picture) with any one of the occupied orbitals. ([45], p. 80).

The phrase *relative sense* implies the consideration of electronic structure and notions from perturbation theory, such as energy differences and strength of first-order interaction matrix elements. For example, when *inner-hole* states are considered, all kinds of possible mixings involving both valence and inner spin orbitals are in principle present. In a related investigation concerning photoelectron spectroscopy [27a–27c], we wrote:

> *The zeroth order is, in general, a multiconfigurational vector which includes those valence configurations which mix heavily and affect the overall character of the wave function the most, together with the 'symmetric-exchange-of-symmetry' (SEOS) correlations. [SEOS correlations in atoms dominate the 'hole-filling' electron rearrangements]. We have called this vector the 'Fermi-sea' vector [7, 26b, 26c]. The function space spanned by the orbitals orthogonal to the FS orbitals is called virtual. For states involved in inner-shell ionization, the corresponding angular symmetries of the subshells entering the Fermi-seas are usually the same. They often play the major role in multiplet and satellite structure in photoelectron spectroscopy.* ([27b], p. 858).

Available information suggests that in searching for good choices of state-specific Fermi-seas to satisfy the criterion $a_0 \approx 1$ in a satisfactory way subject to constraints of computational economy, attention should be given to the following probable causes of strong mixing, taken individually or collectively:

- Hydrogenic near-degeneracies.
- Valence configuration mixing with one or more members of a Rydberg series.
- Mixing of moieties associated with intramolecular charge transfer.
- Simultaneous intra- and intershell near-degeneracies—see Eq. (1) and example (4) of Section 4.
- H_2^+-type and general dissociation degeneracies, involving all the bonding and antibonding orbitals that are directly relevant to the dissociation channels.
- π-electron degeneracies, for example, in states of organic molecules, where judicious choices of active sets of π, π^*, n, and σ orbitals must be made.
- Breakdown of the hydrogenic Aufbau scheme for atoms starting with potassium and the transition metal atom series.

The above cases are functions of the parameters of the electronic Hamiltonian, which affect the spectrum, such as the effective Z and molecular geometry, and hold for both the ground and the excited (especially) states. Presumably, more such identifications are possible in molecules, especially for cases in which chemical transformations are investigated. Keeping track of energy denominators in possible mixings to first order in perturbation theory is a useful heuristic tool.

8.1. Properties of the noble gases: a qualitative application of the concept of the Fermi-sea

The hypothesis that the electronic structures of states of atoms and molecules should be understood and computed within a framework that describes them in zero order in terms of Fermi-seas rather than in terms of the conventional single configurations was first tested [7, 26b, 26c, 45] in terms of its physical relevance on the long-held view in research papers and in books that all noble gases are, par excellence, single-determinantal closed-shell atoms. Such a zero-order description leads to the conclusion that their properties should be roughly the same (hence their common epithet) and that the formalism and efficient methods for the computation of their properties should also be the same.

The initial adoption of the Fermi-seas for atoms in ground states across the Periodic Table, albeit in a rough and heuristic way [7, 26c], indicated to us that for this paradigm of closed-shell structures, there are in fact two categories. One category contains He and Ne, and the other contains Ar, Kr, Xe, and Rn. The latter atomic states were defined as *pseudo-closed-shell* structures since their Fermi-sea contains not only the *ns* and *np* spin orbitals but also the $(n+1)ns$, $(n+1)np$, and *nd* ones.

Given the meaning of the term $a_0\Psi_n^0$ in Eq. (8), it is hypothesized that the response of atoms to perturbations takes place in terms of their Fermi-seas and the superposition of the corresponding SACs.

The understanding and computation of properties of the noble gases must take this basic feature into account. This recognition led us [7, 26c, 45] to a rationalization of the existence of different physical and chemical properties between the two categories, such as the following facts:

1. The chemical reactivity that starts with Ar does not exist for He and Ne as, for example, in the case of the formation of diatomic fluorine ions [98]. In fact, in a review of the subject, Holloway and Hope [99] write that "The inert status for helium and neon remains unchallenged." Indeed, this is in accordance with the prediction that accompanied the introduction of the rough classification of atomic ground states in terms of Fermi-seas [7, 26c, 45].
2. The cross-section minimum in the Ramsaur–Townsend effect, which is present in slow electron–(Ar, Kr, Xe) scattering, is absent in the elastic scattering from He or Ne [100].
3. Photoabsorption transition probabilities and cross-sections for the two categories contain different satellite peaks due to the presence (or absence) of different zero-order Fermi-sea SACs in initial and final states, for example, Ref. [101]. This is in accordance with FOTOS, where, as explained in Section 4, the essential features of the transition probability and the related phenomena are explained by using in the zero-order transition matrix element the Fermi-sea multiconfigurational wavefunctions of the initial and the final states of the transition [26b, 45].

4. The jump in the polarizabilities, α, from Ne to Ar [102]. Starting with Ar, the presence of the unoccupied orbitals of the Fermi-sea facilitates the polarization compared to Ne, just like they facilitate hybridization and bond formation in the case of chemical compounds. Specifically, whereas $\alpha(\mathrm{He}) = 1.4$ a.u. and $\alpha(\mathrm{Ne}) = 2.7$ a.u., a sharp increase holds for argon, $\alpha(\mathrm{Ar}) = 11.1$ a.u., and the rise continues slowly, $\alpha(\mathrm{Kr}) = 16.7$ a.u. and $\alpha(\mathrm{Xe}) = 27.3$ a.u.

9. ANOTHER EXAMPLE OF THE POSSIBLE UTILITY OF THE SMALL FERMI-SEA WAVEFUNCTIONS IN ATOMS: THE CASE OF THE LOW-LYING STATES OF Be

In order to underline the significance of the state-specific nature of the Fermi-sea, on page 111 of the book of Ref. [26c], we gave indicative samples of proposed Fermi-seas for selected states of neutral atoms of atomic ions and diatomics. (See also the discussion linked to the examples of Section 4.) There, one may see that even for the small, four-electron Be atom, the Fermi-seas of the ground state, ^1S, and the lowest lying states of the even and odd symmetries are different. For example, whereas for most of them, the Fermi-sea contains only the $2s$, $2p$ valence orbitals (i.e., $2s^2 \leftrightarrow 2p^2$ mixing for the ^1S symmetry), and for the lowest state of ^1D symmetry, which is normally labeled by the $1s^2 2p^2$ SAC, the Fermi-sea contains as well the $3d$ orbital. (This extension takes into account the criterion of economy.) This fact has repercussions not only on the construction of calculations of atomic properties but also on calculations and analysis of Be-containing molecules.

For example, in 1999, Martin [103], following his extensive "Full CI" calculations, and in 2010, Schmidt, Ivanic and Ruedenberg [95], based on data from systematic calculations, used as "active space" the set of ($2s$, $2p$) spin orbitals and drew conclusions as to higher order virtual excitations and as to the separate significance of the ND and D correlations in the bonding of Be_2. However, things look different when the problem is analyzed in terms of the Fermi-seas of all the low-lying states. This is discussed and demonstrated in the following paragraphs and in Section 10.

9.1. The dependence of the Fermi-sea on symmetry, spin, and the parameters of the Hamiltonian. Valence-Rydberg state mixing

The spectrum of an atom or molecule depends on the parameters in the Hamiltonian and on symmetry (including spin). For example, the conspicuous effects of strong mixing of configurations in zero order on properties such as photoabsorption oscillator strengths can be interpreted in the same way in atoms and diatomics in terms of the dependence of the valence-Rydberg mixed wavefunctions of $\mathbf{H}(Z)$ or $\mathbf{H}(R)$ [104a, 104b].

In order to illustrate by a simple example the consequences of the dependence of the Fermi-sea not only on Z but also on symmetry, here I consider the lowest energy states of each symmetry for the Be isoelectronic sequence, known by the SAC labels $1s^22s^2\ ^1S$, $1s^22s2p\ ^{3,1}P^o$, $1s^22p^2\ ^1D$ and $1s^22p^2\ ^3P$.

In the spin-orbital determinantal H-F sea model, for the first-row atoms, the set of active orbitals has always been chosen as the eight spin orbitals, $2s\alpha$, $2s\beta, \ldots 2p_{-1}\alpha, \ldots 2p_{+1}\beta$, assuming the $1s^2$ core is frozen. On the other hand, in the framework of SACs, the proper choice of the Fermi-sea reveals features that have repercussions on the a priori understanding of certain properties and, of course, on computation. I consider each of the above states separately.

The case of the ground state, ^1S, was already discussed in Section 5, with numerical results for different values of Z. Both the H-F sea and the Fermi-sea zero-order wavefunctions are described by a superposition of the $1s^22s^2\ ^1S$ and $1s^22p^2\ ^1S$ SACs.

The Fermi-sea for the state labeled by $1s^22p^2\ ^3P$ cannot produce another SAC due to symmetry constraints. Therefore, the $1s^22p^2\ ^3P$ SAC, which is represented by one determinant, is an accurate zero-order representation.

The zero-order description of the two states $1s^22s2p\ ^3P^o$and $^1P^o$ exhibits differences that are due to the opposite signs in front of the exchange integral, $G_1(2s, 2p)$, in the corresponding energy expressions. Indeed, state-specific numerical MCHF calculations show that the $^1P^o\ 1s^22s2p$ SAC (two determinants) mixes rather significantly (with consequences for calculations of properties such as transition probabilities), with the Rydberg SAC $1s^22p3d\ ^1P^o$ (six determinants), whereas the $^3P^o 1s^22s2p$ SAC does not do so with $1s^22p3d\ ^3P^o$ (three determinants). Specifically, the corresponding superpositions are as follows:

$$|^3P^o\rangle_{\mathrm{MCHF}} : 0.994(1s^22s2p) - 0.096(1s^22p3d) - 0.042(1s^23s3p) \tag{17a}$$

$$|^1P^o\rangle_{\mathrm{MCHF}} : 0.972(1s^22s2p) - 0.218(1s^22p3d) - 0.089(1s^23s3p) \tag{17b}$$

with corresponding energies,

$$E(^3P^o) = -14.51800\,\text{a.u.}, \quad E(^1P^o) = -14.41658\,\text{a.u.} \tag{17c}$$

The doubly excited configuration $1s^23s3p$, whose coefficient is small in both superpositions, has been added for reasons of stability in the convergence of the solutions.

Not only is the mixing different but also the extent of the $2p$ orbitals in the two states differs. (On the contrary, the $2s$ orbitals are nearly the same, with $\langle r\rangle_{2s} = 2.5$ a.u.). Specifically, for the $^3P^o$ state, $\langle r\rangle_{2p} = 2.87$ a.u., whereas for the $^1P^o$ state, the $2p$ MCHF orbital is much more diffuse, with $\langle r\rangle_{2p} = 3.57$ a.u. This fact implies that the principal state-specific correlation functions from

the pair of the valence electrons are also different, even though the zero-order configurations are the same.

Finally, I come to the state normally labeled by $1s^2 2p^2\ ^1D$. In Ref. [26c], page 111, it was pointed out that the Fermi-sea for this state in Be goes beyond the H-F sea, even though Be is a first-row atom. Specifically, the zero-order self-consistent orbital set must also include the orbital $3d$ from the Rydberg configuration $1s^2 2s3d\ ^1D$. But this holds only for $Z = 4$. When $Z = 5, 6, \ldots$, the HN-D dominates and the significance of the $3d$ orbital, which is due to the strong valence-Rydberg series mixing $2p^2 \leftrightarrow 2snd$, $n = 3, 4, 5 \ldots$, in Be, is reduced considerably for $Z = 4$ and more drastically in the higher-Z isoelectronic ^1D ground states. Therefore, for the ions, the Fermi-sea need not include the $3d$ orbital, and the $1s^2 2p^2$ SAC is a sufficient zero-order label.

In order to make the argument quantitative, below I give a three-term expansion of $\Psi^0(^1D)$ and the corresponding coefficients for Be, B^+, and C^{++}.

$$\Psi^0(^1D) = a(Z)(1s^2 2p^2)\ ^1D + b(Z)(1s^2 2s3d)^1D + c(Z)(1s^2 3d^2)\ ^1D \qquad (18)$$

The $1s^2 2p^2$ SAC is represented by one determinant, the $1s^2 2s3d$ SAC by two, and the $1s^2 3d^2$ SAC by three.

A three-term numerical MCHF calculation gives the coefficients and energies:

$$\mathrm{Be}: a = 0.735, \quad b = 0.677, \quad c = 0.021, \quad E = -14.35583\ \text{a.u.} \qquad (19a)$$

$$\mathrm{B}^+: a = 0.959, \quad b = 0.280, \quad c = 0.045, \quad E = -23.82263\ \text{a.u.} \qquad (19b)$$

$$\mathrm{C}^{++}: a = 0.983, \quad b = 0.181, \quad c = 0.038, \quad E = -35.80617\ \text{a.u.} \qquad (19c)$$

Note that given the nature of the MCHF scheme, the MCHF configuration $1s^2 2s3d$ contains, in the absence of other configurations with structure $1s^2 2sd$, some of the information from the contribution of the higher lying $1s^2 2snd$ Rydberg levels.

9.2. A comment on the presence of the doubly excited configurations in Eqs. (17a, 17b and 18)

At this point, I would like to remark that in spite of their small mixing coefficients, the presence of the doubly excited configurations in Eqs. (17a, 17b and 18) is essential for two reasons that have been recognized after computational experience with diagonalizations of small energy matrices.

The first is the fact that they facilitate the computations in obtaining converged MCHF solutions for lower lying mixed wavefunctions. In fact, being optimized variationally self-consistently, they absorb some of the contribution from other excited configurations with the same structure. Obviously,

closely lying DES such as the $1s^2 3p^2\ {}^1D$ could also be included at a slight expense of the economy of computation. Indeed, such a calculation facilitates convergence of the solution of the MCHF equations for Be ^1D, suggesting the possible utility of the $3p$ orbital in CASSCF calculations of molecules. Specifically, the inclusion of the $1s^2 3p^2\ {}^1D$ SAC (with coefficient d) produces the following MCHF result for Be, to be compared with Eq. (19a),

$$a = 0.761, \quad b = 0.644, \quad c = 0.022, \quad d = -0.065, \quad E = -14.35823\,\text{a.u.} \quad (20)$$

The difference in energy between Eqs. (19a) and (20) is very small while the mixing coefficients of the two main configurations remain essentially the same. In other words, although the presence of the $3p$ orbital is helpful for reasons of computational convergence in the SCF procedure, it does not affect the essence of the result (19a). Furthermore, the presence of the doubly excited $1s^2 3p^2\ {}^1D$ SAC eliminates the need for considering the "semi-internal" $1s^2 2p 3p\ {}^1D$ SAC [82] since its contribution is negligible in the presence of the $1s^2 2p^2$ and $1s^2 3p^2\ {}^1D$ SACs.

The second reason has to do with the need to obtain good relative energies for those configurations that actually mix heavily due to the proximity of their diagonal energies. For example, the presence of the $1s^2 3d^2$ SAC in the MCHF calculation pushes the energy of the $1s^2 2s 3d$ SAC downwards, thereby securing a sufficiently accurate energy difference between $1s^2 2s 3d$ and $1s^2 2p^2$, which is necessary for the coefficients to come out correct (or nearly so). The addition of the $1s^2 3p^2\ {}^1D$ SAC lowers the Fermi-sea energy by only 0.065 eV. Similar considerations hold when examining the mixing of closely lying nonrelativistic states that is caused by the Breit–Pauli relativistic operators. A small correction to the energy difference may have a large effect on the mixing coefficients.

The above two attributes of double (or of multiple) virtual excitations is often important. Therefore, it is necessary to be aware of their possible contributions, even when their direct contribution is small. In other words, care and experience are sometimes needed when deciding a priori to decouple double or multiple excitations from a lower order function space with strongly mixed configurations. In our work on valence-Rydberg state mixing, it has been found advantageous to use experimentally suggested small adjustments of the diagonal energies in order to obtain accurate results. This approach, which was introduced in the 1970s, is discussed again in Ref. [22] as the *down-shift model*. The "down shift" refers to the correction needed when the D electron correlation energy of the valence state is not, and need not be, fully computed.

The example (19, 20) shows that at least for Be, and to a lesser degree for the ions, the adoption of a Fermi-sea, which is not dictated exclusively by the HN-D, leads to a serious correction of the SCA. In other words, by labeling in zero order, the ^1D ground state of Be simply as $1s^2 2p^2\ {}^1D$, and by developing

analysis and computational methodology accordingly, one misses important information already in zero order.

Furthermore, and this is important for the interpretation of the bonding in Be_2 to be discussed below, the results (17–20) show that primarily the state ^1D and to a lesser degree the state $^1P^o$ carry with them a significant $d-wave$ component in their Fermi-sea zero-order wavefunctions. This means that such orbitals should also be considered in the self-consistent, zero-order description of molecules containing Be.

9.3. Excitation energies of the low-lying valence states of Be. Comparison of results from conventional quantum chemistry calculations and from the use of the Fermi-sea energies obtained from numerical MCHF wavefunctions

The aim of the conventional computational methods for the solution of the TISE is to obtain accurate total energies. However, in spite of the impressive algorithmic power that has been developed and implemented by many people over the years, and in spite of the huge number of successful applications, the dependence of the final results on the basis sets remains crucial. Normally, in these methods both the occupied and the unoccupied orbitals are constructed in terms of a single set of basis functions. In contradistinction, the SPSA aims at using separately optimized function spaces, depending on the problem. For example, in atoms and diatomics, we have introduced the methodology of using a mixture of zero-order numerical HF or MCHF orbitals with variationally optimized analytic correlation orbitals.

In order to see the difference in the two approaches, below I focus on the excitation energies, ΔE, of the Be states that are discussed here. The nice thing about atomic spectra of this type is that there is accurate experimental information with which one can compare the results of a theoretical method (See, Tables of NIST, USA, in the WWW). Specifically, I compare the ΔE from the Be Fermi-sea energies for which cancellations on subtraction of total energies are expected, with those obtained from methods that have used one of the known basis sets. I consider two such publications. The first is in 1986 by Graham et al. [105] where a $\langle 9s9p5d \rangle$ contracted GTO basis (61 basis functions) was used for different types of computations. I keep the full CI (FCI) results. The second is in 2003 by Sears, Sherrill and Krylov [106], who studied aspects of "spin-flip" methods and compared them with FCI using the same basis set, which is a 6-31G.

Table 2.7 contains five columns of numbers for excitation energies in Be. The first two are from Ref. [106]. The acronyms SC-SF-CIS and FCI stand for "spin-complete, spin-flip, configuration-interaction singles" and "full configuration interaction," respectively. In this case, the application of SPSA employs the differences of only the Fermi-sea energies given in the previous subsection (15a, 16c, and 19). Also, the Fermi-sea wavefunction for the

Table 2.7 Excitation energies (eV) for the low-lying states of Be

	Theory				
	[106]		[105]	SPSA–Fermi-sea	
	SC-SF-CIS	FCI	FCI		Experiment
$1s^2 2s2p\ ^3P^o$	2.1	2.9	2.7	2.7	2.7
$1s^2 2s2p\ ^1P^o$	6.0	6.6	5.3	5.4	5.3
$1s^2 2p^2\ ^1D$	8.9	8.6	7.1	7.0	7.0
$1s^2 2p^2\ ^3P$	7.0	7.7	7.4	7.6	7.4

$1s^2 2p^2\ ^3P$ state is just the HF wavefunction, whose energy is -14.33631 a.u.. Therefore, the corresponding excitation energy is $\Delta(^3P - {}^1S) = 7.6$ eV. Note that I chose the accuracy of the first decimal digit, although the results of Refs. [105, 106] are given to the third decimal digit.

The, thus computed SPSA-Fermi-sea excitation energies from the ground state are in very good to excellent agreement with the experimental ones. For the results published in Ref. [106], large deviations from experiment are observed, even for the FCI results. Actually, the SC-SF-CIS excitation energy for the $1s^2 2s2p\ ^3P^o$ state is about 0.6 eV smaller than the experimental one.

Note that the often cited Hund's rule does not work here for the $1s^2 2p^2$ configuration. Fermi-sea correlations in ^1D, which are absent in ^3P, are to blame for this failure. This fact is easily recognized in the framework of the SPSA. There are additional observations and conclusions that one can draw from Table 2.7. For reasons of economy, these are not discussed here. It suffices to add that the size of the SPSA calculations is obviously orders of magnitude smaller than that of the other methods.

9.4. Fine and hyperfine structure of the two lowest bound states of Be^-, and their first two ionization thresholds

This is the title of the paper [107], where for the first time such properties, as well as electric dipole transition probabilities, were reported for the bound excited states of the negative ion of Be, namely the $Be^- 1s^2 2s2p^2\ ^4P$ and $1s^2 2p^3\ ^4S^o$, whose existence had previously been predicted theoretically. The paper is cited here in order to provide evidence of the flexibility and efficiency of methods in the framework of the SPSA (Breit–Pauli Hamiltonian) in producing correlated wavefunctions of excited states that are usable toward the calculation of other properties, such as fine and hyperfine structures and oscillator strengths [107]. Note that the computational facilities available to us in the early 1980s were far from optimal.

In addition to such properties of Be^-, we also published results for the hyperfine structure (hfs) of the metastable Be $1s^2 2s2p\ ^3P^o_J$ [107]. The calculated

energy intervals were in excellent agreement with experiment [108]. The hfs parameters were later also computed in terms of very large MCHF wavefunctions (with the number of configurations in the thousands) in [109, 110]. The agreement of the results of [109, 110] with those first predicted from the relatively small wavefunctions of Ref. [107] is very good.

9.5. The Fermi-seas of the Be low-lying states, the corresponding {2*s*, 2*p*, 3*s*, 3*p*, 3*d*} CASSCF model, and the weak bond of Be_2 $X^1\Sigma_g^+$

As explained in the previous sections, in the framework of the SPSA, the response of atomic or molecular states to external perturbations is best described, heuristically and quantitatively, by employing as reference the Fermi-sea wavefunction, Ψ_n^0, followed by the necessary additional corrections. For example, this was outlined in Section 4.3 with the FOTOS.

In a broader sense, similar notions can be applied when chemical binding is investigated. In this case, the "perturbation" of one atom by another atom (in the simplest situation) causes the mixing of low-lying atomic states. The description of these states in zero order by their Fermi-sea wavefunctions can shine light on issues of chemical binding, which are otherwise hidden. In the case of the Be valence states discussed earlier, the possibility arises that even for this small, four-electron atom, *d* orbitals, which are not occupied in the ground or low-lying states according to the single-configuration approximation, play a role in the *zero-order description* of chemical binding. This conjecture, which will be verified in Section 10 via ab initio molecular calculations on the Be_2 bond, is justified as follows:

When the formation of a molecular bond in the ground state is examined theoretically, say that of Be_2 $X^1\Sigma_g^+$, in principle it is not only the two atomic ground states that interact, for example, $^1S + {}^1S$. Instead, the quantum mechanical superposition principle entails that, subject to the constraints of molecular symmetry, a set of (relatively) low-lying states contribute to this interaction, of course with different weights. Indeed, this is the meaning of the early example by Rosen [111] on the hydrogen bond, where the superposition $1s + a2p_o$ was used. This type of superposition is often reduced to the orbital model and is described as $s \rightarrow p$ *hybridization* or, in the language of basis sets, as inclusion of *polarization functions*. Another such example from the early days of quantum chemistry is the formation of CH_4, for which the origin of its four bonds in the shape of a tetrahedron is due to the mixing of the carbon-excited state $1s^2 2s 2p^3\ {}^5S^0$, which is 4.2 eV above the ground state. (For a recent theory of molecular shapes and related issues, see Refs. [112, 113]). Of course, in a MO-CI computational scheme, the relative significance of each atomic state can be inferred only heuristically via arguments that depend on their structure, their symmetry, and their energy in the limiting regions of the united atom and the dissociated molecule.

The above brief commentary allows us to consider the possibility of deducing rational conclusions regarding binding in weakly bonded molecules such as Be_2 $X^1\Sigma_g^+$ (the binding energy is only about 0.1 eV) from the analysis of the Fermi-seas of both the ground and the lowest lying excited states of Be. An example of the consequences of these states in chemical binding is the $^2\Sigma^+$ energy spectrum of BeH [114]. MRCI adiabatic calculations and transformations to quasi-diabatic states revealed the presence of mixings of Rydberg states with valence and with "ion-pair" states as a function of internuclear distance [114].

In the theory of electronic structure and chemical binding, the case of Be and its compounds is special, mainly because the ground state is a ^1S, which is normally represented by a single determinant. Yet, it exhibits the strong effect of $2s^2 \leftrightarrow 2p^2$ mixing. This fact, and the related concept of the chemically important $2s \rightarrow 2p$ hybridization, have been used in the literature as the basic source of possible understanding of the causes of formation of the Be_2 $X^1\Sigma_g^+$ bond. For example, many researchers have tackled this problem computationally by starting with a CASSCF wavefunction that is based on the set $\{2s, 2p\}$ as the active space (Fermi-sea). However, such a CASSCF computation *cannot bind* Be_2 [95, 103].

On the other hand, things look different when the weak chemical bond of Be_2 $X^1\Sigma_g^+$ is interpreted in terms of the superposition of many states. The state-specific Fermi-seas for Be ^1S, $^3P^o$, $^1P^o$, and ^1D states show the following:

1. The thus computed excitation energies from the ground state are in excellent agreement with the experimental ones. (Table 2.7).
2. This agreement between theory and experiment would not happen if the $3d$ orbitals and corresponding Rydberg SACs were not included in the Fermi-sea of the ^1D and $^1P^o$ states.
3. Therefore, contrary to the decades-old lore of electronic structure theory, which assigns to the low-lying Be $^1P^o$ and especially the ^1D state, the labels of just the $1s^2 2s 2p$ $^1P^o$ and $1s^2 2p^2$ ^1D SACs, the state-specific Fermi-sea wavefunctions and energies indicate that in addition to p orbitals, the d orbitals play a significant role in zero order by participating in zero-order components of Rydberg character ($1s^2 2p 3d$ $^1P^o$ and $1s^2 2s 3d$ ^1D). Furthermore, given the strong mixing, the complementary components, which represent higher lying states, may also play an indirect role in the total mixing of the molecular states of the R-dependent spectrum of the molecular symmetry of interest, even though their excitation energy is high.

Hence, it is reasonable to expect that within a self-consistent multiconfigurational Fermi-sea molecular scheme, *d-waves* may have nonnegligible consequences in zero order to cases of Be binding. Such contributions ought to come from the excited states. In other words, apart from the approximate PEC that is associated with the ground atomic states ($^1S - ^1S$), it is

possible that excited states of ${}^1\Sigma_g^+$ symmetry, associated with, say, the $({}^1P^o - {}^1P^o)$, $({}^1S - {}^1D)$, or $({}^1D - {}^1D)$ dissociation channels in which the d-waves are present as Rydberg components, contribute to the character and the stability of the bond in zero order.

Of course, in addition to the above states, there are also low-lying excited Rydberg states, with labels $1s^2 2sns\ {}^{3,1}S$ and $1s^2 2snp\ {}^{3,1}P^o$, $n = 3, 4, \ldots$, which can also combine to form ${}^1\Sigma_g^+$ excited states that can influence the binding in the ground state of Be_2. The experimental excitation energies of the lowest lying ${}^{3,1}P^o$ and ${}^{3,1}S$ Rydberg states are $1s^2 2s3p\ {}^3P^o$: 2.72 eV, $1s^2 2s3p\ {}^1P^o$: 5.28 eV, $1s^2 2s3s\ {}^3S$: 6.46 eV, $1s^2 2s3s\ {}^1S$: 6.78 eV.

9.6. What can the above analysis tell us about the main character and the origin of the Be_2 bond?

There is a plethora of research papers on the formation and characteristics of the Be_2 bond, spanning a few decades. A very recent one by Schmidt, Ivanic and Ruedenberg [95] provides a list of references and, what is most interesting, a detailed discussion that is relevant to the arguments of the analysis and the position of the present paper. Specifically, the authors have carried out a series of calculations on a very large scale and have provided a thorough analysis using as reference point the results that emerge when the normal assumption of a $2s - 2p$ *active space* is made.

I take this opportunity to guide the reader through some of the important differences between the way things are analyzed in Ref. [95] and in this work. In order to be precise, I will quote a few of the phrases in Ref. [95] and will comment on them.

1. Schmidt et al. [95] start their introduction as follows: "A highly unusual bond is formed by two beryllium atoms in as much as the attraction between them results entirely from changes in the dynamic electron correlation." ([95], p. 8687).

   According to the arguments in the text, and as I repeat below, the fundamental contribution of the $3d$ orbitals that is revealed in the computations of [95] are in the function space of the Fermi-sea *nondynamical* electron correlation and not of *dynamical* correlation.
2. In their section IV, Schmidt et al. [95], after they state the long-known fact that the HF calculation produces, incorrectly, a nonbinding (repulsive) potential energy curve and that the $2s \rightarrow 2p$ hybridization improves things but does not correct them, eventually note the following having to do with the basic significance of the $3d$ orbital:
   a. "In addition to hybridization, the MCSCF potential also contains the effects of nondynamical correlations due to excitation from the SCF orbitals into the valence orbitals generated by the $2p$ shell. This near-degeneracy correlation energy lowering also lowers the energy by thousands of wave-numbers. Surprisingly, however, it hardly changes

the shape of the potential and it does not remove the repulsive character of the potential." ([95], p. 8691).

b. "Manifestly, the orbitals that arise from the 3*d* shell are the ones that account for the presence of the bond in Be_2." ([95], p. 8692).

In other words, the CASSCF calculation with the standard $2s-2p$ active space, where no 3*d* orbitals are present (for reasons that were explained above) has led them to the conclusion that the ND correlation effects *do not* produce the chemically correct information.

It is this conclusion of Schmidt et al. [95] (which is in agreement with a previous one by Kutzelnigg—reference cited in [95]) as to the separation of ND from D correlation effects and their significantly distinct roles, which is critically examined here, in view of the fact that the $^1P^o$ state and especially the ^1D state, do contain substantial components with *d*-waves. The participation of these low-lying atomic states to the binding of Be_2 would imply that an active space (Fermi-sea) with added 3*d* orbitals should provide the essence of the origin of the unusual Be_2 bond. In other words, a Ψ_n^0 that is obtained from a CASSCF calculation that includes 3*d* orbitals beyond the standard $\{2s, 2p\}$ set should produce binding, thereby leading to the conclusion that ND correlation suffices to explain semiquantitatively the formation of this bond.

In order to confirm this assertion, I present new results for the binding in Be_2 $X^1\Sigma_g^+$ obtained from two types of calculations of Ψ_n^0. One is a CASSCF, with just the near-degeneracy active space of the $\{2s, 2p\}$ orbitals. The other takes into account the wavefunctions (17b) and (20) and computes a CASSCF wavefunction with $\{2s, 2p, 3s, 3p, 3d\}$ orbitals. I note that the addition into the active space of just the 3*d* orbitals is enough to support the validity of the argument qualitatively. However, better convergence and overall accuracy for the final results on the PEC is obtained when the 3*s* and 3*p* orbitals are also included, and this is why such calculations are also carried out, with results that are shown in the next section.

10. THE Be_2 MOLECULE: ITS BOND IN THE $X^1\Sigma_g^+$ GROUND STATE AND THE $^1\Sigma_g^+$ EXCITED STATES

In 2009, an experimental paper [115] and a related short comment [116] on the issue of the precise characteristics of the PEC of the Be_2 $^1\Sigma_g^+$ state were published in the journal SCIENCE. In their experimental report, whose results resolved previous uncertainties, Merritt, Bondybey and Heaven [115] review and explain briefly the long-held interest in this *70 year-old problem*. They note that "The sensitivity of the Be_2 PEC to the level of theory has made analysis of this molecule a benchmark problem for quantum mechanics and a critical test for new theoretical models and procedures. At present, more than

100 papers devoted to beryllium dimers and clusters have appeared, making the dimer one of the most extensively theoretically studied molecules". In the same spirit, Bernath [116] points out that "Quantum Chemistry attributes the formation of the Be-Be bond and the unusual potential shape to the inclusion of more and more p character in the valence orbitals as the atoms approach each other [103]."

With respect to the last quotation, it is known from the literature on the Be_2 bond, for example, Refs. [95, 103], and is verified here again as part of a series of calculations, that a CASSCF calculation that uses $\{2s, 2p\}$ as the active set of zero-order spin orbitals yields essentially a repulsive curve. This fact has been emphasized in Ref. [95], who carried out not only large-scale calculations but also an *in-depth analysis* of the origin of the Be–Be bond, by emphasizing that "the binding in Be_2 is contingent on the effects of dynamical electron correlation, which is uncommon and therefore of considerable interest." ([95], p. 8687).

Following the spirit of the SPSA, the purpose of the present study and computations was not to produce numerically precise total energies for the PEC, especially since this is a very shallow potential. Instead, as also argued in Ref. [95], the goal was to provide arguments and numerical support as to the essential features of the origin of this bond, in terms of reliable computations that are relevant to this issue.

Thus, according to Eq. (8), I focused on the calculation of $a_0\Psi_n^0 + \Phi_n^{\rm corr}$, where two choices of Ψ_n^0 were made. The first is a CASSCF wavefunction obtained in terms of the $\{2s, 2p\}$ set of active orbitals, which is the choice of the earlier publications by other researchers. This calculation was carried out only for reasons of comparison. The second choice for Ψ_n^0 is the CASSCF solution that is obtained when the Fermi-sea set $\{2s, 2p, 3s, 3p, 3d\}$ is adopted, according to the analysis of the Fermi-seas of the low-lying states of Be presented in the earlier sections. For this case, both the Ψ_n^0 and the $\Psi_n = a_0\Psi_n^0 + \Phi_n^{\rm corr}$ wavefunctions of Eq. (8) were obtained, the latter at the level of MRCISD. On the other hand, I deemed it unnecessary for the economy and the purposes of the problem to account for the (small) changes of electron correlation along the PEC, which are due to the inner electrons, $1s^2$.

By considering that bonding occurs in terms of the superposition of many low-lying Be states, I have already argued in the previous section that the origin of the Be–Be bond must be due not only to p-waves that are present in the Fermi-seas of the ground and the low-lying excited states but also to the contribution of d-waves, which are also in the zero-order Fermi-sea and not only in the function space of D correlations. These come into play from the significant mixing of Rydberg configurations with $3d$ orbitals in the Fermi-seas of the $1s^2 2s 2p\ ^1P^o$ and especially the $1s^2 2p^2\ ^1D$ excited states of Be.

In this section, this is verified via relevant molecular calculations using the code MOLPRO [117, 118]. Specifically, the inclusion of d orbitals in the Fermi-sea (active space), in addition to s and p orbitals, which is a reasonable

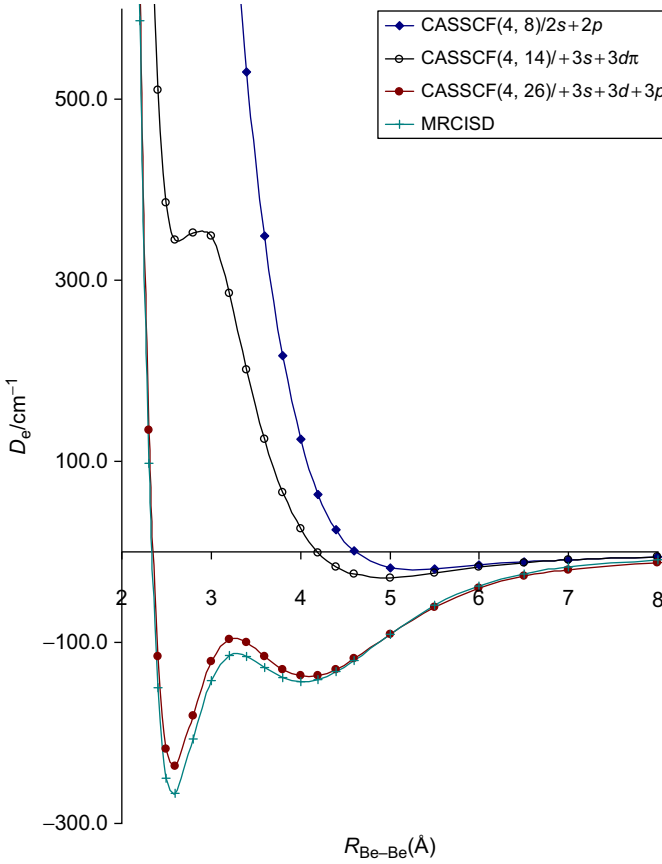

Figure 2.1 A hierarchy of CASSCF calculations that reveal the critical significance of the presence of *d* orbitals in the zero order, "Fermi-sea" set of orbitals. The curve for CASSCF (4, 26)/+3*s*, +3*d*, +3*p* is in essential agreement with that of the MRCISD, whose reference wavefunction is the standard CASSCF (4, 8)/2*s* + 2*p*. (The aug-cc-pVDZ basis set was used).

consequence of the assumption of the role of the Fermi-seas of the excited states of Be, suffices to change a repulsive CASSCF $(4,8)/2s+2p$ PEC for Be_2 $X^1\Sigma_g^+$ into an attractive one.

The first set of calculations (Figure 2.1) was done using Dunning's contracted correlation-consistent basis set of double-zeta quality augmented with a set of diffuse functions, aug-cc-pVDZ (10s5p2d) →[4s3p2d]. Each PEC was obtained from 30–35 calculated points.

Figure 2.1 contains four curves. I use the conventional nomenclature. The first PEC was obtained from a CASSCF $(4,8)/2s+2p$. This is the standard reference zero-order calculation applied in all earlier calculations. The curve

is essentially repulsive. Nothing changes when a $3s$ orbital is included in the Fermi-sea. The curve of CASSCF(4,10)/$2s + 2p + 3s$ is essentially the same as that of CASSCF (4,8)/$2s + 2p$ (not shown).

However, a qualitatively drastic change occurs when $3d\pi$ orbitals are added to the zero-order set. Specifically, the second curve depicts the PEC from a CASSCF (4,14)/$+3s + 3d\pi$ calculation and shows the appearance of a local minimum in the region where, in fact, the exact equilibrium distance is obtained from both experiment [115] and from large-scale computations [95, 103] and below. This is the first suggestion that some type of interaction with higher lying states, induced by the presence of the $3d\pi$ orbitals in the molecular Fermi-sea, is capable of changing qualitatively the initially repulsive character of the PEC in Be_2 into one where the minimum starts appearing in the region of the correct R_{eq}. ($\approx$ 2.5Å). This is in distinct contrast to other types of advanced calculations, in the literature as well as here, where a minimum (invalid) first appears, alone or as a second minimum, in the range 4.0–5.0 Å.

When, according to the structure of the Fermi-seas of the ground and the low-lying excited states of Be, $3p$ orbitals are added together with all $3d$ orbitals to the "active space," the third PEC, labeled as CASSCF (4, 26)/$+3s + 3p + 3d$, is obtained. Now, the new inner minimum acquires a shape that is close to the true one but, of course, with a much smaller dissociation energy than the exact one. The second minimum in the region of about 4.0 Å–4.5 Å is characteristic of all approximate computations of the Be_2 bond, [95, 103] and references there in. It eventually goes away when the size of the calculation increases.

Finally, the last PEC represents $\Psi_n = a_0\Psi_n^0 + \Phi_n^{corr}$ and is obtained from a MRCISD calculation based on the CASSCF (4, 8)/$2s + 2p$ zero-order wavefunction. In such a calculation, the corrections that are taken into account by Φ_n^{corr} are considered part of the D correlation. The difference between the last two curves is very small. Obviously, when additional correlations of the D type (in terms of configurations and basis sets) are included in a full CI computation, the inner minimum goes down close to its true value while the outer one disappears [95, 103, 115]. The same occurs in the present work using the larger CASSCF (4, 26) reference wavefunction with the Be Fermi-sea of $\{2s, 2p, 3s, 3p, 3d\}$ orbitals.

Figure 2.2 depicts the spectrum of the ground and the first 10 excited states of $^1\Sigma_g^+$ symmetry as computed at the level of a state-averaged CASSCF (4, 26)/aug-cc-pVDZ. The PECs of the excited states exhibit clearly the presence of deep minima, of barriers and of avoided crossings.

These results seem to confirm qualitatively the assertion as to the significance of d-waves in the zero-order description of the Be $^1P^o$ and ^1D excited states: when, in addition to p and d orbitals are included in the "active space," the representation of the ground and the excited states in terms of Ψ_n^0, a few of which correlate with the $^1P^o$ and the ^1D states of one atom, indicates that considerable interaction (state mixing) takes place in the region where the

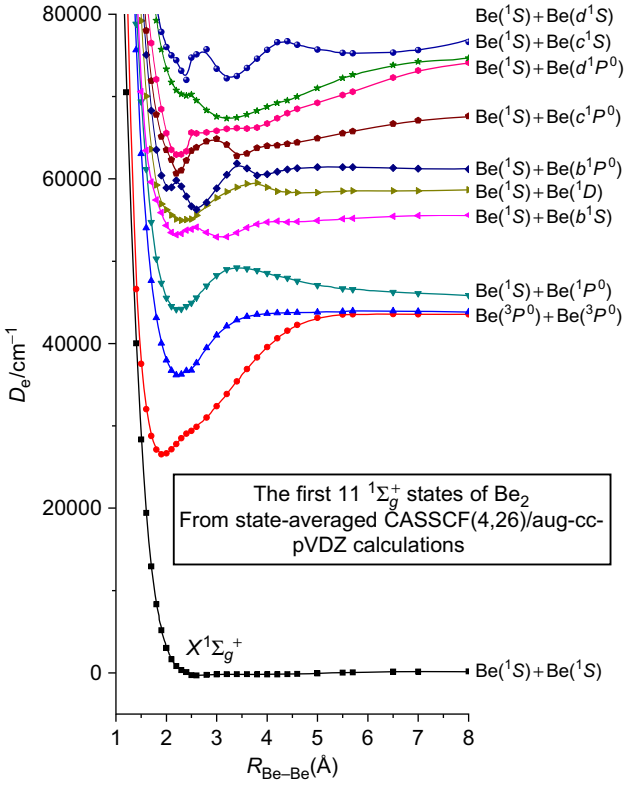

Figure 2.2 The first 11 $^1\Sigma_g^+$ potential energy curves of Be_2 from a state-averaged CASSCF (4, 26)/aug-cc-pVDZ calculation. Considerable state mixing takes place in the region where the weak Be_2 bond of the ground state is formed. See text.

minimum appears, that is, around 2.5 Å. Figure 2.3 presents the PECs of the first seven $\Psi_n = a_0\Psi_n^0 + \Phi_n^{\text{corr}}$ obtained from MRCISD calculations in which Ψ_n^0 is a CASSCF $\{(4, 26)/+3s+3p+3d\}$ reference wavefunction. All these seven $^1\Sigma_g^+$ states are below the ionization threshold of the state $Be_2^+\,{}^2\Sigma_u^+$, which is at about 7.4 eV.

The curves in Figure 2.2 and 2.3 are very similar, indicating that this Ψ_n^0 contains the dominant part of ND electron correlation for much of the spectrum. Indeed, the criterion linked to Eq. (8), $a_0 \approx 1$, is satisfied very well. For example, Table 2.8 contains the values of a_0 for the first four states, at three values of the internuclear distance, $R = 2.5$ Å (equilibrium), $R = 5.0$ Å (intermediate), and $R = 100.0$ Å (dissociation). Their high and nearly constant value along the PEC implies that the choice of the $\{2s, 2p, 3s, 3p, 3d\}$ active set is pertinent.

Finally, Figure 2.4a–2.4d compare the PECs obtained from the CASSCF $\{(4, 26)/+3s+3p+3d\}$ and the corresponding MRCISD calculations, for the first

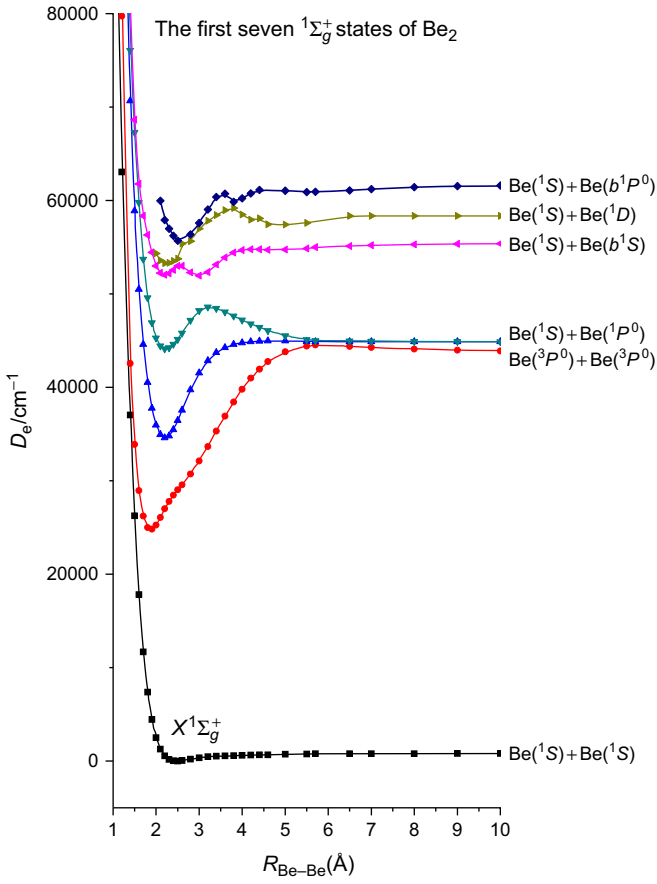

Figure 2.3 The first seven $^1\Sigma_g^+$ states of Be_2 at the state-averaged CASSCF (4e/26o)+1 + 2 (=MRCISD) level of theory, with the aug-cc-pVQZ basis set. The energy minima of all states are below the ionization threshold at about 7.4 eV. ($^2\Sigma_u^+$ state of Be_2^+). At this computational level, with the $1s^2$ electrons kept "frozen," $D_e = 791\,cm^{-1}$ at $R_e = 2.489$ Å.

four $^1\Sigma_g^+$ states with a aug-cc-pVQZ basis set. The Ψ_n^0 has picked up all the significant characteristics while there is very good quantitative agreement, especially for the excited states. I emphasize that, with this basis set, the CASSCF calculation is much more economic than that of the corresponding MRCISD. For the ground state, the MRCISD calculation gives a binding energy of 791 cm^{-1} at the equilibrium distance $R_e = 2.489$ Å.

In conclusion, the results presented in the previous paragraphs and sections as to the choice and significance of Fermi-sea wavefunctions of states of Be and Be_2 ($^1\Sigma_g^+$ symmetry) support the argument that the unusual Be_2 bond is produced predominantly by ND-type correlations, whose characteristics originate from the participation in the bonding of a few low-lying

Table 2.8 Satisfaction of criterion for Eq. (8), $a_0 \approx 1$, in the case of the lowest four Be_2 $^1\Sigma_g^+$ states along the whole PEC, when Ψ_n^0 is the Fermi-sea (CASSCF) wavefunction with active set the Be{2*s*, 2*p*, 3*s*, 3*p*, 3*d*} orbitals[1]

	$R = 2.5$ Å	$R = 5.0$ Å	$R = 100.0$ Å
$X^1\Sigma_g^+$	0.997	0.998	0.997
$1^1\Sigma_g^+$	0.996	0.970	0.724
$2^1\Sigma_g^+$	0.996	0.964	0.998
$3^1\Sigma_g^+$	0.992	0.954	0.978

[1] The total wavefunction $\Psi_n = a_0\Psi_n^0 + \Phi_n^{\text{corr}}$ is obtained from MRCISD at each value of internuclear distance.

states of Be and not just of the $(a1s^22s^2 + b1s^22p^2)$ ^1SBe ground state. In this way, the presence of *d*-waves in the active space makes the difference and induces binding. This conclusion differs from that of Schmidt, Ivanic and Ruedenberg [95] who assume, as others before them, that the "active space" consists of just the {2*s*, 2*p*} of the Be ground state and claim that the weak bond of Be_2 should be attributed exclusively to D-type correlations.

11. SYNOPSIS

For many applications of quantum chemistry, it is not necessary to solve the *time-independent Schrödinger equation* (TISE) to a high level of accuracy for the total energy. In other words, the degree of the effect of electron correlation on properties depends on the problem, for example, Ref. [7]. A simple example is that of the determination of a property of an unperturbed Rydberg wavefunction of a many-electron atom that depends on the outer electron orbital. Say one is interested in the 25th such state. A direct, state-specific numerical solution of a one-electron TISE with an effective potential, with special attention to the proper boundary conditions and to the numerical accuracy in the asymptotic region, will yield a considerably more suitable wavefunction than the one that would be produced by a conventional electron correlation method that is normally applied to *N*-electron ground states (if applicable to the case of such excited states) and aims at the computation of the total energy of the *N*-electron system.

For the multitude of cases in quantum chemistry in which the omnipresence of interelectronic interactions render the use of one-electron models inadequate, simple consideration of the formalism and the meaning of perturbation theory that is based on well-defined zero-order reference wavefunctions indicates that not all terms play the same role as regards their contribution to the eigenfunction of each state. Therefore, depending on the problem under consideration, it may be possible, to a good and practical approximation, to partition the total wavefunction in such a way to

be able to focus on the computation of only those portions that contribute the most to the state and property of interest to avoid the impact of the law of diminishing returns. In other words, such analysis, in conjunction with experience that can be accumulated via appropriate computations on various systems, could provide quantitative insight into fundamental issues of Quantum Chemistry with economy. This is the framework of the *state- and property-specific approach* (SPSA) to Quantum Chemistry.

In symbols, the general compass is the form $a_0\Psi_n^0 + \Phi_n^{\rm corr}$ of the wavefunction of Eq. (8). In principle, the two parts are represented by different function spaces, whose elements and size depend on the problem. The zero-order wavefunction, Ψ_n^0, is normally obtained self-consistently. Its orbitals belong to the state-specific *Fermi-sea*, see below.

Even for ground states, the actual or anticipated prowess of each computational method and its algorithms in handling systems with many electrons and terms of high orders that contribute small amounts to the total energy cannot be dissociated from the fact that the overall accuracy depends on the character and quality of the function space that is used for the calculation of the property of interest. This requirement becomes more stringent when it comes to excited states, especially those that are in the continuous spectrum and produce resonances, for example, Refs. [10, 21]. Regarding the basis set problem, the SPSA seeks after the possibility of optimizing small function spaces.

In particular, as regards its implementation, first to atomic structures and subsequently to diatomic ones, this has been done in the following way: In order to secure the accuracy of the Fermi-sea orbitals, we compute Ψ_n^0 via the numerical solution of the state-specific HF or, most frequently, MCHF equations. The choice of the components of $\Phi_n^{\rm corr}$ that are considered relevant to the overall calculation depends on the desired level of accuracy and the property. They are expressed in terms of analytic functions, whose final optimization is done variationally to all orders.

In certain problems of excited states, depending on the electronic structures of the moieties involved and on the type of superpositions that may be relevant in zero order, actual or effective projections are implemented via the appropriate choice of the functions spaces.

When computing state mixing of separately optimized function spaces, or electron correlation, *nonorthonormal CI* (NONCI) can be applied. Normally, because the number of matrix elements in such SPSA constructions is not very large, the execution of NONCI does not destroy the economy of the overall calculation. Also, in certain types of problems, such as radiative or radiationless transition rates, NON is also taken into account for off-diagonal configurational N-electron matrix elements involving state-specific basis sets that are not orthonormal.

The introduction in the early 1970s of the concept and the methodology of the Fermi-sea as the zero-order orbital set for the construction of the state-specific multiconfigurational wavefunction played on the themes

of the two near-degeneracies (Section 5) and the corresponding HF-sea (Sections 5–7) at a register that may incorporate other types of possible mixings, especially in excited states, such as Hamiltonian parameter-dependent valence-Rydberg channel interactions or intramolecular charge transfer

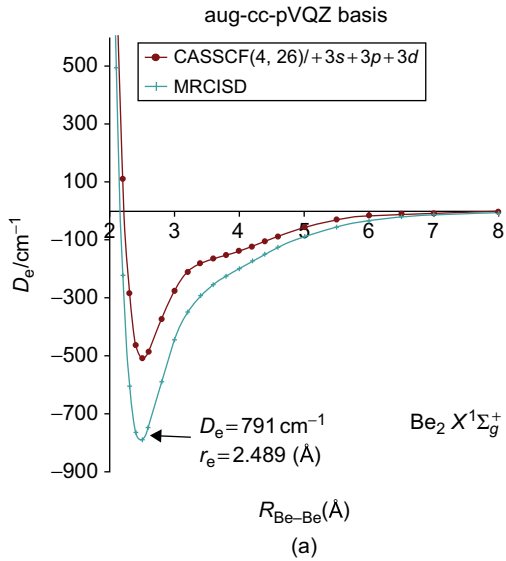

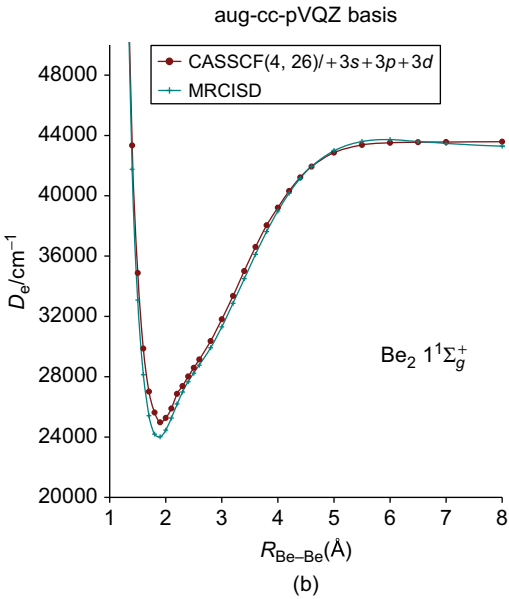

(*Continued*)

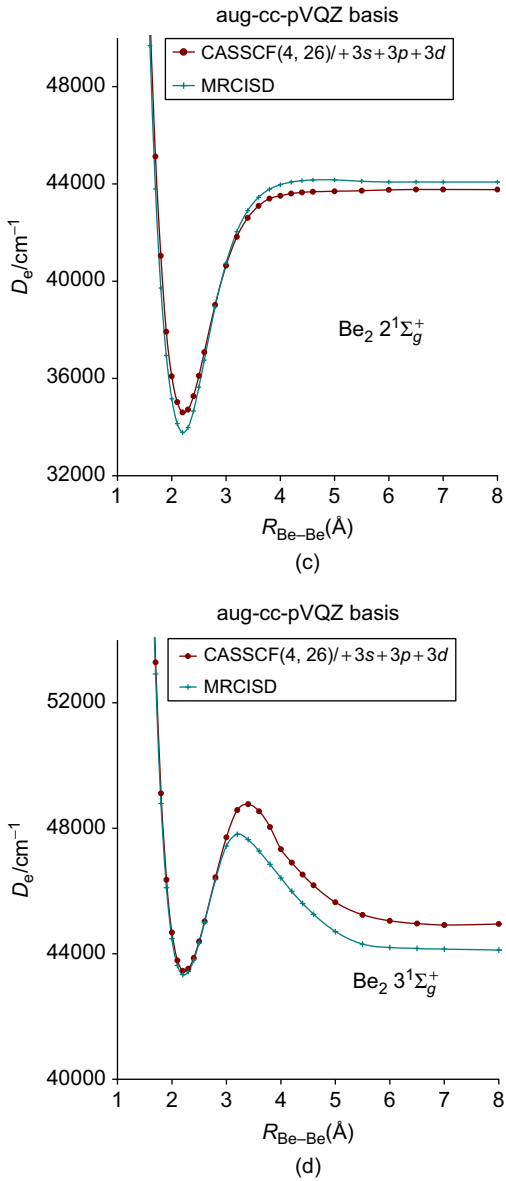

Figure 2.4 (a) Results from CASSCF(4, 26) calculations, where the active space consists of the 2*s*, 2*p*, 3*s*, 3*p*, and 3d orbitals of each Be atom. The basis set was the aug-cc-pVQZ, with the contraction {13*s*7*p*4*d*3*f*2*g*}→[6*s*5*p*4*d*3*f*2*g*]. MRCISD calculations using the CASSCF (4, 26) as reference and keeping "frozen" the two 1*s* orbitals of each Be. The Be_2 binding energy at this MRCI level is 791 cm^{-1} and the bond length, $r_e = 2.489$ Å. (b) As in Figure 2.4a, for the first excited state. (c) As in Figure 2.4a, for the second excited state. (d) As in Figure 2.4a, for the third excited state.

(Section 8), according to the criterion of the SPSA, $a_0 \approx 1$, linked to Eq. (8). Given the progress of quantum chemistry in recent years, this route to the understanding and calculation of electronic structures may be easily recognizable and to some extent executable. However, this was not the case in the period around 1970, especially for excited states in the discrete or the continuous spectrum.

The earlier sections contain a number of prototypical ("proof-of-principle"-type) examples where these ideas and methods can be used. I point out that the possibility of constructing state-specific and, hence, compact and directly interpretable wavefunctions has allowed the implementation of practical methodologies for the ab initio nonperturbative solution of the *complex-eigenvalue Schrödinger equation* for unstable states that are created when *ac* external fields are included [10] and of the *time-dependent Schrödinger equation* for various types of problems [17].

The last two examples (Sections 9 and 10) started with the efficient computation of the Fermi-sea wavefunctions of the low-lying states of Be, whose structure can be utilized in the a priori understanding of the major contributions to the function spaces that are responsible for bonding in Be-containing compounds. Specifically, I discussed the formation of the Be_2 $X^1\Sigma_g^+$ ground state in terms of a Fermi-sea (active space) which, in addition to s and p orbitals, includes d orbitals that correspond to the presence of $3d$ orbitals in the zero-order *valence-Rydberg state mixing* that exists in the ^1D and $^1P^o$ states of Be. In this context, by paying attention to the rough features of the potential energy curves of the first few $^1\Sigma_g^+$ states, it may be concluded that the formation of the weak bond of Be_2 can be called an *excited-states effect*, whose critical component is induced by the activity of d-waves in the *zero-order, nondynamical* function space comprising Ψ_n^0 of Eq. (8). The MRCISD results presented in Figures 2.1–2.4 demonstrate the physical relevance of the active set $\{2s, 2p, 3s, 3p, 3d\}$ that was chosen for the calculation of the CASSCF wavefunctions for this system. These CASSCF wavefunctions satisfy the SPSA criterion of $a_0 \approx 1$ over the whole PEC (Table 2.8).

REFERENCES

[1] B.O. Roos, P.R. Taylor, P.E.M. Siegbahn, A complete active space SCF method (CASSCF) using a density matrix formulated super-CI approach, Chem. Phys. 48 (1980) 157.

[2] P.E.M. Siegbahn, J. Almlöf, A. Heiberg, B.O. Roos, The complete active space SCF (CASSCF) method in a Newton-Raphson formulation with application to the HNO molecule, J. Chem. Phys. 74 (1981) 2384.

[3] B.O. Roos, U. Ryde, Molecular orbital theory (SCF methods and active space SCF), in: Comprehensive Coordination Chemistry II, vol. 2, eds. J.A. McCleverty and T.J. Meyer, Elsevier, Amsterdam, 2003, pages 519–539.

[4] C.C.J. Roothaan, Self-consistent field theory for open shells of electronic systems, Rev. Mod. Phys. 32 (1960) 179.

[5] C.C.J. Roothaan, P.S. Bagus, Atomic self-consistent field calculations by the expansion method, in: Methods in Computational Physics, vol. 2, eds. B. Alder, S. Fernbach and M. Rotenberg, Academic Press, New York, 1963, pages 47–94.
[6] B. Roos, C. Salez, A. Veillard, E. Clementi, A general program for calculation of atomic SCF orbitals by the expansion method, IBM technical report RJ 518 (1968).
[7] D.R. Beck, C.A. Nicolaides, The effect of electron correlation on atomic properties, Int. J. Quantum Chem. Supp. 8 (1974) 17.
[8] C.A. Nicolaides, Theoretical approach to the calculation of energies and widths of resonant (autoionizing) states in many-electron atoms, Phys. Rev. A 6 (1972) 2078.
[9] C.A. Nicolaides, and N.A. Piangos, State-specific approach and computation of resonance states. Identification and properties of the lowest $^2P^o$ and ^2D triply excited states of He^-, Phys. Rev. A 64 (2001) 052505.
[10] C.A. Nicolaides, Theory and state-specific methods for the analysis and computation of field-free and field-induced unstable states in atoms and molecules, in: C.A. Nicolaides, E.J. Brändas (Eds.), Advances in Quantum Chemistry, Academic Press, Boston, vol. 60, 2010, p. 163–267.
[11] S. Salomonson, I. Lindgren, A.-M. Märtensson, Numerical many-body perturbation calculations on Be-like systems using a multi-configurational model space, Phys. Scripta 21 (1980) 351.
[12] U. Kaldor, Intruder states and incomplete model spaces in multireference coupled-cluster theory: The $2p^2$ states of Be, Phys. Rev. A 38 (1988) 6013.
[13] U.S. Mahapatra, S. Chattopadhyay, R.K. Chaudhuri, Second-order state-specific multi-reference Mller-Plesset perturbation theory: Application to energy surfaces of diimide, ethylene, butadiene and cyclobutadiene, J. Comput. Chem. 32 (2011) 325.
[14] U.S. Mahapatra, B. Datta, D. Mukherjee, A state-specific multi-reference coupled cluster formalism with molecular applications, Mol. Phys. 94 (1998) 157.
[15] F.A. Evangelista, J. Gauss, Insights into the orbital invariance problem in state-specific multireference couple cluster theory, J. Chem. Phys. 133 (2010) 044101.
[16] B. Roos, A new method for large-scale CI calculations, Chem. Phys. Lett. 15 (1972) 153.
[17] Th. Mercouris, Y. Komninos, C.A. Nicolaides, The state-specific expansion approach to the solution of the polyelectronic time-dependent Schrödinger equation for atoms and molecules in unstable states, in: C.A. Nicolaides, E. Brändas (Eds.), Unstable States in the continuous spectrum, Part I, Adv. Quantum Chem., vol. 60, Academic Press, London, 2010, p. 333.
[18] C. Froese Fischer, A general multi-configuration Hartree-Fock program, Comput. Phys. Commun. 14 (1978) 145.
[19] E.A. McCullough, Numerical Hartree-Fock methods for diatomic molecules: A partial wave expansion approach, Comp. Phys. Rep. 4 (1986) 265.
[20] C.A. Nicolaides, The state-specific approach to the solution of problems of electronic structure and dynamics involving excited states, Int. J. Quantum Chem. 60 (1996) 119.
[21] C.A. Nicolaides, On the application of conventional quantum chemistry methods of computation to states perturbed by the continuous spectrum, Int. J. Quantum Chem. 71 (1999) 209.
[22] C.A. Nicolaides, On calculations of correlated wave functions with heavy configurational mixing, Int. J. Quantum Chem. 102 (2005) 260.
[23] Y. Komninos, C.A. Nicolaides, Multi-channel reaction matrix theory and configuration-interaction in the discrete and in the continuous spectrum. Inclusion of closed channels and derivation of quantum defect theory, Z. Phys. D 4 (1987) 301.
[24] Y. Komninos, G. Aspromallis, C.A. Nicolaides, Theory and computation of perturbed spectra. Application to the Al^2D relativistic J $= 5/2, 3/2$ spectrum, J. Phys. B 28 (1995) 2049.

[25] Y. Komninos, C.A. Nicolaides, Quantum defect theory for Coulomb and other potentials in the framework of configuration interaction, and implementation to the calculation of ^2D and $^2F^o$ of *Al*, J. Phys. B 37 (2004) 1817.
[26a] D.R. Beck, C.A. Nicolaides, Theory of the one-electron binding energies including correlation, relativistic and radiative effects: Application to free atoms and metals, in: C.A. Nicolaides, D.R. Beck (Eds.), Excited States in Quantum Chemistry, Reidel, Dordrecht, 1978, p. 329.
[26b] C.A. Nicolaides, and D.R. Beck, Many-body theory of photoabsorption in atoms and molecules, in: C.A. Nicolaides, D.R. Beck (Eds.), Excited States in Quantum Chemistry, Reidel, Dordrecht, 1978, p. 143.
[26c] D.R. Beck, C.A. Nicolaides, Theory of the electronic structure of excited states in small systems, with numerical applications to atomic states, in: C.A. Nicolaides, D.R. Beck (Eds.), Excited States in Quantum Chemistry, Reidel, Dordrecht, 1978, p. 105.
[27a] C.A. Nicolaides, Y. Komninos, D.R. Beck, The K-shell binding energy of *Be* and its fluorescence yield, Phys. Rev. A 27 (1983) 1865.
[27b] D.R. Beck, C.A. Nicolaides, Specific correlation effects in inner-electron photoelectron spectroscopy, Phys. Rev. A 26 (1982) 857.
[27c] D.R. Beck, C.A. Nicolaides, Theory of Auger energies in free atoms: Application to the alkaline earths, Phys. Rev. A 33 (1986) 3885.
[28] C.A. Nicolaides, A. Zdetsis, A. Andriotis, State-specific many-electron theory of core levels in metals: The 1*s* binding energy of *Be* metal, Solid State Comm. 50 (1984) 857.
[29] A. Szabo, N.S. Ostlund, Modern Quantum Chemistry, Dover Publications, Mineola, 1996.
[30] O. Sinanoğlu, Many–electron theory of atoms and molecules. I. Shells, electron pairs vs many-electron correlations, J. Chem. Phys. 36 (1962) 706.
[31] R.E. Watson, Approximate wave functions for atomic *Be*, Phys. Rev. 119 (1960) 170.
[32] D.D. Ebbing, Configuration interaction study of the lithium hydride molecule, J. Chem. Phys. 36 (1962) 1361.
[33] E.C. Barnes, G.A. Peterson, MP2/CBS atomic and molecular benchmarks for H through Ar, J. Chem. Phys. 132 (2010) 114111.
[34] C.A. Nicolaides, State-specific theory of quantum chemistry, in: R. Carb (Ed)., Quantum Chemistry- Basic Aspects, Actual Trends", Elsevier, Amsterdam, 1989, p. 343.
[35a] C.A. Nicolaides, A. Zdetsis, Theory of chemical reactions of vibronically excited $H_2\, B^1\Sigma_u^+$. II: Noble gas dihydrides, J. Chem. Phys. 80 (1984) 1900.
[35b] C.A. Nicolaides, N.C. Bacalis, Y. Komninos, Theory for the direct construction of diabatic states and application to the $He_2^+\, ^2\Sigma_g^+$ spectrum, Chem. Phys. Lett. 192 (1992) 486.
[36] I.D. Petsalakis, G. Theodorakopoulos, C.A. Nicolaides, R.J. Buenker, S.D. Peyerimhoff, Nonorthonormal CI for molecular excited states. I. The sudden polarization effect in 90° twisted ethylene, J. Chem. Phys. 81 (1984) 3161.
[37] I.D. Petsalakis, G. Theodorakopoulos, C.A. Nicolaides, R.J. Buenker, Nonothonormal CI for molecular excited states. II. The zwitterionic states of terminally twisted butadiene, J. Chem. Phys. 81 (1984) 5952.
[38] P. Bruckmann, l. Salem, Coexistence of two opossitely polarized zwitterionic forms on the lowest excited singlet surface of terminally twisted butadiene. Two-funnel photochemistry with dual stereochemistry, J. Am. Chem. Soc. 98 (1976) 5037.
[39] B.R. Brooks, H.F. Schaefer III, Sudden polarization: Pyramidalization of twisted ethylene, J. Am. Chem. Soc. 101 (1979) 307.
[40] V. Bonacic-Koutecky, R.J. Buenker, S.D. Peyerimhoff, Use of configuration selection methods to study the sudden polarization effect, J. Am. Chem. Soc. 101 (1979) 5917.
[41] R. Lindh, B.O. Roos, A theoretical study of the diffuseness of the $V(^1B_{1u})$ state of planar ethylene, Int. J. Quantum Chem. 35 (1989) 813.

[42] J. Finley, P-Å. Malmqvist, B.O. Roos, L. Serrano-Andrés, The multi-state CASPT2 method, Chem. Phys. Lett. 288 (1998) 299.
[43] C. Angeli, On the nature of the $\pi \rightarrow \pi^*$ ionic excited states: The V state of ethene as a prototype, J. Comp. Chem. 30 (2009) 1319.
[44] M. Dupuis, D. Spangler, J.J. Wendoloski, Natl. Res. Comp. Chem. Software catalogue 1, Prog. No. QG01 (GAMESS) (1980); B.B. Schlegel, J. Comp. Chem. 3 (1982) 214.
[45] C.A. Nicolaides, and D.R. Beck, Approach to the calculation of the important many-body effects on photoabsorption oscillator strengths, Chem. Phys. Lett. 36 (1975) 79.
[46] C.A. Nicolaides, Multielectron radiative transitions, J. Phys. B 26 (1993) L291.
[47a] C.A. Nicolaides, G. Theodorakopoulos, FOTOS applied to molecules: Oscillator strengths in H_2O, Int. J. Quantum Chem. Symp. 14 (1980) 315.
[47b] G. Theodorakopoulos, I.D. Petsalakis, C.A. Nicolaides, A method for the calculation of transition moments between electronic states of molecules using a different one-electron basis set for each state, Int. J. Quantum Chem. 29 (1986) 399.
[48a] H.P. Saha, C. Froese Fischer, Multiconfiguration Hartree-Fock calculations of the oscillator strength for the $2s2p\,^1P^o \rightarrow 2p^2$, $2snd\,^1D$ $(n = 3 - 6)$ transitions in Beryllium, Phys. Rev. A 35 (1987) 5240.
[48b] I. Bergstrom, J. Bromander, R. Buchta, L. Lundin, I. Martinson, Mean lives of excited terms in *BeI*, *BeII*, *BI*, *BII*, *CII* and *CIII*, Phys. Lett. 28A (1969) 721.
[48c] T. Anderson, J.R. Roberts, G. Sorensen, Mean-life measurements of excited electronic states in perturbed series of $A\ell II$ and *BeI*, Phys. Scr. 4 (1971) 52.
[49] D.R. Beck, C.A. Nicolaides, Electric quadrupole transition probabilities for the lowest ^1D metastable state in *Ca* and *Sr*, J. Phys. B 16 (1983) L627.
[50] C.W. Bauschlicher, S.R. Langhoff, H. Partridge, The radiative lifetime of the $^1D_2$ state of *Ca* and *Sr*: A core-valence treatment, J. Phys. B 18 (1985) 1523.
[51] N. Vaeck, M. Godefroid, J.E. Hansen, MCHF oscillator strength and lifetime calculations in neutral Calcium, J. Phys. B 24 (1991) 361.
[52] N. Beverini, E. Maccioni, F. Sorrentino, V. Baraulia, M. Coca, Measurement of the $4s^{21}S_0 \rightarrow 4s3d^1D_2$ transition probability in Calcium, Eur. Phys. J. D 23 (2003) 223.
[53] S.I. Themelis, C.A. Nicolaides, Dipole polarizabilities and hyperpolarizabilities of excited valence states of *Be*, Phys. Rev. A 52 (1995) 2439.
[54a] D. Bégué, M. Mérawa, C. Pouchan, Dynamic dipole and quadrupole polarizabilities for the ground 2^1S and the low-lying 3^1S and 3^3S states of *Be*, Phys. Rev. A 57 (1998) 2470.
[54b] D. Bégué, M. Mérawa, M. Rérat, C. Pouchan, Dynamic scalar and tensor polarizabilities for the low-lying 2^1P^o and 2^3P^o states of *Be*, J. Phys. B 31 (1998) 5077.
[55] G. Aspromallis, Y. Komninos, C.A. Nicolaides, Electron correlation and relativistic effects on the energies and widths of doubly excited states of *He*, J. Phys. B 17 (1984) L151.
[56a] C.C.J. Roothaan, A.W. Weiss, Correlated orbitals for the ground state of Heliumlike systems, Rev. Mod. Phys. 32 (1960) 194.
[56b] W. Kolos, C.C.J. Roothaan, Correlated orbitals for the ground state of the Hydrogen molecule, Rev. Mod. Phys. 32 (1960) 205.
[57] A.K. Bhatia, A. Temkin, Calculation of aotoionization of *He* and H^- using projection-operator formalism, Phys. Rev. A 11 (1975) 2018.
[58] Y. Komninos, C.A. Nicolaides, Electron correlation, geometry, and energy spectrum of quadruply excited states, Phys. Rev. A 50 (1994) 3782.
[59] Y. Komninos, Th. Mercouris, C.A. Nicolaides, Regular series of doubly excited states inside two-electron continua: Application to $2s^2$-hole states in Neon above the $Ne^{++}1s^22s^22p^4$ and $1s^22s2p^5$ thresholds, Phys. Rev. A 83 (2011) 022501.
[60a] Y. Komninos, C.A. Nicolaides, The Wannier two-electron ionization ladder in many-electron systems: The He $^1P^o$ doubly excited states, J. Phys. B 19 (1986) 1701.
[60b] C.A. Nicolaides, Y. Komninos, The Wannier two-electron ionization ladder of $^1P^o$ symmetry in H^-, *He* and Li^+, Phys. Rev. A 35 (1987) 999.

[61] C.A. Nicolaides, M. Chrysos, Y. Komninos, Li^- resonances: The two-electron ionization ladder of ^1S symmetry, Phys. Rev. A 39 (1989) 1523.
[62] C.A. Nicolaides, M. Chrysos, Y. Komninos, Geometry of the three-electron ionization ladder and its corresponding spectrum, Phys. Rev. A 41 (1990) 5244.
[63] Y. Komninos, M. Chrysos, C.A. Nicolaides, The two-electron ionization ladder for He^- ^2S and H^- ^1S states, J. Phys. B 20 (1987) L791.
[64] S.I. Themelis, C.A. Nicolaides, Energies, widths and $\ell-$dependence of the H^- ^3P and He^- ^4P TEIL states, J. Phys. B 28 (1995) L379.
[65] Y. Komninos, S.I. Themelis, M. Chrysos, C.A. Nicolaides, Properties of the two-electron ionization ladder and related good quantum numbers, Int. J. Quantum Chem. Symp. 27 (1993) 399.
[66] S.I. Themelis, Y. Komninos, C.A. Nicolaides, Properties of doubly excited states of $H^-$and *He* associated with manifolds from N=6 to N=25, Eur. Phys. J. D 18 (2002) 277.
[67] C.A. Nicolaides, S.I. Themelis, Y. Komninos, Degrees of validity of models for the description of doubly excited states of H^- and *He*, J. Phys. B 35 (2002) 1831.
[68] D.R. Herrick, O. Sinanoğlu, Comparison of doubly-excited helium energy levels, isoelectronic series, autoionization lifetimes, and group-theoretical configuration-mixing prediction with large-configuration-interaction calculations and experimental spectra, Phys. Rev. A 11 (1975) 97.
[69] W. Moffit, Configurational interaction in simple molecular orbital theory, J. Chem. Phys. 22 (1954) 1820.
[70] M. Kotani, K. Ohno, K. Kayama, Quantum mechanics of electronic structure of simple molecules, in: S. Flügge (Ed.), Encyclopedia of Physics, Springer–Verlag, Berlin, 1961, pages 1–172.
[71] A.C. Wahl, P.J. Bertoncini, G. Das, T.L. Gilbert, Recent progress beyond the Hartree–Fock method for diatomic molecules: The method of optimized valence configurations, Int. J. Quantum Chem. S 1 (1967) 123.
[72] R.E. Watson, The two-configuration approximation for four-electron ions, Ann. Phys. 13 (1961) 250.
[73] D.R. Hartree, W. Hartree, B. Swirles, Self-consistent field, including exchange and superposition of configurations, with some results for Oxygen, Phil. Trans. Roy. Soc. A 238 (1939) 229.
[74] H.P. Kelly, Many-body perturbation theory applied to atoms, Phys. Rev. 136 (1964) B896.
[75] D.F. Tuan, O. Sinanoğlu, Many-electron theory of atoms and molecules. IV. *Be* atom and its ions, J. Chem. Phys. 41 (1964) 2677.
[76] V. McKoy, O. Sinanoğlu, Many-electron theory of atoms and molecules. V. First row atoms and their ions, J. Chem. Phys. 41 (1964) 2689.
[77] H.J. Silverstone, O. Sinanoğlu, Many-electron theory of non-closed shell atoms and molecules. I. Orbital wavefunctions and perturbation theory, J. Chem. Phys. 44 (1966) 1899.
[78] B. Skutnik, I. Öksüz, O. Sinanoğlu, Correlation effects in the excited states of atoms. The $1s^2 2s^n 2p^m$ configuration of Carbon, Nitrogen and Oxygen, Int. J. Quantum Chem. 2 (1968) 1.
[79] O. Sinanoğlu, I. Öksüz, Theory of atomic structure including electron correlation, Phys. Rev. Lett. 21 (1968) 507.
[80] H.P. Kelly, Many-body perturbation theory applied to open-shell atoms, Phys. Rev. 144 (1966) 39.
[81] J.L. Whitten, M. Hackmeyer, Configuration interaction studies of ground and excited states of polyatomic molecules. I. The CI formulation and studies of formaldehyde, J. Chem. Phys. 51 (1969) 5584.
[82] It is worth recalling that the classification of electron correlation excitations in terms of spin orbitals and Slater determinants does not correspond term by term to the classification that emerges when symmetry-adapted orbitals and SACs are used. The arguments

can be general and formal. However, a simple example suffices: Suppose that an open-shell state of a first-row atom is considered. In this case, the 'Hartree–Fock sea' consists of the ten spin orbitals that close the $n = 1$ and 2 shells. Let the Hamiltonian operator act on the occupied spin orbitals so as to produce virtual excitation of two p electrons, say $2p_o\alpha 2p_o\beta$. Among the double virtual excitations, one will be the excited spin-orbital product $2p_{-1}\alpha f_{p_{+1}}\beta$, which, in the language of [77], is classified as "semi-internal". According to the implementation of [77–79] and of subsequent publications, the 'semi-internal' one-electron function $f_{p_{+1}}$ was chosen as a $3p$-like STO with variationally optimized exponent. However, if the formalism uses symmetry-adapted orbitals, this excitation corresponds to a symmetry-adapted single orbital excitation, e.g., $2p^2 \rightarrow 2p\bar{p}$. Similarly, to a two-orbital excitation there may correspond a triple spin-orbital excitation. It follows that the identification of various correlation effects in open-shell states, especially in excited states, as to their degree of significance with respect to a particular property, differs in the two formalisms and computational methodologies, (spin orbital and Slater determinants vs. symmetry-adapted orbitals and configurations).

[83] O. Sinanoğlu, J. Cižek, Reducible and irreducible pair correlations in benzene, Chem. Phys. Lett. 1 (1967) 337.

[84] D.R. Beck, O. Sinanoğlu, Resonance transition probabilities for third-row atoms and ions ($MgI, SiII - III, PII, PIV, SII - III, ClIII$) including the important correlation effects, Phys. Rev. Lett. 28 (1972) 945.

[85] G. Das, A.C. Wahl, Optimized valence configurations and the F_2 molecule, Phys. Rev. Lett. 24 (1970) 440.

[86] H.F. Schaefer III, Ab initio potential curve for the $^3\Sigma_g^-$ state of O_2, J. Chem. Phys. 54 (1971) 2207.

[87] H.F. Schaefer III, Electron correlation in the lowest $^1\Sigma^+$ state of Beryllium oxide, J. Chem. Phys. 55 (1971) 176.

[88] G. Fogarasi, R. Liu, P. Pulay, Effect of nondynamical electron correlation on the geometries of conjugated π-systems, J. Phys. Chem. 97 (1993) 4036.

[89] B. Datta, D. Mukherjee, Treatment of quasi-degeneracy in single-reference coupled-cluster theory. Separation of dynamical and nondynamical correlation effects, Chem. Phys. Lett. 235 (1995) 31.

[90] D.K.W. Mok, R. Neumann, N.C. Handy, Dynamical and nondynamical correlation, J. Phys. Chem. 100 (1996) 6225.

[91] K. Nakayama, K. Hirao, R. Lindh, Different bases for different correlation effects: Multi-reference Møller-Plesset perturbation theory in the extended basis function space, Chem. Phys. Lett. 300 (1999) 303.

[92] E. Valderrama, J.M. Mercero, J.M. Ugalde, The separation of the dynamical and non-dynamical electron correlation effects, J. Phys. B 34 (2001) 275.

[93] D. Cremer, Density functional theory: Coverage of dynamic and non-dynamic electron correlation effects, Mol. Phys. 99 (2001) 1899.

[94] J.S. Sears, C.D. Sherrill, On the choice of reference in multi-reference electronic structure theory: Minimal references for bond breaking, Mol. Phys. 103 (2005) 803.

[95] M.W. Schmidt, J. Ivanic, K. Ruedenberg, Electronic analysis of the ground-state potential energy curve of Be_2, J. Phys. Chem. A 114 (2010) 8687.

[96] C.A. Nicolaides, D.R. Beck, Variational calculations of correlated wavefunctions and energies for ground, low-lying as well as highly excited discrete states in many-electron atoms, J. Phys. B 6 (1973) 535.

[97] C.A. Nicolaides, Oscillator strengths in first row neutral. Singly and doubly ionized atoms: Comparison of recent theoretical and experimental values, Chem. Phys. Lett. 21 (1973) 242.

[98] J. Berkowitz, W.A. Chupka, Diatomic ions of noble gas fluorides, Chem. Phys. Lett. 7 (1970) 447.

[99] J.H. Holloway, E.G. Hope, Recent advances in noble-gas chemistry, in: Advances in Inorganic Chemistry, vol. 46, ed. A.G. Sykes, Academic Press, Boston, 1999, p. 51.
[100] N.F. Mott, H.S.W. Massey, The Theory of Atomic Collisions, Clarendon Press, Oxford, 1965.
[101] U. Becker, D.A. Shirley, (Eds.), VUV and Soft X-ray Photoionization, Plenum Press, New York, 1996.
[102] R.R. Teachout, T.R. Pack, The static dipole polarizabilities of all the neutral atoms in their ground states, Atomic Data 3 (1971) 195.
[103] J.M.L. Martin, The ground-state spectroscopic constants of Be_2 revisited, Chem. Phys. Lett. 303 (1999) 399.
[104a] C.A. Nicolaides, D.R. Beck, Transfer of oscillator strength in regions of (avoided) crossings I: The two state approximation, Chem. Phys. Lett. 53 (1978) 87.
[104b] D.R. Beck, C.A. Nicolaides, Transfer of oscillator strength in regions of (avoided) crossings II: Atomic spectra for non-integer values of Z. Application to the $NI^4S^o - {}^4P$, Chem. Phys. Lett. 53 (1978) 91.
[105] R.L. Graham, D.L. Yeager, J. Olsen, P. Jørgensen, R. Harrison, S. Zarrabian, R. Bartlett, Excitation energies in Be: A comparison of multiconfigurational linear response and full configuration interaction calculations, J. Chem. Phys. 85 (1986) 6544.
[106] J.S. Sears, C.D. Sherrill, A.I. Krylov, A spin-complete version of the spin-flip approach to bond breaking: What is the impact of obtaining spin eigenfunctions? J. Chem. Phys. 118 (2003) 9084.
[107] D.R. Beck, C.A. Nicolaides, Fine and hyperfine structure of the two lowest states of Be^- and their first two ionization thresholds, Int. J. Quantum Chem. S 18 (1984) 467.
[108] A.G. Blachman, A. Lurio, Hyperfine structure of the metastable $(1s^2 2s 2p)\,{}^3P^o$ of ${}_4Be^9$ and the nuclear electric quadrupole moment, Phys. Rev. 153 (1967) 164.
[109] D. Sundholm, J. Olsen, Large MCHF calculations of the hyperfine structure of $Be({}^3P^o)$: The nuclear quadrupole moment of ${}^9Be$, Chem. Phys. Lett. 177 (1991) 91.
[110] P. Jönsson, C. Froese Fischer, Large-scale MCHF calculations of hyperfine-interaction constants for low-lying states in Beryllium, Born and Carbon, Phys. Rev. A 48 (1993) 4113.
[111] N. Rosen, The normal state of the Hydrogen molecule, Phys. Rev. 38 (1931) 2099.
[112] C.A. Nicolaides, Y. Komninos, Geometrically active atomic states and the formation of molecules in their normal shapes, Int. J. Quantum Chem. 67 (1998) 321.
[113] Y. Komninos, C.A. Nicolaides, Molecular shape, the shape of the geometrically active atomic states and hybridization, Int. J. Quantum Chem. 71 (1999) 25; Erratum, ibid. 74 (1999) 435.
[114] I.D. Petsalakis, G. Theodorakopoulos, C.A. Nicolaides, Adiabatic and quasidiabatic ${}^2\Sigma^+$ states of *BeH*, J. Chem. Phys. 97 (1992) 7623.
[115] J.M. Merritt, V.E. Bondybey, M.C. Heaven, Beryllium dimer- Caught in the act of bonding, Science 324 (2009) 1548.
[116] P.F. Bernath, Extracting potentials from spectra, Science 324 (2009) 1526.
[117] MOLPRO: A package of ab initio quantum chemistry programs designed and maintained by H.-J. Werner, P.J. Knowles, version 2002.6. R.D. Amos, A. Bernhardsson, A. Berning, P. Celani, D.L. Cooper, M.J.O. Deegan, A.J. Dobbyn, F. Eckert, C. Hampel, G. Hetzer, P.J. Knowles, T. Korona, R. Lindh, A.W. Lloyd, S.J. McNicolas, F.R. Manby, W. Meyer, M.E. Mura, A. Nicklass, P. Palmieri, R. Pitzer, G. Rauhut, M. Schütz, A.J. Stone, R. Tarroni, T. Thorsteinsson, H.-J. Werner.
[118] I. Kerkines, C.A. Nicolaides, Theoretical and Physical Chemistry Institute, Hellenic Research Foundation, Athens, Greece, unpublished work, (2010).

CHAPTER 3

Ab initio Electron Propagator Calculations on Electron Detachment Energies of Fullerenes, Macrocyclic Molecules, and Nucleotide Fragments

Viatcheslav G. Zakrzewski[a], **Olga Dolgounitcheva**[a], **Alexander V. Zakjevskii**[a], and **J. V. Ortiz**[a]

Contents

Abstract Transition energies for electron attachment or detachment of closed-shell molecules that are large by contemporary standards of quantum chemistry

[a] Department of Chemistry and Biochemistry, Auburn University, Auburn AL, USA
E-mail address: ortiz@auburn.edu

Advances in Quantum Chemistry, Volume 62
ISSN 0065-3276, DOI: 10.1016/B978-0-12-386477-2.00009-7

calculations may be calculated *ab initio* with various electron propagator methods. Quasiparticle approximations that produce perturbative relaxation and correlation corrections to the results of Koopmans's theorem and renormalized self-energy approximations that retain their validity when the one-electron picture of electron binding energies is questionable have been implemented in efficient computer codes. In the former case, a simplified form of the Dyson equation is easily solved by evaluating diagonal matrix elements of the self-energy operator. In the latter case, strategies for solving eigenvalue problems of large dimension are reviewed. A study of the vertical ionization energies of the C_{60} and C_{70} fullerenes reveals the presence of many closely coinciding cationic states, some of which exhibit strong correlation effects. Vertical ionization energies for C_{96} and C_{144} are reported as well. Calculations on porphyrins and phthalocyanines reveal a nearly complete breakdown of the one-electron picture of electron binding energies. Calculations on the electron detachment energies of an anionic dinucleotide containing two guanine fragments produce many final states and indicate that the final state hole resides on a single guanine moiety.

1. INTRODUCTION

Among the most successful theories of quantum physics are those that have been formulated in terms of propagators. Sequences of propagators, also known as Green's functions, have been used to reformulate many-body problems [1]. Instead of solving the many-body Schrödinger equation, one may introduce a coupling of propagators corresponding to number of particles from one to the full, N-particle limit. The electron propagator, also known as the one-electron Green's function, of an N-electron system is a function with poles (values that yield vanishing denominators and therefore singularities) that correspond to all possible electron binding energies. In molecular calculations subject to the Born–Oppenheimer approximation, these poles are equal to negative vertical detachment energies (VDEs) or negative vertical attachment energies (VAEs). Propagator concepts in molecular electronic structure theory and the breadth of their applications have been discussed in a recent monograph [2].

2. ELECTRON PROPAGATOR THEORY

Poles, the energies that produce singularities, and residues, coefficients of the terms responsible for the singularities [3], provide information on observable quantities. The r,s element of the electron propagator matrix has a spectral

form that reads

$$G_{rs}(E) \equiv \langle\langle a_r^\dagger; a_s \rangle\rangle$$
$$= \lim_{\eta \to 0} \left\{ \sum_n \frac{\langle N|a_r^\dagger|N-1,n\rangle\langle N-1,n|a_s|N\rangle}{E + E_n(N-1) - E_0(N) - i\eta} + \sum_m \frac{\langle N|a_s|N+1,m\rangle\langle N+1,m|a_r^\dagger|N\rangle}{E - E_m(N+1) + E_0(N) + i\eta} \right\}. \quad (1)$$

The indices r and s refer to general, orthonormal spin orbitals, $\phi_r(x)$ and $\phi_s(x)$, respectively, where x is a space–spin coordinate. Integration techniques required in a Fourier transform from the time-dependent representation require that the limit with respect to η be taken [1, 4]. Matrix elements of the corresponding field operators, $a_r^\dagger$ and a_s, are evaluated with respect to an N-electron reference state, $|N\rangle$, and final states with N±1 electrons identified by the indices m and n. Elements of the electron propagator matrix are energy dependent. A pole occurs when E equals a negative VDE, $E_0(N) - E_n(N-1)$, or a negative VAE, $E_m(N+1) - E_0(N)$.

The residues corresponding to these poles are related to the Feynman–Dyson amplitudes (FDAs), where

$$U_{r,n} = \langle N-1,n|a_r|N\rangle \quad (2)$$

or

$$U_{r,n} = \langle N+1,n|a_r^\dagger|N\rangle. \quad (3)$$

The FDAs allow construction of the Dyson orbitals (DOs) for VDEs, where

$$\phi_n^{\text{Dyson},VDE}(x) = \sum_r \phi_r(x) U_{r,n}, \quad (4)$$

and for VAEs, where

$$\phi_n^{\text{Dyson},VAE}(x) = \sum_r \phi_r(x) U_{r,n}. \quad (5)$$

For a given VDE whose final state is labelled by n, the DO is expressed in terms of initial and final state wavefunctions via

$$\phi_n^{\text{Dyson},VDE}(x_1) = \sqrt{N} \int \Psi_N(x_1, x_2, x_3, \ldots, x_N) \times \Psi^*_{N-1,n}(x_2, x_3, x_4, \ldots, x_N) \mathrm{d}x_2 \mathrm{d}x_3 \mathrm{d}x_4 \cdots \mathrm{d}x_N, \quad (6)$$

and for VAEs, the corresponding expression is

$$\phi_n^{\mathrm{Dyson},VAE}(x_1) = \sqrt{N+1}\int \Psi_{N+1,n}(x_1, x_2, x_3, \ldots, x_{N+1}) \times \Psi_N^*(x_2, x_3, x_4, \ldots, x_{N+1})\mathrm{d}x_2\mathrm{d}x_3\mathrm{d}x_4 \cdots \mathrm{d}x_{N+1}. \quad (7)$$

Electron detachment or attachment processes may be qualitatively classified in terms of molecular orbital (MO) configurations. The simplest transitions conform to a one-electron picture of electron detachment (see Figure 3.1) where the usual MO picture applies. For example, a hole may be created in a formerly doubly occupied MO in a reference, determinantal wavefunction. The transition energy can be viewed as a Koopmans's theorem (KT) value adjusted by electron correlation and final-state orbital relaxation corrections. (Greater care must be taken when Kohn–Sham orbital energies are used as a point of departure.) More complicated transitions that are described as shakeup processes also may occur. For example, two electrons may leave an occupied MO with the attachment of an electron to a virtual MO. Such an event is also depicted in Figure 3.1. Such two-hole, one-particle configurations are denoted by the abbreviation 2h1p. 1h configurations correspond to VDEs where the Koopmans picture is qualitatively valid, whereas 1p configurations may be valid for certain VAEs. However, Feshbach resonances, which are often described as electron attachment

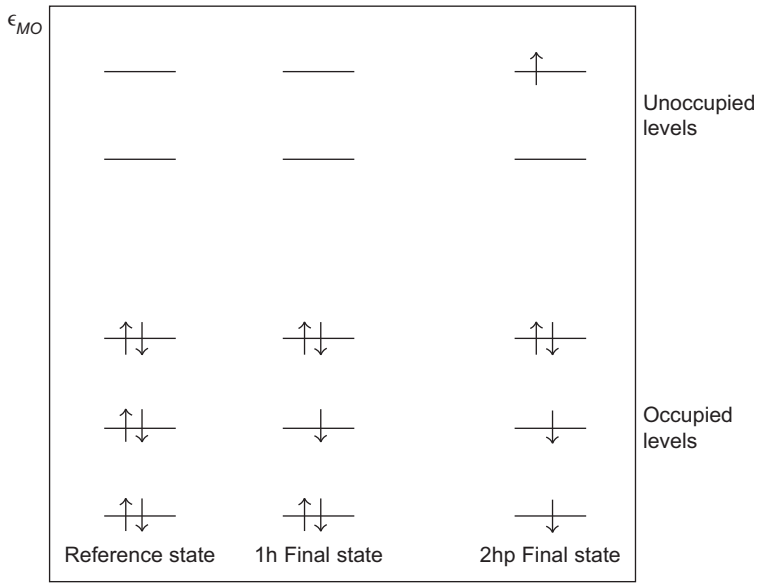

Figure 3.1 Electron detachment from a closed-shell system.

accompanied by a single excitation, may be described by 2p1h configurations. Even more complicated transitions may require the 3h2p or 3p2h configurations for their qualitative description.

Approximate propagators may be designed to provide perturbative corrections to Koopmans results or may have the flexibility to account for correlation states where 1h or 1p descriptions of final states are qualitatively invalid. For the first case, in which the one-electron picture of electron detachment or attachment is adequate, quasiparticle self-energy approximations are suitable. In other cases, nondiagonal self-energy approximations are necessary.

2.1. Self-energy approximations

Dyson orbitals and electron binding energies (i.e., negative VDEs and VAEs) may be obtained from the Dyson equation, which, in its inverse form, relates the electron propagator matrix to its zeroth-order counterpart via

$$\mathbf{G}^{-1}(E) = \mathbf{G}_0^{-1}(E) - \mathbf{\Sigma}(E). \tag{8}$$

A one-electron, zeroth-order Hamiltonian may be used to generate a set of reference spin orbitals and energies (ϵ) such that the matrix elements of the corresponding inverse propagator matrix have the simple form

$$[\mathbf{G}_0^{-1}(E)]_{rs} = (E - \epsilon_r)\delta_{rs}. \tag{9}$$

Whereas many choices for the zeroth-order Hamiltonian are possible, the Fock operator with the usual one-electron, Coulomb and exchange components has been the usual choice in molecular calculations. In the remaining term, $\mathbf{\Sigma}(E)$, the self-energy operator describes the effects of electron correlation and of orbital relaxation in final states. There are energy-independent and energy-dependent components of the self-energy operator:

$$\Sigma(E) = \Sigma(\infty) + \Sigma'(E). \tag{10}$$

These terms are also known respectively as the constant and dynamic self-energy operators; the dynamic part vanishes as the absolute value of E increases without bound. A more intuitively appealing form of the Dyson equation [5–8] emphasizes its connection with self-consistent field theory:

$$[F + \Sigma'(E_p)]\phi_p^{\text{Dyson}} = E_p\phi_p^{\text{Dyson}}, \tag{11}$$

where F is the usual Fock operator of Hartree–Fock theory. Here, the constant self-energy operator is absorbed in F by the generalization of the one-electron density matrix of the reference state.

To discover poles, iteration with respect to E is continued until agreement between the eigenvalue, E_p, and the argument of $\Sigma'(E)$ is achieved.

In practice, approximations in the self-energy operator are needed. Efficient, perturbative improvements to Koopmans results may be produced by the neglect of off-diagonal matrix elements of the self-energy operator in the canonical, Hartree–Fock basis. Such diagonal approximations in the self-energy, which are also known as quasiparticle methods, yield an especially simple form of the Dyson equation,

$$E_p = \epsilon_p + \Sigma_{pp}(E_p), \tag{12}$$

where E_p is an electron binding energy. In recent years, two kinds of quasiparticle methods have been in general use: the Outer Valence Green Function (OVGF) [9] and the Partial Third order (P3) [10–12] approximation. Self-energy terms up to third order in the fluctuation potential are evaluated in both methods, which are intended to provide corrections to Koopmans results for outer valence orbitals. In quasiparticle calculations, the pole strength, P, is a criterion of these methods' validity for a given electron binding energy, ω, and may be calculated as follows:

$$P_q = \left[1 - \frac{\partial \Sigma(\omega)_{qq}}{\partial \omega}\right]^{-1}, \tag{13}$$

where $\Sigma(\omega)_{qq}$ is the qth diagonal element of the self-energy operator. The derivative that appears in this expression is easily evaluated analytically and depends only on the dynamic self-energy. For diagonal self-energy methods and their accompanying perturbative corrections to Koopmans results to be valid, it is necessary that P_q be close to its uncorrelated limit, unity [9].

One approach to the derivation of quasiparticle methods departs [9, 13] from many-body concepts that themselves arose from quantum field theory [4, 14]. Terms in the self-energy may be represented pictorially in terms of Feynman, Goldstone [15], or Hugenholtz [16] diagrams. An initial presentation of the OVGF approximation [17] was followed by a more flexible formulation [9]. Numerical procedures have been described in detail [18].

Alternative derivations of perturbational expansions for the electron propagator employ an algebraic approach based on superoperators [5–8, 19]. This route was taken in obtaining the P3 method [10–12], which has some computational advantages over the OVGF. The latter approximation requires transformed electron repulsion integrals of the form $\langle ab \| cd \rangle$ in the canonical Hartree–Fock basis, where the usual notations for occupied (i,j,k,. . .) and unoccupied (a,b,c,. . .) MOs have been adopted. Explicit computation and storage of these integrals may be avoided by the employment of semidirect algorithms [20, 21]. For cases in which storage of electron repulsion integrals

is limited, the Gaussian suite of programs [22] provides this option at the cost of performing more arithmetic operations. The P3 method does not require transformed integrals with four virtual orbital indices for the calculation of VDEs. (However, these integrals are needed in P3 calculations of VAEs.) There are also arithmetic advantages for P3 over OVGF, for these methods have respectively ov^4 and o^2v^3 scaling factors for VDE calculations, where o and v are the numbers of occupied and virtual MOs.

Use of better methods (with respect to accuracy and generality) is indicated by numerical failures of the quasiparticle approximation (e.g., when pole strengths are not close to unity) or when perturbative arguments based on Koopmans results are likely to be unreliable. Infinite-order or renormalized approximations are needed when relaxation or correlation effects are qualitatively strong. Core ionization energies, for example, require an alternative to P3 and OVGF. Many kinds of final states cannot be described, even qualitatively, by single-determinant wavefunctions. Inner valence regions of gas-phase photoelectron spectra usually do not map onto occupied MOs. Here, shakeup states do not correspond to final-state configurations that differ from a reference determinant by one hole (h) or particle (p) index. Correlation states, where 2h1p configurations are qualitatively important, generally exhibit extensive configuration interaction. To describe such cases, nondiagonal, renormalized self-energy approximations are needed.

Superoperator concepts may be used to derive this class of approximations. Here, one solves for the eigenvalues and eigenvectors of the superoperator Hamiltonian matrix, $\hat{\mathbf{H}}$, instead of focusing attention on the matrix elements of the self-energy operator. Electron binding energies are given by the eigenvalues of $\hat{\mathbf{H}}$ and may correspond to final states where the Koopmans picture breaks down. The corresponding eigenvectors yield Dyson orbitals. A systematic procedure may be followed for the derivation of Hermitian superoperator Hamiltonian matrices. Elements of $\hat{\mathbf{H}}$ that are used in

$$\hat{\mathbf{H}}\mathbf{C} = \mathbf{C}\mathbf{E} \tag{14}$$

depend on field operator products and a reference state, $|ref\rangle$, where

$$(X \mid \hat{H}Y) = \langle ref \mid [X^\dagger, [H, Y]]_+ \mid ref \rangle, \tag{15}$$

and where H is the second-quantized Hamiltonian. In this notation, X and Y are field operator products in which the number of annihilators is one greater than the number of creators. X may be a simple annihilation operator of the 1h type, a_i, for example, and may have couplings with a Y operator of the 2h1p type such as $a_j a_k a_a^\dagger$. Although there are no couplings between np(n-1)h (VAE) and nh(n-1)p (VDE) operators in Hilbert space approaches such as

configuration interaction, in propagator methods, the 1h, 1p, 2h1p, 2p1h, and higher np(n-1)h and nh(n-1)p operators interact. For VDE calculations, the 1h, 2h1p and higher nh(n-1)p operators describe final-state orbital relaxation and configuration mixing, but the 1p, 2p1h and higher np(n-1)h operators treat initial-state correlation. For VAE calculations, the roles of these two sectors of operators are reversed.

For many of the commonly used renormalized methods, such as 2ph–TDA, NR2, and ADC(3), the operator space spans the 1h (h), 1p (p), 2h1p (2hp), and 2p1h (2ph) subspaces of the full operator manifold [9, 23]. Reference states are built from Hartree–Fock determinantal wavefunctions plus corrections from Rayleigh–Schrödinger perturbation theory. The resulting expressions for various blocks of the superoperator Hamiltonian matrix may be evaluated through a given order in the fluctuation potential. The general structure of the superoperator Hamiltonian matrix for the approximations mentioned earlier is as follows:

$$\hat{\mathbf{H}} = \begin{bmatrix} \boldsymbol{\epsilon} + \Sigma(\infty)_{h-h} & \boldsymbol{\Sigma}(\infty)_{h-p} & \hat{\mathbf{H}}_{h-2hp} & \hat{\mathbf{H}}_{h-2ph} \\ \boldsymbol{\Sigma}(\infty)_{p-h} & \boldsymbol{\epsilon} + \Sigma(\infty)_{p-p} & \hat{\mathbf{H}}_{p-2hp} & \hat{\mathbf{H}}_{p-2ph} \\ \hat{\mathbf{H}}_{2hp-h} & \hat{\mathbf{H}}_{2hp-p} & \hat{\mathbf{H}}_{2hp-2hp} & \mathbf{0} \\ \hat{\mathbf{H}}_{2ph-h} & \hat{\mathbf{H}}_{2ph-p} & \mathbf{0} & \hat{\mathbf{H}}_{2ph-2ph} \end{bmatrix}, \tag{16}$$

where $\boldsymbol{\epsilon}$ is a diagonal matrix of orbital energies and $\boldsymbol{\Sigma}(\infty)$ is the static contribution to the self-energy.

The ADC(3), NR2, 2ph–TDA, and BD–T1 [24] approximations display this structure in $\hat{\mathbf{H}}$. In these methods, couplings between simple (h and p) and triple (2hp and 2ph) operators may be evaluated through first or second order in the fluctuation potential. Hilbert space methods of similar computational difficulty, such as IP–CCSD [25], do not have couplings between nh(n-1)p and np(n-1)h sectors. A similar formulation can be achieved by using Kohn–Sham orbitals to define a reference state [26]. Identical expressions for the matrix elements of $\hat{\mathbf{H}}$ can be derived using a diagrammatic approach [27].

For blocks that involve the h and p operator subspaces, the matrix elements are easily stored. Storage may be infeasible for larger blocks, for example, the 2ph–2ph case. These matrix elements may be calculated as needed during matrix–vector multiplications that are repeated in procedures for solving large eigenvalue problems [28]. Whereas application of these procedures to variational methods usually aims at the lowest eigenvalues, here the eigenvalues of interest are somewhere in the middle of the spectrum. An algorithm of this kind [29] has been used to calculate the photoelectron spectrum of the C_{60} [30] and that of a free-base phthalocyanine [31].

From the eigenvectors, **C**, of $\hat{\mathbf{H}}$, one may infer the pole strengths, using

$$P_w = \sum_i |C_{iw}|^2 + \sum_a |C_{aw}|^2, \tag{17}$$

where w is a final–state index. When pole strengths are close to unity, the diagonalization algorithm usually converges rapidly, and therefore one may focus on an individual final state. However, correlation final states may be densely spaced with respect to energy and have low pole strengths. In such cases, a more efficient strategy is to obtain many eigenvectors simultaneously. This kind of problem has an experimental counterpart, for photoelectron spectra often exhibit closely spaced correlation (satellite or shakeup) states, where only broad envelopes, obscured by strong vibronic couplings between electronic states, may be seen. In the inner valence region, eigenvectors for VDEs frequently have qualitatively important entries for h and 2hp operators in final states that have small energy separations. Here, the Koopmans description of final states loses all of its interpretive power. In phthalocyanine, for example, only the lowest VDE has a large pole strength [31], and the other VDEs correspond to **C** vectors with large 2hp elements.

2.2. Solution of Eigenvalue problems

The present eigenvalue problem differs somewhat from multiroot eigenvalue problems encountered in configuration interaction calculations. Here, one must find eigenvalues in a given energy range. To facilitate interpretation of low-intensity features in a photoelectron spectrum, it may be desirable to find eigenvectors with h and p contributions above a chosen threshold that guarantee a minimum pole strength. The Davidson procedure [28] is adapted to these ends in the following manner.

1. Select an orthonormal set of vectors $\mathbf{Y}_I$ ($I = 1, 2, 3, \ldots, \mathrm{K}$).
2. Build a projected matrix **h** with elements

$$h_{IJ} = \mathbf{Y}_I \hat{\mathbf{H}} Y_J. \tag{18}$$

3. Solve the small eigenvalue problem

$$\mathbf{hy} = \mathbf{ey}. \tag{19}$$

4. Build linear combinations of vectors **Y**

$$\tilde{\mathbf{Y}}_J = \sum_i y_I^J \mathbf{Y}_I, \tag{20}$$

where index J refers to the Jth eigenvalue of the projected matrix.

5. Apply energy and pole strength criteria to select vectors.
6. Build residual vectors according to

$$\mathbf{R} = \hat{\mathbf{H}}\tilde{\mathbf{Y}} - e\tilde{\mathbf{Y}}. \tag{21}$$

7. Additional expansion vectors are constructed as

$$\mathbf{S}_I = \mathbf{R}_I/(e - \hat{H}^0_{II}). \tag{22}$$

   Note that in contrast to the procedure used in configuration interaction calculations, only orbital energies and no electron repulsion integrals occur in the denominator.
8. These vectors are orthonormalized with respect to the initial set $\mathbf{Y}$ and are added to enlarge the iterational space.

Application of this algorithm requires some flexibility. Convergence to eigenvectors with large p and h components is generally faster than to eigenvectors with large 2hp or 2ph character. This leads to very small residual vector norms and to division by very small numbers during orthonormalization. Therefore, converged vectors are removed from the iterative process and are saved. Initial guesses may be based upon zero-order diagonal elements of $\hat{\mathbf{H}}$, but they may not produce reasonable approximations to converged shakeup states. Therefore, all vectors that satisfy energy and pole strength criteria during a given number of initial iterations are retained. The remaining iterations then are performed by retaining vectors according to energy, pole strength, and overlap criteria. After a given number of iterations, the process is stopped and another energy range is considered. An alternative procedure is provided by the Lanczos eigensolver [32].

2.3. Closed-shell case for nondiagonal approximations

For closed-shell reference states, doublet final states are of primary interest. Here, one may take spin symmetry into account, as well as molecular point groups. Zeroth-order terms appear only in diagonal elements of the 2hp–2hp block, where

$$\hat{\mathbf{H}}^0_{aij,aij} = -\epsilon_a + \epsilon_i + \epsilon_j, \tag{23}$$

and in diagonal elements of the 2ph–2ph block, where

$$\hat{\mathbf{H}}^0_{iab,iab} = -\epsilon_i + \epsilon_a + \epsilon_b. \tag{24}$$

For closed-shell reference states, spin adaptation of the operator manifolds reduces the rank of $\hat{\mathbf{H}}$. Amplitudes for doublet final states have the following

form [9] for the 2hp case:

$$
\begin{aligned}
Y^S_{a,jk} &= \frac{1}{\sqrt{6}}(2Y_{a\alpha j\alpha k\alpha} + Y_{a\beta j\alpha k\beta} + Y_{a\beta j\beta k\alpha}) \quad j < k \\
Y^S_{a,jj} &= Y_{a\beta j\alpha j\beta} \quad j = k \\
Y^A_{a,jk} &= \frac{1}{\sqrt{2}}(Y_{a\beta j\alpha k\beta} - Y_{a\beta j\beta k\alpha}) \quad j < k.
\end{aligned} \tag{25}
$$

When the last two indices are expanded from lower triangles to squares, symmetric and antisymmetric matrices are formed. The superscripts S and A denote these cases. Diagonal elements for the symmetric case have a different normalization factor. The rank of the spin-adapted $\hat{\mathbf{H}}$ matrix for the closed-shell case is o+v+vo^2+ov^2.

2.3.1. Matrix–vector multiplications

Multiplication of $\hat{\mathbf{H}}$ by trial vectors is required by diagonalization procedures that are appropriate for large matrices. Storage of the 2hp–2hp and 2ph–2ph blocks in memory [9, 32] or on external disks is impractical here, especially for low-symmetry molecules. Transformed electron repulsion integrals with four virtual indices also require large amounts of memory or external storage. In the present algorithm, contributions to the matrix–vector product are obtained either with transformed integrals stored on disk or by recomputation of integrals over atomic basis functions.

Formation of the $\hat{\mathbf{H}}_{2ph-2h}\mathbf{Y}_{2ph}$ product is the most difficult phase of the matrix–vector multiplication. Spin adaptation leads to the following structure:

$$
\begin{pmatrix} \mathbf{X^S} \\ \mathbf{X^A} \end{pmatrix} = \begin{pmatrix} \mathbf{C^{S,S}} & \mathbf{C^{S,A}} \\ \mathbf{C^{A,S}} & \mathbf{C^{A,A}} \end{pmatrix} \begin{pmatrix} \mathbf{Y^S} \\ \mathbf{Y^A} \end{pmatrix}. \tag{26}
$$

Y amplitudes may be considered lower or upper triangles of symmetric and antisymmetric matrices over 2h or 2p pairs of indices. The symmetric case has a special normalization factor ($\sqrt{2}$) when the indices are equal. For the 2ph case,

$$
\tilde{X}^S_{jab} = \sum_{k,c} W_1(kb,jc)\tilde{Y}^S_{k,ac} + \frac{\sqrt{3}}{2}\sum_{kc}\langle kb \mid cj\rangle \tilde{Y}^A_{k,ac} \tag{27}
$$

and

$$
\tilde{X}^A_{jab} = \sum_{k,c} W_2(kb,jc)\tilde{Y}^A_{k,ac} + \frac{\sqrt{3}}{2}\sum_{kc}\langle kb \mid cj\rangle \tilde{Y}^S_{k,ac}, \tag{28}
$$

where intermediates W_1 and W_2 are defined as follows:

$$W_1(ka,jc) = \left(-\langle ka \mid jc\rangle + \frac{1}{2}\langle ka \mid cj\rangle\right) \tag{29}$$

$$W_2(ka,jc) = \left(-\langle ka \mid jc\rangle + \frac{3}{2}\langle ka \mid cj\rangle\right). \tag{30}$$

Elements of $\tilde{\mathbf{Y}}^{\mathbf{S}}$ and $\tilde{\mathbf{Y}}^{\mathbf{A}}$ are defined by

$$\begin{aligned}
\tilde{Y}^S_{kca}|_{c<a} &= Y^S_{kca}|_{c<a} \\
\tilde{Y}^S_{kac}|_{c>a} &= Y^S_{kca}|_{c<a} \\
\tilde{Y}^S_{kca}|_{c=a} &= \sqrt{2}Y^S_{kaa}|_{c=a}
\end{aligned} \tag{31}$$

and

$$\begin{aligned}
\tilde{Y}^A_{kca}|_{c<a} &= +Y^A_{kca}|_{c<a} \\
\tilde{Y}^A_{kac}|_{c>a} &= -Y^A_{kca}|_{c<a} \\
\tilde{Y}^A_{kca}|_{c=a} &= 0.
\end{aligned} \tag{32}$$

Elements of $\mathbf{X}^{\mathbf{S}}$ and $\mathbf{X}^{\mathbf{A}}$ are recovered from $\tilde{\mathbf{X}}^{\mathbf{S}}$ and $\tilde{\mathbf{X}}^{\mathbf{A}}$ according to

$$\begin{aligned}
X^S_{jab}|_{a<b} &= \tilde{X}^S_{jab}|_{a<b} + \tilde{X}^S_{jba}|_{a<b} \\
X^S_{jab}|_{a=b} &= \sqrt{2}\tilde{X}^S_{jab}|_{a=b} \\
X^A_{jab}|_{a<b} &= \tilde{X}^A_{jab}|_{a<b} - \tilde{X}^A_{jba}|_{a<b}.
\end{aligned} \tag{33}$$

After these manipulations are performed, contributions involving integrals with four virtual indices may be considered. This aspect of the calculation requires slightly different organization. If the intermediate, $\langle ab \mid + \mid cd\rangle$ (i.e., $\langle ab \mid cd\rangle + \langle ab \mid dc\rangle$) is available such that $a \le b$ and $c \le d$, then

$$\begin{aligned}
\tilde{Y}^S_{kcd}\big|_{c<d} &= Y^S_{kcd}\big|_{c<d} \\
\tilde{Y}^S_{kcd}\big|_{c>d} &= Y^S_{kcd}\big|_{c<d} \\
\tilde{Y}^S_{kcd}\big|_{c=d} &= \frac{1}{\sqrt{2}}Y^S_{kcd}\big|_{c=d} \\
\tilde{X}^S_{jab}\big|_{a\le b} &\leftarrow \tilde{X}^S_{jab}\big|_{a\le b} + \sum_{c\le d}\langle ab \mid + \mid cd\rangle \tilde{Y}^S_{kcd} \\
X^S_{jab}\big|_{a<b} &= \tilde{X}^S_{jab}\big|_{a<b} \\
X^S_{jab}|_{a=b} &= \frac{1}{\sqrt{2}}\tilde{X}^S_{jab}\big|_{a=b}.
\end{aligned} \tag{34}$$

Contraction of $\mathbf{Y}_A$ with $\langle ab \,||\, cd\rangle$ integrals can be done in a straightforward way:

$$X^A_{jab}|_{a<b} \leftarrow X^A_{jab}|_{a<b} + \sum_{c<d} \langle ab \| cd\rangle Y^A_{cd}. \tag{35}$$

A direct algorithm for contractions involving $\langle ab \mid cd\rangle$ integrals may be employed when storage and recovery of these integrals is not feasible. Here, components of $\tilde{Y}$ are transformed into the atomic basis in their last two indices:

$$\tilde{Y}^{S,A}_{k\rho\sigma} = \sum_{cd} \tilde{Y}^{S,A}_{kcd} C_{\rho c} C_{\sigma d}. \tag{36}$$

These intermediates then are contracted with electron repulsion integrals in the atomic basis that are generated as needed:

$$\tilde{W}^{S,A}_{k\mu\nu}\,|_{\mu\le\nu} = \sum_{\rho\le\sigma} (\mu\rho \mid \nu\sigma)\tilde{Y}^{S,A}_{k\rho\sigma}. \tag{37}$$

The last steps are described by

$$\begin{aligned}
\hat{W}^S_{k\mu\nu}\,|_{\mu\le\nu} &= \frac{1}{2}\tilde{W}^S_{k\mu\nu} \\
\hat{W}^S_{k\mu\nu}\,|_{\mu>\nu} &= \frac{1}{2}\tilde{W}^S_{k\nu\mu} \\
\hat{W}^A_{k\mu\nu}\,|_{\mu<\nu} &= \tilde{W}^A_{k\mu\nu} \\
\hat{W}^A_{k\mu\nu}\,|_{\mu>\nu} &= -\tilde{W}^A_{k\nu\mu},
\end{aligned} \tag{38}$$

which is followed by

$$\begin{aligned}
\tilde{X}^{S,A}_{kab} &= \sum_{\mu\nu} C_{\mu a} C_{\nu b} \hat{W}^{S,A}_{k\mu\nu} \\
X^S_{kab}\,|_{a<b} &= \tilde{X}^S_{kab} + \tilde{X}^S_{kba} \\
X^S_{kaa} &= \sqrt{2}\tilde{X}^S_{kaa} \\
X^A_{kab}\,|_{a<b} &= \tilde{X}^A_{kab}.
\end{aligned} \tag{39}$$

2.3.2. Constant self-energy

Renormalizations in the constant part of the self-energy matrix, $\mathbf{\Sigma}(\infty)$, are often included in ADC(3) calculations. An algorithm for the evaluation of

this matrix [9] that assumed the availability of the $\hat{\mathbf{H}}_{2ph-2ph}$ and $\hat{\mathbf{H}}_{2hp-2hp}$ matrices in diagonal form is impractical for calculations in which ov^2 and vo^2 are large. An alternative approach using the Lanczos diagonalization procedure has been suggested [32, 33].

Here, another method [33] is adopted, where the following intermediates are obtained:

$$\mathbf{V}_{\mathbf{h-2ph}} = (\epsilon_{\mathbf{h}} - \hat{\mathbf{H}}^{\mathbf{0}}_{\mathbf{2ph}} - \mathbf{C}_{\mathbf{2ph-2ph}})^{-\mathbf{1}}\hat{\mathbf{H}}_{\mathbf{2ph-h}} \tag{40}$$

$$\mathbf{V}_{\mathbf{p-2hp}} = (\epsilon_{\mathbf{p}} - \hat{\mathbf{H}}^{0}_{\mathbf{2hp}} - C_{\mathbf{2hp-2hp}})^{-\mathbf{1}}\hat{\mathbf{H}}_{\mathbf{2hp-p}}. \tag{41}$$

The matrix inversions may be done as an expansion about the zeroth-order, diagonal terms. In this case, only the matrix–vector products of the previous section are needed.

The constant part of the self–energy satisfies

$$\Sigma_{pq}(\infty) - \sum_{rs}\langle pr\|qs\rangle\frac{n_r - n_s}{\epsilon_r - \epsilon_s}\Sigma_{rs}(\infty) = \sum_{rs}\langle pr\|qs\rangle Q_{rs}, \tag{42}$$

where n_r and n_s are ordinary occupation numbers. $\mathbf{Q}$ is defined by

$$\begin{aligned} Q_{kl} &= -\sum_{jab} V_{k,jab}V_{l,jab} \\ Q_{ak} &= \left(\sum_{jcd} V_{k,jcd}\hat{H}_{a,jcd} + \sum_{cij} V_{a,cij}\hat{H}_{k,cij}\right)\frac{1}{\epsilon_k - \epsilon_a} \\ Q_{ka} &= Q_{ak} \\ Q_{ab} &= \sum_{cij} V_{a,cij}V_{b,cij}. \end{aligned} \tag{43}$$

$\mathbf{\Sigma}(\infty)$ may be expressed in terms of the correlation contribution to the one-electron density matrix, ρ^c:

$$\Sigma_{tu}(\infty) = \sum_{rs}\langle tr\|us\rangle\rho^c_{rs}. \tag{44}$$

ρ^c, in turn, is related to $\mathbf{Q}$ matrix elements via

$$\rho^c_{tu} - \frac{n_t - n_u}{\epsilon_t - \epsilon_u}\sum_{rs}\langle tr\|us\rangle\rho_{rs} = Q_{tu}. \tag{45}$$

The second term vanishes when the t, u pair pertains to the h–h or p–p blocks of ρ^c. Therefore, after spin adaptation,

$$\rho_{kl} = Q_{kl}$$
$$\rho_{ab} = Q_{ab}$$
$$\rho_{ia} - \frac{1}{\epsilon_i - \epsilon_a} \sum_{jb} \left\{ 2(\langle ij \mid ab \rangle + \langle ib \mid aj \rangle) - (\langle ij \mid ba \rangle + \langle ib \mid ja \rangle) \right\} \rho_{jb} =$$
$$Q_{ia} + \frac{1}{\epsilon_i - \epsilon_a} \left\{ \sum_{kl} \left(2\langle ik \mid al \rangle - \langle ik \mid la \rangle \right) \rho_{kl} + \sum_{cd} \left(2\langle ic \mid ad \rangle - \langle ic \mid da \rangle \right) \rho_{cd} \right\}. \tag{46}$$

The matrix equation for the p–h part of ρ^c has the familiar form **(1-A)X = B**, which occurs in coupled Hartree–Fock theory [34].

3. APPLICATIONS

Examples of electron propagator calculations on relatively large systems are given here. All calculations were performed with Gaussian03 [35] and the development version of Gaussian [36].

3.1. Fullerenes and other carbon clusters

The equilibrium structures of C_{60} and C_{70} were obtained with the B3LYP density functional [37] and the 6–31G(d) basis. The I_h and D_{5h} point groups were imposed for C_{60} and C_{70}, respectively, during the optimization procedure. Semidirect, symmetry-adapted algorithms for electron propagator calculations [20, 21, 29, 38, 39] were employed with the OVGF, ADC(3), and NR2 approximations. The 6–311G(d) basis was used, with the total number of contracted Gaussian functions being 1080 for C_{60} and 1260 for C_{70}.

3.1.1. C_{60}

OVGF calculations were performed with a full active virtual space and then with a truncated active space of 645 virtual MOs. (Virtual space reduction by omission of ordinary canonical Hartree–Fock orbitals resulted in the largest deviation being only 0.06 eV.) 84 occupied and 465 virtual MOs were used in ADC(3) calculations.

Table 3.1 presents ionization energies (IEs) of C_{60} obtained with the OVGF, ADC(3), and NR2 methods [30] together with experimental values [40]. Pole strengths (PSs) are given in parentheses to the right of each energy value.

^2H_u is the first ionized state of C_{60}. An IE value of 7.67 eV is obtained with the OVGF method, and the PS of 0.89 indicates a one-electron process.

Table 3.1 Vertical ionization energies of C_{60}, eV

	Ionization energies, eV				
MO	KT	OVGF[1]	ADC(3)	NR2	Exp. [40, 41]
$6h_u$	7.87	7.67(0.89)	7.68(0.87)	7.47(0.83)	7.64 ± 0.02
$10h_g$	9.65	9.18(0.88)	9.07(0.83)	8.85(0.80)	8.95[2]
			10.49(0.002)		
			10.54(0.02)	10.48(0.01)	
$6g_g$	9.91	9.23(0.87)	9.16(0.84)	8.82(0.80)	
			10.46(0.003)	10.47(0.003)	
$6g_u$	12.59	11.33(0.78)	11.32(0.70)		$10.82 - 11.59$[3]
			9.84(0.02)	9.79(0.07)	
			10.45(0.02)	10.34(0.06)	
$6t_{2u}$	13.06	11.88(0.79)	10.40(0.006)	10.38(0.02)	
			10.66(0.002)		
$5h_u$	13.68	11.79(0.89)		11.29(0.85)	
$9h_g$	14.03	12.13(0.89)		11.65(0.80)	

[1] 645 virtual orbitals retained;
[2] band centroid;
[3] unresolved band.

The ADC(3) method gives 7.68 eV with a PS value of 0.87, thus confirming the one-electron nature of this ionization. Both methods are in excellent agreement with the experimental value [40].

For the second band, two, almost degenerate IEs are obtained. The OVGF and ADC(3) values are very close and correspond qualitatively to the experimental estimates [40, 41].

Four ionized states are predicted for the third band. The OVGF calculations are characterized by low PS values for electron detachments from the first two MOs in this set. Because of this, exact positions of the main lines may be very different from the energy values given in Table 3.1. OVGF and ADC(3) predict the ^2G_u ionized state at essentially the same energy, 11.33 eV versus 11.32 eV. The ADC(3) PS for this energy is 0.70, showing this spectral line to be the most intense. Numerous shakeups characterized by very small PS values appear for this ionization. ADC(3) calculations on a system of this size are not feasible for energies outside of the −15 to 2 eV range. Although a collapse of the one-electron picture of ionization was anticipated for the above two energy levels, the current ADC(3) calculations revealed only two satellite lines for the $^2T_{2u}$ state. A state with a large PS may exist within a larger energy range, or there may be a complete breakdown of the one-electron picture of ionization from this MO.

The one-electron picture of ionization is confirmed for detachments from the $5h_u$ and $9h_g$ levels as the corresponding OVGF PS values are high. No IEs for these levels are found by ADC(3) calculations.

In attempts to find the energies missed by the ADC(3) procedure, NR2 calculations were performed. The NR2 procedure usually converges faster than ADC(3) and gives somewhat smaller IEs. Two missing IEs were found: one for ionization from the $5h_u$ MO that was placed at 11.29 eV and another for ionization from the $9h_g$ level that appeared at 11.65 eV. The PS values imply relatively large one-electron character for both processes.

3.1.2. C_{70}

Vertical IEs of C_{70} are compiled in Table 3.2. The OVGF energies were obtained with different truncations of the active orbital space. In the first truncation scheme, 610 virtual MOs out of 1050 were kept. With the second truncation, all but 100 virtual MOs were kept. No significant differences between OVGF energies obtained with larger and smaller orbital spaces were observed. Excellent agreement with the experimental assignment of Ref. [42]

Table 3.2 Vertical ionization energies of C_{70}, eV

	Ionization energies, eV				
MO	KT	OVGF[1](PS)	NR2[1](PS)	OVGF[2](PS)	Exp. [42]
$14a_2''$	7.54	7.47(0.90)	7.73(0.81)	7.45(0.90)	7.47
			9.86(0.02)		
$19e_1''$	7.60	7.49(0.89)	7.69(0.81)	7.47(0.89)	7.47
$7a_2'$	8.06	7.59(0.88)	7.97(0.82)	7.63(0.88)	7.68
$23e_2'$	8.48	7.90(0.88)	8.22(0.80)	7.94(0.88)	7.96
$19e_2''$	8.58	8.11(0.88)	8.13(0.79)	8.09(0.88)	8.12
$23e_1'$	8.82	8.44(0.88)	8.51(0.80)	8.42(0.88)	8.43
$22e_1'$	10.01	9.14(0.84)	9.22(0.73)	9.17(0.84)	9.04
			10.11(0.05)		
$18e_2''$	10.63	9.67(0.82)	9.70(0.38)	9.69(0.81)	9.28
			9.36(0.17)		
			9.62(0.08)		
			9.82(0.03)		
$18e_1''$	11.03	9.90(0.81)	9.93(0.35)	9.92(0.81)	9.60
			9.69(0.29)		
$22e_2'$	11.20	10.03(0.81)	9.73(0.32)	10.06(0.80)	9.60
			9.79(0.07)		
			10.16(0.06)		

[1] 610 virtual MOs retained in the active space;
[2] 950 virtual MOs retained in the active space.

was achieved for the first seven ionized states. PS values are very high for the first six ionizations. Based on these values, one-electron character can be anticipated for these six ionization events. The PSs for the next five ionizations are somewhat lower and might indicate many-electron (correlation state) character in these transitions.

NR2 calculations were performed on C_{70} with the same active space restrictions as those used with OVGF. These IEs are presented in Table 3.2 next to the OVGF data. As expected, no shakeup states appeared for the first six ionizations. Starting with the seventh ionization, satellite lines are predicted. Complete breakdowns of the one-electron picture of ionization are obvious in the cases of $18e_2''$ and $18e_1''$ MOs where two ionized states of comparable PS values arise. Some of these OVGF energies correspond rather well to the experimental values. For example, the experimental feature at 9.28 eV matches a satellite of the $18e_2''$ MO with an energy of 9.36 eV and the PS of 0.17. Another experimental energy that appears at 9.60 eV might be shaped by three shakeup states with IEs at 9.70 eV, 9.69 eV, and 9.73 eV. These states borrow intensity from the $18e_2''$, $18e_1''$, and $22e_1'$ MOs, respectively.

3.1.3. Predictions for C_{96} and C_{144}

Equilibrium structures of the C_{96} nanodisk and the C_{144} nanocapsule were optimized by Shukla and Leszczynski [43]. D_{6h} symmetry was imposed on these structures. OVGF calculations were performed with the 6–311G(d) basis. The size of the basis was 1728 for C_{96} and 2592 for C_{144}. The active orbital space for C_{96} consisted of 192 occupied MOs and 1025 virtual MOs. 288 occupied and 1115 virtual MOs were involved in the case of C_{144}. Vertical IEs are presented in Tables 3.3 and 3.4, respectively.

There are no experimental gas-phase or thin-film photoelectron spectra (PES) for these two carbon nanostructures. Ultraviolet PES measured in thin films of C_{96} were published [44, 45]. No absolute values were given for the peak positions, instead, the spectra were depicted over the energy scale relative to the Fermi energy level. The low-energy part of this spectrum contains an intense peak followed by a jagged plateau of lower intensity. At least three small peaks are visible on that plateau. The energy difference between the main peak position and the first small peak on the plateau is about 0.5 eV.

Table 3.3 Vertical ionization energies of C_{96}, eV

MO	KT	OVGF(PS)	Exp. [46]
e_{1u}	7.09	6.95(0.88)	6.92
e_{1g}	7.69	7.45(0.89)	
a_{1u}	7.83	7.35(0.87)	
e_{2g}	8.08	7.80(0.88)	
a_{2g}	8.43	7.89(0.86)	

Table 3.4 Vertical ionization energies of C_{144}, eV

MO	KT	OVGF(PS)
e_{2g}	7.04	6.87(0.88)
e_{1u}	7.13	6.86(0.88)
e_{1g}	7.47	7.12(0.88)
b_{2u}	7.85	7.57(0.87)
a_{2g}	7.91	7.31(0.86)

The plateau ends at about 1 eV over the main peak maximum. The adiabatic IE is available for C_{96} [46].

OVGF predicts the first ionized state of C_{96} at 6.95 eV, which is in very good agreement with the adiabatic value of Ref. [46]. (See Table 3.3.) Like most higher carbon clusters, C_{96} has a globular, rigid structure for which no dramatic relaxation upon ionization is expected (except for Jahn–Teller distortion). The first final state of ^2E_u symmetry is well separated from other transitions and, as such, should appear in the PES as a well-resolved peak. The next two final states are predicted at 7.35 eV and 7.45 eV. Relative positions of these two ionizations might be reversed in calculations with larger active spaces. The last two ionizations under consideration are placed at about 0.5 eV higher. According to high PS values, the one-electron picture of ionization should hold for all ionization events discussed above. Thus, the OVGF data give a good description of the low-energy part of the C_{96} spectra of Refs. [44] and [45].

A gradual decrease in IEs of C_n molecules with increasing n was observed experimentally [46]. Our results for C_{60}, C_{70}, and C_{96} follow this pattern. OVGF vertical IEs for the C_{144} nanocapsule are given in Table 3.4. As expected, the first IE value of this large system was smaller than those of other carbon clusters discussed above. The first IE is predicted as a fourfold event that occurs from two almost degenerate sets of e_{2g} and e_{1u} orbitals. The order of these two ionized states might be reversed if a larger active orbital space were engaged in the calculations; however, no drastic increase in energy gap is expected. The second ionization event is predicted at 7.12 eV, rather close to the first one. The next two ionizations are placed at 7.31 and 7.57 eV. A Koopmans's theorem defect (incorrect order of final states) is predicted for these two ionized states. The one-electron picture of ionization holds for the energies presented in Table 3.4.

3.2. Macrocycles: porphyrins and phthalocyanines

Macrocycles such as porphyrins, tetraazaporphyrins, phthalocyanines, and their derivatives are compounds with diverse, applicable properties [47, 48].

Extended conjugated systems of π-electrons make these compounds promising candidates for various electronic devices [49, 50] and solar cell components [51, 52]. These macrocycles provide a variety of substitution sites which can be used to create compounds with controlled electron donor/acceptor properties [53, 54]. In nature, metal-containing macrocycles are present as central structural units in many substances involved in biochemical redox reactions [55].

Chemical reactivity of macrocycles in such events as electron transfer, oxygen transport, oxidation, and reduction is directly related to their ionization energies and electron affinities, which in turn depend upon the chemical environment about the porphyrin unit. MO concepts usually inform theoretical interpretations of experiments that probe the electronic and spectroscopic properties of conjugated macrocyclic compounds. For macrocycles, the four highest occupied levels have been invoked for this purpose [56]. In some cases, MOs of even higher energies were involved in the assignment of electronic spectra [57]. Vertical IEs that can be obtained from PES as peak maxima are usually associated with MO energies.

Examples of electron propagator calculations showing both preservation of the one-electron picture of ionization and its complete breakdown in cases of porphyrins and phthalocyanines are given below.

3.2.1. Porphyrins: Free-base porphine (H_2P), Mg and Zn porphyrins (MgP and ZnP)

Reports of gas-phase ultraviolet PES of porphyrins are available only for free-base porphine (H_2P) and a number of highly substituted (usually, octaethyl and tetraphenyl) porphyrins and metalloporphyrins.

In the PES of H_2P, which first appeared in Ref. [58], there are four well-separated bands within a 6–14 eV energy range. The first appears as a sharp peak at 6.9 eV with an obvious shoulder at 7.1–7.2 eV. The second band consists of a plateau at 8–8.4 eV, followed by a peak at 9.1 eV with a high-energy shoulder. The third band is located between 10 and 11 eV and has significantly less intensity than the previous two. All these bands were assigned to ionizations from π levels, and the rest of the spectrum was not assigned. No experimental spectra exist for either Mg or Zn unsubstituted porphyrins.

Tables 3.5–3.7 present vertical IEs of H_2P, MgP, and ZnP obtained with the P3 and NR2 approximations and the 6–311G(d,p) basis. Equilibrium molecular structures were optimized with the B3LYP and 6–311(d,p) basis (Figure 3.2). Harmonic frequency analysis revealed a D_{2h} minimum for H_2P and D_{4h} minima for MgP and ZnP.

Excellent agreement with experiment was achieved for H_2P in the P3 calculations with no reduction of the virtual space [59]. (Various schemes of active space reduction were discussed in the same paper.) Among the first eight π cationic states, only the two upper states have P3 PS values exceeding 0.84. For the rest of the π states, the P3 PS values varied from 0.67

Table 3.5 Free-base porphine ionization energies, eV

State	KT	P3	PS	NR2	PS	Expt. [58]
$^2B_{3u}$	6.68	6.97	0.85	6.68	0.81	6.9
^2A_u	6.14	6.94	0.85	6.78	0.81	7.1
$^2B_{1g}$	9.13	8.30	0.81	8.10	0.40	~8.0–8.4
				7.61	0.31	
				9.83	0.06	
				10.38	0.04	
				10.84	0.03	
$^2B_{3u}$	9.37	8.50	0.82	8.04	0.67	~8.0–8.4
				9.86	0.08	
$^2B_{2g}$	10.05	9.10	0.68	8.72	0.49	
				8.46	0.10	
				8.86	0.04	
				10.61	0.16	
$^2B_{2g}$	10.24	9.16	0.82	8.86	0.58	
				7.58	0.06	
				8.46	0.05	
				8.72	0.08	
$^2B_{3u}$	10.27	9.22	0.82	8.76	0.67	
				10.66	0.04	
$^2B_{1g}$	10.40	9.38	0.67	8.91	0.43	
				8.10	0.02	
				10.55	0.22	
^2A_g	11.49	9.58	0.86	9.16	0.82	
$^2B_{2u}$	11.56	9.61	0.86	9.17	0.82	
^2A_u	11.94	10.53	0.73	9.88	0.45	
				10.00	0.06	

to 0.82, indicating the breakdown of the one-electron picture of ionization. (See Table 3.5.) Thus, the absolute P3 results cannot be taken at face value.

NR2 calculations confirmed the one-electron picture of ionization for the first two cationic states of H_2P. The PSs are smaller than those obtained with the P3 method. Although the absolute IE values are lower than the P3 results (which is normal for the basis set and the active orbital space used), the energy gap is consistent with the experimental and relative positions of the states. No shakeup states with significant PSs are predicted for these two transitions.

NR2 calculations predict complete breakdowns of the one-electron picture of ionization for higher, $^2B_{1g}$, $^2B_{3u}$, and $^2B_{2g}$ final states with large intensity borrowing between the states of the same symmetry. Although the

Table 3.6 Mg porphyrin ionization energies,[1] eV

State	KT	P3	PS	NR2	PS
$^2A_{1u}$	6.02	6.80	0.85	6.59	0.81
$^2A_{2u}$	6.63	6.80	0.85	6.53	0.81
$^2B_{2u}$	9.38	8.38	0.82	7.93	0.71
				10.08	0.11
^2E_g	9.48	8.42	0.81	8.14	0.48
				7.47	0.17
				8.36	0.12
				10.01	0.04
				10.21	0.03
$^2A_{2u}$	9.84	8.77	0.82	8.29	0.66
				10.24	0.09
^2E_g	10.09	9.06	0.69	8.64	0.48
				8.14	0.05
				10.21	0.08
$^2B_{1g}$	11.78	9.81	0.87	9.38	0.84
$^2B_{1u}$	11.79	10.29	0.74	9.65	0.52
^2E_u	12.68	10.71	0.87	10.25	0.82
$^2B_{2g}$	14.14	12.40	0.87	11.94	0.82

[1] Active orbital space - 367 MOs. Occupied MOs with $\epsilon < -1.09$ a.u. dropped; virtual MOs with $\epsilon > 2.98$ a.u. dropped.

observed correlation effects might have been exaggerated by the NR2 scheme due to the restricted active orbital space, the qualitative picture is rather representative. Each final state mentioned above is characterized by a single, more intense main transition and at least one satellite of lower intensity.

The one-electron picture of ionization is conserved for two σ-type final states that arise after the first π final states. Analogous behavior is observed for MgP and ZnP. (See Tables 3.6 and 3.7.) For the first two IEs and for the σ-hole states, the pole strengths are above 0.8, but strong shakeup character is present in the remaining π-hole IEs.

3.2.2. Phthalocyanines

Ultraviolet PES of gaseous, free-base phthalocyanine (H_2Pc) and metal phthalocyanines (MPc, M = Mg, Fe, Co, Ni, Cu, and Zn) were reported first in Ref. [60]. All spectra were strikingly similar; only fine structures of broad bands differed. A narrow band at about 6.4 eV and a broad band at ~8–10 eV appeared in all spectra. Another band followed at ~10–12 eV. Only tentative positions of several IEs were given in the experimental work [60] with no definite assignments.

Table 3.7 Zn porphyrin ionization energies,[1] eV

State	KT	P3	PS	NR2	PS
$^2A_{1u}$	5.99	6.77	0.85	6.58	0.82
$^2A_{2u}$	6.64	6.82	0.85	6.56	0.82
$^2B_{2u}$	9.44	8.47	0.83	8.03	0.70
				10.13	0.11
^2E_g	9.49	8.44	0.81	8.18	0.49
				7.49	0.16
				8.41	0.12
				10.08	0.05
$^2A_{2u}$	9.85	8.82	0.82	8.35	0.66
				10.30	0.10
				11.13	0.02
^2E_g	10.10	9.10	0.69	8.70	0.47
				8.18	0.04
$^2B_{1g}$	10.83	8.86	0.88	8.40	0.85
$^2B_{1u}$	11.82	10.35	0.73	9.72	0.51
^2E_u	12.85	10.97	0.86	10.55	0.82
$^2B_{2g}$	14.14	12.50	0.87	12.06	0.82
$^2A_{2g}$	14.18	12.38	0.86	11.96	0.80

[1] Active space includes 356 MOs. Occupied MOs with $\epsilon > -1.063$ a.u. and virtual MOs with $\epsilon < 2.973$ a.u. are included.

The molecular structures of H_2Pc, MgPc, and ZnPc were optimized with the B3LYP density functional [37] and the 6–311G(d,p) basis (Figure 3.2). D_{2h} and D_{4h} symmetry point groups were assumed for H_2Pc and MPc, respectively; minima were confirmed by harmonic frequency analysis. Electron propagator calculations were performed in the P3 and ADC(3) approximations with the same basis. High symmetry in these molecular systems permitted calculations to be performed in the full valence active orbital space. The results were very similar for all three systems under consideration, so only the H_2Pc case is discussed below.

Electron propagator VIEs of H_2Pc are tabulated in Table 3.8 together with Koopmans's theorem values and experimental data. Table 3.8 lists ionized states in the order of their Hartree–Fock orbital energies. P3 and ADC(3) IEs with their PSs in parentheses are shown. Only those ADC(3) energies for which a given MO provides a major contribution to the corresponding eigenvector of the superoperator Hamiltonian matrix are given here.

The PS values of the P3 IEs show that among ionizations from π levels, even the first one corresponds only qualitatively to a one-electron process.

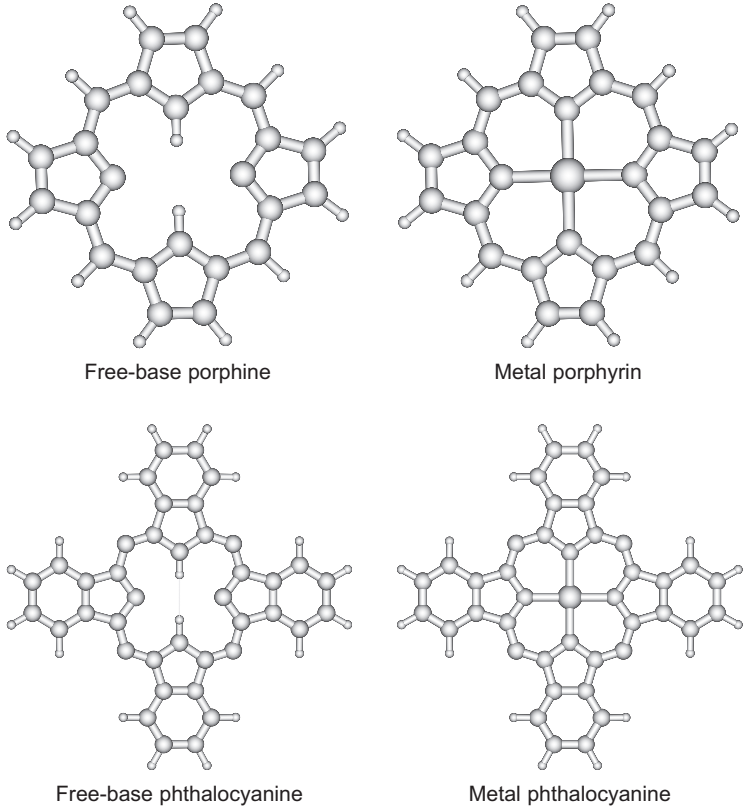

Figure 3.2 Molecular structures of porphyrins and phthalocyanines.

Very good agreement between the P3 IE value for the π_1 MO and the experimental one (6.55 vs 6.41 eV in Ref. [60]) is achieved despite the PS, which is somewhat lower than the 0.85 threshold for the validity of diagonal self-energy calculations. The ADC(3) energy, 6.14 eV, is lower and the PS value is nearly equal to its P3 counterpart. Strong correlation effects are observed for all higher π levels. There are many π-hole final states whose PSs do not exceed 0.65. Numerous satellites with PSs that are less than 0.1 were found in the energy region of 8–10 eV. These are not shown here.

The one-electron picture of transitions belonging to the b_{3u} representation is completely invalid. For the π_2, HOMO–1 case, two main lines with energies of 7.90 and 8.49 eV and PS values near 0.4 are the most prominent. Four satellites with appreciable PSs appear at higher energies. The π_2 MO is the largest contributor for the ionized states with energies of 7.90 eV, 8.49 eV, and 9.88 eV.

Table 3.8 Phthalocyanine ionization energies, eV

State	MO type	KT	P3(PS)	ADC(3)(PS)
^2A_u	π_1	5.23	6.55(0.83)	6.14(0.82)
$^2B_{3u}$	π_2	8.90	8.36(0.80)	7.90(0.43)
				8.49(0.37)
				9.88(0.11)
$^2B_{1g}$	π_3	8.96	8.35(0.78)	7.93(0.41)
				8.65(0.34)
				10.13(0.10)
$^2B_{3u}$	π_4	9.06	8.64(0.79)	8.11(0.42)
				9.97(0.07)
$^2B_{2g}$	π_5	9.25	8.67(0.70)	8.64(0.65)
^2A_u	π_6	9.38	8.86(0.79)	8.57(0.46)
				9.15(0.26)
$^2B_{1g}$	π_7	9.46	8.80(0.65)	8.85(0.50)
				9.10(0.11)
				9.68(0.08)
$^2B_{2g}$	π_8	9.63	8.93(0.77)	8.99(0.30)
				8.25(0.27)
				9.30(0.04)
				9.50(0.11)
				10.58(0.05)
$^2B_{3u}$	π_9	9.94	9.04(0.80)	8.89(0.32)
				9.06(0.10)
				9.55(0.10)
				10.64(0.13)
^2A_u	π_{10}	10.05	9.43(0.78)	9.06(0.25)
				9.52(0.09)
				9.54(0.08)
$^2B_{3g}$	σ_1	11.57	9.56(0.86)	9.75(0.85)
$^2B_{1g}$	π_{11}	11.76	–	10.02(0.11)
				9.56(0.02)
$^2B_{2u}$	σ_2	11.80	9.83(0.85)	10.01(0.84)
^2A_g	σ_3	12.05	10.08(0.85)	10.31(0.84)
$^2B_{2g}$	π_{12}	12.09	–	–
$^2B_{1u}$	σ_4	12.14	10.07(0.86)	10.27(0.84)

An analogous picture is observed for the b_{1g} HOMO–2 orbital, where the P3 energy splits into two major lines and several satellites.

In general, all π MOs lower than the HOMO give rise to more than three IEs. The ADC(3) energy values for these MOs cover the range from 7.9 to over

10 eV with rather small intervals between final states. This very complicated picture of ionization explains the structure of the second energy band, which was completely unresolved in the experimental spectrum [60].

The one-electron picture has somewhat greater validity for ionizations from the first four σ levels, listed at the bottom of Table 3.8. Here, the PSs are 0.84 or greater. The position of a σ_1 MO is predicted at about 9.6–9.7 eV and fits under a broad envelope at ~8–10 eV of the experimental spectrum. Three other σ IEs are very close to each other and probably appear in the experimental spectrum as a weak plateau at ~10.2 eV.

3.3. Dinucleotides

Electron transfer processes in DNA and RNA are very important for biological systems. These processes can initiate changes in genetic material leading to mutations [61, 62]. It is supposed that these processes start with electron detachment from one site in the nucleic acid strand and end with electron attachment to another site of the same or a different strand. It is also believed that an electron deficiency in a DNA fragment may be created initially by ionizing radiation on a guanine site. Otherwise, the hole moves through stacks of bases until it reaches the guanine base [63, 64].

Direct experimental studies of these processes in real DNA or RNA are difficult: these macromolecules and their fragments decompose under harsh conditions of gas-phase ionization experiments. Ionization in aqueous media is accompanied by formation of high amounts of hydroxyl radicals, complicating interpretation of the results [65].

Although nucleic acids are too large for computational studies with reliable theoretical methods, electron transfer phenomena can be studied in their constituents: oligonucleotides and their fragments. An oligonucleotide contains n sugar–base moieties interlinked by $(n-1)$ phosphate groups. Computational studies of neutral, monoanionic, and polyanionic oligonucleotides of this kind are possible. In the case of monoanionic oligonucleotides, only one of the phosphate groups is deprotonated. Therefore, there are three sites in a closed-shell, deprotonated nucleotide anion that an electron may occupy: a base, the phosphate group, and a sugar. Of course, an electron can also be delocalized over the whole anion.

Ionizations from bases are very well documented [66–72]. Excellent agreement has been achieved between electron propagator calculations in the P3 approximation [10–12] and results of ultraviolet PES experiments [73] for all five nucleic acid bases.

Electron detachment from anionic mono-, di-, and trinucleotides was studied experimentally by electrospray photodetachment photoelectron spectroscopy (EPPS) [74]. Substrates did not decompose at the relatively low temperatures of these experiments.

The spectra of anionic mononucleotides ($dXMP^-$, where X = A, C, G, and T) [74] were rather poorly resolved for the first VDEs of $dAMP^-$, $dCMP^-$, and $dTMP^-$, whereas an error bar of ±0.10 eV was determined for the VDE of $dGMP^-$. Theoretical VDE values obtained in the same paper as B3LYP energy differences between anionic and neutral states were about 0.5–0.8 eV off the experimental peak positions for $dTMP^-$, $dCMP^-$, and $dAMP^-$. No interpretation of other possible transitions was given. Excellent agreement with experimental energy values was achieved for VDEs of mononucleotide anions calculated with *ab initio* electron propagator theory [71, 75].

No VDE values were reported for any of 16 possible monoanionic dinucleotides, although the adiabatic electron detachment energies were tabulated [74]. The spectra of eight dinucleotides were displayed in the same publication. These included the spectra of dAA^-, dCC^-, dGG^-, dTT^-, dAG^-, dCG^-, dGA^-, and dTG^-. One common feature is present in the EPPS spectra of all dinucleotides containing a guanine moiety: a low-intensity band centered at about 5.5 eV, well separated from the second envelope arising at higher energies. In the case of dGG^-, the intensity of this particular band was about two times larger than for other guanine-containing dinucleotides. This pecularity lead to a suggestion that the low-energy band in the EPPS of dGG^- contained ionizations from both guanine fragments [74].

Here, we present the results of P3 studies of the VDEs of the most stable conformation of a dinucleotide: 2′,2′-deoxyribo diguanosine-3′,5′-monophosphate anion ($dDGMP^-$ or dGG^-).

The structure depicted in Figure 3.3 seems to be a global minimum. It was found among eighty conformations of dGG^- by means of, first, a Monte Carlo AM1 conformational search with BOSS4.6 [76] and, second, a reoptimization of the structures with the B3LYP/6–311++G(d,p) model. The structure shown in Figure 3.3 is a globular, H-bonded, nonstacked conformation. It contains three H-bonds, two of which are formed by OH groups of each sugar and two O atoms of the PO_4 group. The third H-bond is formed between the amino group of the 5′ guanine (an electron acceptor) and a carbonyl oxygen of the 3′ guanine (an electron donor). The H-bond lengths do not exceed 1.8 Å.

The dinucleotide under consideration is rather large for electron propagator calculations with a full active space of orbitals. The number of basis functions for the 6-311++G(d,p) basis for dGG^- totals 1078. There are 155 valence occupied MOs and 923 virtual MOs. The system has no symmetry, and so P3 calculations with an active orbital space of this size require a very large amount of disk space for storage of intermediate data. A significant reduction of the active space was needed in order to run these calculations. Such a reduction may be achieved through the use of Quasiparticle Virtual Orbitals (QVOs) [77] in which the number of virtual orbitals involved in the electron propagator calculations is reduced without significant loss of accuracy.

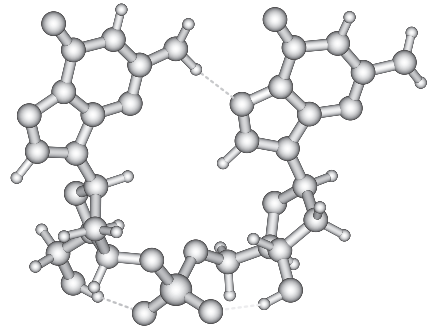

Figure 3.3 The most stable structure of deoxyribo diguanosine monophosphate anion, dGG^-.

Table 3.9 QVOs VDEs of dGG^-, eV

MO	KT	P3	Exp. [74]
π_1 G(5′)	5.71	5.47	∼5.5
PO_4	8.52	6.52	
π_1 G(3′)	6.78	6.60	
S(5′)	8.84	7.03	∼7.1
PO_4	8.92	7.07	∼7.1
G(3′) + S(3′) + PO_4	8.81	7.15	∼7.2
π_2 G(5′)	8.40	7.21	∼7.2

The P3 calculations need ⟨ia‖bc⟩ integrals, and storage requirements for these scale as ov^3. Reduction of the virtual space thus leads to significant savings in disk space. The QVOs method was only recently implemented in the Gaussian suites of programs [77], and its applicability to large systems with no symmetry was tested on anionic mononucleotides [78]. For MOs localized on a base or the phosphate group, a 50% reduction in the number of virtual orbitals introduced numerical deviations no larger than 0.02 eV. Somewhat larger errors were obtained for more delocalized MOs. Disk space required for storage of transformed integrals and intermediates was smaller by a factor of 2.5 than in the case of the full virtual orbital space.

Table 3.9 contains the VDE values obtained for 2′,2′-deoxyribo diguanosine-3′,5′-monophosphate anion (dGG^-) with the 6-311++G(d,p) basis and a 50%-reduced virtual MO space produced by the QVOs procedure.

The first VDE of the most stable conformation of dGG^- is placed at 5.47 eV. This value is in excellent agreement with the maximum of the first band in

the experimental EPPS of dGG^- [74]. This VDE is assigned to electron detachment from the π_1 MO of 5′ guanine. The next two ionization energies are more than 1 eV larger and are assigned to the phosphate MO and the π_1 MO of 3′ guanine. Although there are no distinctive peaks at these energies in the EPPS of [74], the values of 6.52 and 6.60 eV fit well into the envelope of the second band. The next four VDEs are assigned to different fragments of this conformation of dGG^- and correspond very well to some visible peaks in the aforementioned spectrum. The main conclusion here is that electron detachment from only one guanine moiety is responsible for the experimental peak at ∼5.5 eV, at least for the most stable conformation of dGG^-.

4. CONCLUSIONS

Accurate electron binding energies of molecules and molecular ions, including those that pertain to excited final states in a photoelectron experiment, may be obtained efficiently with electron propagator methods. For transition energies where the approximations inherent in Koopmans's theorem are qualitatively reasonable, perturbative, quasiparticle approximations may be used with confidence. In these cases, diagonal elements of the self-energy operator are needed in calculations that employ a highly simplified form of the Dyson equation. When qualitatively important correlation or final-state orbital relaxation effects are present, methods based on renormalized, nondiagonal self-energy expressions should be used. These techniques involve methods for obtaining eigenvalues and eigenvectors of the superoperator Hamiltonian matrix.

Both classes of self-energy approximations yield useful data for C_{60}, C_{70}, and larger fullerenes. Nondiagonal, renormalized methods reveal the presence of correlation states in photoelectron spectra. Electron propagator calculations performed on porphyrins and phthalocyanines indicate the prevalence of strong correlation effects for the lowest cationic states. Quasiparticle calculations on an anionic dinucleotide with two guanine bases exhibit the need for correlated methods in interpreting anion photoelectron spectra of nucleic acid fragments.

ACKNOWLEDGMENTS

This work was supported by the National Science Foundation through grant CHE–0809199 to Auburn University. We thank Professor Jerzy Leszczynski of Jackson State University for optimized geometries of C_{96} and C_{144} and Professor Orlando Acevedo of Auburn University for advice on the use of the BOSS program.

REFERENCES

[1] A.B. Migdal, Theory of Finite Fermi Systems, Wiley–Interscience, New York, 1967.
[2] J. Linderberg, Y. Öhrn, Propagators in Quantum Chemistry, Second ed., Wiley–Interscience, Hoboken, New Jersey, 2004.
[3] The residue corresponding to an electron propagator pole, E_{pole}, is defined by $Res(E_{pole}) = \lim_{E \to E_{pole}} G_{pq}(E)(E - E_{pole})$.
[4] A.A. Abrikosov, L.P. Gorkov, I.E. Dzyaloshinski, Methods of Quantum Field Theory in Statistical Physics, Prentice–Hall, Englewood Cliffs, NJ, 1963.
[5] J.V. Ortiz, V.G. Zakrzewski, O. Dolgounitcheva, in: E.S. Kryachko (Ed.), Conceptual Trends in Quantum Chemistry, Vol. 3, Kluwer, Dordrecht, 1997, p. 465.
[6] J.V. Ortiz, in: J. Leszczynski (Ed.), Computational Chemistry: Reviews of Current Trends, Vol. 2, World Scientific, Singapore, 1997, p. 1.
[7] J.V. Ortiz, Adv. Quantum Chem. 35 (1999) 33.
[8] R. Flores-Moreno, J. Melin, O. Dolgounitcheva, V.G. Zakrzewski, J.V. Ortiz, Int. J. Quantum Chem. 110 (2010) 706.
[9] W. von Niessen, J. Schirmer, L.S. Cederbaum, Comput. Phys. Rep. 1 (1984) 57.
[10] J.V. Ortiz, J. Chem. Phys. 104 (1996) 7599.
[11] J.V. Ortiz, V.G. Zakrzewski, J. Chem. Phys. 105 (1996) 2762.
[12] A.M. Ferreira, G. Seabra, O. Dolgounitcheva, V.G. Zakrzewski, J.V. Ortiz, in: Cioslowski (Ed.), Quantum–Mechanical Prediction of Thermochemical Data, Kluwer, Dordrecht, 2001, p. 131.
[13] L.S. Cederbaum, W. Domcke, Adv. Chem. Phys. 36 (1977) 206.
[14] N.H. March, W.H. Young, S. Sampanthar, The Many–Body Problem in Quantum Mechanics, Cambridge University Press, London, 1967.
[15] J. Goldstone, Proc. Roy. Soc. A 239 (1957) 267.
[16] L. van Hove, L. Hugenholtz, L. Howland, Quantum Theory of Many–Particle Systems, Benjamin, New York, 1961.
[17] L.S. Cederbaum, J. Phys. B 8 (1975) 290; L.S. Cederbaum, Theor. Chim. Acta 31 (1973) 239.
[18] V.G. Zakrzewski, J.V. Ortiz, J.A. Nichols, D. Heryadi, D.L. Yeager, J.T. Golab, Int. J. Quantum Chem. 60 (1996) 29.
[19] Y. Öhrn, G. Born, Adv. Quantum Chem. 13 (1981) 1.
[20] V.G. Zakrzewski, J.V. Ortiz, Int. J. Quantum Chem. S28 (1994) 23.
[21] V.G. Zakrzewski, J.V. Ortiz, Int. J. Quantum Chem. 53 (1995) 583.
[22] GAUSSIAN 09, (Revision A.1): M.J. Frisch, G.W. Trucks, H.B. Schlegel, et al. Gaussian, Inc., Wallingford, CT, 2009 and previous versions such as GAUSSIAN 03, GAUSSIAN 98 and GAUSSIAN 94.
[23] J.V. Ortiz, J. Chem. Phys. 108 (1998) 1008.
[24] J.V. Ortiz, Int. J. Quantum Chem. 75 (1999) 615.
[25] A.A. Golubeva, P.A. Pieniazek, A.I. Krylov, J. Chem. Phys. 130 (2009) 124113.
[26] Y. Shigeta, A.M. Ferreira, V.G. Zakrzewski, J.V. Ortiz, Int. J. Quantum Chem. 85 (2001) 411.
[27] J. Schirmer, L.S. Cederbaum, J. Phys. B 11 (1978) 1889; J. Schirmer, L.S. Cederbaum, O. Walter, Phys. Rev. A 28 (1983) 1237.
[28] E.R. Davidson, J. Comput. Phys. 17 (1975) 87.
[29] V.G. Zakrzewski, O. Dolgounitcheva, J.V. Ortiz, Int. J. Quantum Chem. 75 (1999) 607.
[30] V.G. Zakrzewski, O. Dolgounitcheva, J.V. Ortiz, J. Chem. Phys. 129 (2008) 104306.
[31] V.G. Zakrzewski, O. Dolgounitcheva, J.V. Ortiz, Int. J. Quantum Chem. 109 (2009) 3619.
[32] H.–G. Weikert, H.–D. Meyer, L.S. Cederbaum, J. Chem. Phys. 104 (1996) 7122.
[33] J. Schirmer, G. Angonoa, J. Chem. Phys. 91 (1989) 1754.
[34] J.A. Pople, R. Krishnan, H.B. Schlegel, J.S. Binkley, Int. J. Quantum Chem. S13 (1979) 225.
[35] GAUSSIAN 03, (Revision C.03): M.J. Frisch, G.W. Trucks, H.B. Schlegel, et al. Gaussian, Inc, Wallingford, CT, 2004.

[36] GAUSSIAN Development Version, (Revision H.01): M.J. Frisch, G.W. Trucks, H.B. Schlegel, et al. Gaussian, Inc, Wallingford, CT, 2008.
[37] D.A. Becke, Phys. Rev. A 38 (1988) 3098; T.C. Lee, T. Yang, R.C. Parr, Phys. Rev. B 37 (1988) 785.
[38] V.G. Zakrzewski, W. von Niessen, J. Comput. Chem. 14 (1993) 13.
[39] V.G. Zakrzewski, O. Dolgounitcheva, J.V. Ortiz, Int. J. Quantum Chem. 80 (2000) 836.
[40] D.L. Lichtenberger, K.W. Nebesny, C.D. Ray, D.R. Huffman, L.D. Lamb, Chem. Phys. Lett. 176 (1991) 203.
[41] D.L. Lichtenberger, M. Jatcko, K.W. Nebesny, C.D. Ray, D.R. Huffman, L.D. Lamb, Mat. Res. Soc. Symp. Proc. 206 (1991) 673.
[42] D.L. Lichtenberger, M.E. Rempe, S.B. Gogosha, Chem. Phys. Lett. 198 (1992) 454.
[43] M.K. Shukla, J. Leszczynski, Chem. Phys. Lett. 428 (2006) 317.
[44] S. Hino, H. Takahashi, K. Iwasaki, T. Miyazaki, K. Kikuchi, Y. Achiba, Chem. Phys. Lett. 230 (1994) 165.
[45] S. Hino, K. Kikuchi, Y. Achiba, Synth. Metals 70 (1995) 1337.
[46] O.V. Boltalina, I.N. Ioffe, L.N. Sidorov, G. Seifert, K. Vietze, J. Am. Chem. Soc. 122 (2000) 9745.
[47] K. Kasuga, M. Tsutsui, Coord. Chem. Rev. 32 (1980) 67.
[48] K. Flatz, M. Grobosch, M. Knupfer, J. Chem. Phys. 126 (2007) 214702 and references therein.
[49] J. Danziger, J.–P. Dodelet, P.A. Lee, K.W. Nebesny, N.R. Armstrong, Chem. Mater. 3 (1991) 821.
[50] U. Weiler, T. Mayer, W. Jaegermann, C. Kelting, D. Schlettwein, S. Makarov, et al., J. Phys. Chem. B 108 (2004) 19398.
[51] D. Schlettwein, K. Hesse, N.E. Gruhn, P.A. Lee, K.W. Nebesny, N.R. Armstrong, J. Phys. Chem. B 105 (2001) 4791 and references therein.
[52] M.E. El–Khouly, M. Fujitsuka, O. Ito, J. Porphyrins Phthalocyanines 4 (2000) 591.
[53] D. Pop, B. Winter, W. Freyer, I.V. Hertel, W. Widdra, J. Phys. Chem. B 107 (2003) 11647.
[54] D. Pop, B. Winter, W. Freyer, R. Weber, W. Widdra, I.V. Hertel, J. Phys. Chem. B 108 (2004) 9158 and references therein.
[55] D. Dolphin, R.H. Felton, Acc. Chem. Res. 7 (1974) 26.
[56] N. Kobayashi, H. Konami, J. Porphyrins Phthalocyanines 5 (2001) 233.
[57] A.B.J. Parusel, S. Grimme, J. Porphyrins Phthalocyanines 5 (2001) 225.
[58] P. Dupuis, R. Roberge, C. Sandorfy, Chem. Phys. Lett. 75 (1980) 434.
[59] O. Dolgounitcheva, V.G. Zakrzewski, J.V. Ortiz, J. Phys. Chem. 109 (2005) 11596.
[60] J. Berkowitz, J. Chem. Phys. 70 (1979) 2819.
[61] D. Becker, M.D. Sevilla, in: J.T. Lett, H. Adler (Eds.), Advances in Radiation Biology, Vol. 17, Academic Press, New York, 1993, 121.
[62] B. Giese, Curr. Opin. Chem. Biol. 6 (2002) 612.
[63] S. Steenken, Chem. Rev. 89 (1989) 503.
[64] S. Steenken, V. Jovanovic, J. Am. Chem. Soc. 119 (1997) 617.
[65] T. Melvin, S.W. Botchway, A.W. Parker, P. O'Neill, J. Am. Chem. Soc. 118 (1996) 10031.
[66] O. Dolgounitcheva, V.G. Zakrzewski, J.V. Ortiz, Int. J. Quantum Chem. 80 (2000) 831.
[67] O. Dolgounitcheva, V.G. Zakrzewski, J.V. Ortiz, J. Am. Chem. Soc. 122 (2000) 12304.
[68] O. Dolgounitcheva, V.G. Zakrzewski, J.V. Ortiz, J. Phys. Chem. A 106 (2002) 8411.
[69] O. Dolgounitcheva, V.G. Zakrzewski, J.V. Ortiz, Int. J. Quantum Chem. 90 (2002) 1547.
[70] O. Dolgounitcheva, V.G. Zakrzewski, J.V. Ortiz, in: E.J. Brändas, E.S. Kryachko (Eds.), Fundamental World of Quantum Chemistry: A Tribute to the Memory of Per-Olov Löwdin Kluwer, Dordrecht, 2003, 525.
[71] V.V. Zakjevskii, O. Dolgounitcheva, V.G. Zakrzewski, J.V. Ortiz, Int. J. Quantum Chem. 107 (2007) 2266.
[72] O. Dolgounitcheva, V.G. Zakrzewski, J.V. Ortiz, J. Phys. Chem. A 113 (2009) 14630.
[73] S. Urano, X. Yang, P.R. LeBreton, J. Mol. Struct. 214 (1989) 315, and references therein.

[74] X. Yang, X.B. Wang, E.R. Vorpagel, L.S. Wang, Proc. Nat. Acad. Sci. U.S. 101 (2004) 17588.
[75] V.V. Zakjevskii, S.J. King, O. Dolgounitcheva, V.G. Zakrzewski, J.V. Ortiz, J. Am. Chem. Soc. 128 (2006) 13350.
[76] W.L. Jorgensen, J. Tirado–Rives, J. Comput. Chem. 26 (2005) 1689.
[77] R. Flores–Moreno, J.V. Ortiz, J. Chem. Phys. 128 (2008) 164105.
[78] V.G. Zakrzewski, O. Dolgounitcheva, A.V. Zakjevskii, J.V. Ortiz, Int. J. Quantum Chem. 110 (2010) 2918.

CHAPTER 4

Rotations of Asymmetric Molecules and the Hydrogen Atom in Free and Confined Configurations

Ricardo Méndez-Fragoso[a] and **Eugenio Ley-Koo**[a]

Contents

[a] Instituto de Física, Universidad Nacional Autónoma de México. Apartado Postal, México, D. F., México
E-mail addresses: rmf@fisica.unam.mx (Ricardo Méndez-Fragoso), eleykoo@fisica.unam.mx (Eugenio Ley-Koo)

Advances in Quantum Chemistry, Volume 62
ISSN 0065-3276, DOI: 10.1016/B978-0-12-386477-2.00004-8

Abstract The contribution to the 50th Sanibel Symposium, "Lamé Spheroconal Harmonics in atoms and molecules," is the connecting reference among previous investigations on rotations of free asymmetric molecules and the Hydrogen atom, and recent results on rotations of the same systems in situations of confinement by elliptical cones. This chapter for Advances in Quantum Chemistry is based on both sets of works, presenting them as a review of the exact formulations and evaluations for the rotations of the free systems in Section 2, and as a guide for the results of the confined situations because of the new boundary conditions including elliptical cones in Section 3. Additionally, we report some tools and advances in developing the theory of angular momentum in bases of spheroconal harmonics in Section 4. The list of contents indicates some of the details in the respective sections, of which brief descriptions of the successive references are given next, commenting about their sequence and relationships with emphasis on the open problems and advances in each stage.

1. INTRODUCTION

The contribution to the 50th Sanibel Symposium, "Lamé Spheroconal Harmonics in atoms and molecules" [1], is the connecting reference among previous investigations on rotations of free asymmetric molecules [2–6] and the Hydrogen atom [7], and recent results on rotations of the same systems in situations of confinement by elliptical cones [1, 8]. This chapter for *Advances in Quantum Chemistry* is based on both sets of works, presenting them as a review of the exact formulations and evaluations for the rotations of the free systems in Section 2, and as a guide for the results of the confined situations because of the new boundary conditions including elliptical cones [9] in Section 3. Additionally, we report some tools and advances in developing the theory of angular momentum in bases of spheroconal harmonics in Section 4. The list of contents indicates some of the details in the respective sections, of which brief descriptions of the successive references are given next, commenting about their sequence and relationships with emphasis on the open problems and advances in each stage.

In the review, Refs. [2] and [3] contain two alternative and equivalent, exact formulations for the rotations of asymmetric molecules, whereas [4] concentrates on the numerical solutions for the most asymmetric molecules. Our own Refs. [5] and [6] implement two alternative matrix evaluations of the energy eigenvalues and eigenfunctions of molecules with any asymmetry distribution, using the spherical harmonic bases and constructing directly the spheroconal harmonic bases, respectively; common generating functions for both sets of bases are also identified. Our Ref. [7] deals with the rotations of the hydrogen atom, including the generation of its complete wavefunctions with a common radial factor, and alternative spherical and spheroconal harmonic angular momentum factors.

In fact, Kramers and Ittmann [2] and Piña [3] used spheroconal coordinates in their algebraic and Jacobian elliptical function representations, respectively [10, 11]. While Ref. [2] used the complete Hamiltonian $\hat{H}$ for the molecule in the body frame with coordinate axes oriented along the principal axes and the inverses of the respective moments of inertia a, b, c; [3] reparametrized the diagonal matrix of such inverses of moments of inertia in terms of its averaged trace Q, its traceless contributions Pe_i, such that the total Hamiltonian is the sum of the spherical top Hamiltonian with inverse moment of inertia Q plus the asymmetry Hamiltonian, expressed as the product of the asymmetry magnitude P and an asymmetry distribution Hamiltonian H^* involving linear combinations of the squares of angular momentum components with coefficients e_1, e_2, e_3, of which only one is independent.

The exact solution of the Schrödinger equation for the rotations of asymmetric molecules is possible because of the existence of complete sets of commuting operators, namely the respective Hamiltonians $\hat{H}$ and $\hat{H}^*$, and the square of angular momentum $\hat{L}^2$. The practical advantage of using the Hamiltonian $\hat{H}^*$ over $\hat{H}$ is that the latter involves three independent parameters (a, b, c), whereas H^* involves only one independent parameter.

Both works [2] and [3] show the separations of the eigenvalue equations for $\hat{H}$ and $\hat{L}^2$, and $\hat{H}^*$ and $\hat{L}^2$, in their respective spheroconal coordinates, into Lamé differential equations in the individual elliptical cone angular coordinates. The corresponding solutions are Lamé spheroconal polynomials included in the classic book of Whittaker and Watson [12]. In practice, the numerical evaluation of such Lamé functions was not developed in an efficient manner so that the exact formulation of Ref. [2] did not prosper. Consequently, the analysis of rotations of asymmetric molecules took the route of perturbation theory using the familiar basis of spherical harmonics.

The investigation in Ref. [4] was restricted to the case of the most asymmetric molecules with asymmetry parameters $e_2 = 0$ and $e_1 = -e_3 = \sqrt{3}/2$, and focused on obtaining numerical results. Nevertheless, its penultimate paragraph states that "this investigation will be only the first step in a

perturbation theory starting with the exact case of the most asymmetric molecules."

The obvious need of evaluating reliably, accurately, and efficiently the Lamé spheroconal harmonics, in order to implement the exact formulations of rotations of asymmetric molecules in Refs. [2] and [3], motivated our works of [5] and [6]. Their connections with Refs. [2] and [3] are spelled out in Sections 2.4 and 2.5. In Ref. [5] and Section 2.4, the problem is formulated and solved through the construction and diagonalization of the matrix of the asymmetry distribution Hamiltonian $\hat{H}^*$ in bases of spheroconal harmonics. In Ref. [6] and Section 2.5, the three term recurrence relations for the coefficients in series expansions for the Lamé functions are rewritten as tridiagonal matrices following the method of Ref. [13]. Both cases involve finite-size matrices for any integer value ℓ of the angular momentum label, and consequently the rotational states and energies of a molecule with any asymmetry can be accurately evaluated for any excited state.

The Hamiltonian of the Hydrogen atom [7], and also of any central potential quantum system [1], commutes with the square of the angular momentum. Both operators also commute with any of the cartesian components of the angular momentum, or with any linear combination of the squares of those components. Consequently, they admit alternative spherical harmonic and spheroconal harmonic angular momentum eigenfunctions [14]. We did not know about the latter, until we were involved simultaneously in developing the works [5–7]. Thus, our knowledge of the rotations of asymmetric molecules could be applied to the rotations of the Hydrogen atom as reviewed in Section 2.6.

Concerning the Guide to the rotations of the confined systems, here we give a chronological account of the successive works, warning the reader that in Section 3, our 50th Sanibel Symposium contribution in Section precedes the following two sections for reasons of logical presentation in the chapter. In Ref. [9] and Section 3.1, dealing with the confinement of the Hydrogen atom in semi-infinite spaces with conoidal (paraboloidal, hyperboloidal, and circular cone, including plane) boundaries, it was recognized that other types of natural boundaries of confinement include elliptical cones and dihedral angles, and anticipated our corresponding investigations. The first one has already been reported in Ref. [8] and is discussed in Section 3.3. We realized additionally that we could also extend our experience with the confined hydrogen atom to the rotations of asymmetric molecules confined by elliptical cones, on which we were already working when we decided on the topic of our contribution to the Sanibel Symposium as expressed by its own title. Section 3.4 reports original results on the rotations of asymmetric molecules confined in two alternative families of elliptical cones associated with spheroconal coordinates, which allow the simultaneous separation of the eigenvalue equations of the Hamiltonian and the square of the angular momentum.

The generating functions in Refs. [5–7] are common for the spherical harmonic and spheroconal harmonic angular momentum eigenfunctions. Our investigations of the rotations of asymmetric molecules and Hydrogen atom signal the equal standing of both sets of functions and, at the same time, indicate that the familiar theory of angular momentum in the spherical harmonic basis must have its counterpart in the spheroconal harmonics bases. Section 4 is focused on the way to develop such a counterpart. Most recently, we have identified complete radial and angular momentum raising and lowering operators for the free particle in three dimensions in spherical coordinates, as explained in Section 4.1. Correspondingly, Section 4.2 reports some advances on (1) the actions of the angular momentum operators and (2) the complete radial and angular operators on the spheroconal harmonics, as well as (3) in the identification of spheroconal tools to further develop the theory of angular momentum.

2. REVIEW OF EXACT FORMULATIONS AND EVALUATIONS OF ROTATIONS OF ASYMMETRIC MOLECULES AND THE HYDROGEN ATOM

This section reviews successively the alternative exact formulations of the rotations of asymmetric molecules using the spheroconal coordinates in their algebraic Section 2.1 and Jacobian elliptic function Section 2.2 representations, respectively. Their common features, relationships, and specific differences are recognized in order to understand their respective advantages, disadvantages, and limitations. Section 2.3 develops the formulation of Section 2.2 to evaluate numerically the rotational states of the most asymmetric molecules, on which several comments are formulated. Our own works in Sections 2.4 and 2.5 are focused, respectively, on the matrix evaluations of the rotational states of asymmetric molecules using spherical harmonic bases, and of the Lamé functions needed to construct the alternative spheroconal harmonic bases themselves. In both sections, common generating functions for both harmonic bases are identified. The knowledge about both bases in the molecular rotations is extended in Section 2.6 to the rotations in the hydrogen atom, associated with its complete wavefunctions in spherical and spheroconal coordinates as obtained from a common generating function.

As a prelude to the formulation of the rotations of asymmetric molecules, we review the description of the Euler angles involved in going from the laboratory or inertial frame XYZ to the molecular or body frame xyz.

Figure 4.1(a–c) shows the successive rotations around the $Z = z'$ axis by an angle ψ, around the axis $x' = x''$ by an angle θ, and around the axis $z'' = z$ by an angle φ. The respective angular velocity vectors are described by the

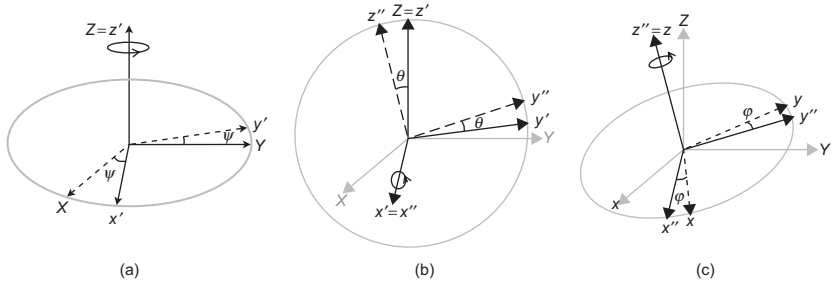

Figure 4.1 Successive rotations in terms of the Euler angles going from the laboratory frame to the body frame.

direction of their axis of rotation and their magnitude as the time rate of change of the associated angle:

$$\vec{\omega}_Z = \hat{\mathrm{k}}'\dot{\psi},\ \vec{\omega}_{x'} = \hat{\mathrm{i}}''\dot{\theta}, \quad \vec{\omega}_{z''} = \hat{\mathrm{k}}\dot{\varphi}. \tag{1}$$

The total angular velocity vector in the body frame is the sum of the successive intermediate contributions in Eq. (1), including the expressions for the unit vectors:

$$\begin{aligned}\hat{\mathrm{i}}'' &= \hat{\mathrm{i}}\cos\varphi - \hat{\mathrm{j}}\sin\varphi,\\ \hat{\mathrm{k}}' &= \hat{\mathrm{k}}''\cos\theta + \hat{\mathrm{j}}''\sin\theta = \hat{\mathrm{k}}\cos\theta + (\hat{\mathrm{i}}\sin\varphi + \hat{\mathrm{j}}\cos\varphi)\sin\theta,\end{aligned} \tag{2}$$

with the end result:

$$\begin{aligned}\vec{\omega}^B = {} & \hat{\mathrm{i}}(\sin\theta\sin\varphi\dot{\psi} + \cos\varphi\dot{\theta}) + \hat{\mathrm{j}}(\sin\theta\cos\varphi\dot{\psi} - \sin\varphi\dot{\theta})\\ & + \hat{\mathrm{k}}(\cos\theta\dot{\psi} + \dot{\varphi}).\end{aligned} \tag{3}$$

Similarly, in the laboratory frame

$$\begin{aligned}\hat{\mathrm{i}}'' &= \hat{\mathrm{i}}' = \hat{\mathrm{i}}^L\cos\psi + \hat{\mathrm{j}}^L\sin\psi,\\ \hat{\mathrm{k}}'' &= \hat{\mathrm{k}}'\cos\theta - \hat{\mathrm{j}}'\sin\theta = \hat{\mathrm{k}}^L\cos\theta - (-\hat{\mathrm{i}}^L\sin\psi + \hat{\mathrm{j}}^L\cos\psi)\sin\theta,\end{aligned} \tag{4}$$

and

$$\vec{\omega}^L = \hat{\mathrm{i}}^L(\sin\theta\sin\psi\dot{\varphi} + \cos\psi\dot{\theta}) + \hat{\mathrm{j}}^L(-\sin\theta\cos\psi\dot{\varphi} + \sin\psi\dot{\theta}) + \hat{\mathrm{k}}^L(\cos\theta\dot{\varphi} + \dot{\psi}). \tag{5}$$

Equation (3) can also be written in the matrix form

$$\begin{pmatrix} \omega_x^B \\ \omega_y^B \\ \omega_z^B \end{pmatrix} = \begin{pmatrix} \sin\theta\sin\varphi & \cos\varphi & 0 \\ \sin\theta\cos\varphi & -\sin\varphi & 0 \\ \cos\theta & 0 & 1 \end{pmatrix} \begin{pmatrix} \dot{\psi} \\ \dot{\theta} \\ \dot{\varphi} \end{pmatrix} \tag{6}$$

identifying the rotation matrix going from the Eulerian angular velocities to the cartesian components of the angular velocity in the body frame, and its determinant is $-\sin\theta$. This matrix and its transpose are used in Refs. [2] and [3], as reviewed in Sections 2.1 and 2.2.

2.1. On the quantization of asymmetric tops

Kramers and Ittmann recognized in their 1929 article [2] that the separation achieved by Reiche for the quantization of asymmetric tops, using the phase integral method [15], could be extended in quantum mechanics leading to the Lamé differential equations. Consequently, the theory of the Lamé functions and their eigenvalues is the appropriate tool to evaluate the eigenfunctions and eigenenergies of asymmetric molecules.

In fact, by that time, Witmer [16] and von Lütgemeier [17] had already started the analysis of the rotations of molecules with small asymmetries using the quantum mechanics perturbation method with the prolate and oblate symmetric molecule known eigenfunctions and eigenenergies as the starting points. In contrast, Ref. [2] emphasizes the identification of the Schrödinger equation for the asymmetric tops with the Lamé equations, as well as their exact eigenfunctions and eigenenergies.

Here, we review the evaluation of the kinetic energy of an asymmetric molecule in the body frame with axes oriented along the principal axes, in terms of the inverses (a,b,c) of the moments of inertia, the Euler angles (ψ,θ,φ), and angular velocities $(\dot{\psi},\dot{\theta},\dot{\varphi})$, the ignorability of the first Euler angle; the replacement of the other two angles by spheroconal coordinates; the construction of the Schrödinger equation and its separation into Lamé ordinary differential equations; and the identifications of its eigenfunctions and eigenvalues in Ref. [2].

Twice the kinetic energy in the body frame x,y,z can be written immediately by using Eq. (3):

$$\begin{aligned} 2T &= \left(\frac{1}{a}\omega_x^2 + \frac{1}{b}\omega_y^2 + \frac{1}{c}\omega_z^2\right) \\ &= \frac{1}{a}\left(\dot{\psi}\sin\theta\sin\varphi + \dot{\theta}\cos\varphi\right)^2 + \frac{1}{b}\left(\dot{\psi}\sin\theta\cos\varphi - \dot{\theta}\sin\varphi\right)^2 \\ &\quad + \frac{1}{c}\left(\dot{\psi}\cos\theta + \dot{\varphi}\right)^2. \end{aligned} \tag{7}$$

The Euler angle ψ does not appear in the kinetic energy, and consequently it is a cyclic or ignorable variable. In the body frame xyz, the other Euler angles θ, φ are the polar coordinates of the Z axis. The determinant of the matrix connecting the two alternative representations in Eq. (7) is $D = \sin^2\theta/abc$.

The change from spherical coordinates to spheroconal coordinates is contained in the transformation equations:

$$\begin{aligned} x &= r\sin\theta\cos\varphi = r\sqrt{\frac{(a-\lambda)(a-\mu)}{(a-b)(a-c)}} \\ y &= r\sin\theta\sin\varphi = r\sqrt{\frac{(b-\lambda)(\mu-b)}{(a-b)(b-c)}} \\ z &= r\cos\theta = r\sqrt{\frac{(\lambda-c)(\mu-c)}{(a-c)(b-c)}} \end{aligned} \tag{8}$$

in which $c \le \lambda \le b \le \mu \le a$. The new coordinates $(q_1 = \lambda, q_2 = \mu, q_3 = \psi)$ have their associated velocities $\dot{q}_1 = \dot{\lambda}, \dot{q}_2 = \dot{\mu}, \dot{q}_3 = \dot{\psi}$, and the kinetic energy becomes a homogeneous quadratic expression in the latter:

$$2T = \sum_{i,j} g_{ij}\dot{q}_i\dot{q}_j. \tag{9}$$

The Schrödinger equation for the stationary states with energy E is constructed as

$$\sum_{i,k} \frac{1}{\sqrt{g}}\frac{\partial}{\partial q_i}\left(\sqrt{g}g^{ik}\frac{\partial}{\partial q_k}\right)\Psi + \frac{2E}{\hbar^2}\Psi = 0, \tag{10}$$

using the determinants and the Jacobian of the successive transformations

$$\sqrt{g} = \sqrt{D}\frac{\partial(\theta,\varphi)}{\partial(\lambda,\mu)} = \frac{\sin\theta}{\sqrt{abc}}\frac{\lambda-\mu}{4\sin\theta\sqrt{-f(\lambda)f(\mu)}}, \tag{11}$$

where $f(\nu) = (a-\nu)(b-\nu)(c-\nu)$.

The metric coefficients are taken from Ref. [15]

$$g^{11} = \frac{2\mu f(\lambda)}{\lambda-\mu}, \quad g^{12} = 0, \quad g^{22} = \frac{2\lambda f(\mu)}{\mu-\lambda}. \tag{12}$$

Substitution of Eqs. (11 and 12) in Eq. (10) gives the latter its final form

$$\left\{\frac{\mu}{\mu-\lambda}\left[\sqrt{-4f(\lambda)}\frac{\partial}{\partial\lambda}\right]^2 + \frac{\lambda}{\mu-\lambda}\left[\sqrt{4f(\mu)}\frac{\partial}{\partial\mu}\right]^2 + \frac{2E}{\hbar^2}\right\}\Psi = 0. \tag{13}$$

This equation is separable admitting factorizable solutions

$$\Psi(\lambda,\mu) = \Lambda(\lambda)M(\mu), \tag{14}$$

which satisfy the respective Lamé ordinary differential equations [12]

$$\left(\sqrt{-4f(\lambda)}\frac{\mathrm{d}}{\mathrm{d}\lambda}\right)^2 \Lambda(\lambda) = \left(-\frac{2E}{\hbar^2} + A\lambda\right)\Lambda(\lambda) \tag{15}$$

$$\left(\sqrt{4f(\mu)}\frac{\mathrm{d}}{\mathrm{d}\mu}\right)^2 M(\mu) = \left(\frac{2E}{\hbar^2} - A\mu\right)M(\mu), \tag{16}$$

where A is the separation constant. The constant is chosen with the value $\ell(\ell+1)$ as the eigenvalue of the square of the angular momentum, which shares the eigenfunctions of Eq. (14). The Laplace equation also shares the same eigenfunctions with radial functions r^ℓ and/or $r^{-(\ell+1)}$. Correspondingly, such eigenfunctions are spheroconal harmonic functions.

The identification of the solutions of Eq. (13) as Lamé spheroconal harmonic functions in the respective coordinates allows writing them as superpositions of the familiar spherical harmonics:

$$L_{\ell n_\lambda}(\lambda)L_{\ell n_\mu}(\mu) = \sum_{m=-\ell}^{\ell} a_m^\ell P_\ell^m(\cos\theta)e^{im\varphi}. \tag{17}$$

We call the attention of the reader on this expression in anticipation of Section 2.4.

Concerning the Lamé functions, Table 1 in Ref. [2] shows their classification, structure, and numbers. In fact, the derivatives of Eq. (8) with respect to λ and μ, allow the identification of the removable singularities in the solutions of Eqs. (15 and 16), respectively:

$$A = 1;\ \sqrt{a-\lambda},\ \sqrt{b-\lambda},\ \sqrt{\lambda-c};$$
$$\sqrt{(b-\lambda)(\lambda-c)},\ \sqrt{(a-\lambda)(\lambda-c)},\ \sqrt{(a-\lambda)(b-\lambda)};\ \sqrt{(a-\lambda)(b-\lambda)(\lambda-c)}.$$
$$B = 1;\ \sqrt{a-\mu},\ \sqrt{\mu-b},\ \sqrt{\mu-c};$$
$$\sqrt{(\mu-b)(\mu-c)},\ \sqrt{(a-\mu)(\mu-c)},\ \sqrt{(a-\mu)(\mu-b)};\ \sqrt{(a-\mu)(\mu-b)(\mu-c)}.$$

They correspond to one type of species 1, three types of species 2, three types of species 3, and one of species 4. The products of such matching species and types lead to the corresponding AB species and types of Lamé spheroconal

harmonic polynomials:

$$1.\ \Psi = \Pi; \quad 2.\ \Psi = x\Pi,\ \ \Psi = y\Pi,\ \ \Psi = z\Pi;$$
$$3.\ \Psi = yz\Pi,\ \ \Psi = xz\Pi,\ \ \Psi = xy\Pi; \quad 4.\Psi = xyz\Pi.$$

They possess well-defined parities under $(x \to -x, y \to -y, z \to -z)$: 1. $(+++)$; 2. $(-++)$, $(+-+)$, $(++-)$; 3. $(+--)$, $(-+-)$, $(--+)$; 4. $(---)$. Each one also has a polynomial factor which is written as the products,

$$\Pi = \prod_{r=1}^{N} \left(\frac{x^2}{a-\theta_r} + \frac{y^2}{b-\theta_r} + \frac{z^2}{c-\theta_r} \right) = \prod_{r=1}^{N} r^2 \frac{(\lambda-\theta_r)(\mu-\theta_r)}{-f(\theta_r)}. \tag{18}$$

For a given even value of the angular momentum label ℓ, the Lamé spheroconal harmonic functions belong to species 1 and 3 with positive parity; there are $(\ell+2)/2$ polynomials of species 1 and degree $\ell/2$, and there are $\ell/2$ polynomials of degree $(\ell-2)/2$ for each of the three types of species 3. For odd values of ℓ, the Lamé functions belong to species 2 and 4 with negative parity; there are $(\ell+1)/2$ polynomials of degree $(\ell-1)/2$ for each of the three types of species 2, and $(\ell-1)/2$ polynomials of degree $(\ell-3)/2$ for the one of species 4. In both cases, the total number of independent eigenfunctions is the same, $2\ell+1$.

Niven established the connections between the ellipsoidal harmonics, expressed in cartesian coordinates, and the spheroconal harmonics, expressed in spheroconal coordinates, in the respective factors of Eq. (18), by requiring that the eigenfunctions Ψ satisfy the Laplace equation [18]. The application of the Laplace operator on the eigenfunctions Ψ with the condition of vanishing leads to the zeros θ_r of the respective polynomials, which are real and different in their respective domains $c < \lambda < b < \mu < a$. For instance, for $\ell = 2$ and species 1, the application of the Laplacian in cartesian coordinates leads to the corresponding condition for its being harmonic

$$\frac{2}{a-\theta_r} + \frac{2}{b-\theta_r} + \frac{2}{c-\theta_r} = 0. \tag{19}$$

This equation is quadratic in θ_r with two zeros for $r = 1, 2$ in the intervals $c < \theta_1 < b < \theta_2 < a$ which are associated with the two independent eigenfunctions

$$\frac{(\lambda-\theta_1)(\mu-\theta_1)}{-f(\theta_1)} \quad \text{and} \quad \frac{(\lambda-\theta_2)(\mu-\theta_2)}{-f(\theta_2)}, \tag{20}$$

with the respective nodes $\lambda = \theta_1$, and $\mu = \theta_2$.

Table 2 in Ref. [2] contains the eigenfunctions and eigenenergies of the asymmetric molecules for $\ell = 0, 1, 2, 3, 4$. The reader can identify the counterparts of Eq. (19), which guarantee the harmonic nature of the eigenfunctions of the other species and degrees. The values of the eigenenergies are linear combinations of the a, b, c parameters and the respective zeros of the above-mentioned equations.

The reader may also profit by looking at the corresponding graphical illustrations in Ref. [2]: Its Figure 2 illustrates the schematic position of the nodes in the successive numbers $\ell = 0, 1, 2, 3, 4$ for the respective states of each species, their distributions in the subintervals $c \leq b \leq a$ depending on the asymmetry, including the symmetric prolate ($c = b$) and oblate ($b = a$) molecules with doubly degenerate states for projections of the angular momentum $m = \pm 1, \pm 2, \ldots, \pm\ell$ along the rotational symmetry axis [19, 20]. While its Figure 3 contains the energy spectra of the asymmetric molecules with $a = 3c$ and $b = c$, $1.1c$, $1.5c$, $3c$ for states $\ell = 4$, for asymmetries interpolating between the symmetric ends with the $m = 0$ state as their lowest energy and highest energy states, respectively, and illustrating the slow removal of the double degeneracy at one end and the restoration of the one corresponding to the other end, as b changes from c to a.

We conclude with the comment that the formulation of the rotations of asymmetric molecules reviewed in this section is mathematically exact. However, its numerical application for higher ℓ excited states was not efficiently implemented. Correspondingly, the perturbation method using the results for the symmetric molecules, like those of Refs. [16, 17, 19, 20], as the nonperturbed starting point became the way to analyze the experimental data on rotational molecular spectroscopy [20–31].

As an Interlude between sections, it is useful to use Eq. (7) to obtain, at once, the general expressions for the angular momenta canonically conjugate to the Euler angles, as well as their relations with the corresponding cartesian components in the body frame. It is straightforward to obtain

$$
\begin{aligned}
L_\psi = \frac{\partial T}{\partial \dot{\psi}} &= \frac{1}{a}\left(\dot{\psi}\sin\theta\sin\varphi + \dot{\theta}\cos\varphi\right)\sin\theta\sin\varphi \\
&\quad + \frac{1}{b}\left(\dot{\psi}\sin\theta\cos\varphi - \dot{\theta}\sin\varphi\right)\sin\theta\cos\varphi \\
&\quad + \frac{1}{c}\left(\dot{\psi}\cos\theta + \dot{\varphi}\right)\cos\theta, \\
L_\theta = \frac{\partial T}{\partial \dot{\theta}} &= \frac{1}{a}\left(\dot{\psi}\sin\theta\sin\varphi + \dot{\theta}\cos\varphi\right)\cos\varphi \\
&\quad - \frac{1}{b}\left(\dot{\psi}\sin\theta\cos\varphi - \dot{\theta}\sin\varphi\right)\sin\varphi, \\
L_\varphi = \frac{\partial T}{\partial \dot{\varphi}} &= \frac{1}{c}\left(\dot{\psi}\cos\theta + \dot{\varphi}\right).
\end{aligned}
\tag{21}
$$

In turn, the respective angular velocity components can also be expressed as linear combinations of the angular momenta:

$$\begin{aligned}
\left(\dot{\psi}\sin\theta\sin\varphi+\dot{\theta}\cos\varphi\right) &= \frac{a}{\sin\theta}\left[\left(L_{\psi}-\cos\theta L_{\varphi}\right)\sin\varphi+\sin\theta\cos\varphi L_{\theta}\right],\\
\left(\dot{\psi}\sin\theta\cos\varphi-\dot{\theta}\sin\varphi\right) &= \frac{b}{\sin\theta}\left[\left(L_{\psi}-\cos\theta L_{\varphi}\right)\cos\varphi-\sin\theta\sin\varphi L_{\theta}\right],\\
\left(\dot{\psi}\cos\theta+\dot{\varphi}\right) &= cL_{\varphi}.
\end{aligned} \tag{22}$$

Then, the kinetic energy or Hamiltonian takes the canonical form

$$H=\frac{1}{2}\left[aL_x^2+bL_y^2+cL_z^2\right], \tag{23}$$

with the identification of the cartesian components of the angular momentum

$$\begin{aligned}
\hat{L}_x &= -i\hbar\left[\frac{\sin\varphi}{\sin\theta}\frac{\partial}{\partial\psi}+\cos\varphi\frac{\partial}{\partial\theta}-\cot\theta\sin\varphi\frac{\partial}{\partial\varphi}\right],\\
\hat{L}_y &= -i\hbar\left[\frac{\cos\varphi}{\sin\theta}\frac{\partial}{\partial\psi}-\sin\varphi\frac{\partial}{\partial\theta}-\cot\theta\cos\varphi\frac{\partial}{\partial\varphi}\right],\\
\hat{L}_z &= -i\hbar\frac{\partial}{\partial\varphi}.
\end{aligned} \tag{24}$$

Similar expressions can be obtained for the components of the angular momentum components in the inertial frame,

$$\begin{aligned}
\hat{M}_X &= -i\hbar\left[-\frac{\sin\psi}{\sin\theta}\frac{\partial}{\partial\varphi}+\cos\psi\frac{\partial}{\partial\theta}+\cot\theta\sin\psi\frac{\partial}{\partial\psi}\right],\\
\hat{M}_Y &= -i\hbar\left[\frac{\cos\psi}{\sin\theta}\frac{\partial}{\partial\varphi}+\sin\psi\frac{\partial}{\partial\theta}+\cot\theta\cos\psi\frac{\partial}{\partial\psi}\right],\\
\hat{M}_Z &= -i\hbar\frac{\partial}{\partial\psi}.
\end{aligned} \tag{25}$$

2.2. Some properties of the spectra of asymmetric molecules

Piña's work [3], to be reviewed in this section, investigates the same problem as Ref. [2], using an alternative parametrization of the asymmetric molecule

inverses of the moments of inertia, and the Jacobian elliptic function representation of spheroconal coordinates.

Here, we call the attention of the reader that our Eq. (24) in the previous interlude correspond to Eqs. (32) in Ref. [3] for the cartesian components of the angular momentum in the body frame and the inertial frame, respectively, in terms of the Euler angles. Notice that the angles ψ and φ in Refs. [2] and [3] are also exchanged. Also, the canonical notation for the forms of our Eqs. (23 and 21) in Ref. [3] for the Hamiltonian are the same. Additionally, the relevant commutation rules from Eq. (22) in Ref. [3], for the analysis of the rotations of asymmetric molecules are as follows:

$$\begin{gathered}\left[\hat{L}_i, \hat{L}_j\right] = -i\epsilon_{ijk}\hbar\hat{L}_k, \quad \left[\hat{M}_i, \hat{M}_j\right] = i\epsilon_{ijk}\hbar\hat{M}_k, \quad \left[\hat{L}_z, \hat{M}_Z\right] = 0, \\ \left[\hat{L}^2, \hat{L}_i\right] = 0, \quad \left[\hat{L}^2, \hat{M}_i\right] = 0, \\ \left[\hat{H}, \hat{L}^2\right] = 0, \quad \left[\hat{H}, \hat{M}_i\right] = 0.\end{gathered} \tag{26}$$

Consequently, $\hat{H}$, $\hat{L}^2$, and $\hat{M}_Z$ form a complete set of commuting operators with common eigenfunctions:

$$\hat{H}\Psi = E\Psi, \quad \hat{L}^2\Psi = \hbar^2\ell(\ell+1)\Psi, \quad \hat{M}_Z\Psi = \hbar M\Psi, \tag{27}$$

where ℓ and M are restricted to being integers and $-\ell \leq M \leq \ell$. However, the raising and lowering operators $\hat{M}_\pm = \hat{M}_X \pm i\hat{M}_Y$ perform such actions on the eigenvalues and eigenfunctions of $\hat{M}_Z$. Since the latter is canonically conjugate with the angle ψ, which is ignorable, Piña chooses the state with $M = 0$, for which the cartesian components of the angular momentum only depend on the two other Euler angles, and the first two Eqs. (24) become

$$\hat{L}_x = -i\hbar\left[\cos\varphi\frac{\partial}{\partial\theta} - \cot\theta\sin\varphi\frac{\partial}{\partial\varphi}\right], \tag{28}$$

$$\hat{L}_y = -i\hbar\left[-\sin\varphi\frac{\partial}{\partial\theta} - \cot\theta\cos\varphi\frac{\partial}{\partial\varphi}\right]. \tag{29}$$

The eigenvalue equations for the square of the angular momentum and the energy take the corresponding forms

$$\left(\hat{L}_x^2 + \hat{L}_y^2 + \hat{L}_z^2\right)\Psi = \hbar^2\ell(\ell+1)\Psi, \tag{30}$$

$$\left(a\hat{L}_x^2 + b\hat{L}_y^2 + c\hat{L}_z^2\right)\Psi = 2E\Psi. \tag{31}$$

The reparametrization of the diagonal (a, b, c) matrix of the inverses of the moments of inertia involves its averaged trace

$$Q = \frac{1}{3}(a + b + c), \tag{32}$$

and its traceless asymmetries for $i = 1, 2, 3$

$$Pe_i = a - Q, \quad b - Q, \quad c - Q, \tag{33}$$

with

$$e_1 + e_2 + e_3 = 0, \tag{34}$$

$$e_1^2 + e_2^2 + e_3^2 = \frac{2}{3}, \tag{35}$$

and

$$P^2 = \frac{2}{9}\left[(a-b)^2 + (a-c)^2 + (b-c)^2\right], \tag{36}$$

measuring the magnitude of the asymmetry.

The two conditions on the three parameters (e_1, e_2, e_3) indicate that only one can be independent. They can also be replaced with a single angular parameter σ, such that

$$e_1 = \cos\sigma, \quad e_2 = \cos(\sigma - 120^\circ), \quad e_3 = \cos(\sigma + 120^\circ). \tag{37}$$

Then the Hamiltonian in the Schrödinger equation, Eq. (31), is separated into its spherical top and asymmetry distribution contributions

$$\begin{aligned} 2\hat{H} &= Q\hat{L}^2 + P\left(e_1\hat{L}_x^2 + e_2\hat{L}_y^2 + e_3\hat{L}_z^2\right) \\ &= Q\hat{L}^2 + 2P\hat{H}^*, \end{aligned} \tag{38}$$

where

$$2\hat{H}^* = e_1\hat{L}_x^2 + e_2\hat{L}_y^2 + e_3\hat{L}_z^2. \tag{39}$$

Notice the additional commutativities

$$\left[\hat{H}, \hat{H}^*\right] = 0, \quad \left[\hat{H}^*, \hat{L}^2\right] = 0. \tag{40}$$

The consequence is that $\hat{H}^*$ also shares the common eigenfunctions of the two other operators

$$2\hat{H}^*\Psi = 2E^*\Psi. \tag{41}$$

The practical advantage of changing from $\hat{H}$ to $\hat{H}^*$ is that while both have energies depending on three parameters $E(a,b,c)$ and $E^*(e_1,e_2,e_3)$, those parameters are independent for the complete Hamiltonian while only one of them is independent for the asymmetry distribution Hamiltonian. Because $\hat{H}^*$ has the same structure as $\hat{H}$, being linear combinations of squares of the cartesian components of the angular momentum, their eigenenergies and eigenfunctions are of the same type with the replacements $a \to e_1$, $b \to e_2$, and $c \to e_3$.

Concerning the spheroconal coordinates expressed through Jacobian elliptic functions used in Ref. [3], its Eq. (50) is reproduced here

$$\hat{u} = \begin{pmatrix} \sin\theta\sin\phi \\ \sin\theta\cos\phi \\ \cos\theta \end{pmatrix} = \begin{pmatrix} \mathrm{dn}(\chi_1|k_1)\mathrm{sn}(\chi_2|k_2) \\ \mathrm{cn}(\chi_1|k_1)\mathrm{cn}(\chi_2|k_2) \\ \mathrm{sn}(\chi_1|k_1)\mathrm{dn}(\chi_2|k_2) \end{pmatrix} \tag{42}$$

as the cartesian components of a unit radial vector in both spherical (θ,φ) and spheroconal coordinates (χ_1,χ_2). The parameters k_1 and k_2 are subject to the restriction $k_1^2 + k_2^2 = 1$.

The eigenvalue Eqs. (30 and 39) admit factorizable eigenfunctions in these coordinates

$$\Psi(\chi_1,\chi_2) = \Lambda(\chi_1)\Lambda(\chi_2), \tag{43}$$

and become simultaneously separable into Lamé differential equations, provided the geometrical parameters k_1^2, k_2^2 and the dynamical parameters e_1, e_2, e_3 are connected through

$$k_1^2 = \frac{e_2 - e_3}{e_1 - e_3}, \quad k_1^2 = \frac{e_1 - e_2}{e_1 - e_3}. \tag{44}$$

In fact, the ordinary differential equations in each variable from such a separation have the standard form of the Lamé equation [12]:

$$\frac{\mathrm{d}^2\Lambda_i}{\mathrm{d}\chi_i^2} - \left[k_i^2\ell(\ell+1)\mathrm{sn}^2(\chi_i|k_i) + h_i\right]\Lambda_i = 0. \tag{45}$$

The eigenvalues h_i are the separation constants and are linear combinations of the eigenvalues $\ell(\ell+1)$ and E^*.

Piña refers the reader to Ref. [12] for the properties of the Lamé functions, illustrating the structures of the eight species and types of the spheroconal harmonics eigenfunctions involving the singularity removing factors 1, $u_y u_z$, $u_x u_z$, $u_x u_y$; u_x, u_y, u_z, $u_x u_y u_z$ multiplied by polynomial factors in the respective coordinates.

The matrix $\mathcal{A}(\alpha_j)$, such that

$$\mathcal{A}^{-1}(\alpha) = \begin{pmatrix} e_1 - \alpha & 0 & 0 \\ 0 & e_2 - \alpha & 0 \\ 0 & 0 & e_3 - \alpha \end{pmatrix} \tag{46}$$

is used to generate the product representation of the polynomial factors

$$\hat{\hat{u}} A^{-1} \hat{u} = \frac{\left[e_3 + (e_2 - e_3)\mathrm{sn}^2(\chi_1|k_1) - \alpha\right]\left[e_1 + (e_2 - e_1)\mathrm{sn}^2(\chi_2|k_2) - \alpha\right]}{(e_1 - \alpha)(e_2 - \alpha)(e_2 - \alpha)} \tag{47}$$

This is the counterpart of Eq. (20) of Ref. [2] with $a = e_1$, $b = e_2$, and $c = e_3$, allowing also the connection between the algebraic and Jacobian elliptical spheroconal coordinates

$$\lambda = e_3 + (e_2 - e_3)\mathrm{sn}^2(\chi_1|k_1) \equiv \mathcal{P}_1(\chi_1), \tag{48}$$

$$\mu = e_1 + (e_2 - e_1)\mathrm{sn}^2(\chi_2|k_2) \equiv \mathcal{P}_2(\chi_2). \tag{49}$$

involving the Weierstrass form of elliptic functions [11].

Reference [3] also includes the eigenfunctions and eigenenergies for $\ell = 1, 2, 3$. The reader may also profit from the comparison with those of Table 2 in Ref. [2], appreciating the simplifications brought in by the condition of Eq. (34).

The work in Ref. [3] also includes sum rules for the energy levels and selection rules for the rotation spectra, as well as some properties of the most asymmetric case. The latter is reviewed in the following section.

The corresponding interlude consists of Tables 4.1 and 4.2, illustrating typical numerical values of the σ, e_i, and k_i parameters, and examples of molecules with their respective asymmetry parameters (a, b, c) and (Q, P, σ) from Refs. [2] and [3], respectively.

2.3. The rotational spectra of the most asymmetric molecules

The investigation in Ref. [4] is based on the general formulation of Ref. [3], which is briefly reviewed in its introduction section. In particular, for the symmetric molecules of the oblate ($\sigma = 60^\circ$, $e_1 = e_2 = 1/2$ and $e_3 = -1$, $k_1^2 = 1$, $k_2^2 = 0$) and prolate ($\sigma = 0^\circ$, $e_1 = 1$ and $e_2 = e_3 = -1/2$, $k_1^2 = 0$, $k_2^2 = 1$) shapes according to (42), the respective spheroconal coordinates become spherical

Table 4.1 Sample of numerical values of alternative molecular asymmetry distribution and elliptical-cone parameter sets, from Eqs. (37 and 44)

σ	0°	15°	30°	45°	60°
e_1	1	$\frac{\sqrt{6}+\sqrt{2}}{4}$	$\frac{\sqrt{3}}{2}$	$\frac{1}{\sqrt{2}}$	$\frac{1}{2}$
e_2	$-\frac{1}{2}$	$\frac{\sqrt{2}-\sqrt{6}}{4}$	0	$\frac{\sqrt{6}-\sqrt{2}}{4}$	$\frac{1}{2}$
e_3	$-\frac{1}{2}$	$-\frac{1}{\sqrt{2}}$	$-\frac{\sqrt{3}}{2}$	$-\frac{\sqrt{6}+\sqrt{2}}{4}$	-1
k_1^2	0	$\frac{3-\sqrt{3}}{3+\sqrt{3}}$	$\frac{1}{2}$	$\frac{2\sqrt{3}}{3+\sqrt{3}}$	1
k_2^2	1	$\frac{2\sqrt{3}}{3+\sqrt{3}}$	$\frac{1}{2}$	$\frac{3-\sqrt{3}}{3+\sqrt{3}}$	0

Table 4.2 Table of some asymmetric molecules with values of their asymmetry parameters $\hat{H}(a,b,c)$, in Eq. (31), and asymmetry distribution parameters, $\hat{H}^*(\sigma)$, according to Eqs. (32–39), [32], [33]*

Molecule	a (cm^{-1})	b (cm^{-1})	c (cm^{-1})	Q (cm^{-1})	P (cm^{-1})	σ (deg)
NH_3	9.44430	9.44430	6.19600	8.3615	2.1655	60.0
C_4H_4O	0.31512	0.30843	0.15580	0.2598	0.1041	57.8727
$C_4H_4N_2$	0.20830	0.19890	0.10180	0.1697	0.0681	55.4280
C_2H_5N	0.75840	0.70690	0.44641	0.6372	0.1931	51.1437
N_2S	10.37400	8.99100	4.73200	8.0323	3.3956	46.3993
C_3H_4	1.00273	0.72803	0.46018	0.7303	0.3132	29.5824
CD_3CDO^*	0.68799	0.52131	0.38934	0.5329	0.1728	26.1617
CH_2	19.80540	11.24890	7.23860	12.7643	7.4120	18.2026
H_2O	27.87700	14.51200	9.28500	17.2247	11.0716	15.8174
D_2O	15.41996	7.27296	4.84530	9.1794	6.3960	12.6584
$C_{10}H_8$	0.10405	0.04113	0.02948	0.0582	0.0463	8.3493
CH_2F_2	1.59213	0.35378	0.30854	0.7515	0.8411	1.7796
CH_2CHCl	1.87324	0.20114	0.18164	0.7520	1.1213	0.5753

coordinates with rotational axes along the z-axis and x-axis, respectively; their corresponding eigenfunctions are spherical harmonics with positive or negative parities $[Y_{\ell m}(\theta_i,\varphi_i) \pm Y^*_{\ell m}(\theta_i,\varphi_i)]/\sqrt{2}$, with $i = x, z$. For the so-called most asymmetric molecules ($\sigma = 30^\circ$, $e_1 = -e_3 = \sqrt{3}/2$ and $e_2 = 0$, $k_1^2 = k_2^2 = 1/2$), the middle asymmetry distribution parameter vanishes, and the two geometric parameters equal one half, expecting some simplification vis-à-vis the general case.

The authors of Ref. [4] chose to solve the Lamé equations from $\hat{H}^*(e_1, e_2, e_3)$ in the algebraic representation of the spheroconal coordinates,

$$\frac{\mathrm{d}^2\Lambda}{\mathrm{d}\lambda^2} + \left[\frac{1/2}{\lambda - e_1} + \frac{1/2}{\lambda - e_2} + \frac{1/2}{\lambda - e_3}\right]\frac{\mathrm{d}\Lambda}{\mathrm{d}\lambda} - \frac{\ell(\ell+1)\lambda - 2E^*/\hbar^2}{(\lambda - e_1)(\lambda - e_2)(\lambda - e_3)}\Lambda = 0. \tag{50}$$

It is recognized that in the most asymmetric case, it is convenient to introduce the scaled variable $w = 2\lambda/\sqrt{3}$ and energy parameter $b = -2E^*/\sqrt{3}\hbar^2$, so that the equation becomes

$$2w(1 - w^2)\frac{\mathrm{d}^2\Lambda(w)}{\mathrm{d}w^2} + (1 - 3w^2)\frac{\mathrm{d}\Lambda(w)}{\mathrm{d}w} - \left(\frac{\ell(\ell+1)}{2}w + b\right)\Lambda(w) = 0. \tag{51}$$

The removing singularity factors 1, $\sqrt{w(1-w)}$, $\sqrt{1-w^2}$, $\sqrt{w(1+w)}$ for ℓ even and $\sqrt{1-w}$, $\sqrt{w}$, $\sqrt{1+w}$, $\sqrt{w(1-w^2)}$ for ℓ odd define the eight types of Lamé functions in their different species, as in Section 2.1, upon multiplication by their respective polynomials $P(w)$.

The change $w \to -w$ changes also the signs of the first two terms in Eq. (51), as well as in the first of the last two terms; for the cases when $b = 0$, the solutions may have a well-defined parity. For the given solution $\Lambda(w)$ with ℓ and b values, if the change $b \to -b$ is also made in Eq. (51), then $\Lambda(-w)$ is also a solution. These simplifications occur only for the most asymmetric molecules. The article first analyses the solutions with $b = 0$, and then goes on to construct systematically the general solutions.

The Eq. (51) for $b = 0$ is shown to be rewritable as the Jacobi differential equation with argument w^2. The reader can see the corresponding solutions of the types 1, $\sqrt{w}$, $\sqrt{1-w^2}$, $\sqrt{w(1-w^2)}$ with orbital angular momentum $\ell = 4n$, $4n+1$, $4n+2$, and $4n+3$, respectively, in Eqs. (38–41) in Ref. [4], as well as ladder operators making ℓ to jump by 4, within the framework of Piña [34].

The general solutions of Eq. (51) for any b require the removal of the successive singularity factors, obtaining the differential equations for the respective companion factors. For the factor 1, the equation remains the same, and for the other ones, we simply quote and adapt Eqs. (49 and 54) for ℓ even and Eqs. (59, 64, and 69) for ℓ odd from Ref. [4]. Specifically,
for $\sqrt{1-w^2}$

$$2w(1 - w^2)\frac{\mathrm{d}^2P}{\mathrm{d}w^2} + (1 - 7w^2)\frac{\mathrm{d}P}{\mathrm{d}w} - \left(\frac{(\ell-2)(\ell+3)}{2}w + b\right)P = 0; \tag{52}$$

for $\sqrt{w(1 \mp w)}$

$$2w(1-w^2)\frac{\mathrm{d}^2P}{\mathrm{d}w^2} + (3 \mp w - 7w^2)\frac{\mathrm{d}P}{\mathrm{d}w} - \left(\frac{(\ell-2)(\ell+3)}{2}w + b \mp \frac{3}{2}\right)P = 0; \tag{53}$$

for $\sqrt{w(1-w^2)}$

$$2w(1-w^2)\frac{\mathrm{d}^2P}{\mathrm{d}w^2} + (3-9w^2)\frac{\mathrm{d}P}{\mathrm{d}w} - \left(\frac{(\ell-3)(\ell+4)}{2}w + b\right)P = 0; \tag{54}$$

for $\sqrt{w}$

$$2w(1-w^2)\frac{\mathrm{d}^2P}{\mathrm{d}w^2} + (1-5w^2)\frac{\mathrm{d}P}{\mathrm{d}w} - \left(\frac{(\ell-1)(\ell+2)}{2}w + b\right)P = 0; \tag{55}$$

for $\sqrt{1 \mp w}$

$$2w(1-w^2)\frac{\mathrm{d}^2P}{\mathrm{d}w^2} + (1 \pm 2w - 5w^2)\frac{\mathrm{d}P}{\mathrm{d}w} - \left(\frac{(\ell-1)(\ell+2)}{2}w + b \pm \frac{1}{2}\right)P = 0. \tag{56}$$

It is instructive to follow the differences in the respective linear and quadratic coefficients of the function and first derivative terms in each equation, in the order of number of factors in the corresponding square roots, or of Eqs. (36, 64, 69, 49, 54 and 59) in Ref. [4]: for P starting with the ℓ-dependent coefficient, their successive values are $\ell(\ell+1)$, $(\ell-1)(\ell+2)$, $(\ell-2)(\ell+3)$, $(\ell-3)(\ell+4)$ for the respective species; b is shifted by one-half up or down in Eq. (56) and by three halves down or up in Eq. (53), and stays the same in the other cases; however, for the derivative, the quadratic term has the negative coefficients 3, 5, 7, and 9, while the respective constant terms are 1 and 3, and the linear terms only appear in Eqs. (53 and 56) again. The changes in the ℓ-dependent coefficients and in the anergy parameters are not exclusively for the most asymmetric molecules. Their counterparts also appear for molecules with any asymmetry, as shown in our Section 4.2.3.

After the singularities in the original Eq. (51) have been removed, the remaining factors in Eqs. (52–56) can be solved by power series expansions

$$P(w) = \sum_s a_s w^s. \tag{57}$$

Because all the equations have the same structure, the corresponding recurrence relation for the respective coefficients also have the same structure.

Specifically, they turn out to be three-term recurrence relations which can be re-expressed as tridiagonal matrices [13]. The diagonalization of such matrices yield the separation constants and the expansion coefficients. For a chosen integer value of ℓ, the matrices turn out to be of finite size, yielding Lamé polynomials of degree ℓ in the numbers already described in our Section 2.1 for the respective species and types.

Tables V-VIII in Ref. [4] report the numerical values of the separation constant b, which is proportional to the energy E^*, for $\ell = 2, \ldots, 15$. For each value of ℓ, there is only one state with $b = 0$, and the other 2ℓ appear in pairs with values $\pm b$. The reader is warned to be careful about the species and type association of the eigenfunctions in Ref. [4]. For ℓ even in Table IV, if we accept the x, y, z identifications for ℓ odd, then the first one is simply xyz, and for ℓ even they become 1, yz, xz, xy, respectively, to be consistent with the classification in Tables II and III in Ref. [4].

We make three remarks on the discussion in the closing section of Ref. [4]:

1. For the original citation of the textbook of their Ref. [11]: "In the highly asymmetric case, as you might guess, the levels may not form any obvious simple pattern and the resulting spectrum can be quite a mess" [31], the remark is that the pattern in Tables V–VIII in Ref. [4] is systematic and simple because $\hat{H}^*(\sigma)$ is used.
2. Concerning "the deuterated acetaldehyde $CD_3 - C = OD$ molecule with $\sigma = 26.16^\circ$," Table 4.2 in our previous interlude shows it after cyclopropene C_3H_4, which is even closer to 30°, corresponding to the most asymmetric molecules.
3. "It is evident that the most asymmetric case studied in this chapter will be only the first step in a perturbation theory for very asymmetric molecules." Instead of doing perturbation theory, the method used in Ref. [4] is applicable to obtain the exact rotational eigenstates for molecules with any asymmetry, as reviewed in Section 2.4.

The interlude between the set of Sections 2.1, 2.2, and 2.3 and the next pair of Sections 2.4 and 2.5 contrasts their different objectives, methods, and results highlighting the respective advances. In fact, the first set focused on the alternative exact formulations of the rotational states in asymmetric molecules including the explicit construction of the lowest eigenstates for any asymmetry and higher excited states for the most asymmetric case. Their formulations start from the Euler angles, taking the ignorability of the first one into account, and replacing the other two with spheroconal coordinates. The operators $\hat{H}$ and $\hat{L}^2$ and $\hat{H}^*$ form complete sets of commuting operators, and their eigenvalue equations with common eigenfunctions separate into Lamé equations. The polynomial Lamé spheroconal harmonics and their properties are simply taken from Ref. [12]. Our starting point involves the representations of the operators as linear combinations of the squares of the

cartesian components of the angular momentum Eqs. (30, 38, and 39). Our aim is to evaluate their eigenfunctions and eigenenergies for any asymmetry and any excitation accurately and efficiently. Section 2.4 uses the familiar spherical harmonic bases to achieve the stated objective. Section 2.5 goes directly from cartesian to spheroconal coordinates, constructing the successive operators in the latter, and constructs the solutions of the ordinary Lamé differential equations for any asymmetry distribution of the molecules using the method of Section 2.3.

2.4. Properties of the spectra of asymmetric molecules: Matrix evaluation in bases of spherical harmonics and generating function

The work [5], to be reviewed in this section, makes use of the asymmetric distribution Hamiltonian, as well as the cartesian component, ladder and square of the angular momentum operators and their actions on the chosen spherical harmonic basis $|\ell m_k\rangle$ for $(i,j,k) = cyc(x,y,z)$. Here, we start from its Eqs. (26–28) for the matrix elements of $\hat{H}^*$ in the alternative bases:

$$\left\langle \ell m_x' \left| \hat{H}^* \right| \ell m_x \right\rangle = \frac{\hbar^2}{2} \left\{ \left[e_1 m_x^2 + \frac{e_2+e_3}{4} \Big(C_+(\ell, m_x - 1) C_-(\ell, m_x) + C_-(\ell, m_x + 1) C_+(\ell, m_x) \Big) \right] \delta_{m_x', m_x} + \frac{e_2 - e_3}{4} \times \left[C_+(\ell, m_x + 1) C_+(\ell, m_x) \delta_{m_x', m_x + 2} + C_-(\ell, m_x - 1) C_-(\ell, m_x) \delta_{m_x', m_x - 2} \right] \right\}, \quad (58)$$

$$\left\langle \ell m_y' \left| \hat{H}^* \right| \ell m_y \right\rangle = \frac{\hbar^2}{2} \left\{ \left[e_2 m_y^2 + \frac{e_3+e_1}{4} \Big(C_+(\ell, m_y - 1) C_-(\ell, m_y) + C_-(\ell, m_y + 1) C_+(\ell, m_y) \Big) \right] \delta_{m_y', m_y} + \frac{e_3 - e_1}{4} \times \left[C_+(\ell, m_y + 1) C_+(\ell, m_y) \delta_{m_y', m_y + 2} + C_-(\ell, m_y - 1) C_-(\ell, m_y) \delta_{m_y', m_y - 2} \right] \right\}, \quad (59)$$

$$\left\langle \ell m_z' \left| \hat{H}^* \right| \ell m_z \right\rangle = \frac{\hbar^2}{2} \left\{ \left[e_3 m_z^2 + \frac{e_1+e_2}{4} \Big(C_+(\ell, m_z - 1) C_-(\ell, m_z) + C_-(\ell, m_z + 1) C_+(\ell, m_z) \Big) \right] \delta_{m_z', m_z} + \frac{e_1 - e_2}{4} \times \left[C_+(\ell, m_z + 1) C_+(\ell, m_z) \delta_{m_z', m_z + 2} + C_-(\ell, m_z - 1) C_-(\ell, m_z) \delta_{m_z', m_z - 2} \right] \right\}, \quad (60)$$

where

$$C_{\pm}(\ell, m) = \sqrt{(\ell \mp m_k)(\ell \pm m_k + 1)} = C_{\mp}(\ell, m_k \mp 1), \tag{61}$$

are the coefficients for the raising and lowering operators.

The readers' attention is called on the following consequences:

1. The angular momentum selection rules $\Delta m_k = 0, \pm 2$, separate the $(2\ell + 1) \times (2\ell + 1)$ matrices into two tridiagonal blocks: one for m_k even of dimensions $(\ell + 1) \times (\ell + 1)$ and one for m_k odd and $\ell \times \ell$ for ℓ even, and the other way around for ℓ odd.
2. The matrices are symmetric with respect to the main diagonal because of the hermiticity of $\hat{H}^*$ and also with respect to the other diagonal because of Eq. (61).
3. The invariance of $\hat{H}^*$ and $\hat{L}^2$ under the parity operations $(x \to -x, y \to -y, z \to -z)$ leads to combinations with well-defined parities $|\ell, m_k\rangle \pm |\ell, -m_k\rangle$ in the bases and in the eigenfunctions.
4. The classification of the latter into their different species and kinds $[1, yz, xz, xy]$ for ℓ even and $[x, y, z, xyz]$ for ℓ odd connects with the results used in Sections 2.1 and 2.2. Their respective parities are $[(+++), (+--), (-+-), (--+)]$ and $[(-++), (+-+), (++-), (---)]$.
5. The diagonalization of the matrices in Eqs. (58–60) leads to the common eigenfunctions

$$|E^*, \ell, n\rangle = \sum_{m_k} a^{\ell n}_{m_k} |\ell m_k\rangle \,, \tag{62}$$

as the ket version of Eq. (17) written by Kramers and Ittmann, yielding the eigenvectors $a_{\ell m_k}$ in the chosen bases and the eigenvalues $E^*_{\ell n}(\sigma)$ in the notation of Ref. [4], independently of the basis, where n counts the order of excitation with $n = 0, 1, 2, \ldots, 2\ell$.

Illustrations of numerical results are provided through Table 4.3 and Figure 4.2 borrowed from Ref. [5]. Table 4.3 lists the numerical values of the eigenenergies for $\ell = 5$ and $n = 1, 2, 3, \ldots, 11$ for $\sigma = 0^\circ, 15^\circ, 30^\circ, 45^\circ$, and 60°.

The entries at the left and right ends correspond to the symmetric prolate and oblate molecules with analytical expressions for their energies

$$E^*_{\ell m_x}(\sigma = 0^\circ) = \frac{\hbar^2}{4}\left(3m_x^2 - \ell(\ell + 1)\right), \tag{63}$$

following directly from Eq. (58) where $e_2 - e_3 = 0$, and

$$E^*_{\ell m_z}(\sigma = 60^\circ) = -\frac{\hbar^2}{4}\left(3m_z^2 - \ell(\ell + 1)\right), \tag{64}$$

from Eq. (60) with $e_1 - e_2 = 0$.

Table 4.3 Energy eigenvalues $E^*_{\ell n}/\hbar^2$, for $\ell = 5$ and successive orders of excitation $n = 0, 1, \ldots, 10$ of molecules with different asymmetries $\sigma = 0^\circ, 15^\circ, \ldots, 60^\circ$

	σ					
$\ell = 5$	n	0°	15°	30°	45°	60°
	0	−7.5	−8.5360900339119	−9.9542229834973	−10.915786939060	−11.25
	1	−6.75	−8.4743820417365	−9.9498743710662	−10.915687010907	−11.25
	2	−6.75	−5.3033008588991	−4.6444340679126	−4.5080411669285	−4.5
	3	−4.5	−4.5	−4.5	−4.5	−4.5
	4	−4.5	−3.2163948301846	−1.1854016127986	0.30918522126180	0.75
	5	−0.75	−0.50016213090185	0	0.50016213090185	0.75
	6	−0.75	−0.30918522126180	1.1854016127986	3.2163948301846	4.5
	7	4.5	4.5	4.5	4.5	4.5
	8	4.5	4.5080411669286	4.6444340679126	5.3033008588991	6.75
	9	11.25	10.915687010907	9.9498743710662	8.4743820417365	6.75
	10	11.25	10.915786939060	9.9542229834973	8.5360900339119	7.5

Notice that these energies have the same numerical values but opposite signs for $m_x = m_z = 0, \pm 1, \pm 2, \ldots, \pm \ell$, as a comparison of the successive entries in the left-end column from top to bottom and in the right-end column from bottom to top indicates. The double degeneracy of the states with $m_x = m_z \neq 0$ and the single states with $m_x = m_z = 0$ are also recognized. The entries for $\sigma = 30^\circ$ corresponding to the most asymmetric molecules coincide with those of Ref. [4]. We identify the zero-energy state at the center of the table, as well as the symmetric displacements in the same column above and below, and in the energy levels on the vertical line at $\sigma = 30^\circ$. The effect of asymmetries of the molecules for values of σ to the right of 0° and to the left of 60° is manifested by the decreasing and increasing of the energy of the $m_x = 0$ and $m_z = 0$ state, respectively, and by the removal of the double degeneracy of the $m_x = m_z \neq 0$ states.

The reader may also repeat the exercise of going down the entries in the column for $\sigma = 15^\circ$ and going up in the column for $\sigma = 45^\circ$ to recognize the same numbers with opposite signs at each step.

The general result can be summarized as the relationship $E_{\ell n_1}(\sigma_1) = -E_{\ell n_2}(\sigma_2)$ for matching asymmetry distributions $\sigma_1 + \sigma_2 = 60^\circ$ and matching states $n_1 + n_2 = 2\ell$. This is a reflexion of the structure of $\hat{H}^*$ as discussed in points 1) $-$ 4) in the previous page. The reader is advised about the typographic error in Ref. [5] where the minus sign in the relationship between the energies is missing, and the shifting of the ordering numbers starting with 0 for the lowest energy states. The systematics and the simplicity recognized in Ref. [4] for the energy levels of the most asymmetric molecules, which are self-matching, is recognized for the energies with any integer ℓ in the σ, n plane.

Figure 4.2 illustrates the energy levels $E^*_{\ell n}(\sigma)$ for $\ell = 1, 2, \ldots, 10, 20, 30$ and asymmetry distributions $0 \leq \sigma \leq 60^\circ$ covering any shape of the molecules. Any of the energy spectra in each entry, under rotation around the axis perpendicular to its plane at the point $E^*(\sigma = 30^\circ) = 0$ by 180°, coincides with its original form, reflecting the relationship described in the previous paragraph.

Additionally, the readers are also invited to look at the illustrative figures for the eigenfunctions obtained for $\ell = 4$ in Ref. [5] and $\ell = 5$ in Ref. [6]. The shapes of the eigenfunctions in the complementary columns and rows are the same but differ in orientations. The number of ℓ nodal elliptical cones is common to all the eigenfunctions with the same value of ℓ. The end columns for the symmetric molecules involve spherical harmonics with circular cones and meridian half-planes as their nodes. The changes of the eigenfunctions with the changes in the asymmetry distribution can also be followed for each state moving along the same row.

It is interesting to recognize that the familiar perturbation method for the analysis of the rotational spectra and the exact evaluations of the eigenenergies and eigenfunctions just reviewed in this section use the same tool,

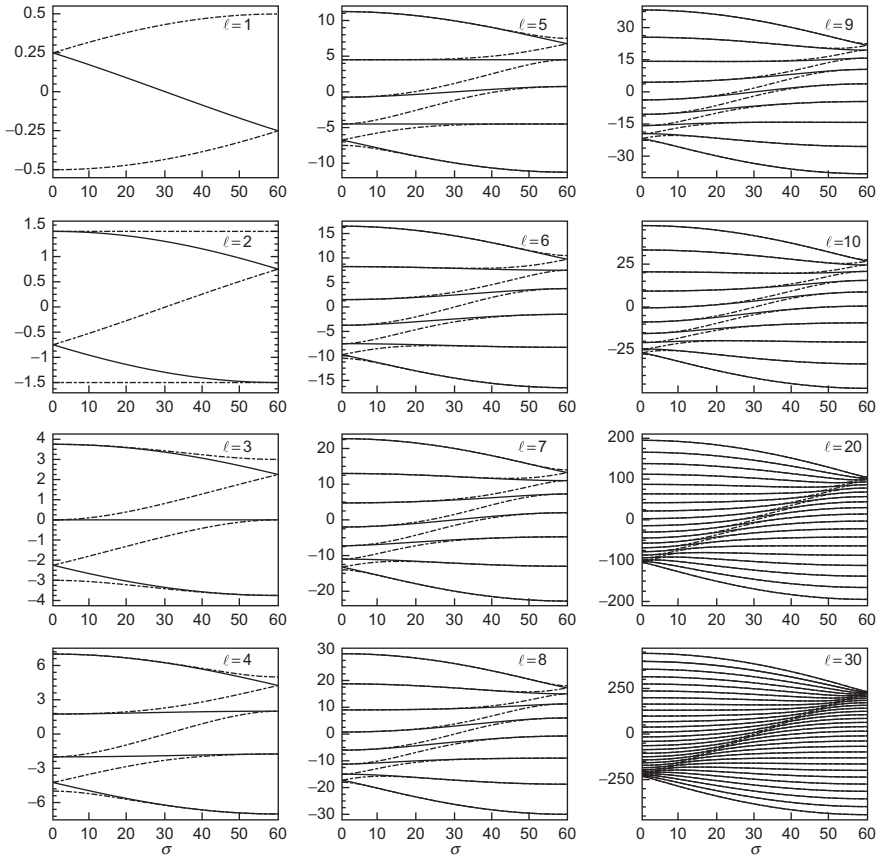

Figure 4.2 Energy spectra, $E^*/\hbar^2$, for states with $\ell = 1, 2, \ldots, 10, 20, 30$ of molecules with different asymmetries $\sigma \in [0^\circ, 60^\circ]$.

namely, spherical harmonics. However, both approaches are different from the very beginning, with their consequent limited and accurate results, respectively.

The generating function of the Lamé polynomials and of the spherical harmonics are familiar since the study of electrostatics

$$\frac{1}{\left|\vec{r} - \vec{r}'\right|} = \sum_{\ell} \frac{r_<^{\ell}}{r_>^{\ell+1}} P_\ell(\hat{r} \cdot \hat{r}'), \tag{65}$$

$$P_\ell(\hat{r} \cdot \hat{r}') = \frac{4\pi}{2\ell + 1} \sum_{m=-\ell}^{\ell} Y^*_{\ell m}(\theta', \varphi') Y_{\ell m}(\theta, \varphi). \tag{66}$$

The expansion of Eq. (62) can be inverted to express the spherical harmonics in terms of spheroconal harmonics, whose completeness in turn leads to the addition theorem in the form

$$P_\ell(\hat{r}\cdot\hat{r}') = \frac{4\pi}{2\ell+1}\sum_{A,B}\sum_{n_1,n_2}\Lambda^A_{n_1}(\chi_1',k_1)\Lambda^B_{n_2}(\chi_2',k_2)\Lambda^A_{n_1}(\chi_1,k_1)\Lambda^B_{n_2}(\chi_2,k_2), \tag{67}$$

for matching values of A and B, and $n_1+n_2=\ell$.

2.5. Rotations of asymmetric molecules revisited: Matrix evaluation and generating function of Lamé functions

This section reviews the simultaneous separations of the eigenvalue equations for the Hamiltonian $\hat{H}^*$ and the square of the angular momentum operators in spheroconal coordinates in the Jacobi elliptical function representation, leading to Lamé ordinary differential equations in the respective variables χ_1 and χ_2. The matrix method to evaluate the solutions of the latter, as well as matching them to construct the Lamé spheroconal harmonic polynomials are also reviewed, following Ref. [6]. Illustrative numerical results for the rotational eigenenergies and eigenstates of asymmetric molecules are discussed, including comparisons with those of the earlier sections.

The respective equations take the forms

$$-\frac{\hbar^2}{1-k_1^2\mathrm{sn}^2(\chi_1|k_1)-k_2^2\mathrm{sn}^2(\chi_2|k_2)}\left\{\left[e_1-(e_1-e_2)\mathrm{sn}^2(\chi_1|k_1)\right]\frac{\partial^2}{\partial\chi_1^2}\right.$$
$$\left.+\left[e_3-(e_2-e_3)\mathrm{sn}^2(\chi_2|k_2)\right]\frac{\partial^2}{\partial\chi_2^2}\right\}\Psi = 2E^*\Psi, \tag{68}$$

$$-\frac{\hbar^2}{1-k_1^2\mathrm{sn}^2(\chi_1|k_1)-k_2^2\mathrm{sn}^2(\chi_2|k_2)}\left[\frac{\partial^2}{\partial\chi_1^2}+\frac{\partial^2}{\partial\chi_2^2}\right]\Psi = \hbar^2\ell(\ell+1)\Psi. \tag{69}$$

They admit factorizable solutions Eq. (43) and can be separated into ordinary differential equations in each variable, provided the geometric and dynamic parameters are related through Eq. (44), so that

$$1-k_1^2\mathrm{sn}^2(\chi_1|k_1)-k_2^2\mathrm{sn}^2(\chi_2|k_2)$$
$$=\frac{1}{e_1-e_3}\left[-e_3-(e_2-e_3)\mathrm{sn}^2(\chi_1|k_1)+e_1-(e_1-e_2)\mathrm{sn}^2(\chi_2|k_2)\right]. \tag{70}$$

The interested reader can see the details in the Appendix of Ref. [6].

The separated equations become

$$\frac{\mathrm{d}^2\Lambda_{n_1}}{\mathrm{d}\chi_1^2} - \left(\ell(\ell+1)k_1^2\mathrm{sn}^2(\chi_1|k_1) + \frac{\ell(\ell+1)e_3}{e_1-e_3} - \frac{2E^*}{\hbar^2\,(e_1-e_3)}\right)\Lambda_{n_1} = 0, \tag{71}$$

$$\frac{\mathrm{d}^2\Lambda_{n_2}}{\mathrm{d}\chi_2^2} - \left(\ell(\ell+1)k_2^2\mathrm{sn}^2(\chi_2|k_2) - \frac{\ell(\ell+1)e_1}{e_1-e_3} + \frac{2E^*}{\hbar^2\,(e_1-e_3)}\right)\Lambda_{n_2} = 0, \tag{72}$$

with the standard form of the Lamé ordinary differential equation [12]

$$\frac{\mathrm{d}^2\Lambda_{n_i}}{\mathrm{d}\chi_i^2} - \left(\ell(\ell+1)k_i^2\mathrm{sn}^2(\chi_i|k_i) + h_i\right)\Lambda_{n_i} = 0, \tag{73}$$

involving the respective eigenvalues

$$h_1 = \frac{\ell(\ell+1)e_3}{e_1-e_3} - \frac{2E^*}{\hbar^2(e_1-e_3)}, \quad h_2 = -\frac{\ell(\ell+1)e_1}{e_1-e_3} + \frac{2E^*}{\hbar^2(e_1-e_3)}. \tag{74}$$

Their linear combinations

$$h_1 + h_2 = -\ell(\ell+1) \tag{75}$$

$$e_1h_1 + e_3h_2 = -\frac{2E^*}{\hbar^2}. \tag{76}$$

connect with the eigenvalues of our physical interest.

The derivatives of the Jacobi elliptical functions

$$\begin{aligned}
\frac{\mathrm{d}}{\mathrm{d}\chi}\mathrm{sn}(\chi|k) &= \mathrm{cn}(\chi|k)\mathrm{dn}(\chi|k),\\
\frac{\mathrm{d}}{\mathrm{d}\chi}\mathrm{cn}(\chi|k) &= -\mathrm{sn}(\chi|k)\mathrm{dn}(\chi|k),\\
\frac{\mathrm{d}}{\mathrm{d}\chi}\mathrm{dn}(\chi|k) &= -k^2\mathrm{sn}(\chi|k)\mathrm{cn}(\chi|k),
\end{aligned} \tag{77}$$

determine the removable singularities in Eq. (73), and the eight species and types of their solutions. They are expressed as the products of the removing

singularity factors and power series in $\mathrm{sn}^2(\chi|k)$:

$$\Lambda^1 = \sum_p a_p^1 \mathrm{sn}^{2p}\left(\chi_i|k_i\right), \tag{78}$$

$$\Lambda^s = \mathrm{sn}\left(\chi_i|k_i\right) \sum_p a_p^s \mathrm{sn}^{2p}\left(\chi_i|k_i\right), \tag{79}$$

$$\Lambda^c = \mathrm{cn}\left(\chi_i|k_i\right) \sum_p a_p^c \mathrm{sn}^{2p}\left(\chi_i|k_i\right), \tag{80}$$

$$\Lambda^d = \mathrm{dn}\left(\chi_i|k_i\right) \sum_p a_p^d \mathrm{sn}^{2p}\left(\chi_i|k_i\right), \tag{81}$$

$$\Lambda^{cs} = \mathrm{cn}\left(\chi_i|k_i\right) \mathrm{sn}\left(\chi_i|k_i\right) \sum_p a_p^{cs} \mathrm{sn}^{2p}\left(\chi_i|k_i\right), \tag{82}$$

$$\Lambda^{ds} = \mathrm{dn}\left(\chi_i|k_i\right) \mathrm{sn}\left(\chi_i|k_i\right) \sum_p a_p^{ds} \mathrm{sn}^{2p}\left(\chi_i|k_i\right), \tag{83}$$

$$\Lambda^{dc} = \mathrm{dn}\left(\chi_i|k_i\right) \mathrm{cn}\left(\chi_i|k_i\right) \sum_p a_p^{dc} \mathrm{sn}^{2p}\left(\chi_i|k_i\right), \tag{84}$$

$$\Lambda^{dcs} = \mathrm{dn}\left(\chi_i|k_i\right) \mathrm{cn}\left(\chi_i|k_i\right) \mathrm{sn}\left(\chi_i|k_i\right) \sum_p a_p^{dcs} \mathrm{sn}^{2p}\left(\chi_i|k_i\right). \tag{85}$$

Substitutions of Eqs. (78–85) in Eq. (73) lead to three-term recurrence relations of the expansion coefficients a_p^A, contained in Eqs. (32–39) in Ref. [6] and not reproduced here for the sake of space. The three-term recurrence relations can be cast onto the form of matrix eigenvalue equations with eigenvalues h^A and the eigenvectors a_p^A, just like in the case of Section 2.3.

The important point is that for integer values of ℓ, the matrices for each species and type become of finite size $N_{\max}^A \times N_{\max}^A$ and the series are polynomials. For ℓ even, the respective sizes are

$$N_{\max}^1 = \frac{\ell+2}{2}, \quad N_{\max}^{cs} = N_{\max}^{ds} = N_{\max}^{dc} = \frac{\ell}{2}; \tag{86}$$

and for ℓ odd,

$$N_{\max}^d = N_{\max}^c = N_{\max}^s = \frac{\ell+1}{2}, \quad N_{\max}^{dcs} = \frac{\ell-1}{2}, \tag{87}$$

with a total of $2\ell+1$ independent states in both cases.

Table II in Ref. [6] illustrates the eigenvalues h^A for the cases of $\ell = 4$ and 5 for the respective species and types of the Lamé polynomials for molecules with the different asymmetry distributions. Figure 1 in Ref. [6] shows the variations of the Lamé polynomials Λ^s, Λ^c, Λ^d (three of each), and Λ^{scd} (two) as functions of their argument and of the asymmetry distribution.

In the table, the readers may play the game of adding the eigenvalues in the end columns, in their neighbors and in the middle going down in one and up the other for $\ell = 4$ and 5 with the common results of -20 and -30, respectively, consistent with Eq. (75). In the figure, they can appreciate the species and type of each function, according to their values or their derivatives at $am(\chi)$ of 0° and 90°, the order of excitation according to their number of nodes, which remain the same as the asymmetry distribution changes in the molecules. Of course, the positions of the zeros change for each state within each column as the parameter k^2 changes from 0 to 1 going down, belonging to symmetric molecules at the top and bottom rows, to the most asymmetric molecules at the middle row with $k^2 = 0.5$, and complementary asymmetry distributions in the second and fourth rows.

The construction of the Lamé spheroconal harmonic polynomials involves Eq. (43) with matching parameters Eq. (44), matching species, and matching excitations of the respective elliptical cone coordinate degrees of freedom. The matching of species and kinds are the following:

$$\Psi^{AB}_{n_1 n_2}(\chi_1, \chi_2) = \Lambda^A_{n_1}(\chi_1, k_1)\Lambda^B_{n_2}(\chi_2, k_2), \tag{88}$$

with A and B in the following form

The matching of excitations involve $n_1 + n_2 = \ell$, as well as Eq. (75), matching eigenvalues determining the eigenenergies $E^*_{n_1 n_2}(\sigma)$ through Eq. (76).

The numerical results for the eigenenergies and eigenfunctions evaluated in Refs. [5] and [6] for molecules with different asymmetry distributions and states are accurate and consistent. The zeros of the individual Lamé functions can be determined with high accuracy, and are illustrated in Figure 1 in Ref. [6]. They allow writing the Lamé polynomial in product forms presented in Sections 2.1 and 2.2. They are also the key to implement the boundary condition for the rotations of molecules confined by elliptical cones as discussed in Section 3.

The Rayleigh expansion of a plane wave in a basis of spherical waves [10],

$$e^{i\vec{k}\cdot\vec{r}} = \sum_\ell i^\ell (2\ell + 1) j_\ell(kr) P_\ell(\hat{k} \cdot \hat{r}), \tag{89}$$

can be identified as a generating function of the Legendre polynomials and/or the spherical Bessel functions. The first ones, in turn, are the generating function for the spherical harmonics and the spheroconal harmonics through the addition theorem as already proven in Section 2.4, Eq. (67).

2.6. Common generating function for three-dimensional hydrogen atom complete wavefunctions

The Laplace equation and the Schrödinger equation for the free particle, the harmonic oscillator, and the hydrogen atom, in different dimensions, are superintegrable, which means that they admit separable and integrable solutions in different coordinate systems [14]. In general, the complete solutions of such equations in the respective coordinate systems can be obtained from common generating functions, as already illustrated in Sections 2.4 and 2.5 for the spherical and spheroconal solutions of the Laplace and Helmholtz equations. Our own works on Mathieu functions [35], spheroidal functions [36], D-dimensional harmonic oscillators [37], two-dimensional Hydrogen atom [38], and three-dimensional hydrogen atom [7] have identified or constructed such common generating functions including their expansions in the complete wavefunctions.

Here, we discuss the last one with focus on the rotations of the hydrogen atom. It is well known that the corresponding Schrödinger equation is separable in spherical, parabolic, and spheroidal prolate coordinates, and also in spheroconal coordinates [14]. In this case, the identification of the common generating function is based on the recognition that the Schrödinger equation separates in parabolic coordinates into equations with the same structure as the radial equations of two-dimensional harmonic oscillators in circular coordinates. Correspondingly, the common generating function for the three-dimensional hydrogen atom in such coordinates is the product of two known generating functions of two-dimensional harmonic oscillators and their expansions in the respective eigenfunctions in parabolic coordinates, with angular dependencies that guarantee the generation of the proper angular eigenfunctions $e^{im\varphi}$.

The transformations from parabolic coordinates into spherical, spheroconal, and prolate spheroidal coordinates allow the rewriting of the generating function in each one of them. Its respective expansions for each case are straightforward, but laborious. For the spherical and spheroidal cases, the common angular eigenfunctions $e^{im\varphi}$ serve as guides to complete the job. In particular, in the spherical case, the complete angular dependence can be expressed as $P_\ell(\hat{r}_0 \cdot \hat{r})$ through the addition theorem, reflecting the rotational invariance of the system. The latter leads to the extension for the spheroconal coordinates, just as in Section 2.4 and 2.5, with common radial functions. The interested reader may follow the details in Ref. [7].

The equal standing of spherical harmonics and spheroconal harmonics is manifested in this case. The rotations of the hydrogen atom are familiarly described through eigenfunctions of $\hat{L}^2$ and $\hat{L}_z$, but they also admit eigenfunctions of $\hat{L}^2$ and $\hat{H}^*$. The same holds for any central potential quantum system. Some of the consequences are illustrated in the following section.

3. A GUIDE TO ROTATIONS OF THE HYDROGEN ATOM AND ASYMMETRIC MOLECULES CONFINED BY ELLIPTICAL CONES

This section deals with the hydrogen atom and rotations of asymmetric molecules in situations of confinement in elliptical cones. The discussion in Section 3.1 deals with the hydrogen atom in semi-infinite spaces limited by conoidal boundaries in general, identifying that the cases of elliptical cone and dihedral boundaries were still open problems. Our contribution to the 50th Sanibel Symposium is the basis of Section 3.2, contrasting the evaluation and application of Lamé spheroconal harmonics in their polynomial and quasi-periodic forms for the description of rotations of quantum systems in their free and confined-by-elliptical-cone configurations, respectively. The specific examples of the free particle and the harmonic oscillator were included in Ref. [1]. The investigations of Sections 3.3 and 3.4, on the hydrogen atom and rotations of asymmetric molecules, respectively, were already on their way when we decided on the topic for the symposium. Although the results on the hydrogen atom have already been published [8], those on the molecules are reported in detail in Section 3.4 for the first time.

3.1. The hydrogen atom confined in semi-infinite spaces limited by conoidal boundaries

This is the title of Chapter 3 in Ref. [9], *Advances in Quantum Chemistry*, Vol. 57, dedicated to confined quantum systems. The conoidal boundaries involve spheres, circular cones, dihedral angles, confocal paraboloids, confocal prolate spheroids, and confocal hyperboloids as natural boundaries of confinement for the hydrogen atom. In fact, such boundaries are associated with the respective coordinates in which the Schrödinger equation is separable and the boundary conditions for confinement are easily implemented. While spheres and spheroids model the confinement in finite volumes, the other surfaces correspond to the confinement in semi-infite spaces.

The chapter contains a review of the free hydrogen atom eigenfunctions in the spherical, spheroconal, parabolic, and prolate spheroidal coordinates; an overview of our own works for confinement by most of the above-mentioned boundaries; and a preview of problems on confined atoms and molecules of current and future investigations.

In particular, for the hydrogen atom, it was recognized that the confinements by elliptical cones and by dihedral angles were pending. Section 5.1 in the Preview of Ref. [9] formulated the problem of the hydrogen atom confined by a family of elliptical cones identified in its Eqs. (123 and 124), with the boundary condition that the wavefunctions vanish in such cones, Eqs. (125 and 126). The corresponding solution [8] is the subject of Section 3.3.

3.2. Lamé spheroconal harmonics in atoms and molecules

This is the title of our contribution to the 50th Sanibel Symposium and its written version [1]. It includes our earlier work on the rotations of asymmetric molecules and the hydrogen atom in free configurations, as discussed in Sections 2.5, 2.6, and 3.1, involving Lamé spheroconal harmonic polynomials. Against this background, we went on to our investigations of the same systems in situations of confinement by elliptical cone boundaries involving Lamé quasi-periodic spheroconal harmonic functions. In this section, the concentration is on the latter, considering that the differential equations of the earlier sections are the same, but the solutions with the new boundary conditions are qualitatively and quantitatively different.

In fact, the impenetrable elliptical cone confinement imposes the boundary conditions

$$\Psi(\chi_1 = \chi_{10}, \chi_2) = 0 \quad \text{or} \quad \Psi(\chi_1, \chi_2 = \chi_{20}) = 0, \tag{90}$$

translating into the vanishing of the respective Lamé functions

$$\Lambda^A(\chi_1 = \chi_{10}) = 0 \quad \text{or} \quad \Lambda^B(\chi_2 = \chi_{20}) = 0. \tag{91}$$

If the position of the boundary $\chi_i = \chi_{i0}$ coincides with the cone of the zeros of the Lamé polynomials of Section 2.5, the corresponding angular momentum label ℓ is an integer for that specific state. In general, for the same boundary other states will not vanish there, requiring noninteger values for the angular momentum label, λ, to satisfy the same boundary condition.

In practical terms, we rewrite the Lamé differential equations to be solved as

$$\frac{\mathrm{d}^2\Lambda_i}{\mathrm{d}\chi_i^2} - \left[\lambda(\lambda+1)k_i^2\mathrm{sn}^2(\chi_i|k_i) + h_i\right]\Lambda_i = 0, \tag{92}$$

$$\frac{\mathrm{d}^2\Lambda_j}{\mathrm{d}\chi_j^2} - \left[\lambda(\lambda+1)k_j^2\mathrm{sn}^2(\chi_j|k_j) + h_j\right]\Lambda_j = 0, \tag{93}$$

with the boundary condition of Eq. (91) for $\chi_i = \chi_{i0}$, and maintaining the parity and periodicity conditions for the complementing factor $\Lambda_j(\chi_j)$. In fact, the presence of the boundary breaks the original parity and periodicity in $\Lambda_i(\chi_i)$ relative to the axis of the cone.

Our experience with the hydrogen atom confined by a circular cone [39] involves going from Legendre polynomials $P_\ell^m(\cos\theta)$ to Legendre functions

$P_\lambda^m(\cos\theta)$, with noninteger values of λ and series expansions in powers of $(1-\cos\theta)/2$. Consequently, we tried solutions in the confined variable of the following forms:

$$\Lambda^1(\chi_i,k_i;\lambda)=\sum_{p=0}^{\infty}b_p^1\left(\frac{1-\mathrm{sn}\left(\chi_i|k_i\right)}{2}\right)^p, \tag{94}$$

$$\Lambda^d\left(\chi_i,k_i;\lambda\right)=\mathrm{dn}\left(\chi_i|k_i\right)\sum_{p=0}^{\infty}b_p^d\left(\frac{1-\mathrm{sn}\left(\chi_i|k_i\right)}{2}\right)^p, \tag{95}$$

$$\Lambda^c\left(\chi_i,k_i;\lambda\right)=\mathrm{cn}\left(\chi_i|k_i\right)\sum_{p=0}^{\infty}b_p^c\left(\frac{1-\mathrm{sn}\left(\chi_i|k_i\right)}{2}\right)^p, \tag{96}$$

$$\Lambda^{dc}\left(\chi_i,k_i;\lambda\right)=\mathrm{dn}\left(\chi_i|k_i\right)\mathrm{cn}\left(\chi_i|k_i\right)\sum_{p=0}^{\infty}b_p^{dc}\left(\frac{1-\mathrm{sn}\left(\chi_i|k_i\right)}{2}\right)^p, \tag{97}$$

to be matched with their respective counterparts $\Lambda^1(\chi_j,k_j;\lambda)$, $\Lambda^s(\chi_j,k_j;\lambda)$, $\Lambda^c(\chi_j,k_j;\lambda)$ and $\Lambda^{sc}(\chi_j,k_j;\lambda)$ in the other variable from Eqs. (25) in Ref. [6] and Eq. (88) in Section 2.5, which maintain their parities and periodicities.

The substitution of Eqs. (94–97) in Eq. (92) leads to four-term-recurrence relations, Eqs. (43–46) in Ref. [1] or Eqs. (33–36) in Ref. [8]. Correspondingly, the recurrence relations can be cast into the form of matrix eigenvalue equations with eigenvectors b_p^A and eigenvalues h_i^A for chosen values of λ and k_i, which may be numerically obtained by diagonalization. Although the matrices in Section 2.5 are of finite sizes, the fact that λ is noninteger implies that the sizes of the new matrices are infinite. Nevertheless, this is no impediment to obtain convergent and accurate values for large-enough finite sizes. The matrices for the companion variable Lamé functions involving three-term-recurrence relations also become of infinite size, and the diagonalizations of their matrices yield the eigenvectors a_p^B and eigenvalues h_j^B.

The complete Lamé spheroconal harmonic quasi-periodic functions, satisfying the respective boundary conditions in Eq. (91), involve matching the corresponding factors of Table 4.4 and their counterparts. For the boundary

Table 4.4 Matching species of Lamé functions whose products are Lamé spheroconal harmonic functions with defined parities

A	1	d	c	s	cs	ds	dc	dcs
B	1	s	c	d	cd	sd	sc	scd
AB	1	x	y	z	yz	xz	xy	xyz

$\chi_1 = \chi_{10}$, the 1, x and y parities survive, and the z parity is broken:

$$\Psi^{1}_{n_1 n_2}(\chi_1, \chi_2; \lambda) = \Lambda^{1}_{n_1}(\chi_1; k_1, \lambda = \lambda_{n_1+1})\Lambda^{1}_{n_2}(\chi_2; k_2, \lambda = \lambda_{n_1+1}), \tag{98}$$

$$\Psi^{x}_{n_1 n_2}(\chi_1, \chi_2; \lambda) = \Lambda^{d}_{n_1}(\chi_1; k_1, \lambda = \lambda_{n_1+1})\Lambda^{s}_{n_2}(\chi_2; k_2, \lambda = \lambda_{n_1+1}), \tag{99}$$

$$\Psi^{y}_{n_1 n_2}(\chi_1, \chi_2; \lambda) = \Lambda^{c}_{n_1}(\chi_1; k_1, \lambda = \lambda_{n_1+1})\Lambda^{c}_{n_2}(\chi_2; k_2, \lambda = \lambda_{n_1+1}), \tag{100}$$

$$\Psi^{xy}_{n_1 n_2}(\chi_1, \chi_2; \lambda) = \Lambda^{dc}_{n_1}(\chi_1; k_1, \lambda = \lambda_{n_1+1})\Lambda^{sc}_{n_2}(\chi_2; k_2, \lambda = \lambda_{n_1+1}), \tag{101}$$

where n_1 and n_2 are the number of nodes in the respective functions without counting the one at the boundary. For the boundary $\chi_2 = \chi_{20}$, the 1, y and z parities survive, and the x parity is broken:

$$\Psi^{1}_{n_1 n_2}(\chi_1, \chi_2; \lambda) = \Lambda^{1}_{n_1}(\chi_1; k_1, \lambda = \lambda_{n_2+1})\Lambda^{1}_{n_2}(\chi_2; k_2, \lambda = \lambda_{n_2+1}), \tag{102}$$

$$\Psi^{y}_{n_1 n_2}(\chi_1, \chi_2; \lambda) = \Lambda^{c}_{n_1}(\chi_1; k_1, \lambda = \lambda_{n_2+1})\Lambda^{c}_{n_2}(\chi_2; k_2, \lambda = \lambda_{n_2+1}), \tag{103}$$

$$\Psi^{z}_{n_1 n_2}(\chi_1, \chi_2; \lambda) = \Lambda^{s}_{n_1}(\chi_1; k_1, \lambda = \lambda_{n_2+1})\Lambda^{d}_{n_2}(\chi_2; k_2, \lambda = \lambda_{n_2+1}), \tag{104}$$

$$\Psi^{yz}_{n_1 n_2}(\chi_1, \chi_2; \lambda) = \Lambda^{sc}_{n_1}(\chi_1; k_1, \lambda = \lambda_{n_2+1})\Lambda^{dc}_{n_2}(\chi_2; k_2, \lambda = \lambda_{n_2+1}). \tag{105}$$

The first set corresponds to Eqs. (29–32) chosen for the hydrogen atom in Ref. [8] and to Eqs. (55–58) in Ref. [1]. The second set coincides with Eqs. (56–62) in Ref. [1]. Both sets are needed and used for molecules in Section 3.4. Here we have added their k_i parameters and common λ eigenvalue, explicity.

The Lamé quasi-periodic functions are common eigenfunctions of the operators $\hat{L}^2$ and $\hat{H}^*$ as discussed in Sections 2.2 and 2.5. In Refs. [1] and [8], we chose the notation of $\hat{G}$ for the latter in order to emphasize that it represents the geometry of the spheroconal elliptical cone confinement, in contrast with its dynamical character for the rotations of asymmetric molecules. The eigenvalues h_1^A and h_2^B are numerically found to satisfy the relationships

$$h_1^A + h_2^B = -\lambda(\lambda + 1), \quad e_1 h_1 + e_3 h_2 = -2E^*. \tag{106}$$

as the counterparts of Eqs. (75 and 76).

Because the Hamiltonian of any central potential quantum system, $\hat{H}_{\text{cp}}$, commutes with the operators $\hat{L}^2$ and $\hat{H}^*$, they also have common eigenfunctions, including the situation of confinement by elliptical cones. Although Ref. [8] focused on the hydrogen atom, Ref. [1] included the examples of the free particle confined by elliptical cones with spherical caps, and the harmonic oscillator confined by elliptical cones. They all share the angular momentum eigenfunctions of Eqs. (98–101), which were evaluated in Ref. [8] and could be borrowed immediately. Their radial functions and their

energy eigenvalue equations in the free configuration involving the angular momentum quantum label ℓ can be immediately transformed into the corresponding forms for the confined configurations by the replacement $\ell \to \lambda$.

Readers are invited to do their own reading of Ref. [1], including the effects of the confinement by elliptical cones on the energy spectra and eigenfunctions of the familiar free particle and harmonic oscillator.

3.3. The hydrogen atom confined in semi-infinite space with an elliptical cone boundary

This is the title of our reference [8] with the novel element of confinement of the hydrogen atom by elliptical cones. We were in a position to investigate such a system after becoming aware of the separability of its Schrödinger equation in spheroconal coordinates, as already discussed in Section 2.6, with the consequent recognition that the associated elliptical cones are natural boundaries of confinement allowing the integration of the corresponding angular equations, as anticipated in Section 3.1. The solution of the problem led us to develop the matrix method to evaluate the Lamé functions of Eqs. (94–97) satisfying the boundary conditions of Eqs. (90 and 91), and their companions in the other elliptical-cone coordinate, and matching them to construct the quasi-periodic Lamé spheroconal harmonics of Eqs. (98–105), as discussed in Section 3.2. The boundary condition introduces noninteger values for the angular momentum label λ, and eigenfunctions breaking the original parity symmetry of the hydrogen atom. Notice that reference [8] was multicited because it was the original work available at the time of the Sanibel Symposium.

In the following, the radial differential equation for the confined hydrogen atom,

$$\left\{-\frac{\hbar^2}{2m_e}\left[\frac{1}{r^2}\frac{\mathrm{d}}{\mathrm{d}r}r^2\frac{\mathrm{d}}{\mathrm{d}r}-\frac{\lambda(\lambda+1)}{r^2}\right]-\frac{e^2}{r}\right\}R = ER, \tag{107}$$

is considered, taking into account that its rotational kinetic energy or centrifugal potential term involves noninteger values of λ, as established in the previous paragraph. The corresponding radial eigenfunctions and energy eigenvalues become

$$R_{n_r\lambda}(r) = N_{n_r\lambda}r^{\lambda}e^{-\frac{r}{\nu a_0}}{}_1F_1\left(-n_r, 2\lambda+2; \frac{2r}{\nu a_0}\right), \tag{108}$$

$$E_\nu = -\frac{e^2}{2a_0\nu^2}, \quad \nu = n_r + \lambda + 1, \tag{109}$$

involving also noninteger values of the energy principal quantum label ν that replaces the integer n of the free hydrogen atom. Obviously, for such values of λ and ν, the behaviors of the radial function close to the origin $r \to 0$, asymptotically $r \to \infty$, and in between $0 < r < \infty$, differ quantitatively from those of the familiar $n\ell = 1s, 2s, 2p, \ldots$ states. The same holds for the eigenenergies with the removal of the also familiar degeneracy of order n^2 when the atom is not confined.

The geometry of the confining elliptical cone defined by the values of the shape σ and the aperture $\mathrm{sn}(\chi_{10}|\sigma)$ parameters, determines the energy spectra through the dependence of the total energy quantum label on such parameters $\nu(\sigma, \mathrm{sn}(\chi_{10}|\sigma))$, as determined by Eqs. (91 and 109), for different eigenstates $n_r, \lambda(An_1, Bn_2)$ from Eqs. (98–101, and 108). It is assumed that the nucleus is at the position $(x = 0, y = 0, z = 0^+)$ infinitesimally above the origin, with the z-axis as the axis of the confining cones. First, the shapes of the families of cones are recognized to interpolate between circular cones and dihedral angles with the x-axis as their edge, as the parameter takes the successive values $\sigma = 60^\circ$, 45°, 30°, 15°, 0°, involving ellipses with increasing eccentricities from zero to 1. The apertures of the ellipses cover the range $-1 \leq \mathrm{sn}(\chi_{10}|\sigma) \leq 1$ going from the quasi-free atom lower limit to the maximum confinement upper limit; the intermediate value $\mathrm{sn}(\chi_{10} = 0|\sigma) = 0$ corresponds to the equatorial plane $z = 0$, which is the common shape of the cones for all values of σ, and corresponds to Levine's plane [40]. In particular, the quasi-free atom has its electron excluded from the negative z-axis for $\sigma = 60^\circ$, from increasing angles in the xz plane with negative z-axis as their bisector for $60^\circ > \sigma > 0^\circ$, and from the lower xz-half-plane for $\sigma = 0^\circ$. However, in the limit of maximum confinement, the electron is restricted to move inside a circular cone closing around the positive z-axis for $\sigma = 60^\circ$, inside decreasing angles in the xz-plane with the positive axis as their bisector for $60^\circ > \sigma > 0^\circ$, and inside the dihedral angle closing around the upper xz-half-plane for $\sigma = 0^\circ$.

The variations of the energy eigenvalues $E^{AB}_{n_r\lambda(n_1,n_2)}(\sigma, \mathrm{sn}(\chi_{10}|\sigma))$ depending on the shape and aperture parameters of the confining elliptical cones can be qualitatively described in parallel with the geometrical variations of the previous paragraph. Readers may also follow them quantitatively in Ref. [8]. In the quasi-free atom limit, the energies of the ground state for the maximum aperture of the cones $\mathrm{sn}(\chi_{10}|\sigma) = -1$ are lower for larger values of σ, as it can be appreciated by comparing the regions of exclusion of the electron of the negative z-axis and of the lower xz-plane and in between. As the aperture decreases and $\mathrm{sn}(\chi_{10}|\sigma)$ increases, all the levels have increasing energies. By the time that all cones become the equatorial plane $\mathrm{sn}(\chi_{10}|\sigma) = 0$, the eigenstates become those of the hydrogen atom with $(\ell - m)$ odd, including their Levine degeneracies [40]. For larger apertures $\mathrm{sn}(\chi_{10}|\sigma) > 0$, the order of some levels is reversed. In the limit of maximum confinement, the values of λ increase considerably, and so do those of ν, Eqs. (109), with the consequent

vanishing of the energies of all levels, which become infinitely degenerate at the ionization threshold. This is a signature of the hydrogen atom confined in semi-infinite spaces [9].

One of the consequences of the parity symmetry breaking effect in the hydrogen atom, because of its confinement in an elliptical cone, is that it acquires an electric dipole moment because the center of electric charge of the electron does not coincide with the position of the nucleus. Reference [8] contains its evaluation for the ground state, exhibiting its variations $\vec{d}(\sigma, \mathrm{sn}(\chi_{10}|\sigma))$ with the shape and aperture parameters of the confining cones. For the confining cones below the xz-plane, the magnitudes are such that

$$d\,(\mathrm{sn}(\chi_{10}|60^\circ) < 0) < d\,(\mathrm{sn}(\chi_{10}|60^\circ > \sigma > 0^\circ) < 0) < d\,(\mathrm{sn}(\chi_{10}|0^\circ) < 0);$$

for the equatorial plane $d(\mathrm{sn}(\chi_{10}|\sigma) = 0) = 3.75ea_0$ [40]; and for cones above the xz-plane

$$d\,(\mathrm{sn}(\chi_{10}|60^\circ) > 0) > d\,(\mathrm{sn}(\chi_{10}|60^\circ > \sigma > 0^\circ) > 0)) > d\,(\mathrm{sn}(\chi_{10}|0^\circ) > 0).$$

Another property of interest in the confined hydrogen atom is the pressure distribution on the walls of the confining surface. Reference [8] adapted the method introduced for the case of confinement by paraboloids [41] using Hirschfelder's work on the mechanical properties of quantum systems [42], for the specific case of confinement by elliptical cones. Table V and Figure 3 in Ref. [8] illustrate the variations of the pressure in different radial positions r and angular positions $\mathrm{sn}(\chi_2|\sigma)$ on the walls of some confining cones $\mathrm{sn}(\chi_{10}|\sigma)$.

3.4. Rotations of asymmetric molecules in semi-infinite spaces with elliptical cone boundaries

The early antecedent of the investigation presented in this section is Sommerfeld and Hartmann's work on the rotor constrained in a circular cone [43]. That work and also the hydrogen atom in the same situation of confinement [39] involve eigenfunctions described by Legendre functions vanishing at the circular cone boundaries

$$P_\lambda^m(\cos\theta = \cos\theta_0) = 0, \tag{110}$$

in which the angular momentum label λ is no longer an integer.

The rotations of asymmetric molecules confined by the two alternative families of spheroconal elliptical cone boundaries $\chi_1 = \chi_{10}$ and $\chi_2 = \chi_{20}$ is a richer problem compared with the previous ones. In fact, the boundary

conditions become

$$\Psi(\chi_1 = \chi_{10}, \chi_2) = 0 \quad \text{or} \quad \Lambda_{\lambda n_1}(\chi_1 = \chi_{10}) = 0, \tag{111}$$

$$\Psi(\chi_1, \chi_2 = \chi_{20}) = 0 \quad \text{or} \quad \Lambda_{\lambda n_2}(\chi_2 = \chi_{20}) = 0, \tag{112}$$

involving the angular momentum λ no longer integer and quasi-periodic Lamé functions. Although the investigations in Sections 3.2 and 3.3 for central potential systems can be limited to either of the Eqs. (111 and 112) leading to equivalent solutions because of the intrinsic rotational invariance of the system, for the asymmetric molecules, the eigenfunctions satisfying the respective boundary conditions are different and have different eigenenergies. Nevertheless, the mathematics involved is the same, as already developed and used in Sections 3.2 and 3.3. Obviously, the numerical implementation and the results are multiplied on account of the asymmetry distribution in the molecules. Section 3.4.1 reports original results on the eigenenergies $E^*(\sigma, \chi_{10})$ and $E^*(\sigma, \chi_{20})$ for the different eigenstates, with specific discussions on their similarities and differences, as well as compared with those of Sections 3.2 and 3.3.

The complete solutions, Eq. (43), of the eigenvalue Eqs. (68 and 69), are constructed by multiplying the matching Lamé functions in the respective coordinates introduced in Section 3.2. The matching covers the restrictions in the coordinate parameters, after Eq. (42), their relations with the asymmetry distribution parameters, Eq. (44), the relationships among the eigenvalues, Eqs. (106), with common values of λ and E^* and the species of Lamé functions according to Table 4.4.

For the symmetric molecules with $\sigma = 0^\circ$ ($k_1^2 = 0, k_2^2 = 1$) or $\sigma = 60^\circ$ ($k_1^2 = 1$, $k_2^2 = 0$), the confinement by the associated circular cones or dihedral angles is susceptible to a simple analysis of its eigenvalues and eigenfunctions, through Eqs. (92 and 93). In fact, for $k_i^2 = 0$, the argument χ_i becomes the meridian half-plane angular coordinate, and the eigenvalue equation admits $\sin n_f\varphi$ or $\sin \mu\varphi$ solutions with n_f integer in the nonconfined coordinate and $\mu = n_c\pi/\varphi_0$ in the confined coordinate, with the respective eigenvalues

$$h_f^B = -n_f^{B^2} \tag{113}$$

and

$$h_c^A = -\mu^2, \tag{114}$$

respectively. The corresponding matching eigenvalues for the eigenfunctions in the complementary coordinates are

$$h_c^A = -\lambda(\lambda + 1) + n_f^{B^2}, \tag{115}$$

for the confinement in circular cones, and

$$h_f^B = -\lambda(\lambda+1) + \mu^2, \tag{116}$$

for confinement in the dihedral angle. The eigenfunctions are the Legendre associated functions subject to the boundary condition in Eq. (110) with $m = n_f^B$, involving noninteger values of λ, coinciding with those of Sommerfeld and Hartmann [43], and the cones for the hydrogen atom in the same type of confinement [39]. For confinement in the dihedral angle, the eigenfunctions are associated Legendre polynomials of order μ and degree n_f^A [9], $P^{\mu}_{n_f^A+\mu}(\cos\theta_f)$, so that additionally, the eigenvalues become

$$\lambda = n_f^A + \mu, \quad h_f^B = -\lambda(2n_f^A+1) + {n_f^A}^2. \tag{117}$$

For the asymmetric molecules $0^\circ < \sigma < 60^\circ$, the eigenvalues and eigenfunctions associated with the respective elliptical-cone coordinates, interpolate between the above limiting cases.

3.4.1. Numerical results and discussion

This section contains an illustrative sample of numerical results, for chosen values of λ, of (1) the eigenvalues h_c^A and h_f^B of the matching Lamé functions as solutions of Eqs. (92) and (93) in the confining and free elliptical-cone coordinates, from Eqs. (94–97) and Eqs. (78–85), respectively, and evaluated from the diagonalization of the tetradiagonal matrices associated with the confined coordinate, and the corresponding tridiagonal matrices associated with the free coordinate, and (2) the energy eigenvalues E^* as evaluated from Eq. (106) for the ground state and successive excited states of the asymmetric molecules in the respective positions of the confining elliptical cones $\mathrm{sn}(\chi_{10}|\sigma)$ and $\mathrm{sn}(\chi_{20}|\sigma)$ determined by the boundary condition of Eqs. (111) and (112).

In fact, Table 4.5 reports the first eigenvalue h_c^1 and matching h_f^1 for the respective Lamé functions in the λ interval $(0, 5]$ and diminishing values $1 \geq k_c^2 \geq 0$ from left to right, corresponding to the confinement by elliptical cones of increasing eccentricities interpolating between circular cones and dihedral angles. The reader may check that $h_c^1 + h_f^1$ add up to $-\lambda(\lambda+1)$, as required by Eq. (106). While for circular cones $h_c^1 = -\lambda(\lambda+1)$ and $h_f^1 = 0$, on the left, as we move to the right in each row to elliptical cones with increasing eccentricities the ratio h_c^1/h_f^1 diminishes, until we arrive to the dihedral angles on the right in which $h_c^1 = -\lambda^2$ and $h_f^1 = -\lambda$. The empty spaces in the top and right corner of the table indicate that there are no matching values of h_c^1 and h_f^1 for chosen values of λ and confining elliptical cones.

Table 4.6 contains the corresponding information for the second eigenvalue h_c^1 and matching h_f^1 in the lambda interval $[2.5, 5]$. Again the matching

Table 4.5 First eigenvalue h_c^1 and matching h_f^1 of the respective Lamé functions as functions of angular momentum values λ for the successive families of elliptical cones $1 \geq k_c^2 \geq 0$

	$k_c^2 = 1$		$k_c^2 = 0.732050807$		$k_c^2 = 0.5$		$k_c^2 = 0.267949192$		$k_c^2 = 0$	
λ	h_c	h_f	h_c	h_f	h_c	h_f	h_c	h_f	h_c	h_f
$\to 0$	$\to 0^-$	0.0								
0.1	−0.11	0.0								
0.2	−0.24	0.0								
0.3	−0.39	0.0	−0.336112373	−0.053887626	−0.285747506	−0.104252493				
0.4	−0.56	0.0	−0.482871465	−0.077128534	−0.411333857	−0.148666142	−0.331391092	−0.228608907		
0.5	−0.75	0.0	−0.647074929	−0.102925070	−0.552434941	−0.197565058	−0.448100671	−0.301899328	−0.25	−0.5
0.6	−0.96	0.0	−0.828782218	−0.131217781	−0.709295760	−0.250704239	−0.579597706	−0.380402293	−0.36	−0.6
0.7	−1.19	0.0	−1.028058914	−0.161941085	−0.882184461	−0.307815538	−0.726593714	−0.463406285	−0.49	−0.7
0.8	−1.44	0.0	−1.244976626	−0.195023373	−0.107139035	−0.368609645	−0.889826260	−0.550173739	−0.64	−0.8
0.9	−1.71	0.0	−1.479612854	−0.230387145	−0.127722123	−0.432778763	−1.070037421	−0.639962578	−0.81	−0.9
1	−2	0.0	−1.732050807	−0.267949192	−1.5	−0.5	−1.267949192	−0.732050807	−1	−1
1.5	−3.75	0.0	−3.264543598	0.485456401	−2.879896763	−0.870103236	−2.544046410	−1.205953589	−2.25	−1.5
2	−6	0.0	−5.257252559	−0.742747440	−4.732050807	−1.267949192	−4.329049329	−1.670950670	−4	−2
2.5	−8.75	0.0	−7.724405344	−0.102559465	−7.084828627	−1.665171372	−6.631832145	−2.118167854	−6.25	−2.5
3	−12	0.0	−10.67940027	−1.320599720	−9.949489742	−2.050510257	−9.445574503	−2.554425496	−9	−3
3.5	−15.75	0.0	−14.13252839	−1.617471601	−13.32609001	−2.423909980	−12.76433282	−2.985667175	−12.25	−3.5
4	−20	0.0	−18.08991550	−1.910084499	−17.21110255	−2.788897449	−16.58512631	−3.414873682	−16	−4
4.5	−24.75	0.0	−22.55399937	−2.196000626	−21.60120130	−3.148798695	−20.90670758	−3.843292412	−20.25	−4.5
5	−30	0.0	−27.52484001	−2.475159987	−26.49414663	−3.505853361	−25.72859436	−4.271405637	−25	−5

Table 4.6 Second eigenvalue h_c^1 and matching h_f^1 of the respective Lamé functions as functions of angular momentum values λ for the successive families of elliptical cones $1 \geq k_c^2 \geq 0$

	$k_c^2 = 1$		$k_c^2 = 0.732050807$		$k_c^2 = 0.5$		$k_c^2 = 0.267949192$		$k_c^2 = 0$	
λ	h_c	h_f	h_c	h_f	h_c	h_f	h_c	h_f	h_c	h_f
2.5	−4.75	−4	−3.963048059	−4.786951940	−3.024057143	−5.725942856	−1.882189563	−6.867810436	−0.25	−8.5
3	−8	−4	−6.641107796	−5.358892203	−5.050510257	−6.949489742	−3.233917420	−8.766082579	−1	−11
3.5	−11.75	−4	−9.699163988	−6.050836011	−7.366414871	−8.383585128	−4.865445971	−10.88455402	−2.25	−13.5
4	−16	−4	−13.13622696	−6.863773031	−10	−10	−6.863773031	−13.13622696	−4	−16
4.5	−20.75	−4	−16.95594558	−7.794054416	−12.98661903	−11.76338096	−9.323145779	−15.42685422	−6.25	−18.5
5	−26	−4	−21.16549569	−8.834504306	−16.36878388	−13.63121611	−12.30988140	−17.69011859	−9	−21

condition of Eq. (106) can be verified in the pairs of entries in each row. Now, for the circular cones $h_c^1 = -\lambda(\lambda+1)+4$, $h_f^1 = -4$, for the elliptical cones with increasing eccentricities, the ratio h_c^1/h_f^1 diminishes more noticeably than in Table 4.5 as we move to the right in each row, and for the dihedral angle $h_c^1 = -(\lambda-2)^2$, $h_f^1 = -5\lambda+4$. Similar behaviors can be recognized in the successive Tables 4.7–4.9. Indeed in Tables 4.7 and 4.8 sharing the common λ interval $[1.5, 5]$ and the common entries on the left for circular cones $h_c^c = -\lambda(\lambda+1)+1$, $h_f^c = -1$, and $h_c^d = -\lambda(\lambda+1)+1$, $h_f^s = -1$, their entries for dihedral angles on the right differ in their values $h_c^c = -\lambda^2$, $h_c^c = -\lambda$, versus $h_c^d = -(\lambda-1)^2$, $h_f^s = -3\lambda+1$. The reader may also follow the changes of the respective ratios h_c^c/h_f^c and h_c^d/h_f^s for the elliptical cones with increasing eccentricities when moving from left to right on each row. However, Table 4.9 shares the same λ interval $[2.5, 5]$ and entries in the left columns for circular cones with $h_c^{dc} = -\lambda(\lambda+1)+4$, $h_f^{sc} = -4$ with Table 4.6, and they differ in the dihedral angle entries on the right with $h_c^{dc} = -(\lambda-1)^2$, $h_f^{sc} = -3\lambda+1$. In general, the reader can check that the regularities described in this paragraph follow from Eqs. (113–116, and 117).

From the diagonalization of the tetradiagonal matrices of Eqs. (43–46) in Ref. [1], the eigenvectors of the expansion coefficients b_N^A in the Lamé functions of Eqs. (94–97) are also obtained. The next step is to determine their respective zeros $\mathrm{sn}(\chi_{c0}|k_c^2)$ guaranteeing that the boundary condition of Eq. (111) or (112) is satisfied for the corresponding position of the confining elliptical cone. The eigenvectors a_N^A in the periodic Lamé functions of Eqs. (78–85) are also obtained from the diagonalization of the associated tridiagonal matrices.

The energy eigenvalues follow from Eq. (106) with the previously evaluated h_c^A and h_f^B Lamé eigenvalues of Tables 4.5–4.9. Correspondingly Tables 4.10 and 4.11 illustrate the numerical values of the energy eigenvalues $E^*_{n_1^A n_2^B}(\chi_{10}, \sigma)$ and $E^*_{n_2^B n_1^A}(\chi_{20}, \sigma)$ for the ground state $n_1^1 = n_2^1 = 0$ and other values for the excited states, respectively, as functions of λ for the molecules with different asymmetry distributions $60^\circ \geq \sigma \geq 0^\circ$ confined by the complementary families of confining elliptical cones with their respective positions $\mathrm{sn}(\chi_{10}|\sigma)$ and $\mathrm{sn}(\chi_{20}|\sigma)$.

First, we describe the variations of the energy eigenvalues of the ground state and the positions of the confining elliptical cones $E^*_{0^1 0^1}(\chi_{10}, \sigma)$ and $E^*_{0^1 0^1}(\chi_{20}, \sigma)$ as reported in Table 4.10 for the increasing values of $0 < \lambda \leq 5$. The molecule is assumed to be at the origin $(x = 0^+, y = 0, z = 0^+)$. Let us start with the left-column entries for $\sigma = 60^\circ$ $(e_1 = \frac{1}{2}, e_2 = \frac{1}{2}, e_3 = -1)$ symmetric oblate molecules invariant under rotations around the z-axis in the two situations of confinement by circular cones $\mathrm{sn}(\chi_{10}|60^\circ)$ and dihedral angles $\mathrm{sn}(\chi_{20}|60^\circ)$, respectively. The upper entries cover the intervals $0 < E_1^* < 7.5$ and $-1 < \mathrm{sn}(\chi_{10}|60^\circ) < 1$ from the quasi-free molecule limit excluding the system from the negative z-axis, slowly increasing energies

Table 4.7 First eigenvalue h_c^c and matching h_f^c of the respective Lamé functions as functions of angular momentum values λ for the successive families of elliptical cones $1 \geq k_c^2 \geq 0$

	$k_c^2 = 1$		$k_c^2 = 0.732050807$		$k_c^2 = 0.5$		$k_c^2 = 0.267949192$		$k_c^2 = 0$	
λ	h_c	h_f	h_c	h_f	h_c	h_f	h_c	h_f	h_c	h_f
1.5	−2.75	−1	−2.630300448	−1.119699551	−2.521550253	−1.228449746	−2.405432781	−1.344567218	−2.25	−1.5
2	−5	−1	−4.732050807	−1.267949192	−4.5	−1.5	−4.267949192	−1.732050807	−4	−2
2.5	−7.75	−1	−7.308915620	−1.441084379	−6.947076201	−1.802923798	−6.607596025	−2.142403974	−6.25	−2.5
3	−11	−1	−10.36479261	−1.635207380	−9.872983346	−2.127016653	−9.436589388	−2.563410611	−9	−3
3.5	−14.75	−1	−13.90355152	−1.846448472	−13.28560292	−2.464397075	−12.76115077	−2.988849229	−12.25	−3.5
4	−19	−1	−17.92880708	−2.071192918	−17.19041575	−2.809584240	−16.58403594	−3.415964058	−16	−4
4.5	−23.75	−1	−22.44375332	−2.306246679	−21.59090529	−3.159094700	−20.90634314	−3.843656855	−20.25	−4.5
5	−29	−1	−27.45107218	−2.548927817	−26.48912529	−3.510874706	−25.72847490	−4.271525094	−25	−5

Table 4.8 First eigenvalue h_c^d and matching h_f^s of the respective Lamé functions as functions of angular momentum values λ for the successive families of elliptical cones $1 \geq k_c^2 \geq 0$

	$k_c^2 = 1$		$k_c^2 = 0.732050807$		$k_c^2 = 0.5$		$k_c^2 = 0.267949192$		$k_c^2 = 0$	
λ	h_c	h_f	h_c	h_f	h_c	h_f	h_c	h_f	h_c	h_f
1.5	−2.75	−1	−2.127708493	−1.622291506	−1.582350663	−2.167649336	−1.024276187	−2.725723812	−0.25	−3.5
2	−5	−1	−3.928203230	−2.071796769	−3	−3	−2.071796769	−3.928203230	−1	−5
2.5	−7.75	−1	−6.138681537	−2.611318462	−4.777572575	−3.972427424	−3.487043983	−5.262956016	−2.25	−6.5
3	−11	−1	−8.766082579	−3.233917420	−6.949489742	−5.050510257	−5.358892204	−6.641107795	−4	−8
3.5	−14.75	−1	−11.81946675	−3.930533243	−9.558122235	−6.191877764	−7.748158236	−8.001841763	−6.25	−9.5
4	−19	−1	−15.31024264	−4.689757357	−12.64575131	−7.354248688	−10.66922649	−9.330773508	−9	−11
4.5	−23.75	−1	−19.25208253	−5.497917463	−16.24297610	−8.507023891	−14.11291300	−10.63708699	−12.25	−12.5
5	−29	−1	−23.66025403	−6.339745962	−20.36293051	−9.637069481	−18.06855744	−11.93144255	−16	−14

Table 4.9 First eigenvalue h_c^{dc} and matching h_f^{sc} of the respective Lamé functions as functions of angular momentum values λ for the successive families of elliptical cones $1 \geq k_c^2 \geq 0$

	$k_c^2 = 1$		$k_c^2 = 0.732050807$		$k_c^2 = 0.5$		$k_c^2 = 0.267949192$		$k_c^2 = 0$	
λ	h_c	h_f	h_c	h_f	h_c	h_f	h_c	h_f	h_c	h_f
2.5	−4.75	− 4	−4.109745588	−4.640254411	−3.546675294	−5.203324705	−2.969444443	−5.780555556	−2.25	−6.5
3	−8	− 4	−6.928203230	−5.071796769	−6	−6	−5.071796769	−6.928203230	−4	−8
3.5	−11.75	− 4	−10.19157680	−5.558423192	−8.875812187	−6.874187812	−7.609004833	−8.140995166	−6.25	−9.5
4	−16	− 4	−13.90454401	−6.095455982	−12.19041575	−7.809584240	−10.60829900	−9.391700994	−9	−11
4.5	−20.75	− 4	−18.07220773	−6.677792260	−15.95933207	−8.790667928	−14.08808045	−10.66191954	−12.25	−12.5
5	−26	− 4	−22.69996090	−7.300039091	−20.19615242	−9.803847577	−18.05894475	−11.94105524	−16	−14

Table 4.10 Table of energy eigenvalues, E_1^* and E_2^*, for the respective positions, $\mathrm{sn}(\chi_{10}|\sigma)$ and $\mathrm{sn}(\chi_{20}|\sigma)$, of the confining boundaries for the ground state of the successive asymmetric molecules $60^\circ \geq \sigma \geq 0^\circ$

			$\sigma = 60^\circ$		$\sigma = 45^\circ$		$\sigma = 30^\circ$		$\sigma = 15^\circ$		$\sigma = 0^\circ$	
			E_1^*	$\mathrm{sn}(\chi_{10}\|\sigma)$	E_1^*	$\mathrm{sn}(\chi_{10}\|\sigma)$	E_1^*	$\mathrm{sn}(\chi_{10}\|\sigma)$	E_1^*	$\mathrm{sn}(\chi_{10}\|\sigma)$	E_1^*	$\mathrm{sn}(\chi_{10}\|\sigma)$
n_c^A	n_f^B	λ	E_2^*	$\mathrm{sn}(\chi_{20}\|\sigma)$	E_2^*	$\mathrm{sn}(\chi_{20}\|\sigma)$	E_2^*	$\mathrm{sn}(\chi_{20}\|\sigma)$	E_2^*	$\mathrm{sn}(\chi_{20}\|\sigma)$	E_2^*	$\mathrm{sn}(\chi_{20}\|\sigma)$
0^1	0^1	$\to 0$	$\to 0^+$	$\to -1^+$								
0^1	0^1										$\to 0^-$	$\to -1^+$
		0.1	0.0275	−0.999906976								
											−0.0275	−0.999906976
		0.2	0.06	−0.985274627								
											−0.06	−0.985274627
		0.3	0.0975	−0.916431613	0.092807943	−0.973150793	0.078589646	−0.9999666195				
							−0.078589646	−0.9999666195	−0.092807943	−0.973150793	−0.0975	−0.916431613
		0.4	0.14	−0.796957609	0.133470622	−0.855037074	0.113738457	−0.913212272	0.079224097	−0.974767243		
					−0.079224097	−0.974767243	−0.113738457	−0.913212272	−0.133470622	−0.855037074	−0.14	−0.796957609
		0.5	0.1875	−0.652229531	0.179066543	−0.701678296	0.153663166	−0.757287892	0.109678432	−0.833768778	0.0	−1
			0.0	−1	−0.109678432	−0.833768778	−0.153663166	−0.757287892	−0.179066543	−0.701678296	−0.1875	−0.652229531
		0.6	0.24	−0.502236678	0.229645441	−0.540800620	0.198575953	−0.585675586	0.145431679	−0.651477301	0.03	−0.866025403
			−0.03	−0.866025403	−0.145431679	−0.651477301	−0.198575953	−0.585675586	−0.229645441	−0.540800620	−0.24	−0.502236678
		0.7	0.2975	−0.358314457	0.285262176	−0.385914744	0.248709039	−0.418295992	0.187078931	−0.466440018	0.07	−0.623489801
			−0.07	−0.623489801	−0.187078931	−0.466440018	−0.248709039	−0.418295992	−0.285262176	−0.385914744	−0.2975	−0.358314457
		0.8	0.36	−0.225741316	0.345976650	−0.243106520	0.304312973	−0.263405573	0.235237288	−0.293357797	0.12	−0.382683432
			−0.12	−0.382683432	−0.235237288	−0.293357797	−0.304312973	−0.263405573	−0.345976650	−0.243106520	−0.36	−0.225741316
		0.9	0.4275	−0.106309837	0.411853694	−0.114455616	0.365654317	−0.123878442	0.290527482	−0.137512007	0.18	−0.173648177
			−0.18	−0.173648177	−0.290527482	−0.137512007	−0.365654317	−0.123878442	−0.411853694	−0.114455616	−0.4275	−0.106309837

1	0.5	0.0	0.482962913	0.0	0.433012701	0.0	0.353553390	0.0	0.25	0.0
	−0.25	0.0	−0.353553390	0.0	−0.433012701	0.0	−0.482962913	0.0	−0.5	0.0
1.5	0.9375	0.372342908	0.919733020	0.399471690	0.870266125	0.426849829	0.802311084	0.458159450	0.75	0.5
	−0.75	0.5	−0.802311084	0.458159450	−0.870266125	0.426849829	−0.919733020	0.399471690	−0.9375	0.372342908
2	1.5	0.577350269	1.5	0.616787519	1.5	0.650115167	1.5	0.679702285	1.5	0.707106781
	−1.5	0.707106781	−1.5	0.679702285	−1.5	0.650115167	−1.5	0.616787519	−1.5	0.577350269
2.5	2.1875	0.698270708	2.235665517	0.742236912	2.346780431	0.772153705	2.454043546	0.793164389	2.5	0.809016994
	−2.5	0.809016994	−2.454043546	0.793164389	−2.346780431	0.772153705	−2.235665517	0.742236912	−2.1875	0.698270708
3	3.0	0.774596669	3.137937490	0.818895387	3.420358449	0.842675531	3.658736383	0.856568346	3.75	0.866025403
	−3.75	0.866025403	−3.658736383	0.856568346	−3.420358449	0.842675531	−3.137937490	0.818895387	−3.0	0.774596669
3.5	3.9375	0.825549012	4.215424536	0.867934044	4.720782434	0.885825812	5.109106612	0.895006230	5.25	0.900968867
	−5.25	0.900968867	−5.109106612	0.895006230	−4.720782434	0.885825812	−4.215424536	0.867934044	−3.9375	0.825549012
4	5.0	0.861136311	5.473250986	0.900514202	6.244997998	0.913700362	6.802660752	0.919917063	7.0	0.923879532
	−7.0	0.923879532	−6.802660752	0.919917063	−6.244997998	0.913700362	−5.473250986	0.900514202	−5.0	0.861136311
4.5	6.1875	0.886922240	6.913456090	0.922891659	7.990124710	0.932595140	8.738355336	0.936938999	9.0	0.939692620
	−9.0	0.939692620	−8.738355336	0.936938999	−7.990124710	0.932595140	−6.913456090	0.922891659	−6.1875	0.886922240
5	7.5	0.906179845	8.536090033	0.938735129	9.954222983	0.945939809	10.91578693	0.949070763	11.25	0.951056516
	−11.25	0.951056516	−10.91578693	0.949070763	−9.954222983	0.945939809	−8.536090033	0.938735129	−7.5	0.906179845

Table 4.11 Table of energy eigenvalues E_1^* and E_2^* versus positions of the confining elliptical cones, $\mathrm{sn}(\chi_{10}|\sigma)$ and $\mathrm{sn}(\chi_{20}|\sigma)$, respectively, for the successive excited states of asymmetric molecules $60^\circ \geq \sigma \geq 0^\circ$

			$\sigma = 60^\circ$		$\sigma = 45^\circ$		$\sigma = 30^\circ$		$\sigma = 15^\circ$		$\sigma = 0^\circ$	
n_c^A	n_f^B	λ	E_1^* E_2^*	$\mathrm{sn}(\chi_{10}\|\sigma)$ $\mathrm{sn}(\chi_{20}\|\sigma)$	E_1^* E_2^*	$\mathrm{sn}(\chi_{10}\|\sigma)$ $\mathrm{sn}(\chi_{20}\|\sigma)$	E_1^* E_2^*	$\mathrm{sn}(\chi_{10}\|\sigma)$ $\mathrm{sn}(\chi_{20}\|\sigma)$	E_1^* E_2^*	$\mathrm{sn}(\chi_{10}\|\sigma)$ $\mathrm{sn}(\chi_{20}\|\sigma)$	E_1^* E_2^*	$\mathrm{sn}(\chi_{10}\|\sigma)$ $\mathrm{sn}(\chi_{20}\|\sigma)$
1^1	0^1	1.5	0.9375	−0.903776130	0.919733020	−0.957844724	0.870266125	−0.987158646	0.802311084	−0.998368542	0.75	−1
0^1	1^1		−0.75	−1	−0.802311084	−0.998368542	−0.870266125	−0.987158646	−0.919733020	−0.957844724	−0.9375	−0.903776130
		2	1.5	−0.577350269	1.5	−0.616787519	1.5	−0.650115167	1.5	−0.679702285	1.5	−0.707106781
			−1.5	−0.707106781	−1.5	−0.679702285	−1.5	−0.650115167	−1.5	−0.616787519	−1.5	−0.577350269
		2.5	2.1875	−0.255466238	2.235665517	−0.272228853	2.346780431	−0.285278981	2.454043546	−0.296724240	2.5	−0.309016994
			−2.5	−0.309016994	−2.454043546	−0.296724240	−2.346780431	−0.285278981	−2.235665517	−0.272228853	−2.1875	−0.255466238
		3	3.0	0.0	3.137937490	0.0	3.420358449	0.0	3.658736383	0.0	3.75	0.0
			−3.75	0.0	−3.658736383	0.0	−3.420358449	0.0	−3.137937490	0.0	−3.0	0.0
		3.5	3.9375	0.193626778	4.215424536	0.204648448	4.720782434	0.211331392	5.109106612	0.216766598	5.25	0.222520933
			−5.25	0.222520933	−5.109106612	0.216766598	−4.720782434	0.211331392	−4.215424536	0.204648448	−3.9375	0.193626778
		4	5.0	0.339981043	5.473250986	0.357786920	6.244997998	0.367415487	6.802660752	0.375006209	7.0	0.382683432
			−7.0	0.382683432	−6.802660752	0.375006209	−6.244997998	0.367415487	−5.473250986	0.357786920	−5.0	0.339981043
		4.5	6.1875	0.451789833	6.913456090	0.473495760	7.990124710	0.484099967	8.738355336	0.492199252	9.0	0.5
			−9.0	0.5	−8.738355336	0.492199252	−7.990124710	0.484099967	−0.451789833	0.473495760	−4.5	0.451789833
		5	7.5	0.538469310	8.536090033	0.562187138	9.954222983	0.572774363	10.91578693	0.580594195	11.25	0.587785252
			−11.25	0.587785252	−10.91578693	0.580594195	−9.954222983	0.572774363	−8.536090033	0.562187138	−7.5	0.538469310
0^d	1^s	1.5	0.1875	−0.419443051	−0.031248079	−0.469729143	−0.253441759	−0.533574063	−0.469001484	−0.638522998	−0.75	−1
1^s	0^d		0.75	−1	0.469001484	−0.638522998	0.253441759	−0.533574063	0.031248079	−0.469729143	−0.1875	−0.419443051
		2	0.75	0.0	0.388228567	0.0	0.0	0.0	−0.388228567	0.0	−0.75	0.0
			−0.75	0.0	−0.388228567	0.0	0.0	0.0	0.388228567	0.0	0.75	0.0
		2.5	1.4375	0.269702885	0.909181699	0.301531586	0.348638076	0.339924904	−0.176623024	0.395686832	−0.5	0.5
			0.5	0.5	0.176623024	0.395686832	−0.348638076	0.339924904	−0.909181699	0.301531586	−1.4375	0.269702885
		3	2.25	0.447213595	1.537416039	0.498939888	0.822282237	0.556868073	0.240160011	0.626781082	0.0	0.707106781
			0.0	0.707106781	−0.240160011	0.626781082	−0.822282237	0.556868073	−1.537416039	0.498939888	−2.25	0.447213595

		3.5	3.1875	0.568586940	2.280510761	0.632655791	1.457626613	0.697235557	0.912994787	0.758908841	0.75	0.809016994
			−0.75	0.809016994	−0.912994787	0.758908841	−1.457626613	0.697235557	−2.280510761	0.632655791	−3.1875	0.568586940
		4	4.25	0.654653670	3.148009322	0.726048414	2.291287847	0.788692290	1.853914096	0.835393915	1.75	0.866025403
			−1.75	0.866025403	−1.853914096	0.835393915	−2.291287847	0.788692290	−3.148009322	0.726048414	−4.25	0.654653670
		4.5	5.4375	0.717658320	4.151348822	0.792855660	3.349765571	0.848533226	3.055235401	0.881606386	3.0	0.900968867
			−3.0	0.900968867	−3.055235401	0.881606386	−3.349765571	0.848533226	−4.151348822	0.792855660	−5.4375	0.717658320
		5	6.75	0.765055323	5.303300858	0.841466140	4.644434068	0.888083683	4.508041166	0.911074757	4.5	0.923879532
			−4.5	0.923879532	−4.508041166	0.911074757	−4.644434068	0.888083683	−5.303300858	0.841466140	−6.75	0.765055323
0^c	1^c	1.5	0.1875	−0.419443051	0.389178284	−0.434617873	0.559928944	−0.450078620	0.686358524	−0.468879397	0.75	−0.5
1^c	0^c		−0.75	−0.5	−0.686358524	−0.468879397	−0.559928944	−0.450078620	−0.389178284	−0.434617873	−0.1875	−0.419443051
		2	0.75	0.0	1.060660171	0.0	1.299038105	0.0	1.448888739	0.0	1.5	0.0
			−1.5	0.0	1.448888739	0.0	−1.299038105	0.0	−1.060660171	0.0	−0.75	0.0
		2.5	1.4375	0.269702885	1.888101588	0.279096322	2.227483330	0.287847589	2.433769635	0.297230671	2.5	0.309016994
			−2.5	0.309016994	−2.433769635	0.297230671	−2.227483330	0.287847589	−1.888101588	0.279096322	−1.4375	0.269702885
		3	2.25	0.447213595	2.874763053	0.462131865	3.354101966	0.474766606	3.651220188	0.486890769	3.75	0.5
			−3.75	0.5	−3.651220188	0.486890769	−3.354101966	0.474766606	−2.874763053	0.462131865	−2.25	0.447213595
		3.5	3.1875	0.568586940	4.023881650	0.586620303	4.685719582	0.600337994	5.106444772	0.612140725	5.25	0.623489801
			−5.25	0.623489801	−5.106444772	0.612140725	−4.685719582	0.600337994	−4.023881650	0.586620303	−3.1875	0.568586940
		4	4.25	0.654653670	5.338481167	0.674282715	6.227082711	0.687602900	6.801748634	0.697974016	7.0	0.707106781
			−7.0	0.707106781	−6.801748634	0.697974016	−6.227082711	0.687602900	−5.338481167	0.674282715	−4.25	0.654653670
		4.5	5.4375	0.717658320	6.821233469	0.737909686	7.981208108	0.750131786	8.738050474	0.758849549	9.0	0.766044443
			−9.0	0.766044443	−8.738050474	0.758849549	−7.981208108	0.750131786	−6.821233469	0.737909686	−5.4375	0.717658320
		5	6.75	0.765055323	8.474382041	0.785301918	9.949874371	0.796166307	10.91568701	0.803357689	11.25	0.809016994
			−11.25	0.809016994	−10.91568701	0.803357689	−9.949874371	0.796166307	−8.474382041	0.785301918	−6.75	0.765055323
2^1	0^1	2.5	2.1875	−0.956364707	2.235665517	−0.994443960	2.346780431	−0.999636813	2.454043546	−0.999916274	2.5	−1
0^1	2^1		−2.5	−1	−2.235665517	−0.999916274	−2.346780431	−0.999636813	−2.235665517	−0.994443960	−2.1875	−0.956364707
		3	3.0	−0.774596669	3.137937490	−0.818895386	3.420358449	−0.842675531	3.658736383	−0.856568346	3.75	−0.866025403
			−3.75	−0.866025403	−3.658736383	−0.856568346	−3.420358449	−0.842675531	−3.137937490	−0.818895386	−3.0	−0.774596669
		3.5	3.9375	−0.551448547	4.215424536	−0.582214507	4.720782434	−0.599512329	5.109106612	−0.612073618	5.25	−0.623489801
			−5.25	−0.623489801	−5.109106612	−0.612073618	−4.720782434	−0.599512329	−4.215424536	−0.582214507	−3.9375	−0.551448547

(*Continued*)

Table 4.11 (*Continued*)

			$\sigma = 60^\circ$		$\sigma = 45^\circ$		$\sigma = 30^\circ$		$\sigma = 15^\circ$		$\sigma = 0^\circ$	
n_c^A	n_f^B	λ	$\frac{E_1^*}{E_2^*}$	$\frac{\mathrm{sn}(\chi_{10}\|\sigma)}{\mathrm{sn}(\chi_{20}\|\sigma)}$	$\frac{E_1^*}{E_2^*}$	$\frac{\mathrm{sn}(\chi_{10}\|\sigma)}{\mathrm{sn}(\chi_{20}\|\sigma)}$	$\frac{E_1^*}{E_2^*}$	$\frac{\mathrm{sn}(\chi_{10}\|\sigma)}{\mathrm{sn}(\chi_{20}\|\sigma)}$	$\frac{E_1^*}{E_2^*}$	$\frac{\mathrm{sn}(\chi_{10}\|\sigma)}{\mathrm{sn}(\chi_{20}\|\sigma)}$	$\frac{E_1^*}{E_2^*}$	$\frac{\mathrm{sn}(\chi_{10}\|\sigma)}{\mathrm{sn}(\chi_{20}\|\sigma)}$
		4	5.0	−0.339981043	5.473250986	−0.357786920	6.244997998	−0.367415487	6.802660752	−0.375006209	7.0	−0.382683432
			−7.0	−0.382683432	6.802660752	−0.375006209	−6.244997998	−0.367415487	−5.473250986	−0.357786920	−5.0	−0.339981043
		4.5	6.1875	−0.155672711	6.9134560902	−0.163246711	7.990124710	−0.167140948	8.738355336	−0.170319359	9.0	−0.173648177
			−9.0	−0.173648177	−7.990124710	−0.170319359	−7.990124710	−0.167140948	−6.9134560902	−0.163246711	−6.1875	−0.155672711
		5	7.5	0.0	8.536090033	0.0	9.954222983	0.0	10.915786939	0.0	11.25	0.0
			−11.25	0.0	−10.915786939	0.0	−9.954222983	0.0	−8.536090033	0.0	−7.5	0.0
1^d	1^s	2.5	1.4375	−0.736331247	0.909181699	−0.819793782	0.348638076	−0.904939760	−0.176623024	−0.978590760	−0.5	−1
1^s	1^d		0.5	−1	0.176623024	−0.978590760	−0.348638076	−0.904939760	−0.909181699	−0.819793782	−1.4375	−0.736331247
		3	2.25	−0.447213595	1.537416039	−0.498939888	0.822282237	−0.556868073	0.240160011	−0.626781082	0.0	−0.707106781
			0.0	−0.707106781	−0.240160011	−0.626781082	−0.822282237	−0.556868073	−1.537416039	−0.498939888	−2.25	−0.447213595
		3.5	3.1875	−0.199684372	2.280510761	−0.222542889	1.457626613	−0.247089818	0.912994787	−0.274746628	0.75	−0.309016994
			−0.75	−0.309016994	−0.912994787	−0.274746628	−1.457626613	−0.247089818	−2.280510761	−0.222542889	−3.1875	−0.199684372
		4	4.25	0.0	3.148009322	0.0	2.291287847	0.0	1.853914096	0.0	1.75	0.0
			−1.75	0.0	−1.853914096	0.0	−2.291287847	0.0	−3.148009322	0.0	−4.25	0.0
		4.5	5.4375	0.158787692	4.151348822	0.176143637	3.349765571	0.191765703	3.055235401	0.206147948	3.0	0.222520933
			−3.0	0.222520933	−3.055235401	0.206147948	−3.349765571	0.191765703	−4.151348822	0.176143637	−5.4375	0.158787692
		5	6.75	0.285231516	5.303300858	0.315411866	4.644434067	0.339744318	4.508041166	0.360478745	4.5	0.382683432
			−4.5	0.382683432	−4.508041166	0.360478745	−4.644434067	0.339744318	−5.303300858	0.315411866	−6.75	0.285231516
1^c	1^c	2.5	1.4375	−0.736331247	1.888101588	−0.759967778	2.227483330	−0.778345570	2.433769635	−0.794265787	2.5	−0.809016994
1^c	1^c		−2.5	−0.809016994	−2.433769635	−0.794265787	−2.227483330	−0.778345570	−1.888101588	−0.759967778	−1.4375	−0.736331247
		3	2.25	−0.447213595	2.874763053	−0.462131865	3.354101966	−0.474766606	3.651220188	−0.486890769	3.75	−0.5
			−3.75	−0.5	−3.651220188	−0.486890769	−3.354101966	−0.474766606	−2.874763053	−0.462131865	−2.25	−0.447213595
		3.5	3.1875	−0.199684372	4.023881650	−0.206233368	4.685719582	−0.211638027	5.106444772	−0.216792669	5.25	−0.222520933
			−5.25	−0.222520933	−5.106444772	−0.216792669	−4.685719582	−0.211638027	−4.023881650	−0.206233368	−3.1875	−0.199684372
		4	4.25	0.0	5.338481167	0.0	6.227082711	0.0	6.801748634	0.0	7.0	0.0
			−7.0	0.0	−6.801748634	0.0	−6.227082711	0.0	−5.338481167	0.0	−4.25	0.0

		4.5	5.4375	0.158787692	6.821233469	0.163633069	7.981208108	0.167179637	8.738050474	0.170320812	9.0	0.173648177
			−9.0	0.173648177	−8.738050474	0.170320812	−7.981208108	0.167179637	−6.821233469	0.163633069	−5.4375	0.158787692
		5	6.75	0.285231516	8.474382041	0.293559503	9.949874371	2.992486165	10.915687010	0.304082431	11.25	0.309016994
			−11.25	0.309016994	−10.915687010	0.304082431	−9.949874371	2.992486165	−8.474382041	0.293559503	−6.75	0.285231516
0^1	2^1	2.5	−0.8125	−0.331861432	−0.910771175	−0.362206548	−1.169950832	−0.410180944	−1.519109911	−0.505036522	−2.0	−1
2^1	0^1		2.0	−1	1.519109911	−0.505036522	1.169950832	−0.410180944	0.910771175	−0.362206548	0.8125	−0.331861432
		3	0.0	0.0	−0.240160011	0.0	−0.822282237	0.0	−1.537416039	0.0	−2.25	0.0
			2.25	0.0	1.537416039	0.0	0.822282237	0.0	0.240160011	0.0	0.0	0.0
		3.5	0.9375	0.221852139	0.506842927	0.243742713	−0.440447641	0.278282258	−1.498441022	0.339203149	−2.25	0.5
			2.25	0.5	1.498441022	0.339203149	0.440447641	0.278282258	−0.506842927	0.243742713	−0.9375	0.221852139
		4	2.0	0.377964473	1.329409766	0.416399032	0.0	0.474766606	−1.329409766	0.565687027	−2.0	0.707106781
			2.0	0.707106781	1.329409766	0.565687027	0.0	−0.474766606	−1.329409766	0.416399032	−2.0	0.377964473
		4.5	3.1875	0.491843740	2.230592825	0.543064297	0.529677622	0.616455952	−0.951482970	0.712621225	−1.5	0.809016994
			1.5	0.809016994	0.951482970	0.712621225	−0.529677622	0.616455952	−2.230592825	0.543064297	−3.1875	0.491843740
		5	4.5	0.577350269	3.216394830	0.638502612	1.185401612	0.719488320	−0.309185221	0.804834735	−0.75	0.866025403
			0.75	0.866025403	0.309185221	0.804834735	−1.185401612	0.719488320	−3.216394830	0.638502612	−4.5	0.577350269
0^{dc}	2^{sc}	2.5	−0.8125	−0.331861432	−0.788056301	−0.356968138	−0.717350237	−0.385038412	−0.609603477	−0.423202332	−0.5	−0.5
2^{sc}	0^{dc}		0.5	−0.5	0.609603477	−0.423202332	0.717350237	−0.385038412	0.788056301	−0.356968138	0.8125	−0.331861432
		3	0.0	0.0	0.0	0.0	0.0	0.0	0.0	0.0	0.0	0.0
		3	0.0	0.0	0.0	0.0	0.0	0.0	0.0	0.0	0.0	0.0
		3.5	0.9375	0.221852139	0.918754277	0.238295992	0.866728779	0.255681178	0.796590696	0.277072140	0.75	0.309016994
			−0.75	0.309016994	−0.796590696	0.277072140	−0.866728779	0.255681178	−0.918754277	0.238295992	−0.9375	0.221852139
		4	2.0	0.377964473	1.972119503	0.405345379	1.896955692	0.432531458	1.802947261	0.462736147	1.75	0.5
			−1.75	0.5	−1.802947261	0.462736147	−1.896955692	0.432531458	−1.972119503	0.405345379	−2.0	0.377964473
		4.5	3.1875	0.491843740	3.164364318	0.526510845	3.104122629	0.558429902	3.034462570	0.590147847	3.0	0.623489801
			−3.0	0.623489801	−3.034462570	0.590147847	−3.104122629	0.558429902	−3.164364318	0.526510845	−3.1875	0.491843740
		5	4.5	0.577350269	4.5	0.616787519	4.5	0.650115167	4.5	0.679702285	4.5	0.707106781
			−4.5	0.707106781	−4.5	0.679702285	−4.5	0.650115167	−4.5	0.616787519	−4.5	0.577350269

$0 < E_1^* \leq 0.5$ for cones in the $z < 0$ hemisphere $-1 < \mathrm{sn}(\chi_{10}|60^\circ) \leq 0$ up to the equatorial plane $z = 0$; and faster increasing energies $0.5 < E_1^* \leq 7.5$ for cones in the $z > 0$ hemisphere $0 < \mathrm{sn}(\chi_{10}|60^\circ) \leq 0.906179845$, including their asymptotic extrapolations $E^* \to \infty$ as the cone closes around the positive z axis $\mathrm{sn}(\chi_{10}|60^\circ) \to 1$. The lower entries cover the interval $0 \geq E_2^* \geq -11.25$ and $-1 \leq \mathrm{sn}(\chi_{20}|60^\circ) \leq 0.951056516$, going from the limit in which the molecule is excluded from the half plane ($-\infty < x < 0$, $y = 0, -\infty < z < \infty$), slowly decreasing energies $0 \geq E_2^* \geq -0.25$ and $-1 \leq \mathrm{sn}(\chi_{20}|60^\circ) \leq 0$ for excluded dihedral angles up to the $x = 0$ plane, faster decreasing energies $-0.25 \geq E_2^* \geq -11.25$ for closing dihedral angles $0 \leq \mathrm{sn}(\chi_{20}|60^\circ) \leq 0.951056516$, including their asymptotic extrapolations $E_2^* \to -\infty$ and $\mathrm{sn}(\chi_{20}|60^\circ) \to 1$, when the dihedral angle closes around the half plane ($0 < x < \infty, y = 0, -\infty < z < \infty$). The difference in signs of E_1^* and E_2^* can be understood from Eq. (106) as a result of the combination of the values e_1, e_2, e_3 and the exchange $h_1 = h_c$, $h_2 = h_f$ to $h_1 = h_f$, $h_2 = h_c$ when going from circular cones to dihedral angles. Next, let us move to the right-column entries for $\sigma = 0^\circ$ ($e_1 = 1, e_2 = -\frac{1}{2}, e_3 = -\frac{1}{2}$), symmetric prolate molecules invariant under rotations around the x-axis in the two situations of confinement by dihedral angles $\mathrm{sn}(\chi_{10}|0^\circ)$ and circular cones $\mathrm{sn}(\chi_{20}|0^\circ)$, respectively. The reader may notice the switching of the order of the shapes on the confining boundaries in the new situation compared with the previous one; as well as $e_1(\sigma = 0^\circ) = -e_3(\sigma = 60^\circ)$, $e_2(\sigma = 0^\circ) = -e_2(\sigma = 60^\circ)$, and $e_3(\sigma = 0^\circ) = -e_1(\sigma = 60^\circ)$. The latter relationships, combined with given values of h_c and h_f to evaluate the energies through Eq. (106), translate into the additional relationships $E_2^*(\mathrm{sn}(\chi_{20}|0^\circ)) = -E_1^*(\mathrm{sn}(\chi_{10}|60^\circ))$ for the eigenenergies of the symmetric molecules confined by circular cones and dihedral angles, with the same values of $\mathrm{sn}(\chi_{c0}|k_c)$, respectively. In fact, the readers can follow the entries in the left and right columns together to check such relationships. The interpolations of the energy eigenvalues and positions of the confining elliptical cones for the molecules with $\sigma = 45^\circ$, 30°, and 15° between their values for the symmetric molecules in the left and right columns can be read horizontally across the middle columns, and from top to bottom within the table for the increasing values of λ. The general relationships $e_1(\sigma = \sigma_0) = -e_3(\sigma = 60^\circ - \sigma_0)$, $e_2(\sigma = \sigma_0) = -e_2(\sigma = 60^\circ - \sigma_0)$, and $e_3(\sigma = \sigma_0) = -e_1(\sigma = 60^\circ - \sigma_0)$ between the asymmetry distribution parameters, already recognized in Table 4.1, extend to the relationships between the energy eigenvalues $E_2^*(\mathrm{sn}(\chi_{20}|\sigma_0)) = -E_1^*(\mathrm{sn}(\chi_{10}|60^\circ - \sigma_0))$ and $E_1^*(\mathrm{sn}(\chi_{10}|\sigma_0)) = -E_2^*(\mathrm{sn}(\chi_{20}|60^\circ - \sigma_0))$ entered in the columns equidistant from the central one. In particular, in the central column itself $E_1^*(\mathrm{sn}(\chi_{10}|30^\circ)) = -E_2^*(\mathrm{sn}(\chi_{20}|30^\circ))$ and $\mathrm{sn}(\chi_{10}|30^\circ) = \mathrm{sn}(\chi_{20}|30^\circ)$ for the most asymmetric molecules, with both energies vanishing when their respective quantum numbers are the same, $n_1^A = n_2^B$. Also notice that for $\lambda = 1$ all molecules share the same plane boundaries $\mathrm{sn}(\chi_{10}|\sigma) = 0$ equivalent

to the $z = 0$ plane Eq. (42) and $\mathrm{sn}(\chi_{20}|\sigma) = 0$ equivalent to the plane $x = 0$ plane Eq. (42), but each type of molecule has its own eigenenergies for the respective confinements. For smaller values of λ between one and towards zero, $\mathrm{sn}(\chi_{c0}|\sigma) \to -1$ approaching the quasi-free molecule limit in which the confining elliptical cone becomes a triangle bisected by the negative z-axis (or x-axis), and interpolating between such an axis and the $(-\infty < x < 0, y = 0, -\infty < z < \infty)$ or $(-\infty < x < \infty, y = 0, -\infty < z < 0)$ half planes. On the other hand, for larger values of λ from one to infinite an increasing number of confining cones appear successively with eigenenergies $E_1^*(\mathrm{sn}(\chi_{10}|\sigma)) \to \infty$ and $E_2^*(\mathrm{sn}(\chi_{20}|\sigma)) \to -\infty$, as $\mathrm{sn}(\chi_{c0}|\sigma) \to 1$ corresponding to triangles, from half lines to half planes, closing around the positive z-axis or x-axis, respectively.

Now we go on with the entries in Table 4.11 for the energies $E^*_{n_1^A n_2^B}(\mathrm{sn}(\chi_{10}|\sigma))$ and $E^*_{n_2^B n_1^A}(\mathrm{sn}(\chi_{20}|\sigma))$ of the lower excited state of the molecules and the positions of the respective confining elliptical cones. The shifting of the starting values of λ with higher order excitations should be noted to begin with. For the successive excited states $(1^1 0^1)$, $(0^d 1^s)$, $(0^c 1^c)$, $(2^1 0^1)$, $(1^d 1^s)$, $(1^c 1^c)$, $(0^1 2^1)$, $(0^{dc} 2^{sc})$ and their partners with the quantum numbers exchanged, the following points of reference may help the reader: (1) the double-zero entries for the positions of the boundaries, corresponding to $z = 0$ or $x = 0$ planes, are common to all the types of molecules, (2) the entries above them involve negative values for the position of the confining boundaries in the respective negative hemispheres, $z < 0$ or $x < 0$, (3) while the entries below involve positive values for the boundaries in the positive hemispheres, $z > 0$ or $x > 0$, (4) the common energies of degeneracy of the states of the symmetric molecules in the entries in the left or right columns for $d(k^2 = 1) \to c$ and $c \rightleftarrows s$: Specifically $0^c 1^c$ and $0^d 1^s$, $1^c 1^c$ and $1^d 1^s$, $0^1 2^1$ and $0^{dc} 2^{sc}, \ldots$ are doubly degenerate for prolate symmetric molecules in circular cones at the same positions, and likewise for the states with the exchanged quantum numbers for oblate symmetric molecules in circular cones, (5) the removal of such degeneracies for the asymmetric molecules in the middle columns, (6) the connections $E^*_{n_1^A n_2^B}(\mathrm{sn}(\chi_{10}|\sigma_0)) = -E^*_{n_2^B n_1^A}(\mathrm{sn}(\chi_{20}|60^\circ - \sigma_0))$ and $\mathrm{sn}(\chi_{10}|\sigma_0) = \mathrm{sn}(\chi_{20}|60^\circ - \sigma_0)$ for entries in the same row in columns equidistant from the central one, and (7) the asymptotic limits $E^*_{n_1^A n_2^B}(\mathrm{sn}(\chi_{10}|\sigma_0) \to 1) \to \infty$ and $E^*_{n_2^B n_1^A}(\mathrm{sn}(\chi_{20}|\sigma_0) \to 1) \to -\infty$.

Figures 4.3–4.5 present graphically the information on the energy spectra as functions of the positions of the confining elliptical cones for the ground and successive excited states, for the sample of types of molecules illustrated in the five columns of Tables 4.5–4.11. The upper and lower entries in each figure are in a one-to-one correspondence with the respective entries in the successive rows of Tables 4.10 and 4.11, with positive and

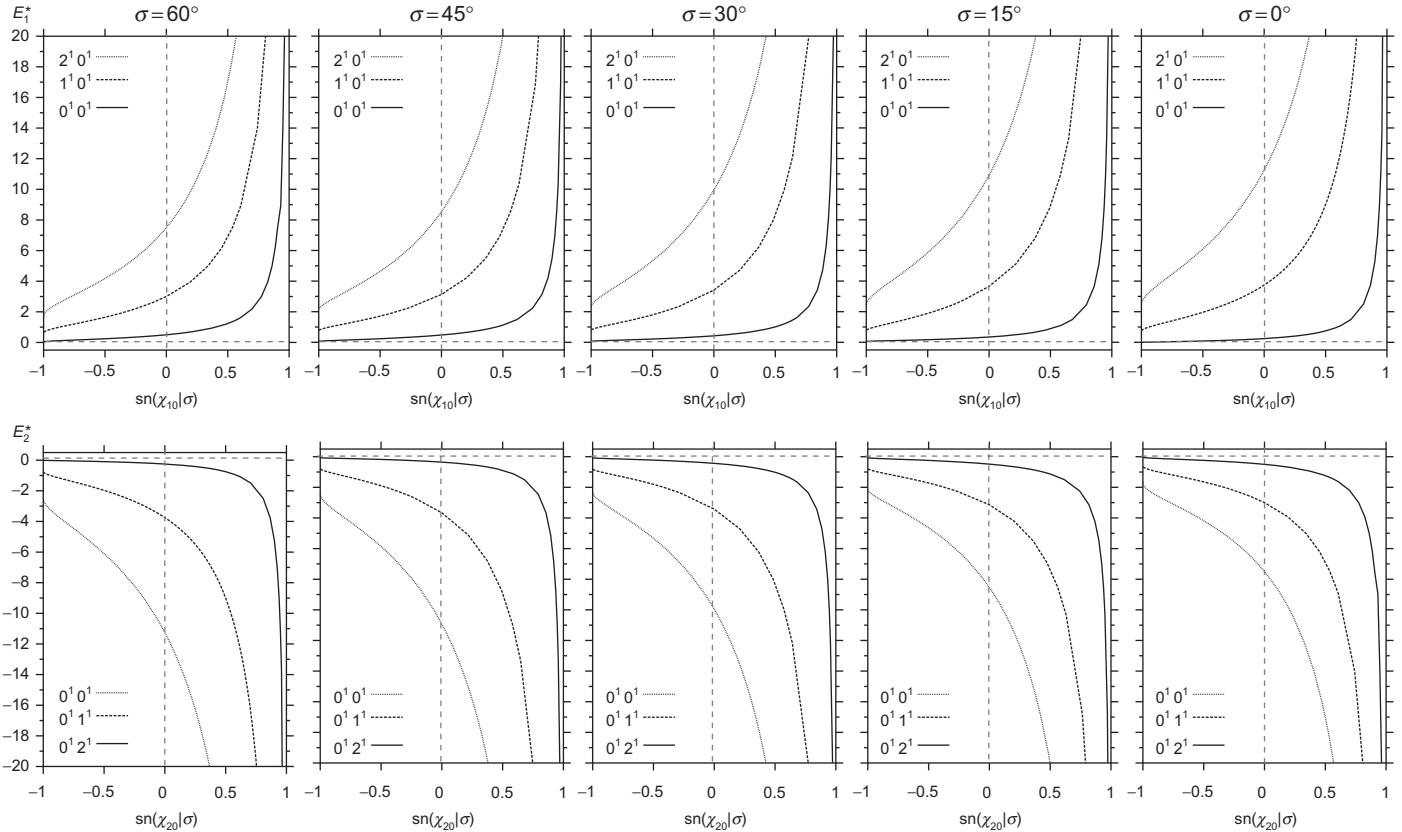

Figure 4.3 Energy spectra $E^*_{n_1^1\,0^1}$ $(\mathrm{sn}(\chi_{10}|\sigma))$ and $E^*_{0^1\,n_1^1}$ $(\mathrm{sn}(\chi_{20}|\sigma))$ as functions of the positions $\mathrm{sn}(\chi_{c0}|\sigma)$ of the confining elliptical-cones for asymmetric molecules $60^\circ \geq \sigma \geq 0^\circ$.

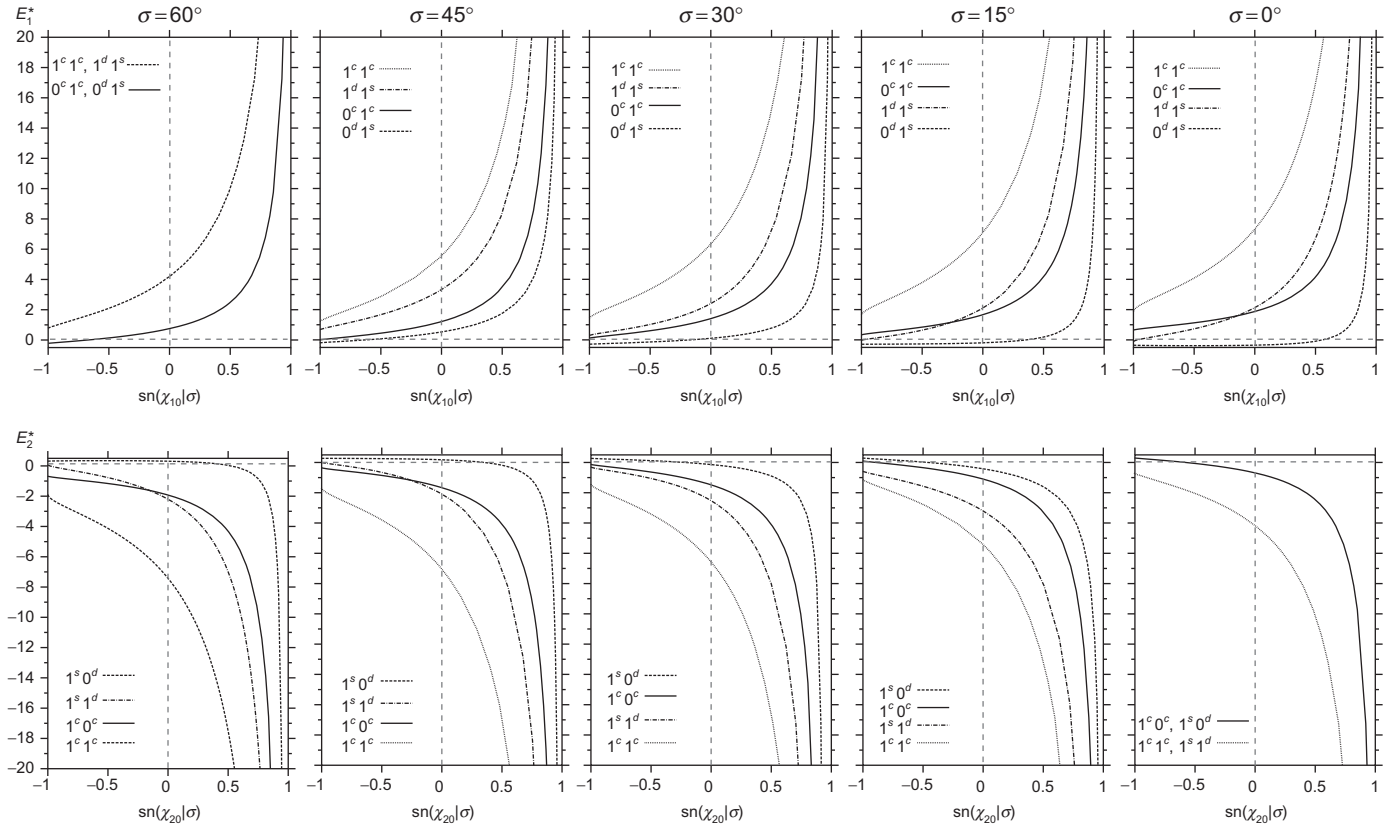

Figure 4.4 Energy spectra $E^*_{n_1^A\,1^B}(\mathrm{sn}(\chi_{10}|\sigma))$ and $E^*_{1^B\,n_1^A}(\mathrm{sn}(\chi_{20}|\sigma))$ as functions of the positions $\mathrm{sn}(\chi_{c0}|\sigma)$ of the confining elliptical-cones for asymmetric molecules $60^\circ \geq \sigma \geq 0^\circ$.

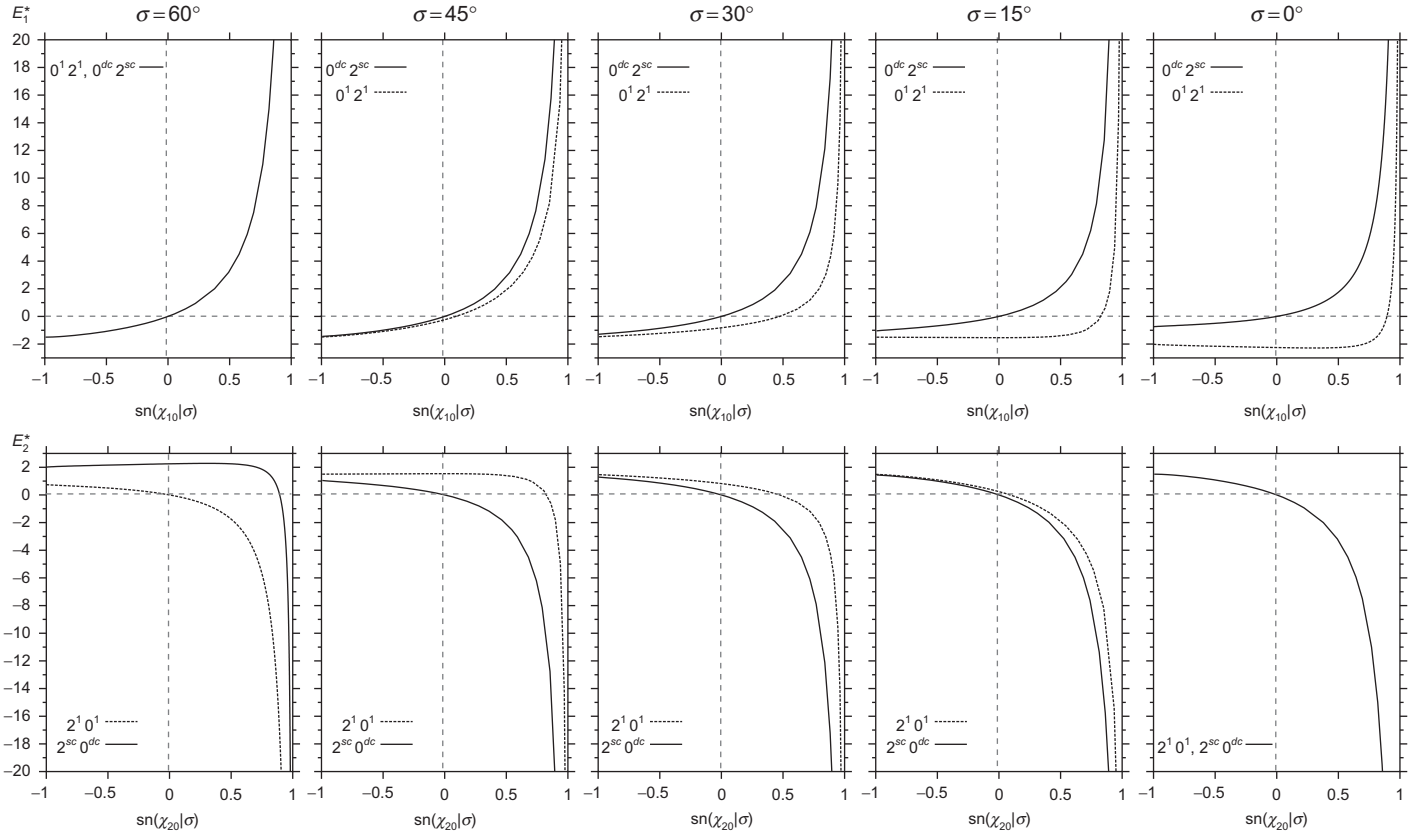

Figure 4.5 Energy spectra $E^*_{n_1^A\, 2^B}$ $(\mathrm{sn}(\chi_{10}|\sigma))$ and $E^*_{2^B\, n_1^A}$ $(\mathrm{sn}(\chi_{20}|\sigma))$ as functions of the positions $\mathrm{sn}(\chi_{c0}|\sigma)$ of the confining elliptical-cones for asymmetric molecules $60^\circ \geq \sigma \geq 0^\circ$.

negative energy eigenvalues E_1^* and E_2^*, respectively. Their respective monotonic increasing and decreasing as functions of the position of the confining elliptical cones from the quasi-free molecule to the most complete confinement can be followed in each individual figure, for the successive distributions of asymmetry $\sigma = 60^\circ, 45^\circ, 30^\circ, 15^\circ, 0^\circ$. Although in Figure 4.3 each energy level is an individual one, in Figures 4.4 and 4.5, the energy levels in the upper left and lower right corners, for the oblate and prolate symmetric molecules in circular cones, respectively, are doubly degenerate as already described in point (4) of the previous paragraph. The removal of such degeneracies for the other molecules can be followed from left to right in the upper row of individual figures, and from right to left in the lower one, including the occurrences of energy level crossings. In the three figures, the reader may also appreciate the meaning of the relationships of point (6) of the previous paragraph, upon recognition that, by referring to the rows (upper $= U$ and lower $= L$) and to the columns ($N = 1 - 5$) to locate each individual entry, in general UN and $L(6 - N)$ are the same figures, except for a flipping which considers the change of sign associated with the exchange $U \rightleftarrows L$. The reader may also appreciate the difference of the energy spectra for the different molecules in the common situations of confinement by planes, singularized by the vertical lines for $\mathrm{sn}(\chi_{c0} = 0|\sigma) = 0$.

The numerical results of Tables 4.10–4.11 and Figures 4.3–4.5 have been centered in the energies E^*, because they reflect the symmetries and relationships discussed in the last two paragraphs for the entire set of asymmetric molecules. Naturally, the complete energy spectra for each individual molecule is given by the eigenvalues E_1 and E_2 of the Hamiltonian of Eq. (38), with its symmetric molecule contribution $\frac{1}{2}Q\lambda(\lambda + 1)$ and its asymmetry contribution PE^*, where the magnitude of the asymmetry intensity parameter P is given by Eq. (36). While E_1^* and E_2^* are positive and negative, and their magnitudes grow without limit as the confinement intensifies, $\mathrm{sn}(\chi_{c0}|\sigma) \to 1$, the symmetric contribution to the total energy increases gradually as $\lambda(\lambda + 1)$ and dominates, so that both E_1 and E_2 become positive for molecules confined by sufficiently closed elliptical cones. Table 4.2 contains a sample of molecules with their respective moments of inertia [32] and the corresponding alternative Q, P, and σ parameters from which E_1 and E_2 can be calculated by using the values of λ, E_1^* and E_2^* in Tables 4.10–4.11 and Figures 4.3–4.5. Additional values of the energies, between the reported values and beyond, can be evaluated systematically by choosing interpolated and extrapolated values for the parameters of the molecules of specific interest.

We conclude this discussion by making a comparison of this work with our recent one on the hydrogen atom in the same situations of confinement [8]. Both problems involve the same equations, the same boundary conditions, and the same angular eigenfunctions. Their difference resides in the

exchanged roles of the $\hat{H}^*$ operator for the molecule and the $\hat{L}^2$ operator for the atom as the relevant parts of their respective Hamiltonians, while the same operators $\hat{L}^2$ and $\hat{G} \equiv \hat{H}^*$, commute with each other as well as with the respective complete Hamiltonians. In the notation of Eq. (38), the molecules involve both terms, and the atom involves only the spherical term with $Q = 1/mr^2$ since $P = 0$. The commutativity of the respective pairs of operators is the reason behind the simultaneous separability of the respective eigenvalue equations in spheroconal coordinates. In the article on the hydrogen atom, we chose the symbol $\hat{G}$ for the operator in order to emphasize its geometric character and its independence of the associated Hamiltonian. The additional condition for separability is the connection between the geometric parameters of the spheroconal coordinates and the dynamic parameters of $\hat{H}^*$, or geometric parameters of $\hat{G}$, Eqs. (44). Because the hydrogen atom is spherically symmetric it was sufficient to study explicitly its confinement in one of the angular coordinates $\mathrm{sn}(\chi_{10}|\sigma)$. The case of the molecules requires the study of both situations of confinement by cones $\mathrm{sn}(\chi_{10}|\sigma)$ and $\mathrm{sn}(\chi_{20}|\sigma)$, which are different due to their different distribution of asymmetries. Obviously, the energy spectra of the hydrogen atom and asymmetric molecules in the same situations of confinement, as determined by their respective complete Hamiltonians and common boundary conditions, are different. The results for the hydrogen atom can be extended for any central potential quantum system in the corresponding situations of confinement by elliptical cones. Our contribution to the 50th Sanibel Symposium illustrated the cases of the free particle and the harmonic oscillator, emphasizing the role and the matrix evaluation of the Lamé spheroconal harmonics in their polynomial and quasi-periodic forms [1].

4. ON DEVELOPING THE THEORY OF ANGULAR MOMENTUM IN BASES OF LAMÉ SPHEROCONAL HARMONICS

Our works [5, 6] reviewed in Sections 2.4 and 2.5 were focused on the accurate evaluation of the rotational states of asymmetric molecules. At the same time, we recognized the equal standing of the familiar spherical harmonics, common eigenfunctions of the operators $\hat{L}^2$ and $\hat{L}_z$, and the not-so-familiar spheroconal harmonics, common eigenfunctions of the operators $\hat{L}^2$ and $\hat{H}^*$. We tried to emphasize such an equal standing when we identified common generating functions for both bases of harmonic functions; specifically, the Coulomb potential and the plane wave are familiar generating functions for the Legendre polynomials and for the spherical harmonics, through the addition theorem, and in Refs. [5] and [6], their respective expansions in spheroconal harmonics were also proven. However, on page 168 of Ref. [6], a comparison was made on the advantages and disadvantages of

the respective methods developed in Ref. [5], using the familiar spherical harmonics bases, and in Ref. [6], constructing the spheroconal harmonics themselves. Although the familiarity with the first set has favored its use, it is most advantageous to become familiar with both the sets. In particular, it may be worthwhile exploring the extension of the theory of angular momentum based on spheroconal harmonics.

The idea of superintegrability is very useful for the problem at hand because it involves solutions in different coordinate systems. Two of its consequences are the existence of common generating functions for the respective solutions, and also the construction of solutions by the factorization method [44, 45].

In Section 4.1, the identification of complete radial and angular momentum raising and lowering operators for the familiar spherical harmonics is presented in our own version, as a point of reference for some extensions in Section 4.2 for the spheroconal harmonics. The results in Section 4.1 have been known in the literature [44, 46], but here the interest is in their adaptation and extension to eigenfunctions of $\hat{L}^2$ and $\hat{L}_k^2$, and $\hat{L}^2$ and $\hat{H}^*$.

4.1. Complete radial and angular momentum raising and lowering operators for a free particle in three dimensions

This section identifies and proves that the components of the linear momentum $\hat{\vec{p}} = \frac{1}{2}(\hat{\imath} - i\hat{\jmath})\hat{p}_+ + \frac{1}{2}(\hat{\imath} + i\hat{\jmath})\hat{p}_- + \hat{k}\hat{p}_z$ play the role of complete radial and angular momentum raising and lowering operators, when acting on the eigenfunctions of the free particle with a fixed energy $E = \hbar^2 k^2/2M$, expressed as products of spherical Bessel and spherical harmonic functions $z_\ell(kr)Y_{\ell m}(\theta, \varphi)$. It is also shown that the Hamiltonian can be written in the alternative forms $2M\hat{H} = (\hat{p}_r - i\hbar(\ell+2)/r)(\hat{p}_r + i\hbar\ell/r) = (\hat{p}_r + i\hbar(\ell - 1)/r)(\hat{p}_r - i\hbar(\ell+1)/r)$ obtained from the successive applications of the raising-and-lowering or lowering-and-raising operators, respectively. These results extend, generalize, and connect with two recent works [47, 48].

The contents of this section were motivated by the recent identifications by Liu, Xun, and Shan of the raising and lowering operators for the ℓ orbital angular momentum [47], and by Sun and Dong of the new radial and angular momentum operators shifting the m quantum number for the circular well potential in two dimensions [48]. Although the last investigation was focused on the circular well potential, its results are applicable in general for the free particle, with a fixed-energy eigenvalue, including not only the ordinary Bessel functions but also those of the Neumann and Hankel types [11]. However, the work in Ref. [47] improves Ka's original results in terms of the ℓ orbital angular momentum number [49], by replacing the latter with the appropriate square root of the square of angular momentum operators. The inclusion of the radial part together with the angular momentum part to obtain complete raising and lowering ℓ operators is the aim in what follows.

The Schrödinger equation for a free particle of mass M in spherical coordinates,

$$\left\{-\frac{\hbar^2}{2M}\left[\frac{\partial^2}{\partial r^2}+\frac{2}{r}\frac{\partial}{\partial r}\right]+\frac{\hat{\vec{L}}\cdot\hat{\vec{L}}}{2Mr^2}\right\}\Psi(\vec{r})=E\Psi(\vec{r}), \tag{118}$$

admits separable solutions

$$\Psi(\vec{r})=z_\ell(kr)Y_{\ell m}(\theta,\varphi), \tag{119}$$

involving the product of radial spherical Bessel functions $z_\ell(kr)=j_\ell(kr)$, $y_\ell(kr)$, $h_\ell^{(1)}(kr)$, $h_\ell^{(2)}(kr)$ and spherical harmonics of order ℓm, eigenfunctions of the square and of the z-component of the orbital angular momentum operators, and the energy eigenvalues $E=\hbar^2k^2/2M$.

The problem of our interest is the identification and construction of operators raising and lowering the ℓ quantum number simultaneously for both radial and angular functions in Eq. (119), thereby making it possible to connect all the eigenstates with different values of ℓ and m for the same energy. In particular, starting from the state $z_0(kr)Y_{00}(\theta,\varphi)$, the raising operators may generate by successive applications any state of the basis of Eq. (119).

The starting point for the identification at hand is to write the linear momentum vector in terms of its radial and transverse components, recognizing that the latter involve the angular momentum vector:

$$\hat{\vec{p}}=\hat{\vec{r}}(\hat{\vec{r}}\cdot\hat{\vec{p}})-\hat{\vec{r}}\times\frac{\hat{\vec{L}}}{r}. \tag{120}$$

The components of the unit radial vector and their representations in terms of angular momentum eigenstates $|\ell=1,m_2\rangle$,

$$\begin{aligned}\sin\theta e^{i\varphi}&=-\sqrt{\frac{8\pi}{3}}\,|1,1\rangle,\\ \sin\theta e^{-i\varphi}&=\sqrt{\frac{8\pi}{3}}\,|1,-1\rangle,\\ \cos\theta&=\sqrt{\frac{8\pi}{3}}\frac{1}{\sqrt{2}}\,|1,0\rangle,\end{aligned} \tag{121}$$

lead to the practical representation of the operators of our interest:

$$\hat{\vec{p}}=\sqrt{\frac{8\pi}{3}}\left\{\frac{1}{2}(\hat{\imath}-i\hat{\jmath})\left[-\hat{p}_r\,|1,1\rangle-\frac{i}{r}\left(|1,1\rangle\,\hat{L_z}+\frac{1}{\sqrt{2}}\,|1,0\rangle\,\hat{L_+}\right)\right]\right.$$

$$+\frac{1}{2}(\hat{\imath}+i\hat{\jmath})\left[\hat{p}_r\,|1,-1\rangle-\frac{i}{r}\left(\,|1,-1\rangle\,\hat{L_z}-\frac{1}{\sqrt{2}}\,|1,0\rangle\,\hat{L_-}\right)\right]$$
$$+\hat{k}\left[\hat{p}_r\frac{1}{\sqrt{2}}\,|1,0\rangle-\frac{i}{2r}\left(-|1,1\rangle\,\hat{L_-}-|1,-1\rangle\,\hat{L_+}\right)\right]\Bigg\}. \tag{122}$$

In fact, the $\hat{L}_+$, $\hat{L}_-$, and $\hat{L}_z$ operators are known to raise, lower, and measure the m quantum number in the eigenstates $|\ell,m\rangle$ maintaining the value ℓ unchanged. The presence of the states $|1,m_2\rangle$ is the key element for raising and lowering by one the eigenvalue ℓ. Specifically, the evaluation of the effect of applying the operators $\hat{p}_+$, $\hat{p}_-$, and $\hat{p}_z$ of the successive rows in the last equation on the eigenstate $z_\ell(kr)\,|\ell m\rangle$, involving the coupling of angular momenta $\ell+1=\ell'$ and the rewriting of the states $|\ell m\rangle\,|1m_2\rangle$ as superpositions of the states $|\ell 1\ell' m'\rangle$ with $\ell'=\ell+1$ and $\ell-1$, lead to the results:

$$\hat{p}_+ z_\ell(kr)\,|\ell m\rangle =$$
$$=\sqrt{\frac{8\pi}{3}}\Bigg[-\left(\hat{p}_r+\frac{i\hbar\ell}{r}\right)z_\ell(kr)\,|\ell 1\;\ell+1\;m+1\rangle\,\langle\ell\,1\;\ell+1\;m+1|\ell m11\rangle$$
$$-\left(\hat{p}_r-\frac{i\hbar(\ell+1)}{r}\right)z_\ell(kr)\,|\ell 1\;\ell-1\;m+1\rangle\,\langle\ell 1\;\ell-1\;m+1|\ell m11\rangle\Bigg], \tag{123}$$

$$\hat{p}_- z_\ell(kr)\,|\ell m\rangle =$$
$$=\sqrt{\frac{8\pi}{3}}\Bigg[\left(\hat{p}_r+\frac{i\hbar\ell}{r}\right)z_\ell(kr)\,|\ell 1\;\ell+1\;m-1\rangle\,\langle\ell 1\;\ell+1\;m-1|\ell m1-1\rangle$$
$$+\left(\hat{p}_r-\frac{i\hbar(\ell+1)}{r}\right)z_\ell(kr)\,|\ell 1\;\ell-1\;m-1\rangle\,\langle\ell 1\;\ell-1\;m-1|\ell m1-1\rangle\Bigg], \tag{124}$$

$$\hat{p}_z z_\ell(kr)\,|\ell m\rangle =$$
$$=\sqrt{\frac{8\pi}{3}}\Bigg[\left(\hat{p}_r+\frac{i\hbar\ell}{r}\right)z_\ell(kr)\,|\ell 1\;\ell+1\;m\rangle\,\frac{1}{\sqrt{2}}\,\langle\ell 1\;\ell+1\;m|\ell m10\rangle$$
$$+\left(\hat{p}_r-\frac{i\hbar(\ell+1)}{r}\right)z_\ell(kr)\,|\ell 1\;\ell-1\;m\rangle\,\frac{1}{\sqrt{2}}\,\langle\ell 1\;\ell-1\;m|\ell m10\rangle\Bigg]. \tag{125}$$

The three terms in each operator of Eq. (122) share the total $\hat{L}_z$ eigenvalues $m+1, m-1$, and m, respectively, leading to the common Clebsch–Gordan coefficients $\langle\ell 1\ell' m'|\ell m1m_2\rangle$ for $m_2=1,-1,0$, Table 27.9.2 [11], in

Eqs. (123–125). The combinations of the other factors $m+(\ell-m), m-(\ell+m)$, and $(\ell-m)+(\ell+m)$ for $\ell'=\ell+1$, and $-m-(\ell-m+1), m-(\ell+m+1)$, and $(\ell-m+1)+(\ell+m+1)$ for $\ell'=\ell-1$, associated with the last two terms in each operator of Eq. (122), lead to the common radial factors in Eqs. (123–125) without any m dependence.

So far, we have only examined the effect of the raising and lowering operators on the angular eigenstates. Next, we include the remaining effect on the companion radial eigenstates $z_\ell(kr)$. For the $\ell'=\ell+1$ and $\ell-1$ states, the recurrence relations for the spherical Bessel functions 10.1.22 and 10.1.21 [11] show that the radial eigenfunctions have indeed their ℓ labels raised and lowered by one unit, matching the changes in their companion angular eigenstates:

$$\begin{aligned}\left(\hat{p}_r+\frac{i\hbar\ell}{r}\right)z_\ell(kr) &= (-i\hbar)k\left[\frac{\mathrm{d}}{\mathrm{d}(kr)}-\frac{\ell}{kr}\right]z_\ell(kr)\\ &= (-i\hbar)k\Big[-z_{\ell+1}(kr)\Big], \qquad (126)\\ \left(\hat{p}_r-\frac{i\hbar(\ell+1)}{r}\right)z_\ell(kr) &= (-i\hbar)k\left[\frac{\mathrm{d}}{\mathrm{d}(kr)}+\frac{\ell+1}{kr}\right]z_\ell(kr)\\ &= (-i\hbar)k\Big[z_{\ell-1}(kr)\Big]. \qquad (127)\end{aligned}$$

Thus, the combination of Eqs. (123–125) and (126)–(127) proves that the $\hat{p}_+, \hat{p}_-$, and $\hat{p}_z$ acting on the eigenfunctions of the free particle, Eq. (119), transform them into the l-raised projected states $z_{\ell+1}(kr)\,|\ell 1\,\ell+1, m'\rangle$ and the ℓ-lowered projected states $z_{\ell-1}(kr)\,|\ell 1\,\ell-1, m'\rangle$ with $m'=m+1, m-1$, and m, respectively.

The closing of this section includes the analysis of the additional application of the lowering radial operators to the states with $\ell'=\ell+1$ and of the raising radial operators to the states with $\ell'=\ell-1$, both leading back to the $z_\ell(kr)\,|\ell m\rangle$ eigenstates, and to the two alternative representations of the Hamiltonian. Because of the spherical symmetry of the free particle, the m dependence is not affected, and attention is concentrated on the ℓ' dependence for each case. Going from $\ell'=\ell+1$ to l naturally involves the lowering operator and from $\ell'=\ell-1$ to ℓ the raising operator. Thus, we write the respective sequences of raising-and-lowering and lowering-and-raising operators from right to left acting on the eigenstates of Eq. (119):

$$\begin{aligned}&\left(\hat{p}_r-\frac{i\hbar(\ell+2)}{r}\right)\left(\hat{p}_r+\frac{i\hbar\ell}{r}\right)z_\ell(kr)\,|\ell m\rangle\\ &\quad=\left(\hat{p}_r-\frac{i\hbar(\ell+2)}{r}\right)(i\hbar k)z_{\ell+1}(kr)\,|\ell+1 m\rangle=(-i\hbar k)(i\hbar k)z_\ell(kr)\,|\ell, m\rangle\,, \qquad (128)\end{aligned}$$

$$\left(\hat{p}_r + \frac{i\hbar(\ell-1)}{r}\right)\left(\hat{p}_r - \frac{i\hbar(\ell+1)}{r}\right) z_\ell(kr)\,|\ell m\rangle$$
$$= \left(\hat{p}_r + \frac{i\hbar(\ell-1)}{r}\right)(-i\hbar k) z_{\ell-1}(kr)\,|\ell-1\, m\rangle = (i\hbar k)(-i\hbar k) z_\ell(kr)\,|\ell m\rangle. \quad (129)$$

The Hamiltonian can be identified as the products of the radial operators in both equations,

$$2M\hat{H} = \left(\hat{p}_r - \frac{i\hbar(\ell+2)}{r}\right)\left(\hat{p}_r + \frac{i\hbar\ell}{r}\right)$$
$$= \left(\hat{p}_r + \frac{i\hbar(\ell-1)}{r}\right)\left(\hat{p}_r - \frac{i\hbar(\ell+1)}{r}\right), \quad (130)$$

and its eigenvalues $\hbar^2k^2/2M$ follow from the right-hand sides. Additionally, it can be directly established that both representations coincide with that of Eq. (118).

The aim of this work of identifying the complete radial and angular momentum raising and lowering operators is implemented by Eqs. (120–122). The proof of their actions on any of the eigentstates of Eq. (119) is illustrated by Eqs. (123–125) for the angular part including the factorization of the radial parts, whose actions are exhibited by Eqs. (126 and 127). Their combined effects of Eqs. (128 and 129) lead to the two alternative representations of the Hamiltonian in Eq. (130).

The two-dimensional case in Ref. [48] follows from Eq. (122) by dropping the terms with $|10\rangle$ and $\hat{L}_\pm$. The results of [47] involve the $\hat{\vec{r}} \times \hat{\vec{L}}/r$ term in Eq. (120) plus minus the square roots of the square of the angular momentum, which appear in our complete radial operators of Eqs. (126–130) in the notation of Ref. [49].

The method and results of this section also illuminate some of our works on rotations of asymmetric molecules, the hydrogen atom and any central potential in the direction of developing the theory of angular momentum in the Lamé spheroconal harmonic bases, as discussed in the following sections.

4.2. Angular momentum transformations of Lamé spheroconal harmonic polynomials

The familiar theory of angular momentum, based on spherical harmonics, eigenfunctions of $\hat{L}^2$ and $\hat{L}_z$ operators of angular momentum, also uses the ladder operators $\hat{L}_\pm$, which for a given value of ℓ connect all the $2\ell+1$ successive states $|\ell m\rangle$ with $m = -\ell, -\ell+1, \ldots, -1, 0, 1, \ldots, \ell-1, \ell$. Section 4.2.1 illustrates the counterpart for the spheroconal harmonics or the spherical harmonics with well-defined parities under the application of the operators

$\hat{L}_x$, $\hat{L}_y$, $\hat{L}_z$. Correspondingly, Section 4.2.2 illustrates for the spheroconal harmonics what has been rigorously proven for spherical harmonics in Section 4.1. Then, Section 4.2.3 identifies some spheroconal tools to further explore the development of the theory of angular momentum.

4.2.1. Transformations under $\hat{L}_x$, $\hat{L}_y$, and $\hat{L}_z$

It is interesting that Refs. [2–4] did not include the explicit expressions for the cartesian components of the angular momentum operator in their respective spheroconal coordinates. The Appendix of Ref. [6] does have such expressions for the spheroconal coordinates in the Jacobi elliptic function representation. The interested reader is invited to see them and understand their structure.

Here, we follow Niven's example [18] in using the operators in their cartesian coordinate representations directly:

$$\hat{L}_i = -i\hbar \left[x_j \frac{\partial}{\partial x_k} - x_k \frac{\partial}{\partial x_j} \right], \tag{131}$$

with $(i, j, k) = cyc(1, 2, 3)$, in order to analyze their effects on the eigenfunctions of angular momentum with well-defined parities, 1; x, y, z; yz, xz, xy; xyz, and at the appropriate moment connect them with their spherical and spheroconal counterparts.

For the polynomial of degree zero, the three operators lead to the eigenvalues zero for any $\hat{L}_i$ and $\hat{L}^2$, as it should be.

For the polynomials of degree 1, the familiar result is

$$\hat{L}_i x_j = i\hbar \epsilon_{ijk} x_k, \tag{132}$$

where $\epsilon_{ijk} = 1$ for $i, j, k = cyc(1, 2, 3)$ and -1 for odd permutations of $1, 2, 3$ and zero otherwise. In other words, the application of $\hat{L}_i$ on x_i gives the eigenvalue zero associated to such an eigenfunction. The application on any of the other two x_j or x_k gives the other one. The spherical or spheroconal harmonics follows directly from the transformation equation to cartesian coordinates, Eq. (42).

For the polynomials of degrees $\ell = 2$ and 3, we include the results in Tables 4.11 and 4.12, going beyond the initial eigenstates because additional eigenstates appear in a natural way.

The last entry in the first column is the difference between those in the fifth and fourth rows. The underlined eigenfunctions in the Table 4.11 are identified as the eigenstates $r^2 \sin\theta \cos\theta \sin\varphi, r^2 \sin\theta \cos\theta \cos\varphi, r^2 \sin^2\theta \sin\varphi \cos\varphi$, $r^2 \sin^2\theta \cos 2\varphi$, and $r^2(3\cos^2\theta - 1)$ in spherical coordinates with parities $(+--)$, $(-+-)$, $(--+)$, $(+++)$, and $(+++)$, respectively. They also correspond to spheroconal harmonics of the species and types

Table 4.11 Angular momentum operators $\hat{L}_x$, $\hat{L}_y$, $\hat{L}_z$ acting on cartesian angular momentum harmonic eigenfunctions in first column produce eigenfunctions of the same type with $\ell = 2$

	$\hat{L}_x/(-i\hbar)$	$\hat{L}_y/(-i\hbar)$	$\hat{L}_z/(-i\hbar)$
yz	$y^2 - z^2$	$-xy$	xz
zx	yx	$z^2 - x^2$	$-yz$
xy	$-zx$	yz	$x^2 - y^2$
$y^2 - z^2$	$-4yz$	$2xz$	$2xy$
$z^2 - x^2$	$2yz$	$-4xz$	$2xy$
$x^2 - y^2$	$2yz$	$2xz$	$-4xy$
$2z^2 - x^2 - y^2$	$6yz$	$-6xz$	0

Table 4.12 Angular momentum operators $\hat{L}_x$, $\hat{L}_y$, $\hat{L}_z$ acting on cartesian angular momentum harmonic eigenfunctions with $\ell = 3$ lead to functions of the same family

	$\hat{L}_x/(-i\hbar)$	$\hat{L}_y/(-i\hbar)$	$\hat{L}_z/(-i\hbar)$
xyz	$x(y^2 - z^2)$	$y(z^2 - x^2)$	$z(x^2 - y^2)$
$x(y^2 - z^2)$	$-4xyz$	$z(2x^2 + y^2 - z^2)$	$y(2x^2 - y^2 + z^2)$
$y(z^2 - x^2)$	$z(2y^2 + x^2 - z^2)$	$-4xyz$	$x(2y^2 - x^2 + z^2)$
$z(x^2 - y^2)$	$y(2z^2 + x^2 - y^2)$	$x(2z^2 - x^2 + y^2)$	$-4xyz$
$z(2z^2 - 3x^2 - 3y^2)$	$3y(4z^2 - x^2 - y^2)$	$-3x(4z^2 - x^2 - y^2)$	0
$y(3x^2 - y^2)$	$-3z(x^2 - y^2)$	$6xyz$	$3x(x^2 - 3y^2)$
$x(x^2 - 3y^2)$	$6xyz$	$3z(x^2 - y^2)$	$-3y(3x^2 - y^2)$
$y(4z^2 - x^2 - y^2)$	$z(11y^2 + x^2 - 4z^2)$	$-10xyz$	$x(4z^2 - x^2 - y^2)$
$x(4z^2 - x^2 - y^2)$	$10xyz$	$-z(11x^2 + y^2 - 4z^2)$	$-y(4z^2 - x^2 - y^2)$

$\Lambda_1^{cs}(\chi_1)\Lambda_1^{cd}(\chi_2)$, $\Lambda_1^{ds}(\chi_1)\Lambda_1^{sd}(\chi_2)$, $\Lambda_1^{dc}(\chi_1)\Lambda_1^{sc}(\chi_2)$ the first three ones; and two orthogonal linear combinations of $\Lambda_2^1(\chi_1)\Lambda_0^1(\chi_2)$ and $\Lambda_0^1(\chi_1)\Lambda_2^1(\chi_2)$ the last two ones. In turn, the latter can be written as orthogonal linear combinations of the spherical harmonics with the common $(+++)$ parities as evaluated in Ref. [6].

The fifth entry in the first column is the negative of the sum of the second row and third column plus third row and second column entries. The sixth entry in the first column is twice the entry in the second row in the fourth column minus the entry in the fourth row in the second column, eliminating the terms in z^2. Similarly, the seventh row in the first column is the entry in the fourth row in the third column minus twice the entry in the third row of the fourth column. The eighth entry in the

first column is the entry in the fifth row in the second column, and the ninth entry in the first row is the entry in the eighth row in the third column. All the entries are harmonic functions as the reader can check directly. The ones that are underlined in the first column are spherical harmonics $r^3 \sin^2\theta \cos\theta \sin\varphi \cos\varphi$, $r^2 \sin^2\theta \cos\theta \cos 2\varphi$, $r^3(5\cos^2\theta - 3\cos\theta)$, $r^3 \sin^3\theta \sin 3\varphi$, $r^3 \sin^3\theta \cos 3\varphi$, $r^3(5\cos^2\theta - 1)\sin\varphi$, $r^3(5\cos^2\theta - 1)\cos\varphi$. The third one is the eigenfunction of $\hat{L}_z$ with eigenvalue zero. The next two pairs are exchanged under the action of $\hat{L}_z$, and the same happens for the first pair. Their respective parities are identified to be $(---)$, $(++-)$, $(++-)$, $(+-+)$, $(-++)$, $(+-+)$, and $(-++)$, respectively. Although the first is the single spheroconal harmonic $\Lambda^{dcs}(\chi_1)\Lambda^{scd}(\chi_2)$, the other three pairs are linear combinations of two independent spheroconal harmonics of species and types $\Lambda^s(\chi_1)\Lambda^d(\chi_2)$, $\Lambda^c(\chi_1)\Lambda^c(\chi_2)$, $\Lambda^d(\chi_1)\Lambda^s(\chi_2)$.

In conclusion, the application of the cartesian operators to any angular momentum eigenfunction leads to its companions with the same label ℓ. Then the identification of their spherical or spheroconal representations follow as discussed in Refs. [5] and [6], including their identifications by species and types with their respective numbers depending on whether ℓ is even or odd.

4.2.2. Complete radial and angular momentum raising and lowering transformations

This section is the counterpart of Section 4.1 aimed to illustrate the generation of the complete radial and spheroconal angular momentum eigenfunction for the free particle in three dimensions using an alternative representation of the same operator.

In fact, Section 4.1 is geared to the spherical harmonic representation emphasizing that the functions involved are eigenfunctions of $\hat{L}^2$ and $\hat{L}_z$, for which the unit vectors $\hat{\imath} \pm i\hat{\jmath}$ matching the eigenfunctions $e^{\mp im\varphi}$ are appropriate. Now the functions involved are common eigenfunctions of $\hat{L}^2$, $\hat{H}^*$, and the parity operators, calling for the representation

$$\hat{\vec{p}} = \hat{\imath}\left[\frac{x}{r}\hat{p}_r - \frac{1}{r^2}\left(y\hat{L}_z - z\hat{L}_y\right)\right] + \hat{\jmath}\left[\frac{y}{r}\hat{p}_r - \frac{1}{r^2}\left(z\hat{L}_x - x\hat{L}_z\right)\right] + \hat{\mathrm{k}}\left[\frac{x}{r}\hat{p}_r - \frac{1}{r^2}\left(x\hat{L}_y - y\hat{L}_x\right)\right]. \tag{133}$$

We consider, in the following, the successive application of this operator on the lower angular momentum eigenstates, starting with that for $\ell = 0$, $z_0(kr)$. The application of the angular momentum operators give zero and the net result is as follows:

$$\hat{\vec{p}} z_0(kr) = -i\hbar\left[\hat{\imath}\frac{x}{r} + \hat{\jmath}\frac{y}{r} + \hat{\mathrm{k}}\frac{z}{r}\right]\frac{\mathrm{d}}{\mathrm{d}r} z_0(kr). \tag{134}$$

Here, we identify the angular momentum spheroconal eigenfunctions $\mathrm{dn}(\chi_1|k_1)\ \mathrm{sn}(\chi_2|k_2)$, $\mathrm{cn}(\chi_1|k_1)\mathrm{cn}(\chi_2|k_2)$, and $\mathrm{sn}(\chi_1|k_1)\mathrm{dn}(\chi_2|k_2)$ in the respective directions, as well as the radial momentum eigenvalue $\hbar k$ and eigenfunction

$$\frac{\mathrm{d}}{\mathrm{d}(kr)} z_0(kr) = -z_1(kr), \tag{135}$$

with $\ell = 1$. This is the identification of the raising action of the operators $\hat{p}_x$, $\hat{p}_y$, and $\hat{p}_z$.

Next, we apply the operator on the $\ell = 1$ eigenfunctions:

$$\hat{\hat{p}}\left[\frac{x}{r} z_1(kr)\right] = \left\{\hat{\imath}\left[\frac{x^2}{r^2}\hat{p}_r - \frac{i\hbar}{r^3}(y^2+z^2)\right] + \hat{\jmath}\left[\frac{xy}{r^2}\hat{p}_r - \frac{i\hbar}{r^3}(xy)\right] + \hat{\mathrm{k}}\left[\frac{zx}{r^2}\hat{p}_r - \frac{i\hbar}{r^3}(-xz)\right]\right\} z_1(kr), \tag{136}$$

$$\hat{\hat{p}}\left[\frac{y}{r} z_1(kr)\right] = \left\{\hat{\imath}\left[\frac{xy}{r^2}\hat{p}_r + \frac{i\hbar}{r^3}(yx)\right] + \hat{\jmath}\left[\frac{y^2}{r^2}\hat{p}_r - \frac{i\hbar}{r^3}(z^2+x^2)\right] + \hat{\mathrm{k}}\left[\frac{zy}{r^2}\hat{p}_r - \frac{i\hbar}{r^3}(-yz)\right]\right\} z_1(kr), \tag{137}$$

$$\hat{\hat{p}}\left[\frac{z}{r} z_1(kr)\right] = \left\{\hat{\imath}\left[\frac{xz}{r^2}\hat{p}_r - \frac{i\hbar}{r^3}(-zx)\right] + \hat{\jmath}\left[\frac{yz}{r^2}\hat{p}_r - \frac{i\hbar}{r^3}(-zy)\right] + \hat{\mathrm{k}}\left[\frac{z^2}{r^2}\hat{p}_r - \frac{i\hbar}{r^3}(x^2+y^2)\right]\right\} z_1(kr). \tag{138}$$

We identify the common factorizable terms in the above equations:

$$\hat{p}_y\left[\frac{x}{r} z_1(kr)\right] = \hat{p}_x\left[\frac{y}{r} z_1(kr)\right] = \frac{yx}{r^2}\left[\hat{p}_r + \frac{i\hbar}{r}\right] z_1(kr), \tag{139}$$

$$\hat{p}_z\left[\frac{x}{r} z_1(kr)\right] = \hat{p}_x\left[\frac{z}{r} z_1(kr)\right] = \frac{xz}{r^2}\left[\hat{p}_r + \frac{i\hbar}{r}\right] z_1(kr), \tag{140}$$

$$\hat{p}_z\left[\frac{y}{r} z_1(kr)\right] = \hat{p}_y\left[\frac{z}{r} z_1(kr)\right] = \frac{yz}{r^2}\left[\hat{p}_r + \frac{i\hbar}{r}\right] z_1(kr). \tag{141}$$

They involve the respective $\ell = 2$ spheroconal harmonic polynomials $\mathrm{dn}(\chi_1|k_1)\ \mathrm{cn}(\chi_1|k_1)\mathrm{sn}(\chi_2|k_2)\mathrm{cn}(\chi_2|k_2)$, $\mathrm{dn}(\chi_1|k_1)\mathrm{sn}(\chi_1|k_1)\mathrm{sn}(\chi_2|k_2)\mathrm{dn}(\chi_2|k_2)$,

$\mathrm{cn}(\chi_1|k_1)\ \mathrm{sn}(\chi_1|k_1)\mathrm{cn}(\chi_2|k_2)\mathrm{dn}(\chi_2|k_2)$, and the common

$$-i\hbar k\left(\frac{\mathrm{d}}{\mathrm{d}(kr)}-\frac{1}{kr}\right)z_1(kr)=i\hbar k z_2(kr) \tag{142}$$

radial spherical Bessel function of the same order $\ell=2$. The raising action of the linear momentum operators on the $\ell=1$ eigenstates is illustrated again. From the other equations, we form the following successive combinations

$$\begin{aligned}&\hat{p}_x\left[\frac{x}{r}z_1(kr)\right]+\hat{p}_y\left[\frac{y}{r}z_1(kr)\right]+\hat{p}_z\left[\frac{z}{r}z_1(kr)\right]\\&\quad=\left[\frac{x^2+y^2+z^2}{r^2}\hat{p}_r-\frac{2i\hbar}{r^3}(x^2+y^2+z^2)\right]z_1(kr)\\&\quad=\left(\hat{p}_r-\frac{2i\hbar}{r}\right)z_1(kr)=-i\hbar k\left(\frac{\mathrm{d}}{\mathrm{d}(kr)}+\frac{2}{r}\right)z_1(kr)=-i\hbar k z_0(kr).\end{aligned} \tag{143}$$

This shows the combined lowering action of the operators $\hat{p}_x$, $\hat{p}_y$, and $\hat{p}_z$ when applied to the three $\ell=1$ eigenstates of the free particle and leading to the $\ell=0$ single eigenstate, complementing the one in Eq. (134). The other two combinations

$$\hat{p}_x\left[\frac{x}{r}z_1(kr)\right]-\hat{p}_y\left[\frac{y}{r}z_1(kr)\right]=\frac{x^2-y^2}{r^2}\left[\hat{p}_r+\frac{i\hbar}{r}\right]z_1(kr), \tag{144}$$

$$\begin{aligned}&-\hat{p}_x\left[\frac{x}{r}z_1(kr)\right]-\hat{p}_y\left[\frac{y}{r}z_1(kr)\right]+2\hat{p}_z\left[\frac{z}{r}z_1(kr)\right]\\&\qquad=\frac{-x^2-y^2+2z^2}{r^2}\left[\hat{p}_r+\frac{i\hbar}{r}\right]z_1(kr),\end{aligned} \tag{145}$$

lead to the same radial linear momentum eigenvalue and eigenfunctions in Eqs. (139–142), and the respective spherical harmonic functions $\sin^2\theta\cos 2\varphi$ and $P_2(\cos\theta)$, with $\ell=2$. The latter are linear combinations of the Lamé spheroconal harmonic polynomials $\Lambda^1_2(\chi_1)\Lambda^1_0(\chi_2)$ and $\Lambda^1_0(\chi_1)\Lambda^1_2(\chi_2)$, [5, 6]. The latter together with the three of Eqs. (139–141) form the family of five for $\ell=2$.

Of the nine combinations of the three operators and three functions in Eqs. (136–138), we recognize that three pairs lead to common results, Eqs. (139–141). Of the remaining three, we formed three new combinations, one of which belongs to $\ell=0$ through the lowering action, and the other two belong with the previous three with $\ell=2$, having been obtained by the raising action of the operators.

The application of the three operators $\hat{p}_x$, $\hat{p}_y$, and $\hat{p}_z$ to the five linearly independent functions $\frac{yz}{r^2}z_2(kr)$, $\frac{zx}{r^2}z_2(kr)$, $\frac{xy}{r^2}z_2(kr)$, $\frac{x^2-y^2}{r^2}z_2(kr)$, and $\frac{2z^2-x^2-y^2}{r^2}z_2(kr)$

lead to 15 combinations. Three of them,

$$\hat{p}_x\left[\frac{yz}{r}z_2(kr)\right]=\hat{p}_y\left[\frac{xz}{r}z_2(kr)\right]=\hat{p}_z\left[\frac{xy}{r}z_2(kr)\right]$$
$$=\left[\frac{xyz}{r^3}\hat{p}_r+\frac{2i\hbar}{r}xyz\right]z_2(kr)=\frac{xyz}{r^3}(-i\hbar k)\left[\frac{\mathrm{d}}{\mathrm{d}(kr)}-\frac{2}{kr}\right]z_2(kr)$$
$$=\frac{xyz}{r^3}(i\hbar k)z_3(kr), \tag{146}$$

lead to the $\ell=3$ spheroconal harmonic $\mathrm{dn}(\chi_1|k_1)\mathrm{cn}(\chi_1|k_1)\mathrm{sn}(\chi_1|k_1)\mathrm{sn}(\chi_2|k_2)$ $\mathrm{cn}(\chi_2|k_2)\mathrm{dn}(\chi_2|k_2)$ and the spherical Bessel function of the same order. The remaining combinations come in the following sets from the other two operators acting on the same functions

$$\hat{p}_y\left[\frac{yz}{r^2}z_2(kr)\right]=\left[\frac{y^2z}{r^3}\hat{p}_r+\frac{i\hbar}{r^4}\left(z(y^2-z^2)-x^2z\right)\right]z_2(kr), \tag{147}$$

$$\hat{p}_z\left[\frac{yz}{r^2}z_2(kr)\right]=\left[\frac{yz^2}{r^3}\hat{p}_r+\frac{i\hbar}{r^4}\left(-x^2y-y(y^2-z^2)\right)\right]z_2(kr), \tag{148}$$

$$\hat{p}_x\left[\frac{xz}{r^2}z_2(kr)\right]=\left[\frac{x^2z}{r^3}\hat{p}_r+\frac{i\hbar}{r^4}\left(-y^2z-z(z^2-x^2)\right)\right]z_2(kr), \tag{149}$$

$$\hat{p}_z\left[\frac{xz}{r^2}z_2(kr)\right]=\left[\frac{xz^2}{r^3}\hat{p}_r+\frac{i\hbar}{r^4}\left(x(z^2-x^2)-y^2x\right)\right]z_2(kr), \tag{150}$$

$$\hat{p}_x\left[\frac{xy}{r^2}z_2(kr)\right]=\left[\frac{x^2y}{r^3}\hat{p}_r+\frac{i\hbar}{r^4}\left(y(x^2-y^2)-z^2y\right)\right]z_2(kr), \tag{151}$$

$$\hat{p}_y\left[\frac{xy}{r^2}z_2(kr)\right]=\left[\frac{xy^2}{r^3}\hat{p}_r+\frac{i\hbar}{r^4}\left(-z^2x-x(x^2-y^2)\right)\right]z_2(kr), \tag{152}$$

and the other sets result from the application of the three operators on the other two functions

$$\hat{p}_x\left[\frac{x^2-y^2}{r^2}z_2(kr)\right]=\left[\frac{x(x^2-y^2)}{r^3}\hat{p}_r+\frac{i\hbar}{r^4}\left(-4xy^2-2xz^2\right)\right]z_2(kr), \tag{153}$$

$$\hat{p}_y\left[\frac{x^2-y^2}{r^2}z_2(kr)\right]=\left[\frac{y(x^2-y^2)}{r^3}\hat{p}_r+\frac{i\hbar}{r^4}\left(2yz^2+4x^2y\right)\right]z_2(kr), \tag{154}$$

$$\hat{p}_z\left[\frac{x^2-y^2}{r^2}z_2(kr)\right]=\left[\frac{z(x^2-y^2)}{r^3}\hat{p}_r+\frac{i\hbar}{r^4}\left(2x^2z-2y^2z\right)\right]z_2(kr), \tag{155}$$

$$\hat{p}_x\left[\frac{2z^2-x^2-y^2}{r^2}z_2(kr)\right]=\left[\frac{x(2z^2-x^2-y^2)}{r^3}\hat{p}_r+\frac{i\hbar}{r^4}\left(6xz^2\right)\right]z_2(kr), \tag{156}$$

$$\hat{p}_y\left[\frac{2z^2-x^2-y^2}{r^2}z_2(kr)\right]=\left[\frac{y(2z^2-x^2-y^2)}{r^3}\hat{p}_r+\frac{i\hbar}{r^4}\left(6yz^2\right)\right]z_2(kr), \tag{157}$$

$$\hat{p}_z\left[\frac{2z^2-x^2-y^2}{r^2}z_2(kr)\right]$$
$$=\left[\frac{z(2z^2-x^2-y^2)}{r^3}\hat{p}_r+\frac{i\hbar}{r^4}\left(-6x^2z-6y^2z\right)\right]z_2(kr), \tag{158}$$

The differences between Eqs. (152)−(150), (148)−(151), and (149)−(147) lead to other $\ell=3$ eigenfunctions

$$\frac{x(y^2-z^2)}{r^3}z_3(kr),\quad \frac{y(z^2-x^2)}{r^3}z_3(kr),\quad \frac{z(x^2-y^2)}{r^3}z_3(kr). \tag{159}$$

Similarly, $\frac{z(2z^2-3x^2-3y^2)}{r^3}z_3(kr)$ is obtained from $(158)-2(147)-2(149)$; $\frac{y(3x^2-y^2)}{r^3}$ $z_3(kr)$ from $2(151)+(154)$; $\frac{x(x^2-3y^2)}{r^3}z_3(kr)$ from $-2(152)+(153)$; $\frac{y(4z^2-x^2-y^2)}{r^3}z_3(kr)$ from $2(148)+(157)$; and $\frac{x(4z^2-x^2-y^2)}{r^3}z_3(kr)$ from $2(150)+(156)$. Notice that according to Table 4.12 only the seven underlined functions are linearly independent.

In going from the $\ell=2$ to the $\ell=3$ eigenfunctions, the raising actions of the $\hat{\vec{p}}$ operators is implemented. The translations into spherical or spheroconal harmonics follow by using coordinate transformation equations and the addition theorem [5, 6].

The three combinations of Eqs. (150) + 2(152) + (153), (148) + 2(152) − (154), and 3(147) + 3(149) + (158) involving the factors $x^2+y^2+z^2=r^2$ and $\left(\hat{p}_r-\frac{3i\hbar}{r}\right)z_2(kr)=-i\hbar k z_1(kr)$ lead to the $\ell=1$ eigenfunctions

$$\frac{x}{r}z_1(kr),\quad \frac{y}{r}z_1(kr),\quad \frac{z}{r}z_1(kr), \tag{160}$$

exhibiting the combined lowering action of the operators $\hat{\vec{p}}$.

The generalization by mathematical induction is described next, without including the proof. In fact, the application of the three operators $\hat{p}_x$, $\hat{p}_y$, $\hat{p}_z$ on the $2\ell+1$ linearly independent cartesian angular momentum eigenfunctions multiplied by the radial Bessel function $z_\ell(kr)$ lead to the following results for ℓ even and odd, respectively.

Of the $3(4n+1)$ combinations for $\ell=2n$, there are $2(2n+1)+1$ with $\ell=2n+1$ and $2(2n-1)+1$ with $\ell=2n-1$ factorizable linearly independent combinations, which can be identified with cartesian angular momentum eigenfunctions of odd degrees $2n+1$ and $2n-1$, respectively, multiplied by the respective $z_{2n+1}(kr)$ and $z_{2n-1}(kr)$ radial functions. The combinations for the latter contain additionally the factor $x^2+y^2+z^2=r^2$.

Similarly, of the $3(4n+3)$ combinations for $\ell = 2n+1$, there are $2(2n+2)+1$ with $\ell = 2n+2$ and $2(2n)+1$ with $\ell = 2n$ linearly independent combinations, which can be identified with cartesian angular momentum eigenfunctions of even degrees $2n+2$ and $2n$, respectively, multiplied by their respective $z_{2n+2}(kr)$ and $z_{2n}(kr)$ radial functions. The combinations for the latter are also identified through their additional common factor $x^2+y^2+z^2=r^2$.

In both cases, the total numbers of independent states, $4n+3+4n-1=2(4n+1)$ and $4n+5+4n+1=2(4n+3)$, coincide with the number in Section 4.1 obtained by using the selection rules $\ell' = \ell+1$ and $\ell-1$, which is $2\ell+3+2\ell-1=2(2\ell+2)$.

Of course, the connection between Sections 4.1 and 4.2.2 is provided by Euler's formula $e^{\pm im\varphi} = \cos m\varphi \pm i \sin m\varphi$. Thus, the simultaneous raising and lowering actions of the linear momentum operators on the order of the angular momentum and radial eigenfunctions is established for cartesian, spherical, and spheroconal representations.

4.2.3. A spheroconal toolbox to continue the construction of the theory

This section contains some tools that we have identified as worth exploring in the ongoing development of the theory of angular momentum with a strictly spheroconal basis. We share them with the readers hoping that some may want to join in the task and develop tools of their own:

Vector operators $\hat{\vec{L}}$ and

$$\vec{e} \cdot \hat{\vec{L}} = \hat{\imath} e_1 \hat{L}_x + \hat{\jmath} e_2 \hat{L}_y + \hat{\mathrm{k}} e_3 \hat{L}_z. \tag{161}$$

Their scalar product

$$\hat{\vec{L}} \cdot \vec{e} \cdot \hat{\vec{L}} = 2H^*. \tag{162}$$

The linear momentum operator and its connection with the angular momentum operator in spheroconal and cartesian components:

$$\hat{\vec{p}} = (-i\hbar)\left[\hat{r}\frac{\partial}{\partial r} + \frac{\hat{\chi}_1}{h_\chi}\frac{\partial}{\partial \chi_1} + \frac{\hat{\chi}_2}{h_\chi}\frac{\partial}{\partial \chi_2}\right]. \tag{163}$$

The unit vectors $(\hat{r}, \hat{\chi}_1, \hat{\chi}_2)$ and scale factors $h_{\chi_1} = h_{\chi_2}$ can be found in the Appendix in Ref. [6],

$$\hat{\vec{L}} = \hat{\chi}_1 \hat{L}_{\chi_1} + \hat{\chi}_2 \hat{L}_{\chi_2}, \tag{164}$$

$$\hat{r} \times \hat{\vec{L}} = \hat{\chi}_2 \hat{L}_{\chi_1} - \hat{\chi}_1 \hat{L}_{\chi_2} = \frac{i\hbar r}{h_\chi}\left(\hat{\chi}_1 \frac{\partial}{\partial \chi_1} + \hat{\chi}_2 \frac{\partial}{\partial \chi_2}\right), \tag{165}$$

where in the last result, Eq. (120) has been used. Therefore,

$$\hat{L}_{\chi_1} = \frac{i\hbar r}{h_\chi}\frac{\partial}{\partial \chi_2}, \quad \hat{L}_{\chi_2} = -\frac{i\hbar r}{h_\chi}\frac{\partial}{\partial \chi_1}, \tag{166}$$

and

$$\hat{\vec{L}} = -\frac{i\hbar r}{h_\chi}\left(-\hat{\chi}_1\frac{\partial}{\partial \chi_2} + \hat{\chi}_2\frac{\partial}{\partial \chi_1}\right). \tag{167}$$

By using the unit vectors $\hat{\chi}_1$ and $\hat{\chi}_2$ in terms of the cartesian ones $\hat{\imath}$, $\hat{\jmath}$, $\hat{k}$, Eqs. (A.11–A.12) in Ref. [6], the cartesian components of the angular momentum are obtained as

$$\hat{L}_x = -i\hbar\left[\frac{\mathrm{cn}(\chi_2|k_2)\mathrm{dn}(\chi_1|k_1)\mathrm{dn}(\chi_2|k_2)}{1-k_1^2\mathrm{sn}^2(\chi_1|k_1)-k_2^2\mathrm{sn}^2(\chi_2|k_2)}\frac{\partial}{\partial\chi_1} + \frac{k_1^2\mathrm{sn}(\chi_1|k_1)\mathrm{sn}(\chi_2|k_2)\mathrm{cn}(\chi_1|k_1)}{1-k_1^2\mathrm{sn}^2(\chi_1|k_1)-k_2^2\mathrm{sn}^2(\chi_2|k_2)}\frac{\partial}{\partial\chi_2}\right], \tag{168}$$

$$\hat{L}_y = -i\hbar\left[\frac{\mathrm{sn}(\chi_1|k_1)\mathrm{cn}(\chi_2|k_2)\mathrm{dn}(\chi_1|k_1)}{1-k_1^2\mathrm{sn}^2(\chi_1|k_1)-k_2^2\mathrm{sn}^2(\chi_2|k_2)}\frac{\partial}{\partial\chi_2} - \frac{\mathrm{cn}(\chi_1|k_1)\mathrm{sn}(\chi_2|k_2)\mathrm{dn}(\chi_2|k_2)}{1-k_1^2\mathrm{sn}^2(\chi_1|k_1)-k_2^2\mathrm{sn}^2(\chi_2|k_2)}\frac{\partial}{\partial\chi_1}\right], \tag{169}$$

$$\hat{L}_z = i\hbar\left[\frac{k_2^2\mathrm{sn}(\chi_1|k_1)\mathrm{sn}(\chi_2|k_2)\mathrm{cn}(\chi_2|k_2)}{1-k_1^2\mathrm{sn}^2(\chi_1|k_1)-k_2^2\mathrm{sn}^2(\chi_2|k_2)}\frac{\partial}{\partial\chi_1} + \frac{\mathrm{cn}(\chi_1|k_1)\mathrm{dn}(\chi_1|k_1)\mathrm{dn}(\chi_2|k_2)}{1-k_1^2\mathrm{sn}^2(\chi_1|k_1)-k_2^2\mathrm{sn}^2(\chi_2|k_2)}\frac{\partial}{\partial\chi_2}\right], \tag{170}$$

coinciding with Eqs. (A.15–A.17) in Ref. [6].

The linear momentum becomes

$$\begin{aligned}\hat{\vec{p}} = \hat{\imath}\Big[&\mathrm{dn}(\chi_1|k_1)\mathrm{sn}(\chi_2|k_2)\hat{p}_r \\ &-\frac{1}{r}\left(\mathrm{cn}(\chi_1|k_1)\mathrm{cn}(\chi_2|k_2)\hat{L}_z - \mathrm{sn}(\chi_1|k_1)\mathrm{dn}(\chi_2|k_2)\hat{L}_y\right)\Big] \\ &+\hat{\jmath}\Big[\mathrm{cn}(\chi_1|k_1)\mathrm{cn}(\chi_2|k_2)\hat{p}_r \\ &-\frac{1}{r}\left(\mathrm{sn}(\chi_1|k_1)\mathrm{dn}(\chi_2|k_2)\hat{L}_x - \mathrm{dn}(\chi_1|k_1)\mathrm{sn}(\chi_2|k_2)\hat{L}_z\right)\Big]\end{aligned}$$

$$+\hat{\mathrm{k}}\Big[\mathrm{sn}(\chi_1|k_1)\mathrm{dn}(\chi_2|k_2)\hat{p}_r - \frac{1}{r}\left(\mathrm{dn}(\chi_1|k_1)\mathrm{sn}(\chi_2|k_2)\hat{L}_y - \mathrm{cn}(\chi_1|k_1)\mathrm{cn}(\chi_2|k_2)\hat{L}_z\right)\Big], \quad (171)$$

using the cartesian unit vectors and the operators in their spheroconal coordinate representations.

We also include the differential equations for the remaining factor in the Lamé functions after removing the singularity factors

$$\Lambda^A(\chi_i) = f_A(\chi_i)P^A(\chi_i), \quad (172)$$

which become

$$f_A\frac{\mathrm{d}^2P^A}{\mathrm{d}\chi_i^2} + 2\frac{\mathrm{d}f_A}{\mathrm{d}\chi_i}\frac{\mathrm{d}P^A}{\mathrm{d}\chi_i} + \frac{\mathrm{d}^2f_A}{\mathrm{d}\chi_i^2}P^A - \left[\ell(\ell+1)k_i^2\mathrm{sn}^2(\chi_i|k_i) + h_i^A\right]P^A = 0. \quad (173)$$

They are the general counterpart of Eqs. (36), (44), (49), (54), (59), (64), (69) in Ref. [4], which for the most asymmetric molecules with vanishing separation constant allowed the identification of four-step ladder operators, Eqs. (42 and 43) in Ref. [4]. In our case, the general equations for $A = d, c, s, cs, sd, dc, dcs$ are:

$$\mathrm{dn}(\chi_i|k_i)\frac{\mathrm{d}^2P^d}{\mathrm{d}\chi_i^2} - 2k_i^2\mathrm{sn}(\chi_i|k_i)\mathrm{cn}(\chi_i|k_i)\frac{\mathrm{d}P^d}{\mathrm{d}\chi_i} - \left[(\ell(\ell+1)-2)k_i^2\mathrm{sn}^2(\chi_i|k_i) + (h_i^d - k_i^2)\right]P^d = 0, \quad (174)$$

$$\mathrm{cn}(\chi_i|k_i)\frac{\mathrm{d}^2P^c}{\mathrm{d}\chi_i^2} - 2\mathrm{sn}(\chi_i|k_i)\mathrm{dn}(\chi_i|k_i)\frac{\mathrm{d}P^c}{\mathrm{d}\chi_i} - \left[(\ell(\ell+1)-2)k_i^2\mathrm{sn}^2(\chi_i|k_i) + (h_i^c - 1)\right]P^c = 0, \quad (175)$$

$$\mathrm{sn}(\chi_i|k_i)\frac{\mathrm{d}^2P^s}{\mathrm{d}\chi_i^2} + 2\mathrm{cn}(\chi_i|k_i)\mathrm{dn}(\chi_i|k_i)\frac{\mathrm{d}P^s}{\mathrm{d}\chi_i} - \left[(\ell(\ell+1)-2)k_i^2\mathrm{sn}^2(\chi_i|k_i) + (h_i^s + 1)\right]P^s = 0, \quad (176)$$

$$\mathrm{cn}(\chi_i|k_i)\mathrm{sn}(\chi_i|k_i)\frac{\mathrm{d}^2P^{cs}}{\mathrm{d}\chi_i^2} - 2\mathrm{dn}(\chi_i|k_i)[1-2\mathrm{sn}^2(\chi_i|k_i)]\frac{\mathrm{d}P^{cs}}{\mathrm{d}\chi_i} - \left[(\ell(\ell+1)-6)k_i^2\mathrm{sn}^2(\chi_i|k_i) + (h_i^{cs} - 4 - k_i^2)\right]P^{cs} = 0, \quad (177)$$

$$\mathrm{sn}(\chi_i|k_i)\mathrm{dn}(\chi_i|k_i)\frac{\mathrm{d}^2P^{sd}}{\mathrm{d}\chi_i^2}+2\mathrm{cn}(\chi_i|k_i)[1-2k_i^2\mathrm{sn}^2(\chi_i|k_i)]\frac{\mathrm{d}P^{sd}}{\mathrm{d}\chi_i}$$
$$-\left[(\ell(\ell+1)-6)k_i^2\mathrm{sn}^2(\chi_i|k_i)+(h_i^{sd}+4+k_i^2)\right]P^{sd}=0, \quad (178)$$

$$\mathrm{dn}(\chi_i|k_i)\mathrm{cn}(\chi_i|k_i)\frac{\mathrm{d}^2P^{dc}}{\mathrm{d}\chi_i^2}+2\mathrm{dn}(\chi_i|k_i)[-1+2k_i^2\mathrm{sn}^2(\chi_i|k_i)]\frac{\mathrm{d}P^{dc}}{\mathrm{d}\chi_i}$$
$$-\left[(\ell(\ell+1)-6)k_i^2\mathrm{sn}^2(\chi_i|k_i)+(h_i^{dc}+1)\right]P^{dc}=0, \quad (179)$$

$$\mathrm{dn}(\chi_i|k_i)\mathrm{cn}(\chi_i|k_i)\mathrm{sn}(\chi_i|k_i)\frac{\mathrm{d}^2P^{dcs}}{\mathrm{d}\chi_i^2}$$
$$+2[1-2(1+k_i^2)\mathrm{sn}^2(\chi_i|k_i)+3k_i^2\mathrm{sn}^4(\chi_i|k_i)]\frac{\mathrm{d}P^{dcs}}{\mathrm{d}\chi_i}$$
$$-\left[(\ell(\ell+1)-12)k_i^2\mathrm{sn}^2(\chi_i|k_i)+(h_i^{dcs}+2(1+k_i^2))\right]P^{dcs}=0. \quad (180)$$

Notice that the coefficient $\ell(\ell+1)$ in the original equation becomes $(\ell-1)(\ell+2)$, $(\ell-2)(\ell+3)$, and $(\ell-3)(\ell+4)$ for the successive species being the same as Eqs. (52–56), while the eigenvalues h_i^A are also shifted depending on the coefficients involved in the second derivatives of $f_A(\chi_i)$. These changes are reminiscent of the familiar ones for the ordinary and associated Legendre polynomials, and their connections with the actions of ladder operators. We are exploring the possibilities for the Lamé functions themselves and their connections with Section 4.2.2.

For the mathematically inclined Volkmer's Chapter 29 on Lamé functions in the *NIST Handbook of Mathematical Functions* [50], and the article "A new basis for the representations of the rotational group. Lamé and Heun polynomials" [51] are parts of the toolbox.

5. DISCUSSION

The topics of this chapter, listed in the Contents and outlined in the Introduction, discuss the rotations of asymmetric molecules and the hydrogen atom in their natural free configurations as reviewed in Section 2; changes in the properties of the same systems in configurations of confinement by elliptical cones are reported, including new results for asymmetric molecules, in Section 3; and some advances in developing the theory of angular momentum in spheroconal harmonic bases, as well as some possible routes under exploration are presented in Section 4.

The exact nature of the formulations of the problem of rotations of symmetric molecules in spheroconal coordinates, in Sections 2.1 and 2.2, is emphasized, recognizing also their points of contact and differences. The

latter reside in their respective algebraic and Jacobi elliptic function representations of the spheroconal coordinates, uses of the complete Hamiltonian $H(a,b,c)$ with three independent parameters and asymmetry distribution Hamiltonian $\hat{H}^*(e_1,e_2,e_3) = \hat{H}^*(\sigma)$ with one independent parameter. Their points of contact are given through Eqs. (8 and 42) for the respective coordinate transformations, and Eqs. (32–38) for the parameter transformations, establishing the equivalence of both formulations. Of course, the one parameter dependence of $\hat{H}^*$ gives it advantage over the three parameter dependence of $\hat{H}$; nevertheless, because they commute with each other and with $\hat{L}^2$, they all share common Lamé spheroconal harmonic polynomial eigenfunctions. They also shared the limitation of not having had a reliable numerical method to evaluate the latter, with the consequence that the analysis of the rotational spectra followed the perturbation theory route starting from the symmetric prolate and oblate molecules. Section 2.3 focused on the most asymmetric molecules with the idea of using it also as the starting point for perturbation theory.

Our works reviewed in Sections 2.4 and 2.5 were focused on matrix evaluations of the exact rotational eigenstates of molecules with any asymmetry, using the spherical harmonic bases and constructing the individual and matching Lamé functions, respectively. Both methods lead to the same numerical results for the eigenenergies $E^*_{n_1 n_2}(\sigma)$ and eigenstates $\Psi^{AB}_{n_1 n_2}(\sigma)$, with $n_1 + n_2 = \ell$ for any integer value of ℓ. The energy spectra and eigenfunctions for the entire range of the asymmetry distribution parameter $0^\circ < \sigma < 60^\circ$ reflect the symmetries of $\hat{H}^*(\sigma)$.

Section 2.6 recognizes that for the hydrogen atom, its Hamiltonian also commutes with $\hat{L}^2$ and $\hat{H}^*$; correspondingly, it also admits solutions with Lamé spheroconal harmonics polynomial eigenfunctions. It also shares the same radial eigenfunction with the familiar solution with spherical harmonics, and additionally both can be obtained from a common generating function and both satisfy the addition theorem.

The Guide in Section 3 covers in succession: 3.1 Going from the free hydrogen atom to its confinement by any of its natural conoidal boundaries including elliptical cone boundaries. 3.2 The same commutation rules apply for any central potential, admitting in consequence Lamé spheroconal harmonic polynomial eigenfunctions when free, and Lamé spheroconal harmonic quasi-periodic functions when confined by an elliptical cone boundary. 3.3 The confined hydrogen atom required the matrix construction of the matching Lamé spheroconal harmonic quasi-periodic functions with broken parity symmetry relative to the axis of the confining elliptical cone. 3.4 Since the hydrogen atom and the asymmetric molecules share commuting operators and common eigenfunctions, in both free and confined by elliptical cone configurations, the study in this section concentrated on the construction of the energies $E^*_{n_1 n_2}(\sigma, \chi_{i0})$ for $i = 1$ and 2 for the molecules.

Although our motivation in Refs. [5] and [6] was the accurate evaluation of the rotational eigenenergies and eigenstates of the asymmetric molecules, our motivation in the writing of the review in Section 2 has been the identification of the elements to develop the theory of angular momentum in bases of spheroconal harmonics as presented in Section 4. In fact, Sections 4.1, 4.2.1, and 4.2.2 are geared to the connections among the familiar spherical harmonics, the spherical harmonics with definite parities, and the spheroconal harmonics. From those connections, we have recognized some of the tools to hopefully construct the theory of angular momentum on a strictly spheroconal harmonic basis.

The methods and results reviewed in Section 2, guided in Section 3, and explored in Section 4 have validity beyond the specific topics of rotations of asymmetric molecules and the hydrogen atom discussed in this chapter. They may be useful and find applications in other areas of Chemistry and Physics as already pointed out in Ref. [1].

ACKNOWLEDGMENTS

The authors sincerely thank Prof. John Sabin, Editor of *Advances in Quantum Chemistry*, for his encouraging invitation to write this chapter. They also gratefully acknowledge the financial support from SNI-1796 CONACYT for the research reported herein.

Additional thanks are expressed with pleasure to Prof. Eduardo Piña, Universidad Autónoma Metropolitana - Iztapalapa, for sharing his expertise on classical and quantum rotations; to Prof. Hans Volkmer, University of Wisconsin - Milwaukee, for discussions on how to evaluate Lamé functions; and to Prof. Jocele Allegra Wild Wolf for proof reading and sustained encouragement.

REFERENCES

[1] R. Mendez-Fragoso, E. Ley-Koo, Lamé spheroconal harmonics in atoms and molecules. Int. J. Quant. Chem. 110 (2010) 2765.
[2] H.A. Kramers, G.P. Ittmann, Zeits. Phys. 53 (1929) 553.
[3] E. Piña, J. Mol. Struct. (THEOCHEM) 493 (1999) 159.
[4] M.T. Valdés, E. Piña, Rev. Mex. Fís. 52 (2006) 220.
[5] E. Ley-Koo, R. Méndez-Fragoso, Rev. Mex. Fís. 54 (2008) 69.
[6] E. Ley-Koo, R. Méndez-Fragoso, Rev. Mex. Fís. 54 (2008) 162.
[7] E. Ley-Koo, A. Góngora-T, The hydrogen atom in a semi-infinite space with an elliptical cone boundary. Int. J. Quant. Chem. 109 (2009) 790.
[8] R. Méndez-Fragoso, E. Ley-Koo, Int. J. Quant. Chem. (Published Online: May 18 2010) DOI 10.1002/qua.22569.
[9] E. Ley-Koo, Adv. Quant. Chem. 57 (2009) 79.
[10] P.M. Morse, H. Feshbach, Methods of Theoretical Physics, Mc Graw-Hill, New York, 1953.

[11] M. Abramowitz, I.A. Stegun, Handbook of Mathematical Functions, Dover, New York, 1965.
[12] E.T. Whittaker, G.N. Watson, A Course of Modern Analysis, Cambridge University Press, United Kingdom, 1927.
[13] G. Hunter, H.O. Pritchard, J. Chem. Phys. 46 (1967) 2146.
[14] E. Kalnins, W. Miller, P. Winternitz, P. SIAM, J. Appl. Math. 30 (1976) 360.
[15] F. Reiche, Zeits. Phys. 19 (1918) 394.
[16] E.E. Witmer, Proc. Natl. Acad. Am. 12 (1926) 602.
[17] F. Lütgemeier, Zeits. Phys. 38 (1926) 251.
[18] C. Niven, Philos Transact R Soc Lond 171 (1880) 117.
[19] F. Reiche, H. Rademacher, Zeits. Phys. 39 (1926) 444.
[20] R. de, L. Kronig, J.J. Rabi, Phys. Rev. 29 (1927) 262.
[21] B.S. Ray, Zeits. Phys. 78 (1932) 74.
[22] R. Mecke, Zeits. Phys. 81 (1933) 313.
[23] G.W. King, R.M. Hainer, P.C. Cross, J. Chem. Phys. 11 (1943) 27.
[24] G.W. King, R.M. Hainer, P.C. Cross, J. Chem. Phys. 12 (1944) 210.
[25] G.W. King, R.M. Hainer, P.C. Cross, J. Chem. Phys. 15 (1947) 820.
[26] C. Van Winter, Physica 20 (1954) 274.
[27] J.M. Bennett, I.G. Ross, E.J. Wells, J. Mol. Spectrosc. 4 (1960) 342.
[28] J.D. Louck, J. Mol. Spectrosc. 10 (1963) 163.
[29] J.D. Louck, J. Mol. Spectrosc. 10 (1965) 83.
[30] J.E. Wollrab, Rotational Spectra and Molecular Structure, Academic Press, New York, 1967.
[31] H.W. Kroto, Molecular Rotation Spectra, John Wiley & Sons, Great Britain, 1975.
[32] NIST Computational Chemistry Comparison and Benchmark Database, NIST Standard Reference Database Number 101 Release 15a, April 2010, Editor: Russell D. Johnson III http://cccbdb.nist.gov/
[33] C.H. Townes, A.L. Schawlow, Microwave Spectroscopy, Dover, New York, 1975.
[34] E. Piña, Rev. Mex. Fís. 41 (1995) 913.
[35] L. Chaos-Cador, E. Ley-Koo, Rev. Mex. Fís. 48 (2002) 67.
[36] N. Aquino, E. Castaño, E. Ley-Koo, Rev. Mex. Fís. 48 (2002) 277.
[37] L. Chaos-Cador, E. Ley-Koo, Int. J. Quantum Chem. 97 (2004) 844.
[38] L. Chaos-Cador, E. Ley-Koo, Int. J. Quantum Chem. 103 (2005) 369.
[39] E. Ley-Koo, S. Mateos-Cortés, Am. J. Phys. 61 (1993) 246.
[40] J.D. Levine, Phys. Rev. A 140 (1965) 586.
[41] E. Ley-Koo, R.M.G. García-Castelán, J. Phys. A 24 (1991) 1481.
[42] J.O. Hirschfelder, J. Chem. Phys. 68 (1978) 5151.
[43] A. Sommerfeld, H. Hartmann, Ann. Phys. 5 (1940) 333.
[44] L. Infeld, T.E. Hull, Rev. Mod. Phys. 23 (1951) 21.
[45] S.H. Dong, Factorization Method in Quantum Mechanics, The Netherlands, Springer, 2007.
[46] M.E. Rose, Elementary Theory of Angular Momentum, Dover, New York, NY, USA, 1995.
[47] Q.H. Liu, D.M. Xun, L. Shan, Int. J. Theor. Phys. 49 (2010) 2164.
[48] G.H. Sun, S.H. Dong, Phys. Lett. A 374 (2010) 4112.
[49] X.L. Ka, Lamé Functions. Advanced Quantum Mechanics, Higher Education, Beijing, New York, NY, USA, 2001, p. 135.
[50] H. Volkmer, in: F.W.J. Oliver, D.W. Lozier, R.F. Boisvert, C.W. Clark (Eds.), NIST Handbook of Mathematical Functions, Cambridge University Press, New York, NY, USA, 2010 (chap. 29.).
[51] J. Patera, P. Winternitz, J. Math. Phys. 14 (1973) 1130.

CHAPTER 5

Mean Excitation Energies for Biomolecules: Glycine to DNA

Stephan P. A. Sauer[a], **Jens Oddershede**[b,c], and **John R. Sabin**[b,c]

Contents

Abstract The effects of energy transfer from swift ion radiation to biomolecules are best described by the stopping cross section of the target for the projectile ion. In turn, the mean excitation energy of the target is the determining

[a] Department of Chemistry, University of Copenhagen, Copenhagen, Denmark
E-mail address: sauer@kiku.dk
[b] Department of Physics and Chemistry, University of Southern Denmark, Odense Denmark
E-mail address: sabin@qtp.ufl.edu
[c] Quantum Theory Project, Department of Physics, University of Florida, Gainesville, Florida, USA
E-mail address: jod@sdu.dk

Advances in Quantum Chemistry, Volume 62
ISSN 0065-3276, DOI: 10.1016/B978-0-12-386477-2.00011-5

factor in the stopping cross section. Using polarization propagator methodology, the mean excitation energies of components of several biomolecular systems, ranging from amino acids to nucleotides, have been reported. The calculated mean excitation energies could then be used to determine the stopping cross sections of the various biomolecular systems.

1. INTRODUCTION

Although the bulk of biological damage resulting from exposure to radiation comes from either single (SSB) or double (DSB) strand breaks in DNA, relatively few such breaks are produced by direct hits of ions or photons on DNA. Rather, because it is ubiquitous in the cell, most damage arises from decay products of the interaction of radiation with water: from δ- (or secondary) electrons that can interact either directly or indirectly through water with a biomolecule, as well as from O- and OH-free radicals. For massive ionizing radiation such as protons and alpha particles, this is almost entirely the case, whereas for photons, there is a larger possibility of exciting a molecule somewhat larger than water, or localized fragment of a molecule, causing electronic excitation which is followed by fragmentation or decomposition into radicals and electrons. Understanding the interaction of radiation, both massive and mass-less particles, with biological targets becomes increasingly important as we seek to protect healthy cells from radiation damage and to selectively target therapeutic radiation on pathologic cells.

The problem of describing and explaining the effects of radiological action on biological systems is tremendous [1, 2], as the problem extends over many orders of magnitude in complexity, timescale, and size, as the effects of the interaction of radiation with matter become more complicated. In any such process, where there is exposure of a biological entity to radiation, be it for therapeutic or malevolent purposes, there are long chains of sequential and parallel actions, as well as possible nonlinearities between initial radiogenic molecular changes and final biological effects [3]. The chain of events can be viewed in a hierarchical scheme beginning with the initial interaction of the radiation with a molecule in a biological sample: Initial reactions of radiation with biomolecules, diffusion, de-excitation and/or dissociation, effects on DNA (such as strand breaks), followed by effects on the cell, on tissue, on organs, and finally, effects on the organism. All of these processes must be well understood in order to deal effectively with problems such as radiation protection and radiation therapy.

There are, in principle, two general ways to approach such a problem: either top down or bottom up. Both are valid, and they contribute greatly to the final understanding of the process. In this work, we take the bottom up approach, and, more particularly, apply quantum mechanical molecular electronic structure theory to the problem.

The interaction of radiation with biomolecular targets has broad and deep implications in modern life. Some modern speculation involves the interaction of swift ions and/or photons (γ-radiation) with interstellar protobiotic molecules to produce glycine, a precursor of life [4]. The interaction of ions and gamma rays can be used to treat, or cause, cancers, depending on the point of application and the nature of the radiation. Single, double, or multiple strand breaks in DNA can cause damage with resulting repair, mutation, or cell death.

There are several sorts of radiation and particles that are of interest when one is concerned with the interaction of radiation with biological matter, and how they interact with biomolecules in somewhat different ways. In this study, we concentrate on massive particles, which deposit energy in a molecule by collision with either the electrons (the dominant mechanism at higher collision energies) or the nucleus of the molecule (more important at lower collision energies). The collision typically results in electronic excitation of the target molecule, followed by ionization, decay, emission of secondary radiation, and/or fragmentation. In the cases discussed here, namely that of swift ions colliding with biomolecules, the energy deposition is done predominantly at the end of the ion's track through the target, and the Bragg peak (the maximum in the energy deposition per unit path length) comes just before the particle comes to rest.

Perhaps the most spectacular form of radiation resulting from the large amount of energy that it can deposit in matter comes from impact of highly charged, high-energy heavy ions (e.g., Xe^{18+}) with biomaterials. Such ions blast through a biological system wrecking havoc along the track. Although there may be few direct hits on biomolecules when fast ions impact biological materials, there are some, and it is those direct hits that we are concerned with here. Concomitantly, under these circumstances water is ionized and fragmented abundantly, and the resulting radicals and δ-electrons cause great damage. Most ionic radiation is not so spectacular, however, and consists of the much more mundane, more common, and better understood swift protons and alpha particles. These particles also ionize and fragment water as well as causing damage by direct hits.

Here, we consider the very first steps in the energy deposition by a fast ion colliding with a biomolecule. The single materials parameter that best describes the propensity for energy transfer from the projectile to the target, the stopping power of the target molecule for the ion, is the mean excitation energy (vide infra) of the target, and that is the quantity that we focus on here. We summarize a program of calculations of mean excitation energies from the simplest of protobiologic molecules, namely formaldehyde, to RNA and DNA [5–10].

Although not the subject of this study, other forms of radiation such as electrons, photons, neutrons, etc. also have great significance in radiation biology. These particles interact with biomolecules in a very different way than do the heavy ions.

2. BETHE'S THEORY OF STOPPING

One of the simpler, and first truly quantum mechanical, treatments of energy transfer by a fast ion of mass M and charge $+Ze$ to a target atom or molecule is that of Bethe [11].

Energy transfer to a molecule by a fast ion is frequently described in terms of the so-called linear energy transfer (LET), or stopping power $-\mathrm{d}E/\mathrm{d}x$, of the target molecule [12, 13]. To avoid problems when comparing stopping in targets of different densities, one frequently considers the stopping cross section $S(v)$:

$$-\frac{\mathrm{d}E}{\mathrm{d}x} = NS(v) \tag{1}$$

where N is the number density of the scatterers, and v is the projectile velocity. The cross section is derived by standard time-dependent perturbation theory [11, 14]. The Hamiltonian $\hat{H}$ of the total system, a molecule interacting with a fast ion, is thereby partitioned in a zeroth-order part, describing the unperturbed molecule $\hat{H}_{\mathrm{mol}}$ and a fast moving ion $\hat{H}_{\mathrm{p}}$, and a perturbation term $\hat{H}_{\mathrm{int}}$, which describes the interaction between the molecule and the fast ion. The unperturbed, time-dependent wavefunctions for the system before the collision $|0,k\rangle$ and for any of the possible excited states $|n,k_n\rangle$ that the target may be excited into after the inelastic scattering event takes place are simple product functions of wavefunctions for the molecule $\{\Psi_0, \Psi_n\}$ with energies $\{E_0, E_n\}$ and plane wave functions for the ion times the time-dependent phase factor, that is,

$$|0,k\rangle = \Psi_0 e^{i\vec{k}\cdot\vec{R}} e^{i\left(E_0+\frac{\hbar^2k^2}{2M}\right)\frac{t}{\hbar}} \tag{2}$$

$$|n,k_n\rangle = \Psi_n e^{i\vec{k}_n\cdot\vec{R}} e^{i\left(E_n+\frac{\hbar^2k_n^2}{2M}\right)\frac{t}{\hbar}} \tag{3}$$

where $\vec{R}$ is the vector from the center of mass of the molecule to the ion and $\{\vec{k},\vec{k}_n\}$ are the wave vectors of the ion before and after the collision. Because we are concerned with fast ions, where the interaction is primarily with the electrons of the molecule, we make use of the Born–Oppenheimer approximation and replace the molecular wavefunctions and energies by the electronic wavefunctions and energies for an equilibrium geometry.

Expanding the time-dependent wavefunction for the interacting system in this basis of unperturbed functions, Eqs. (2) and (3), and using the machinery of time-dependent perturbation theory yields the differential cross section $\sigma_n(q)\mathrm{d}q$ as function of the momentum transfer q

$$\sigma_n(q)\mathrm{d}q = \frac{1}{2\pi}\frac{q}{\hbar^2v^2}\left|\langle n,k_n|\hat{H}_{\mathrm{int}}|0,k\rangle\right|^2\mathrm{d}q \tag{4}$$

The differential cross section is essentially the number of ions experiencing a momentum transfer $q = |\vec{q}| = |\vec{k} - \vec{k}_n|$ in the inelastic scattering while leaving the molecule in the excited state $|\Psi_n\rangle$ with energy E_n. The total cross section is obtained by summing over all excited electronic states of the molecule, bound as well as continuum states, and integrating over all possible values of the momentum transfer q

$$-\frac{\mathrm{d}E}{\mathrm{d}x} = N \int_{q_{\min}}^{q_{\max}} \sum_{n>0} (E_n - E_0)\sigma_n(q)\mathrm{d}q \tag{5}$$

However, before doing so, one has to evaluate the matrix elements of the interaction operator $\hat{H}_{\mathrm{int}}$, which consists of the electrostatic repulsion of the positively charged ion by the nuclei in the molecule and the attraction by the N_{e} electrons in the molecule, that is,

$$\hat{H}_{\mathrm{int}} = Ze^2 \left(\sum_{M}^{\text{nuclei}} \frac{Z_M}{|\vec{R} - \vec{R}_M|} - \sum_{j}^{N_{\mathrm{e}}} \frac{1}{|\vec{R} - \vec{r}_j|} \right) \tag{6}$$

where the nuclear and electronic position vectors $\{\vec{R}_M, \vec{r}_j\}$ are also taken with respect to the center of mass of the molecule. Because we are considering only exited electronic states, the matrix element of $\hat{H}_{\mathrm{int}}$ reduces to

$$\langle n, k_n | \hat{H}_{\mathrm{int}} | 0, k \rangle = -\frac{4\pi e^2 Z}{q^2} \left\langle \Psi_n \left| \sum_{j}^{N_{\mathrm{e}}} e^{i\vec{q}\cdot\vec{r}_j} \right| \Psi_0 \right\rangle \tag{7}$$

and the differential cross section becomes

$$\sigma_n(q)\mathrm{d}q = \frac{8\pi e^4 Z^2}{\hbar^2 v^2} \left| \langle \Psi_n | \sum_{j}^{N_{\mathrm{e}}} e^{i\vec{q}\cdot\vec{r}_j} | \Psi_0 \rangle \right|^2 \frac{\mathrm{d}q}{q^3} \tag{8}$$

The total cross section is then calculated as

$$-\frac{\mathrm{d}E}{\mathrm{d}x} = N \frac{8\pi e^4 Z^2}{\hbar^2 v^2} \int_{q_{\min}}^{q_{\max}} \sum_{n>0} (E_n - E_0) \left| \langle \Psi_n | \sum_{j}^{N_{\mathrm{e}}} e^{i\vec{q}\cdot\vec{r}_j} | \Psi_0 \rangle \right|^2 \frac{\mathrm{d}q}{q^3} \tag{9}$$

where the quantity

$$F_{0n}(\vec{q}) = \frac{2m_{\mathrm{e}}}{\hbar^2 q^2} (E_n - E_0) \left| \langle \Psi_n | \sum_{j}^{N_{\mathrm{e}}} e^{i\vec{q}\cdot\vec{r}_j} | \Psi_0 \rangle \right|^2 \tag{10}$$

is known as the generalized oscillator strength (GOS) [15]. The cross section can then be obtained by performing the integration and summation in Eq. (9) over these generalized oscillator strengths [16, 17]. However, in most cases, the GOS is approximated by expanding the exponential operator $e^{i\vec{q}\cdot\vec{r}_j} = 1 + i\vec{q}\cdot\vec{r}_j + \cdots$ and keeping only the first two terms, yielding:

$$F_{0n}(\vec{q}) \approx f_{0n} + \cdots \tag{11}$$

where f_{0n} is the dipole oscillator strength of optical spectroscopy in dipole length formulation,

$$f_{0n} = \frac{2}{3}\frac{m_e}{\hbar^2}(E_n - E_0)\left|\langle\Psi_n|\sum_j^{N_e}\vec{r}_j|\Psi_0\rangle\right|^2 \tag{12}$$

which is independent of the momentum transfer q. If the square of the norm is "interpreted" as the dot product of the indicated matrix element and its adjoint, then Eq. (12) represents the directionally averaged dipole oscillator strength. For the dipole oscillator strength for a particular direction, the coordinate in the expectation value should be that direction and the prefactor should be 2 instead of 2/3. The complete set of dipole oscillator strengths corresponding to excitations to all bound and continuum states of a molecule is called the dipole oscillator strength distribution (DOSD), which summed fulfills Thomas–Reiche–Kuhn (TRK) sum rule [18–20]

$$S_0 = \sum_{n>0} f_{0n} = N_e \tag{13}$$

This holds not only for oscillator strengths calculated from the exact eigenstates of the molecular Hamiltonian, but also for oscillator strengths obtained with certain approximate methods, vide infra.

Finally carrying out the summation over all excited electronic states of the molecule, bound as well as continuum states, and integrating over all possible values of the momentum transfer q one obtains

$$S(v) = \frac{4\pi e^4 Z^2 N_e}{m_e v^2}\ln\frac{2m_e v^2}{I_0} \tag{14}$$

where the quantity I_0 is known as the mean excitation energy of the target and is defined as the first energy-weighted moment of the dipole oscillator strength distribution (DOSD) of the target

$$\ln I_0 = \frac{\sum_{n>0} f_{0n}\ln(E_n - E_0)}{\sum_{n>0} f_{0n}} \tag{15}$$

where $\sum_{n>0}$ again implies summation over all bound excited states with energy E_n and integration over all excited continuum states of the target molecule.

Using individual Cartesian components of the dipole moment operator $\sum_j^{N_e} \vec{r}_j$ in the dipole oscillator strength, Eq. (12), we can obtain directional components I_0^x, I_0^y, and I_0^z of the mean excitation energy from Eq. (15), which are related to their isotropic value as

$$I_0 = (I_0^x I_0^y I_0^z)^{\frac{1}{3}} \tag{16}$$

Using the directional components of the mean excitation energy, one can calculate the stopping power for a particular orientation of the target molecule with respect to the beam and the total stopping power can then be decomposed into components with the incident beam either parallel or perpendicular to the plane of e.g., a nucleobase or amino as done in the following:

$$S(v) = \frac{2}{3} S_{\parallel}(v) + \frac{1}{3} S_{\perp}(v). \tag{17}$$

Here the symbols $\perp$ and $\parallel$ refer to the orientation of the projectile beam with respect to the molecular plane. As only excitations with polarization perpendicular to the projectile velocity can contribute to the stopping power [21], and because we will generally place the molecules considered here in the xy-plane, the projectiles moving perpendicular to the plane are described by I_0^x and I_0^y while those moving in the molecular plane are described by either I_0^x and I_0^z or by I_0^y and I_0^z. The perpendicular and parallel components of the stopping power of a molecule placed in the xy-plane can then be expressed as

$$S_{\perp}(v) = \frac{4\pi e^4 Z^2 N_e}{m_e v^2} \ln \frac{2 m_e v^2}{(I_0^x I_0^y)^{\frac{1}{2}}} \tag{18}$$

and

$$S_{\parallel}(v) = \frac{4\pi e^4 Z^2 N_e}{m_e v^2} \ln \frac{2 m_e v^2}{(I_0^x I_0^y (I_0^z)^2)^{\frac{1}{4}}} \tag{19}$$

Furthermore, one can define an anisotropy, A, in the energy deposition [22] arising from the relative orientation of the projectile direction with respect to the plane of the nucleobase or amino acid in terms of the directional components as

$$A = -N_e \ln \frac{I_0^x I_0^y}{(I_0^z)^2} = -4 N_e \ln \frac{I_0^{\perp}}{I_0^{\parallel}} \tag{20}$$

Inokuti pointed out [23] that "The mean excitation energy, I_0, is the sole nontrivial property of matter appearing in Bethe's expression for the stopping power for a charged particle at high speed." The mean excitation energy measures the difficulty with which a target molecule can absorb energy from a massive projectile. Large mean excitation energies correspond to greater difficulty for the absorption of energy by a target molecule, and thus lead to lower stopping power. We will thus concentrate on the mean excitation energies of the biomolecules as descriptors of their interaction with swift ions.

In this simplest version of stopping theory according to Bethe [11], it is assumed that the projectile velocity v is considerably larger than the velocity of the electrons in the target molecule. In order to extend the treatment to the case of smaller projectile velocity, Eqn. (14) can be generalized to

$$S(v) = \frac{4\pi e^4 Z^2 N_e}{m_e v^2} L(v), \tag{21}$$

where the stopping number, $L(v)$, is extended by so-called shell corrections, $-\frac{C(v)}{N_e}$, that is,

$$L(v) = \ln \frac{2m_e v^2}{I_0} - \frac{C(v)}{N_e} \tag{22}$$

which approach zero for increasing projectile velocities.

3. DIPOLE OSCILLATOR STRENGTH DISTRIBUTIONS OBTAINED FROM POLARIZATION PROPAGATORS

The vertical electronic excitation energies, $E_n - E_0$, and associated electronic transition dipole moments $\langle \Psi_n | \sum_j^{N_e} \vec{r}_j | \Psi_0 \rangle$ for a molecule that are needed in order to obtain the mean excitation energies according to Eq. (15) can conveniently be extracted from the linear response function or polarization propagator [24], as can be seen from its spectral representation in the basis of the eigenstates $\{|\Psi_0\rangle, |\Psi_n\rangle\}$ of the molecular Hamiltonian $\hat{H}_{\text{mol}}$:

$$\left\langle\left\langle \hat{P}; \hat{Q} \right\rangle\right\rangle_E = \sum_{n \neq 0} \left[\frac{\langle \Psi_0 | \hat{P} | \Psi_n \rangle \langle \Psi_n | \hat{Q} | \Psi_0 \rangle}{E - E_n + E_0} + \frac{\langle \Psi_0 | \hat{Q} | \Psi_n \rangle \langle \Psi_n | \hat{P} | \Psi_0 \rangle}{E + E_n - E_0} \right], \tag{23}$$

where the sum is over all excited states $\{|\Psi_n\rangle\}$ of the system. The poles and residues of the propagator are the excitation energies and transition matrix elements, $\langle \Psi_0 | \hat{P} | \Psi_n \rangle$, of the operators $\hat{P}$ and $\hat{Q}$, respectively. If we choose $\hat{P} = \hat{Q} = \sum_j^{N_e} \vec{r}_j$, then the residues may be used to compute the dipole

oscillator strengths of the system in the length formulation (all quantities are in Hartree atomic units), while choices of $\hat{P} = \hat{Q} = \sum_j^{N_e} \hat{\vec{p}}_j$ or $\hat{P} = \sum_j^{N_e} \vec{r}_j$ and $\hat{Q} = \sum_j^{N_e} \hat{\vec{p}}_j$ lead to dipole oscillator strengths in the velocity and mixed formulations, respectively. We note that all the quantities reported here are calculated in the dipole length formulation.

However, in order to obtain excitation energies and transition moments from the polarization propagator, one has to have another way of obtaining the propagator. This is provided by using the property that polarization propagators are the linear responses to number conserving external perturbations. Using this approach, one may express the propagator in terms of a set of matrices as

$$\left\langle\left\langle \hat{P}; \hat{Q} \right\rangle\right\rangle_E = \tilde{\mathbf{T}}^{[1]}(\hat{P})(E\mathbf{S}^{[2]} - \mathbf{E}^{[2]})^{-1}\mathbf{T}^{[1]}(\hat{Q}), \tag{24}$$

where $\mathbf{E}^{[2]}$ and $\mathbf{S}^{[2]}$ are the molecular Hessian and overlap matrices

$$(\mathbf{E}^{[2]})_{ij} = \langle\Psi_0|[h_i, [\hat{H}, h_j^\dagger]]|\Psi_0\rangle \tag{25}$$

$$(\mathbf{S}^{[2]})_{ij} = \langle\Psi_0|[h_i, h_j^\dagger]|\Psi_0\rangle \tag{26}$$

and $\tilde{\mathbf{T}}^{[1]}(\hat{P})$ and $\mathbf{T}^{[1]}(\hat{Q})$ are property gradient vectors

$$(\tilde{\mathbf{T}}^{[1]}(\hat{P}))_i = \langle\Psi_0|[\hat{P}, h_i]|\Psi_0\rangle \tag{27}$$

$$(\mathbf{T}^{[1]}(\hat{Q}))_i = \langle\Psi_0|[h_i^\dagger, \hat{Q}]|\Psi_0\rangle \tag{28}$$

Choosing the operators $\{h_i\}$ to be the state-transfer operators $\{|\Psi_n\rangle\langle\Psi_0|; |\Psi_0\rangle\langle\Psi_n|\}$ would lead us back to the spectral representation, Eq. (23). In practical applications, however, the exact ground state of the system $|\Psi_0\rangle$ is replaced by some approximate wave function $|\Phi\rangle$, which is a linear combination of antisymmetrized products of molecular orbitals, so-called Slater determinants, while the operators $\{h_i\}$ replace one or more of the occupied molecular orbitals by virtual orbitals (excitations) in the Slater determinants or virtual orbitals by occupied orbitals (de-excitations). Approximations to the vertical electronic excitation energies $E_n - E_0$ are then obtained by solving the generalized eigenvalue problem

$$[\mathbf{E}^{[2]} - (E_n - E_0)\mathbf{S}^{[2]}]\mathbf{X}_{0n} = \mathbf{0} \tag{29}$$

and the corresponding approximations to the transition matrix elements are calculated from the eigenvectors $\mathbf{X}_{0n}$ as

$$\langle\Psi_0|\hat{P}|\Psi_n\rangle = \tilde{\mathbf{T}}^{[1]}(\hat{P})\mathbf{X}_{0n} \tag{30}$$

This approach yields a finite number of excitations. As a result, the integrations over the continuum states in Eqs. (13) and (15) are done numerically using the excitation energies with energies larger than the first ionization energy of the system, called pseudostates, as integration points. We have found that this discretization of the continuum works well provided sums over the entire excitation spectrum are taken [25]. It should be noted that energy-weighted oscillator strength sums can also be obtained directly from matrices used in the polarization propagator [26, 27], but the direct sum over states was used in this application as it was more convenient. The DOSD sum rules and mean excitation energies in Eq. (15) are then obtained by explicit summation of the oscillator strengths to all bound states and to the discrete continuum pseudostates. Experience indicates that about 10% to 15% of the mean excitation energy is because of excitation to bound states, while the remaining 85% to 90% comes from transitions into the pseudostates for the biomolecules considered here [5].

Different types of reference wave functions $|\Phi\rangle$ and corresponding sets of excitation operators $\{h_i\}$ can be used in Eqs. (25–28). Experience also shows [11, 28] that some amount of electron correlation is needed in order to calculate reliable spectral moments of the DOSD. One needs to calculate the propagator at least at the level of the time-dependent Hartree–Fock, also called the random phase approximation (RPA) [18, 24, 29, 30], which implies using a Hartree–Fock self-consistent field wavefunction as the reference wave function for the linear response function. In this approximation, we are also restricting the excitation operators $\{h_i\}$ to the excitations from a single occupied molecular orbital to one virtual molecular orbital or vice versa. The RPA adds correlation in both ground and excited states in a balanced way [31]. Alternatively, time-dependent density functional theory (TD-DFT) [32, 33] can successfully be used in the calculation of DOSDs and thus mean excitation energies [7–10].

It should be noted that in the RPA, the dipole oscillator strengths calculated in dipole velocity, dipole length, or mixed representation and all sum rules would be identical, and the TRK sum rule, Eq. (13), would be fulfilled exactly, that is, be equal to the number of electrons if the computational basis were complete [30, 34, 35]. Comparison of the oscillator strengths calculated in the different formulations thus gives a measure of the completeness of the computational basis in addition to the fulfillment of the Thomas–Reiche–Kuhn sum rule (vide infra).

4. INITIAL CALCULATIONS

Mean excitation energies and their directional components for several atoms and smaller molecules, including He [36], H_2 [25, 37], H_2O [25, 37], N_2 [38], and CO [39], have been calculated using the scheme described above. All show good agreement with other results, experimental and theoretical.

In addition, two more systematic studies of the mean excitation energies, their directional components, and TRK sum rules for a series of small molecules have also been made [9, 22]. In the first study [22], 20 molecules containing approximately 20 electrons each were calculated at the RPA level using the RPAC 9.0 program package [40], and using Gaussian basis sets of approximately (9*s*9*p*5*d*2*f*) quality for first row atoms and (5*s*4*p*1*d*) for hydrogen. All these bases have been previously used with good results [41–44]. In the second study [9], mean excitation energies were calculated for nine simple organic molecules consisting of methane, ethane, ethene, ethyne, methanol, methanal, methanamine, methanimine, and methanethiol in addition to calculations on H_2O, H_2S, NH_3, and CO_2 using the Turbomole program [45, 46] at the TD-DFT level using the B3LYP functional [47] and the aug-cc-pCVTZ-CTOCD-uc basis sets [9, 48, 49].

The conclusion is that the polarization propagator scheme outlined in Section 3, when implemented at the RPA or TD-DFT level with a reasonable basis set, and utilizing the discrete representation of the continuum, will give a good prediction of molecular mean excitation energies. This should consequently also be true for most biological systems, which consist mostly of first row atoms and hydrogen.

The first calculations made on biomolecules (excepting water) were on glycine [5], H_2N-CH_2-COOH, the simplest of the amino acids, containing 40 electrons, and on alanine [7] (H_2N-$CHCH_3$-COOH), the next larger amino acid with 48 electrons. Minimum energy structures of the neutral molecules were determined with density functional theory, using the B3LYP functional [47] and a standard 6-31+G(d,p) [50] basis using the Gaussian 03 program [51]. After the structures of interest were determined, the molecules were reoriented in such a way that the carboxyl group was placed in the *xy*-plane.

For the neutral molecules, three local minima were found as shown in Figure 5.1 and Figure 5.2. The most stable structure (a), which corresponds to the experimental structures [52, 53], has both the C–N and O–H bonds synperiplanar to the C=O bond, so there is a bifurcated hydrogen bond from the amino group to the carbonyl oxygen, $NH_2 \cdots O{=}C$. There is also a second hydrogen bond internal to the carboxyl group, from the hydroxyl group

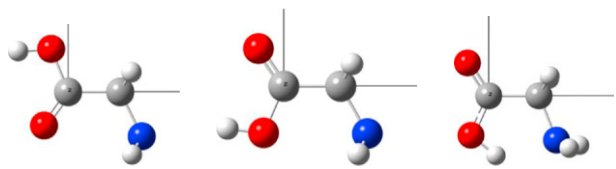

Figure 5.1 Optimized geometries of the three local minima of glycine. The carboxyl group lies in the *xy*-plane with the *y*-axis pointing upward and the *x*-axis to the right.

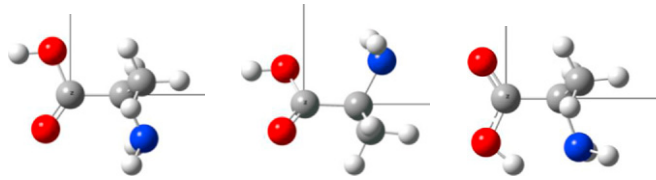

Figure 5.2 Optimized geometries of the three local minima of alanine. The carboxyl group lies in the *xy*-plane with the *y*-axis pointing upward and the *x*-axis to the right.

to the carbonyl oxygen, OH···O=C. In the next most stable structure (b), the O–H and C=O groups are also synperiplanar, so there is still a hydrogen bond within the carboxyl group, but the C–N bond is now antiperiplanar to the C=O bond. Thus, there is only a weak bifurcated hydrogen bond between the amino and hydroxyl groups $NH_2 \cdots O-H$. The next higher energy structure (c) has both C–N and O–H bonds antiperiplanar to the C=O bond.

The mean excitation energies were then determined at the RPA level, again using RPAC and Turbomole and tailor-made basis sets of approximately 200 contracted functions. For details of the calculation, including basis set details, and its results, see Refs. [5] and [7]. However, we should emphasize here our finding that sufficiently converged results for the mean excitation energies can only be obtained either with standard basis sets of at least quintuple zeta quality and augmented with enough polarization and diffuse functions or with specifically tailor-made basis sets of at least triple zeta quality [5]. The latter approach was chosen for glycine [5] and alanine [7].

The isotropic mean excitation energies, I_0, and anisotropies, A, for the three conformers of glycine and alanine are given in Table 5.1. For both amino acids, one observes that the isotropic mean excitation energy is basically the same in all three conformations. This applies also to the anisotropy of glycine, while somewhat larger variations are observed for the anisotropy of alanine. Furthermore, the anisotropy—and to a lesser extent also the mean excitation energy—is larger for glycine than for alanine.

For these prototypical amino acids, we had also investigated the effect of using time-dependent density functional theory (TD-DFT) instead of RPA in the calculation of the mean excitation energies [7]. In Table 5.2, the RPA results for the isotropic mean excitation energies, I_0, and anisotropies, A, of conformer A of glycine and alanine are thus compared with the results of TD-DFT calculations using the B3LYP [47], PBE0 [54, 55], and PBE [56] functionals showing that the variation is only small. However, recalling that PBE is a generalized gradient approximation functional, while PBE0 and B3LYP are hybrid functionals including a certain amount of exact Hartree–Fock exchange and RPA includes, of course, the full exact Hartree–Fock exchange,

Table 5.1 Isotropic mean excitation energies I_0 and anisotropies A for various conformations of glycine and alanine

	Glycine		Alanine	
Conformation	I_0 (eV)	A	I_0 (eV)	A
Conformer (A)	71.10	9.21	67.37	7.32
Conformer (B)	71.08	9.23	67.36	5.72
Conformer (C)	71.03	9.41	67.36	8.07

Table 5.2 Isotropic mean excitation energies I_0 and anisotropies A of conformer A of glycine and alanine calculated at the RPA level and TD-DFT level using the B3LYP, PBE0, and PBE functionals

	Glycine		Alanine	
Method	I_0 (eV)	A	I_0 (eV)	A
RPA	71.10	9.21	67.37	7.32
TD-DFT/B3LYP	70.79	9.51	67.09	7.55
TD-DFT/PBE0	70.64	9.54	66.95	7.54
TD-DFT/PBE	70.43	9.67	66.73	7.61

we notice a small but systematic variation in the isotropic mean excitation energy as well as in the anisotropy with the amount of exact Hartree–Fock exchange.

As a biomolecule in a cell is surrounded by water, it is of interest to determine also the direct effect of solvation on the mean excitation energy of biomolecules, in this case glycine [8], in addition to the effect through changes in the geometry alone. Consequently, we calculated the mean excitation energy of one glycine molecule surrounded by 511 rigid water molecules using the polarizable quantum-mechanics/molecular-mechanics (QM/MM) model [57, 58], which can model solute–solvent interactions in an accurate way. The zwitterionic geometry of glycine was optimized with the PCM model [59] at the B3LYP/aug-cc-pVTZ level using the Gaussian 03 program [51]. The electronic structure and excitation energies of glycine are determined quantum mechanically at the Hartree–Fock and density functional theory level using the Dalton 2.0 program [60] and the same basis set as in the gas phase study [5], while the 511 water molecules were treated with molecular mechanics. All excitation allowed by the finite basis are included, and the discrete representation of the continuum is used. Finally, the mean excitation energy is calculated as a statistical average over the mean excitation energies of glycine in 120 molecular configurations extracted from a MD

simulation of the rigid glycine plus 511 rigid water molecules system using the Molsim program [61]. The mean excitation energy of solvated glycine calculated in this way was found to be 69.79 ± 0.01 eV, which is only marginally smaller than in the gas phase.

Keeping in mind that the mean excitation energy enters the Bethe formula for the stopping power, Eq. (14), through its logarithm, we can summarize that the conclusions from the calculations reported above is that, at least as far as energy deposition from fast ions in glycine and alanine is concerned, neither the conformation of the amino acid nor solvation nor the precise choice of propagator method for the calculation of the DOSD affects its energy-absorption properties significantly. However, using a sufficiently large and flexible basis set for such calculations is essential.

5. THE BRAGG RULE FOR FRAGMENTS

Glycine is perhaps, other than water, the smallest molecule with biological relevance. However, calculation of the full excitation spectrum and thus the mean excitation energy of a molecule of the size of glycine are computationally demanding. As direct computation of significantly larger systems such as the larger amino acids, base pairs, or helix fragments is thus untenable, calculations for larger biomolecules have been based on the premise that the energy transfer or stopping cross section for an aggregate system $S(v)^{\text{molecule}}$ may be determined from a weighted sum of the atomic stopping cross sections, $S_i(v)$:

$$S(v)^{\text{molecule}} = \sum_{i=\text{atoms}} S_i(v) \tag{31}$$

Such a notion that the total stopping cross section can be represented as the sum of its parts is known as the Bragg Rule [62]. One might expect that the Bragg Rule, originally formulated as the molecular stopping cross section is the sum of its atomic constituents, cannot be particularly accurate because it represents a molecule as an aggregate of atoms, as it thus neglects chemical-binding effects. However, guided by chemistry, one might formulate a Bragg Rule for molecular fragments, or other aggregates, which includes terms for bonding and thus recover the effects of chemical bonding within each fragment. We have implemented this scheme for small molecules in a cores and bonds approach [63, 64], in which the mean excitation energies corresponding to specific bonds and atomic cores were calculated and used to determine molecular stopping cross sections. It should also be noted that the molecular mean excitation energy is dominated by the atomic core values, and that bonding effects are small perturbations on the sums of the atomic mean excitation energies. That is the main reason for the validity of

the Bragg Rule irrespective of its actual implementations, be it in terms of atoms of molecular fragments.

The Bragg Rule can also be somewhat generalized so that a system is composed of a number of polyatomic fragments, akin to functional groups (vide infra):

$$S(v)^{\text{aggregrate}} = \sum_{i=\text{fragments}} S_i(v) \tag{32}$$

As the mean excitation energy is simply related to the stopping number (Eq. (14)), it is also possible to write a combination law for fragment mean excitation energies, which is consistent with the Bragg Rule. In this case, the mean excitation energy, I_0, for a molecule containing N_e electrons and divided into fragments, each with fragment mean excitation energy I_0^i and associated with ω_i electrons would be as follows:

$$\ln I_0^{\text{aggregate}} = \frac{1}{N_e} \sum_{i=\text{fragments}} \omega_i \ln I_0^i, \tag{33}$$

where N_e is the total number of electrons in the aggregate/molecule. This is the formulation that we have used to calculate the mean excitation energies for some amino acids and nucleotides. We will compare the results calculated using a Bragg rule formulation to those obtained from whole molecule calculations on the amino acids.

6. THE MEAN EXCITATION ENERGY OF THE AMINO ACIDS AND POLYPEPTIDES

As the amino acids are among the smaller of the biologically significant molecules, we consider their mean excitation energies first, using the methodology [6, 9] described in sections 2–4. The core mean excitation energies were taken from earlier work [65], while the bond mean excitation energies were recalculated using the consistent set of mean excitation energies of small inorganic and organic molecules [9] discussed in section 4.

The fragment mean excitation energies were obtained individually by application of Eq. (33) and the core data in Ref. [65] and bond data in Ref. [9]. In some cases, Eq. (33) may be applied in two ways. For example, the mean excitation energy of the methyl group (–CH_3) can be obtained either by subtracting a C–H bond from the experimental mean excitation energy of methane [66], or by combining three C–H bonds and a carbon atom core according to Eq. (33). The two schemes give mean excitation energies of 48.3 and 47.1 eV, respectively. As the mean excitation energy enters the stopping cross section under the logarithm, this difference is well within

Table 5.3 Fragment mean excitation energies and weights

Fragment	Construction	I_0 (eV)	ω
–CH2–	Addition of two C–H bonds and C_{core}	60.6	6
–CH3	Addition of three C–H bonds and C_{core}	47.1	8
–COOH	Addition of C–O, C=O, O–H bonds and C_{core} and twice O_{core}	65.8	22
–C6H5(–Phe)	Experimental $I_{benzene}$ minus a C–H Bond	77.8	40
–NH2	Addition of two N–H bonds and N_{core}	58.7	22/3
–OH	Addition of one O–H bond and O_{core}	104.4	6
–C6H11(–Ch)	Addition of eleven C–H bonds and six C_{core}	54.3	46

acceptable error. A similar comparison on the cyclohexyl group, a significantly larger system, gives values of 58.6 and 54.3 eV, a somewhat larger difference, but still acceptable. Other group mean excitation energies were obtained as follows:

All amino acids can be viewed as a central carbon connected to an amino group, a carboxylic acid group, a hydrogen atom, and a further group, generally denoted as R. The variation in "–R" is what distinguishes among the amino acids. Thus, one may write an amino acid as $H_2NCHRCOOH$, or A–R, where A is $–CH(NH_2)COOH$. Combining the appropriate groups, one obtains $I_0^A = 78.8$ eV with $\omega = 38$ for the amino acid common fragment. These quantities can then be used with the entries of Table 5.3 and Eq. (33) to construct mean excitation energies for the amino acids through:

$$\ln I_0 = \frac{1}{\omega_R + 38}[38 \ln I_0^A + \omega_R \ln I_0^R] \tag{34}$$

The mean excitation energies (I_0) for several amino acids, along with the few other values available from experiment (E) and theory (T), and are given in Table 5.4.

In the treatment described here, details of molecular connectivity and conformation are not considered, as the mean excitation energy calculated with a Bragg-like rule depends only on the various fragments that make up the molecule and not on their arrangement. Thus, for example, the mean excitation energies of leucine and isoleucine are calculated to be the same, as they differ only in connectivity.

Furthermore, all of the calculations here are made on the neutral forms of the amino acids, not the zwitterion forms. In the studies on glycine [5] and alanine [7], we found a variation of only a fraction of an electron volt

Table 5.4 Calculated Mean excitation energies of some amino acids

Amino acid	R	I_0 (eV)	Other values
Glutamine	$-(CH_2)_2-CO-NH_2$	71.8	71.9(E^{66})
Phenylalanine	$-CH_2-Phe$	74.0	
Tyrosine	$-CH_2-Phe-OH$	66.8	
Lysine	$-(CH_2)_4-NH_2$	65.3	
Glycine	–H	74.0	71.1($T^{5,7}$)
Alanine	$-CH_3$	72.0	71.9(T^7E^{66})
Serine	$-CH_2-OH$	74.0	
Glutamic acid	$-(CH_2)_2-COOH$	67.4	
Aspartic acid	$-CH_2-COOH$	69.4	
Threonine	$-CHOHCH_3$	70.9	
Leucine	$-CH_2-CH(CH_3)_2$	63.4	
Asparagine	$-CH_2-CO-NH_2$	74.4	
Isoleucine	$-CHCH_3-CH_2-CH_3$	63.4	
Valine	$-CH(CH_3)_2$	65.0	67.7(E^{66})

in the mean excitation energy among various molecular conformations, both neutral and zwitterion, and therefore conclude that the use of the neutral form of the molecule will introduce only small errors into the calculation.

Comparison of these calculated numbers with the little experimental and other theoretical data available (see Table 5.4) indicates that the numbers produced here should produce amino acid mean excitation energies reliable at the level of a few percent.

In the simple Bethe theory of energy deposition, see Eqs. (1), (14) and (21), the mean excitation energy measures the difficulty of depositing energy in a target molecule by a swift ion. As the stopping power decreases proportionally as $\ln I_0$, see Eqs. (1) and (14)) the amino acids with low I_0, namely valine, isolucine, and lysine, will be most efficient in absorbing energy, and thus will have the largest stopping powers. These are the amino acids with the longest carbon chains in –R. However, amino acids with short carbon chains, such as glycine, alanine, and serine have much higher mean excitation energies, and thus are less capable of readily absorbing energy. In many cases, addition of a methylene group to –R decreases the mean excitation energy by 2–3 eV (asparagine/glutamine, aspartic acid/glutamic acid, valine/leucine). This is as expected, because addition of a methylene group will increase the density of states in the excitation spectrum, and make energy absorption easier.

The explanation for this behavior is quite clear. As one adds a methylene group to a molecule, in Eq. (34), one adds eight electrons to the denominator in the prefactor (N_e in Eq. (33)), and adds the terms $6 \ln I_{CH_2}$ and $2 \ln I_{C-C}$ under the sum. Adding eight to N_e lowers the first term in the brackets of

Eq. (34) more than the additional logarithm terms increase it, and thus the mean excitation energy decreases when a methylene is added. This is consistent with the experimental mean excitation energies of the alkanes [66], which increase with addition of methyl groups, as the dominance of the two contributions is reversed.

As the amino acids have mean excitation energies in the narrow range of 60–75 eV, one would expect that the mean excitation energies of small polypeptides will also be quite close to 70 eV, the average value of those in Table 5.4. For example, the mean excitation energy of the glycine dipeptide is calculated to be 73.49 eV, very close to the monomer value. The mean excitation energy of an n-mer of glycine would be calculated by increasing by n, both N_e and the term in the bracket in Eq. (34), with no net effect. The extension to mixed polypeptides is easy as well.

7. MEAN EXCITATION ENERGIES OF THE NUCLEOBASES

The next step up from the amino acids in biochemical complexity is the nucleobases. As in the study of the two amino acids glycine and alanine [5, 7], we have optimized the geometries of the five nucleobases at the density functional theory (DFT) level with the B3LYP functional [47] and the 6-31+G(d,p) [50] one-electron basis. No searches of different rotamers/conformers were carried out. Instead, we started the optimizations from geometries that had already been optimized at the MP2/6-31G* level [67]. After the geometry optimization the molecules were reoriented in such a way that the heterocycles are placed in the xy-plane as shown in Figure 5.3 for the pyrimidine bases and Figure 5.4 for the purine bases [10]. Once the minimum energy molecular geometries of the nucleobases were established, vertical singlet excitation energies and associated electronic transition dipole moments were calculated with the Turbomole program [45, 46] using linear response or polarization propagator methods at the level of the random phase approximation.

As the basis sets developed for glycine produced excellent results for that amino acid (see Table 5.1 of Ref. [31] for details), we chose to use the same basis also for the present calculations [68]. Preliminary calculations were also carried out at the level of time-dependent density functional theory (TD-DFT) using the PBE functional [56]. However, the results differed by less than 1% from the RPA result and are thus not reported here.

As noted earlier, in the complete basis set limit of the RPA the Thomas–Reiche–Kuhn (TRK) sum rule should be equal to the number of electrons N_e and the mean excitation energies calculated from oscillator strengths in the length, mixed, or velocity representation should have the same values. The fulfillment of Eq. (13) and the agreement between the mean excitation energies in different representations thus provide figures of merit for the basis

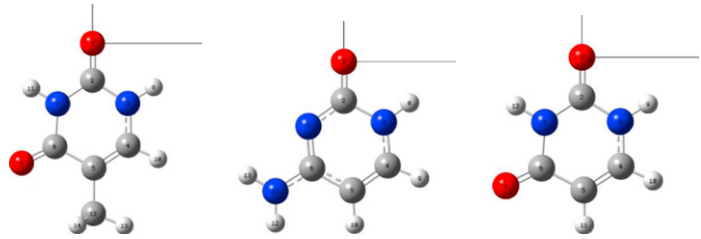

Figure 5.3 Optimized geometries of the pyrimidine nucleobases thymine (a), cytosine (b), and uracil (c). The molecules lie in the *xy*-plane with the *y*-axis point upward and the *x*-axis to the right.

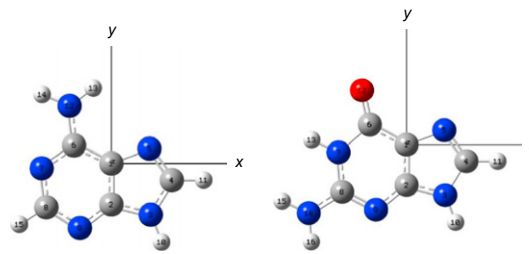

Figure 5.4 Optimized geometries of the purine nucleobases adenine (a) and guanine (b). The molecules lie in the *xy*-plane as indicated.

set used in calculation. In Table 5.4, we have listed the TRK sum rules in the length representation and the mean excitation energies. We observe excellent agreement for the length representation of the Thomas–Reiche–Kuhn sum rule and can therefore conclude that our tailor-made basis set is not only suitable for the amino acids glycine and alanine, but for the nucleobases, it is also sufficiently close to the basis set limit.

The initial observation concerning the isotropic mean excitation energies is that they do not differ among the nucleobases by more than a few percent, similar to the case of the amino acids. This is a consequence of the fact that all of the bases have a similar electronic structure. They are made up of the same sorts of atomic cores and chemical bonds. They all contain many electrons ($N > 55$), so small differences in the oscillator strength distributions are minimized by the large denominator in Eq. (15). Another way of interpreting this is related to the fact that for increasingly large molecules, the density of states in the continuum, which, for example, in alanine contributed almost 90% to the mean excitation energy [5] becomes so dense that adding additional atoms will not make a significant difference.

In comparison, the amino acids, glycine and alanine, are considerably smaller, with less than 50 electrons, so that the small differences in electronic structure are not as easily obscured. In very small systems, such as C_2H_6O ($N = 26$), electronic structure and chemical bonding effects become more important, and the differences in mean excitation energies between isomers such as Me_2O and EtOH are meaningful [69]. Indeed, the interpretation given here is much in line with using a Bragg-like cores and bonds sum rule [6, 9]. Using the core and bond mean excitation energies from Ref. [6] in Eq. (33), we find isotropic mean excitation energies for uracil and adenine of 80.83 and 69.73 eV, respectively; about the accuracy that one might expect from such an approximation.

Although there has been no systematic experimental study of the mean excitation energies of the nucleobases, experimental values of 71.40 and 75.00 eV have been reported [70] for adenine and guanine, respectively, in reasonable agreement with our results as reported in Table 5.5. There is also a set of mean excitation energies calculated for the nucleobases using a dielectric model and an evaluation of the optical energy loss function [71]. Those results are somewhat larger than the ones obtained here, with an average mean isotropic excitation energy of 75.25 eV as opposed to the average over the five nucleobases of 70.67 eV calculated here; thus acceptable agreement.

Although the nucleobases have very similar isotropic mean excitation energies, thus all having similar propensities to absorb energy from a swift ion, they differ significantly in their directional mean excitation energies, that is, the mean excitation energies differ when the target molecule has a specific orientation with respect to the projectile beam. The Cartesian components of the mean excitation energies and their anisotropies (see Eq. (21)) are reported in Table 5.6.

It is known [21] that electronic excitations in a target molecule can only occur for excitations with polarization directions perpendicular to the direction of projectile motion. In the work reported here, the nucleobases are

Table 5.5 The number of electrons, the Thomas–Reiche–Kuhn sum rule in the length representation S_0, and the mean excitation energy, I_0, for the nucleobases

	N_e	S_0	I_0 (eV)
Cytosine	58	58.00	69.60
Uracil	58	58.03	73.13
Thymine	66	66.01	70.00
Adenine	70	70.01	69.06
Guanine	78	78.05	71.58

Table 5.6 Calculated components and anisotropy of the mean excitation energies of the nucleobases

	I_0^x (eV)	I_0^y (eV)	I_0^z (eV)	A
Cytosine	66.10	62.65	81.26	27.06
Uracil	68.72	66.97	84.86	25.97
Thymine	66.92	63.43	80.73	28.30
Adenine	69.06	62.63	81.84	35.57
Guanine	64.62	67.03	84.51	39.01

placed in the *xy*-plane. For the nucleobases, the mean excitation energy is quite anisotropic, and in all cases, I_0^z is considerably (∼30%) larger than either I_0^x or I_0^y, which are approximately equal for the bases. Thus, projectiles traveling perpendicular to the molecular plane are expected to deposit more energy into the target base than projectiles traveling in the molecular plane.

The anisotropy of the purine nucleobases is larger than that of the pyrimidines, which is attributable to the larger physical extension in the direction of the molecular plane. The mean excitation energy of the nucleobases is also more anisotropic than in the case of the amino acids, which is caused by the fact that the nucleobases include planar heterocycles with conjugated π-bonds.

8. MEAN EXCITATION ENERGIES OF THE NUCLEOSIDES

Nucleosides are the next step in complexity after the nucleobases on the path to RNA and DNA. A nucleoside is a combination of a nucleobase connected to a ribose, which is a five-carbon cyclic sugar ($C_5O_5H_{10}$). Although we have not calculated the mean excitation energy of the nucleosides directly, because of the computational requirements of such a calculation, we can estimate the effect on the mean excitation energy of a nucleobase using the cores and bonds approach mentioned earlier [6, 9] (Eq. (33)) [10]. Using a Bragg Rule fragment approach [6, 9] one can write an equation for the mean excitation energy of a nucleoside (I_{NS}) in terms of the mean excitation energy of a ribose fragment missing an –OH group ($I_{R'}$), the mean excitation energy of the parent nucleobase (I_{NB}), and the number of electrons in the nucleobase (N) and the mean excitation energy of an N–H bond:

$$\ln I_{NS} = \frac{1}{72+N}[80 \ln I_{R'} + (N-4) \ln I_{NB} - 4 \ln I_{N-H}] \tag{35}$$

Table 5.7 Mean excitation energies of five nucleosides

Nucleoside	I_0 (eV)
Cytidine	69.96
Uridine	71.41
Methyl uridine	70.12
Adenosine	69.68
Guanosine	70.89

The results using this approach for the five nucleosides are presented in Table 5.7.

Comparison with Table 5.5 shows that increasing the complexity of the system, in this case, by forming the nucleoside from the nucleobase has little effect on the mean excitation energy of the system.

9. FORMATION OF NUCLEOTIDES

The next step toward the formation of RNA and DNA is the formation of nucleotides from a nucleoside together with one to three phosphate groups. Strands of nucleotides make up the nucleic acids. To determine the energy-absorption properties, that is, the mean excitation energies of the nucleotides, we first calculate the mean excitation energy of PO_4^{3-}. Using the methods described for the nine small organic molecules in section 4 [9], the mean excitation energy of the phosphate is determined to be 95.88 eV at the RPA level using the aug-cc-pCVTZ-CTOCD-uc basis set [49, 72].

Consider a nucleotide made up of a nucleoside and one to three phosphate groups. If the nucleoside is composed of a nucleobase containing N electrons, and there are M phosphate groups in the nucleotide, then the mean excitation energy of the nucleotide can be written as follows:

$$\ln I_0^{\mathrm{NT}} = \frac{1}{42M + (135 + N)} [42M \ln I_0^{\mathrm{P}} + (135 + N \ln I_0^{\mathrm{NS}})], \tag{36}$$

where I_0^{NT} is the mean excitation of the nucleotide and I_0^{NS} is the mean excitation energy of the nucleoside.

Using cytidine mono-, di-, and triphosphate as an example, the mean excitation energies are found to be 74.00, 76.96, and 79.22 eV, respectively. The variation in the other nucleotides with phosphate number is expected to parallel this behavior. Again, variation of the details of the biomolecule structure makes little difference.

10. HYDROGEN BONDING

In either the conventional Watson–Crick or Hoogsteen base pairing in DNA or RNA, base pairs are combined with two (adenine–thymine in DNA or adenine–uracil in RNA) or three (guanine–cytosine) hydrogen bonds. Although these hydrogen-bonded systems have been studied computationally [73], the effect of hydrogen bonding on mean excitation energy has not been reported. The effect of hydrogen bonds for the hydrogen-bonded base pairs was not investigated directly in this work, as this would require prohibitively extensive calculations. However, in accordance with the discussion above, we expect to see the largest effect arising from hydrogen bond formation in smaller complexes. As the hydrogen bonds among nucleobases all involve O and N, we have therefore investigated the water and ammonia dimers as well as a water–ammonia complex [10].

Using the same basis sets and methods described above, the mean excitation energies of water, ammonia, and their hydrogen-bonded pairs were calculated. They are given in Table 5.8. The complex geometries were determined by energy minimization. The mean excitation energies are in excellent agreement with previous calculations [9, 37], which found the mean excitation energies of water and ammonia to be 73.31 and 55.24 eV, respectively.

The calculated mean excitation energies of the water dimer and the ammonia dimer are smaller only by less than a percent from those of the monomers. Similarly, calculation of a mean excitation energy using a Bragg-like rule [$\ln I_0^{H_2O/NH_3} = 1/20(10 \ln I_0^{H_2O} + 10 \ln I_0^{NH_3})$] for the mixed dimer, H_2O-NH_3, gives a result of 63.75 eV. Using this as the analog of the nonhydrogen-bonded system, again hydrogen bonding only slightly reduces the mean excitation energy of the molecules. Because one would expect that any effect of hydrogen bonding on the mean excitation energy would be larger in small molecules (vide supra), we conclude that hydrogen bonding will not change the mean excitation energies of the nucleobases, nucleosides, or nucleotides, significantly.

Table 5.8 Mean excitation energies of some hydrogen-bonded species

System	I_0 (eV)
H_2O	73.56
$(H_2O)_2$	73.18
NH_3	55.25
$(NH_3)_2$	54.89
H_2O-NH_3	63.24

11. SUMMARY

The summary of these studies [5–10] reviewed here is that the amino acids and the nucleic acids all have similar properties with regard to absorption of energy from swift ions. All of the biomolecules reported here, including water, have mean excitation energies in the neighborhood of 70 eV. Thus, neither malevolent nor therapeutic radiation would be expected to preferentially interact with any particular class of biomolecules.

The details of the cellular environment are also apparently unimportant. Although the directional dependence of the mean excitation energy with regard to the direction of the beam with respect to the nucleobase plane is significant, in vivo the biomolecules would not be expected to maintain any particular orientation.

Similarly, apparently neither solvation nor hydrogen bonding seems to have any effect on any of the systems examined here.

In fact, these results are not surprising. As most biological molecules are primarily hydrides of the later first row atoms, they all have quite similar excitation spectra, and consequently quite similar mean excitation energies. The Bragg Rule is well obeyed in these systems, as the mean excitation energies of biological systems is both stable and consistent.

ACKNOWLEDGMENTS

S.P.A.S. thanks the Danish Center for Scientific Computing (DCSC), the Danish Natural Science Research Council/The Danish Councils for Independent Research and the Carlsberg Foundation for support.

REFERENCES

[1] C. von Sonntag, The Chemical Basis for Radiation Biology, Taylor and Francis, London, 1987.
[2] C. von Sonntag, Free-Radical DNA Damage and its Repair-A Chemical Perspective, Springer Verlag, Heidelberg, 2005.
[3] T. Schlathölter, F. Alvarado, R. Hoekstra, Ion-biomolecule interactions and radiation damage, Nucl. Inst. Meth. B 233 (2005) 62.
[4] *Cf. e.g.* E. Wilson, Interstellar glycine search intensifies, Chem. Eng. News 83(7) (2005), 14 February, p. 44.
[5] S.P.A. Sauer, J. Oddershede, J.R. Sabin, Directional Dependence of the Mean Excitation Energy and Spectral Moments of the Dipole Oscillator Strength Distribution of Glycine and its Zwitterion, J. Phys. Chem. A 110 (2006) 8811.
[6] J.R. Sabin, J. Oddershede, S.P.A. Sauer, Amino Acid Mean Excitation Energies and Directional Dependencies from Core and Bond Calculations, AIP Conf. Proc. CP1080 (2008) 138.

[7] S. Bruun-Ghalbia, S.P.A. Sauer, J. Oddershede, J.R. Sabin, Comparison of the Directional Characteristics of Swift Ion Excitation for Two Small Biomolecules: Glycine and Alanine, Eur. Phys. J. D 60 (2010) 71.
[8] K. Aidas, J. Kongsted, J.R. Sabin, J. Oddershede, K.V. Mikkelsen, S.P.A. Sauer, The Effect of Solvation on the Mean Excitation Energy of Glycine, J. Phys. Chem. Lett. 1 (2010) 242.
[9] S. Bruun- Ghalbia, S.P.A. Sauer, J. Oddershede, J.R. Sabin, Mean Excitation Energies and Energy Deposition Characteristics of Bio-organic Molecules, J. Phys. Chem. B 114 (2010) 633.
[10] S.P.A. Sauer, J. Oddershede, J.R. Sabin, The Mean Excitation Energies and Their Directional Characteristics for Energy Deposition by Swift Ions on the DNA and RNA Nucleobases, J. Phys. Chem. C 114 (2010) 20335–20341.
[11] H. Bethe, Zur Theorie des Durchgangs schneller Korpuskularstrahlen durch Materie, Ann. Phys. (Leipzig) 5 (1930) 325; H. A. Bethe, Bremsformel für Elektronen relativistischer Geschwindigkeit, Z. Phys. 76 (1932) 293.
[12] J.F. Ziegler, J.P. Biersack, U. Littmark, The Stopping and Range of Ions in Solids, Vol. 1 of the Stopping and Ranges of Ions in Matter, Pergamon Press, Oxford, 1985.
[13] J.F. Janni, Proton range-energy tables 1 keV–10 GeV, At. Data Nucl. Data Tables 27 (1982) 147.
[14] E. Bonderup, Penetration of Charged Particles through Matter, second ed., Fysik Instituts Trykkeri, Aarhus Universitet, Århus, 1981.
[15] M. Inokuti, Inelastic collisions of fast charged particles with atoms and molecules - the Bethe theory revisited, Rev. Mod. Phys. 43 (1971) 297.
[16] E.H. Mortensen, J. Oddershede, J.R. Sabin, Polarization Propagator Calculations of Generalized Oscillator Strengths and Stopping Cross Sections of He, Nucl. Inst. Meth. B69 (1992) 24.
[17] R. Cabrera-Trujillo, J.R. Sabin, J. Oddershede, S.P.A. Sauer, The Bethe Sum Rule and Basis Set Quality in the Calculation of Generalized Oscillator Strengths, Adv. Quantum Chem. 35 (1999) 175.
[18] W. Thomas, Über die Zahl der Dispersionselektronen, die einem stationären Zustand zugeordnet sind, Naturwiss. 13 (1925) 627.
[19] W.Z. Kuhn, Über die Gesamtstärke der von einem Zustande ausgehenden Absorptionslinien, Z. Phys. 33 (1925) 408.
[20] F. Reiche, W. Thomas, Über die Zahl der Dispersionselektronen, die einem stationären Zustand zugeordnet sind, Z. Phys. 34 (1925) 510.
[21] H.H. Mikkelsen, J. Oddershede, J.R. Sabin, E. Bonderup, A Bethe Theory for Directional Dependence of Stopping by Molecules, Nucl. Inst. Meth. B 100 (1995) 451.
[22] S.P.A. Sauer, J.R. Sabin, J. Oddershede, Molecular Mean Excitation Energies for Some Small Molecules, Nucl. Inst. Meth. B 100 (1995) 458.
[23] M. Inokuti, W. Karstens, E. Shiles, D.Y. Smith, Mean Excitation Energy for the Stopping Power of Silicon from Oscillator-Strength Spectra, Presented at the 2005 APS March Meeting, Los Angeles, California, March 21–25, 2005, http://meetings.aps.org/link/BAPS.2005.MAR.R1.55 (accessed 15.09.10).
[24] For a review of the theory and implementation of the polarization propagator method, see: J. Oddershede, P. Jørgensen, D.L. Yaeger, Polarization Propagator Methods in Atomic and Molecular Calculations, Compt. Phys. Rep. 2 (1984) 33; J. Oddershede, Propagator Methods, Adv. Chem. Phys. 69 (1987) 201; S.P.A. Sauer, Molecular Electromagnetism. A Computational Chemistry Approach, Oxford University Press, 2011, chapters 2 & 10.
[25] J. Geertsen, J. Oddershede, J.R. Sabin, Calculation of Molecular Mean Excitation Energies via the Polarization Propagator Formalism: H_2 and H_2O, Phys. Rev. A 34 (1986) 1104.
[26] P. Jørgensen, J. Oddershede, N.H.F. Beebe, Polarization propagator calculations of frequency-dependent polarizabilities, Verdet constant, and energy weighted sum rules, J. Chem. Phys. 68 (1978) 2527.

[27] S.P.A. Sauer, G.H.F. Diercksen, J. Oddershede, Second Order Polarization Propagator Calculations of Dynamic Polarizabilities and C_6 Coefficients, Int. J. Quantum Chem. 39 (1991) 667.
[28] J. Oddershede, J.R. Sabin, The Effect of Correlation on the Mean Excitation Energy of Beryllium, Phys. Rev. A 39 (1989) 5565.
[29] A.D. McLachlan, M.A. Ball, Time-Dependent Hartree-Fock Theory for Molecules Rev. Mod. Phys. 36 (1964) 844.
[30] D.J. Rowe, Equations-of-Motion Method and the Extended Shell Model, Rev. Mod. Phys. 40 (1968) 153.
[31] Aa.E. Hansen, T.D. Bouman, Hypervirial relations as constraints in calculations of electronic excitation properties: The random phase approximation in configuration interaction language, Mol. Phys. 37 (1979) 1713.
[32] E. Runge, E.K.U. Gross, Density-Functional Theory for Time-Dependent Systems, Phys. Rev. Lett. 52 (1984) 997; A. Dreuw, M. Head-Gordon, Single-Reference ab Initio Methods for the Calculation of Excited States of Large Molecules, Chem. Rev. 105 (2005) 4009.
[33] J. Schirmer, A. Dreuw, Critique of the foundations of time-dependent density-functional theory, Phys. Rev. A 75 (2007) 022513.
[34] R.A. Harris, Oscillator strengths and rotational strengths in Hartree–Fock theory, J. Chem. Phys. 50 (1969) 3947.
[35] P. Jørgensen, J. Oddershede, Equivalence between perturbatively calculated transition moments, J. Chem Phys. 78 (1983) 1898.
[36] J.R. Sabin, J. Oddershede, G.H.F. Diercksen, Moments of the Dipole Oscillator Strength Distribution and Mean Excitation Energies of Helium, Phys. Rev. A 42 (1990) 1302.
[37] S.P.A. Sauer, J.R. Sabin, J. Oddershede, Directional Characteristics of the Moments of the Dipole Oscillator Strength Distribution of Molecules: H_2 and H_2O, Phys. Rev. A 47 (1993) 1123.
[38] G.H.F. Diercksen, J. Oddershede, I. Paidarová, J.R. Sabin, Calculation of the Isotropic and Anisotropic Spectral Moments of the Dipole Oscillator Strength Distribution of N_2, Int. J. Quantum Chem. 39 (1991) 755.
[39] E.K. Dalskov, J. Oddershede, J.R. Sabin, Generalized Oscillator Strengths for Calculation of Molecular Stopping Properties, Some Preliminary Results: CO, AIP Conf. Proc. CP392 (1997) 1373.
[40] T.D. Bouman, Aa. Hansen, RPAC Molecular Properties Package, Version 9.0, Copenhagen University, 1990.
[41] S.P.A. Sauer, T. Enevoldsen, J. Oddershede, Paramagnetism of Closed Shell Diatomic Hydrides with Six Valence Electrons, J. Chem. Phys. 98 (1993) 9748.
[42] S.P.A. Sauer, I. Paidarová, J. Oddershede, Correlated and Gauge Origin Independent Calculations of Magnetic Properties. I. Triply Bonded Molecules, Mol. Phys. 81 (1994) 87.
[43] S.P.A. Sauer, J. Oddershede, Correlated Polarization Propagator Calculations of Static Dipole Polarizabilities, Int. J. Quantum Chem. 50 (1994) 317.
[44] S.P.A. Sauer, I. Paidarová, J. Oddershede, Correlated and Gauge Origin Independent Calculations of Magnetic Properties. II. Shielding Constants of Simple Singly Bonded Molecules, Theoret. Chim. Acta 88 (1994) 351.
[45] R. Ahlrichs, M. Bär, M. Häser, H. Horn, C. Kölmel, Electronic structure calculations on workstation computers: The program system Turbomole, Chem. Phys. Lett. 162 (1989) 165; M. Häser, R. Ahlrichs, Improvements on the direct SCF method, J. Comput. Chem. 10 (1989) 104; O. Treutler, R. Ahlrichs, J. Chem. Phys. 102 (1995) 346; R. Bauernschmitt, R. Ahlrichs, Treatment of Electronic Excitations within the Adiabatic Approximation of Time Dependent Density Functional Theory, Chem. Phys. Lett. 256 (1996) 454; S. Grimme, F. Furche, R. Ahlrichs, An improved method for density functional calculations of the frequency-dependent optical rotation, Chem. Phys. Lett. 361 (2002) 321; F. Furche,

D. Rappoport, Computational photochemistry, in: M. Olivucci, (Ed.), Computational and Theoretical Chemistry, Vol. 16, Elsevier, Amsterdam, 2005, Chapter 3; M. Arnim, R. Ahlrichs, Geometry optimization in generalized natural internal Coordinates, J. Chem. Phys. 111 (1999) 9183.

[46] TURBOMOLE V6.0 2009, a development of University of Karlsruhe and Forschungszentrum Karlsruhe GmbH, 1989–2007, TURBOMOLE GmbH, since 2007; available from http://www.turbomole.com (accessed 4.05.11).

[47] C. Lee, W. Yang, R.G. Parr, Development of the Colle-Salvetti correlation-energy formula into a functional of the electron density Phys. Rev. B 37 (1988) 785; A.D. Becke, Density-Functional Thermochemistry. III. The Role of Exact Exchange, J. Chem. Phys. 98 (1993) 5648.

[48] A. Ligabue, S.P.A. Sauer, P. Lazzeretti Correlated and Gauge Invariant Calculations of Nuclear Magnetic Shielding Constants Using the Continuous Transformation of the Origin of the Current Density Approach, J. Chem. Phys. 118 (2003) 6830.

[49] A. Ligabue, S. P. A. Sauer, P. Lazzeretti, Gauge invariant calculations of nuclear magnetic shielding constants using the continuous transformation of the origin of the current density approach. II. Density-functional and coupled cluster theory, J. Chem. Phys. 126 (2007) 154111.

[50] W.J. Hehre, R. Ditchfield, J.A. Pople, Self—Consistent Molecular Orbital Methods. XII. Further Extensions of Gaussian—Type Basis Sets for Use in Molecular Orbital Studies of Organic Molecules, J. Chem. Phys. 56 (1972) 2257; T. Clark, J. Chandrasekhar, P.V.R. Schleyer, Efficient diffuse function-augmented basis sets for anion calculations. III. The 3-21+G basis set for first-row elements, Li–F, J. Comput. Chem. 4 (1983) 294.

[51] M.J. Frisch, G.W. Trucks, H.B. Schlegel, G.E. Scuseria, M.A. Robb, J.R. Cheeseman, et al., Gaussian 03, revision C.02; Gaussian, Inc.: Wallingford, CT, 2004.

[52] P.D. Godfrey, R.D. Brown, Shape of Glycine, J. Am. Chem. Soc. 117 (1995) 2019.

[53] K. Iijima, B. Beagley, An electron diffraction study of gaseous a-alanine, $NH_2CHCH_3CO_2H$, J. Mol. Struct. 248 (1991) 133; P.D. Godfrey, S. Firth, L.D. Hatherley, R.D. Brown, A.P. Pierlot, Millimeter-wave spectroscopy of biomolecules: alanine, J. Am. Chem. Soc. 115 (1993) 9687; S.G. Stepanian, I.D. Reva, E.D. Radchenko, L. Adamowicz, Conformational Behavior of a-Alanine. Matrix-Isolation Infrared and Theoretical DFT and ab Initio Study, J. Phys. Chem. A 102 (1998) 4623; B. Lambie, R. Ramaekers, G. Maes, On the contribution of intramolecular H-bonding entropy to the conformational stability of alanine conformations, Spectrochim. Acta A 59 (2003) 1387.

[54] M. Ernzerhof, G.E. Scuseria, Assessment of the Perdew-Burke-Ernzerhof Exchange-Correlation Functional, J. Chem. Phys. 110 (1999) 5029.

[55] C. Adamo, V. Barone, Toward Reliable Density Functional Methods without Adjustable Parameters: The PBE0 Model, J. Chem. Phys. 110 (1999) 6158.

[56] J.P. Perdew, K. Burke, M. Ernzerhof, Generalized Gradient Approximation Made Simple, Phys. Rev. Lett. **77** (1996) 3865.

[57] J. Kongsted, A. Osted, K.V. Mikkelsen, O. Christiansen, The QM/MM Approach for Wavefunctions, Energies and Response Functions within Self-Consistent Field and Coupled Cluster Theories, Mol. Phys. 100 (2002) 1813; J. Kongsted, K. Aidas, K. V. Mikkelsen, S. P. A. Sauer, On the accuracy of density functional theory to predict shifts in nuclear magnetic resonance shielding constants due to hydrogen bonding, J. Chem. Theory Comput. 4 (2008) 267; A. Møgelhøj, K. Aidas, K. V. Mikkelsen, S. P. A. Sauer, J. Kongsted, Prediction of Spin-Spin Coupling Constants in Solution based on Combined Density Functional Theory/Molecular Mechanics, J. Chem. Phys. 130 (2009) 134508.

[58] K. Aidas, Whirlpool: A QM/MM analysis program, Copenhagen University, 2009. For more information contact: kestas@theory.ki.ku.dk.

[59] J. Tomasi, B. Mennucci, R. Cammi, Quantum Mechanical Continuum Solvation Models, Chem. Rev. 105 (2005) 2999.

[60] Dalton: A molecular electronic structure program, release 2.0, 2005. See http://daltonprogram.org/ (accessed 4.05.11).
[61] P. Linse, MOLSIM is an integrated MD/MC/BD simulation program belonging to the MOLSIM package, version 3.3.0, December 05, 2001.
[62] W.H. Bragg, R. Kleeman, On the alpha particles of radium, and their loss of range in passing through various atoms and molecules, Philos. Mag. 10 (1905) 318.
[63] J.R. Sabin, J. Oddershede, Theoretical Stopping Cross Sections for C-H, C-C and C=C Bonds, Nucl. Inst. Meth. B 27 (1987) 280.
[64] J. Oddershede, J.R. Sabin, Bragg Rule Additivity of Bond Stopping Cross Sections, Nucl. Inst. Meth. B 42 (1989) 7.
[65] J. Oddershede, J.R. Sabin, Orbital and Whole Atom Stopping Power and Shell Corrections for Atoms with Z ¡ 36, At. Data Nuc. Data Tables 31 (1984) 275.
[66] From the US National Institute of Standards and Technology: http://www.nist.gov/pml/data/star/index.cfm (accessed 4.05.11).
[67] M. Schreiber, M.R. Silva-Junior, S.P.A Sauer, W. Thiel, Benchmarks for electronically excited states: CASPT2, CC2, CCSD, and CC3, J. Chem. Phys. 128 (2008) 134110; M.R. Silva-Junior, M. Schreiber, S.P.A. Sauer, W. Thiel, Benchmarks for electronically excited states: Time-dependent density functional theory and density functional theory based multireference configuration interaction, J. Chem. Phys. 129 (2008) 104103; S.P.A. Sauer, M. Schreiber, M.R. Silva-Junior, W. Thiel, Benchmarks for Electronically Excited States: A Comparison of Noniterative and Iterative Triples Corrections in Linear Response Coupled Cluster Methods: CCSDR(3) versus CC3, J. Chem. Theory Comput. 5 (2009) 555; M.R. Silva-Junior, S.P.A. Sauer, M. Schreiber, W. Thiel, Basis set effects on coupled cluster benchmarks of electronically excited states: CC3, CCSDR(3) and CC2, Mol. Phys. 108 (2010) 453; M.R. Silva-Junior, M. Schreiber, S.P.A. Sauer, W. Thiel, Benchmarks of electronically excited states: basis set effects on CASPT2 results, J. Chem. Phys. 133 (2010) 174318.
[68] The orbital exponents and contraction coefficients for the basis are given in Tables 2–5 of Ref. 5.
[69] J.R. Sabin, J. Oddershede, Status of the Calculation of the Energy Loss of Swift Ions in Molecules, Nucl. Inst. Meth. B 64 (1992) 678.
[70] From the U.S. National Institute of Standards and Technology ASTAR database: http://physics.nist.gov/cgi-bin/Star/compos.pl?175 (accessed 1.03.10).
[71] Z. Tan, Y. Xia, M. Zhao, X. Liu, Proton stopping power in a group of bioorganic compounds over the energy range of 0.05–10 MeV, Nucl. Inst. Meth. B 248 (2006) 1.
[72] The aug-cc-pCVTZ-CTOCD-uc basis set for phosphorus was generated from the original aug-cc-pCVTZ basis set by removing the two core-valence s-type functions, decontraction of all p-type functions, and addition of three sets of p-type functions (with exponents 38180, 9030, 2136), three sets of d-type functions (with exponents 40.971, 25.232, 1.968), and one set of f-type functions with exponent 1.238.
[73] E.E. Kryachko, J.R. Sabin, Quantum Chemical Study of the Hydrogen-Bonded Patterns in the AT Base Pair of DNA: The Origins of Tautomeric Mispairs, Base Flipping, and Watson-Crick Hoogsteen Conversion, Int. J. Quantum Chem. 91 (2003) 695.

CHAPTER 6

High-Resolution Signal Processing in Magnetic Resonance Spectroscopy for Early Cancer Diagnostics

Dževad Belkić[a] and **Karen Belkić**[a,b]

Contents

[a] Nobel Medical University, Karolinska Institute, Department of Oncology and Pathology, Stockholm, Sweden

[b] Claremont Graduate University, School of Community and Global Health, Claremont, California, US University of Southern California, School of Medicine, Institute for Health Promotion and Disease Prevention Research, Los Angeles, California, US

Advances in Quantum Chemistry, Volume 62
ISSN 0065-3276, DOI: 10.1016/B978-0-12-386477-2.00006-1

Abstract This paper is on the theory and practice of spectral analysis as it applies to the quantification of a wide class of biomedical time signals. The presented methodology is general and can be applied to many other interdisciplinary fields that need not necessarily overlap with biomedicine. The principal method selected for this challenging task of solving inverse synthesis-type problems in data interpretation is the fast Padé transform (FPT). This method, which can autonomously pass from the time to the frequency domain with no recourse to Fourier integrals, represents a novel unification of the customary Padé approximant and the causal Padé z-transform. The FPT automatically and simultaneously performs interpolation and extrapolation of the examined data. The idea is to synthesize time signals in a search for an adequate explanation of the observed variation in studied phenomena. This consists of composite effects with the aim of finding a subclass of simpler constituent elements related to the fundamental structure of the examined system, which produces a response to external perturbations. Such decomposition of complicated effects into simpler ones is the heart of the problem of quantifying time signals through their parametrizations.

Finding a relatively small number of fundamental parameters eliciting poles and zeros, which could capture the main features of the investigated system associated with a given time signal, is of paramount theoretical and practical importance. In this way, theoretical explanations of phenomena involving time signals exhibit a great potential to simplify the initial task and coordinate its various parts by the decomposition analysis of observed composite phenomena. As such, remarkably, the theory of time signals becomes an essential complement of the corresponding measurements. This complementarity does not stop with theoretical explanations and interpretations. It also provides practical tools that enable interpolation, where measured data have not been recorded, and extrapolation to the ranges where predictions could be made about the possible behavior of the system under study. Measurements in this field yield time signals, but it is the theory that provides frequency spectra and decomposition of encoded data into their constituent fundamental elements. Such inverse problems are difficult due to mathematical ill-conditioning, and the possible solutions are further hampered by inevitable noise.

This type of problem, known as quantification, spectral analysis or harmonic inversion, can be solved by the FPT for any theoretically generated/simulated time signals or experimentally measured data. The obtained solutions gain in their value by the manner in which the accompanying and unavoidable problem of noise is solved. This is done by unequivocal

disentangling of the genuine from spurious information using the concept of Froissart doublets. Spurious information is precisely identified by strong coupling of unphysical poles and zeros through their strict coincidences and zero-valued amplitudes. Such pole–zero confluences are totally absent for physical, genuine resonances. Hence, exact noise separation is a novel paradigm in data analysis.

In the reported thorough illustrations on magnetic resonance spectroscopy for diagnostic purposes in clinical oncology, special attention is paid to current obstacles in this problem area of medicine. Our aim is to demonstrate the potential usefulness of the Padé-optimized quantification for the analysis and interpretation of encoded time signals typical of normal and malignant samples from ovarian cyst fluid, as well as from breast and prostate tissues.

1. INTRODUCTION

This paper deals with the general problem of mathematical optimization as applied to medical diagnostics, within the framework of magnetic resonance spectroscopy (MRS). Of late, magnetic resonance (MR) established itself as one of the key modalities, particularly in cancer diagnostics due to its noninvasiveness and lack of ionizing radiation. This permits repeated usage not only in diagnostics but also for screening and post-therapeutic followup. To supplement magnetic resonance imaging (MRI), which displays anatomical/morphological structures, MRS provides information related to the biochemical content of the scanned tissue. This additional insight from MRS can reveal the minute cellular changes on the molecular level that almost always precede anatomical manifestations. Hence, there is invaluable possibility for early tumor diagnostics. When detected sufficiently early, the potential for cure is greatly enhanced.

According to the promising results, as analyzed in this paper, MRS has already made important strides, especially for breast, ovarian, and prostate cancer, that are of high prevalence. This initial success was achieved on the basis of only a handful of clinically relevant metabolites, the concentrations of which were estimated from time signals encoded from patients. Despite these encouraging developments, however, MRS has not yet reached the stage of being a routine clinical modality in cancer diagnostics.

The reasons for this are primarily because of

1. the lack of uniform mathematical optimization,
2. the difficulties in separating noise from the physical content in measured signals.

These obstacles can be removed by applying the Padé approximant (PA). In the realm of signal processing, the term fast Padé transform (FPT) has been used as an alternative to the conventional acronym PA [1]. Formally, this was done to make an implicit reference to the integral transformation

from the originally measured time domain to the subsequently analyzed frequency domain. Thus far, the most often employed method for this type of transformation has been the fast Fourier transform (FFT), which is commercially used in MRS in medicine. Uniquely, the FPT need not rely on the FFT during the passage from the time to frequency domain and vice versa.

Disadvantageously, the FFT can provide only the overall total shape spectrum in the frequency domain, which represents an envelope of all the existing molecular concentrations. The goal, however, is to precisely extract the information that is underneath this envelope, namely the component spectrum corresponding to MR-visible molecules, many of which are diagnostically important metabolites. Since this is impossible within the FFT, the customary procedure has been to fit the total shape spectrum from the FFT by adjusting the entire envelope to a preselected number of components. This is pure guess work, since the true number of metabolites and, by implication, their concentrations can only be surmised through least square fitting recipes. A major drawback of this conventional procedure for MRS is the lack of uniqueness, since any number of preassigned peaks can be fitted to a given envelope within a prescribed level of accuracy. This technique has been limited in the clinical applications because, invariably, physical metabolites are missed and unphysical ones are spuriously predicted.

With regard to point (2) mentioned earlier, because of its linearity, the FFT imparts noise as unaltered from the time domain to the frequency domain. Moreover, the FFT has no possibility of separating noise from the true signal. In an attempt to improve resolution, one tries in vain to increase the total acquisition time, but for longer signals, noise becomes the major content to the encoded signals or free induction decay (FID) curves.

Each metabolite has one or more resonant frequencies. Besides concentrations, the task is also to reconstruct these frequencies, known as chemical shifts. The FFT cannot retrieve them because it is limited to the preassigned Fourier grid frequencies as a function of the total acquisition time. Overall, the FFT by itself cannot reconstruct chemical shifts or the actual heights of the components, since it can only provide the total shape spectra. Thus, as mentioned earlier, in practice, such spectra are typically postprocessed via fitting, with the attendant drawbacks.

The fast Padé transform successfully overcomes the problems of the FFT. As a nonlinear transform, the FPT suppresses noise from the analyzed time signals. Most importantly, the FPT completely obviates postprocessing via fitting or any other subjective adjustments. This is accomplished by a direct quantification of the time signal under study through exact spectral analysis, which provides the unique solutions for the inverse harmonic (HI) problem [1, 2]. The solution of the HI problem contains four real-valued spectral parameters (one complex frequency and one complex amplitude) for each resonance or peak in the associated frequency spectrum. From these spectral parameters, the metabolite concentrations are unequivocally extracted. This bypasses the ubiquitous uncertainties inherent to fitting, such

as under-fitting (undermodeling) associated with missing genuine metabolites and over-fitting (overmodeling) corresponding to the production of unphysical resonances. The FPT solves the most difficult problem in spectral analysis of time signals, namely noise corruption. This is accomplished by exact separation of signal from noise [3–5]. Identification of noise and noise-like information is achieved in the FPT through the appearance of Froissart doublets where poles and zeros coincide in the analyzed spectrum. As a double signature for signal–noise separation, the FPT detects zero amplitudes for Froissart doublets. In this way, genuine and spurious resonances are unmistakably disentangled within the FPT.

The expounded features of the FPT have thus far been tested in theoretically generated and experimentally measured time signals [1–15]. The FPT has been found to work with unprecedented success using synthesized time signals through machine accurate reconstruction for all the input spectral parameters and for the exact number of resonances [5, 13]. For experimentally measured time signals, the FPT is also highly successful and outperforms all the other signal processing methods in MRS [1, 5, 6]. The present investigation confirms this experience with time signals reminiscent of data encoded via MRS corresponding to benign and malignant samples from human breast, ovary, and prostate. Heretofore, such stringent testings of theory on signal processing have been scarce in the literature on MRS for these specific problem areas. The present paper is meant to bridge this gap and highlight the most recent achievements. It is remarkable that the Padé approximant, the applications of which have brought enviable fruits across interdisciplinary research over decades, has only recently entered into the challenging new arena—cancer diagnostics. It is anticipated the Padé optimization therein will provide substantial aid to this area, which is of major public health concern.

2. THE NEED FOR ADVANCED SIGNAL PROCESSING IN BIOMEDICINE

This review might at first seem quite distant for clinical researchers and practitioners, including especially oncologists. However, with a second look coupled with reflection about the actual barriers to reliable applications of MRS and magnetic resonance spectroscopic imaging (MRSI) for early cancer diagnostics, a different perspective can emerge.

Clinical MR scanners offer the possibility of automatically generating MR spectra. This opportunity is naturally welcomed by diagnosticians who increasingly recognize that the anatomic information provided by MRI, though vital, is still insufficient for unequivocal identification of cancer and its clear distinction from benign pathologies. Indeed, in the recent period, the role of in vivo MRS for cancer diagnostics has been highlighted, especially for neuro-oncology and prostate cancer. Breast cancer detection has also been

improved by MRS. Unfortunately, however, when one examines these automatically generated spectra, innumerable dilemmas arise. The interpretation of these spectra is often hampered by ambiguities. In actual clinical practice, the frequent outcome of this endeavor is to return to the familiar realm of customary anatomical diagnostic modalities. As a consequence, the potentially most valuable diagnostic information is left by the wayside. In fact, MRS has yet to become a standard diagnostic tool in the area where it is needed the most, for clinical oncology, including especially cancer screening and surveillance.

Technological improvements have been sought in attempts to solve these dilemmas. Needless to say, meticulous attention to coil design, shimming, water suppression, as well as the use of appropriate encoding sequences are a prerequisite for proper acquisition of MR time signals. Albeit at higher cost, higher field MR scanners with stronger static magnetic fields obviously provide better signal-to-noise ratio (SNR), thereby yielding improved spectral quality.

Notwithstanding the importance of these technical, that is, hardware considerations and the need for further advances in this area, the critical limitation of current applications of MRS and MRSI is directly related to reliance on the conventional signal processing method, the fast Fourier transform, and the accompanying postprocessing via fitting and/or peak integrations. The more advanced mathematical methods that are the focus of this review are the indispensable remedy. The strategic importance of robust and uniform data processing of MRS signals has been strongly emphasized at, for example, the expert meeting on MRS for oncology, held recently by the U.S. National Cancer Institute, as well as at a special conference in November 2006 on Data Processing in MR Spectroscopy and Imaging by the International Society for Magnetic Resonance in Medicine.

Some may wonder: how could mathematics play such a critical role in medical diagnostics? This is because data encoded directly from patients by means of existing imaging techniques, for example, computerized tomography, positron emission tomography, single photon emission tomography, ultrasound, as well as MRI, MRS and MRSI are not at all amenable to direct interpretation, which therefore need mathematics via signal processing.

The starting point for grasping the basics of signal processing in medical diagnostics is the concept of "conjugate variables." Unfortunately, this concept is rarely formulated in an adequate manner for those whose primary expertize is distant from the realm of mathematics and physics. Rather, far too prematurely, technical terminology is usually introduced, and this is done with inadequate definition. The result is hazy thinking about such important relationships as that between the so-called k-space (momentum space) and the image obtained from the MR scanner. It is rarely pointed out that this relationship is closely analogous to that between time signals and their spectral representation.

Biomedical researchers and clinicians should readily appreciate that diagnostically important information can sometimes be difficult to quantify and may not even be apparent in the domain in which it is recorded. Important examples include slow activity on the electroencephalogram, 60–120 Hz late potentials and heart rate variability in the 0.15–0.4 Hz range on the electrocardiogram. The reason for which spectral analysis of these physiological signals is justified is that time and frequency are complementary representations or conjugate variables. We also proceed to another set of conjugate variables, momentum and position, from whence the *k*-space representation is transformed into an MR image in the more familiar coordinate spatial representation. The next logical step is to examine the mathematical procedures needed to achieve this transformation.

In MRS, the encoded data are heavily packed time signals that decay exponentially in an oscillatory manner. These time domain data are not directly interpretable. The corresponding total shape spectrum is obtained by mathematical transformation of the FID into its complementary representation in the frequency domain. This total shape spectrum provides qualitative information, but not the quantitative one about the actual number of metabolites that underlie each peak or the relative strength of individual components, their abundance, etc. At best, the FFT takes us only to this second step. More information is needed before the metabolites can be identified and their concentrations reliably determined, and from the total shape spectrum alone, this can only be guessed.

This undetected information can be extracted by novel and self-contained data analysis, namely the fast Padé transform. In this chapter, we review the current status of the FPT regarding the most stringent criteria imposed by clinical disciplines such as oncology for MRS. The high resolution and stability of the FPT have been clearly confirmed in the previous studies of MR total shape spectra, thereby overcoming one of the major hindrances to wider application of MRS in clinical oncology. However, as stated, total shape spectra do not provide the information needed to determine how many metabolite resonances are actually present in the tissue and in which concentrations. It is this information that is essential for improving the accuracy of MRS in early cancer diagnostics. It has been demonstrated that the FPT provides exact quantification of MR signals, and thereby metabolite concentrations are reliably and unequivocally obtained with an intrinsic and robust error analysis.

We emphasize that there is an urgent need for accurate quantification to determine metabolite concentrations, so that MRS can be better used to detect and characterize cancers, with clear distinction from nonmalignant processes. As presently reviewed, this can be clearly illustrated by applying the FPT to time signals that were generated according to in vitro MRS data as encoded from (1) malignant and benign ovarian cysts, (2) breast cancer, fibroadenoma, and normal breast tissue, and (3) for cancerous prostate,

and normal stromal and glandular prostate. We chose these problem areas to address in the present work because of their major impact on public health.

This approach was made possible by widening the horizons of signal processing through finding its natural framework in a larger and well-established physics theory—quantum mechanics. By identifying the quantification problem in signal processing by quantum-mechanical spectral analysis, the key door was opened for using a highly developed mathematical apparatus to overcome the otherwise insurmountable difficulties of the FFT, fittings, and other similar techniques. It is through this direct connection of signal processing with quantum physics that a veritable paradigm shift has been established, and the stage set for the emergence of modern and advanced spectral analyzers, such as the fast Padé transform.

3. THEORY

3.1. The role of quantum physics and chemistry in spectral analysis of time signals

Quantum physics can answer the critical question in general signal processing: does any improvement beyond the Fourier resolution contradict the Heisenberg uncertainty principle $\Delta\omega\Delta t \geq \hbar$? The correct answer requires a sharp distinction between the informational content and the resolving power. Reliability of the FPT and FFT will be guaranteed only if they preserve information from the original time signal. They actually both do, the FFT in a linear and the FPT in a nonlinear manner. The resolution of the FFT is determined from the onset by the preselected time-bandwidth. This resolution is given by the smallest possible distance called the Rayleigh limit or bound $\Delta\omega_{\min} = 2\pi/T$ between any two adjacent equidistant Fourier frequencies for the chosen total acquisition time T. It is this Rayleigh bound $\Delta\omega_{\min}$ that inherently limits the resolution in the FFT. Across interdisciplinary research on spectral analysis, the Heisenberg uncertainty principle for the conjugate pair, time-frequency, from quantum physics has been repeatedly evoked to claim that no theoretical processing method can surpass the Rayleigh limit $\Delta\omega_{\min}$. However, this claim is confusing and misleading. The Heisenberg principle demands that any two conjugate observables $\mathcal{A}$ and $\mathcal{B}$, described by the operators A and B that do not commute ($AB \neq BA$), cannot be measured simultaneously. This means that a measurement of, for example, $\mathcal{A}$ precludes the knowledge of $\mathcal{B}$. Any attempt to determine $\mathcal{B}$ experimentally would destroy the knowledge of $\mathcal{A}$. The Heisenberg principle is one of the cornerstones of quantum physics, which is the only theory to date determining what actually cannot be measured experimentally,

irrespective of any conceivable advance in instrumentation. However, this uncertainty principle has nothing to do with the resolution limit $\Delta\omega_{\min}$ on the frequency within the FFT. This is simply because in the considered phenomenon, there is only one physical quantity that is subject to measurement and that is the time signal $c(t)$. By contrast, the corresponding spectrum $F(\omega)$ is not measured experimentally, but rather obtained theoretically through numerical computations. Since signal processing, which is, at any rate, used after completion of the experiment, cannot possibly destroy the measurement of $c(t)$, it follows that the Rayleigh bound $\Delta\omega_{\min}$ could only be a limitation of theoretical tools of linear analysis, such as the one used in the FFT. The FPT as a nonlinear processor takes full advantage of that opportunity and achieves the frequency resolution, which could be better than $\Delta\omega_{\min}$. The resolution in the FPT is given by the average separation $\Delta\omega_{\text{ave}}$, which is usually smaller than $\Delta\omega_{\min}$ in a chosen window. Therefore, the FPT can surpass the Rayleigh limit $\Delta\omega_{\min} = 2\pi/T$. The resolution $2\pi/T$ of the FFT is limited by a sharp cutoff of $c(t)$ at $t = T$. By contrast, the FPT extrapolates the time signal $c(t)$ to $t > T$, and this can yield a resolution better than $2\pi/T$.

It is also important to ask another key question: why should quantum physics be used in processing time signals that originate from magnetic resonance? It definitely should because such time signals $c(t)$ stem from purely quantum-mechanical phenomena. The function $c(t)$ itself is the overall result of the induced transitions between two quantum mechanically allowed states of a sample, perturbed by static and varying magnetic fields, as well as radio waves tuned to a resonant frequency of the investigated spin-active nuclei with nonzero values of the magnetic moment. Moreover, quantum physics is the only complete theory that can provide both data driven and purely mechanistic descriptions of spectra and time signals $c(t)$. For example, in mechanistic modeling by quantum physics, one would insert the known spin–spin and spin–lattice interactions into the Hamiltonian of the studied system and predict a functional dependence of $c(t)$, which turns out to fully agree with experimentally encoded time signals. The same analysis also leads to a quantum-mechanical spectrum that could be reduced to the Fourier spectrum only under certain restrictive approximations. For instance, in the setting of the nearest neighbor approximation, while applying the strategy of the well-known inverse scattering problem to the measured $c(t)$, quantum physics can retrieve interactions (e.g., protein–protein interactions in tissue) as the most important part of the dynamics that produces the encoded time signals. Furthermore, quantum physics and quantum chemistry are used to design modern experiments from the realm of nuclear magnetic resonance (NMR) in chemistry and biology through practically infinite possibilities of manipulations with spins of nuclei.

3.2. The concept of quantum-mechanical signal processing

In quantum physics, the dynamics of physical systems that evolve in time are described by the nonstationary Schrödinger equation $\widehat{\mathrm{U}}(\tau)|\Upsilon_k) = u_k|\Upsilon_k)$ where $u_k = \exp(-i\omega_k\tau)$. This represents the eigenvalue problem of the evolution operator $\widehat{\mathrm{U}} = \exp(-i\widehat{\Omega}\tau)$ where $\widehat{\Omega}$ is the system operator that generates the dynamics. To secure decay to zero of u_k at the infinite time, we must have $\mathrm{Im}(\omega_k) < 0$. Physically, $\widehat{\Omega}$ is the energy operator associated with the Hamiltonian, which is the total energy (kinetic plus potential) of the whole system. For resonances with complex energies, the operator $\widehat{\Omega}$ is non-Hermitean, $\widehat{\Omega}^\dagger \neq \widehat{\Omega}$. Given a "Hamiltonian" $\widehat{\Omega}$ of the studied system, direct spectral analysis deals with extraction of the spectral set with all the fundamental eigenfrequencies and eigenfunctions $\{\omega_k, \Upsilon_k\}$. Such a task is usually accomplished by solving the Schrödinger eigenvalue problem via, for example, diagonalization of $\widehat{\Omega}$ by employing certain basis functions from a set that is complete, or locally complete. For practical purposes, all one needs are the complex fundamental frequencies $\{\omega_k\}$ and the corresponding complex amplitudes $\{d_k\}$. By definition, the amplitudes follow from the squared projection of the full state vector Υ_k onto the initial state Φ_0 of the system, $d_k = (\Phi_0|\Upsilon_k)^2$. In particular, the absolute values $\{|d_k|\}$ are the intensity of spectral lineshapes, whereas $\{\mathrm{Re}(\omega_k)\}$ and $\{\mathrm{Im}(\omega_k)\}$ are, respectively, equal or proportional to the positions and widths of the resonances in the spectrum of the investigated system[1]. Thus, by extracting all the spectral parameters $\{\omega_k, d_k\}$ for the given system operator $\widehat{\Omega}$, quantum physics can examine the structure of matter on any concrete level (nuclear, atomic, molecular, etc.). This is known as the direct quantification problem.

The rationale for calling the quantity $\widehat{\mathrm{U}}$, the evolution operator, can at once be appreciated by inspecting the nonstationary Schrödinger equation $(i\partial/\partial t)\Phi(t) = \widehat{\Omega}\Phi(t)$. "Hamiltonian" operator $\widehat{\Omega}$ is stationary for conservative systems, in which case the solution $\Phi(t)$ of the Schrödinger equation can be generated simply through the relation $\Phi(t) = \widehat{\mathrm{U}}(t)\Phi(0)$. In other words, $\Phi(t)$ at an arbitrary time $t > 0$ is obtained by subjecting $\Phi(0)$ to the action of the operator $\widehat{\mathrm{U}}(t)$. Therefore, given the operator $\widehat{\Omega}$, the state of the system $\Phi(t)$ at any instant t will be known if the initial state $\Phi(0) = \Phi(t = 0) \equiv \Phi_0$ is specified at $t = 0$. This is the origin of determinism of quantum mechanics. This mapping justifies the name of the time evolution operator for $\widehat{\mathrm{U}}$. Spectral problems can alternatively be solved by reliance on another powerful quantum-mechanical formalism called the Green operator $\widehat{\mathrm{G}}(u)$ that is defined as the resolvent operator, $\widehat{\mathrm{G}}(u) = (u\widehat{1} - \widehat{\mathrm{U}})^{-1}$.

All physical systems develop in time via their correlated dynamics. Correlations between any two states of the system are contained in the

[1]Hereafter, the notation $\mathrm{Re}(z)$ and $\mathrm{Im}(z)$ will be used to label the real and imaginary parts of the complex quantity z, respectively.

evolution operator $\widehat{\mathrm{U}}(t)$ that connects $\Phi(0)$ with $\Phi(t)$. Since operators are not observables, that is, they cannot be measured directly in experiments, certain related scalar quantities are needed. For instance, the projection technique can be used to project one state onto the other via the scalar or inner product. Thus, to correlate $\Phi(t)$ and $\Phi(0)$ with the ensuing scalar result, one can make the inner product of these two states, $C(t) \equiv (\Phi(0)|\Phi(t))$. The obtained quantity $C(t)$ is known as the autocorrelation function because it correlates the same system to itself via two different states $\Phi(t)$ and $\Phi(0)$. Furthermore, using $\Phi(t) = \widehat{\mathrm{U}}\Phi(0)$, it follows that $C(t)$ basically correlates the state $\Phi(0)$ to the same vector $\Phi(0)$ "weighted" with the evolution operator $\widehat{\mathrm{U}}$, such that $C(t) = (\Phi_0|\hat{\mathrm{U}}(t)|\Phi_0)$.

The chief working hypothesis of quantum mechanics asserts that the entire information about any given system is ingrained in the wavefunction of the system. These stationary and nonstationary wavefunctions are the state vectors Υ and $\Phi(t)$, respectively. The mathematical formula that encapsulates this postulate is given by the requests of the existence of the global (or at least the local) completeness relation $\sum_{k=1}^{K} \widehat{\pi}_k = \widehat{1}$, where $\widehat{\pi}_k$ is the projection operator $\widehat{\pi}_k = |\Upsilon_k)(\Upsilon_k|$. The term "completeness" refers explicitly to the complete information. To interpret the completeness relation, one resorts to the probabilistic meaning of quantum mechanics and all its entities. Thus, the state vector $|\Upsilon_k)$ and its dual counterpart $(\Upsilon_k|$ are the probability densities to find the system in the state described by these wavefunctions. Plausibly, knowing everything about the system under study is equivalent to achieving the maximum probability, which is equal to 1. This is precisely what is stated by the completeness relation in its operator form. The same statement can also be expressed in the scalar form by putting the operator completeness relation in a matrix element between the initial states $|\Phi_0)$ and its dual counterpart $(\Phi_0|$. The result reads as $\sum_{k=1}^{K} d_k = 1$ where d_k is the scalar amplitude given by $d_k = (\Phi_0|\widehat{\pi}_k|\Phi_0) = (\Phi_0|\Upsilon_k)^2$, which agrees with the above-quoted formula for d_k. Therefore, one of the ways of checking the completeness relation is to verify whether the sum of all the amplitudes $\{d_k\}$ $(1 \leq k \leq K)$ is equal to unity. It should also be noted that every form (operational or scalar) of the completeness relation implicitly contains the whole information about the fundamental frequencies $\{\omega_k\}$, since Υ_k and d_k correspond to ω_k.

The quantities that hold the complete information, the states vectors Υ and $\Phi(t)$, can be derived from the system operator $\widehat{\Omega}$. This, in turn, means that the entire sought information is also present in $\widehat{\Omega}$ or, equivalently, in $\widehat{\mathrm{U}}(t)$. The total evolution operator $\widehat{\mathrm{U}}(t)$ itself is the major physical content of $C(t)$. Hence, the stated quantum-mechanical postulate on completeness implies that everything one could possibly learn about any considered system is also contained in the autocorrelation function $C(t)$. Despite the fact that the same full information is available from Υ, $\Phi(t)$, $\widehat{\Omega}$, $\widehat{\mathrm{U}}(t)$, and $C(t)$, the autocorrelation functions are more manageable in practice, since they are observables. As a scalar, the quantity $C(t)$ has a functional form that is defined by its

dependence on the independent variable t. Therefore, since $C(t)$ ingrains the whole information about the studied generic system, it is critically important to have the quantum-mechanical prediction for the shape of the autocorrelation function. To obtain the explicit form of the autocorrelation function $C(t)$ for varying time t, one can use the spectral representation of $\widehat{\mathrm{U}}(t)$. This representation is easily obtained via multiplication of the defining exponential $\exp(-i\widehat{\Omega}t)$ for $\widehat{\mathrm{U}}(t)$ by the unity operator $\widehat{1}$, which is taken from the completeness relation. The end result is $\widehat{\mathrm{U}}(t) = \sum_{k=1}^{K} \exp(-i\omega_k t)\widehat{\pi}_k$. Therefore, preservation of the entire information from the system imposes the form of the spectral representation of the evolution operator given by the sum of K damped complex exponentials with the operator amplitudes $\widehat{\pi}_k$. Substituting such a representation for $\widehat{\mathrm{U}}(t)$ into $C(t)$ yields $C(t) = \sum_{k=1}^{K} d_k \exp(-i\omega_k t)$. Thus, the obtained shape of the quantum-mechanical autocorrelation functions represents a linear combination of K damped complex exponentials with the scalar amplitudes d_k. Crucially, this is not a fitting model for $C(t)$ introduced by hand. Rather, it is the shape of the autocorrelation function demanded by the form $\exp(-i\widehat{\Omega}t)$ of the quantum-mechanical evolution operator $\widehat{\mathrm{U}}(t)$. The derived form of $C(t)$ corresponds precisely to time signals $c(t)$ in many research branches. Critically, such time signals are measured in experiments across interdisciplinary fields, including NMR and MRS.

The outlined procedure establishes the equivalence between time signals and autocorrelation functions from quantum mechanics. This leads to a direct link between quantum mechanics and signal processing as two otherwise separated branches. Such a connection is of fundamental importance because a correct mathematical modeling in signal processing can only be done with a proper physical description of the investigated phenomenon. As seen, quantum mechanics amply fulfills this strict requirement. The whole field of signal processing benefits by being situated in a larger framework, such as quantum physics. However, quantum physics and chemistry can also gain from bridging to signal processing, which can offer its multitude of specialized algorithms on optimization and stabilization of physical systems.

3.3. Rational functions in the theory of approximations

We shall now outline the principal characteristics of the fast Padé transform in a larger mathematical theory. The stage is set for the natural emergence of the FPT by reference to the major features of rational functions. General rational functions $R(z^{-1})$ are defined as quotients of two other functions $f(z^{-1})$ and $g(z^{-1})$:

$$R(z^{-1}) = \frac{f(z^{-1})}{g(z^{-1})}. \tag{1}$$

Here, for convenience, the independent variable z^{-1} is chosen as the inverse of a general complex variable z. These rational functions represent the leading class of functions from mathematics with a myriad of applications across interdisciplinary research fields, ranging from physics to life sciences. This is primarily due to the main features of rational approximations, as they apply to analysis and interpretation of data that can stem from either experimental measurements or from theory by means of numerical computations. Such features are interpolation and extrapolation. By interpolation, one attempts to reliably generate the values of the observables in certain ranges or points where measured data are unavailable. By extrapolation, one tries to accurately predict the values that would have been measured had the experiment continued beyond the last recorded data point of the studied physical quantity. Both processes are of great practical importance, since a reliable method would save extra measurements and time-consuming numerical computations. Yet, the goal of an optimal theory is not to try in vain to achieve physically adequate interpolation and extrapolation by fitting with unavoidable nonuniqueness, subjectivity, and bias. Rather, the aim is to ingrain these two features into adequate mathematical models without adjustable parameters for the purpose of description of measured phenomena. The most suitable framework for solving this challenging simultaneous interpolation–extrapolation problem is provided precisely by rational functions of the general type (1).

3.4. Padé approximant in the theory of rational functions

The simplest and the most powerful rational function, is the Padé approximant, $R^{(\mathrm{PA})}(z^{-1})$, which is introduced by a ratio of two polynomials $P_L^-(z^{-1})$ and $Q_K^-(z^{-1})$ of degrees L and K [1]:

$$R^{(\mathrm{PA})}(z^{-1}) = \frac{P_L^-(z^{-1})}{Q_K^-(z^{-1})}, \tag{2}$$

$$P_L^-(z^{-1}) = \sum_{r=0}^{L} p_r^- z^{-r}; \qquad Q_K^-(z^{-1}) = \sum_{s=0}^{K} q_s^- z^{-s}, \tag{3}$$

where $\{p_r^-, q_s^-\}$ are the expansion coefficients of $P_L^-(z^{-1})$ and $Q_K^-(z^{-1})$. The most stable are the diagonal and para-diagonal PA as obtained for $L = K$ and $L - 1 = K$, respectively. The polynomial ratio from Eq. (2) becomes unique if it is taken to approximate a given Maclaurin series:

$$G(z^{-1}) = \sum_{n=0}^{\infty} c_n z^{-n}, \tag{4}$$

where the elements c_n of infinite set $\{c_n\}$ are the known expansion coefficients that can be any set of numbers and not only time signal points. In applications to signal processing in many fields, the c_n's from Eq. (4) are time signal points or autocorrelation functions [1]. These are given by linear combinations of decaying trigonometric functions that are complex-valued damped exponentials called fundamental harmonics (transients):

$$c_n = \sum_{k=0}^{K} d_k z_k^n; \qquad z_k = \mathrm{e}^{i\omega_k \tau}, \qquad \mathrm{Im}(\omega_k) > 0. \tag{5}$$

Here, τ is the sampling or dwell time, whereas $\{\omega_k, d_k\}$ are the nodal angular frequencies and the associated amplitudes, respectively. By inserting (5) into $G(z^{-1})$ from Eq. (4), the infinite sum over n can be carried out using the exact result for the geometric series $\sum_{n=0}^{\infty}(z_k/z)^n = 1/(1 - z_k/z) = z/(z - z_k)$. The obtained fraction $z/(z - z_k)$ is the simplest first-order diagonal ($L = K = 1$) rational polynomial in the variable $z^{+1} \equiv z$. To cohere with Eq. (5), general variable z can also be written in the harmonic form $z = \exp(i\omega\tau)$, where ω is a running complex angular frequency. A sum of K fractions $z/(z - z_k)$ via $G(z^{-1}) = \sum_{n=0}^{\infty} c_n z^{-n} = \sum_{k=1}^{K} d_k \sum_{n=0}^{\infty}(z_k/z)^n = \sum_{k=1}^{K} z d_k/(z - z_k)$ represents the Kth-order diagonal ($L = K$) rational polynomial $P_K^+(z)/Q_K^+(z)$:

$$G(z^{-1}) = \sum_{k=1}^{K} \frac{z d_k}{z - z_k} \equiv \frac{P_K^+(z)}{Q_K^+(z)}, \tag{6}$$

$$P_L^+(z) = \sum_{r=1}^{L} p_r^+ z^r, \qquad Q_K^+(z) = \sum_{s=0}^{K} q_s^+ z^s. \tag{7}$$

Thus, for the expansion coefficients $\{c_n\}$ in the form of geometric progression (5), the exact result for the infinite sum in Eq. (4) is given precisely by the rhs of Eq. (6), which can alternatively be rewritten as:

$$G(z^{-1}) = R^{(\mathrm{PzT})}(z), \qquad R^{(\mathrm{PzT})}(z) \equiv \frac{P_K^+(z)}{Q_K^+(z)}. \tag{8}$$

Here, the acronym PzT stands for the so-called Padé z-transform. Distinguishing PA from PzT is essential, due to the subtle, but the following critical differences between these two methods:

1. The standard Padé approximant is invariably introduced in the literature on this method as the rational polynomial $P_L^-(z^{-1})/Q_K^-(z^{-1})$ from Eq. (2) in the same variable z^{-1} as the original function $G(z^{-1})$ from Eq. (4). On the other hand, we can alternatively interpret (4) as the usual z-transform in variable z^{-1} [1]. As such, subsequently using geometric progression (5)

for the c_n's, the resulting rational function $R^{(\mathrm{PzT})}(z) = P_K^+(z)/Q_K^+(z)$ from Eq. (8) becomes the exact Padé polynomial quotient, but in the new variable z relative to the z-transform, $G(z^{-1})$. Thus, given $G(z^{-1})$, the first key difference between the PA and PzT is that the former and the latter are defined in variables z^{-1} and z, respectively. Of course, since the PzT is also a rational polynomial, the PzT and PA both belong to the same family of Padé approximants, albeit with two different tasks. To specify these tasks, given (4), we can consider two regions $|z| > 1$ and $|z| < 1$ in the complex $z-$plane. For $|z| > 1$ and $|z| < 1$, the series $G(z^{-1})$ from Eq. (4) will converge (say, slowly) and diverge, respectively. Therefore, the rational polynomial $P_K^-(z^{-1})/Q_K^-(z^{-1})$ from the usual PA in the same variable z^{-1} with respect to $G(z^{-1})$ accelerates the already existing convergence of (4) for $|z| > 1$. For the opposite case $|z| < 1$, the input series (4) diverges. However, for the same case $|z| < 1$, the rational polynomial $P_K^+(z)/Q_K^+(z)$ from the standard PzT converges, as it is defined in terms of the variable z as opposed to z^{-1} from $G(z^{-1})$. In this way, by means of the Cauchy analytical continuation, the PzT effectively induces convergence into the originally divergent series $G(z^{-1})$ for $|z| < 1$. This is how the same Padé methodology can achieve two opposite mappings via transforming divergent series into convergent ones and converting slowly into faster converging series (hence acceleration) [1].

2. The numerator polynomial $P_K^-(z^{-1})$ in, for example, the diagonal PA generally possesses the constant expansion coefficient ($p_0^- \neq 0$), such that the sum over r in Eq. (3) can start from $r = 0$ yielding:

$$P_K^-(z^{-1}) = p_0^- + p_1^- z^{-1} + p_2^- z^{-2} + \cdots + p_K^- z^{-K} \qquad (p_0^- \neq 0). \tag{9}$$

However, by definition, the corresponding expansion coefficient p_0^+ of the numerator polynomial $P_K^+(z)$ in the diagonal PzT is zero. Hence, this time, the sum over r in Eq. (7) for $P_K^+(z)$ begins with $r = 1$ with no free, z-independent term, thus producing:

$$P_K^+(z) = p_1^+ z + p_2^+ z^2 + \cdots + p_K^+ z^K \qquad (p_0^+ = 0). \tag{10}$$

The mentioned uniqueness of the Padé approximant for the given input Maclaurin series (4) represents a critical feature of this method. In other words, the ambiguities encountered in other mathematical modelings are eliminated from the outset already at the level of the definition of the PA. Moreover, this definition contains its "figure of merit" by revealing how well the PA can really describe the function $G(z^{-1})$ to be approximated. More precisely, given the infinite sum $G(z^{-1})$ via Eq. (4), the key question to raise is about the best agreement between $R^{(\mathrm{PA})}(z^{-1})$ from Eq. (2) and $G(z^{-1})$ from Eq. (4). This question can be easily answered by expanding $R^{(\mathrm{PA})}(z^{-1})$ as

an infinite sum in powers of z^{-1} around the point z_∞ located at infinity, $z = z_\infty \equiv \infty$. The result can be symbolically expressed by:

$$G(z^{-1}) - \frac{P_L^-(z^{-1})}{Q_K^-(z^{-1})} \approx \mathcal{O}^-(z^{-L-K-1}), \quad z \longrightarrow \infty, \tag{11}$$

where $\mathcal{O}^-(z^{-L-K-1})$ is the remainder of power series expansions around $z = z_\infty = \infty$. The function $\mathcal{O}^-(z^{-L-K-1})$, as an explicit error of the approximation $G(z^{-1}) \approx P_L^-(z^{-1})/Q_K^-(z^{-1})$, itself represents a power series with the expansion terms z^{-L-K-m} $(m = 1, 2, 3, \ldots, \infty)$. In other words, the mentioned "figure of merit" is explicitly given by the easily obtainable error term $\mathcal{O}^-(z^{-L-K-1})$, which is an infinite sum with higher order expansion terms than those retained in the Maclaurin series for the polynomial quotient $P_L^-(z^{-1})/Q_K^-(z^{-1})$ from the PA.

The definition (11) of the PA is reminiscent of a variance-type estimate given as the difference between the input data (observed, measured, encoded), $G(z^{-1})$ and output (modeled) function, $P_L^-(z^{-1})/Q_K^-(z^{-1})$:

$$\begin{aligned} \text{Padé Variance} &= \mathcal{O}^-(z^{-L-K-1}) \\ &\approx G(z^{-1})\,\{\text{input data (observed, measured)}\} \\ &- \frac{P_L^-(z^{-1})}{Q_K^-(z^{-1})}\,\{\text{output data (modeled, objective function)}\}. \end{aligned} \tag{12}$$

However, and this is what sets the PA apart from other methods, this "built-in" Padé variance is not an adjustable function, which can be used as a fitting recipe for producing anything which one subjectively decides to be "sufficiently good." Rather, the variance in the PA is free from any adjustable parameter and, as such, it is fully and objectively controlled solely by the structure of the input data $G(z^{-1})$. The Padé variance for the alternative version $P_L^+(z)/Q_K^+(z)$ is introduced in a similar way from the definition $G(z^{-1}) - P_L^+(z)Q_K^+(z) \approx \mathcal{O}(z^{L+K+1})$.

The possibility of being able to explicitly compute the difference term or the error estimate via $\mathcal{O}^-(z^{-L-K-1})$ in the Padé estimate $G(z^{-1}) \approx P_L^-(z^{-1})/Q_K^-(z^{-1})$ is the basis of the error analysis of proven validity in the PA. Padé approximants can be computed through many different numerical algorithms, including the most stable numerical computations via continued fractions. Moreover, unlike any other related method, for the known $G(z^{-1})$, both Padé polynomials $P_L^-(z^{-1})$ and $Q_K^-(z^{-1})$ in the PA can be extracted by purely analytical means in their simple and concise closed forms [1]. This represents the gold standard against which all the corresponding numerical algorithms should be benchmarked for their stability and robustness.

Outside mathematics, per se, theoretical physicists are most appreciative of the power and usefulness of the PA, which they began to use more than

half a century ago in many problems, ranging from the Brillouin–Wigner perturbation series to divergent expansions in quantum chromodynamics in the theory of strong interactions of elementary particles [1, 5]. The reason for such a widespread usage of this method in theoretical physics is that, in fact, the most interesting and also the most important series expansions emanating from realistic problems are divergent. Other frequently encountered series, although convergent in principle, often converge so slowly that they become virtually impractical in exhaustive applications. The PA comes to rescue the situation in both cases by converting divergent into convergent series and accelerating slowly converging series. The reason why the same method is able to tackle these diametrically opposing tasks (analytical continuations and convergence accelerations) is in the nonlinearity of the PA, as is obvious from the definition (11).

3.5. Cross-validation by two Padé variants in the complex frequency plane

The two main features of the Padé functions via its two wings, the PA (convergence rate enhancement of slowly convergent series or sequences), and the PzT (forced convergence of originally divergent series) are jointly embodied into the FPT. In the fast Padé transform, the PzT and PA are relabeled as $\mathrm{FPT}^{(+)}$ and $\mathrm{FPT}^{(-)}$, respectively, where the superscripts $\pm$ refer to the employed independent variables, $z^{+1} \equiv z$ and $z^{-1} = 1/z$. By definition, the $\mathrm{FPT}^{(+)}$ accomplishes analytical continuation through the forced convergence of divergent series. Likewise, the $\mathrm{FPT}^{(-)}$ achieves acceleration of slowly converging series or sequences. Given a Maclaurin series (4), the $\mathrm{FPT}^{(+)}$ and $\mathrm{FPT}^{(-)}$ are aimed at approximating the same function $G(z^{-1})$:

$$G(z^{-1}) \approx R^{(\mathrm{FPT})\pm}(z^{\pm 1}). \tag{13}$$

Functions $R^{(\mathrm{FPT})\pm}(z^{\pm 1})$ are explicitly defined as rational polynomials:

$$R^{(\mathrm{FPT})\pm}(z^{\pm 1}) \equiv \frac{P_L^{\pm}(z^{\pm 1})}{Q_K^{\pm}(z^{\pm 1})}, \tag{14}$$

$$P_L^{\pm}(z^{\pm 1}) = \sum_{r=1,0}^{L} p_r^{\pm} z^{\pm r}, \qquad Q_K^{\pm}(z^{\pm 1}) = \sum_{s=0}^{K} q_r^{\pm} z^{\pm s}, \tag{15}$$

where $r = 0$ and $r = 1$ correspond to $P_L^{-}(z^{-1})$ and $P_L^{+}(z)$, respectively. As in Eq. (11), the qualities of the $\mathrm{FPT}^{(\pm)}$, that is, the adequacy of the two approximations in Eq. (13), are governed by the explicit definitions:

$$\sum_{n=0}^{\infty} c_n z^{-n} - \frac{P_L^{\pm}(z^{\pm 1})}{Q_K^{\pm}(z^{\pm 1})} \approx \mathcal{O}(z^{\pm(L+K+1)}), \tag{16}$$

for $z \to 0$ and $z \to \infty$, respectively. The remainders or error functions $\mathcal{O}^{\pm}(z^{\pm(L+K+1)})$ follow by developing $R^{(\mathrm{FPT})\pm}(z^{\pm 1})$ in their power series. Such developments imply that both rational functions $P_L^{\pm}(z^{\pm 1})/Q_K(z^{\pm 1})$ are able to exactly reproduce the first $L+K$ terms from the infinite set $\{c_n\}$ of the input Maclaurin series (13). By definition, the rational polynomials $P_L^{+}(z)/Q_K^{+}(z)$ and $P_L^{-}(z^{-1})/Q_K^{-}(z^{-1})$ from the FPT$^{(+)}$ and FPT$^{(-)}$ yield the series expansions in powers of z and $1/z$. Therefore, the remainders $\mathcal{O}(z^{L+K+1})$ and $\mathcal{O}(z^{-L-K-1})$ from Eq. (16) are themselves power series expansions around the points $z=0$ and $z=\infty$. When z is a harmonic variable as in MRS, where $z = \exp(i\omega\tau)$ and $\mathrm{Re}(\omega) > 0$, the FPT$^{(+)}$ and FPT$^{(-)}$ converge inside and outside the unit circle $|z| < 1$ and $|z| > 1$, respectively. However, being in the family of Padé approximants, the FPT$^{(+)}$ and FPT$^{(-)}$ (just like the PzT and PA) converge, as well, in the complementary regions $|z| > 1$ and $|z| < 1$, respectively, by virtue of their analytical continuations. In other words, the FPT$^{(\pm)}$ are defined throughout the complex $z-$plane with the exception of K poles $z = z_k^{\pm}$ $(1 \le k \le K)$ of $P_K^{\pm}(z^{\pm 1})/Q_K^{\pm}(z^{\pm 1})$, where $z_k^{\pm}$ are zeros of the denominator polynomials, $Q_K^{\pm}(z_k^{\pm}) = 0$.

The outlines from Sections 3.3 and 3.4 emphasize the universal importance of rational functions and their most powerful proponent—Padé approximants. This led to a straightforward identification of the origin of the fast Padé transforms, via the FPT$^{(-)}$ and FPT$^{(+)}$, as the standard PA (acceleration of slowly converging series) and the PzT (transformation of diverging into converging series), respectively. However, in addition to convergence acceleration and induced convergence, the FPT can be applied to signal processing, where the main task is to carry out spectral analysis, that is, to solve the quantification problem. In this latter research area, a sampled time signal $\{c_n\}$ is available either from computations or measurements. Particularly in MRS, magnetic resonance physics dictates that each c_n is indeed a sum of K damped complex exponentials, as in Eq. (5). Here, we are given a set of N sampled time signal points $\{c_n\}$ $(0 \le n \le N-1)$, where the dwell time τ and the total signal length N are also known. As stated, the principal goal in parametric signal processing is to solve the quantification problem as an inverse problem. For the given input data $\{c_n\}$ $(0 \le n \le N-1)$, with the known N and τ, this inverse problem amounts to finding the unique solutions for the three types of unknown quantities that are the complex fundamental frequencies $\{\omega_k\}$ and the corresponding complex amplitudes $\{d_k\}$, as the building elements of each c_n. In this quantification problem, the third unknown quantity is the number of genuine resonances with the spectral parameters $\{\omega_k, d_k\}$.

The FPT provides the exact separation of genuine (physical) from spurious (unphysical, noise and/or noise-like) information encountered either in theory or measurements involving time signals. This is accomplished by means of Froissart doublets [16] that are coincident pairs of poles $z_k^{\pm} \equiv z_{k,Q}^{\pm}$ and zeros $z_{k,P}^{\pm}$ in the response functions or complex-valued spectra $P_K^{\pm}(z^{\pm 1})/Q_K^{\pm}(z^{\pm 1})$

from the FPT$^{(\pm)}$. Here, $z^{\pm}_{k,P}$ and $z^{\pm}_{k,Q}$ are the solutions of the numerator and denominator characteristic or secular equations:

$$P^{\pm}_{K}(z^{\pm}_{k,P}) = 0, \qquad z^{\pm}_{k,P} = \mathrm{e}^{\pm i\omega^{\pm}_{k,P}\tau}, \tag{17}$$

$$Q^{\pm}_{K}(z^{\pm}_{k,Q}) = 0, \qquad z^{\pm}_{k,Q} = \mathrm{e}^{\pm i\omega^{\pm}_{k,Q}\tau}. \tag{18}$$

Froissart pole–zero confluences are synchronized with the corresponding zero values obtained for Froissart amplitudes:

$$\text{Spurious:} \quad z^{\pm}_{k,Q} = z^{\pm}_{k,P} \quad \therefore \ \{d^{\pm}_{k}\}_{z^{\pm}_{k,Q}=z^{\pm}_{k,P}} = 0. \tag{19}$$

By changing the degree K of the polynomials in the diagonal FPT$^{(\pm)}$ from $P^{\pm}_{K}(z^{\pm 1})/Q^{\pm}_{K}(z^{\pm 1})$, Froissart doublets unpredictably and uncontrollably alter their positions in the complex $z^{\pm 1}-$planes. They never converge (stabilize) even when the whole signal length is exhausted. Therefore, these latter resonances that roam around in the complex planes are considered as spurious or unphysical. As such, these unstable resonances are identified by their twofold signature: pole–zero coincidences and zero amplitudes for noise-free time signals. The same type of signature also applies to noise-corrupted time signals (theoretically generated or experimentally measured), but with the approximations $z^{\pm}_{k,Q} \approx z^{\pm}_{k,P}$ and $d^{\pm}_{k} \approx 0$. Crucially, however, although Froissart doublets are unstable against even the smallest external perturbation (e.g., altering the degree of the Padé polynomial, adding noise, etc), they nevertheless consistently preserve the relationships in Eq. (19) or $z^{\pm}_{k,Q} \approx z^{\pm}_{k,P}$ and $d^{\pm}_{k} \approx 0$.

By contrast, there are retrieved resonances with spectral parameters that converge, and these are viewed as stable, genuine, or physical resonances. The signatures of all such genuine resonances are:

$$\text{Genuine:} \quad z^{\pm}_{k,Q} \neq z^{\pm}_{k,P} \quad \therefore \ \{d^{\pm}_{k}\}_{z^{\pm}_{k,Q}\neq z^{\pm}_{k,P}} \neq 0. \tag{20}$$

Amplitudes $d^{\pm}_{k}$ are the Cauchy residues of quotients $P^{\pm}_{K}(z^{\pm 1})/Q^{\pm}_{K}(z^{\pm 1})$ taken at the poles $z^{\pm}_{k,Q}$. Here, the word residues has the transparent meaning of the residual differences that remain after the values of the poles are subtracted from the zeros, implying that $d^{\pm}_{k}$ are proportional to $z^{\pm}_{k,Q} - z^{\pm}_{k,P}$ in the sense of a metric via:

$$d^{\pm}_{k} \propto z^{\pm}_{k,Q} - z^{\pm}_{k,P}. \tag{21}$$

Thus, the distances between poles $z^{\pm}_{k,Q}$ and zeros $z^{\pm}_{k,P}$ are proportional to the amplitudes $d^{\pm}_{k}$. Hence, $d^{\pm}_{k} \equiv 0$ for the exact pole–zero coincidences in the Froissart doublets (19). It is vital to have full control over the locations of all

the zeros of $Q_K^{\pm}(z^{\pm 1})$ in the Padé quotients $P_K^{\pm}(z^{\pm 1})/Q_K^{\pm}(z^{\pm 1})$ from the FPT$^{(\pm)}$. Such control is possible in the FPT$^{(+)}$ and FPT$^{(-)}$ because all the genuine zeros of $Q_K^{+}(z)$ and $Q_K^{-}(z^{-1})$ are inside and outside the unit circle, respectively. However, despite our prior knowledge about such precise locations before reconstructing these zeros, as soon as the systematically increased degree K of $Q_K^{\pm}(z^{\pm 1})$ surpasses the unknown true order $K_{\rm G}$, spurious roots $\{z_{k,Q}^{\pm}\}$ of the characteristic equations $Q_K^{\pm}(z^{\pm 1}) = 0$ would inevitably appear. For the same reason, spurious zeros $\{z_{k,P}^{\pm}\}$ will also emerge from the accompanying secular equations of the numerator polynomials $P_K^{\pm}(z^{\pm 1}) = 0$. This is where the Froissart concept comes into play to take advantage of the spuriousness in the set $\{z_{k,Q}^{\pm}\}$. Namely, the two types of spuriousness from the two sources $Q_K^{\pm}(z^{\pm 1}) = 0$ and $P_K^{\pm}(z^{\pm 1}) = 0$ are strongly coupled together. As a result, spurious Froissart poles $\{z_{k,Q}^{\pm}\}$ and zeros $\{z_{k,P}^{\pm}\}$ are always born out as pairs. It is in this way that Froissart doublets manifest themselves through pole–zero coincidences, $\{z_{k,Q}^{\pm}\} = \{z_{k,P}^{\pm}\}$, as in Eq. (19). Such an occurrence cancels the entire spuriousness from the polynomial quotients $P_K^{\pm}(z^{\pm 1})/Q_K^{\pm}(z^{\pm 1})$. This becomes particularly apparent when these ratios are written in their canonical forms:

$$\frac{P_K^{\pm}(z^{\pm 1})}{Q_K^{\pm}(z^{\pm 1})} = \frac{p_K^{\pm}}{q_K^{\pm}} \prod_{k=1}^{K} \frac{\left(z^{\pm 1} - z_{k,P}^{\pm}\right)}{\left(z^{\pm 1} - z_{k,Q}^{\pm}\right)}. \tag{22}$$

If the running degree K is larger than the number of genuine resonances $K_{\rm G}$, then all the terms $(z^{\pm 1} - z_{k,P}^{\pm})/(z^{\pm 1} - z_{k,Q}^{\pm})$ from Eq. (22) for $K - K_{\rm G} > 0$ would contain spurious Froissart poles $z_{k,Q}^{\pm}$ and zeros $z_{k,P}^{\pm}$. Hence, pole–zero cancellations leading to $(z^{\pm 1} - z_{k,P}^{\pm})/(z^{\pm 1} - z_{k,Q}^{\pm}) = 1$ for Froissart doublets $z_{k,Q}^{\pm} = z_{k,P}^{\pm}$, as per Eq. (19).

The ensuing consequence of these pole–zero cancellations onto the corresponding amplitudes of Froissart resonances can be seen at once from the explicit formulae for $d_k^{\pm}$ in terms of all the recovered poles and zeros:

$$d_k^{\pm} = \frac{p_K^{\pm}}{q_K^{\pm}} \prod_{k'=1}^{K} \frac{\left(z_{k,Q}^{\pm} - z_{k',P}^{\pm}\right)}{\left(z_{k,Q}^{\pm} - z_{k',Q}^{\pm}\right)_{k' \neq k}}. \tag{23}$$

Here, in the numerator, it is permitted to have $k' = k$, in which case every Froissart doublet from Eq. (19) would produce zero-valued terms $(z_{k,Q}^{\pm} - z_{k,P}^{\pm})$, and thus the whole product in Eq. (23) will become zero. As mentioned earlier, this yields $d_k^{\pm} = 0$ for $z_{k,Q}^{\pm} = z_{k,P}^{\pm}$, according to Eq. (19). It can also be seen that Eq. (21) and expression (23) are compatible with each other. In computations, expression (23) should not be used to obtain the amplitudes $d_k^{\pm}$ in the FPT$^{(\pm)}$. This is because formula (23) employs the whole set of the reconstructed amplitudes to compute $d_k^{\pm}$ for the kth resonance. Therefore, even the slightest inaccuracy, such as near cancellations of poles and zeros, rather than

the theoretically exact cancellations, could spoil the precision of the sought $d_k^{\pm}$ for the given k. Instead, we use the alternative and equivalent expressions:

$$d_k^{\pm} = \frac{P_K^{\pm}(z_{k,Q}^{\pm})}{Q_K^{\pm'}(z_{k,Q}^{\pm})}; \qquad Q_K^{\pm'}(z_{k,Q}^{\pm}) \neq 0, \tag{24}$$

where $Q_K^{\pm'}(z^{\pm 1}) = (\mathrm{d}/\mathrm{d}z^{\pm 1})Q_K^{\pm}(z^{\pm 1})$. Here, each kth amplitude on the lhs depends only on one, that is, the kth value of the rhs of Eq. (23), and hence no other resonance can deteriorate the accuracy of the retrieved $d_k^{\pm}$.

Overall, it is clear from these remarks that the FPT$^{(\pm)}$ possess a very elegant, simple, and powerful solution for the exact identification of all spurious Froissart resonances [5]. When these are discarded, only genuine resonances are left in the output line list of the reconstructed spectral parameters. This yields the exact solution of the quantification problem.

In the next section, we shall illustrate the performance of the FPT on time signals reminiscent of those encoded via MRS. These are from three problem areas within cancer diagnostics: ovarian, breast, and prostate. Similar applications can be done using many other time signals and spectra encountered across interdisciplinary research, including physics, chemistry, biology and medicine.

4. MRS DATA FOR BENIGN AND MALIGNANT OVARIAN CYST FLUID

4.1. Clinical background

Ovarian cancer is the seventh leading cause of cancer deaths among women worldwide [17]. In many developed countries, it is the most common cause of death from gynecological malignancies. This malignancy is most often detected after spread beyond the true pelvis, when the prognosis is very poor, whereas stage Ia disease has better than a 90% chance of 5-year survival. Unfortunately, early detection is still beyond current reach with standard diagnostic methods. Consequently, despite progress in treatment, mortality rates from ovarian cancer have not declined substantially over the last 30 years [18].

Although helpful in surveillance of patients with diagnosed ovarian cancer, the tumor marker CA-125 does not improve early detection of ovarian cancer when used alone [5]. Investigations examining genomic and proteomic patterns as possible complementary biomarkers for early ovarian cancer have shown some promise. However, further study is necessary to ascertain whether these biomarkers provide sufficient improvement in diagnostic accuracy to justify their more widespread application for ovarian cancer screening [19].

Albeit sensitive, transvaginal ultrasound (TVUS) lacks adequate specificity to distinguish benign from malignant adnexal changes [20]. Among nearly 40000 women within the population-based Prostate, Lung, Colorectal and Ovarian (PLCO) Cancer Screening Trial, the positive predictive value was only 23.5% for the combination of abnormal values of CA-125 plus findings suggesting ovarian malignancy by TVUS. This meant that in order to actually find 26 cases of ovarian cancer (plus three other malignancies), 570 women underwent a surgical procedure [20]. The consequences of such poor specificity included lowered adherence to the PLCO Trial, as well as emotional distress. Because of the potentially deleterious consequences of false positive findings, the U.S. Preventive Services Task Force has recommended against routine screening for this malignancy [21].

Ovarian cancer can be identified more accurately by MRI. In a meta-analytical comparison of morphological imaging modalities, MRI was of greatest incremental value in identifying ovarian cancer when the nature of adnexal mass was considered uncertain by TVUS [22]. Nevertheless, even with contrast-enhanced MRI, 60 of 241 (24.9%) false positive findings from initial TVUS were not recognized as benign lesions [22]. By detecting metabolic features characteristic of ovarian cancer, MRS could potentially enhance the specificity of MRI with regard to the diagnosis of this malignancy. Since molecular changes often precede morphologic alterations, MRS might further improve sensitivity, as well. However, in our recent review of the published studies, in vivo MRS was not found to adequately distinguish malignant from benign ovarian lesions [5]. Poor resolution and SNR have been major problems for in vivo MRS of this small, moving organ [5].

Clinical scanners use the fast Fourier transform to convert the encoded time signal into its spectral representation in the frequency domain. As discussed, the FFT is a low-resolution spectral estimator, which can give only a total shape spectrum (envelope). Since the FFT requires postprocessing via fitting that is nonunique, the stated number of metabolites is actually just a guess. Consequently, estimates of metabolite concentrations could well be far from the true values, particularly when the resonances are closely overlapping [1]. Earlier in this chapter, we have also explained why the fast Padé transform is especially suitable for in vivo MRS [1–15]. We noted that the FPT has high resolution due to its nonlinearity, interpolation and extrapolation capabilities. Crucially, the FPT is a stable parametric signal processor, which unambiguously determines the number of true metabolites and their spectral parameters from which metabolite concentrations can be reliably reconstructed [1–5].

Recently, in Refs. [7, 8], we compared the resolution performance of the FPT and the FFT with time signals that were generated according to in vitro MRS data as encoded from malignant and benign ovarian cyst fluid.

The encoded data were from Ref. [23]. We also examined how the FPT reconstructs the spectral parameters from this MRS data for malignant and benign ovarian cyst fluid. Thereby, we computed the metabolite concentrations that are clinically the most relevant MRS data for distinguishing cancerous from benign ovarian lesions. The detailed mathematical analysis, extensive presentation of the convergence performance of the FPT and the FFT, as well as the full numerical results are reported in Refs. [5, 7, 8]. Herein, we examine how the Padé-optimized MRS might be used to improve ovarian cancer detection. Our emphasis is on the resolution performance of the FPT compared with Fourier-based conventional processing of magnetic resonance time signals.

4.2. Signal processing

We applied the FPT to FIDs according to those encoded in vitro at a magnetic field strength of $B_0 \approx 14.1$T in a 600 MHz NMR spectrometer from benign and neoplastic ovarian cyst fluid, as per Ref. [23]. Two FIDs of the type from Eq. (5) were synthesized, with 12 damped complex exponentials. We then quantified the FIDs as described in Ref. [2] via the FPT.

We generated the input data for the spectral parameters from the median concentrations $\{C_k\}_{k=1}^{12}$ (in μM/L ww) of 12 metabolites typical of benign ovarian cyst fluid from Ref. [23]. These concentrations reported in Ref. [23] were based on 23 patients with benign ovarian cysts. For the cancerous ovarian cyst fluid, the concentrations of metabolites were derived from the median values from 12 patients, as reported in Ref. [23]. The latter were taken as the input data for the cancerous ovaries. In Table 6.1, we present these input data.

The FIDs in Ref. [23] were recorded at a bandwidth of 6667 Hz. We use the inverse of this bandwidth for the sampling time τ in our synthesized time signals. We chose the total signal length N from Ref. [23] based on the Fourier resolving power $\Delta\omega_{\min} = 2\pi/T$. This was done in order to attain a spectral resolution $\Delta\omega = 0.02$ ppm, which would distinguish the two most closely lying metabolites: isoleucine and valine. The closest integer in the form 2^m for the time signal length as required by the FFT is therefore $N = 2^{15} = 32768 = 32$ K(K = 1kilobyte = 1024). In Ref. [23], the FFT spectrum was computed by zero-filling the two encoded time signals to 64 K.

Since, as noted, the FPT resolution is not predetermined by $2\pi/T$, a shorter time signal length is likely to be sufficient, and herein we used a total signal length $N = 1024$. Via the expression $|d_k| = 2C_k/C_{\text{ref}}$, the input peak amplitudes were extracted from the data in Ref. [23].

We took the reference concentration C_{ref} as median lactate concentration in the malignant ovarian samples, since that was the highest value (6536 μM/L ww) from Ref. [23] where the tissue wet weight is abbreviated

Table 6.1 Input data for synthesized FIDs based on in vitro MRS data as encoded from nonmalignant and cancerous ovarian cyst fluid [23]. Quantity $\mathrm{Re}(\nu_k)$ denotes the chemical shift as the relative frequency in parts per million (ppm). The acronym for arbitrary units is au.

Input Data: Spectral Parameters, Concentrations and Metabolite Assignments					
n_k^o (Metabolite # k)	$\mathrm{Re}(\nu_k)$ (ppm)	$\mathrm{Im}(\nu_k)$ (ppm)	$\lvert d_k\rvert$ (au)	C_k (μM/L ww)	M_k (Assignment)
			(i) Benign		
1	1.020219	0.000818	0.003060	10	Isoleucine (Iso)
2	1.040048	0.000821	0.034578	113	Valine (Val)
3	1.330124	0.000822	0.027540	90	Threonine (Thr)
4	1.410235	0.000828	0.758570	2479	Lactate (Lac)
5	1.510318	0.000824	0.089657	293	Alanine (Ala)
6	1.720125	0.000823	0.030906	101	Lysine (Lys)
7	2.130246	0.000819	0.002142	7	Methionine (Met)
8	2.470118	0.000825	0.084149	275	Glutamine (Gln)
9	3.050039	0.000822	0.019278	63	Creatine (Cr)
10	3.130227	0.000821	0.020808	68	Creatinine (Crn)
11	3.190136	0.000820	0.004590	15	Choline (Cho)
12	5.220345	0.000829	0.424419	1387	Glucose (Glc)
			(ii) Malignant		
1	1.020219	0.000828	0.024174	79	Isoleucine (Iso)
2	1.040048	0.000831	0.120869	395	Valine (Val)
3	1.330124	0.000832	0.075887	248	Threonine (Thr)
4	1.410235	0.000838	2.000000	6536	Lactate (Lac)
5	1.510318	0.000834	0.179315	586	Alanine (Ala)
6	1.720125	0.000833	0.149939	490	Lysine (Lys)
7	2.130246	0.000829	0.018972	62	Methionine (Met)
8	2.470118	0.000835	0.253366	828	Glutamine (Gln)
9	3.050039	0.000832	0.020196	66	Creatine (Cr)
10	3.130227	0.000831	0.024174	79	Creatinine (Crn)
11	3.190136	0.000830	0.012852	42	Choline (Cho)
12	5.220345	0.000839	0.079559	260	Glucose (Glc)

by ww. The line widths in Ref. [23] were approximately 1 Hz. We permitted small variations within $\{8.20, 8.39\} \times 10^{-4}$ ppm (labeled as $\mathrm{Im}(\nu_k)$ in the Tables) in the line width. Since the phases ϕ_k $(1 \leq k \leq 12)$ from d_k were all set to zero, each amplitude d_k was real, $d_k = |d_k|$. The area under a given resonance is proportional to the metabolite concentration, relative to the reference concentration, 6536 μM/L ww. In the FPT$^{(-)}$, we thereby computed the metabolite concentrations $\{C_k^-\}$ via $C_k^- = 3268\,|d_k^-|\,\mu$M/L ww.

Table 6.2 Reconstruction by the FPT of spectral parameters and concentrations of metabolites for a synthesized time signal based on MRS data as encoded in vitro in Ref. [23] from cyst fluid of benign ovaries. Convergence is attained at $N/16 = 64$ ($N = 1024$; middle panel (ii)).

Convergence of Spectral Parameters and Concentrations in FPT$^{(-)}$; Signal Length: $N/M, N = 1024, M = 8 - 32$					
n_k^o (Metabolite # k)	Re(ν_k^-) (ppm)	Im(ν_k^-) (ppm)	$\lvert d_k^- \rvert$ (au)	C_k^- (μM/L ww)	M_k (Assignment)
(i) $N/32 = 32$ (Benign)					
2	1.040033	0.001124	0.038143	124	Valine (Val)
4	1.409673	0.001117	0.796643	2603	Lactate (Lac)
5	1.482370	0.005257	0.081645	266	Alanine (Ala)
6	1.706966	0.009141	0.035360	115	Lysine (Lys)
7	2.207406	0.216536	0.005435	17	Methionine (Met)
8	2.470151	0.000826	0.082607	270	Glutamine (Gln)
9	3.058390	0.001607	0.020043	65	Creatine (Cr)
10	3.141312	0.002566	0.024686	80	Creatinine (Crn)
12	5.220345	0.000829	0.424418	1387	Glucose (Glc)
(ii) $N/16 = 64$ (Benign)					
1	1.020219	0.000818	0.003060	10	Isoleucine (Iso)
2	1.040048	0.000821	0.034578	113	Valine (Val)
3	1.330124	0.000822	0.027540	90	Threonine (Thr)
4	1.410235	0.000828	0.758570	2479	Lactate (Lac)
5	1.510318	0.000824	0.089657	293	Alanine (Ala)
6	1.720125	0.000823	0.030906	101	Lysine (Lys)
7	2.130246	0.000819	0.002142	7	Methionine (Met)
8	2.470118	0.000825	0.084149	275	Glutamine (Gln)
9	3.050039	0.000822	0.019278	63	Creatine (Cr)
10	3.130227	0.000821	0.020808	68	Creatinine (Crn)
11	3.190136	0.000820	0.004590	15	Choline (Cho)
12	5.220345	0.000829	0.424419	1387	Glucose (Glc)
(iii) $N/8 = 128$ (Benign)					
1	1.020219	0.000818	0.003060	10	Isoleucine (Iso)
2	1.040048	0.000821	0.034578	113	Valine (Val)
3	1.330124	0.000822	0.027540	90	Threonine (Thr)
4	1.410235	0.000828	0.758570	2479	Lactate (Lac)
5	1.510318	0.000824	0.089657	293	Alanine (Ala)
6	1.720125	0.000823	0.030906	101	Lysine (Lys)
7	2.130246	0.000819	0.002142	7	Methionine (Met)
8	2.470118	0.000825	0.084149	275	Glutamine (Gln)
9	3.050039	0.000822	0.019278	63	Creatine (Cr)
10	3.130227	0.000821	0.020808	68	Creatinine (Crn)
11	3.190136	0.000820	0.004590	15	Choline (Cho)
12	5.220345	0.000829	0.424419	1387	Glucose (Glc)

4.2.1. Benign ovarian cyst fluid

In Table 6.2, we present the FPT-reconstructed spectral parameters for the benign ovarian data. These are displayed for signal lengths $N/32 = 32, N/16 = 64$, and $N/8 = 128$. The top panel ($N/32 = 32$) shows reconstructed spectral parameters for only 9 of the 12 resonances. At $N/32$, isoleucine and threonine were not detected, and between 3.06 and 5.22 ppm only one peak was identified. The computed concentration and spectral parameters were completely correct only for one metabolite: glucose. Thus, 32 signal points were not sufficient for the FPT to reconstruct or even to identify all the physical resonances.

At $N/16 = 64$ (middle panel) of Table 6.2, for each of the 12 resonances, the FPT is seen to *exactly* reconstruct all the spectral parameters with six-digit accuracy. The metabolite concentrations are also seen to be identical to the input concentrations (see Table 6.1 for comparison). Stable convergence is demonstrated by inspection of the bottom panel of Table 6.2. At $N/8 = 128$, all the spectral parameters are exactly the same as those at $N/16 = 64$. We have also confirmed that this convergence is stable at longer partial signal lengths N/M ($M < 8$) and at full signal length $N = 1024$ ($M = 1$).

We display the convergence performance of the FFT (left panels) versus the FPT (right panels) for the absorption total shape spectra in Figure 6.1. The partial signal lengths are $N/32 = 32$ (top, (i)), $N/16 = 64$ (middle, (ii)), and $N/8 = 128$ (bottom, (iii)). The FFT-generated spectra provide no meaningful information, whereas the FPT yield reasonably appearing spectra even prior to convergence at $N/32 = 32$, although only 9 of the 12 metabolites are delineated. As expected from Table 6.2, at $N/16 = 64$ and $N/8 = 128$, the peak heights are correct for all 12 metabolites in the Padé-generated spectra.

Figure 6.2 provides a further comparison of the convergence performance of the FFT and FPT. The upper panels show the rapid convergence of the FPT at $N/16 = 64$ signal points (top right panel). At these signal lengths $N/32 = 32$ and $N/16 = 64$, the FFT provides no meaningful information (middle panels in Figure 6.2). The lower panels of Figure 6.2 show the absorption spectra generated by the FFT at $N = 8\text{K} = 8192, N = 32\text{K} = 32768$ where $\text{K} = 1024$. The first signal length for which the positive-definite Fourier absorption spectra are obtained is very long ($N = 8\text{K}$). Although the 12 resonances are resolved in the FFT at $N = 8\text{K}$ on the bottom left panel of Figure 6.2, a number of peak heights are not correct. Consequently, several of the metabolite concentrations estimated from the Fourier spectra by either fitting or peak integrations will not be accurate even at $N = 8\text{K}$. It should also be noted that at $N = 8\text{K}$ baseline distortions are present, which could further undermine the accuracy of both fitting and numerical peak integrations. The FFT converges finally at $N = 32\text{K} = 32768$.

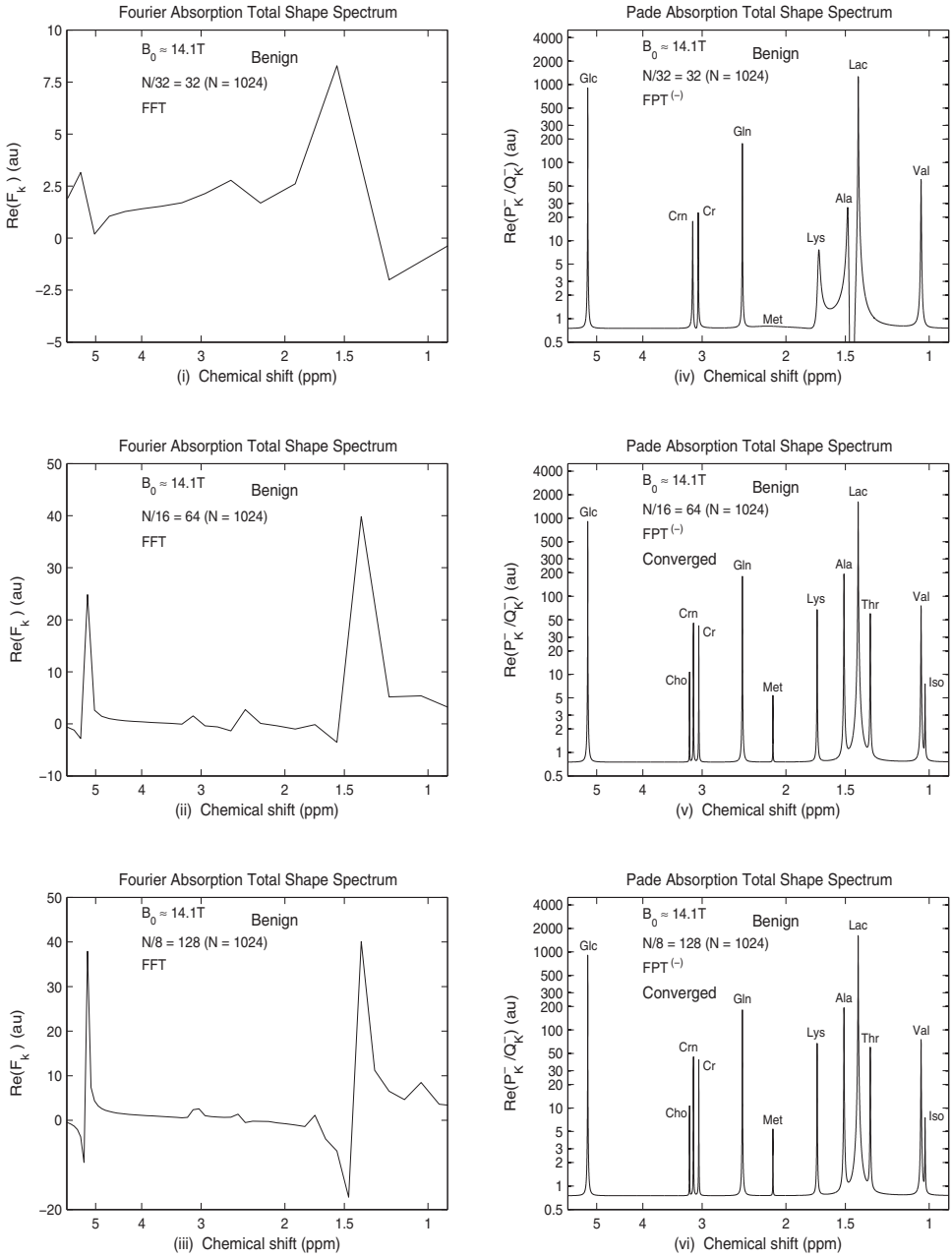

Figure 6.1 Absorption total shape spectra for the benign ovarian cyst fluid from input data derived from Ref. [23]. The signal lengths are $N/32 = 32$ (top panels (i), (iv)), $N/16 = 64$ (middle panels (ii), (v)), and $N/8 = 128$ (bottom panels (iii), (vi)), where N is the full signal length ($N = 1024$). Spectra generated by the FFT are shown on the left panels and by the FPT on the right panels.

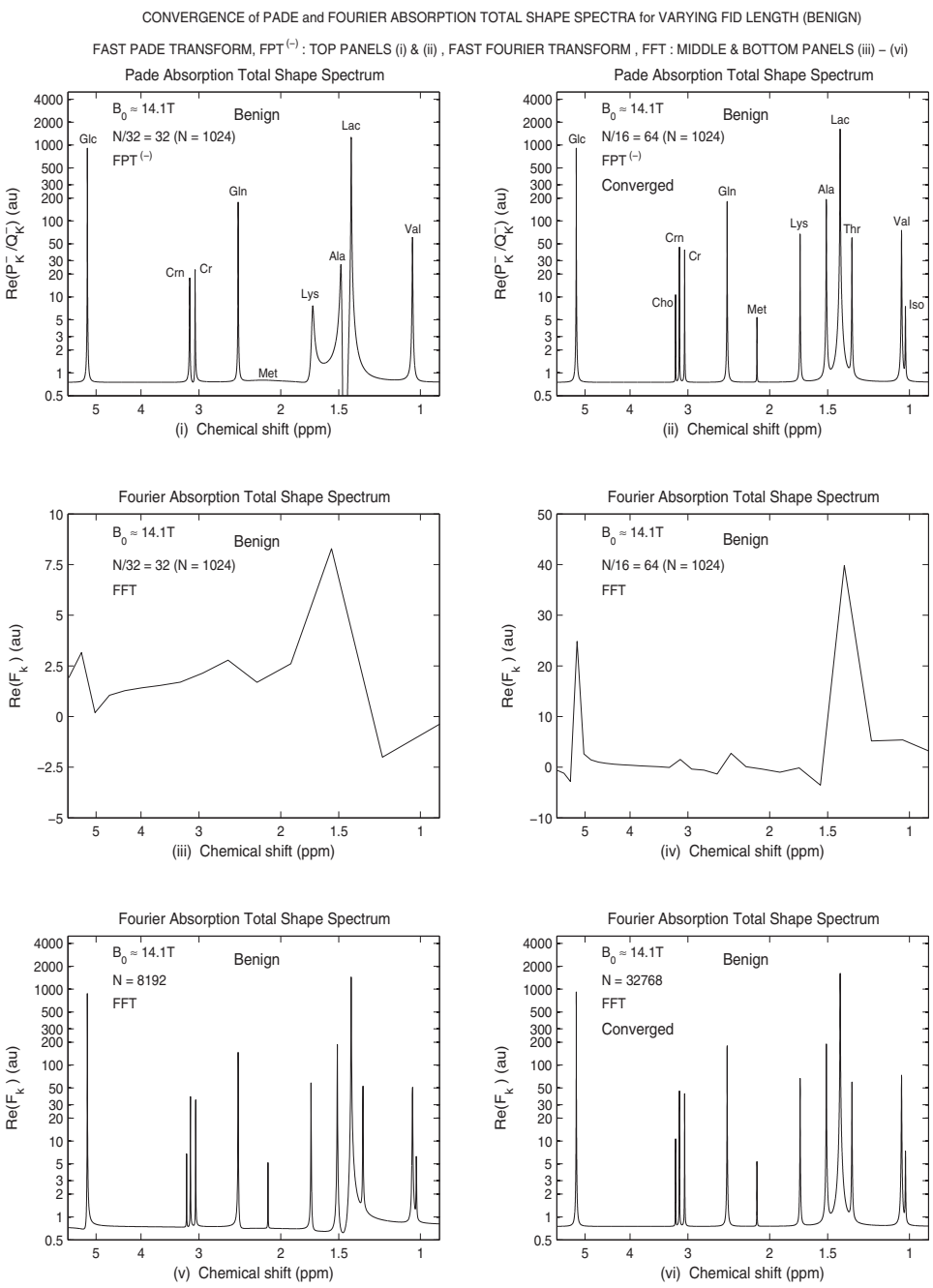

Figure 6.2 Absorption total shape spectra for the benign ovarian cyst fluid from input data derived from Ref. [23]. Top panels are the spectra generated by the FPT at (i) [$N/32 = 32$] and (ii) [$N/16 = 64$]. Middle panels are the FFT-generated spectra at (iii) [$N/32 = 32$] and (iv) [$N/16 = 64$]. Bottom panels are the FFT-generated spectra at (v) [$N = 8192$] and (vi) [$N = 32768$].

Table 6.3 Reconstruction by the FPT of spectral parameters and concentrations of metabolites for a synthesized time signal based on MRS data as encoded in vitro in Ref. [23] from cyst fluid of malignant ovaries. Convergence is attained at $N/16 = 64$ ($N = 1024$; middle panel (ii)).

Convergence of Spectral Parameters and Concentrations in FPT$^{(-)}$; Signal Length: N/M, $N = 1024, M = 8 - 32$					
n_k^o (Metabolite # k)	Re(ν_k^-) (ppm)	Im(ν_k^-) (ppm)	$\lvert d_k^- \rvert$ (au)	C_k^- (μM/L ww)	M_k (Assignment)
(i) $N/32 = 32$ (Malignant)					
2	1.039257	0.001406	0.148343	484	Valine (Val)
4	1.409062	0.001372	2.046372	6688	Lactate (Lac)
5	1.446902	0.008300	0.196825	643	Alanine (Ala)
6	1.712040	0.004160	0.174575	570	Lysine (Lys)
7	2.101571	0.031100	0.028695	93	Methionine (Met)
8	2.470096	0.000838	0.251929	823	Glutamine (Gln)
9	3.069839	0.003200	0.028376	92	Creatine (Cr)
10	3.165277	0.003440	0.028617	93	Creatinine (Crn)
12	5.220345	0.000839	0.079557	260	Glucose (Glc)
(ii) $N/16 = 64$ (Malignant)					
1	1.020219	0.000828	0.024174	79	Isoleucine (Iso)
2	1.040048	0.000831	0.120869	395	Valine (Val)
3	1.330124	0.000832	0.075887	248	Threonine (Thr)
4	1.410235	0.000838	2.000000	6536	Lactate (Lac)
5	1.510318	0.000834	0.179315	586	Alanine (Ala)
6	1.720125	0.000833	0.149939	490	Lysine (Lys)
7	2.130246	0.000829	0.018972	62	Methionine (Met)
8	2.470118	0.000835	0.253366	828	Glutamine (Gln)
9	3.050039	0.000832	0.020196	66	Creatine (Cr)
10	3.130227	0.000831	0.024174	79	Creatinine (Crn)
11	3.190136	0.000830	0.012852	42	Choline (Cho)
12	5.220345	0.000839	0.079559	260	Glucose (Glc)
(iii) $N/8 = 128$ (Malignant)					
1	1.020219	0.000828	0.024174	79	Isoleucine (Iso)
2	1.040048	0.000831	0.120869	395	Valine (Val)
3	1.330124	0.000832	0.075887	248	Threonine (Thr)
4	1.410235	0.000838	2.000000	6536	Lactate (Lac)
5	1.510318	0.000834	0.179315	586	Alanine (Ala)
6	1.720125	0.000833	0.149939	490	Lysine (Lys)
7	2.130246	0.000829	0.018972	62	Methionine (Met)
8	2.470118	0.000835	0.253366	828	Glutamine (Gln)
9	3.050039	0.000832	0.020196	66	Creatine (Cr)
10	3.130227	0.000831	0.024174	79	Creatinine (Crn)
11	3.190136	0.000830	0.012852	42	Choline (Cho)
12	5.220345	0.000839	0.079559	260	Glucose (Glc)

4.2.2. Malignant ovarian cyst fluid

Table 6.3 presents the Padé-reconstructed spectral parameters for the data corresponding to cancerous ovarian cyst fluid. The three signal lengths shown are $N/32 = 32, N/16 = 64$, and $N/8 = 128$. For $N/32 = 32$ signal points as shown on the top panel in Table 6.3, there were only nine delineated resonances: isoleucine and threonine were not identified, and just one resonance was detected between 3.07 and 5.22 ppm. Once again, glucose was the only metabolite for which the spectral parameters and computed concentration were nearly all correct. Consequently, 32 signal points were not enough for the FPT to converge.

It can be seen on the middle panel of Table 6.3 that for data derived from malignant ovarian cyst fluid, the FPT *exactly* reconstructed all the spectral parameters for all 12 peaks using $N/16 = 64$ signal points (compare Tables 6.1 and 6.3 with the input and reconstructed data, respectively). The lower panel of Table 6.3 illustrates stable convergence at $N/8 = 128$. We confirmed that all the peak parameters reconstructed by the FPT remained constant for the malignant ovarian data at higher fractions $N/M\,(M < 8)$ of the full time signal including $N = 1024\,(M = 1)$.

The Padé-generated absorption total shape spectra, as displayed in the right panels of Figure 6.3, are consistent with the tabular reconstructions. Thus, at $N/32 = 32$, some 9 of the 12 metabolites are delineated by the FPT (top panel (iv)), whereas isoleucine, threonine, and choline require 64 signal points to be identified. At $N/16 = 64$, all the peak heights are correct, and the total absorption shape spectrum is completely converged (right middle panel (v)). At $N/8 = 128$ (right bottom panel) the convergence is stable. In sharp contrast, the Fourier-generated absorption spectra shown on the left panels of Figure 6.3, at $N/32 = 32$ (top, (i)), $N/16 = 64$ (middle, (ii)) and $N/8 = 128$ (bottom, (iii)) are devoid of meaningful information.

We continue with our comparison of the convergence performance of the FFT and FPT for the cancerous ovarian data in Figure 6.4. The upper two panels recapitulate the rapid convergence of the FPT attained at $N/16 = 64$ signal points (top right panel). The middle panels in Figure 6.4 recapitulate the rough and uninformative total absorption spectra generated by the FFT at $N/32 = 32$ and $N/16 = 64$. The lower panels of Figure 6.4 demonstrate the performance of the FFT at $N = 8\text{K} = 8192, N = 32\text{K} = 32768$. It is first at $N = 8\text{K}$ that the positive-definite Fourier absorption spectra are obtained. Although all 12 peaks are resolved in the FFT at $N = 8\text{K}$ (lower left panel in Figure 6.4), several of the peak heights are not correct. As was true for the benign ovarian case, at $N = 8\text{K}$ major baseline distortions are observed, which, as noted, would preclude accuracy with attempts at fitting, as well as for numerical peak integrations. The total absorption spectrum converges for the FFT for the cancerous ovarian case at $N = 32\text{K} = 32768$ (bottom right panel in Figure 6.4).

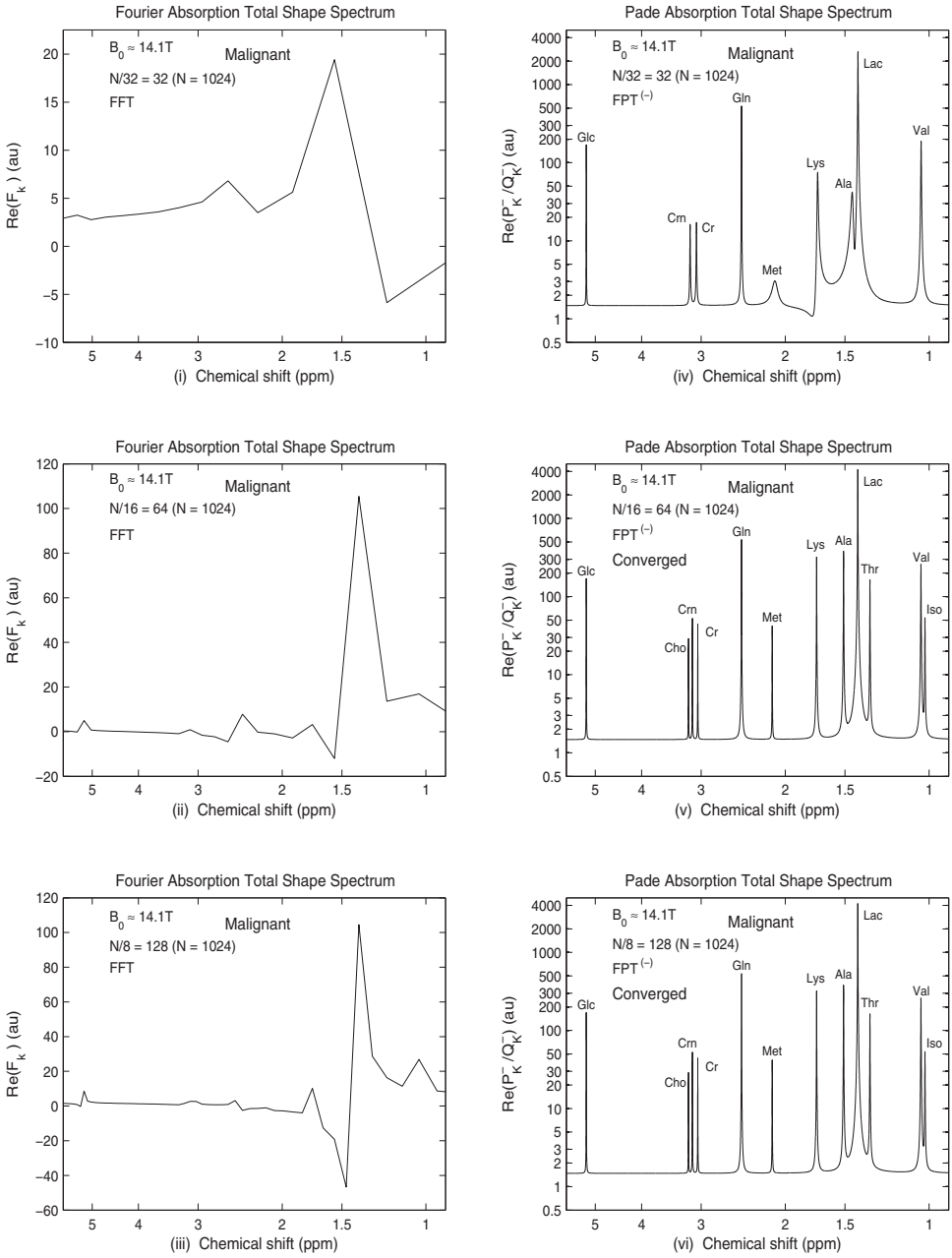

Figure 6.3 Absorption total shape spectra for the cancerous ovarian cyst fluid from input data derived from Ref. [23]. The signal lengths are $N/32 = 32$ (top panels (i), (iv)), $N/16 = 64$ (middle panels (ii), (v)), and $N/8 = 128$ (bottom panels (iii), (vi)), where N is the full signal length ($N = 1024$). Spectra generated by the FFT are shown on the left panels and by the FPT on the right panels.

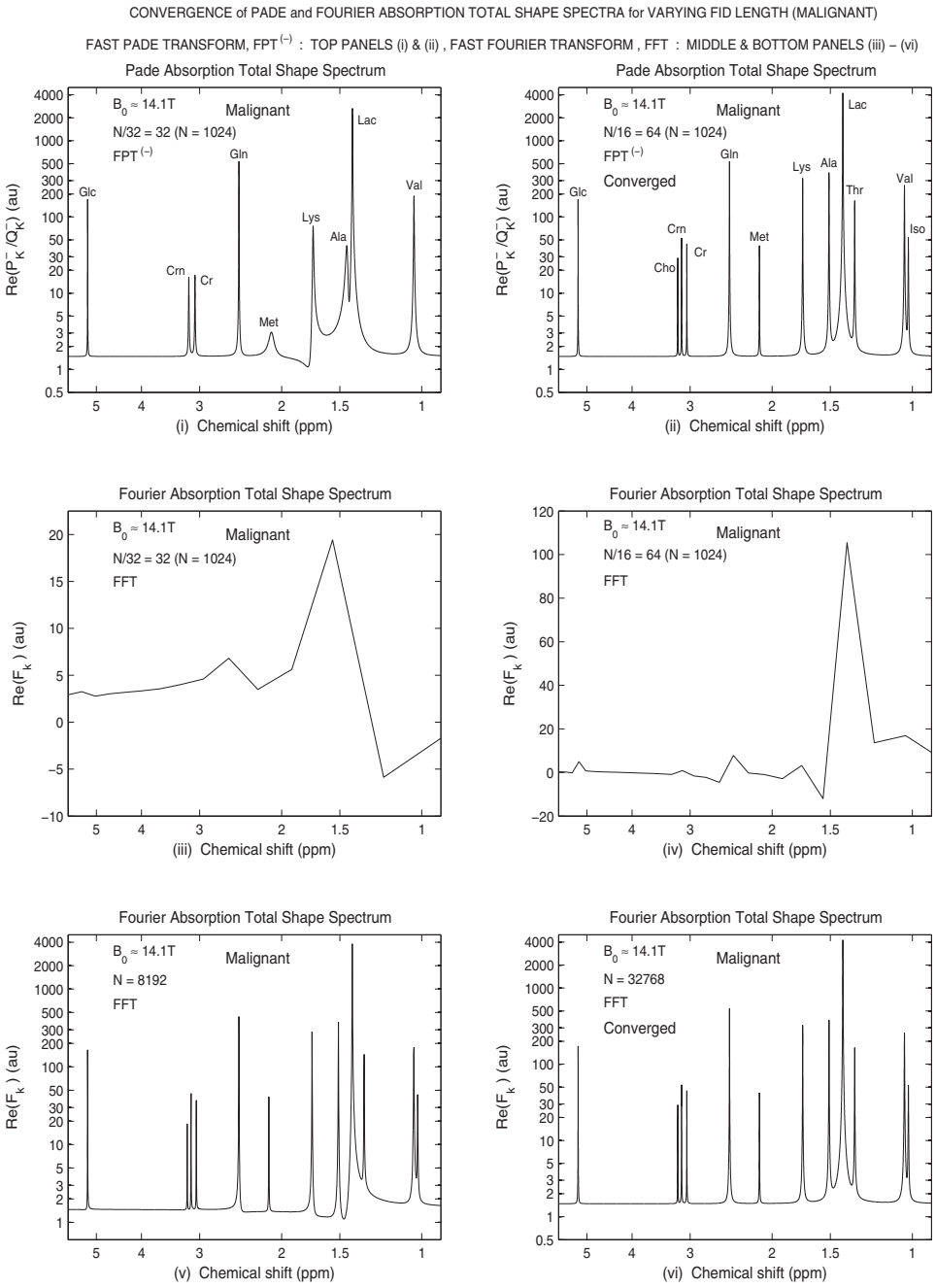

Figure 6.4 Absorption total shape spectra for the cancerous ovarian cyst fluid from input data derived from Ref. [23]. Top panels are the spectra generated by the FPT at (i) [$N/32 = 32$] and (ii) [$N/16 = 64$]. Middle panels are the FFT-generated spectra at (iii) [$N/32 = 32$] and (iv) [$N/16 = 64$]. Bottom panels are the FFT-generated spectra at (v) [$N = 8192$] and (vi) [$N = 32768$].

4.2.3. Comparisons of MRS data for benign and malignant ovarian cyst fluid

In Table 6.4, we summarize the convergence performance of the FPT at three partial signal lengths: $N/32 = 32, N/16 = 64$, and $N/8 = 128$ for the MRS data derived from benign (left panel) and malignant (right panel) ovarian cyst fluid. Since the spectral parameters for all 12 metabolites are exact to 6 decimal places at $N/16 = 64$, the computed concentrations for the benign and malignant cases are completely correct. Convergence is seen to be stable at $N/8 = 128$.

Absorption total shape spectra generated by the FFT at three much longer signal lengths: $N = 8\text{K} = 8192$ (top panels), $N = 16\text{K} = 16384$ (middle panels), and $N = 32\text{K} = 32768$ (bottom panels) are shown in Figure 6.5. The left panel corresponds to the benign ovarian case and the right panel to the cancerous ovarian case. To recapitulate, at $N = 8\text{K} = 8192$ although the 12 resonances are resolved, their peak heights are not correct in either of the two cases. Even at $N = 16\text{K} = 16384$, the heights of the resonances are not yet correct.

To attain the correct heights, $N = 32\text{K} = 32768$ signal points are needed for both the benign and malignant ovarian cases. In other words, 32768 signal points are needed for convergence of the absorption total shape generated by the FFT. Figure 6.5 underscores the need to ascertain the point of convergence. Prior to that point, incorrect peak heights together with baseline distortions would greatly undermine any attempts to compute metabolite concentrations.

Figure 6.6 summarizes the convergence patterns of the Padé-reconstructed absorption total shape spectra via the FPT for the benign (left panels) and malignant (right panels) ovarian cyst fluid. The signal lengths are $N/32 = 32$ (top panels), $N/16 = 64$ (middle panels), and $N/8 = 128$ (bottom panels). Convergence is achieved for both cases at $N/16 = 64$.

In Figure 6.7, we compare the signal length at which convergence is achieved by the FPT and the total shape spectrum generated via the FFT at the same signal length. The FPT yielded completely converged absorption total shape spectra with only $N/16 = 64$ signal points, for the benign ovarian case (upper right panel (iii)) and ovarian cancer (lower right panel (iv)). The FFT provided spectra completely devoid of meaningful information at that signal length (upper left panel (i), benign case; lower left panel (ii), malignant case).

In Figure 6.8, we show the convergence patterns for the metabolite concentrations for benign and cancerous ovarian data as computed via the FPT. Along the abscissae are the chemical shifts for panels (i)–(vi); the ordinates correspond to the concentrations. The symbol x denotes the input data, and the data reconstructed by the FPT are represented by open circles. The left ((i)–(iii)) and right panels ((iv)–(vi)), respectively, correspond to the benign and malignant cases. At $N/32 = 32$ (upper panels (i) and (iv)), completely correct concentrations were obtained only for glucose at 5.22 ppm (1387

Table 6.4 Spectral parameters reconstructed by the FPT from synthesized MR time signals according to data as encoded in vitro from benign and malignant ovarian cyst fluid [23]. The reconstructed data converged at $N/16 = 64$ ($N = 1024$) as seen on the middle panels (ii) and (v), respectively, for benign and malignant ovarian data.

Convergence of Spectral Parameters and Concentrations in FPT$^{(-)}$; Signal Length : $N/M, N = 1024, M = 8 - 32$											
n_k^o (# k)	Re(ν_k^-) (ppm)	Im(ν_k^-) (ppm)	$\lvert d_k^- \rvert$ (au)	C_k^- (μM/L ww)	M_k	n_k^o (# k)	Re(ν_k^-) (ppm)	Im(ν_k^-) (ppm)	$\lvert d_k^- \rvert$ (au)	C_k^- (μM/L ww)	M_k
(i) $N/32 = 32$ (Benign)						(iv) $N/32 = 32$ (Malignant)					
2	1.040033	0.001124	0.038143	124	Val	2	1.039257	0.001406	0.148343	484	Val
4	1.409673	0.001117	0.796643	2603	Lac	4	1.409062	0.001372	2.046372	6688	Lac
5	1.482370	0.005257	0.081645	266	Ala	5	1.446902	0.008300	0.196825	643	Ala
6	1.706966	0.009141	0.035360	115	Lys	6	1.712040	0.004160	0.174575	570	Lys
7	2.207406	0.216536	0.005435	17	Met	7	2.101571	0.031100	0.028695	93	Met
8	2.470151	0.000826	0.082607	270	Gln	8	2.470096	0.000838	0.251929	823	Gln
9	3.058390	0.001607	0.020043	65	Cr	9	3.069839	0.003200	0.028376	92	Cr
10	3.141312	0.002566	0.024686	80	Crn	10	3.165277	0.003440	0.028617	93	Crn
12	5.220345	0.000829	0.424418	1387	Glc	12	5.220345	0.000839	0.079557	260	Glc
(ii) $N/16 = 64$ (Benign)						(v) $N/16 = 64$ (Malignant)					
1	1.020219	0.000818	0.003060	10	Iso	1	1.020219	0.000828	0.024174	79	Iso
2	1.040048	0.000821	0.034578	113	Val	2	1.040048	0.000831	0.120869	395	Val
3	1.330124	0.000822	0.027540	90	Thr	3	1.330124	0.000832	0.075887	248	Thr
4	1.410235	0.000828	0.758570	2479	Lac	4	1.410235	0.000838	2.000000	6536	Lac
5	1.510318	0.000824	0.089657	293	Ala	5	1.510318	0.000834	0.179315	586	Ala
6	1.720125	0.000823	0.030906	101	Lys	6	1.720125	0.000833	0.149939	490	Lys
7	2.130246	0.000819	0.002142	7	Met	7	2.130246	0.000829	0.018972	62	Met

8	2.470118	0.000825	0.084149	275	Gln	8	2.470118	0.000835	0.253366	828	Gln
9	3.050039	0.000822	0.019278	63	Cr	9	3.050039	0.000832	0.020196	66	Cr
10	3.130227	0.000821	0.020808	68	Crn	10	3.130227	0.000831	0.024174	79	Crn
11	3.190136	0.000820	0.004590	15	Cho	11	3.190136	0.000830	0.012852	42	Cho
12	5.220345	0.000829	0.424419	1387	Glc	12	5.220345	0.000839	0.079559	260	Glc
(iii) $N/8 = 128$ (Benign)						(vi) $N/8 = 128$ (Malignant)					
1	1.020219	0.000818	0.003060	10	Iso	1	1.020219	0.000828	0.024174	79	Iso
2	1.040048	0.000821	0.034578	113	Val	2	1.040048	0.000831	0.120869	395	Val
3	1.330124	0.000822	0.027540	90	Thr	3	1.330124	0.000832	0.075887	248	Thr
4	1.410235	0.000828	0.758570	2479	Lac	4	1.410235	0.000838	2.000000	6536	Lac
5	1.510318	0.000824	0.089657	293	Ala	5	1.510318	0.000834	0.179315	586	Ala
6	1.720125	0.000823	0.030906	101	Lys	6	1.720125	0.000833	0.149939	490	Lys
7	2.130246	0.000819	0.002142	7	Met	7	2.130246	0.000829	0.018972	62	Met
8	2.470118	0.000825	0.084149	275	Gln	8	2.470118	0.000835	0.253366	828	Gln
9	3.050039	0.000822	0.019278	63	Cr	9	3.050039	0.000832	0.020196	66	Cr
10	3.130227	0.000821	0.020808	68	Crn	10	3.130227	0.000831	0.024174	79	Crn
11	3.190136	0.000820	0.004590	15	Cho	11	3.190136	0.000830	0.012852	42	Cho
12	5.220345	0.000829	0.424419	1387	Glc	12	5.220345	0.000839	0.079559	260	Glc

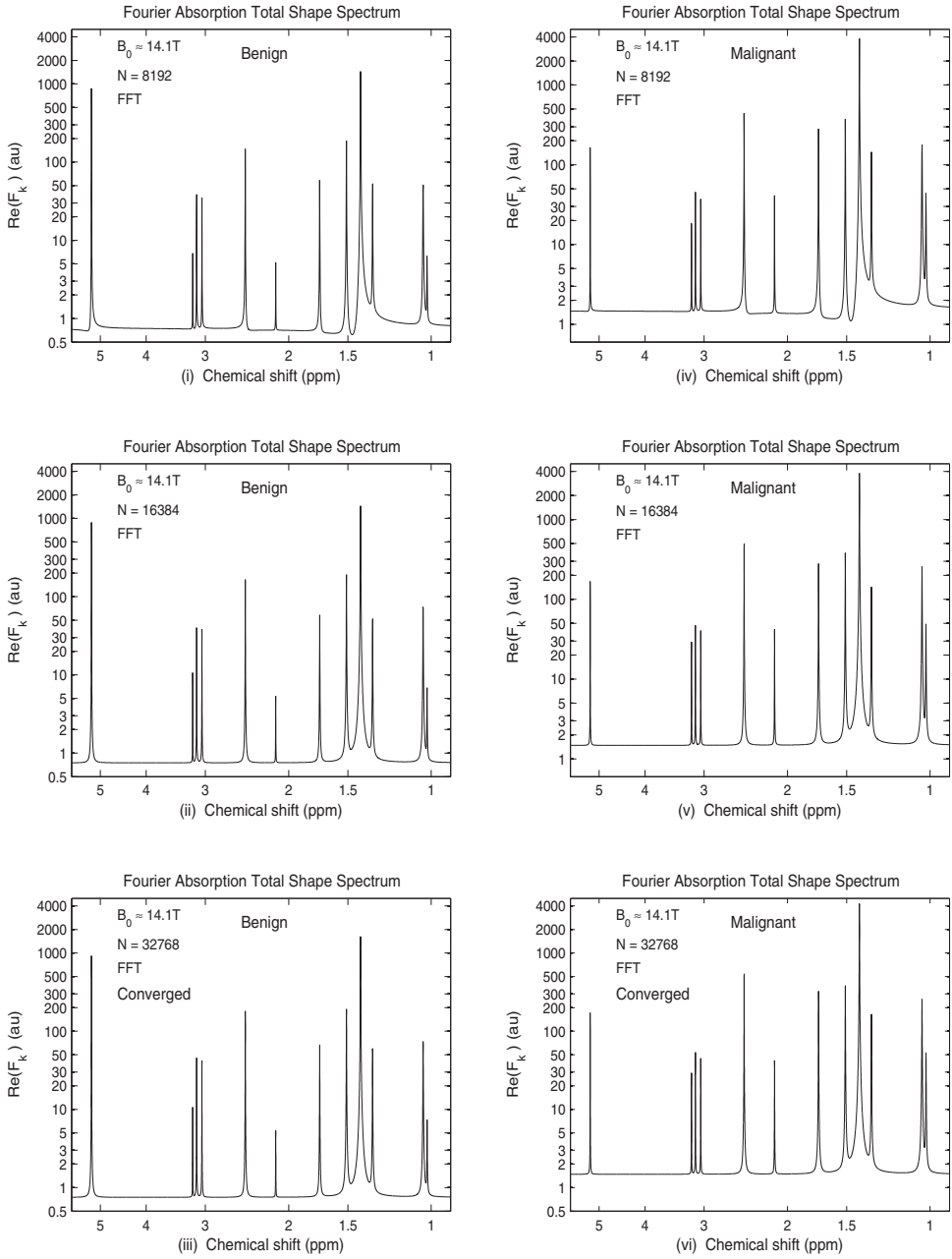

Figure 6.5 Absorption total shape spectra generated by the FFT for the benign and malignant ovarian cyst fluid using input data derived from Ref. [23]. The signal lengths are $N = 8192$ (upper panels), $N = 16384$ (middle panels) and $N = 32768$ (lower panels, where the spectra converge). The benign and malignant cases are shown respectively on the left and right columns.

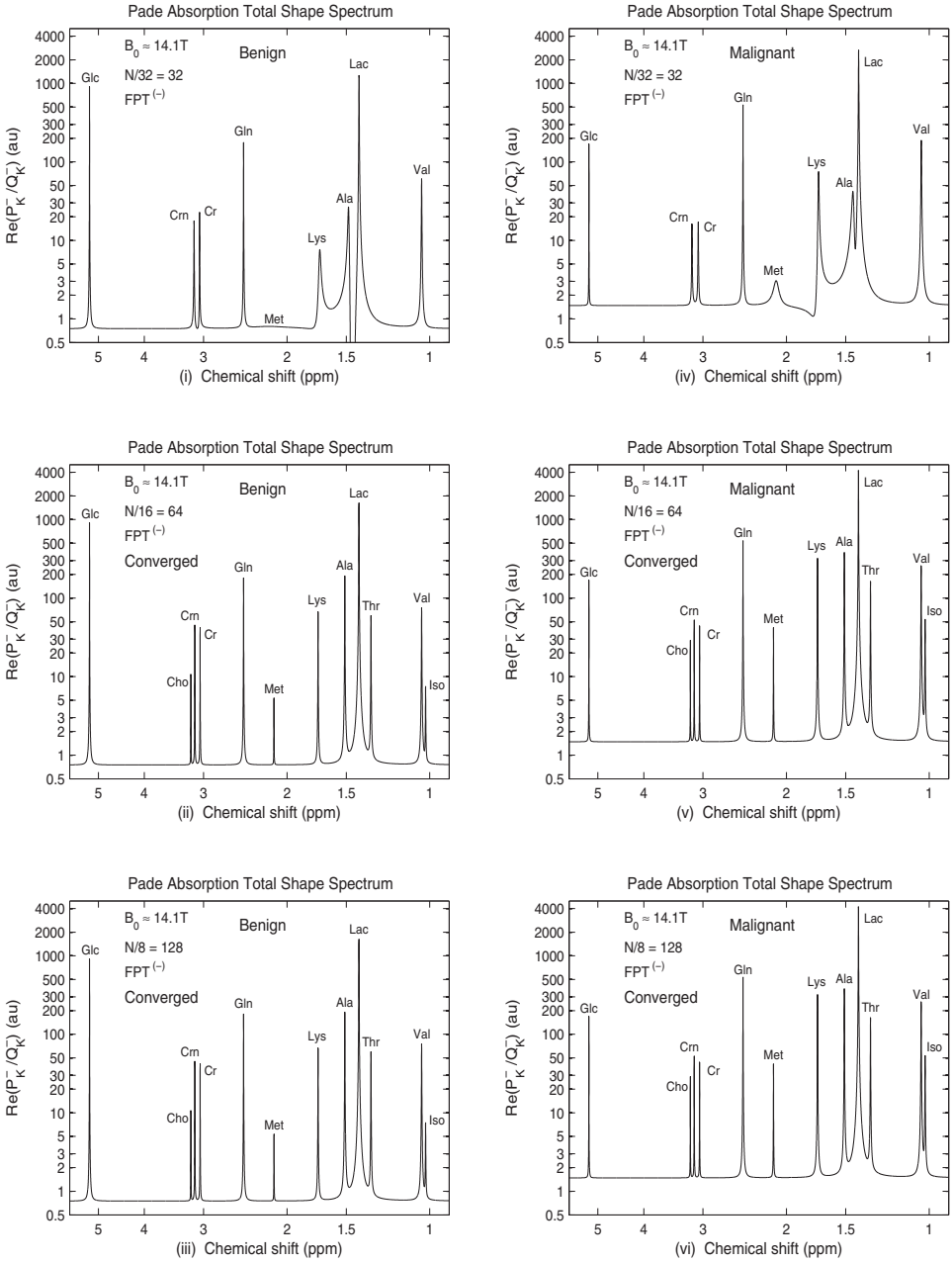

Figure 6.6 Absorption total shape spectra generated by the FPT for the benign and malignant ovarian cyst data derived from Ref. [23]. The signal lengths are $N/32 = 32$ (top panels (i), (iv)), $N/16 = 64$ (middle panels (ii), (v)), and $N/8 = 128$ (bottom panels (iii), (vi)), where N is the full signal length ($N = 1024$). The left panels correspond to benign ovarian data and the right panels to malignant ovary.

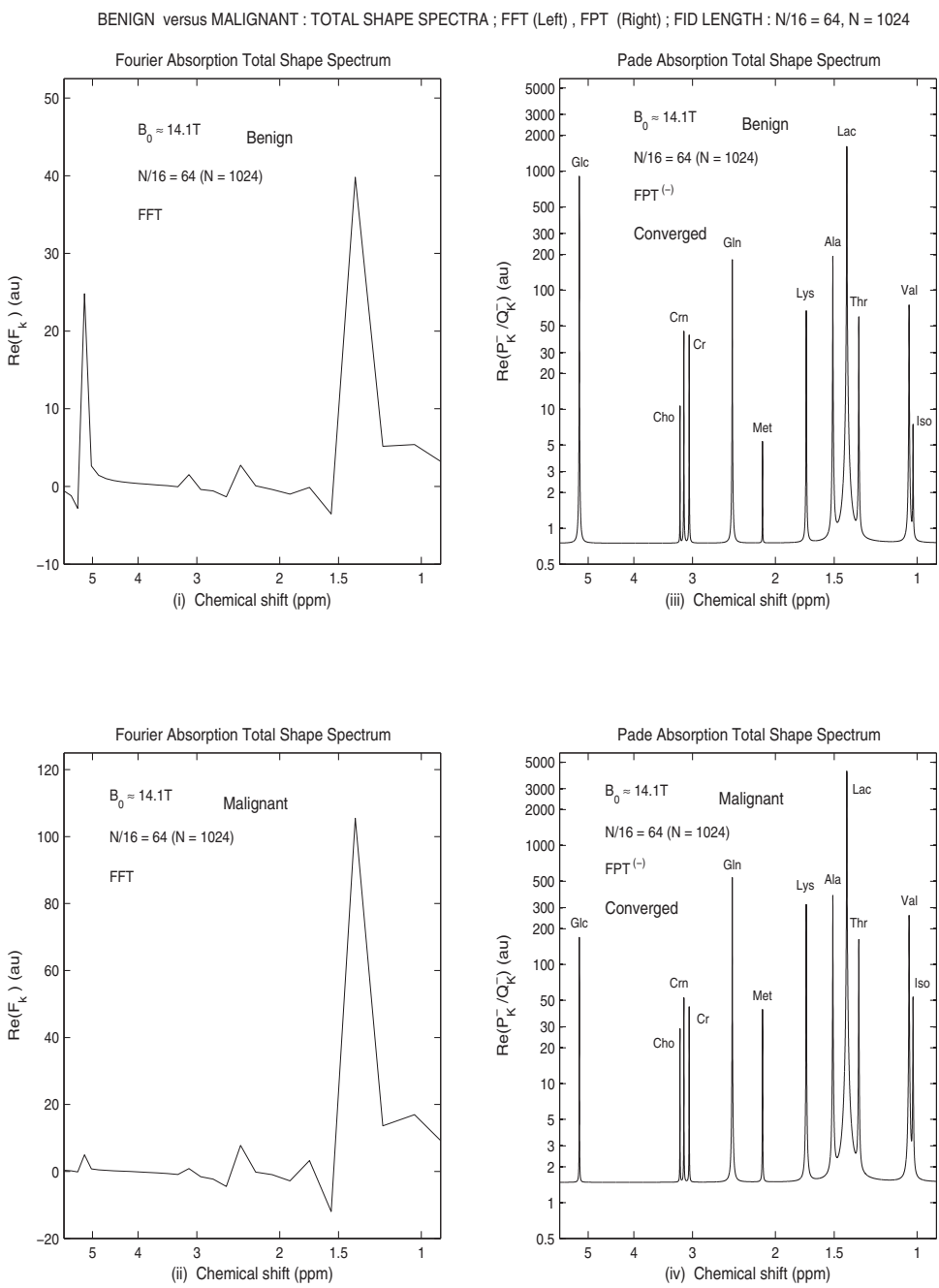

Figure 6.7 Absorption spectra for cases derived from benign and malignant ovarian cyst in vitro encoded MRS data from Ref. [23]. Upper panels show the performance of the FFT (left (i)) and FPT (right (iii)) at $N/16 = 64$, where $N = 1024$ for the benign ovary. The FPT is fully converged, whereas the FFT-generated spectra are not interpretable. For ovarian cancer (lower panels, FFT (left (ii), FPT (right (iv)), a similar pattern is seen.

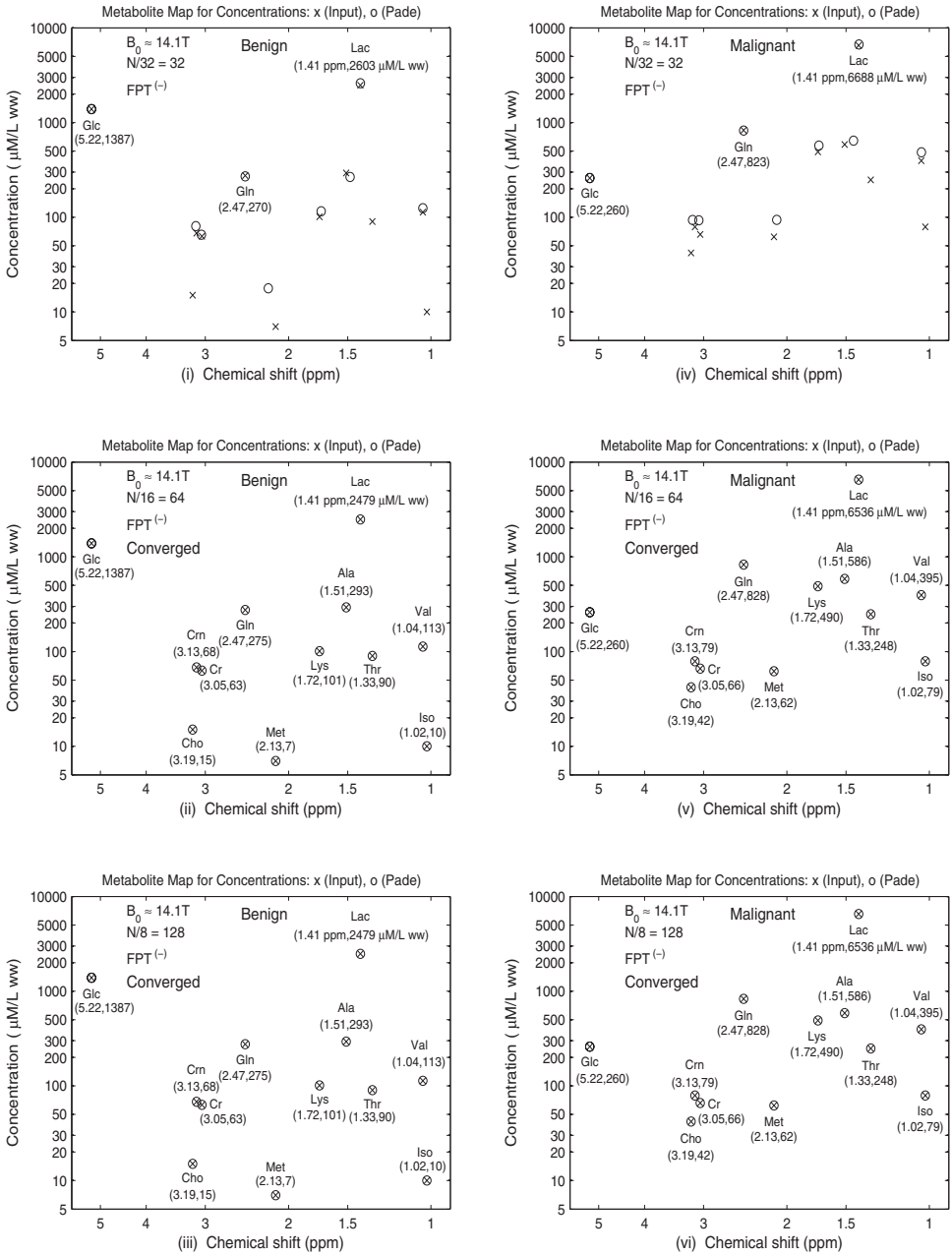

Figure 6.8 Convergence of the metabolite concentrations as reconstructed by the FPT for benign (left column) and malignant (right column) ovarian cyst data from Ref. [23]. Convergence has not occurred at $N/32 = 32$ (upper panels (i) and (iv)). The Padé-reconstructed concentrations at $N/16 = 64$, are converged for all 12 metabolites (middle panels (ii) and (v)). Stable convergence is shown at $N/8 = 128$ on the lower panels (iii) and (vi) and was verified explicitly at $N/4 = 256, N/2 = 512$, and $N = 1024$.

μM/L ww (benign) and 260 μM/L ww (malignant), respectively). At $N/16 = 64$ (middle panels (ii) and (v)) and $N/8 = 128$ (lower panels (iii) and (vi)), all of the reconstructed metabolite concentrations are completely correct. This is shown numerically, as well as via the graphic representations. Consequently, the x's are precisely centered within the open circles for $N/16$ and $N/8$, that is, there was complete agreement between the input and reconstructed data.

In Figure 6.9, we present the absorption spectra together with the metabolite concentrations at $N/16 = 64$ when full convergence is achieved via Padé reconstruction. Therein, we have a graphic illustration that the FPT can generate a shape estimation and provide exact quantification. This is achieved without postprocessing, and no other estimator is needed. Figure 6.9 is particularly helpful for clinicians who can thereby better understand how Padé reconstruction actually works. Figure 6.9 thus brings together key concepts of signal processing: line-shape estimation and quantification. Of vital importance in the clinical setting, all the reconstructed concentrations for the benign and malignant cases can be readily appreciated.

4.2.4. Discussion

Applied to these MRS data of the ovary, the resolution performance of the fast Padé transform is striking, particularly in comparison with the FFT. Padé reconstruction of MR data from benign and cancerous ovarian cyst fluid illustrates the powerful extrapolation and interpolation features of the FPT. Using a mere 64 data points, the absorption spectra generated by the FPT are fully converged. Even the closely lying resonances such as alanine, lactate, and threonine in the region between 1.3 and 1.51 ppm, and the nearly overlapping isoleucine and valine, which are separated by only 0.02 ppm, are reliably generated. Fourier processing could not provide any meaningful spectral information whatsoever at these short signal lengths. We have noted earlier that the envelopes of MR time signals decay exponentially, and thus the signal intensity is the highest early in the encoding. Consequently, it is desirable to encode the FIDs very rapidly in order to avoid long T when predominantly noise will be measured, particularly with clinical scanners of lower magnetic field strengths.

In this clinical framework, it is relevant to recall that the FPT yields not only the shape spectra but also the essential parametric analysis, namely the quantification from which the metabolite concentrations are computed. In the present cases based on ovarian cyst fluid, with only 64 data points of 1024 sampled data, the FPT exactly reconstructed all the spectral parameters to 6 decimal place accuracy for each of the 12 metabolites. The spectral parameters were then utilized to compute metabolite concentrations in a straightforward manner. This stands in sharp contrast to the conventional Fourier approach, whereby metabolite concentrations are estimated from the total shape spectra by either fitting the peaks to a subjectively chosen number of Lorentzians and/or Gaussians or integrating peak areas. Even for distinct

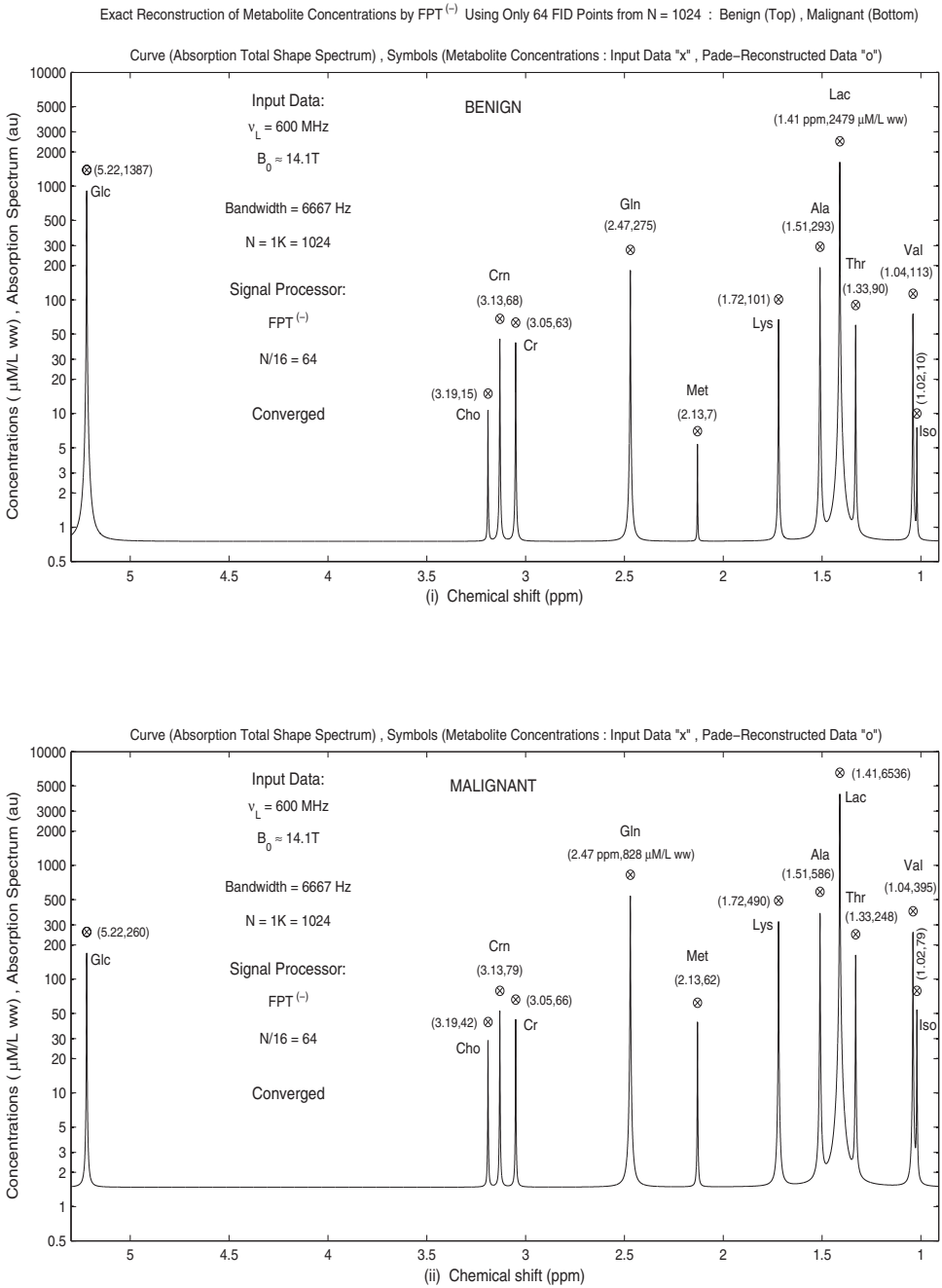

Figure 6.9 Converged total absorption spectra ($N/16 = 64$) achieved by Padé reconstruction. The time signals corresponding to benign (upper panel (i)) and cancerous (lower panel (ii)) ovarian cyst fluid were derived from data encoded in Ref. [23]. The reconstructed chemical shifts and concentrations of the 12 metabolites are shown above the corresponding peak.

peaks, the numerical quadrature procedure is subjective, since there is uncertainty concerning lower and upper integration limits. When the peaks overlap, "spectral crowding" is recognized to create major quantification problems. "Spectral crowding" is not an issue for the FPT. Via parametric analysis, the FPT generates reliable information used to compute metabolite concentrations irrespective of whether or not the peaks are overlapping [1, 2].

By applying in vitro MRS with high magnetic field strengths and sophisticated laboratory processing techniques, several MR-visible compounds have been identified that help distinguish benign and cancerous ovarian lesions [23, 25]. In particular, the concentrations of closely lying peaks: threonine (1.33 ppm), lactate (1.41 ppm), and alanine (1.51 ppm) and the almost overlapping peaks: isoleucine and valine between 1.02 to 1.04 ppm show significant differences in noncancerous and malignant ovarian cyst fluid [23]. In the latter, higher concentrations of the branched-chain amino acids are interpreted as being protein breakdown products from necrosis and proteolysis. Notwithstanding these important findings, no metabolite alone or in combination with others could be found that completely differentiated noncancerous from malignant ovarian lesions. Although the differences in concentrations were highly statistically significant in Ref. [23], the concentration ranges were not entirely distinct. Further studies are ongoing in which the FPT is being applied to larger scale in vitro MRS data from nonmalignant and cancerous ovarian lesions. Padé reconstructions from MRS data could provide the needed standards with regard to metabolite concentrations that characterize normal ovary, as well as benign and malignant ovarian lesions.

Massuger and colleagues [25] consider that in vivo MRS could become the method of choice for early-stage ovarian cancer detection, if the obstacles hindering the acquisition of high-quality time signals and subsequent reliable analysis of spectra can be surmounted. The results presented in this chapter suggest that Padé-optimized MRS could contribute to this aim.

Effective strategies for accurately detecting ovarian cancer in its early stages are urgently needed. Given that MR-based modalities do not entail exposure to ionizing radiation, insofar as their diagnostic accuracies were improved, magnetic resonance imaging and spectroscopy could have more widespread application in screening surveillance for early ovarian cancer detection. Padé-optimized MRS could help achieve that goal.

5. MRS DATA FOR NORMAL, FIBROADENOMA, AND MALIGNANT BREAST TISSUES

5.1. Clinical background

Magnetic resonance-based modalities provide a sensitive means of detecting breast cancer without exposing the breast, a radio-sensitive tissue, to ionizing

radiation. However, contrast-enhanced MRI has poor specificity, resulting in high biopsy rates with fewer than 50% of these actually being malignant [26]. Fibroadenomas and other benign lesions may be difficult to distinguish from breast cancer on MRI [27]. These issues are of particular concern for women at high risk of breast cancer. Our recent review [28] reveals a clear benefit of MRI for women with increased breast cancer risk. However, the large number of false positive findings generated by MRI can have a negative impact on the quality of life. Since it reflects the metabolic characteristics of tissue, MRS can improve the specificity of MRI with regard to breast cancer detection [5, 29, 30]. Data have been published for over 100 malignant and 100 benign breast lesions examined using in vivo MRS, as reviewed recently in Ref. [5]. These studies were primarily based on total choline levels. However, relying on the composite choline peak can undermine diagnostic accuracy, since choline may also be observed in fibroadenomas and other benign breast lesions. On the other hand, small malignant breast lesions have been misclassified as benign when the composite choline peak was undetected [29].

We have pointed out that signal processing in MRS has mainly been based on the conventional fast Fourier transform for converting the encoded time signal into its spectral representation in the frequency domain. The FFT has a number of major drawbacks pertinent to breast cancer diagnostics via MRS. These problems include poor resolution and SNR. Furthermore, with Fourier processing, MRS of the breast has mainly been relied on estimates of total choline [5, 9, 10]. Compared with in vivo MRS, in vitro NMR yields richer information about the metabolic activity of malignant breast tissue. In our multivariate analyses [9] of such in vitro NMR data from extracted breast specimens [31], we found that spectroscopic information from closely overlapping resonances was particularly helpful for identifying breast cancer. It was concluded that there is a need to apply improved signal processing methods to quantify MR-visible characteristics of benign and malignant breast lesions [9].

As reviewed, the fast Padé transform is particularly well suited for MRS [1–15]. We have recently examined the performance of the FPT applied to noiseless time signals that were generated according to in vitro MRS data as encoded from extracted breast specimens [5, 10]. Therein, we found that the FPT resolved and precisely quantified the physical resonances as encountered in benign versus malignant breast. The FPT unambiguously delineated and quantified diagnostically important metabolites such as lactate and phosphocholine (PCho), which very closely overlaps with glycerophosphocholine (GPC) and phosphoethanolamine (PE), and it may represent an MR-visible molecular marker of breast cancer.

In this section, we will focus on the performance of the FPT as applied to MR time signals generated according to in vitro MRS data as encoded from extracted breast cancer, fibroadenoma, and normal breast specimens. In this

fully controlled setting, we thereby compare the resolution performance of the FPT for this clinical problem, as a key preparatory step for application to MR time signals encoded in vivo and in vitro from breast cancer and benign breast lesions.

5.2. Signal processing

Herein, we apply the FPT to time signals that are similar to in vitro MRS data as encoded from extracted breast specimens [31]. Three FIDs of the type given by Eq. (5) with 9 damped complex exponentials are synthesized. Quantification of the time signals via the FPT is as per Ref. [2].

Based on median concentrations $\{\mathrm{C}_k\}_{k=1}^{9}$ (expressed in μM/g ww) of 9 metabolites as encoded in vitro in Ref. [31] from 12 patients, we derived the input data for the d_k's for normal breast tissue. The concentrations of the nine metabolites from a single fibroadenoma as encoded in Ref. [31] were used to derive the input d_k's for benign breast tissue. The input d_k's for breast cancer were based on median concentrations from a total of 14 samples taken from 12 patients as encoded in Ref. [31] (for two patients, two samples each had been taken). Not all the concentrations of metabolites were computed for all the samples, however. For β-glucose and myoinositol, respectively, metabolite concentrations were computed in only six and nine breast cancer samples.

In Ref. [31], the FIDs were recorded with a static magnetic field strength $B_0 \approx 14.1$T (Larmor frequency of 600 MHz). We used a bandwidth of 6 kHz (the inverse of this bandwidth is the sampling time τ) and set the total signal length $N = 2048$. The resonances were grouped into two bands, one from 1.3 to 1.5 ppm and the other from 3.2 to 3.3 ppm. In the latter band, there were seven resonances, including two that were almost degenerate at 3.22 ppm: phosphocholine ($k = 4$) and phosphoethanolamine ($k = 5$) separated by a mere 2.03×10^{-4} ppm.

We used the formula $|d_k| = 2\mathrm{C}_k/\mathrm{C}_{\mathrm{ref}}$ where $\mathrm{C}_{\mathrm{ref}} = 0.05\,\mu$M/g ww to compute the input peak amplitudes $\{|d_k|\}$ from the reported concentrations $\{\mathrm{C}_k\}$. The internal reference was TSP (3-trimethylsilyl-3,3,2,2-tetradeuteropropionic acid), as per Ref. [31]. Accordingly, $|d_k| = \mathrm{C}_k/(25\mu\mathrm{M/g\ ww})$.

In Ref. [31], the T_2 relaxation times were not reported. We designated the full widths at half maximum to be approximately 1 Hz with small variations. The line widths are proportional to $\mathrm{Im}(\nu_k)$. We also deemed the peaks to be Lorentzians. The smallest chemical shift difference was $\approx 2 \times 10^{-4}$ ppm. This is some four times less than the usual line width of 8×10^{-4} ppm. Since the phases ϕ_k ($1 \leq k \leq 9$) from d_k were all set to zero, each amplitude d_k was real, $d_k = |d_k|$.

The input data for the normal breast tissue (upper panel (i)), fibroadenoma (middle panel (ii)), and breast cancer (bottom panel (iii)) are presented in Table 6.5. In the FPT$^{(-)}$, we computed the kth metabolite concentration

Table 6.5 Input data and computed metabolite concentrations corresponding to: normal breast tissue (upper panel (i)), benign pathology (fibroadenoma; middle panel (ii)) and malignant breast tissue (lower panel (iii)) derived from in vitro data of Ref. [31]. Acronyms: ppm indicate parts per million, au arbitrary units, ww wet weight, M_k indicates metabolite assignment, C_k indicates concentration of M_k, Abbreviations: Lac for lactate, Ala alanine, Cho choline, PCho phosphocholine, PE phosphoethanolamine, GPC glycerophosphocholine, β-Glc beta-glucose, Tau taurine, m-Ins myoinositol.

Input Data: Spectral Parameters, Concentrations and Metabolite Assignments					
n_k^o (Metabolite # k)	Re(ν_k) (ppm)	Im(ν_k) (ppm)	$\lvert d_k \rvert$ (au)	C_k (μM/g ww)	M_k (Assignment)
(i) Normal					
1	1.330413	0.000834	0.02016	0.5040	Lac
2	1.470313	0.000832	0.00350	0.0875	Ala
3	3.210124	0.000831	0.00068	0.0170	Cho
4	3.220012	0.000833	0.00076	0.0190	PCho
5	3.220215	0.000834	0.00516	0.1290	PE
6	3.230412	0.000832	0.00128	0.0320	GPC
7	3.250224	0.000833	0.01800	0.4500	β-Glc
8	3.270141	0.000831	0.00530	0.1325	Tau
9	3.280132	0.000832	0.01144	0.2860	m-Ins
(ii) Fibroadenoma					
1	1.330413	0.000832	0.05928	1.4820	Lac
2	1.470313	0.000834	0.00440	0.1100	Ala
3	3.210124	0.000833	0.00088	0.0220	Cho
4	3.220012	0.000832	0.00432	0.1080	PCho
5	3.220215	0.000831	0.01476	0.3690	PE
6	3.230412	0.000833	0.00276	0.0690	GPC
7	3.250224	0.000832	0.03912	0.9780	β-Glc
8	3.270141	0.000834	0.01352	0.3380	Tau
9	3.280132	0.000831	0.01860	0.4650	m-Ins
(iii) Malignant					
1	1.330413	0.000831	0.32474	8.1185	Lac
2	1.470313	0.000832	0.03156	0.7890	Ala
3	3.210124	0.000834	0.00446	0.1115	Cho
4	3.220012	0.000831	0.02448	0.6120	PCho
5	3.220215	0.000832	0.07776	1.9440	PE
6	3.230412	0.000833	0.00936	0.2340	GPC
7	3.250224	0.000832	0.02882	0.7205	β-Glc
8	3.270141	0.000831	0.11182	2.7955	Tau
9	3.280132	0.000833	0.03564	0.8910	m-Ins

C_k^- from the absolute value $|d_k^-|$ of the reconstructed amplitude d_k^- as $C_k^- = 25|d_k^-|C_{\text{ref}}\ \mu$M/g ww.

The signal length was systematically augmented for the same bandwidth (i.e., three acquisition times) to show that the spectral parameters were constant for all three signals. We examined the spectral parameters at total orders $K = 500, 750$, and 1000, where $2K = N_P$ and N_P denotes partial signal length. For all three time signals, convergence took place at $K = 750$ and continued to be stable subsequently.

Reconstructed resonances were assessed as to whether they were genuine via the concept of Froissart doublets. This was done throughout the entire Nyquist range, with special attention to the range between 1.3 and 3.3 ppm, that is, the range of interest. Of a total of 750 resonances, 741 were found to be spurious, that is, with zero amplitudes and the pole–zero coincidences. For each of the three time signals, there were nine true resonances.

5.2.1. Normal breast tissue

The Padé-reconstructed data corresponding to normal breast tissue is presented in Table 6.6 at three partial signal lengths that are $N_P = 1000, 1500$, and 2000. On the top panel (i) at $N_P = 1000$, one of the nine peaks is missing. Only one peak was identified at 3.220189 ppm, although there should be two: PCho ($k = 4$) at 3.220012 ppm and PE ($k = 5$) at 3.220215 ppm. The reconstructed amplitudes and the concentrations for the single resonances were approximately the sum of (PCho + PE) at $N_P = 1000$. The spectral parameters were reconstructed exactly at that signal length for five of the metabolites: lactate (Lac, $k = 1$) at 1.330413 ppm, alanine (Ala, $k = 2$) at 1.470313 ppm, β-glucose (β-Glc, $k = 7$) at 3.250224 ppm, taurine ($k = 8$) at 3.270141 ppm, and myoinositol (m-Ins, $k = 9$) at 3.280132 ppm.

At $N_P = 1500$, all the reconstructed parameters for all nine resonances completely converged, as seen in the middle panel (ii) of Table 6.6. On the bottom panel (iii) in Table 6.6, it is seen that convergence remained stable at $N_P = 2000$. We have verified that this stability continued at higher N_P and at the full signal length N.

We present the absorption component shape spectra and the total shape spectra as reconstructed by the FPT for the normal breast data in Figure 6.10 at three partial signal lengths $N_P = 1000, 1500$, and 2000. The top right panel (iv) indicates that at $N_P = 1000$, the absorption total shape spectrum has converged. In contrast, for the component shape spectrum (top left panel (i)), there is only one peak (phosphoethanolamine, $k = 5$) at 3.22 ppm that has been overestimated, whereas phosphocholine, ($k = 4$) has not been detected.

On the middle left panel (ii) of Figure 6.10 at $N_P = 1500$, the component shape spectrum has converged with resolution of both peaks $k = 4$ and 5. The correct heights are now displayed for these and all the other peaks. Note that the phosphocholine peak is very small and completely underneath the phosphoethanolamine peak. The bottom panels of Figure 6.10 display the

Table 6.6 Padé-reconstructed spectral parameters and metabolite concentrations corresponding to normal breast tissue from the input data derived from Ref. [31].

Convergence of Spectral Parameters and Concentrations in FPT$^{(-)}$: Partial Signal Lengths $N_P = 1000, 1500, 2000$					
n_k^o (Metabolite # k)	Re(ν_k^-) (ppm)	Im(ν_k^-) (ppm)	$\lvert d_k^- \rvert$ (au)	C_k^- (μM/g ww)	M_k (Assignment)
(i) Pade-Reconstructed Data (Normal): $N_P = 1000$ (# 4 PCho: Unresolved, # 5 PE: Overestimated)					
1	1.330413	0.000834	0.02016	0.5040	Lac
2	1.470313	0.000832	0.00350	0.0875	Ala
3	3.210123	0.000830	0.00068	0.0170	Cho
5	3.220189	0.000836	0.00592	0.1480	PE
6	3.230412	0.000831	0.00128	0.0320	GPC
7	3.250224	0.000833	0.01800	0.4500	β-Glc
8	3.270141	0.000831	0.00530	0.1325	Tau
9	3.280132	0.000832	0.01144	0.2860	m-Ins
(ii) Pade-Reconstructed Data (Normal): $N_P = 1500$ (Converged)					
1	1.330413	0.000834	0.02016	0.5040	Lac
2	1.470313	0.000832	0.00350	0.0875	Ala
3	3.210124	0.000831	0.00068	0.0170	Cho
4	3.220012	0.000833	0.00076	0.0190	PCho
5	3.220215	0.000834	0.00516	0.1290	PE
6	3.230412	0.000832	0.00128	0.0320	GPC
7	3.250224	0.000833	0.01800	0.4500	β-Glc
8	3.270141	0.000831	0.00530	0.1325	Tau
9	3.280132	0.000832	0.01144	0.2860	m-Ins
(iii) Pade-Reconstructed Data (Normal): $N_P = 2000$ (Converged)					
1	1.330413	0.000834	0.02016	0.5040	Lac
2	1.470313	0.000832	0.00350	0.0875	Ala
3	3.210124	0.000831	0.00068	0.0170	Cho
4	3.220012	0.000833	0.00076	0.0190	PCho
5	3.220215	0.000834	0.00516	0.1290	PE
6	3.230412	0.000832	0.00128	0.0320	GPC
7	3.250224	0.000833	0.01800	0.4500	β-Glc
8	3.270141	0.000831	0.00530	0.1325	Tau
9	3.280132	0.000832	0.01144	0.2860	m-Ins

absorption component shape spectrum (iii) and the total shape spectrum (vi) at $N_P = 2000$. Therein, stable convergence is seen.

The convergence of the metabolite concentrations for the normal breast data at partial signal lengths: $N_P = 1000, 1500$, and 2000 is shown in Figure 6.11. The symbol "x" represents the input data, and open circles

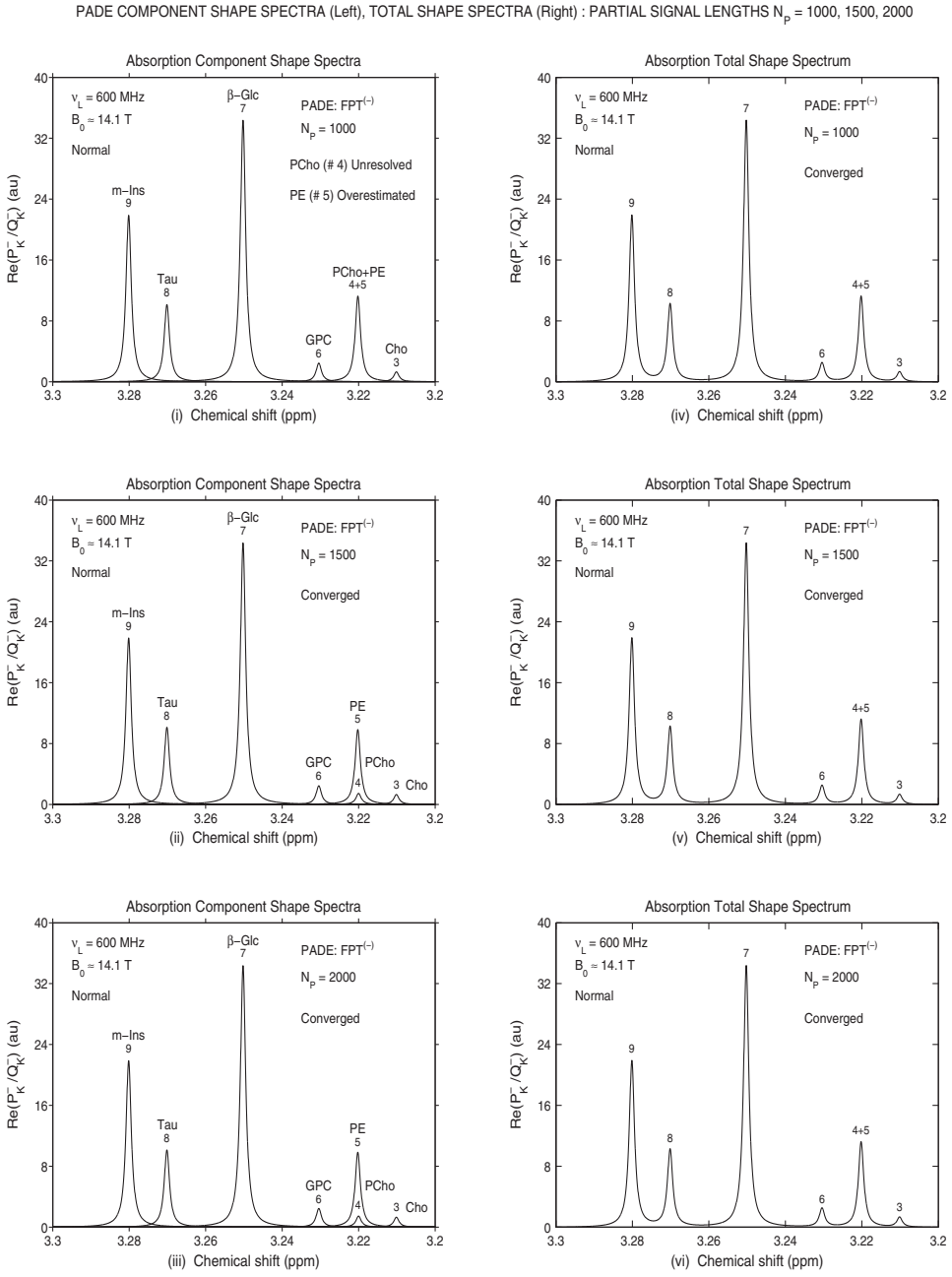

Figure 6.10 Absorption component spectra (left panels) and total shape spectra (right panels) reconstructed by the FPT for normal breast as per in vitro MRS data from Ref. [31].

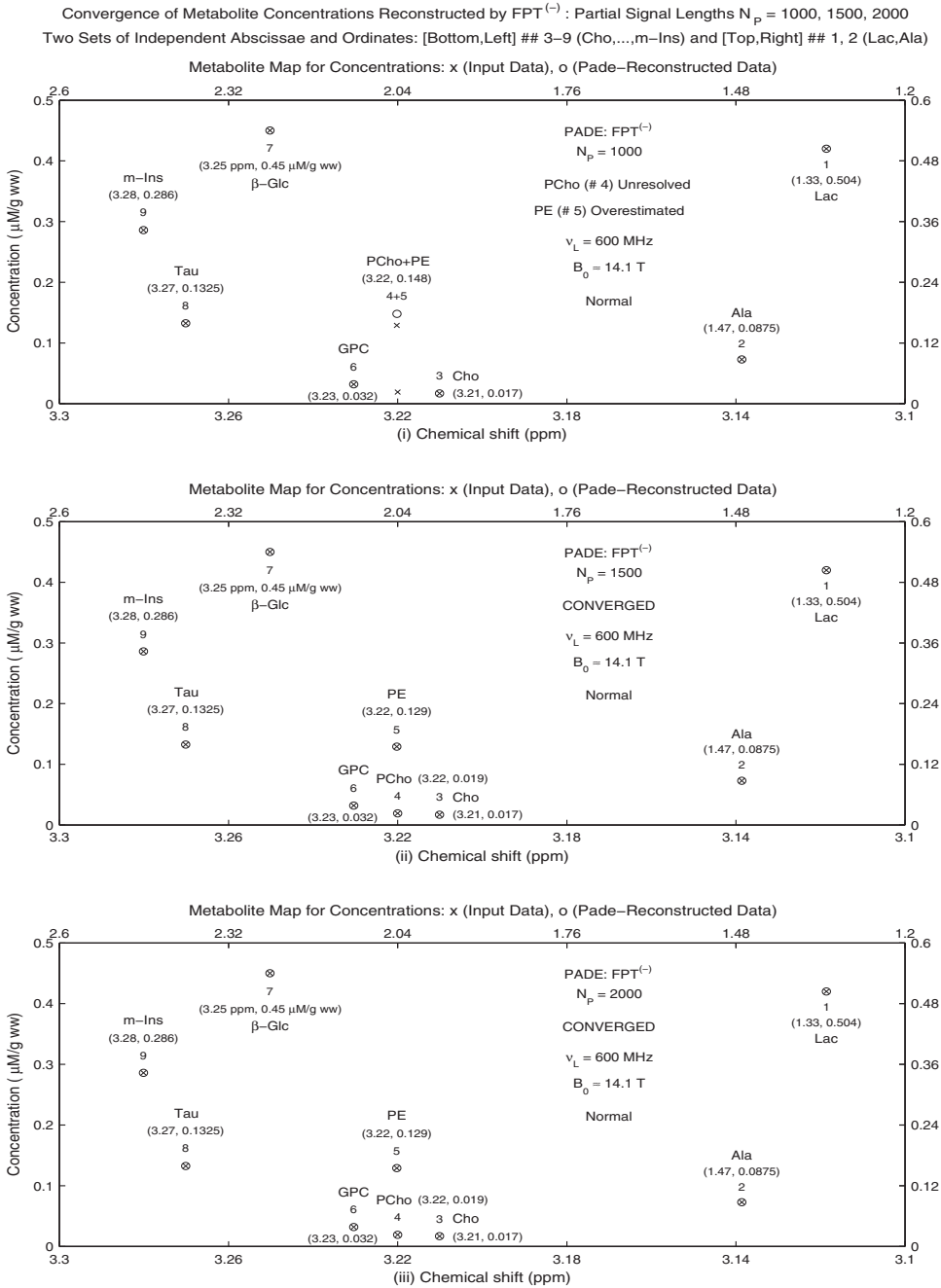

Figure 6.11 Metabolite concentrations reconstructed by the FPT for normal breast as per in vitro MRS data from Ref. [31].

correspond to data reconstructed by the FPT. At $N_P = 1000$ (upper panel (i)), prior to convergence, the concentrations of PCho and PE are incorrectly assessed in the reconstruction. The remaining metabolite concentrations are correct, however. The middle panel (ii) corresponding to $N_P = 1500$ and the lower panel (iii) at $N_P = 2000$ show that all of the computed metabolite concentrations are exact. This is presented numerically and graphically such that each "x" is centered within the open circles, indicating full agreement between the input and reconstructed data.

5.2.2. Fibroadenoma breast tissue

In Table 6.7, the Padé-reconstructed data are presented for the fibroadenoma at $N_P = 1000, 1500$, and 2000. On the top panel (i) of Table 6.7 at $N_P = 1000$, one of the nine resonances was not identified. Only one peak was detected at 3.220169 ppm, although there should be two peaks: phosphocholine ($k = 4$) at 3.220012 ppm and phosphoethanolamine ($k = 5$) at 3.220215 ppm. At $N_P = 1000$, the reconstructed amplitude and the concentration for that one peak were approximately the sum of (PCho + PE). At $N_P = 1000$, the reconstructed spectral parameters were fully exact for five of the peaks: Lac ($k = 1$), Ala ($k = 2$), β-Glc ($k = 7$), Tau ($k = 8$), and m-Ins ($k = 9$). Convergence was attained at $N_P = 1500$ for all the reconstructed parameters for all nine resonances (middle panel (ii) of Table 6.7) in the case of the fibroadenoma data. At $N_P = 2000$ (bottom panel (iii) of Table 6.7), it is shown that convergence is maintained. We have also confirmed the stability of convergence at longer partial signal lengths, and the full signal length N.

Figure 6.12 displays the Padé-reconstructed absorption component shape spectra and the total shape spectra at $N_P = 1000, 1500$, and 2000 for the benign breast pathology: fibroadenoma. Although the absorption total shape spectrum is converged at $N_P = 1000$ (top right panel (iv)), the component shape spectrum (top left panel (i)) was not. Namely, only one peak (PE, $k = 5$) was resolved at 3.22 ppm but overestimated, whereas PCho ($k = 4$) is not detected. The left middle panel (ii) of Figure 6.12 at $N_P = 1500$ shows convergence of the component shape spectrum. Peaks $k = 4$ and 5 are clearly distinguished and their peak heights are correct. This is also the case for the other peaks. Underlying phosphoethanolamine, the small phosphocholine peak is observed. The bottom panels corresponding to $N_P = 2000$ show the stable convergence of both the absorption component shape spectrum (iii) and the total shape spectrum (vi). We have verified this to be the case for longer partial signals lengths and for the full signal length N.

Figure 6.13 presents the convergence pattern for the metabolite concentrations at $N_P = 1000, 1500$, and 2000 with regard to the fibroadenoma data. The concentrations of phosphocholine and phosphoethanolamine are not correctly assessed at $N_P = 1000$ (upper panel (i)). There are small discrepancies as well in the computed concentrations of Cho ($k = 3$) and GPC ($k = 6$). All

Table 6.7 Padé-reconstructed spectral parameters and metabolite concentrations for fibroadenoma. The input data is derived from Ref. [31].

Convergence of Spectral Parameters and Concentrations in FPT$^{(-)}$: Partial Signal Lengths $N_P = 1000, 1500, 2000$					
n_k^o (Metabolite # k)	Re(ν_k^-) (ppm)	Im(ν_k^-) (ppm)	$\lvert d_k^- \rvert$ (au)	C_k^- (μM/g ww)	M_k (Assignment)
(i) Pade-Reconstructed Data (Fibroadenoma): $N_P = 1000$ (# 4 PCho: Unresolved, # 5 PE: Overestimated)					
1	1.330413	0.000832	0.05928	1.4820	Lac
2	1.470313	0.000834	0.00440	0.1100	Ala
3	3.210122	0.000830	0.00088	0.0219	Cho
5	3.220169	0.000835	0.01909	0.4773	PE
6	3.230413	0.000831	0.00276	0.0689	GPC
7	3.250224	0.000832	0.03912	0.9780	β-Glc
8	3.270141	0.000834	0.01352	0.3380	Tau
9	3.280132	0.000831	0.01860	0.4650	m-Ins
(ii) Pade-Reconstructed Data (Fibroadenoma): $N_P = 1500$ (Converged)					
1	1.330413	0.000832	0.05928	1.4820	Lac
2	1.470313	0.000834	0.00440	0.1100	Ala
3	3.210124	0.000833	0.00088	0.0220	Cho
4	3.220012	0.000832	0.00432	0.1080	PCho
5	3.220215	0.000831	0.01476	0.3690	PE
6	3.230412	0.000833	0.00276	0.0690	GPC
7	3.250224	0.000832	0.03912	0.9780	β-Glc
8	3.270141	0.000834	0.01352	0.3380	Tau
9	3.280132	0.000831	0.01860	0.4650	m-Ins
(iii) Pade-Reconstructed Data (Fibroadenoma): $N_P = 2000$ (Converged)					
1	1.330413	0.000832	0.05928	1.4820	Lac
2	1.470313	0.000834	0.00440	0.1100	Ala
3	3.210124	0.000833	0.00088	0.0220	Cho
4	3.220012	0.000832	0.00432	0.1080	PCho
5	3.220215	0.000831	0.01476	0.3690	PE
6	3.230412	0.000833	0.00276	0.0690	GPC
7	3.250224	0.000832	0.03912	0.9780	β-Glc
8	3.270141	0.000834	0.01352	0.3380	Tau
9	3.280132	0.000831	0.01860	0.4650	m-Ins

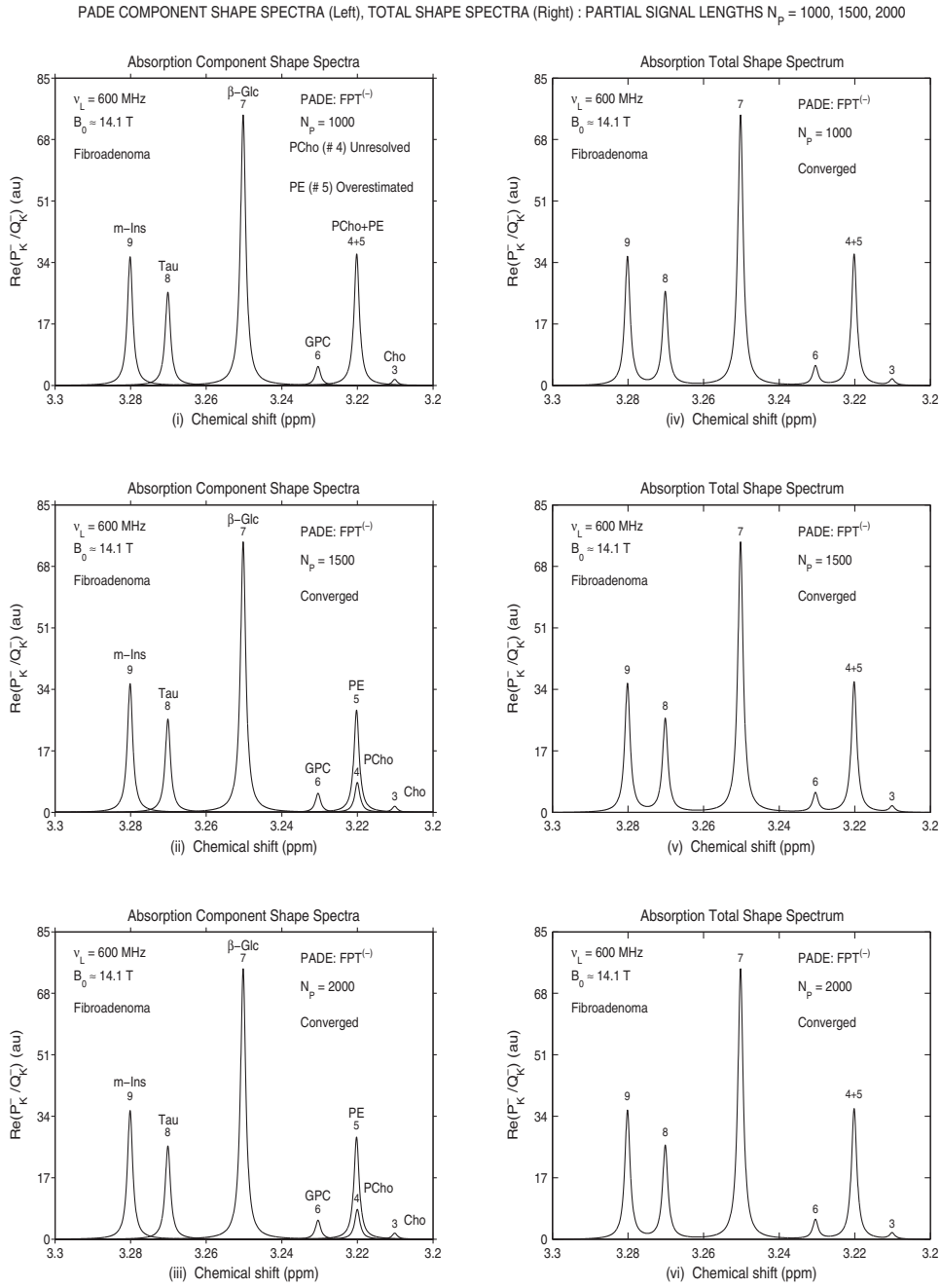

Figure 6.12 Absorption component spectra (left panels) and total shape spectra (right panels) reconstructed by the FPT corresponding to fibroadenoma, according to in vitro MRS data from Ref. [31].

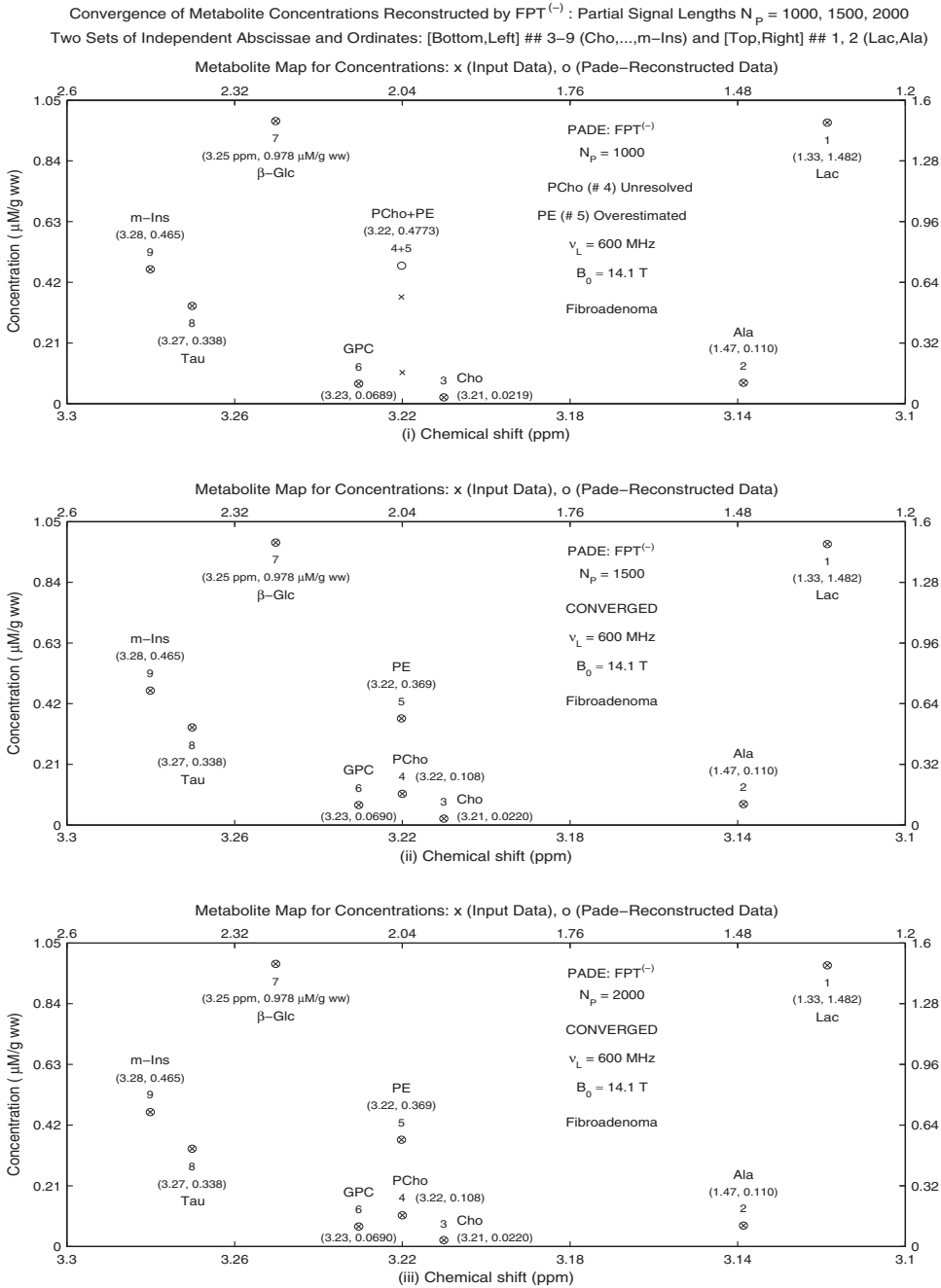

Figure 6.13 Metabolite concentrations reconstructed by the FPT for benign breast tissue (fibroadenoma) derived from in vitro MRS data of Ref. [31].

the metabolite concentrations are correct at $N_P = 1500$ (middle panel (ii)) and $N_P = 2000$ (lower panel (iii)). We have also confirmed that the metabolite concentrations are correct at even higher partial signal lengths and at the full signal length.

5.2.3. Malignant breast tissue

The Padé-reconstructed data for malignant breast tissue at $N_P = 1000, 1500,$ and 2000 are displayed in Table 6.8. Again, one of the nine resonances was not detected at $N_P = 1000$ as seen in the top panel (i) of Table 6.8. Instead of the two peaks, PCho at 3.220012 ppm and PE at 3.220215 ppm, only one was detected at 3.220166 ppm. The reconstructed amplitudes and concentrations for that resonance were approximately equal to the sum of those for PCho plus PE. The reconstructed spectral parameters were exact only for three resonances: Lac ($k = 1$), Ala ($k = 2$), and m-Ins ($k = 9$), at $N_P = 1000$.

At $N_P = 1500$, convergence was achieved for all the reconstructed parameters of all nine resonances corresponding to malignant breast tissue (middle panel (ii) of Table 6.8). On the bottom panel (iii) of Table 6.8, stable convergence is maintained at $N_P = 2000$. For the malignant case, we have also confirmed that convergence of the reconstructed spectral parameters remains stable for longer partial signal lengths and for the full signal length N.

Figure 6.14 shows the absorption component shape spectra and the total shape spectra reconstructed by the FPT for the malignant breast data at $N_P = 1000, 1500,$ and 2000. On the top right panel (iv) at $N_P = 1000$, the absorption total shape spectrum has converged. However, the top left panel (i) displays the component shape spectrum with only one resonance at 3.22 ppm, which was overestimated, whereas the other peak was not detected. The middle left panel (ii) of Figure 6.14 at $N_P = 1500$ shows that the component shape spectrum has converged such that resonances $k = 4$ and 5 are distinguished and their heights are correct. This was also the case for all the other resonances. The bottom panels (iii) and (vi) corresponding to $N_P = 2000$ indicate that convergence is stable. We have also verified stable convergence of the absorption spectra for yet higher partial signal lengths and for the full signal length for both the absorption component shape spectra and the total shape spectrum. Figure 6.15 presents the convergence of metabolite concentrations for the cancerous breast data at $N_P = 1000, 1500,$ and 2000. At $N_P = 1000$, the computed concentrations of PCho and PE are not accurate, as seen in the upper panel (i). The concentrations of peaks $k = 3$ (Cho), $k = 6$ (GPC), $k = 7$ (β-Glc), and $k = 8$ (Tau) are not fully correct, either, at $N_P = 1000$. The middle (ii) ($N_P = 1500$) and bottom panels (iii) ($N_P = 2000$) of Figure 6.15 show that all of the metabolite concentrations are correct. We have confirmed that the metabolite concentrations are correct for higher N_P, and for the full signal length N.

Table 6.8 Padé-reconstructed spectral parameters and metabolite concentrations for cancerous breast tissue. Input data are derived from Ref. [31].

Convergence of Spectral Parameters and Concentrations in FPT$^{(-)}$: Partial Signal Lengths $N_P = 1000, 1500, 2000$					
n_k^o (Metabolite # k)	Re(ν_k^-) (ppm)	Im(ν_k^-) (ppm)	$\lvert d_k^- \rvert$ (au)	C_k^- (μM/g ww)	M_k (Assignment)
(i) Pade-Reconstructed Data (Malignant): $N_P = 1000$ (# 4 PCho: Unresolved, # 5 PE: Overestimated)					
1	1.330413	0.000831	0.32474	8.1185	Lac
2	1.470313	0.000832	0.03156	0.7890	Ala
3	3.210122	0.000830	0.00444	0.1111	Cho
5	3.220166	0.000836	0.10230	2.5575	PE
6	3.230414	0.000829	0.00933	0.2332	GPC
7	3.250224	0.000832	0.02882	0.7204	β-Glc
8	3.270141	0.000831	0.11182	2.7954	Tau
9	3.280132	0.000833	0.03564	0.8910	m-Ins
(ii) Pade-Reconstructed Data (Malignant): $N_P = 1500$ (Converged)					
1	1.330413	0.000831	0.32474	8.1185	Lac
2	1.470313	0.000832	0.03156	0.7890	Ala
3	3.210124	0.000834	0.00446	0.1115	Cho
4	3.220012	0.000831	0.02448	0.6120	PCho
5	3.220215	0.000832	0.07776	1.9440	PE
6	3.230412	0.000833	0.00936	0.2340	GPC
7	3.250224	0.000832	0.02882	0.7205	β-Glc
8	3.270141	0.000831	0.11182	2.7955	Tau
9	3.280132	0.000833	0.03564	0.8910	m-Ins
(iii) Pade-Reconstructed Data (Malignant): $N_P = 2000$ (Converged)					
1	1.330413	0.000831	0.32474	8.1185	Lac
2	1.470313	0.000832	0.03156	0.7890	Ala
3	3.210124	0.000834	0.00446	0.1115	Cho
4	3.220012	0.000831	0.02448	0.6120	PCho
5	3.220215	0.000832	0.07776	1.9440	PE
6	3.230412	0.000833	0.00936	0.2340	GPC
7	3.250224	0.000832	0.02882	0.7205	β-Glc
8	3.270141	0.000831	0.11182	2.7955	Tau
9	3.280132	0.000833	0.03564	0.8910	m-Ins

5.2.4. Comparisons of MRS data for normal, fibroadenoma, and malignant breast tissues

In Figure 6.16, the converged absorption component shape spectra (left panels) and total shape spectra (right panels) are compared for normal

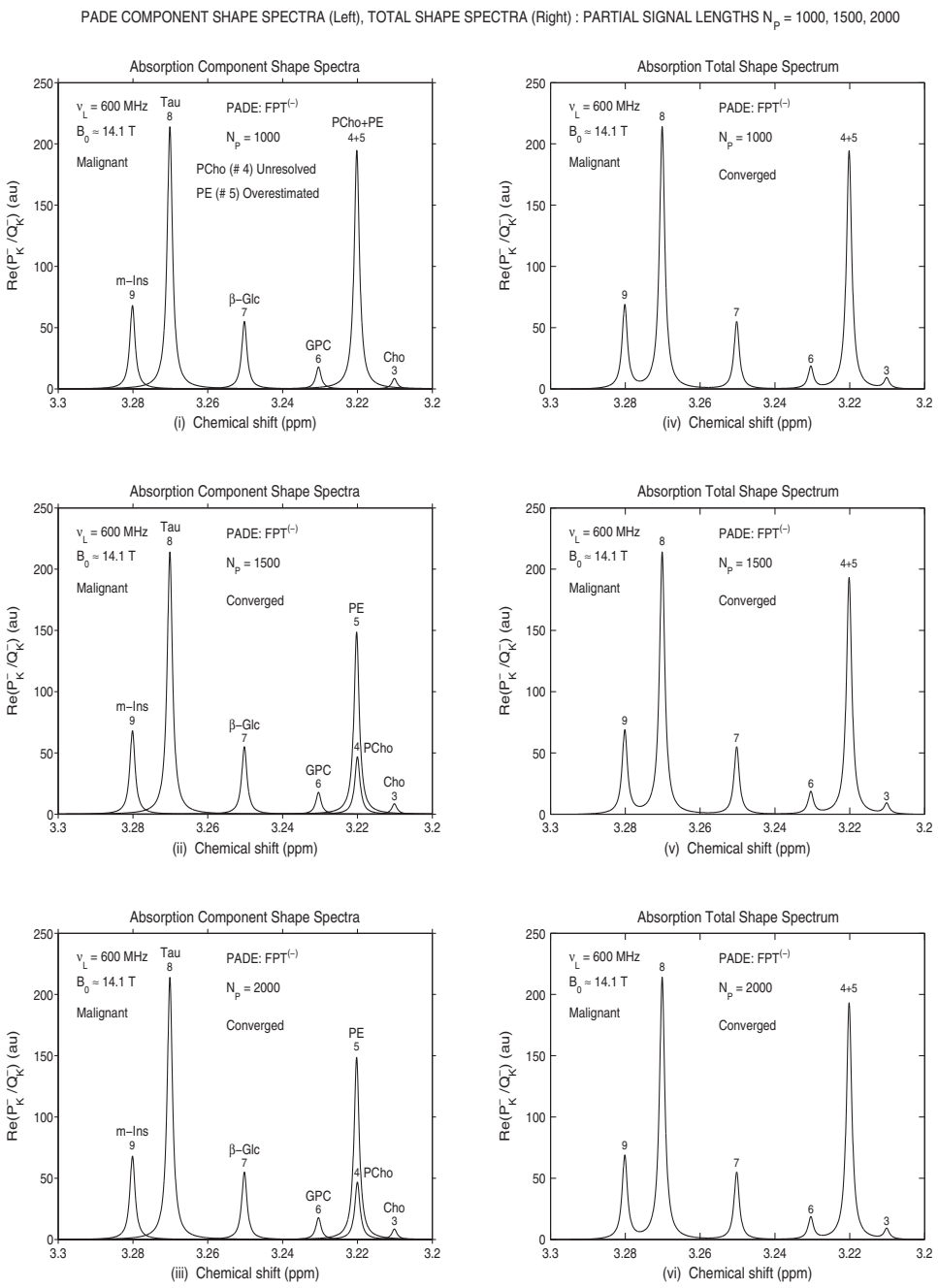

Figure 6.14 Absorption component spectra (left panels) and total shape spectra (right panels) for breast cancer as reconstructed by the FPT, as derived from in vitro MRS data of Ref. [31].

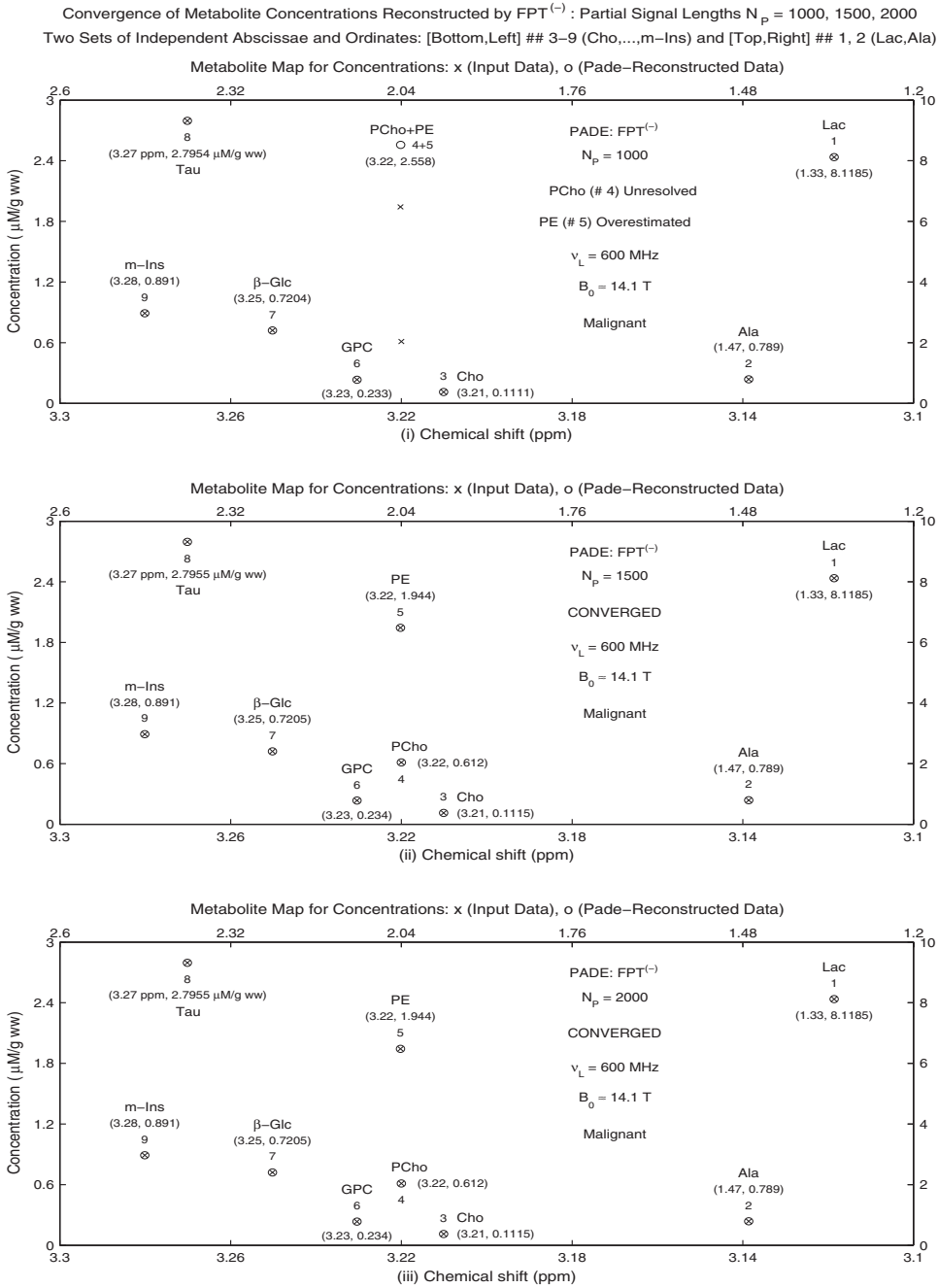

Figure 6.15 Metabolite concentrations reconstructed by the FPT for cancerous breast tissue from in vitro MRS data of Ref. [31].

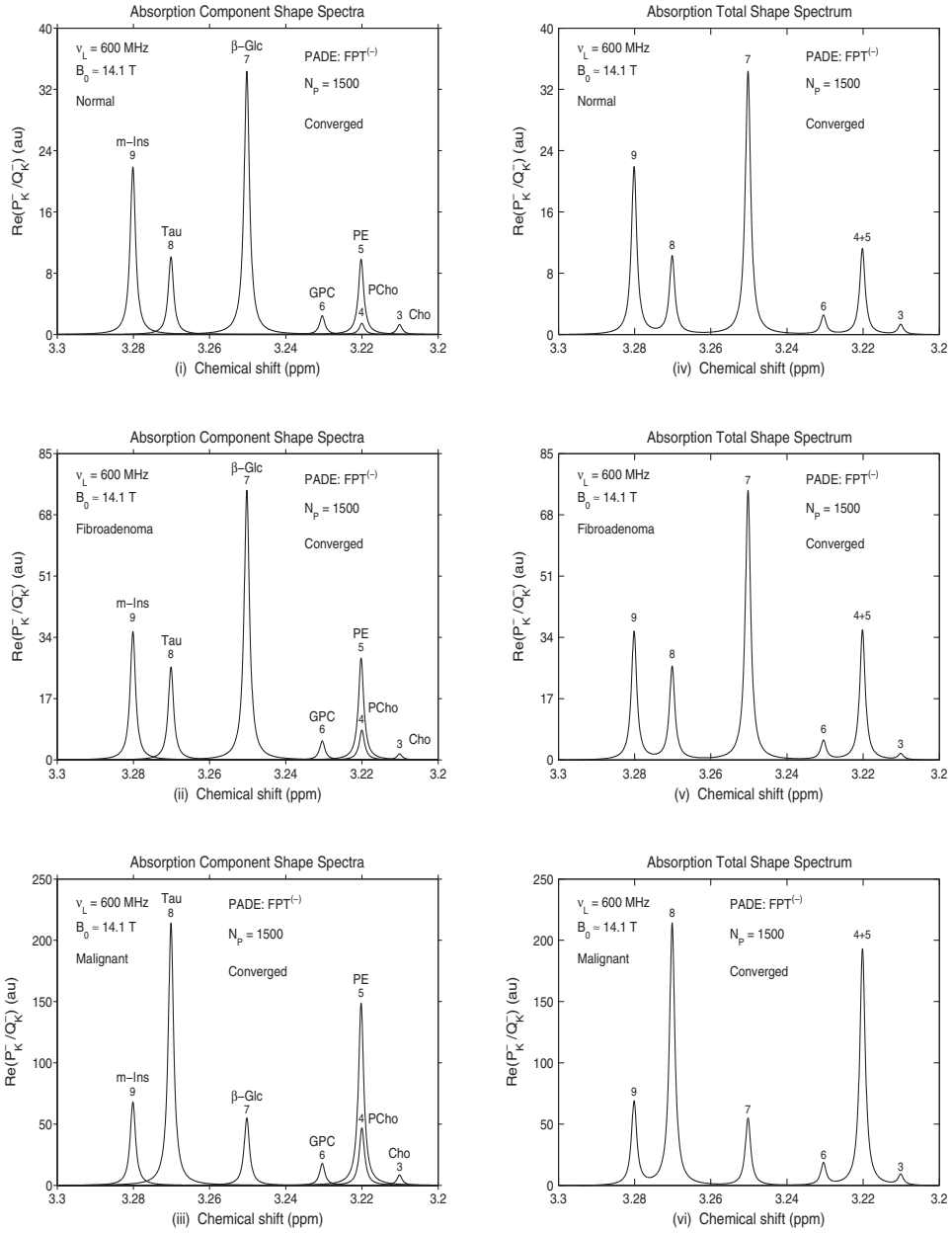

Figure 6.16 Converged absorption component spectra (left panels) and total shape spectra (right panels) as reconstructed by the FPT at $N_P = 1500$. The upper panels (i) and (iv) correspond to normal breast tissue, the middle panels (ii) and (v) to fibroadenoma and the lower panels (iii) and (vi) to malignant breast, derived from in vitro data in Ref. [31].

breast tissue, fibroadenoma, and malignant breast in the range between 3.2 and 3.3 ppm. The upper panels (i) and (iv) of Figure 6.16 display the reconstructed spectra for the normal breast, the spectra for fibroadenoma are in the middle panels (ii) and (v), and that for cancerous breast data in the lower panels (iii) and (vi). The peak heights of all the metabolites within this frequency range are low for normal breast, with β-glucose at 3.25 ppm ($k = 7$) and myoinositol ($k = 9$) at 3.28 ppm as the largest resonances. Phosphocholine is very small. For the fibroadenoma, the peaks within the range of 3.2 and 3.3 ppm are all higher compared with the normal breast spectra. While myoinositol is clearly larger than the resolved peaks $k = 4$ (PCho) and $k = 5$ (PE) at 3.22 ppm in the converged component shape spectrum, for the total shape spectrum peak ($k = 4 + 5$) at 3.22 ppm is approximately the same height as myoinositol ($k = 9$ at 3.28 ppm). Within the range of 3.2–3.3 ppm, spectra from the malignant breast are quite distinct. The largest resonance is taurine ($k = 8$) at 3.27 ppm, and β-Glc peak at 3.25 ppm is among the smaller peaks. The difference between the component and total shape spectra is the most striking, whereby the PCho + PE peak at 3.22 ppm is almost as tall as the taurine peak, whereas in the component spectrum with PE and PCho well demarcated, it is clear that each is much smaller than taurine.

The Padé-reconstructed converged metabolite maps for normal breast (upper panel (i)), fibroadenoma (middle panel (ii)), and for malignant breast (lower panel (iii)) are presented in Figure 6.17. Lactate ($k = 1$) has the highest concentration (0.5040 μM/g ww) in normal breast tissue, followed by β-glucose ($k = 7$) (0.4500 μM/g ww). In the normal breast, the median lactate concentration is approximately 0.34 times lower than that in the fibroadenoma. For the malignant breast, the median lactate concentration is more than five times higher than in fibroadenoma.

5.2.5. Discussion

A major advantage of the fast Padé transform for analysis of MRS signals is its capability to resolve and precisely quantify closely overlapping resonances. Particularly for distinguishing MR signals from noncancerous and malignant breast, this capability of the FPT is most clearly seen in the spectrally dense region between 3.21 and 3.23 ppm. Therein, phosphocholine and phosphoethanolamine are nearly completely overlapping, separated by a mere 0.0002 ppm. Nevertheless at convergence, the input parameters for these two resonances are still reliably reconstructed by the FPT. In other clinically relevant examples, the FPT also exactly reconstructs all the resonances, including those that are extremely closely overlapping, from time signals similar to the ones encoded via MRS from the brain of a healthy volunteer [2, 13], and from normal and cancerous prostate [5, 14], as will be shown in the next section. In each of these examples, it was striking that convergence of the total shape spectrum did not necessarily mean that the component spectra converged. It is indeed precarious to guess how many

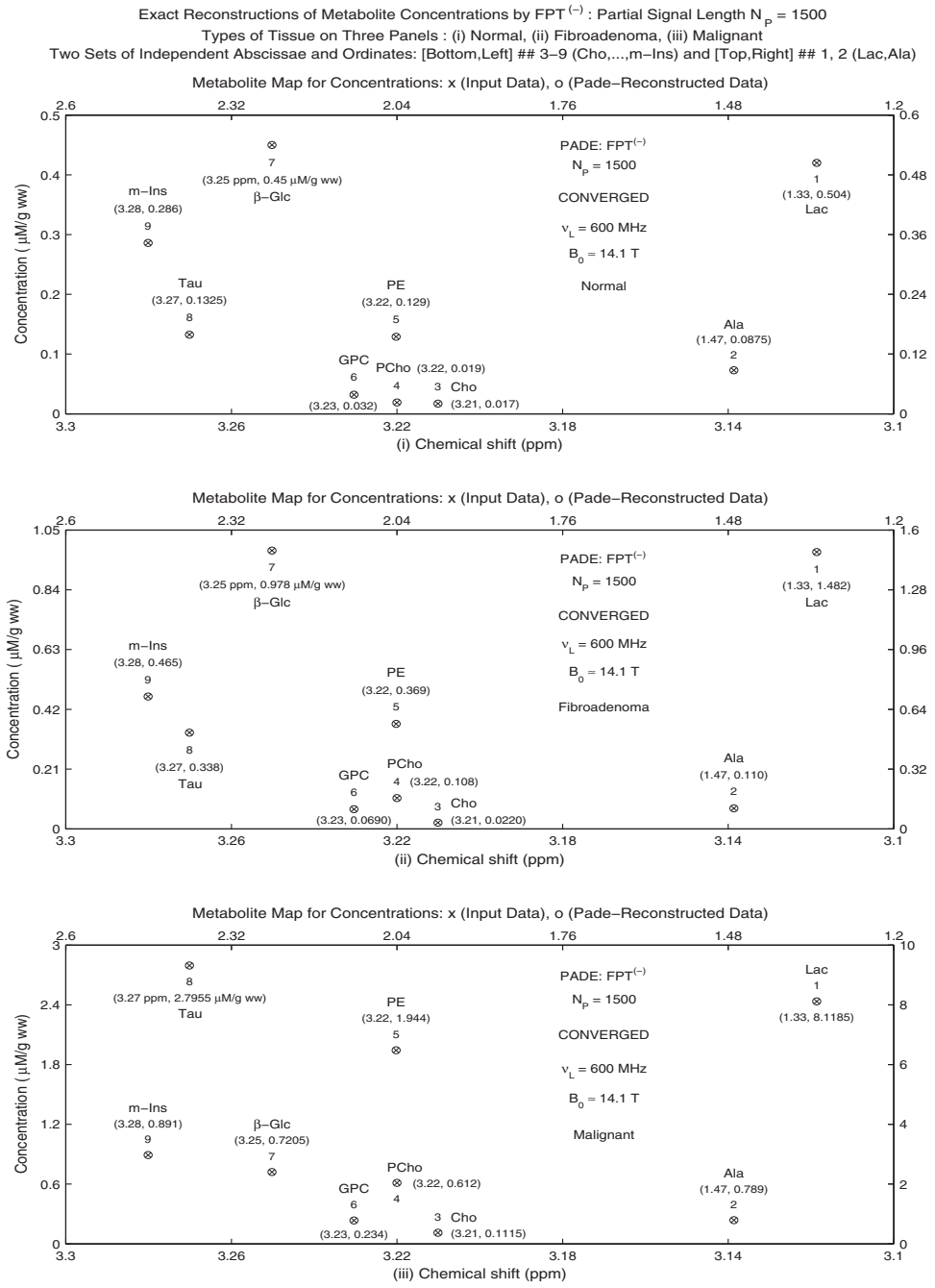

Figure 6.17 Converged metabolite concentration maps at $N_P = 1500$ as reconstructed by the FPT for normal breast tissue (upper panel (i)), fibroadenoma (middle panel (ii)), and malignant breast (lower panel (iii)) derived from in vitro data in Ref. [31].

resonances underlie a given peak, as is done by postprocessing fitting algorithms used in MRS [32–34]. Yet, as noted, this is what is done when relying on Fourier-based processing, which can only generate the envelope or total shape spectrum. On the other hand, the FPT not only extracts the spectral parameters exactly but also determines with certainty the number the resonances that are present [1–3].

Spurious resonances appear with all the parametric estimators that must use more than twice the number of unknown frequencies and amplitudes. This leads to an overdetermined system of linear equations yielding more resonances than the actual number present in the analyzed signal. Only the FPT can use pole–zero cancellation (Froissart doublets) [3] to unequivocally distinguish true from spurious resonances. Spurious resonances act as "noise." The task is to identify and discard them. The number of spurious resonances is always several times greater than that of the true metabolites. In the present cases related to normal, benign and malignant breast, fewer than 2% of the reconstructed resonances were genuine, underscoring the vital importance of this reliable method for signal–noise separation.

For breast cancer diagnostics, it is very important to identify and quantify the components of total choline. Our earlier analyses show that the ratio of PCho/GPC is significantly higher in the malignant compared with normal breast tissue samples [15]. Research from human breast cell lines elucidate a "glycerophosphocholine to phosphocholine switch." This occurs with malignant transformation [35] and is related to overexpression of the enzyme choline kinase responsible for PCho synthesis [36, 37]. Choline metabolism proceeds via the cytosine diphosphate (CDP)-choline pathway [37], wherein choline (3.21 ppm), PCho (3.22 ppm), and GPC (3.23 ppm) are MR-visible compounds. Thus, it becomes possible to evaluate the relationship among these closely overlapping resonances. However, when these three metabolites are summed up as total choline, as is done with Fourier-based in vivo MRS, clinically important information for breast cancer diagnostics is likely to be missed. The distinction between, for example, fibroadenoma and breast cancer could be facilitated, since the PCho concentration was approximately 5.7 times lower in the fibroadenoma than the median PCho concentration for breast cancer. This was percentually a greater difference than for PE or GPC. Thus, accurate quantification of the components of total choline might well aid the development of reliable databases to facilitate distinguishing benign from cancerous breast pathology.

The input data for the analyses performed herein is from a relatively small number of malignant and normal breast samples and from only a single fibroadenoma. Thus, it is not yet entirely clear which metabolites would best detect the presence of breast cancer and distinguish this from benign lesions. Nonetheless, it should be noted that in our multiple logistic regression analysis [9, 15] of these data [31], only lactate showed 100% diagnostic accuracy for identifying malignant breast. Concordant findings concerning lactate are

reported by Sharma et al. [38] who employed in vitro two-dimensional MRS to compare involved and uninvolved lymph nodes from patients with breast cancer. These authors found a highly significant difference between the lactate concentrations in involved and cancer-free lymph nodes. The increased lactate levels are related to the presence of malignant cells whose energy source is from the anaerobic glycolytic pathway. Animal models of breast cancer further confirm the importance of assessing the rate of glycolysis and lactate clearance with regard to breast cancer diagnostics [39].

From this section, we conclude that Padé-optimized MRS can certainly contribute to improved breast cancer detection. We anticipate that this advance will diminish the number of false positive findings of MRI and could even further improve its already excellent sensitivity. Once these goals have been achieved, and in light of the fact that MR-based methods entail no exposure to ionizing radiation, new avenues open up for screening and surveillance. Notably, Padé-optimized MRS could be used at short time intervals to monitor younger women at high risk for breast cancer.

6. MRS DATA FOR NORMAL AND MALIGNANT PROSTATE TISSUES

6.1. Clinical background

Prostate cancer is cited as the most common cancer among men in the European Union and the United States [40–42]. Mortality rates from prostate cancer have been declining since the late 1980s in Western Europe and North America [41, 43, 44]. This favorable trend is related, in large part to early detection using prostate-specific antigen (PSA) [41, 43, 44]. Yet, there are no designated cut points for PSA that provide optimal diagnostic accuracy [45]. For men over age 75, the U.S. Preventive Services Task Force recommends *against* screening for prostate cancer and considers the current evidence insufficient for making a decision regarding men below age 75 [46]. When prostate cancer is suspected from an abnormal PSA, prostate biopsy guided by transurethral ultrasound (TRUS) is recommended. However, TRUS has limited sensitivity; even with 8–12 cores, about 20% of prostate cancers will not be detected [40]. Conversely, up to 75% of patients biopsied for high PSA levels do not have prostate cancer [47].

Magnetic resonance imaging is a sensitive method for diagnosing, staging, and managing prostate cancer. However, MRI poorly distinguishes benign from cancerous prostatic lesions, and many unnecessary biopsies are performed based on suspicious MRI findings [48]. In vivo MRS and MRSI are becoming an important tool for prostate cancer diagnostics. In comparison to MRI alone, MRSI can enhance the accuracy of detecting prostate cancer and distinguishing it from benign prostatic hypertrophy (BPH). The best sites for biopsy are also often better identified by MRSI than MRI. Most applications

of in vivo MRS and MRSI in prostate cancer diagnostics rely on the ratio of choline at approximately 3.2 ppm and citrate (at approximately 2.5–2.7 ppm). Citrate is considered to reflect healthy secretory activity of prostate epithelium, whereas choline is an indicator of phospholipid metabolism of cell membranes and is used as a general marker for membrane damage and cellular proliferation. However, low citrate is also seen in normal stromal prostate and in metabolic atrophy. On the other hand, high citrate is usually observed in BPH, even with coexistent malignancy [49]. Other limitations of current applications of MRS and MRSI in prostate cancer diagnostics include poor resolution [41] and lack of consistent, added diagnostic value when used with PSA or MRI [50, 51]. Another drawback of MRSI is low sensitivity for detecting smaller prostate cancers [52]. For these reasons, MRSI is still not considered to have a role in screening the general population [53].

Many of the limitations of current applications of MRS and MRSI for prostate cancer diagnostics are due to reliance on conventional data analysis via the FFT. As noted, FFT is a nonparametric, low-resolution spectral estimator, yielding only a total shape spectrum and thus requires postprocessing fitting to obtain rough estimates of metabolite concentrations [1]. In vitro NMR applied to extracted specimens reveals that spectra from the prostate are exceedingly rich. Notably, these spectra are replete with closely overlapping, multiplet resonances that pose a major challenge for quantification [54]. The fast Padé transform is well suited to tackle the challenge entailed in processing MRS and MRSI signals from the prostate [5, 14]. In particular, the capabilities of the FPT has been shown to handle very closely overlapping resonances, such as those encountered in the spectra from the prostate [5, 14].

The FPT has been recently applied to time signals generated according to in vitro MRS data, as encoded from extracted prostate specimens [54]. We have presented the extensive numerical results and analytical background in Refs. [5, 14]. In this section, our attention will be directed to how Padé-optimized MRS could be used to improve prostate cancer diagnostics. We will scrutinize the resolution performance of the FPT on these MRS signals from the prostate, as well as the capacity of the FPT to quantify multiplet resonances and closely overlapping resonances of different metabolites seen in normal and malignant prostate.

6.2. Signal processing

We synthesized three time signals in the form from Eq. (5) with a total of 27 damped complex exponentials [14]. These were then quantified using the FPT, according to Ref. [2]. The bandwidth was 6000 Hz, where the inverse of this bandwidth is the sampling time τ. We set the total signal length to be $N = 1024$.

We generated the input data for the absolute values of amplitudes based on the mean metabolite concentrations and also the description of multiplets and the total shape spectra for normal prostate tissues (glandular and stromal) and for the prostate cancer from Ref. [54]. We split the total metabolite concentrations into multiplets with the aim of attaining correspondence to the spectra of Ref. [54].

We deduced the absolute values $\{|d_k|\}$ of the input amplitudes $\{d_k\}$ from the reported metabolite concentrations. We took the reference material to be the TSP molecule, and we computed the reference concentration of TSP, C_{ref} as per the data from Ref. [54]. There was a total of $(TSP + D_2O) = 3.79$ mg, where TSP comprised 0.75% of that weight and altogether 0.02845 mg of TSP [54]. Since the molecular weight of TSP = 172.23 g, there were 0.1652 μM of TSP and the mass of wet tissue =15.11 mg. Thus, the concentration of TSP was 0.1652 μM/15.11 mg ww = 10.93 μM/g ww. The phases ϕ_k $(1 \leq k \leq 27)$ from complex-valued d_k were all set to zero such that each d_k became real $d_k = |d_k|$.

In Tables 6.9, 6.10, and 6.11, the input data for the normal glandular, for normal stromal prostate, and for prostate cancer are presented. The spectral parameters $\{\omega_k^-, d_k^-\}$ $(1 \leq k \leq K)$ of every physical resonance are extracted by the FPT$^{(-)}$ using only the raw input time signal. No editing or other modification is performed. We computed the kth metabolite concentration C_k^- of the tissue wet weight from the absolute value $|d_k^-|$ of the reconstructed amplitude d_k^- as $C_k^- = |d_k^-| C_{ref}/2 = 5.465\,|d_k^-|$ μM/g ww.

We gradually augmented the signal length for the same bandwidth to confirm the constancy of the spectral parameters for all three signals. The spectral parameters were examined at total orders $K = 250$, 300, and 350, where $2K = N_P$ and N_P denotes partial signal length. For the cases of normal glandular and normal stromal prostate and for prostate cancer, convergence occurred at $K = 350, 300$, and 300, respectively. After initial convergence, stability was maintained at longer partial signal lengths. We also verified the constancy in nonparametric signal processing by computing a sequence of the Padé shape spectra $\{P^-_{K_c+m}/Q^-_{K_c+m}\}$ $(m = 1, 2, 3, \ldots)$ for the entire Nyquist range, including the interval of interest between 1.3 and 4.2 ppm. Here, K_c is the value of the polynomial degree K when convergence of the Padé spectra has been recorded for the first time.

We evaluated whether a given reconstructed resonance was genuine by computing signal poles and zeros, as described in Ref. [3]. Recall that spurious resonances have zero amplitudes, since the poles and zeros of the Padé complex-valued spectrum coincide. Of the 350 total resonances for normal glandular prostate, 323 were identified as spurious because of their zero amplitudes and the pole–zero coincidences, thus yielding the 27 true resonances. Of the 300 total resonances for both the normal stromal tissue and prostate cancer, a total of 273 were spurious by their zero amplitudes and the pole–zero coincidences, and the remaining 27 resonances were genuine.

Table 6.9 Input data for normal glandular prostate: spectral parameters and metabolite concentrations based on in vitro data from Ref. [54]. Acronyms as previously are ppm for parts per million, au arbitrary units, M_k denotes metabolite assignment, C_k denotes concentration of M_k. Abbreviations: Lac denotes lactate, Ala alanine, Cit citrate, Cr creatine, PA polyamines, Cho choline, PCho phosphocholine, GPC glycerophosphocholine, s-Ins scylloinositol, Tau taurine, m-Ins myoinositol.

Input Data (Normal Glandular): Spectral Parameters, Concentrations and Metabolite Assignments					
Phases of All Harmonics are Set Equal to Zero: $\phi_k = 0\,(k = 1, \ldots, K; K = 27)$					
n_k^o (Metabolite # k)	Re(ν_k) (ppm)	Im(ν_k) (ppm)	$\lvert d_k \rvert$ (au)	C_k (μM/g ww)	M_k (Assignment)
1	1.330148	0.013213	7.374199	40.3	Lac
2	1.490417	0.030361	1.579140	8.63	Ala
3	2.515197	0.008242	1.500457	8.20	Cit
4	2.540235	0.009624	2.616651	14.3	Cit
5	2.720146	0.010205	2.525160	13.8	Cit
6	2.750328	0.007014	1.244282	6.80	Cit
7	3.040309	0.006951	1.661482	9.08	Cr
8	3.100416	0.021432	2.104300	11.5	PA
9	3.140263	0.025760	1.280878	7.00	PA
10	3.210152	0.002367	0.644099	3.52	Cho
11	3.230242	0.010313	0.181153	0.99	PCho
12	3.240318	0.003014	0.468435	2.56	GPC
13	3.250298	0.004362	0.384263	2.10	Tau
14	3.260429	0.005921	0.823422	4.50	Tau
15	3.275351	0.005671	0.219579	1.20	Tau
16	3.350137	0.007324	0.331199	1.81	s-Ins
17	3.420319	0.004290	0.201281	1.10	Tau
18	3.430241	0.005014	0.329369	1.80	Tau
19	3.440448	0.004721	0.182983	1.00	Tau
20	3.533243	0.006432	0.534309	2.92	m-Ins
21	3.550326	0.009324	1.557182	8.51	m-Ins
22	3.563639	0.007291	0.795974	4.35	m-Ins
23	3.626378	0.006952	0.589204	3.22	m-Ins
24	3.640411	0.009850	1.374199	7.51	m-Ins
25	3.655389	0.005812	0.444648	2.43	m-Ins
26	4.070235	0.012823	0.962489	5.26	m-Ins
27	4.120142	0.019891	1.134492	6.20	Lac

6.2.1. Normal glandular prostate tissue

Table 6.12 displays the Padé-reconstructed data for the normal glandular prostate at partial signal lengths $N_P = 600$ and $N_P = 700$. The spectral reconstructed parameters are listed with six decimals. However, the input concentrations are given with one or maximum two decimals to be consistent with the data from Ref. [54].

Table 6.10 Input data for normal stromal prostate: spectral parameters and metabolite concentrations based on in vitro data of Ref. [54].

Input Data (Normal Stromal): Spectral Parameters, Concentrations and Metabolite Assignments					
Phases of All Harmonics are Set Equal to Zero: $\phi_k = 0\,(k = 1, \ldots, K; K = 27)$					
n_k^o (Metabolite # k)	Re(ν_k) (ppm)	Im(ν_k) (ppm)	$\lvert d_k \rvert$ (au)	C_k (μM/g ww)	M_k (Assignment)
1	1.330148	0.013214	7.154620	39.1	Lac
2	1.490417	0.030360	1.244282	6.80	Ala
3	2.515197	0.010242	0.559927	3.06	Cit
4	2.540235	0.012151	0.977127	5.34	Cit
5	2.720146	0.012203	0.944190	5.16	Cit
6	2.750328	0.009014	0.464776	2.54	Cit
7	3.040309	0.006132	1.396157	7.63	Cr
8	3.100416	0.018432	0.345837	1.89	PA
9	3.140263	0.022761	0.230558	1.26	PA
10	3.210152	0.002613	0.495883	2.71	Cho
11	3.230242	0.010314	0.221409	1.21	PCho
12	3.240318	0.005121	0.572736	3.13	GPC
13	3.250298	0.004132	0.329369	1.80	Tau
14	3.260429	0.003821	0.708143	3.87	Tau
15	3.275351	0.005670	0.188472	1.03	Tau
16	3.350137	0.005022	0.364135	1.99	s-Ins
17	3.420319	0.003690	0.175663	0.96	Tau
18	3.430241	0.003012	0.287283	1.57	Tau
19	3.440448	0.004123	0.159195	0.87	Tau
20	3.533243	0.006432	0.420860	2.30	m-Ins
21	3.550326	0.009324	1.225984	6.70	m-Ins
22	3.563639	0.007290	0.625801	3.42	m-Ins
23	3.626378	0.005951	0.462946	2.53	m-Ins
24	3.640411	0.007432	1.081427	5.91	m-Ins
25	3.655389	0.004814	0.351327	1.92	m-Ins
26	4.070235	0.010123	0.753888	4.12	m-Ins
27	4.120142	0.019891	1.097896	6.00	Lac

The top panel (i) at $N_P = 600$ shows resolution of 25 of the 27 peaks. The two undetected resonances are phosphocholine ($k = 11$) at 3.230242 ppm and one of the taurine triplets ($k = 13$) at 3.250298 ppm. Although some of the computed concentrations were correct, for example, for the polyamine resonance peak $k = 8$ and lactate at 1.330148 ppm, the doublets of citrate and for creatine, the spectral parameters were not fully exact for any of the resonances. At $N_P = 600$, the closest to being completely correct were the spectral parameters and computed concentrations for the peaks at the outermost regions of the spectrum ($k = 1 - 8$ and $k = 25 - 27$). However, in the region of highest spectral density, there were some notable deviations. In particular, the concentration of GPC was computed to be 5.83 μM/g ww at $N_P = 600$,

Table 6.11 Input data for prostate cancer: spectral parameters and metabolite concentrations based on in vitro data of Ref. [54].

Input Data (Malignant): Spectral Parameters, Concentrations and Metabolite Assignments					
Phases of All Harmonics are Set Equal to Zero: $\phi_k = 0$ ($k = 1, \ldots, K; K = 27$)					
n_k^o (Metabolite # k)	Re(ν_k) (ppm)	Im(ν_k) (ppm)	$\lvert d_k \rvert$ (au)	C_k (μM/g ww)	M_k (Assignment)
1	1.330148	0.013213	11.07045	60.5	Lac
2	1.490417	0.030362	2.305581	12.6	Ala
3	2.515197	0.016240	0.680695	3.72	Cit
4	2.540235	0.020952	1.185727	6.48	Cit
5	2.720146	0.020204	1.152790	6.30	Cit
6	2.750328	0.018213	0.567246	3.10	Cit
7	3.040309	0.006951	1.780421	9.73	Cr
8	3.100416	0.021434	0.580055	3.17	PA
9	3.140263	0.032762	0.386093	2.11	PA
10	3.210152	0.002814	0.823422	4.50	Cho
11	3.230242	0.003952	1.235133	6.75	PCho
12	3.240318	0.005890	0.473925	2.59	GPC
13	3.250298	0.004123	0.364135	1.99	Tau
14	3.260429	0.003141	0.781336	4.27	Tau
15	3.275351	0.005672	0.208600	1.14	Tau
16	3.350137	0.004324	0.459286	2.51	s-Ins
17	3.420319	0.003626	0.190302	1.04	Tau
18	3.430241	0.001426	0.312900	1.71	Tau
19	3.440448	0.003821	0.173833	0.95	Tau
20	3.533243	0.006434	0.548948	3.00	m-Ins
21	3.550326	0.010323	1.601098	8.75	m-Ins
22	3.563639	0.007291	0.817932	4.47	m-Ins
23	3.626378	0.005952	0.611162	3.34	m-Ins
24	3.640411	0.009434	1.425435	7.79	m-Ins
25	3.655389	0.004812	0.461116	2.52	m-Ins
26	4.070235	0.012421	0.993596	5.43	m-Ins
27	4.120142	0.012890	1.701738	9.30	Lac

rather than the correct concentration of 2.56 μM/g ww. The bottom panel of Table 6.12 shows that at $N_P = 700$, all the reconstructed parameters and computed concentrations exactly converged for the 27 resonances. We confirmed that this convergence was stable at higher partial signal lengths and at the total signal length $N = 1024$.

The Padé-reconstructed absorption component shape spectra for the normal glandular prostate are shown in Figure 6.18 at $N_P = 54$ and $N_P = 800$. The upper panel reveals that at $N_P = 54$, only 12 of the 27 resonances were resolved. These correctly resolved peaks were mainly at the two extremes of the spectrum (lactate and alanine at 1.33 and 1.49 ppm and myoinositol

Table 6.12 Spectral parameters and metabolite concentrations for normal glandular prostate as reconstructed by the FPT based on input data from Ref. [54].

Convergence of Spectral Parameters and Concentrations in FPT$^{(-)}$: Partial Signal Lengths $N_P = 600, 700$					
n_k^o (Metabolite # k)	Re(ν_k^-) (ppm)	Im(ν_k^-) (ppm)	$\lvert d_k^- \rvert$ (au)	C_k^- (μM/g ww)	M_k (Assignment)
(i) Reconstructed Data (Normal Glandular): $N_P = 600$; Missing Resonances: # 11 (PCho) and # 13 (Tau)					
1	1.330148	0.013213	7.374172	40.3	Lac
2	1.490419	0.030353	1.577285	8.62	Ala
3	2.515197	0.008242	1.500502	8.20	Cit
4	2.540235	0.009624	2.616647	14.3	Cit
5	2.720146	0.010205	2.525202	13.8	Cit
6	2.750328	0.007014	1.244305	6.80	Cit
7	3.040309	0.006951	1.661438	9.08	Cr
8	3.100415	0.021427	2.103129	11.5	PA
9	3.140287	0.025772	1.282285	7.01	PA
10	3.210129	0.002369	0.643592	3.52	Cho
12	3.242549	0.011163	1.066128	5.83	GPC
14	3.262437	0.006985	0.865424	4.73	Tau
15	3.274335	0.005416	0.254324	1.39	Tau
16	3.350141	0.007318	0.330869	1.81	s-Ins
17	3.420373	0.004365	0.208105	1.14	Tau
18	3.430250	0.004800	0.313167	1.71	Tau
19	3.440350	0.004816	0.191041	1.04	Tau
20	3.533241	0.006444	0.535570	2.93	m-Ins
21	3.550328	0.009301	1.551185	8.48	m-Ins
22	3.563630	0.007305	0.799499	4.37	m-Ins
23	3.626376	0.006939	0.587325	3.21	m-Ins
24	3.640406	0.009865	1.377351	7.53	m-Ins
25	3.655393	0.005808	0.443946	2.43	m-Ins
26	4.070235	0.012823	0.962450	5.26	m-Ins
27	4.120142	0.019890	1.134339	6.20	Lac
(ii) Reconstructed Data (Normal Glandular): $N_P = 700$; Converged (All Resonances Resolved)					
1	1.330148	0.013213	7.374199	40.3	Lac
2	1.490417	0.030361	1.579140	8.63	Ala
3	2.515197	0.008242	1.500457	8.20	Cit
4	2.540235	0.009624	2.616651	14.3	Cit
5	2.720146	0.010205	2.525160	13.8	Cit
6	2.750328	0.007014	1.244282	6.80	Cit
7	3.040309	0.006951	1.661482	9.08	Cr
8	3.100416	0.021432	2.104300	11.5	PA
9	3.140263	0.025760	1.280878	7.00	PA
10	3.210152	0.002367	0.644099	3.52	Cho

(*Continued*)

Table 6.12 (*Continued*)

n_k^o (Metabolite # k)	Re(ν_k^-) (ppm)	Im(ν_k^-) (ppm)	$\lvert d_k^- \rvert$ (au)	C_k^- (μM/g ww)	M_k (Assignment)
(ii) Reconstructed Data (Normal Glandular): $N_P = 700$; Converged (All Resonances Resolved)					
11	3.230242	0.010313	0.181153	0.99	PCho
12	3.240318	0.003014	0.468435	2.56	GPC
13	3.250298	0.004362	0.384263	2.10	Tau
14	3.260429	0.005921	0.823422	4.50	Tau
15	3.275351	0.005671	0.219579	1.20	Tau
16	3.350137	0.007324	0.331199	1.81	s-Ins
17	3.420319	0.004290	0.201281	1.10	Tau
18	3.430241	0.005014	0.329369	1.80	Tau
19	3.440448	0.004721	0.182983	1.00	Tau
20	3.533243	0.006432	0.534309	2.92	m-Ins
21	3.550326	0.009324	1.557182	8.51	m-Ins
22	3.563639	0.007291	0.795974	4.35	m-Ins
23	3.626378	0.006952	0.589204	3.22	m-Ins
24	3.640411	0.009850	1.374199	7.51	m-Ins
25	3.655389	0.005812	0.444648	2.43	m-Ins
26	4.070235	0.012823	0.962489	5.26	m-Ins
27	4.120142	0.019891	1.134492	6.20	Lac

and lactate at about 4.07 and 4.12 ppm, respectively). However, in the central region between $\approx$ 2.5 and 3.70 ppm, 15 of the 23 peaks were missing at $N_P = 54$. Moreover, the absorption and dispersive modes both appeared such that negative intensities are seen on the ordinate axis. The relative heights of the doublet citrate peak near 2.5 ppm are reversed, that is, the peak at about 2.52 ppm is larger than the one at about 2.54 ppm. The second citrate peak near 2.75 ppm appears as a singlet, whereas it should be a doublet, and the myoinositol resonances at 3.55 and 3.65 ppm likewise show up as singlets, rather than triplets. Although there should be 10 peaks between 3.0 and 3.3 ppm, only three wide resonances appear, each of which has dispersive features with negative intensities. At $N_P = 800$ (bottom panel of Figure 6.18), the dispersive modes have disappeared and all 27 peaks are resolved. Moreover, their heights are correct. This is true not only for isolated resonances but also for the multiplets, as well as the overlapping peaks of phosphocholine at 3.23 ppm and glycerophosphocholine at 3.24 ppm.

The reason why we show the case with $N_P = 54$ is that this is the least number of signal points that is theoretically needed to resolve 27 resonances. (27 unknown frequencies and 27 unknown amplitudes considered in concert require 54 linear equations.) This algebraic condition of completeness ($N_P = 2K = 2 \times 27$) is entirely insufficient mainly because of the high density of states. In fact, not $2K$ but over $10K$ signal points are required to resolve such closely packed spectra.

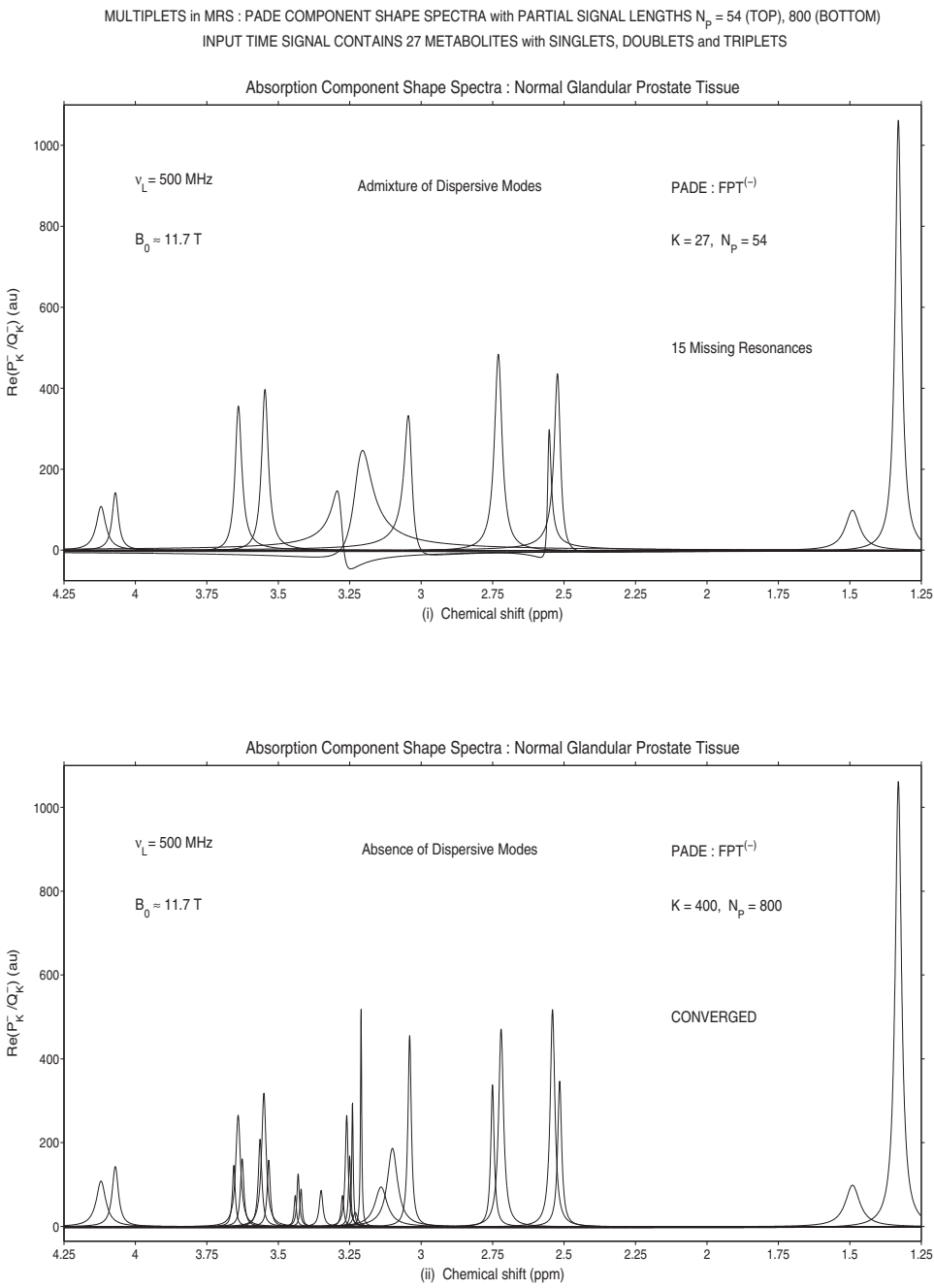

Figure 6.18 Absorption component spectra for normal glandular prostate as reconstructed by the FPT based on in vitro MRS data from Ref. [54].

The Padé-reconstructed total absorption shape spectra for the normal glandular prostate data at the same two partial signal lengths $N_P = 54$ (upper panel (i)) and $N_P = 800$ (lower panel (ii)) are presented in Figure 6.19. Several of the features observed in the component shape spectra at $N_P = 54$ can also be seen here. For example, the relative heights of the doublet citrate peak near 2.5 ppm are reversed, the resonance at approximately 2.52 ppm is higher than the one at 2.54 ppm, and the second citrate peak near 2.75 ppm seems as a singlet, rather than a doublet. The myoinositol resonances around 3.55 and 3.65 ppm appear as singlets, although they should be triplets. Only peaks at the two extremes of the total shape spectrum show correct heights and widths. The admixture of absorption and dispersive modes can also be appreciated from 3.0 to 3.3 ppm. This is reflected in three wide peaks with diminished heights and upward distortion. The converged total absorption shape spectrum at $N_P = 800$ is displayed in the lower panel of Figure 6.19.

Figure 6.20 provides a comparison for normal glandular prostate in the region between 2.40 and 3.70 ppm of the converged absorption component shape spectrum (upper panel (i)) and total absorption shape spectrum (lower panel (i); $N_P = 800$). A number of striking differences are noted. The multiplets of myoinositol and taurine are clearly demarcated as triplets on the component shape spectrum, whereas the three serrations on these structures in the total shape spectrum could at best only hint that there are actually three components. The polyamine doublet centered at about 3.1 ppm is well defined on the component spectrum but is merely suggested by the broad structure on the total shape spectrum. Although PCho at 3.23 ppm and GPC at 3.24 ppm are clearly distinguished in the component shape spectrum (top panel), only one peak appears in that region on the total shape spectrum (bottom panel).

6.2.2. Normal stromal prostate tissue

The Padé-reconstructed data for normal stromal prostate at $N_P = 500$ and $N_P = 600$ are presented in Table 6.13. For $N_P = 500$ (top panel (i)), the findings are similar to those seen for the normal glandular prostate data. There were also two undetected peaks: $k = 11$, PCho at 3.230242 ppm and $k = 13$, the component of the taurine triplet at 3.250298 ppm. For peaks $k = 1$ and $k = 5$, lactate and one of the citrate doublets, the reconstructed spectral parameters and computed concentrations were fully correct. The other spectral parameters and concentrations in the outermost regions of the spectrum ($k = 2, 3, 6$–7 and $k = 25$–27) were almost correct. However, in the middle, denser region between 3.14 and 3.65 ppm, there were more discrepancies, although most of computed concentrations had the correct first digits. The two exceptions were glycerophosphocholine ($k = 12$) and taurine ($k = 14$), which were both overestimated. These two peaks were adjacent to the missed resonances. At $N_P = 600$ (lower panel (ii) of Table 6.13), complete convergence was achieved for all the reconstructed parameters

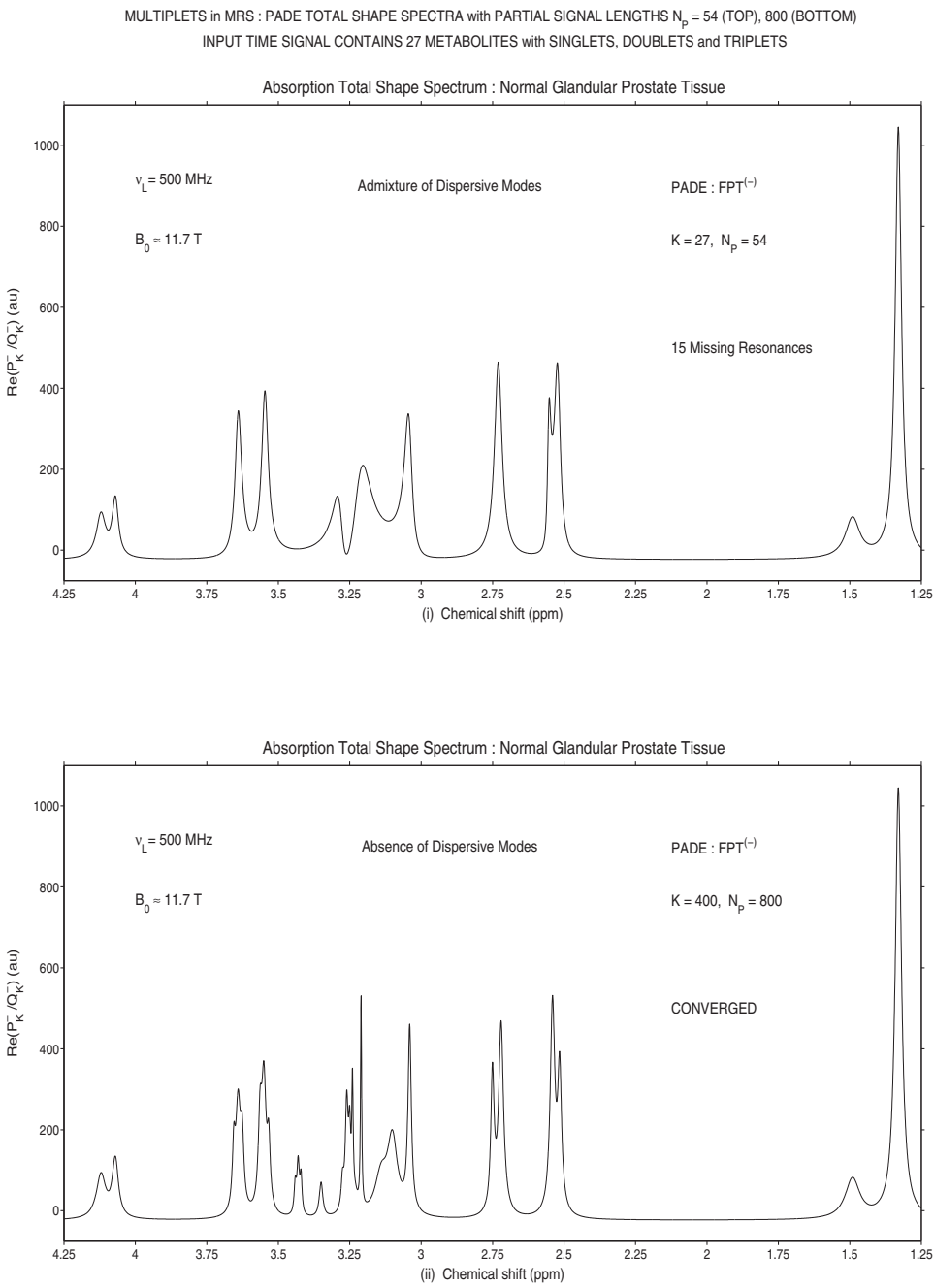

Figure 6.19 Absorption total shape spectra for normal glandular prostate reconstructed by the FPT based on in vitro MRS data from Ref. [54]. The top panel (i) is at $N_P = 54$, and the converged spectrum at $N_P = 800$ is shown on the bottom panel (ii).

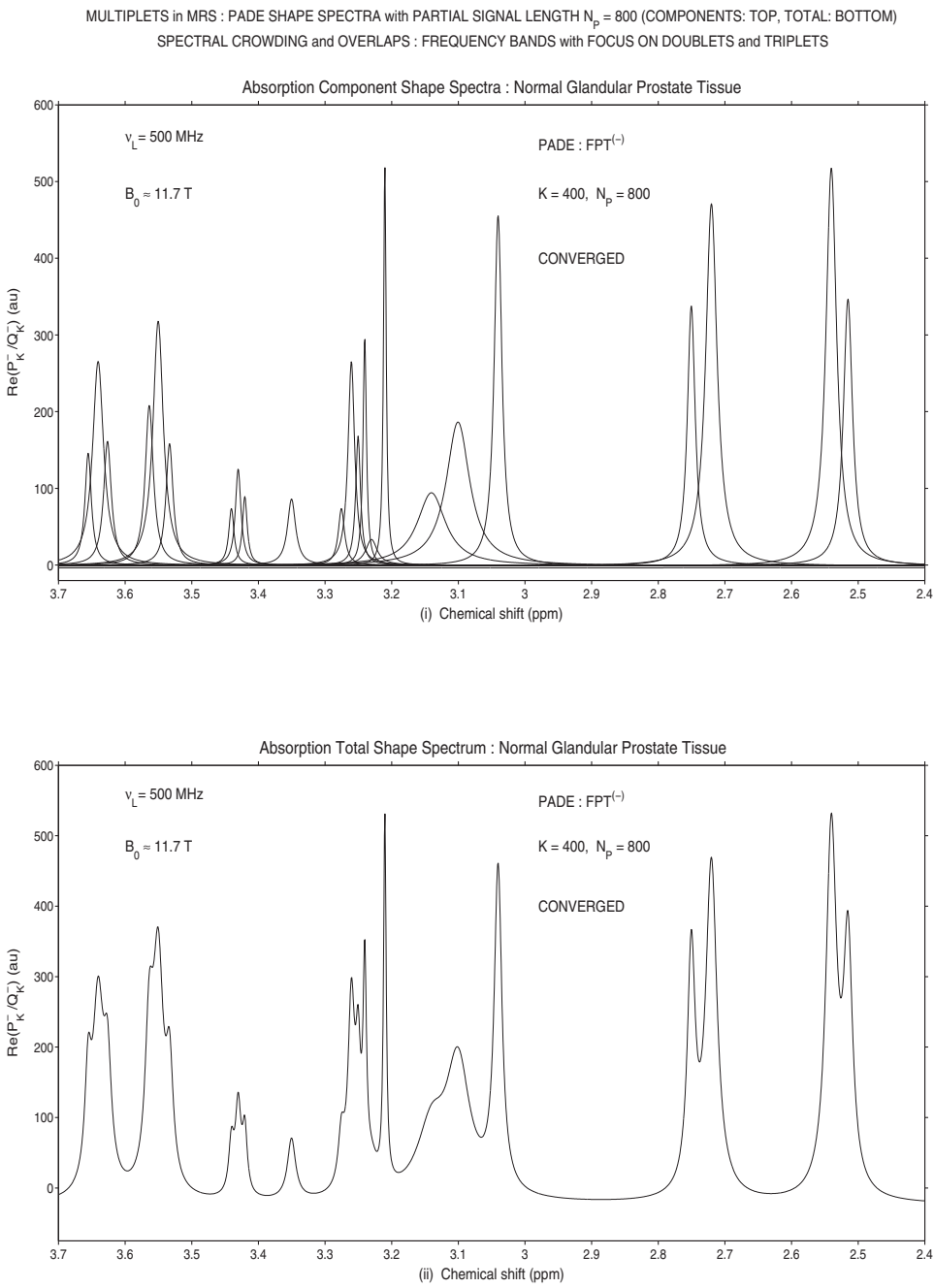

Figure 6.20 Converged absorption component shape spectra (top panel (i)) and converged absorption total shape spectra (bottom panel (ii)) both reconstructed by the FPT based on in vitro MRS data from Ref. [54] for normal glandular prostate.

Table 6.13 Spectral parameters and metabolite concentrations for normal stromal prostate as reconstructed by the FPT based on input data from Ref. [54].

Convergence of Spectral Parameters and Concentrations in FPT$^{(-)}$: Partial Signal Lengths $N_P = 500, 600$					
n_k^o (Metabolite # k)	Re(ν_k^-) (ppm)	Im(ν_k^-) (ppm)	$\lvert d_k^- \rvert$ (au)	C_k^- (μM/g ww)	M_k (Assignment)
(i) Reconstructed Data (Normal Stromal): $N_P = 500$; Missing Resonances: # 11 (PCho) and # 13 (Tau)					
1	1.330148	0.013214	7.154620	39.1	Lac
2	1.490417	0.030360	1.244279	6.80	Ala
3	2.515197	0.010242	0.559928	3.06	Cit
4	2.540235	0.012151	0.977128	5.34	Cit
5	2.720146	0.012203	0.944190	5.16	Cit
6	2.750328	0.009014	0.464780	2.54	Cit
7	3.040309	0.006132	1.396156	7.63	Cr
8	3.100411	0.018433	0.345788	1.89	PA
9	3.140292	0.022726	0.229955	1.26	PA
10	3.210122	0.002639	0.498355	2.72	Cho
12	3.240382	0.010395	1.112238	6.08	GPC
14	3.261970	0.004502	0.765134	4.18	Tau
15	3.273710	0.005855	0.266296	1.46	Tau
16	3.350145	0.005025	0.364284	1.99	s-Ins
17	3.420144	0.003587	0.165519	0.91	Tau
18	3.430355	0.003221	0.304644	1.66	Tau
19	3.440427	0.003932	0.153322	0.84	Tau
20	3.533254	0.006419	0.420171	2.30	m-Ins
21	3.550303	0.009344	1.228695	6.71	m-Ins
22	3.563658	0.007292	0.624220	3.41	m-Ins
23	3.626374	0.005949	0.462618	2.53	m-Ins
24	3.640413	0.007434	1.081656	5.91	m-Ins
25	3.655388	0.004813	0.351285	1.92	m-Ins
26	4.070235	0.010123	0.753887	4.12	m-Ins
27	4.120142	0.019891	1.097886	6.00	Lac
(ii) Reconstructed Data (Normal Stromal): $N_P = 600$; Converged (All Resonances Resolved)					
1	1.330148	0.013214	7.154620	39.1	Lac
2	1.490417	0.030360	1.244282	6.80	Ala
3	2.515197	0.010242	0.559927	3.06	Cit
4	2.540235	0.012151	0.977127	5.34	Cit
5	2.720146	0.012203	0.944190	5.16	Cit
6	2.750328	0.009014	0.464776	2.54	Cit
7	3.040309	0.006132	1.396157	7.63	Cr
8	3.100416	0.018432	0.345837	1.89	PA
9	3.140263	0.022761	0.230558	1.26	PA
10	3.210152	0.002613	0.495883	2.71	Cho
11	3.230242	0.010314	0.221409	1.21	PCho

(*Continued*)

Table 6.13 (*Continued*)

n_k^o (Metabolite # k)	$\mathrm{Re}(\nu_k^-)$ (ppm)	$\mathrm{Im}(\nu_k^-)$ (ppm)	$\lvert d_k^- \rvert$ (au)	C_k^- (μM/g ww)	M_k (Assignment)
(ii) Reconstructed Data (Normal Stromal): $N_P = 600$; Converged (All Resonances Resolved)					
12	3.240318	0.005121	0.572736	3.13	GPC
13	3.250298	0.004132	0.329369	1.80	Tau
14	3.260429	0.003821	0.708143	3.87	Tau
15	3.275351	0.005670	0.188472	1.03	Tau
16	3.350137	0.005022	0.364135	1.99	s-Ins
17	3.420319	0.003690	0.175663	0.96	Tau
18	3.430241	0.003012	0.287283	1.57	Tau
19	3.440448	0.004123	0.159195	0.87	Tau
20	3.533243	0.006432	0.420860	2.30	m-Ins
21	3.550326	0.009324	1.225984	6.70	m-Ins
22	3.563639	0.007290	0.625801	3.42	m-Ins
23	3.626378	0.005951	0.462946	2.53	m-Ins
24	3.640411	0.007432	1.081427	5.91	m-Ins
25	3.655389	0.004814	0.351327	1.92	m-Ins
26	4.070235	0.010123	0.753888	4.12	m-Ins
27	4.120142	0.019891	1.097896	6.00	Lac

and computed concentrations for all 27 resonances. Stable convergence was verified at higher partial signal length and the full signal length N.

The absorption component shape spectra at $N_P = 54$ and $N_P = 800$ for the normal stromal prostate data reconstructed by the FPT are presented in Figure 6.21. Eleven of the 27 peaks were identified at $N_P = 54$ (top panel (i)). Only at the two extremes of the spectrum were the peaks resolved with nearly correct heights (lactate and alanine at 1.33 and 1.49 ppm and myoinositol and lactate at 4.07 and 4.12 ppm, respectively). Also, the absorption and dispersive modes were mixed therein. In the dense region from 2.5 to 3.65 ppm, 16 of the 23 peaks were missing. Most of the structures in that region that should have been doublets or triplets, appear as single peaks. For example, the peaks near 3.55 and 3.65 ppm corresponding to myoinositol were seen as singlets, rather than triplets. At $N_P = 800$ (lower panel (ii) of Figure 6.21), all 27 peaks are resolved with the correct heights, including the multiplets and the overlapping peaks of PCho at ≈ 3.23 ppm and GPC at ≈ 3.24 ppm. No dispersive modes appear at $N_P = 800$.

Figure 6.22 displays the Padé-reconstructed total absorption shape spectra at $N_P = 54$ (upper panel (i)) and $N_P = 800$ (bottom panel (ii)) for the normal stromal prostate. As was seen at $N_P = 54$ for the component spectrum, the resonances at the two extremes of the spectrum were resolved and the heights were nearly correct. Within the middle portion of the spectrum, many of the peaks are missing or appear to be single rather than showing serration indicating possible multiplet resonances. For example, two single

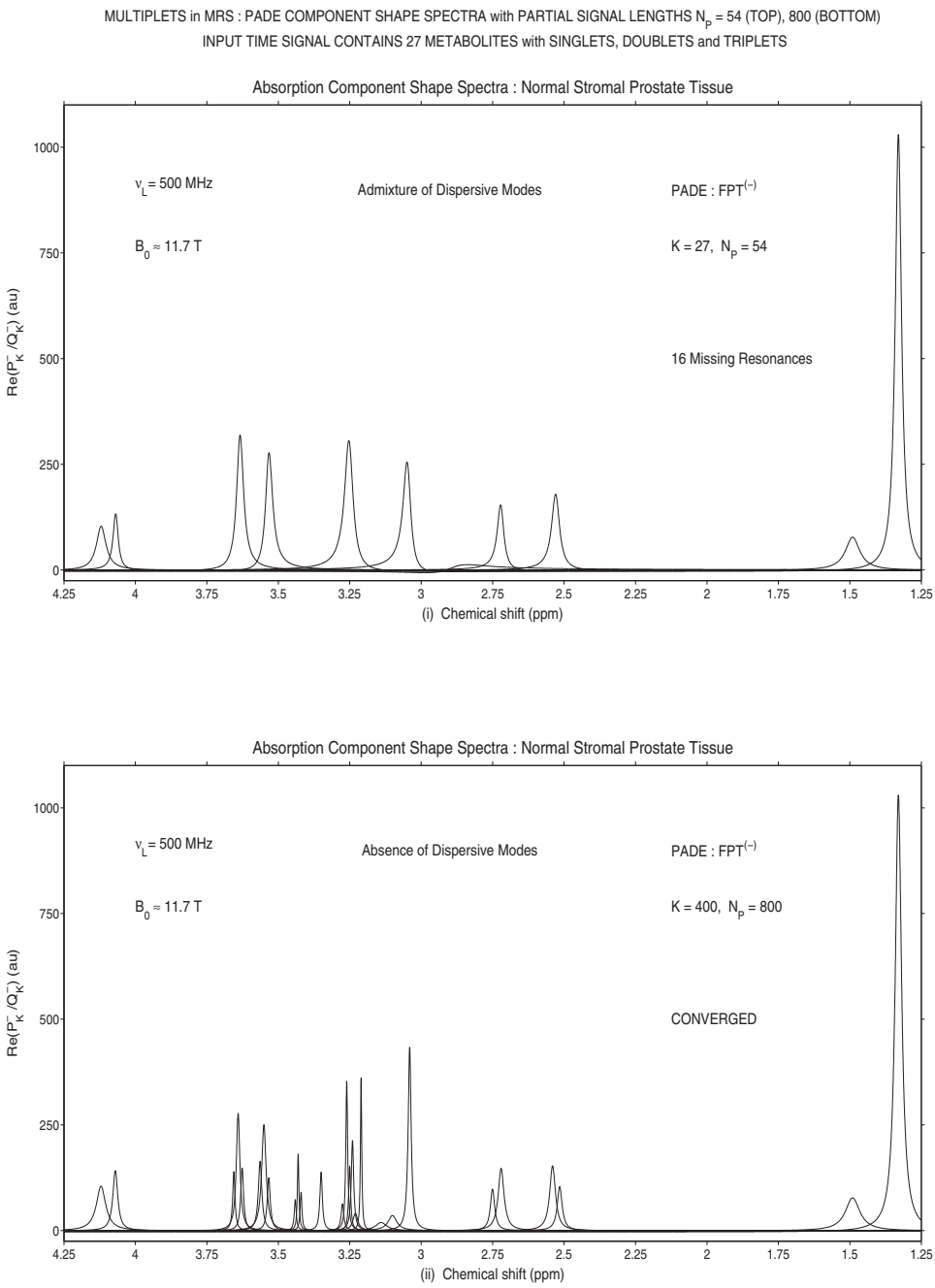

Figure 6.21 Absorption component spectra for normal stromal prostate as reconstructed by the FPT at $N_P = 54$ (top panel (i)) and $N_P = 800$ (bottom panel (ii)), based on in vitro MRS data from Ref. [54].

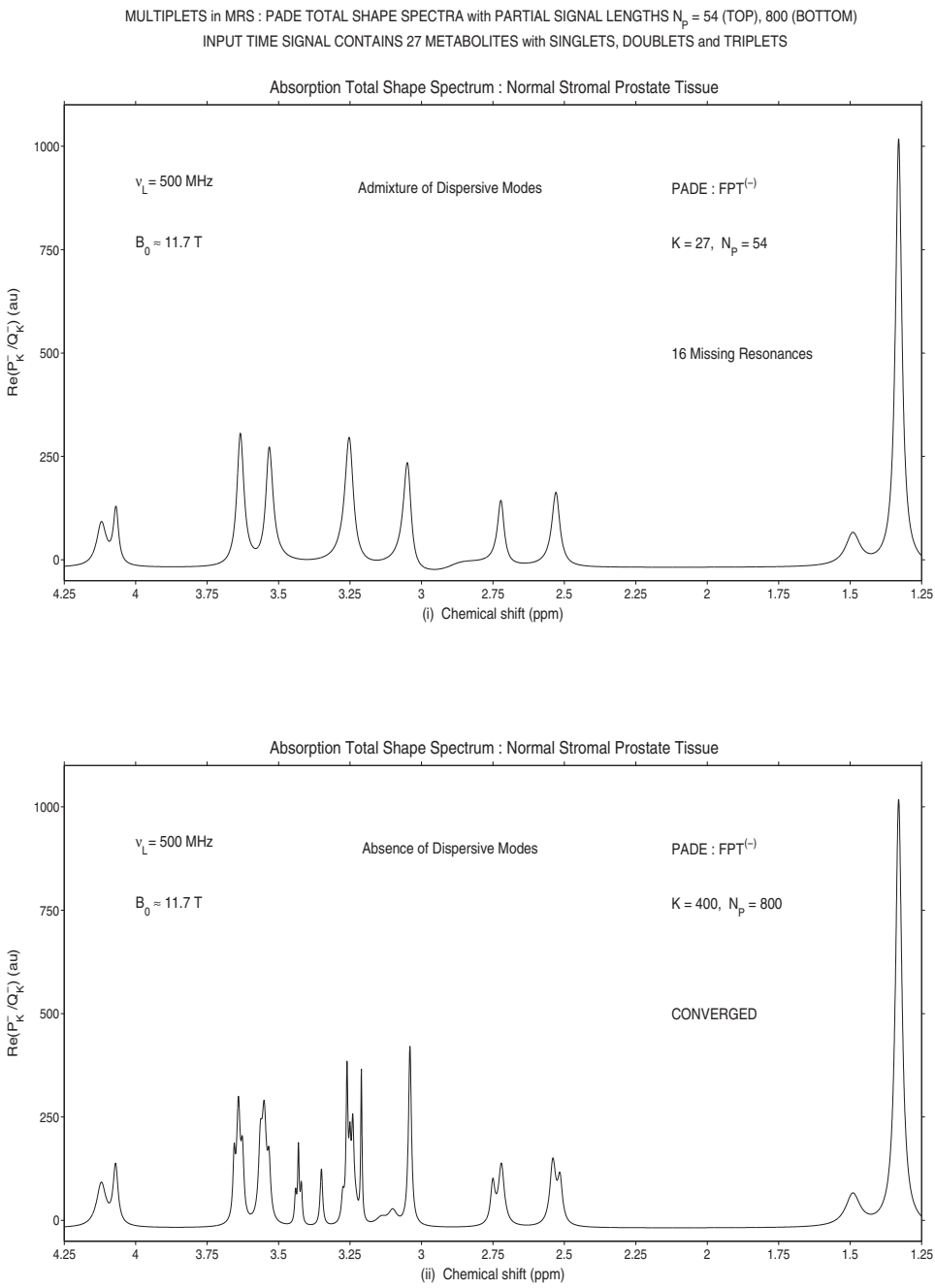

Figure 6.22 Absorption total spectra for normal stromal prostate as reconstructed by the FPT at $N_P = 54$ (top panel (i)) and $N_P = 800$ (bottom panel (ii)), based on in vitro MRS data from Ref. [54].

peaks appear near 3.56 ppm and at 3.64 ppm corresponding to myoinositol, where each should be triply serrated. The lower panel of Figure 6.22 displays the converged total absorption shape spectrum at $N_P = 800$ for normal stromal prostate. Figure 6.23 shows the converged absorption component spectra (upper panel) and the total shape spectrum (lower panel) for normal stromal prostate. Phosphocholine at 3.23 ppm and glycerophosphocholine at 3.24 ppm are clearly distinguished in the component shape spectrum, whereas only one resonance is seen on the total shape spectrum. For the normal stromal prostate, the polyamine peaks are quite minimal, and it would be even more difficult than for the glandular case to specify from the total shape spectrum with certainty that indeed there are exactly two polyamine components.

6.2.3. Malignant prostate tissue

The data for malignant prostate, as reconstructed at $N_P = 500$ and $N_P = 600$ by the FPT are shown in Table 6.14. Prior to convergence at $N_P = 500$ (top panel (i)), one of the 27 resonances, the taurine triplet at 3.250298 ppm, was missing. Lactate at 1.330148 ppm ($k = 1$) and at 4.12042 ($k = 27$) and the myoinositol singlet ($k = 26$) at 4.079235 ppm were reconstructed exactly, whereas Padé-reconstruction of most of the other resonances in the outer regions was nearly so. Most of the computed concentrations had the correct first digits, with the exception of GPC ($k = 12$) that was computed to be twice what it should be. For the malignant prostate data, complete convergence via the FPT was achieved at $N_P = 600$ (bottom panel (ii) of Table 6.14). As reported in the previous cases, convergence was stable at higher partial signal length and at the full signal length N for the malignant prostate data reconstruction.

The absorption component shape spectra for prostate cancer reconstructed by the FPT at $N_P = 54$ and $N_P = 800$ are presented in Figure 6.24. In contrast to the normal prostate spectra, no dispersive modes were observed at $N_P = 54$ (top panel (i)). Sixteen of the 27 peaks were missing at $N_P = 54$. As was observed in the previous two cases, the resonances were resolved with nearly correct heights at the outermost parts of the spectrum. In the spectrally dense middle region, 16 of 23 peaks were missing. The citrate resonances around 2.5 and 2.75 ppm were seen as single peaks, rather than the two doublets that should have appeared. The myoinositol resonances around 3.55 and 3.65 ppm also were single, when there should be triplets. On the lower panel (ii) of Figure 6.24, at $N_P = 800$, it is seen that all 27 resonances were resolved with the correct heights, positions, and widths.

The total absorption shape spectra reconstructed by the FPT at $N_P = 54$ (upper panel (i)) and $N_P = 800$ (lower panel (ii)) for the prostate cancer data are shown in Figure 6.25. Similar to what was seen for the component absorption spectrum for the prostate cancer data, lactate and alanine at 1.33 ppm and 1.49 ppm and myoinositol and lactate at 4.07 ppm and

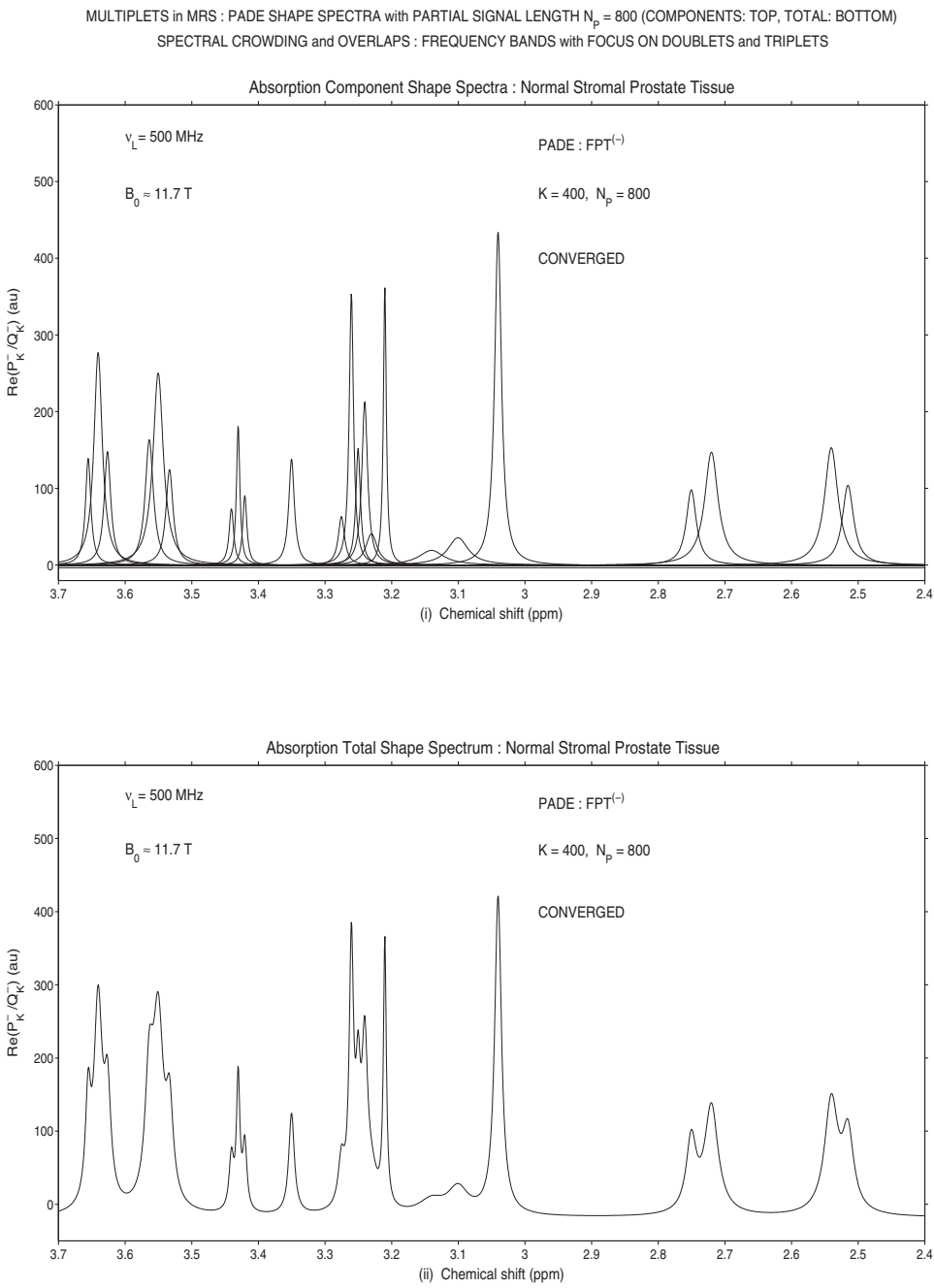

Figure 6.23 Converged absorption component shape spectra (panel (i)) and converged absorption total shape spectra (panel (ii)) for normal stromal prostate reconstructed by the FPT based on in vitro MRS data derived from Ref. [54].

Table 6.14 Spectral parameters and metabolite concentrations reconstructed by the FPT for cancerous prostate with the input data based on Ref. [54].

Convergence of Spectral Parameters and Concentrations in FPT$^{(-)}$: Partial Signal Lengths $N_P = 500, 600$					
n_k^o (Metabolite # k)	Re(ν_k^-) (ppm)	Im(ν_k^-) (ppm)	$\lvert d_k^- \rvert$ (au)	C_k^- (μM/g ww)	M_k (Assignment)
(i) Reconstructed Data (Malignant): $N_P = 500$; Missing Resonance: # 13 (Tau)					
1	1.330148	0.013213	11.07045	60.5	Lac
2	1.490417	0.030362	2.305586	12.6	Ala
3	2.515197	0.016240	0.680689	3.72	Cit
4	2.540235	0.020952	1.185733	6.48	Cit
5	2.720146	0.020204	1.152776	6.30	Cit
6	2.750328	0.018213	0.567253	3.10	Cit
7	3.040309	0.006951	1.780424	9.73	Cr
8	3.100418	0.021437	0.580318	3.17	PA
9	3.140233	0.032708	0.384660	2.10	PA
10	3.210153	0.002834	0.829223	4.53	Cho
11	3.229878	0.004204	1.252506	6.84	PCho
12	3.246399	0.012406	0.950890	5.20	GPC
14	3.261533	0.002729	0.625188	3.42	Tau
15	3.274760	0.006965	0.288772	1.58	Tau
16	3.350140	0.004321	0.458939	2.51	s-Ins
17	3.420142	0.003723	0.187071	1.02	Tau
18	3.430390	0.001404	0.309790	1.69	Tau
19	3.440276	0.003813	0.180274	0.98	Tau
20	3.533235	0.006428	0.547676	2.99	m-Ins
21	3.550337	0.010342	1.605352	8.77	m-Ins
22	3.563644	0.007281	0.815504	4.46	m-Ins
23	3.626378	0.005954	0.611484	3.34	m-Ins
24	3.640413	0.009432	1.424954	7.79	m-Ins
25	3.655388	0.004812	0.461176	2.52	m-Ins
26	4.070235	0.012421	0.993596	5.43	m-Ins
27	4.120142	0.012890	1.701738	9.30	Lac
(ii) Reconstructed Data (Malignant): $N_P = 600$; Converged (All Resonances Resolved)					
1	1.330148	0.013213	11.07045	60.5	Lac
2	1.490417	0.030362	2.305581	12.6	Ala
3	2.515197	0.016240	0.680695	3.72	Cit
4	2.540235	0.020952	1.185727	6.48	Cit
5	2.720146	0.020204	1.152790	6.30	Cit
6	2.750328	0.018213	0.567246	3.10	Cit
7	3.040309	0.006951	1.780421	9.73	Cr
8	3.100416	0.021434	0.580055	3.17	PA
9	3.140263	0.032762	0.386093	2.11	PA
10	3.210152	0.002814	0.823422	4.50	Cho

(*Continued*)

Table 6.14 (*Continued*)

n_k^o (Metabolite # k)	Re(ν_k^-) (ppm)	Im(ν_k^-) (ppm)	$\lvert d_k^- \rvert$ (au)	C_k^- (μM/g ww)	M_k (Assignment)
(ii) Reconstructed Data (Malignant): $N_P = 600$; Converged (All Resonances Resolved)					
11	3.230242	0.003952	1.235133	6.75	PCho
12	3.240318	0.005890	0.473925	2.59	GPC
13	3.250298	0.004123	0.364135	1.99	Tau
14	3.260429	0.003141	0.781336	4.27	Tau
15	3.275351	0.005672	0.208600	1.14	Tau
16	3.350137	0.004324	0.459286	2.51	s-Ins
17	3.420319	0.003626	0.190302	1.04	Tau
18	3.430241	0.001426	0.312900	1.71	Tau
19	3.440448	0.003821	0.173833	0.95	Tau
20	3.533243	0.006434	0.548948	3.00	m-Ins
21	3.550326	0.010323	1.601098	8.75	m-Ins
22	3.563639	0.007291	0.817932	4.47	m-Ins
23	3.626378	0.005952	0.611162	3.34	m-Ins
24	3.640411	0.009434	1.425435	7.79	m-Ins
25	3.655389	0.004812	0.461116	2.52	m-Ins
26	4.070235	0.012421	0.993596	5.43	m-Ins
27	4.120142	0.012890	1.701738	9.30	Lac

4.12 ppm were resolved and heights were nearly correct at $N_P = 54$. The expected serrations in a number of the resonances are missing, so that singlets appear, for example, for the citrate peaks near 2.5 and 2.75 ppm, and several peaks are entirely absent such as scylloinositol at 3.35 ppm. At $N_P = 800$, the total absorption shape spectrum is converged (bottom panel of Figure 6.25).

The converged absorption component shape spectrum (top panel (i)) and total absorption shape spectrum (lower panel (ii)) for prostate cancer between 2.40 and 3.70 ppm at $N_P = 800$ are compared in Figure 6.26. Strikingly, the serrated peaks on the total shape spectrum only suggest the number of underlying resonances. The converged component spectrum is essential to visualize the actual number and structure of resonances. For example, from the small polyamine peaks, it would be difficult to know that there are actually two components.

On the total shape spectrum, the citrate doublets around 2.53 and 2.73 ppm look like broad peaks, and there is only a hint of the doublet structures shown in the component spectra. Although phosphocholine at 3.23 ppm and glycerophosphocholine at 3.24 ppm are clearly distinguished in the component shape spectrum, that is not at all true on the total shape spectrum.

6.2.4. Comparisons of MRS data for normal and malignant prostate

The absorption component shape spectra for normal glandular prostate (upper panel (i)), normal stromal prostate (middle panel (ii)), and prostate

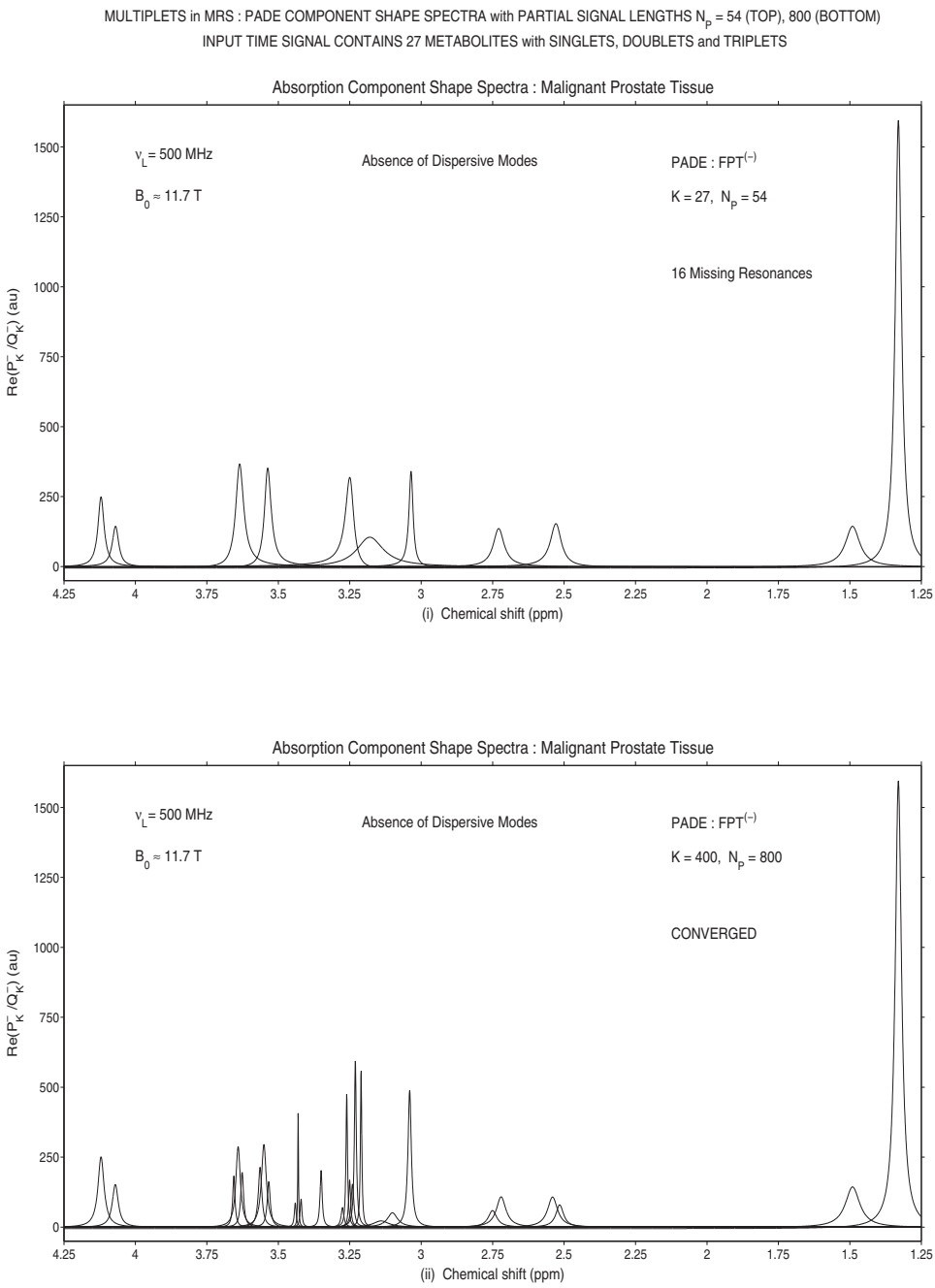

Figure 6.24 Convergence of the absorption component spectra in the FPT for prostate cancer based on in vitro MRS data from Ref. [54].

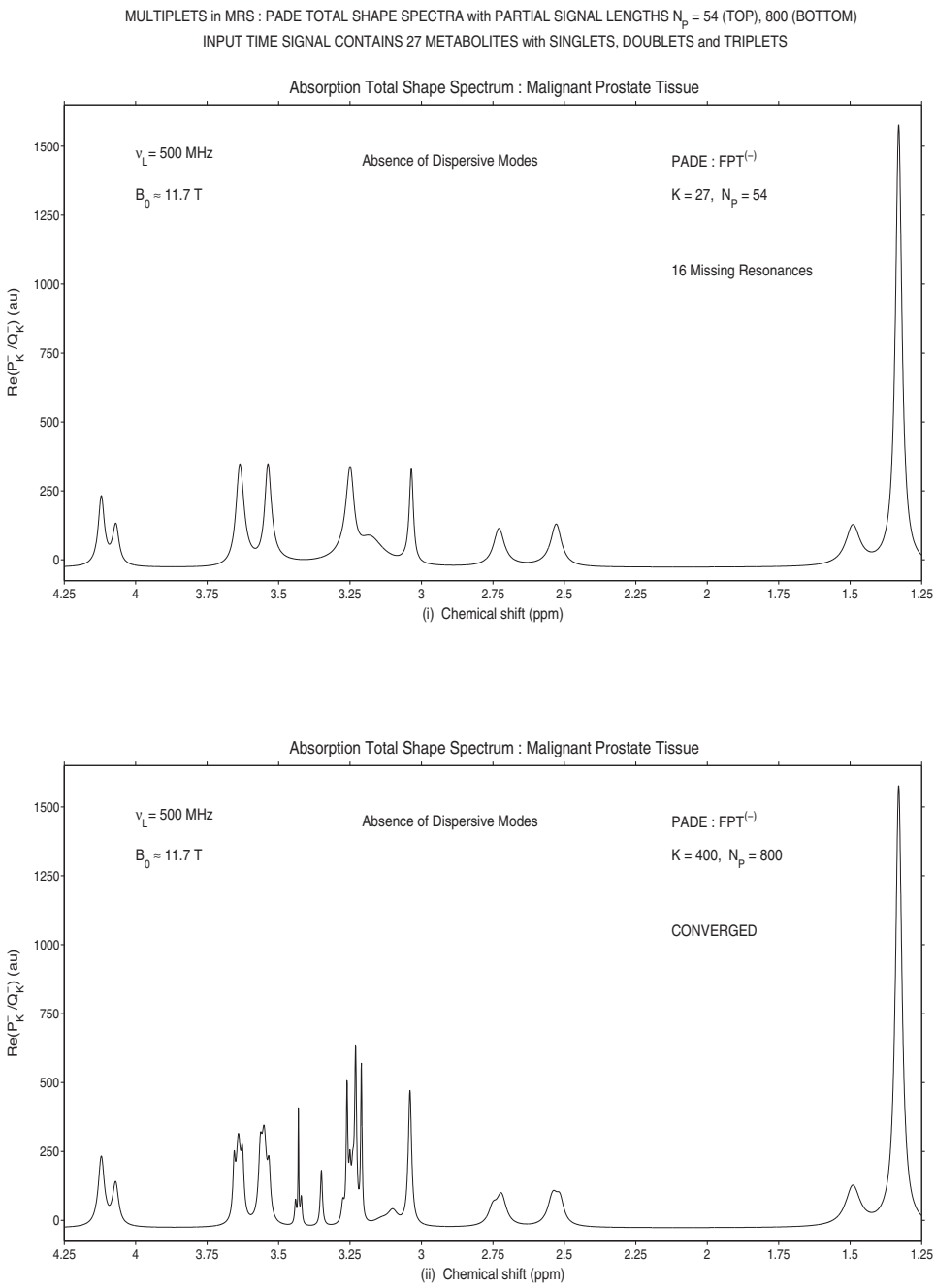

Figure 6.25 Absorption total shape spectra reconstructed by the FPT for MRS prostate cancer data as encoded in vitro in Ref. [54]. The upper panel (i) is at $N_P = 54$ and the converged spectrum at $N_P = 800$ is shown on the lower panel (ii).

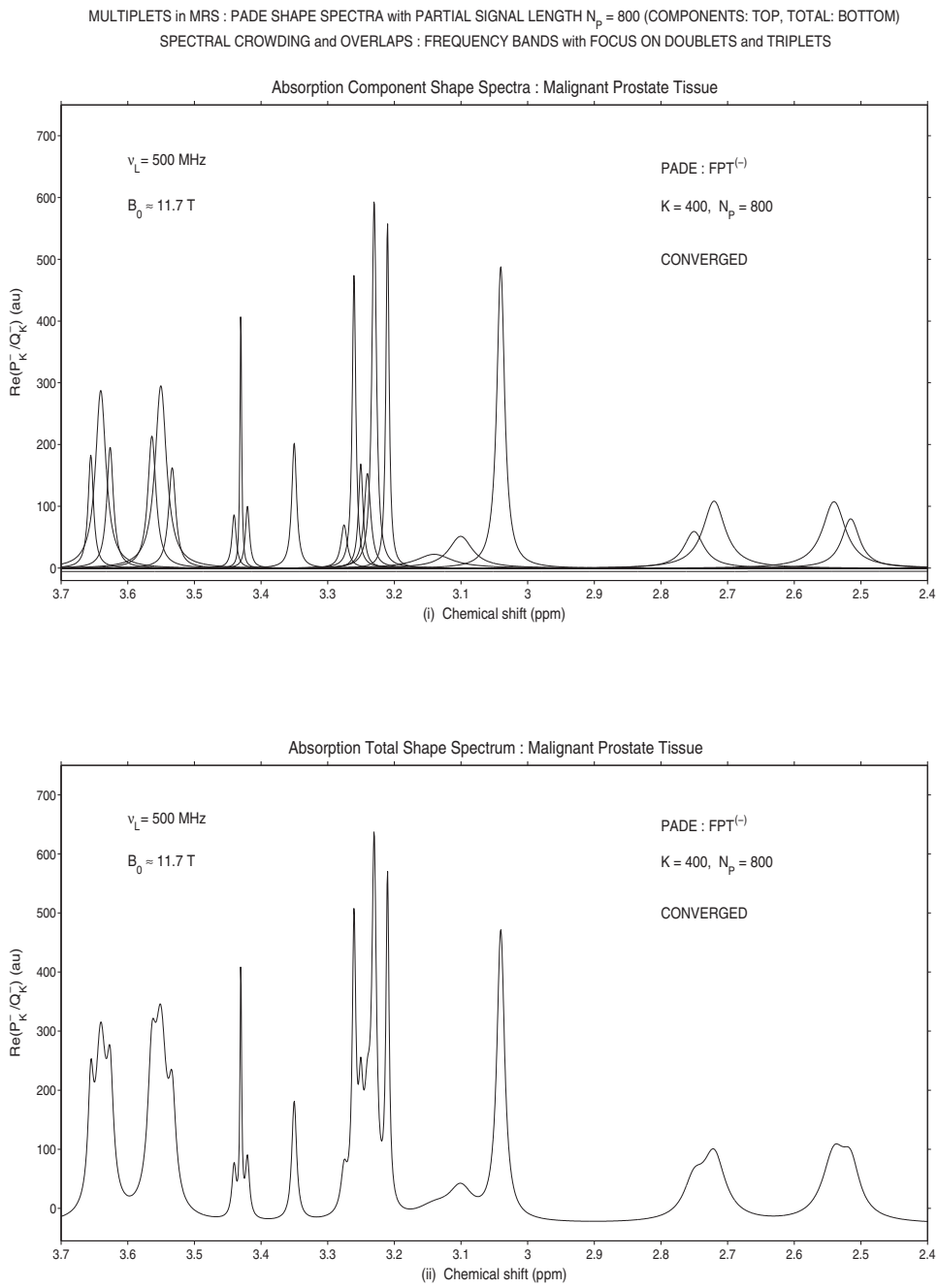

Figure 6.26 Converged absorption component shape spectra (panel (i)) and converged absorption total shape spectra (panel (ii)) for prostate cancer data as reconstructed by the FPT based on in vitro MRS data from Ref. [54].

cancer data (lower panel (iii)) are compared in Figure 6.27. Figure 6.28 presents the converged total shape spectra for these three cases. The largest resonances for the normal glandular prostate besides the lactate peak at 1.33 ppm are the doublets of citrate at 2.5 and 2.75 ppm, creatine at 3.04 ppm, and tall, narrow choline peak at 3.21 ppm. The two polyamine peaks centered at 3.10 and 3.14 ppm are broad, large, and distinct on the absorption component shape spectrum. In contradistinction, on the total shape spectrum for the glandular prostate, the suggestion of a leftward shoulder around 3.14 ppm is the only hint that there is a second polyamine component.

Normal glandular and normal stromal prostate show markedly different spectral patterns. Most notably, the resonances are much smaller in the stromal tissue. Lactate at 1.33 ppm and creatine at 3.04 ppm are the most prominent structures. The lactate peaks at 1.33 and 4.12 ppm are larger in the prostate cancer spectra compared with the two normal prostate tissues. The choline components at 3.21–3.24 ppm (i.e., total choline) are more abundant than creatine at 3.04 ppm. The spectrum for prostate cancer differs most clearly from that of normal glandular prostate, particularly in the spectrum for prostate cancer the citrate doublet peaks and the two polyamine resonances are much smaller than the components of choline.

Figures 6.29 and 6.30, respectively, show the converged absorption component and total shape spectra for normal glandular prostate (upper panels (i)), normal stromal prostate (middle panels (ii)), and prostate cancer data (lower panels (iii)) within the spectral region between 2.40 and 3.70 ppm at $N_P = 800$. The component spectra clearly distinguish PCho and GPC, which is not the case for the total shape spectra.

6.2.5. Discussion

In this section concerning normal and malignant prostate tissue, it is demonstrated that the FPT clearly resolves and precisely quantifies multiplet resonances. This is particularly noteworthy for regions with otherwise very high spectral density. Relying on the FFT and fitting via the Levenberg–Marquardt algorithm, it is stated in Ref. [54] that overlapping resonances undermine the accuracy of quantification. Integrating peak areas in total absorption spectra as generated by the FFT is inevitably a tenuous procedure. Notably, the upper and lower integration limits are set in an arbitrary, subjective manner even if the peaks are isolated. Whenever there is peak overlap, the obstacles to quantification become practically insurmountable [55]. The FPT not only provides the possibility to exactly extract all the complex frequencies and amplitudes for all the resonances but also determines their true number with complete certainty. Hence, unique and reliable quantification, even for the highly challenging problem of multiplet resonances, is seen in prostate spectra. As discussed, the "spectral crowding" problem does not hamper the FPT. Via parametric analysis, without fitting or numerical integration of peak

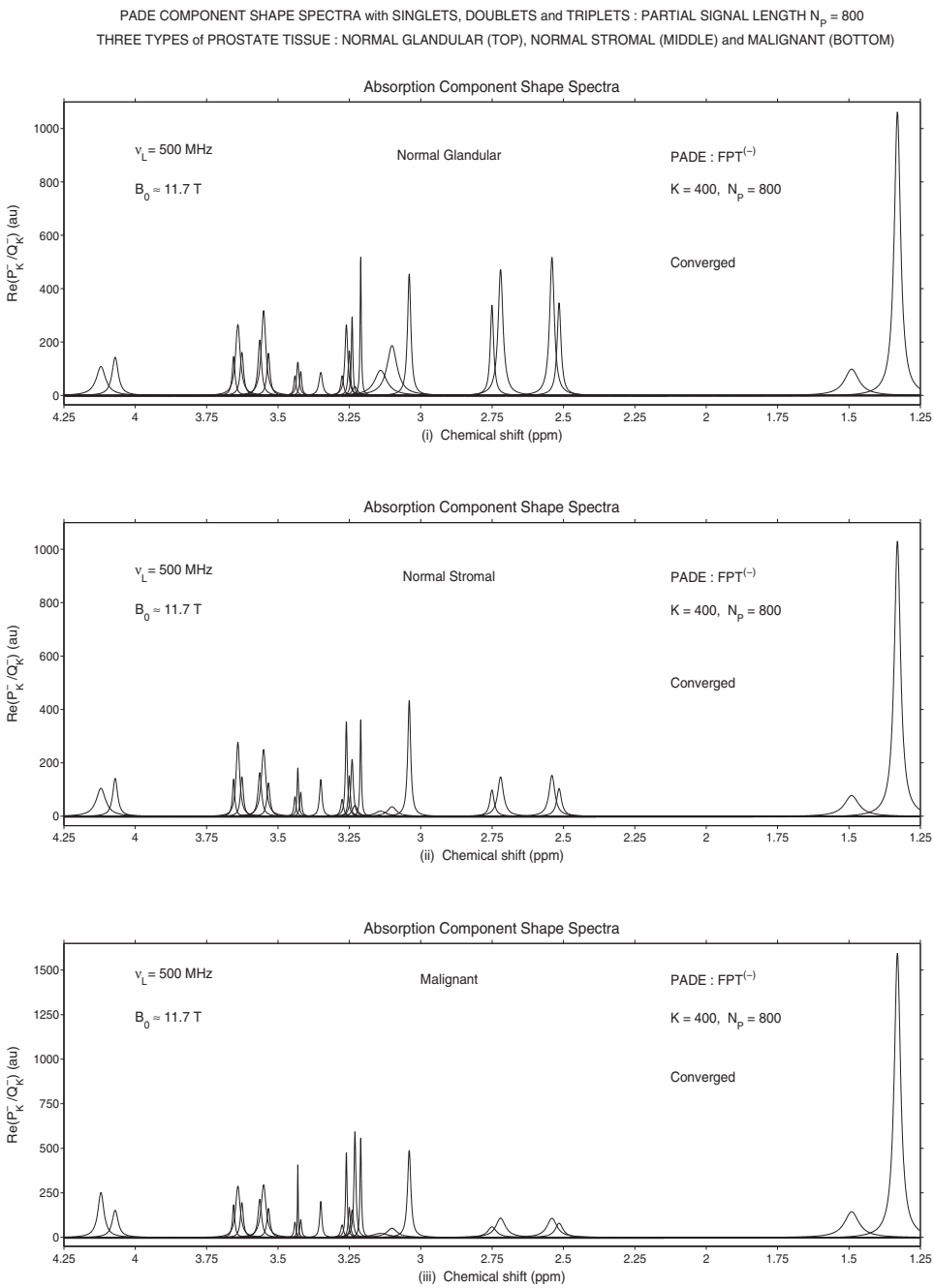

Figure 6.27 Absorption component spectra at $N_P = 800$ (converged) for normal glandular prostate (panel (i)), normal stromal prostate (panel (ii)) and prostate cancer(panel (iii)) based on in vitro MRS data from Ref. [54].

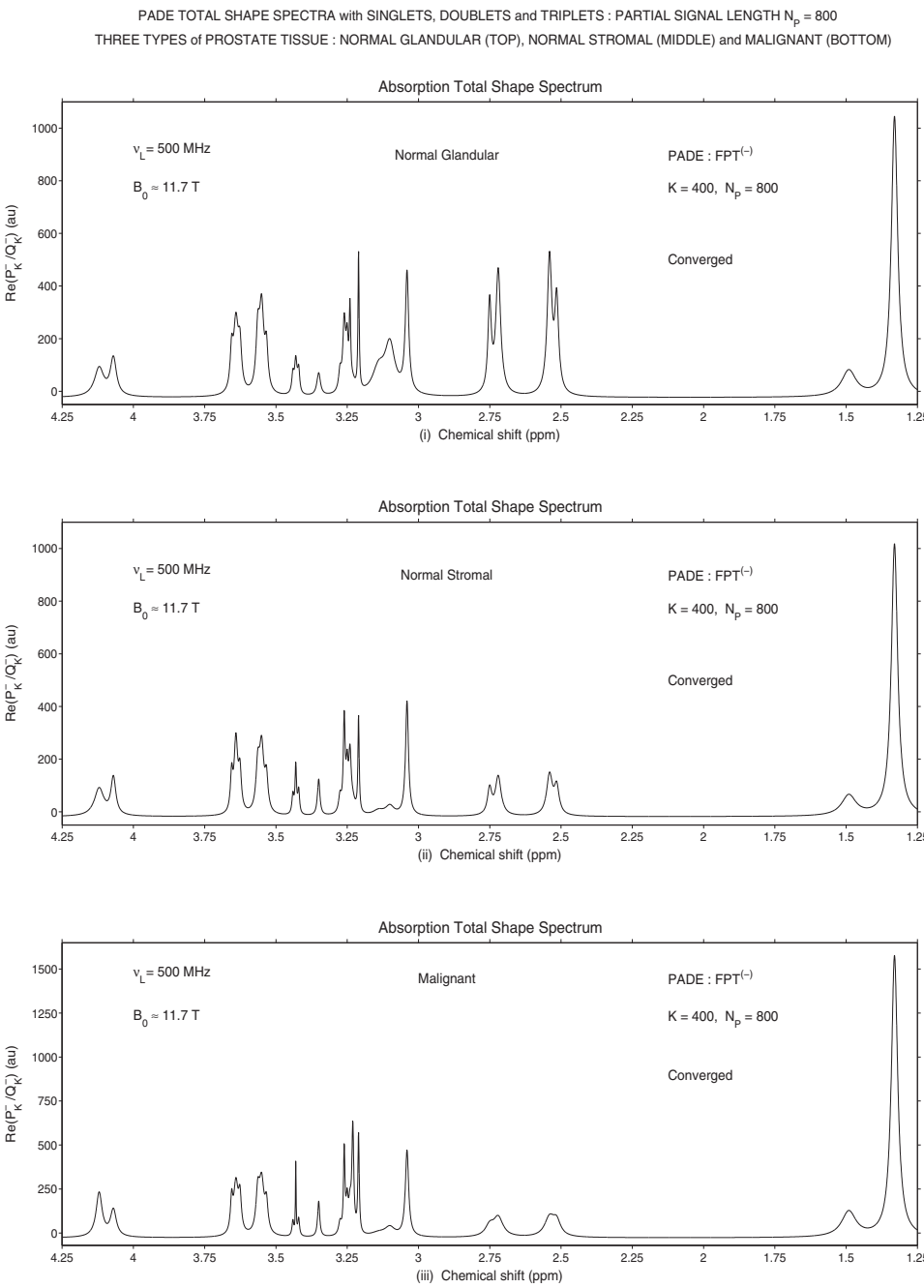

Figure 6.28 Absorption total shape spectra at $N_P = 800$ (converged) for normal glandular prostate (panel (i)), normal stromal prostate (panel (ii)) and prostate cancer (panel (iii)) based on in vitro MRS data from Ref. [54].

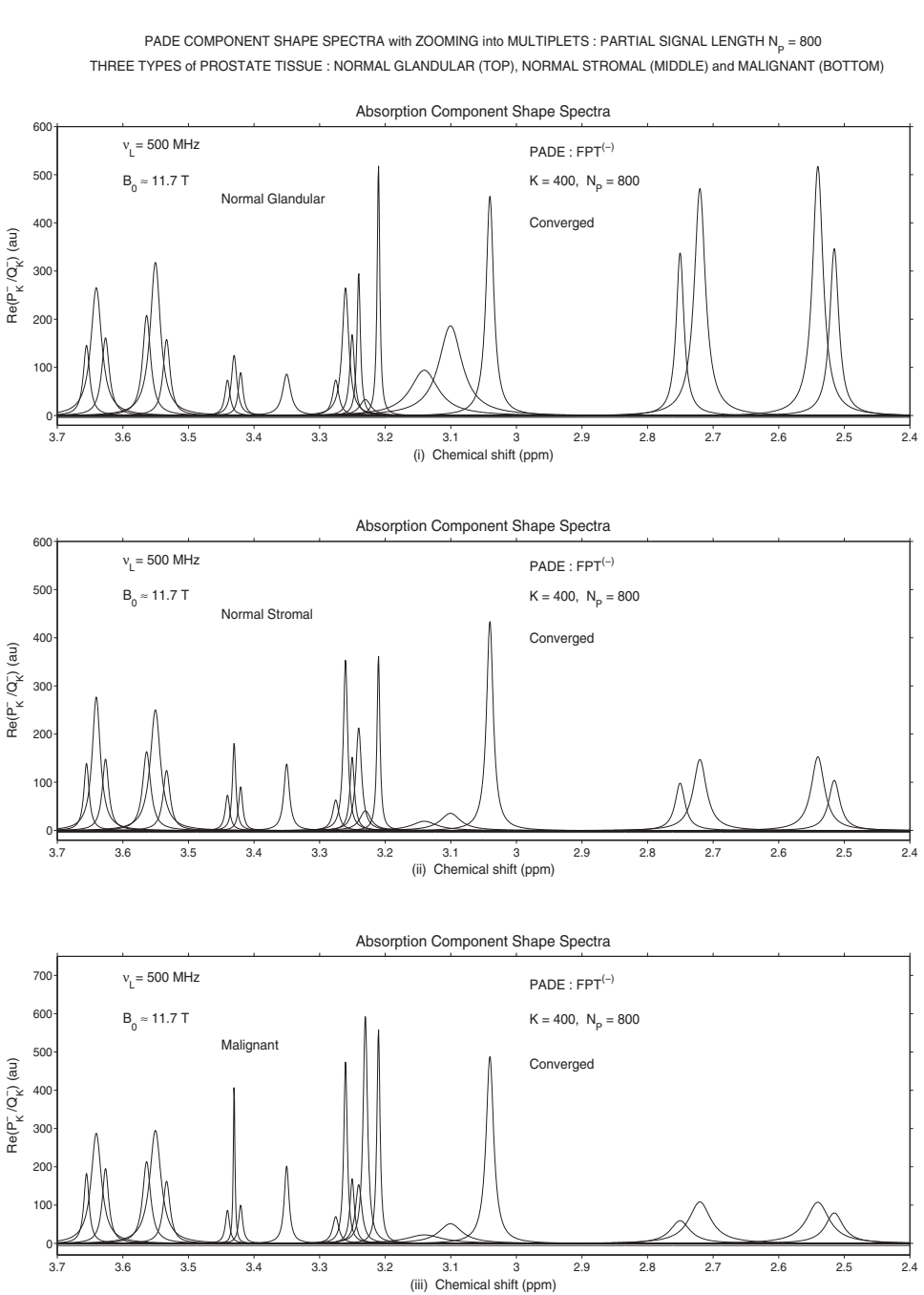

Figure 6.29 Absorption component spectra at $N_P = 800$ (converged) as reconstructed by the FPT for normal glandular prostate (panel (i)), normal stromal prostate (panel (ii)) and prostate cancer (panel (iii)) within the spectral region between 2.4 and 3.7 ppm based on in vitro MRS data from Ref. [54].

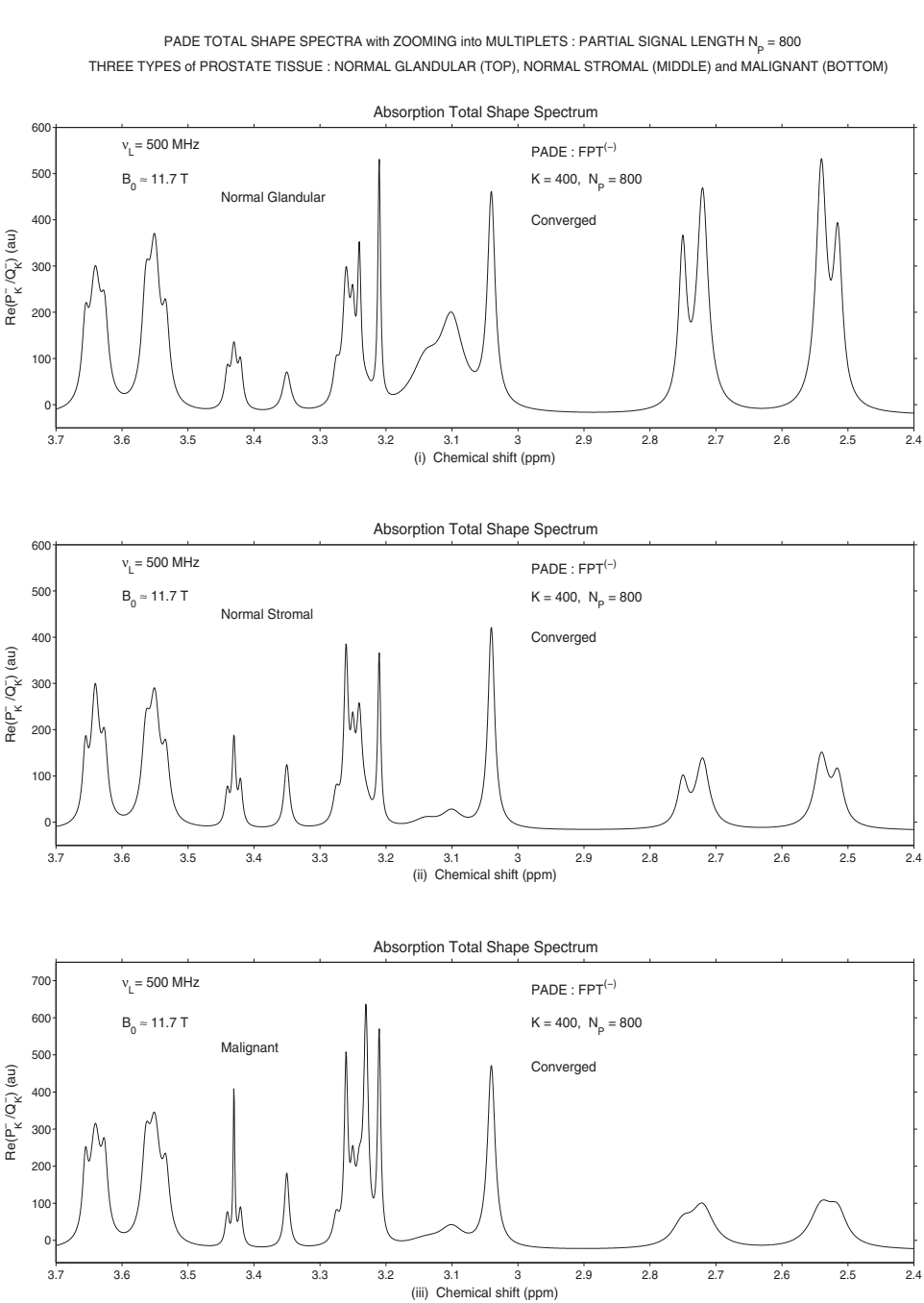

Figure 6.30 Absorption total shape spectra at $N_P = 800$ (converged) as reconstructed by the FPT for normal glandular prostate (panel (i)), normal stromal prostate (panel (ii)) and prostate cancer (panel (iii)) within the spectral region between 2.4 and 3.7 ppm based on in vitro MRS data from Ref. [54].

areas, the FPT reconstructed all the multiplets and closely overlying peaks from different metabolites for all three prostate problems examined herein.

Convergence was achieved at $N_P = 700$ for normal glandular prostate data, whereas for the normal stromal and the malignant data, this occurred at $N_P = 600$. Since $2K = N_P$, there were 350, 300, and 300 resonances, respectively for the normal glandular prostate, normal stromal tissue, and cancerous prostate. However, only 27 of these resonances were genuine, the remaining 323 and 273, respectively, were spurious. The latter were identified as such by their zero amplitudes and the pole–zero coincidences. Consequently, there were more than a factor of 10 more spurious resonances than genuine ones. The ratio of spurious to genuine resonances for the prostate spectra was much larger than for the ovarian spectra, but fewer than for the breast spectra, as presented in the preceding sections. This seems to reflect rather subtle aspects of spectral processing, such as the smallest distance among the poles and zeros, the density of poles and zeros in the complex plane, as well as interseparations among poles and zeros [3].

For these prostate spectra, theoretically it would be possible to retrieve all 27 input resonances at $N_P = 54$, since there are 54 unknowns (27 complex frequencies and 27 complex amplitudes) with 54 linear equations and 54 signal points needed. In fact, at $N_P = 54$, precisely 27 resonances were retrieved. However, 15 of these were spurious for the normal glandular prostate, and 16 were spurious for the normal stromal prostate and malignant prostate. The pole–zero cancellations with zero-valued amplitudes were used to identify these resonances as spurious.

It appears that convergence began in the outermost spectral regions. The most spectrally dense inner region achieved convergence subsequently. The last resonances to converge were those closest to the real axis, and thus having the smallest imaginary part of ν_k^-. Interestingly, at a very few signal points before convergence, an admixture of the absorption and dispersive modes was still apparent for the two normal prostate problems. However, once convergence occurred, and thereafter, the dispersive mode completely disappeared such that the absorption spectrum was entirely in the absorption mode, in other words, the real part of the complex-valued spectrum.

The stability of convergence was confirmed at longer partial signal lengths and at the total signal length for the three prostate cases. This has been true as well for our other applications of the FPT to MRS time signals as noted in the previous sections. Near convergence, at partial signal lengths $N_P = 600$ for the normal glandular data and at $N_P = 500$ for the normal stromal data, the phosphocholine resonance was still not resolved. Consequently, the retrieved concentration of glycerophosphocholine was overestimated by approximately the amount of the missing concentration of PCho. Even for the malignant prostate data, although PCho was resolved prior to convergence, at $N_P = 500$, the concentration of GPC was still overestimated by

about a factor of two. Recall that the so-called "glycerophosphocholine to phosphocholine switch" is reportedly an indicator of malignant transformation for breast [35]. The demonstrated capacity of the FPT to determine the precise point of convergence and then to exactly quantify these very closely overlying components of choline thus becomes very relevant for possibilities to improve cancer diagnostics through MRS.

In the present section, we have focused on prostate cancer, which is the most common cancer among men in the United States and in much of Europe, and a major cause of cancer deaths worldwide. We have discussed the dilemmas concerning screening, early detection, and aspects of clinical decision making regarding prostate cancer. Relying on conventional Fourier-based data analysis, in vivo MRSI has made important strides in improving the accuracy with which prostatic tumor and extracapsular extension are identified, as well as helping to distinguish cancerous prostate from benign prostatic hypertrophy.

In vivo MRSI has also contributed to various aspects of clinical management of this malignancy. Nevertheless, major challenges and difficulties remain, and as of today, none of the existing noninvasive methods for prostate cancer diagnostics have sufficient sensitivity and specificity to be broadly recommended for screening and other aspects of surveillance. It would obviously be premature to render definitive conclusions about the role of the Padé-optimized MRSI in solving these dilemmas. From the input data of Ref. [54] for a fairly small number of prostate cancer samples, it cannot be stated with certainty which metabolites are best for identifying prostate cancer and distinguishing this from normal stromal and glandular prostate. Moreover, unfortunately, only the means and standard deviations of the computed concentrations were given in Ref. [54] for the three types of tissue. Data from the individual patients or the minimum and maximum of the computed concentrations would have been valuable. Notwithstanding these limitations, it is still clear that there is a far richer source of spectral information to identify prostate cancer than is currently used with Fourier-based in vivo MRS. Padé-optimized MRSI with its capability to unequivocally resolve and quantify multiplet resonances and otherwise exceedingly challenging spectra with many overlapping resonances could undoubtedly provide valuable information for improving prostate cancer diagnostics.

Given the density of the MR spectra of the prostate, with the challenge of deciphering numerous multiplet resonances, the FPT resolved these spectra at relatively short signal lengths. This rapid and stable convergence provided by the FPT could improve resolution, which, despite technological advances in, for example, coil design [56] or use of increased magnetic field strength [57], represents a major limitation to wider application of MRS and MRSI for prostate cancer diagnostics [41]. On the basis of these results, we conclude that Padé optimization of MRS is a promising avenue of research

for improving prostate cancer diagnostics. Considering that prostate cancer is a major cause of morbidity and mortality among men in many developed countries, progress in this area would have important public health implications.

7. CONNECTION OF MRS DIAGNOSTICS WITH DOSE-PLANNING SYSTEMS IN RADIOTHERAPY

In this section, we shall address a potentially useful link of MRS diagnostics with radiotherapy. One of the possibilities in this direction could be the use of the cell survival probabilities to assess changes in MRS-quantified metabolite concentrations after radiotherapy. This could help in delineating the target volume for patients who undergo re-irradiation. Experimental data exist on integral intensities $I(D)$ of spectral lineshapes with the underlying concentrations of a number of diagnostically relevant metabolites (NAA, Cre, Cho,...) as a function of the absorbed dose D. Such observables for cyclic variations of concentrations of K metabolites in an irradiated tissue with J compartments could be modeled via $I(D) = \sum_{j=1}^{J} A_j \sum_{k=1}^{K} S_{jk}(D)$, where A_j are the oscillation amplitudes. Here, $S_{jk}(D)$ are the cell-surviving fractions for which many mathematical expressions have been accumulated over a period longer than a half century in the abundant literature on the related radiobiological modelings. Both accurate reconstructions of metabolite concentrations for the MRS data and reliable radiobiological modelings of cell-surviving fractions are critical to the success of analysis, interpretation, and possible usefulness of $I(D)$ in the target volume definition for dose-planning systems in radiotherapy. The Padé-based quantification of MRS data is accurate and, therefore, the fast Padé transform is deemed the most appropriate to provide the reliable concentrations as the diagnostic part of the input to $I(D)$. As to the radiotherapeutic part of $I(D)$ in regard to dose-planning systems, we shall analyze in this section the well-known linear-quadratic (LQ) model with the conventional cell kill and cell repair, both of which will be originally derived here from the mechanistic viewpoint. Further, by exploiting the unprecedented power of the Padé approximant across interdisciplinary research, we will presently derive an alternative and more realistic theory called the Padé linear-quadratic (PLQ) model for cell-surviving fractions after irradiation. In a forthcoming publication, we shall connect the two parts, diagnostics by MRS and dose-planning systems via radiobiological modeling of cell-surviving fractions, into a single, comprehensive theory for $I(D)$. Having shown the reliability of the Padé-based MRS diagnostics via the fast Padé transform, we will now assess the performance of the Padé-optimized cell-surviving fractions after irradiation by using the PLQ model.

7.1. PLQ model for cell survival probabilities after irradiation

The two most salient aspects of the cell-surviving fraction, $S_F(D)$, are the direct cell kill and cell repair. They can be simultaneously taken into account by introducing a biological dose D_B to be determined for the given physical dose D. The sought dose D_B can be found from the Poisson statistics. In the context of radiation damage, the targeted cell is certain to survive if it receives no dose when the dose D_B is expected to be absorbed. The chance for such an event to occur is given by the Poisson probability $P(0) = e^{-\mu D_B}$, where μ is a constant in units of Gy^{-1}. The constant $\mu \geq 0$ is related to the repair time τ during which the cell becomes effectively insensitive to any two consecutive hits (events, particle, or ray traversals through the treated tissue) whenever they follow each other within the time interval Δt which is smaller than τ. When the repair mechanism is activated, the administered physical dose D is only apparent, whereas the true dose, which is actually received by the cell, is the biological dose D_B. Repair modulates D and transforms it to D_B. The only difference between D and D_B is that the latter accounts for a correction due to the missed/wasted hits during the time lag $\Delta t < \tau$ whenever $\tau > 0$. Such a discrepancy between D and D_B is given precisely by the said Poisson probability $P(0)$. This settles the problem of the definition of D_B for a fixed D as $D_B P(0) = D$, or $D_B e^{-\mu D_B} = D$. If D_B were known, the dose which was applied to the tissue could be retrieved by a direct and straightforward computation of the Ricker function $D_B e^{-\mu D_B}$, which would then give D. In reality, however, the biological dose D_B is unknown, but could nevertheless be determined by finding the inverse function of the Ricker function. This exact inverse gives D_B through the Lambert W or Euler tree T function, as recently discussed by Belkić [58]. As a plausible alternative, we shall presently derive a more manageable approximate solution for D_B from the stated implicit, transcendental equation, $D_B = De^{\mu D_B}$, by using only the simplest elementary functions. Assuming that the recovery time is short ($\tau \ll 1$) or $\mu \ll 1$, we are justified to retain only the first two terms of the series $e^{\mu D_B} = 1 + (\mu D)/1! + (\mu D)^2/2! + \cdots$, so that $D_B = De^{\mu D_B} \approx D(1 + \mu D_B)$ or $D_B \approx D/(1 - \mu D)$. Here, the expression $D/(1 - \mu D)$ is the first-order diagonal Padé approximant [1/1] in the variable D. This Padé approximant can further be simplified by employing the binomial series $1/(1 - \mu D) = 1 + (\mu D) + (\mu D)^2 + \cdots$ and consistently keeping solely the first two terms for $\mu \ll 1$. We then finally arrive at $D_B \approx D(1 + \mu D)$. The obtained approximate solution of the equation $D_B e^{-\mu D_B} = D$ for D_B is the sum of the linear ($\sim D$) and quadratic ($\sim D^2$) terms. Without repair, all the impinging radiation quanta would be absorbed by the targeted cell, so that $\tau = 0\,(\mu = 0)$, which gives $D_B = D$. However, with repair, there will be some wasted radiation quanta, as if they were removed from the beam or annihilated in the traversed tissue, in which case $\tau > 0\,(\mu > 0)$, and this gives the quadratic term $\sim D^2$. Our derivation shows that the quadratic term $\sim D^2$

is directly rooted in the cell-repair mechanism and brought about by reconstruction of the unknown biological dose D_{B} from the given physical dose D. This gives an approximate and plausible answer to the inverse dose problem: given the physical dose D applied to the irradiated cells, what would be the biological dose D_{B} received by the cells when the cell repair system is active? The derived answer $D_{\mathrm{B}} \approx D(1+\mu D)$ represents an approximate dose–effect relationship. In radiobiological modeling of cell-surviving fractions, the word "effect" actually refers to the quantity $\mathrm{E}(D) \equiv \alpha D_{\mathrm{B}}$, where $\alpha \geq 0$ is the radiation sensitivity parameter, which is expressed in units of Gy^{-1}. Thus, we can write $\mathrm{E}(D) \approx \alpha D + \beta D^2$, where $\beta = \mu\alpha \geq 0$. Parameters α and β are usually associated in a distinct way with the cell kill and cell repair per Gy^{-1} and Gy^{-2}. However, in the present derivation of the effect $\mathrm{E}(D)$, these two parameters are not independent of each other due to their correlation via $\beta = \alpha\mu$. Thus, if μ were known, only α would be a free parameter when reconstructing $\mathrm{E}(D)$ from its adjustment to the corresponding experimental data. Parameter $\mu = \beta/\alpha$ is the measure of the deviation of the parabola $\alpha D + \beta D^2$ from the straight line αD plotted versus D as the abscissa. The higher the μ, the more parabolic $\mathrm{E}(D)$ and the more significant the repair pathway, βD^2. Conversely, the lower the μ, the more straight-line behavior of $\mathrm{E}(D)$ and the more pronounced the cell kill, αD. Such a feature is also directly reflected in the Poisson-prescribed cell-surviving function $S_{\mathrm{F}}(D)$ which is introduced by taking the exponential of the effect via $S_{\mathrm{F}}(D) \equiv \mathrm{e}^{-\mathrm{E}(D)}$ which gives $S_{\mathrm{F}}(D) = \mathrm{e}^{-\alpha D - \beta D^2}$. This is recognized as the LQ model, $S_{\mathrm{F}}^{(\mathrm{LQ})}(D) \equiv \mathrm{e}^{-\alpha D_{\mathrm{B}}} = \mathrm{e}^{-\alpha D - \beta D^2}$. In a semilogarithmic plot, the curve for $S_{\mathrm{F}}^{(\mathrm{LQ})}(D)$ is mainly exponential $S_{\mathrm{F}}^{(\mathrm{LQ})}(D) \sim \mathrm{e}^{-\alpha D}$ and Gaussian $S_{\mathrm{F}}^{(\mathrm{LQ})}(D) \sim \mathrm{e}^{-\beta D^2}$ at small and large values of D, respectively. A stronger repair, with significant μ, is seen in this plot as a more pronounced shoulder due to the Gaussian with its quadratic term, βD^2, which yields a curvier function $S_{\mathrm{F}}^{(\mathrm{LQ})}(D)$. For small μ, the cell kill prevails and $S_{\mathrm{F}}^{(\mathrm{LQ})}(D)$ is less curvy because of the dominance of the exponential function. As such, the ratio $\beta/\alpha = \mu$ appears as a measure of the curvature of $S_{\mathrm{F}}^{(\mathrm{LQ})}(D)$ and this influences the cell response to radiation. The smaller β/α implies that the dose–response relationship will be less sensitive to fractionation when fractionated radiotherapy is applied. Conversely, the larger β/α means that sublethal damage was accumulated to a sufficient level to produce lesions and sublesions in DNA, which is considered as the principal target molecule in assessments of the radiation-damaged tissue. In such a case, the enzyme molecules are triggered more actively, so that repair of lesions and sublesions can become an important factor in determining the overall biological response to radiation. The number of lesions could be assumed to be proportional to D. Therefore, the effect $\mathrm{E}(D) = (\alpha D)(1+\mu D)$, interpreted as the yield of elementary lesions, is proportional to the product of the average number of primary sublesions ($\sim D$) and the average deposited energy around the sublesions ($\sim \{1+\mu D\}$), which is equivalent

to $\sim (\xi + D)$. Here ξ, as the reciprocal of μ, is the average specific energy defined as the energy per unit mass per unit volume deposited per event per cell nucleus. The present biological dose D_B coincides with the so-called biologically effective dose (BED), which is especially important for fractionated radiotherapy. This is a convenient quantity because it depends only on the ratio of α and β, through $\mu = \beta/\alpha$, but not on the individual values of these two parameters. Based upon the LQ model, the ratios α/β are estimated to be about 3 and 10 Gy for healthy and tumorous tissues, respectively. It should be emphasized, however, that the numerical values for α/β can be meaningful only if they are provided by an adequate radiobiological model. In exhaustive comparisons with many measured cell-surviving fractions after exposure to a number of radiation modalities, the LQ model was fairly good, primarily at lower and intermediate doses around the shoulder, but failed at high doses that are encountered especially in stereotactic radiosurgery (hypofractionated radiotherapy). At larger values of D, experimental data for $S_F(D)$ exhibit an exponential fall-off, $S_F(D) \sim e^{-D/D_0}$, where D_0 is the dose at which the surviving fraction is reduced by $1/e \approx 1/2.7183 \approx 0.3678$ or by 36.78%. In other words, the final slope of most measured curves for cell-surviving fractions is given by $1/D_0$. This is opposed to the high-dose dominance of the Gaussian in the LQ model $S_F^{(LQ)}(D) \sim e^{-\beta D^2}$, which continues to bend with no final slope. In the LQ model, the initial slope, determined by the low-dose asymptote $S_F^{(LQ)}(D) \sim e^{-\alpha D}$, is given by α which is here associated with single radiation events (single hits) in a sensitive part of the cell. Even in the low-dose limit, the LQ model was often seen to deviate from experimental data which gives different numerical values for α than those from $S_F^{(LQ)}(D)$. According to the above derivation, α is also present in β. Hence, the said drawbacks of the LQ model at both low- and high-dose asymptotic regions could partially be attributed to the assumption that radiosensitivity parameter α is uniformly the same (constant) at all doses. It is more plausible to conceive radiosensitivity as being non-uniform such that α is gradually damped as the dose is progressively augmented. To this end, we shall modify the LQ model by introducing a biologically modulated radiosensitivity parameter α_B defined implicitly by $\alpha_B e^{\lambda \alpha_B D} = \alpha$. Here, α is the constant, dose-independent radiosensitivity in Gy^{-1} from the LQ model and $\lambda \geq 0$ is a dimensionless exponential screening factor. Rather than using the Lambert or Euler tree function in the case of the exact solution for α_B of the transcendental equation, $\alpha_B e^{\lambda \alpha_B D} = \alpha$, we shall again devise a simplified and more manageable description. With this goal, we replace the exponential $e^{\lambda \alpha_B D}$ by its first-order diagonal Padé approximant [1/1] in variable D as $e^{-\lambda \alpha_B D} \approx (1 - \lambda \alpha_B D/2)/(1 + \lambda \alpha_B D/2)$. This transforms the transcendental equation into a simple quadratic equation for the unknown α_B via $(\lambda/2)\alpha_B^2 + (1 + \lambda \alpha D/2)\alpha_B - \alpha = 0$ with only one physical root ($\alpha_B \geq 0$) given by $\alpha_B = (Q/\lambda)(-1 + \sqrt{1 + 2\lambda\alpha/Q^2})$ where $Q = 1 + \gamma D$ and $\gamma \equiv \lambda \alpha/2$. Expanding

$(1+2\lambda\alpha/Q^2)^{1/2}$ in a series with powers of $2\lambda\alpha/Q^2$ via $(1+2\lambda\alpha/Q^2)^{1/2} = 1+\lambda\alpha/Q^2+\cdots$, and retaining only the first two terms, $(1+2\lambda\alpha/Q^2)^{1/2} \approx 1+\lambda\alpha/Q^2$, yields the final result $\alpha_{\mathrm{B}} \approx \alpha/Q = \alpha/(1+\gamma D)$. When γ is written explicitly, it is seen that the approximate biological radiosensitivity α_{B} is the first-order diagonal Padé approximant [1/1] in α for a fixed dose, $\alpha_{\mathrm{B}} = \alpha/(1+\lambda D\alpha/2)$. On the other hand, for a fixed α, it follows that α_{B} is the first-order paradiagonal Padé approximant [0/1] in variable D via $\alpha_{\mathrm{B}} = \alpha/(1+\gamma D)$. As such, the biologically modulated radiosensitivity α_{B} is damped via a hyperbola at large doses $\alpha_{\mathrm{B}} \sim \alpha/(\gamma D) \equiv \alpha_{\mathrm{B}_\infty}$, but attains its constant value α through $\alpha_{\mathrm{B}} \sim \alpha \equiv \alpha_{\mathrm{B}_0}$ for small D. The result $\alpha_{\mathrm{B}} = \alpha/(1+\lambda D\alpha/2)$ can also be obtained directly by means of the well-known two-point Padé approximant built from the two asymptotes α_{B_0} and $\alpha_{\mathrm{B}_\infty}$ at $D=0$ and $D=\infty$, respectively. The same result is obtained by taking the halved harmonic average of α_{B_0} and $\alpha_{\mathrm{B}_\infty}$ via $1/\alpha_{\mathrm{B}} = 1/\alpha_{\mathrm{B}_0} + 1/\alpha_{\mathrm{B}_\infty}$, which gives $\alpha_{\mathrm{B}} = \alpha_{\mathrm{B}_0}\alpha_{\mathrm{B}_\infty}/(\alpha_{\mathrm{B}_0}+\alpha_{\mathrm{B}_\infty}) = \alpha/(1+\gamma D)$. Replacing the uniform α by the non-uniform biological radiosensitivity α_{B} yields the Padé-based effect, $\mathrm{E_P} = \alpha_{\mathrm{B}}(D+\mu D)$ or $\mathrm{E_P} = (\alpha D+\beta D^2)/(1+\gamma D)$, which is the para-diagonal Padé approximant [2/1] in variable D. This can be rewritten as $\mathrm{E_P} = v(1+\mu D)$ where $v = \alpha D/(1+\gamma D)$ is the Michaelis–Menten dose-dependent dimensionless velocity/rate for a non-reversible reaction with formation and destruction of the enzyme-substrate complexes, $[\widetilde{\mathrm{E}}]+[\widetilde{\mathrm{S}}] \longrightarrow [\widetilde{\mathrm{E}}\widetilde{\mathrm{S}}] \longrightarrow [\widetilde{\mathrm{R}}]+[\widetilde{\mathrm{E}}]$. Here $[\widetilde{\mathrm{E}}], [\widetilde{\mathrm{S}}], [\widetilde{\mathrm{E}}\widetilde{\mathrm{S}}]$, and $[\widetilde{\mathrm{R}}]$ are the concentrations of the free enzyme molecules, substrate (lesions/sublesions as DNA molecules), enzyme-substrate (or enzyme-lesion) complex, and product (repaired lesion/sublesion), respectively. In this chemical reaction, the free enzyme molecule $\widetilde{\mathrm{E}}$ binds the radiation-damaged DNA molecule (a lesion or sublesion) into an intermediate and temporarily living complex molecule $\widetilde{\mathrm{E}}\widetilde{\mathrm{S}}$. This compound facilitates the enzymatic synthesis of DNA by rejoining single- and double-strand breaks. After completion of this intermediate stage of the reaction, the complex $\widetilde{\mathrm{E}}\widetilde{\mathrm{S}}$ decays, thus producing the repaired lesions $\widetilde{\mathrm{R}}$ and enzymes $\widetilde{\mathrm{E}}$ that are again free for further bindings. As mentioned earlier, the number of lesions is assumed to be proportional to the dose, $[\widetilde{\mathrm{S}}] \sim D = \zeta D$, where ζ is a constant. The respective rate coefficients k_1 and k_2 for formation and destruction of the intermediate complex molecule $\widetilde{\mathrm{E}}\widetilde{\mathrm{S}}$ are embedded in the constant γ as $K_{\mathrm{M}} \equiv \zeta/\gamma$, where K_{M} is the Michaelis constant, $K_{\mathrm{M}} = k_2/k_1$. This enables re-writing v via the authentic Michaelis–Menten expression, $v = v_{\max}[\widetilde{S}]/(K_{\mathrm{M}}+[\widetilde{S}])$, with $[\widetilde{S}] = \zeta D$ where $v_{\max} = k_2[\widetilde{\mathrm{E}}]_0$ is the maximal velocity and $[\widetilde{\mathrm{E}}]_0$ is the initial concentration (the number of enzymes at the onset of the reaction). In our case, $v_{\max} \equiv \alpha/\gamma = 2/\lambda$ which permits connecting, for example, λ with the enzyme kinetic parameters as $\lambda = 2/(k_2[\widetilde{\mathrm{E}}]_0)$. At high doses, the enzyme-lesion reaction velocity v is approximately reduced to the constant value $v_{\max}$, which is the fastest rate possible for the given enzyme concentration $[\widetilde{\mathrm{E}}]_0$. This means that the rectangular curve for $v = \alpha D/(1+\gamma D)$ as a function of D has reached a plateau at larger doses. Stated equivalently, the curve for

$v = v_{\max}[\widetilde{S}]/(K_M + [\widetilde{S}])$, as a function of $[\widetilde{S}]$ is leveled off for higher lesion concentrations, $[\widetilde{S}]$. Such a high-dose or high-lesion concentrations described by the function v in terms of the independent variable D or $[\widetilde{S}]$ is due to the limited amount of the enzymes (∼100 enzymes per lesion) that are available for repair of radiation-damaged cells. At high doses, the average number of lesions is sufficiently large to overwhelm and thus inactivate the enzyme repair system, after which point every radiation damage is essentially lethal. This saturation of the enzyme repair system is the signature for the switch from the cell repair to the cell kill mechanism. Of direct relevance for cell-surviving fractions after irradiation, we emphasize that the Padé-based effect E_P is a linear function of D in the low and high-dose limits, $E_P \sim \alpha D$ and $E_P \sim (\beta/\gamma)D$ with the initial and final slopes α and β/γ, respectively. The ensuing Padé-designed surviving fraction based upon $E_P(D) = \alpha_B(D)D_B$ can now be introduced through the definition:

$$S_F^{(PLQ)}(D) \equiv e^{-E_P(D)} = e^{-\alpha_B(D)D_B} = e^{-\frac{\alpha D + \beta D^2}{1+\gamma D}}. \tag{25}$$

This completes the derivation of the PLQ model which has briefly been analyzed in our previous studies [58, 59]. The discussed behavior of the Padé-designed, biologically optimized effect $E_P(D)$ yields the sought requirements for the two asymptotes $S_F^{(PLQ)}(D) \sim e^{-\alpha D}$ and $S_F^{(PLQ)}(D) \sim e^{-\beta D/\gamma}$ at small and large values of D, respectively. At large doses, by setting $\gamma \equiv \beta D_0$, we can alternatively write $S_F^{(PLQ)}(D) \sim e^{-D/D_0}$. Thus, when γ is constrained to the relation $\gamma = \beta D_0$, the high-dose limit of the PLQ model becomes $S_F^{(PLQ)}(D) \sim e^{-D/D_0}$, as required by experimental data. Moreover, $\gamma = \beta D_0$ yields $\lambda = 2\beta D_0/\alpha = 2\mu D_0$. Irrespective of whether or not γ is preassigned to be of the form $\gamma = \beta D_0$, which is optional rather than mandatory, all the three parameters α, β, and γ are mutually dependent. Specifically, they are intercorrelated by the general relations $\beta = \mu\alpha$ and $\gamma = \lambda\alpha$. As such, the unconstrained version of the PLQ model is negligibly more involved than the LQ model from the computational viewpoint due to the presence of one additional parameter, γ. However, the constrained variant of the PLQ model, with γ fixed by the prescription $\gamma = \beta D_0$, has only two parameters α and β, since D_0 can be considered as the input data to be read from the final slope of the experimentally measured cell-surviving fraction at larger values of D. In either case, the advantage of the PLQ over the LQ model is twofold: (1) a richer mechanistic description rooted in the Michaelis–Menten enzymatic repair kinetics and (2) a smooth switch from the incorrect quadratic (Gaussian) to the correct (exponential) asymptote at high doses, as required by measurements. A distinctly clear outperformance of the PLQ over the LQ model is evident from Figure 6.31, which compares theoretical and experimental cell-surviving fractions after X-ray irradiation [60]. The present study

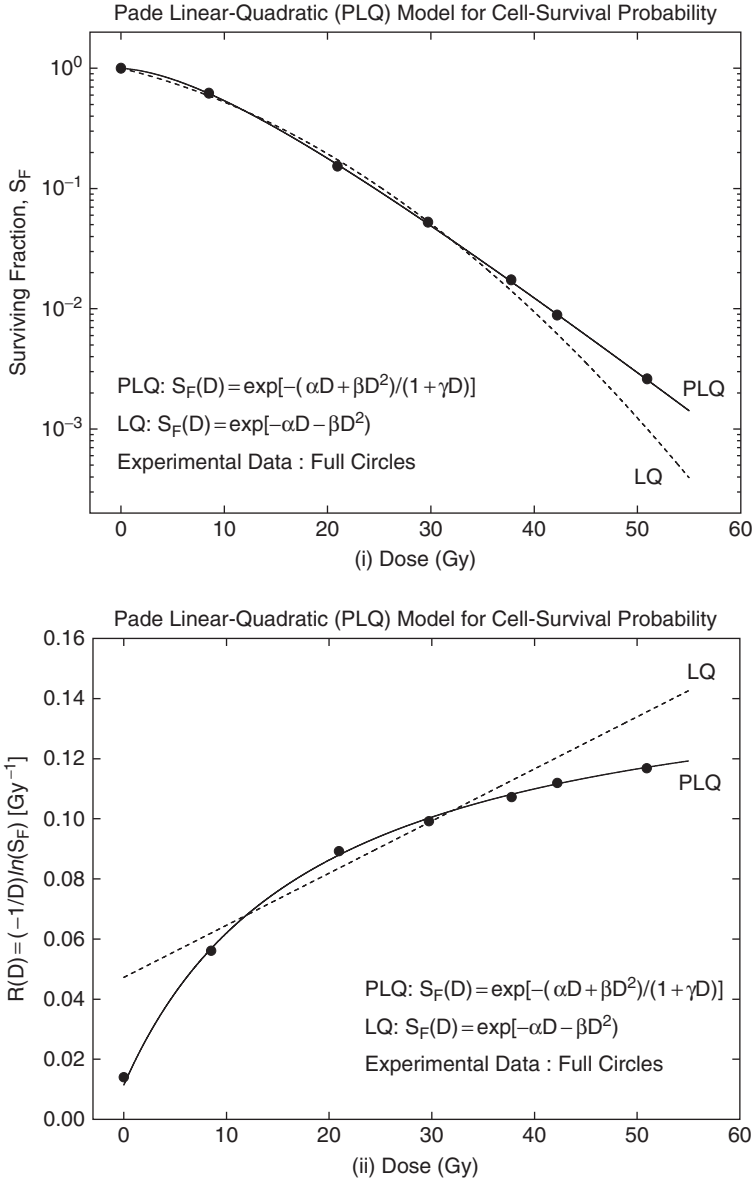

Figure 6.31 Cell-surviving fractions $S_F(D)$ as a function of radiation dose D in Gy (top panel (i)). Bottom panel (ii), as the Fe-plot (Full effect), shows the so-called reactivity $R(D)$ given by product of the reciprocal dose D^{-1} and the negative natural logarithm of $S_F(D)$, as the ordinate versus D as the abscissa. Any departure of experimental data from a straight line indicates inadequacy of the LQ model for the Fe-plot. Experiment (symbols) [60]: the mean clonogenic surviving fractions $S_F(D)$ (panel (i)) and $R(D) \equiv -(1/D)\ln(S_F)$ (panel (ii)) for the asynchronous V79 Chinese hamster cells irradiated hypoxically by 250 kVp X-ray with a concurrent 30 min exposure to the sulfhydryl-binding agent, *N*-ethylmaleimide, of low-concentration 0.75 μM. Theories (present computations): solid curve – PLQ (Padé linear-quadratic) model and dotted curve – LQ model (the straight-line $\alpha + \beta D$ on the bottom panel).

is further expanded in Ref. [61] with a particular focus on several subjects in radiobiological modelings of cell-surviving fractions: (1) a detailed theoretical analysis of the enzymatic lesion repair reactions, (2) simultaneous inclusion of the two active variables (dose D and time t), and (3) an extension to higher order mechanisms for enzyme–lesion interactions modeled by higher order diagonal Padé approximants as the unique ratios of two polynomials of any fixed degree in terms of D or $[\widetilde{S}]$.

8. OVERVIEW

We have shown in this chapter that the FPT can resolve and exactly quantify all the genuine resonances as encountered in MRS data for benign and malignant ovarian, breast, and prostate samples. This quantification is performed with a remarkably small number of signal points, thereby holding promise for substantial improvements in resolution for in vivo MRS. In vivo MRS could certainly benefit from the resolution capabilities of the fast Padé transform.

As discussed, noninvasive ovarian cancer detection via MRS has been particularly hindered by problems of resolution and poor SNR. Insofar as the current obstacles hindering acquisition of high-quality FIDs and the reliance upon the FFT could be overcome, in vivo MRS has the potential to become the method of choice for ovarian cancer screening. The results presented in this chapter suggest that Padé-optimized MRS could contribute toward this goal. An important step in this process would be comparisons between in vitro and in vivo MRS findings together with histopathological results. Further pursuit of this is of high priority, since early ovarian cancer detection is a goal that is still elusive and achievement of which would confer a major survival benefit. This approach would provide the needed validation. Within the clinical setting, the metabolite concentration maps could be quite helpful as a hands-on tool. This would promote a fuller grasp of Padé-based signal processing, as well as facilitate interpretation of diagnostically important information.

Padé-optimized MRS could also benefit breast cancer diagnostics. Again, validation studies will be needed among the in vitro and in vivo MRS and histopathology. We predict that with Padé optimization, the specificity of MR-based modalities could be substantially improved. Insofar as this prediction is confirmed in practice, new avenues could open up for breast cancer screening and early detection, particularly since MR does not expose the patient to ionizing radiation. This would be an important advantage for women at risk, since the screening could begin at an early age and the surveillance frequency could be safely increased.

We have seen that the FPT resolves and quantifies the many overlapping resonances, including multiplets of metabolites in the exceedingly

difficult spectra from malignant prostate and two very different types of normal prostate tissue. Remarkably, short time signals were needed. Work is underway with encoded data from normal, hypertrophic, and cancerous tissue, in vitro, as well as in vivo.

9. PERSPECTIVES

Early cancer detection is critical for improving prognosis, often with improved quality of life since the chances for cure are greater with less radical treatment. This is the basis for screening programs aimed at early detection of highly prevalent malignancies, most notably breast cancer. These programs have demonstrated survival benefits. Ovarian cancer remains as an important cause of death among women precisely due to the lack of early detection.

Particularly for screening and whenever increased surveillance frequency is needed, MR-based modalities are advantageous since there is no exposure to ionizing radiation. Notably, MRI is very sensitive but has poor specificity. The key complementary information provided by MRS is metabolic information. Thus far, MRS and MRSI have made great strides in cancer diagnostics by relying on just a handful of metabolites. Yet, these methods still are not in widespread use. As a field of clinical research and diagnostic modality, MRS is considered to be on the verge of a "veritable renaissance." Beginning as nuclear magnetic resonance, NMR, in physics and analytical chemistry, MRS has come to the point in medicine that it is currently being viewed by experts as the diagnostic modality which could revolutionize cancer diagnostics. Increasingly, there is a search for metabolic markers of cancer. This search needs to be linked to optimization of MRS and MRSI.

What has primarily hampered MRS and MRSI from realizing their potential in cancer diagnostics is the dependence on total shape spectra without reliable quantification. There is a vital need to reconstruct component spectra and the spectral parameters from which metabolite concentrations are computed. The critical role here is played by mathematics by which the measured time signals are transformed into spectra. Spectroscopic methods are the key strategy for investigating the structure and content of matter. Physics and chemistry developed their full potential by means of these methods. Medical diagnostics need to take full advantage of such developments.

Clinical MR scanners used for MRI all rely on the FFT. By inertia, this has continued for MRS, despite the fact that with the FFT the rich information content of a given tissue cannot be unfolded. The more appropriate spectroscopic methods based on quantum physics should have been transferred to MRS. Fitting has been used in attempts to deal with the lack of quantification of the FFT. However, as we have seen, this is an inadequate approach and in fact is just a form of guesswork. Fundamentally, it is not a question

of which fitting algorithm should be used, but rather to understand that fitting is an inappropriate strategy. Underestimation via underfitting (missing true metabolites) and overestimation through overfitting ("prediction" of false, nonexistent metabolites) are completely anathema in the clinical setting. Fitting can provide no certainty about the true, physical components underlying a given envelope. This will always be subjective in all fitting techniques that are overwhelmingly in use in MRS and MRSI.

We should then ask: What is the alternative to the conventional Fourier processing and fitting approach? First, it is necessary to properly define the task of quantification in MRS. This entails the determination of metabolite concentrations that are the norms and then the identification of various patterns of deviation from normal as indicative of cancer versus other, nonmalignant disease processes. Here is the role for clinical interpretation. Realization of this task will be greatly facilitated by a broader view. Namely, to provide cross-fertilization about how spectral analysis, which is quantification, has been successfully achieved in other branches of science. Mathematics is the key, with rational response functions being the leading tool. The Padé approximant is especially well suited since it uniquely solves the quantification problem. In this chapter, we have provided clinically-relevant examples of the performance of the FPT. We have handled fully controlled problems with synthesized FIDs that were based on actually measured data.

Within MRS, obtaining the needed spectral parameters is a key task. These include the complex frequencies and amplitudes, from which metabolite concentrations are computed. There is also a critical unknown parameter: the number of genuine resonances in a given spectrum. Without this latter information, underfitting or overfitting will inevitably occur such that peaks will be missed and/or falsely detected. Both of these failures are totally unacceptable for early cancer diagnostics. In fact, for this reason, clinicians have been highly skeptical of fitting-type data analyses in MRS and MRSI. In sharp contrast, by employing the powerful concept of Froissart doublets, it is demonstrated that exact signal–noise separation can be indeed accomplished within the FPT such that all false resonances are clearly identified and completely separated from the true information content.

In the applications of the FPT presented in this chapter, with direct relevance to early cancer diagnostics, we used noise-free theoretically generated FIDs to set up the standard with a high level of control to solve the quantification problem. We are currently extending our analysis to both noise-corrupted synthesized data (still well controlled) and to encoded time signals. We envisage the subsequent steps as application of the FPT in combined studies of malignant versus benign lesions, in which in vitro and in vivo FIDs encoded by MRS and MRSI are directly and comparatively analyzed, together with histopathology for cross-validation. This type of image-histopathology correlation is deemed especially promising for improving the accuracy of MRS in the realm of cancer diagnostics.

It will be essential to perform Padé optimization for FIDs encoded by in vivo MRS in conjunction with various cancers and noncancerous tissue that have presented differential diagnostic dilemmas, especially benign tumors, infectious or inflammatory lesions. The quantitative biochemical information provided by Padé processing should help in the development of normative databases to aid in cancer diagnostics by identifying cancerous versus benign disease with specific patterns of departures from normal metabolite concentrations.

We conclude with the anticipation that Padé-based optimization of MRS, as illustrated in this chapter, will help realize the full potential of MRS and MRSI in early cancer diagnostics.

ACKNOWLEDGMENTS

This work was supported by the Swedish Cancer Society Research Fund (Cancerfonden), the King Gustav the 5th Jubilee Foundation, Karolinska Institute Research Fund, the Signe and Olof Wallenius Stiftelse and by the Center for Gender Medicine, Karolinska Institute, Stockholm, Sweden.

REFERENCES

[1] Dž. Belkić, Quantum Mechanical Signal Processing and Spectral Analysis, Institute of Physics Publishing, Bristol, 2005.
[2] Dž. Belkić, Exact quantification of time signals in Padé-based magnetic resonance spectroscopy, Phys. Med. Biol. 51 (2006) 2633.
[3] Dž. Belkić, Exact signal-noise separation by Froissart doublets in the fast Padé transform for magnetic resonance spectroscopy, Adv. Quantum Chem. 56 (2009) 95.
[4] Dž. Belkić, K. Belkić, The general concept of signal-noise separation (SNS): Mathematical aspects and implementation in magnetic resonance spectroscopy, J. Math. Chem. 45 (2009) 563.
[5] Dž. Belkić, K. Belkić, Signal Processing in Magnetic Resonance Spectroscopy with Biomedical Applications, Taylor & Francis Group, London, 2010.
[6] Dž. Belkić, Strikingly stable convergence of the fast Padé transform (FPT) for high resolution parametric and nonparametric signal processing of Lorentzian and non-Lorentzian spectra, Nucl. Instr. Meth. Phys. Res. A 525 (2004) 366.
[7] K. Belkić, Resolution performance of the fast Padé transform: Potential advantages for magnetic resonance spectroscopy in ovarian cancer diagnostics, Nucl. Instr. Meth. Phys. Res. A 580 (2007) 874.
[8] Dž. Belkić, K. Belkić, Mathematical modeling applied to an NMR problem in ovarian cancer detection, J. Math. Chem. 43 (2008) 395.
[9] K. Belkić, Magnetic resonance spectroscopic imaging in breast cancer detection: Possibilities beyond the conventional theoretical framework for data analysis, Nucl. Instr. Meth. Phys. Res. A 525 (2004) 313.
[10] Dž. Belkić, K. Belkić, Exact quantification of time signals from magnetic resonance spectroscopy by the fast Padé transform with applications to breast cancer diagnostics, J. Math. Chem. 45 (2009) 790.

[11] Dž. Belkić, Exact analytical expressions for any Lorentzian spectrum in the fast Padé transform (FPT), J. Comp. Meth. Sci. Eng. 3 (2003) 109.
[12] Dž. Belkić, K. Belkić, The fast Padé transform in magnetic resonance spectroscopy for potential improvements in early cancer diagnostics, Phys. Med. Biol. 50 (2005) 4385.
[13] Dž. Belkić, Machine accurate quantification in magnetic resonance spectroscopy, Nucl. Instr. Meth. Phys. Res. A 580 (2007) 1034.
[14] Dž. Belkić, K. Belkić, Unequivocal resolution of multiplets in MR Spectra for prostate cancer diagnostics achieved by the fast Padé transform, J. Math. Chem. 45 (2009) 819.
[15] Dž. Belkić, K. Belkić, Mathematical optimization of *in vivo* NMR chemistry through the fast Padé transform: Potential relevance for early breast cancer detection by magnetic resonance spectroscopy, J. Math. Chem. 40 (2006) 85.
[16] M. Froissart, Approximation de Padé: Application à la physique des particules élémentaires, in: J. Carmona, M. Froissart, D.W. Robinson, D. Ruelle (Eds.), Recherche Coopérative sur Programme (RCP), Centre National de la Recherche Scientifique (CNRS), Strasbourg, L 8470, No. 25, 1969, p. 1.
[17] S. Pecorelli, G. Favalli, L. Zigliani, F. Odicino, Cancer in women, Int. J. Gynecol. Obstet. 82 (2003) 369.
[18] E.R. Woodward, H.V. Sleightholme, A.M. Considine, S. Williamson, J.M. McHugo, D.G. Cruger, Annual surveillance by CA125 and transvaginal ultrasound for ovarian cancer in both high-risk and population risk women is ineffective, Br. J. Obstet. Gynecol. 114 (2007) 1500.
[19] E.P. Diamandis, Cancer biomarkers: Can we turn recent failures into success? J. Natl. Cancer Inst. 102 (2010) 1462.
[20] S.S. Buys, E. Partridge, M.H. Greene, P.C. Prorok, D. Reding, T.L. Riley, et al., the PLCO Project Team; Ovarian cancer screening in the Prostate, Lung, Colorectal and Ovarian (PLCO) cancer screening trial: Findings from the initial screen of a randomized trial, Am. J. Obstet. Gynecol. 193 (2005) 1630.
[21] U.S. Preventive Services Task Force, Screening for ovarian cancer: Recommendation statement, Ann. Fam. Med. 2 (2004) 260.
[22] K. Kinkel, Y. Lu, A. Mehdizade, M.-F. Pelte, H. Hričak, Indeterminate ovarian mass at US: Incremental value of second imaging test for characterization: Meta-analysis and Bayesian analysis, Radiol. 236 (2005) 85.
[23] E.A. Boss, S.H. Moolenaar, L.F.A.G. Massuger, H. Boonstra, U.F. Engelke, J.G. de Jong, et al., High-resolution proton nuclear magnetic resonance spectroscopy of ovarian cyst fluid, NMR Biomed. 13 (2000) 297.
[24] I.C. Smith, D.E. Blandford, Diagnosis of cancer in humans by 1H NMR of tissue biopsies, Biochem. Cell. Biol. 76 (1998) 472.
[25] L.F.A.G. Massuger, P.B.J. van Vierzen, U.F. Engelke, A. Heerschap, R.A. Wevers, 1H-magnetic resonance spectroscopy: A new technique to discriminate benign from malignant ovarian tumors, Cancer 82 (1998) 1726.
[26] D. Saslow, C. Boetes, W. Burke, S. Harms, M.O. Leach, C.D. Lehman, et al., American Cancer Society Breast Cancer Advisory Group; American Cancer Society guidelines for breast screening with MRI as an adjunct to mammography, CA Cancer J. Clin. 57 (2007) 75–89.
[27] S. Lipnick, X. Liu, J. Sayre, L.W. Bassett, N. DeBruhl, M.A. Thomas, Combined DCE-MRI and single-voxel 2D MRS for differentiation between benign and malignant breast lesions, NMR Biomed. 23 (2010) 922.
[28] K. Belkić, M. Cohen, M. Márquez, M. Mints, B. Wilczek, A.H. Berman, et al., Screening of high-risk groups for breast and ovarian cancer in Europe: A focus on the Jewish population, Oncol. Rev. 4 (2010) 233.
[29] R. Katz-Brull, P.T. Lavin, R.E. Lenkinski, Clinical utility of proton magnetic resonance spectroscopy in characterizing breast lesions, J. Natl. Cancer Inst. 94 (2002) 1197.

[30] G.M. Tse, D.K. Yeung, A.D. King, H.S. Cheung, W.T. Yang, in vivo proton magnetic resonance spectroscopy of breast lesions: an update, Breast Cancer Res. Treat. 104 (2007) 249.
[31] I.S. Gribbestad, B. Sitter, S. Lundgren, J. Krane, D. Axelson, Metabolite composition in breast tumors examined by proton nuclear magnetic resonance spectroscopy, Anticancer Res. 19 (1999) 1737.
[32] J.W. van der Veen, R. de Beer, P.R. Luyten, D. van Ormondt, Accurate quantification of *in vivo* 31P NMR signals using the variable projection method and prior knowledge, Magn. Reson. Med. 6 (1988) 92.
[33] L. Vanhamme, A. van den Boogaart, S. van Haffel, Improved method for accurate and efficient quantification of MRS data with use of prior knowledge, J. Magn. Reson. 29 (1997) 35.
[34] S.W. Provencher, Estimation of metabolite concentrations from localized *in vivo* proton NMR spectra, Magn. Reson. Med. 30 (1993) 672.
[35] E.O. Aboagye, Z.M. Bhujwalla, Malignant transformation alters membrane choline phospholipid metabolism of human mammary epithelial cells, Cancer Res. 59 (1999) 80.
[36] R. Katz-Brull, D. Seger, D. Rivenson-Segal, E. Rushkin, H. Degani, Metabolic markers of breast cancer, Cancer Res. 62 (2002) 1966.
[37] K. Glunde, C. Jie, Z.M. Bhujwalla, Molecular causes of the aberrant choline phospholipid metabolism in breast cancer, Cancer Res. 64 (2004) 4270.
[38] U. Sharma, A. Mehta, V. Seenu, N.R. Jagannathan, Biochemical characterization of metastatic lymph nodes of breast cancer patients by *in vitro* 1H magnetic resonance spectroscopy: A pilot study, Magn. Reson. Imaging 22 (2004) 697.
[39] D. Rivenzon-Segal, R. Margalit, H. Degani, Glycolysis as a metabolic marker in orthotopic breast cancer, monitored by *in vivo* 13C MRS, Am. J. Physiol. Endocrinol. Metab. 283 (2002) E623.
[40] A. Horwich, C. Parker, V. Kataja, ESMO Guidelines Working Group; Prostate cancer: ESMO clinical recommendations for diagnosis, treatment and follow-up, Ann. Oncol. 19 (Suppl 2) (2008) ii45.
[41] V. Kundra, P.M. Silverman, S.F. Matin, H. Choi, Imaging in oncology from the University of Texas M. D. Anderson Cancer Center: diagnosis, staging, and surveillance of prostate cancer, Am. J. Roentgenol. 189 (2007) 830.
[42] L.S. Lim, K. Sherin, ACPM Prevention Practice Committee, for prostate cancer in U.S. men: ACPM position statement on preventive practice, Am. J. Prev. Med. 34 (2008) 164.
[43] C. Bosetti, P. Bertuccio, F. Levi, F. Lucchini, E. Negri, C. La Vecchia, Mortality in the European Union, 1970 2003, with a joinpoint analysis, Ann. Oncol. 123 (2008) 421.
[44] C. Bouchardy, G. Fioretta, E. Rapiti, H.M. Verkooijen, C.H. Rapin, F. Schmidlin, et al., Recent rends in prostate cancer mortality show a continuous decrease in several countries, Int. J. Cancer 123 (2008) 421.
[45] I.M. Thompson, D.K. Pauler, P.J. Goodman, C.M. Tangen, M.S. Lucia, H.L. Parnes, et al., Prevalence of prostate cancer among men with a prostate-specific antigen level $\leq$ 4.0 ng per milliliter, N. Engl. J. Med. 350 (2004) 2239.
[46] U.S. Preventive Services Task Force Screening for Prostate Cancer, U.S. Preventive Services Task Force recommendation statement, Ann. Intern. Med. 149 (2008) 185.
[47] D.K. Ornstein, J. Kang, How to improve prostate biopsy detection of prostate cancer, Curr. Urology Rep. 2 (2001) 218.
[48] Y. Mazaheri, A. Shukla-Dave, H. Hričak, S.W. Fine, J. Zhang, G. Inurrigarro, et al., Identification with combined diffusion-weighted MR imaging and 3D 1H MR spectroscopic imaging: Correlation with pathologic findings, Radiol. 246 (2008) 480.
[49] K. Belkić, Molecular Imaging through Magnetic Resonance for Clinical Oncology, Cambridge International Science Publishing, Cambridge, 2004.

[50] S. Cirillo, M. Petracchini, P. Della Monica, T. Gallo, V. Tartaglia, E. Vestita, et al., Value of endorectal MRI and MRS in patients with elevated prostate-specific antigen levels and previous negative biopsies to localize peripheral zone tumors, Clin. Radiol. 63 (2008) 871.
[51] J. Weis, H. Ahlström, P. Hlavčak, M. Häggman, F. Ortiz-Nieto, A. Bergman, Two-dimensional spectroscopic imaging for pre-treatment evaluation of prostate cancer: Comparison with the step-section history after radical prostatectomy, Magn. Reson. Imaging 27 (2009) 87.
[52] J.M. Garcia-Segura, M. Sanchez-Chapad, C. Ibarburen, J. Viaño, J.C. Angulo, J. González, et al., *In vivo* proton magnetic resonance spectroscopy of diseased prostate: spectroscopic features of malignant versus benign pathology, Magn. Reson. Imaging 17 (1999) 755.
[53] A.C. Westphalen, D.A. McKenna, J. Kurhanewicz, F.V. Coakley, Role of magnetic resonance imaging and magnetic resonance spectroscopic imaging before and after radiotherapy for prostate cancer, J. Endourol. 22 (2008) 789.
[54] M.G. Swanson, A.S. Zektzer, Z.L. Tabatabai, J. Simko, S. Jarso, K.R. Keshari, et al., Quantitative analysis of prostate metabolites using 1H HR-MAS spectroscopy, Magn. Reson. Med. 55 (2006) 1257.
[55] J.K. Nicholson, I.D. Wilson, High resolution proton magnetic resonance spectroscopy of biological fluids, Prog. NMR Spectrosc. 21 (1989) 449.
[56] X. Wu, S.J. Dibiase, R. Gullapalli, C.X. Yu, Deformable image registration for the use of magnetic resonance spectroscopy in prostate treatment planning, Int. J. Radiat. Oncol. Biol. Phys. 58 (2004) 1577.
[57] C.K. Kim, B.K. Park, Update of prostate magnetic resonance imaging at 3T, J. Comput. Assist. Tomogr. 32 (2008) 163.
[58] Dž. Belkić, Parametric analysis of time signals and spectra from perspective of quantum physics and chemistry, Adv. Quantum Chem. 61 (2011) 145.
[59] Dž. Belkić, K. Belkić, Padé-Froissart exact signal-noise separation in nuclear magnetic resonance spectroscopy, J. Phys. B: At. Mol. Opt. Phys. 44 (2011) 125003.
[60] B.F. Kimler, W.K. Sinclair, M.M. Elkind, N-ethylmaleimide sensitization of X-irradiated hypoxic Chinese hamster cells, Rad. Res. 71 (1977) 204.
[61] Dž. Belkić, Cell surviving fractions after irradiation: novel radiobiological models with the Michaelis-Menten enzyme kinetics and the Lambert W function, J. Math. Chem. 49 (2011) 1618.

INDEX

Note: The letters '*f*' and '*t*' following locators denote figures and tables respectively.